Room Temperature Phosphorescence (RTP): Experimental And Theoretical Studies on Boron-Containing Materials

Dissertation zur Erlangung des naturwissenschaftlichen Doktorgrades

der Julius-Maximilians-Universität Würzburg

vorgelegt von

Zhu Wu

aus Suqian City, Jiangsu Province, P. R. China

Würzburg 2022

Eingereicht bei der Fakultät für Chemie und Pharmazie am

_____

Gutachter der schriftlichen Arbeit:

1. Gutachter: Prof. Dr. Dr. h.c. Todd B. Marder

2. Gutachter: Prof. Dr. Maik Finze

Prüfer des öffentlichen Promotionskolloquiums

1. Prüfer: Prof. Dr. Dr. h.c. Todd B. Marder

2. Prüfer: Prof. Dr. Maik Finze

3. Prüfer: Lecturer Dr. Florian Beuerle

Datum des öffentlichen Promotionskolloquiums

_____

Doktorurkunde ausgehändigt am

_____

For my future wife and family

Genius only means hard-working all one's life.

--Mendeleyev (Russian chemist)

Die Experimente zur vorliegenden Arbeit wurden in der Zeit von Oktober 2017 bis Februar 2022 am Institut für Anorganische Chemie der Julius-Maximilians-Universität Würzburg unter der Aufsicht von Prof. Dr. Dr. h.c. Todd B. Marder durchgeführt.

Acknowledgments

First of all, I thank **Prof. Dr. Dr. h.c. Todd B. Marder** for offering me the opportunity to be a member of the "**AK Marder**". I appreciate that you gave me a lot of freedom to do scientific research and numerous chances to get in touch with researchers from other universities and institutions. Thank you for the enormous number of dicussions and revising my papers many times. With your kind help, I made a trip to Durham University in the UK to take an intensive course on crystallography which improved my crystal structure solving skills greatly. In addition, I saw and talked with young researchers in this course from all over the world, which definitely opened my mind. Thank you also for bringing me to many kinds of conferences. I really enjoyed sharing my work at the conferences. Especially, thank you for sharing your valuable life experiences when travelling around the world. The four-years of doctoral life in Wuerzburg with you has no doubt been the most important period in my life and I will always be proud to be one of the "**Marder family**". Thanks.

I thank **Prof. Christel M. Marian** from the Universität Düsseldorf and her research group for doing the (TD-) DFT calculations on the triarylboranes at a very high level. I am grateful for the dicussions and revisons of our collaborative papers on RTP. I thank **Fabian Dinkelbach** for countless calculations for our joint papers.

I thank **Dr. Alexandra Friedrich** for helping me measure and solve a lot of crystal structures. With her help, the crystallographic parts of my papers were greatly improved. Especially, I would like to thank her for giving the very nice lectures on the theory of crystallography and telling me a lot about how to measure sensitive crystals.

I thank **Prof. Lei Ji** for teaching me how to use our spectrometer and high vacuum line. I am glad to have had a such good supervisor and friend. I really miss the times when we exchanged and thought up ideas about how to design novel organic molecular strutures. I still remember that you said that organic radicals could be used in OLEDs, which was published half a year later in Nature by Feng Li and coworkers.

I thank **Dr. Jörn Nitsch** and **Dr. Florian Rauch** for tremendous discussions about chemistry (spectroscopic measurements and photophysical theory) and life topics (German beer and society). I appreciate that you helped me to revise my papers so many times and to install the solid absorption device in the Carry 5E to measure the solid state absorption spectrum of boric acid. I am looking forward to your visit to China in the near future.

I thank **Dr. Julia Schuster**, **Dr. Katharina Edkins**, **Juan Carlos Roldao**, **Marcel Loebnitz**, **Dr. Johannes Gierschner**, **Dr. Vladimir Stepanenko** and **Prof. Dr. Frank Würthner**. I am grateful for your suggestions and proof-reading of our joint papers. Thank you, Vladimir, for SEM measurements and discussions.

I thank **Dr. Ivo Krummenacher** for the EPR and cyclic voltammetry measurements and helpful discussions. I thank Michael Moos for the spectroelectrochemical and cyclic voltammetry measurements.

I thank my intern student **Christoph Herok** for helping me to synthesize many aryl-Bpin compounds. I thank all intern students of the AK Marder.

I thank **Dr. Stephan Wagner** for maintance of the GC-MS and dealing with the safety issues in the lab, **Dr. Rüdiger Bertermann** for keeping the NMR machines running and for the specific solid state boron NMR spectra.

I thank **Dr. Xiaoning Guo** (for helpful discussions and proof-reading), **Dr. Jiefeng Hu** (for buying chemicals for me from China), **Dr. Xiaocui Liu** (for inviting me to having delicious dinners after work), **Dr. Yaming Tian** (for being a member of the lunch group), **Maria Eckhardt** (for sorting out travel expenses), **Eva Wittenberg** (for sorting out contracts), **Dr. Wenbo Ming** (for being a good friend and lab member, and for much help in chemistry and life), **Johannes Krebs** (for countless discussions oncrystallography, life, and chemistry), **Dr. Julia Merz** (for organising a lot of fun activities held in the group), **Sabine Lorenzen** (for being in charge of the whole group and freely talking about interesting topics in life and chemistry), **Dr. Stefanie Griesbeck** (for her kind guidance in the beginning of my doctoral studies in Germany), **Christoph Mahler** (for a number of HRMS measurements and patient and detailed explanations), **Dr. Matthias Ferger** (for help with some photophysical measurements and proofreading of the doctoral thesis), **Dr. Sarina Berger** (for organising the daily life of our group, especially in the pandemic period), **Dr. Florian Kerner** (for maintenance of glove-boxes and some crystal structure measurements), **Robert Ricker** (for countless help in life and chemistry), and **Dr. Jan Maier** (for taking pictures for our group).

I thank **Dr. Yudha Budiman** (for discussions about football and life in Germany), and **Dr. Goutam Kumar Kole** (for helping me solving crystal structures).

I thank the members of AK Steffen, **Dr. Markus Gernert** (for guidance and discussions on photophysics), **Dr. Benjamin Hupp** (for teaching me how to use a glove-box), and **Prof. Dr. Andreas Steffen** (for interesting discussions about football). I thank the members of AK

Radius, **Dr. Laura Kuehn** (for lending me chemicals), and **Steffen Föhrenbacher** (for teaching me how to use the infrared spectrometer).

I thank all other group members: **Dr. He Jiang**, **Dr. Xiangqing Jia**, **Dr. Hua Wang**, **Dr. Zhiqiang Liu**, **Dr. Jian Zhao**, **Mingming Huang**, **Dr. Xiaolei Zhang** and **Dr. Weipeng Li** for the numerous happy parties we had at home and travelling in Germany.

I thank the current group members, **Dr. Hamad Al Mamari** (for discussions about family), **Maria-Victoria Benicke Rojas** for buying chemicals, and **Julie Borel** (for discussions about France).

I thank all members in the chemistry institute for your kind help. Without your efforts, my work would not have been possible.

I thank my parents for their support and my sister for her sense of humour. Thank you for bringing me so much support and love.

I thank chinese scholarship council (CSC) for their generous final support.

List of Publications

The publications listed below are partly reproduced in this dissertation with permission from Wiley-VCH. The table itemizes at which position in this work the papers have been reproduced.

Publication	**Position**
[1] Z. Wu, J. Nitsch, T. B. Marder, *Adv. Opt. Mater.* **2021**, *9*, 2100411.	Chapter 1
[2] Z. Wu, J. Nitsch, J. Schuster, A. Friedrich, K. Edkins, M. Loebnitz, F. Dinkelbach, V. Stepanenko, F. Würthner, C. M. Marian, L. Ji, T. B. Marder, *Angew. Chem. Int. Ed.* **2020**, *59*, 17137-17144.	Chapter 2
[3] Z. Wu, F. Dinkelbach, F. Kerner, A. Friedrich, L. Ji, V. Stepanenko, F. Würthner, C. M. Marian, T. B. Marder, *submitted*	Chapter 3
[4] Z. Wu, J. C. Roldao, F. Rauch, A. Friedrich, M. Ferger, F. Würthner, J. Gierschner, T. B. Marder, *Angew. Chem. Int. Ed*. **2022**, https://doi.org/10.1002/anie.202200599.	Chapter 4

Further publications:

X. Jia, J. Nitsch, Z. Wu, A. Friedrich, J. Krebs, I. Krummenacher, F. Fantuzzi, H. Braunschweig, M. Moos, C. Lambert, B. Engels, T. B Marder, *Chem. Sci*. **2021**, *12*, 11864-11872.

Y. M. Tian, X. N. Guo, Z. Wu, A. Friedrich, S. Westcott, H. Braunschweig, U. Radius, T. B Marder, *J. Am. Chem. Soc*. **2020**, *142*, 13136-13144.

Y. M. Tian, X. N Guo, I. Krummenacher, Z. Wu, J. Nitsch, H. Braunschweig, U. Radius, T. B Marder, *J. Am . Chem. Soc*. **2020**, *142*, 18231-18242.

List of Abbreviations

Å	Ångström (1 Å = 10^{-10} m)
A	acceptor
Abs	absorption
AIE	aggregation-induced emission
APCI	atmospheric-pressure chemical ionization
ASAP	atmospheric solids analysis probe
BA	boric acid
Bd	1H-benzo[f]indole
CCDC	Cambridge crystallographic data center
CDs	carbon dots
CIE	Commission Internationale de l'Eclairage
CT	charge transfer
Cz	carbazole
D	donor
DAE	diarylethene
DBBP	4,4’-dibromobiphenyl
DCM	dichloromethane
DFT	density functional theory
DFT/MRCI	multireference configuration interaction
DMF	dimethyl formamide
DRTP	dual room temperature phosphorescence
ESIPT	excited state intramolecular proton transfer
FC	Franck-Condon
$\Phi_{\iota\sigma\chi}$	quantum yield of inter-system crossing
Φ_{π}	quantum yield of phosphorescence

HFC	hyperfine-coupling
HOMO	highest occupied molecular orbital
HPLC	high-pressure liquid chromatography
i	iso
IC	internal conversion
ICSD	inorganic crystal structure database
ICT	intramolecular charge transfer
ISC	inter-system crossing
k_f	fluorescence decay rate
k_{ic}	internal conversion
k_{isc}	inter-system crossing
k_{nr}	nonradiative decay rate
k_p	rate constant of phosphorescence
k_q	quenching rate
LE	locally excited
LUMO	lowest unoccupied molecular orbital
MS	mass spectrometry
ms	millisecond
NA	1,8-naphthalic anhydride
NB	bulky norbornyl
NIR	near infrared ray
NMR	nuclear magnetic resonance
NPs	nanoparticles
ns	nanosecond
NTO	natural transition orbital
OLEDs	organic light-emitting diodes

OSSL	organic solid-state laser
PET	photo-induced electron transfer
PHOLEDs	phosphorescence organic light-emitting diodes
PMMA	poly(methyl methacrylate)
PNA	N-phenylnaphthalen-2-amine
PT	phthalide
PVA	poly(vinyl alcohol)
pXRD	powder X-ray diffraction
r.t.	room temperature
RTP	room temperature phosphorescent
SEM	scanning electron microscope
SMWLE	single-molecule white light emission
SOC	spin–orbit coupling
SOCMEs	spin–orbit coupling matrix elements
t	tert
TADF	thermally activated delayed fluorescence
TCI	Tokyo Chemical Industry
TD-DFT	time-dependent density functional theory
THF	tetrahydrofuran
τ_π	lifetime of phosphorescence
TTA	triplet-triplet annihilation
UV	Ultraviolet
Vis	Visible

Table of Contents

CHAPTER ONE

–

INTRODUCTION

Persistent Room-Temperature Phosphorescence from Purely Organic Molecules and Multi–Component Systems

1.1 Introduction

Persistent room temperature phosphorescent (RTP) luminophores have gained remarkable interest recently for a number of applications in security printing,[1] OLEDs,[2] optical storage,[3] time-gated biological imaging[4] and oxygen sensors[5] due to their unique long emission lifetimes, excellent signal-to-noise ratio, large Stokes shifts and simple operation. At present, the majority of persistent RTP materials are heavy metal-containing complexes, in which charge transfer between metal and ligand mixes singlet and triplet excitons and strong SOC improves the rate of ISC, and enhances the rate of phosphorescence decay.[6] However, many metal-based phosphors are toxic, high in cost and difficult to process compared to organic RTP materials which are environmental friendly, inexpensive and convenient to prepare.[7] Thus, the demand to develop novel purely organic RTP materials has grown recently. Unlike transition metal-containing phosphors, organic materials with persistent luminescent phosphorescence emission are still limited because both the radiative pathway from T_1 to S_0 is spin forbidden and the ISC rate from excited singlet to triplet states is relatively slow.[8] The major challenge is to suppress nonradiative pathway from T_n, which is usually a fast process. Therefore, specific strategies are designed to enhance the quantum yield and lifetime of RTP by promoting the rate of ISC and, at the same time, restricting the nonradiative relaxation of the triplet states,[9] including incorporating heavy atoms,[10] introducing carbonyl groups bearing lone pairs,[11] polymerization methods,[12] constructing a supramolecular framework based on self-assembly properties,[13] utilizing host-guest systems[14] or carbon dots (CDs).[15] Although many approaches have been developed to populate triplet excitons by enhancing SOC, which can be achieved by taking full advantage of El-Sayed's rule,[16] organic phosphors are still limited to certain categories of compounds, such as phenazine,[17] phenothiazine,[18] naphthylamide,[19] and boronic acid[20] and boronic ester[21] derivatives. More recently, our group reported the first triarylborane compounds without lone pairs which exhibit persistent RTP.[22] Bechtold *et al*. also reported a phosphorescent arene in which the non-planar configuration leads to enhanced SOC and a high energy of the T_1 state with a quantum yield up to 5.6%.[23] All of these findings greatly expand the types of organic RTP materials. Moreover, they give useful guidance to understand the relationships between structure and property.[24]

It is important to note that for RTP, which has in many cases an intrinsic low photoluminescence quantum yield, special attention must be paid to how the measurements are performed and to

the purity of the sample under examination, since the smallest impurity can lead to a completely wrong or at least misleading conclusion.[25] Phosphors derived from carbazole and related functional groups should be re-examined carefully with respect to possible impurities, as pointed out recently by Liu *et al*.[26] At the same time, it should be noted that confirmed, pure carbazole-based molecules do exhibit persistent phosphorescence at room temperature.[27] Carbazole-based phosphors are indeed interesting and still promising, but require extremely careful study.[28-44] Most published reviews do not clearly indicate the significance of impurity effects, and may lead to misunderstandings about RTP research.[45] Indeed, we note that extra care needs to be taken to avoid the possibility that RTP phenomena result from trace impurities, as the problem may extend well beyond the carbazole systems. In our review, we present the results and explanations offered by the original authors. We hope that this encourages others to explore the field, and perhaps to re-examine some of the previously reported examples.

This review is structured as follows. In Section 2, the photophysical parameters (Φ_{isc}, Φ_p, τ_p) required for RTP are presented.[46] In Section 3, purely organic room temperature phosphors are classified according to their categories of functional groups which include amide derivatives, boron- and sulfur-containing compounds, quinoxaline derivatives, siloxy group-induced and carbazole-based phosphors. In the last part of Section 3, several nonclassical RTP materials are also introduced. Section 4 provides a summary of multi-component RTP systems, and popular, current strategies to construct multi-component RTP materials are presented, host-guest systems, and supramolecular systems. As it is hard to distinguish whether carbon dots (CDs) are purely organic or multicomponent systems in some cases, we introduce them in Section 5. In the last two sections, we give our future perspectives and conclusion.

1.2 Physical Parameters of RTP

As described in Figure 1-1, electrons of organic RTP molecules are excited from the S_0 state to S_1-S_n states. The excited singlet state can fluoresce and also undergo nonradiative decay to the ground state or relax to a triplet state through an intersystem crossing process when the SOC is strong enough and when the energy gap ΔE_{ST} between the states is sufficient small enough. According to Kasha's rule,[47] if the populated triplet excited state T_n is a higher lying state, it decays quickly to T_1 through internal conversion (IC). Triplet to singlet ground state transitions through radiative decay leads to phosphorescence which is often a slow process (ms) compared to the lifetime of fluorescence (ns), due to the forbidden nature of transitions from T_1 to S_0. This is also the reason that our naked eye can observe the afterglow of phosphorescence. The rate of

nonradiative decay is often higher than the radiative decay rate from T_1 to S_0 at room temperature. Besides oxygen and moisture quenchers, molecular motion (rotations and vibrations) play an important role in nonradiative decay processes. Therefore, phosphorescence from pure organic molecules is typically observed under an inert atmosphere and at low temperature. Approaches such as imbedding the emitter into a rigid matrix or crystallization are used to restrict molecular motions to restrict nonradiative decay for achieving long-lived room temperature phosphorescence according to Equation (1):[48]

$$\tau_p = 1 / (k_p + k_{nr} + k_q) \quad (1)$$

where τ_p is the intrinsic phosphorescence lifetime, k_p is the radiative decay rate and k_{nr} is the non-radiative decay rate from T_1 to S_0 states, and k_q is the quenching rate of the triplet excited state by quenching species. In addition, in organic systems, ISC is often not efficient, but can be accelerated by SOC utilizing heavy atoms (Br, I) or by n-π^* transitions by introducing elements bearing lone pairs (N, O, S). Based on El-Sayed's rule,[16] the ISC rate constant will be enhanced when the two electronic transition states involved belong to different orbital types ($^1n\pi^*$ - $^3\pi\pi^*$ or $^1\pi\pi^*$- $^3n\pi^*$), leading to an increased phosphorescence quantum yield according to Equations (2) and (3):[48]

$$\Phi_{isc} = k_{isc} / (k_f + k_{ic} + k_{isc}) \quad (2)$$

$$\Phi_p = \Phi_{isc} k_p / (k_p + k_{nr} + k_q) \quad (3)$$

where k_f is the fluorescence decay rate from S_1 to S_0 state, k_{ic} is the internal conversion rate from S_1 to S_0, k_{isc} is the ISC rate from S_1 to T_1, and Φ_{isc} is the ISC quantum yield from S_1 to T_1. In some cases, the triplet state in purely organic materials can be stabilized by intermolecular interactions even under ambient conditions, while triplet-triplet annihilation (TTA) is effectively suppressed, resulting in persistent RTP.[49]

1.3 Single Component RTP Systems

1.3.1 Amide Derivative-Based RTP Systems

To develop metal-free RTP materials, heteroatoms are commonly used elements as they provide lone pairs which speed up the ISC process. In addition, hydrogen bond interactions also suppress nonradiative decay. Amides and their derivatives are good candidates for the

construction of RTP materials. In 2018, Shi *et al.* reported **ImBr** (Figure 1-2a) with a dual emission, emitting white-light due to the mixture of blue fluorescence and yellow phosphorescence.[50] Persistent RTP from **ImBr** is likely induced by the bromine atom which

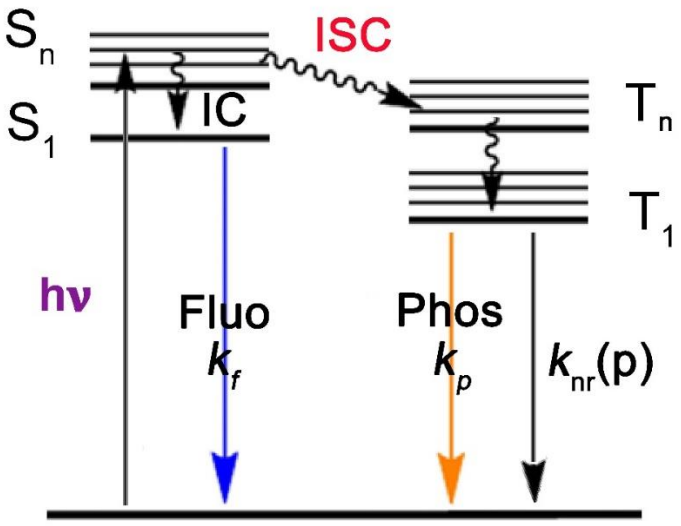

Figure 1-1. Jablonski diagram.

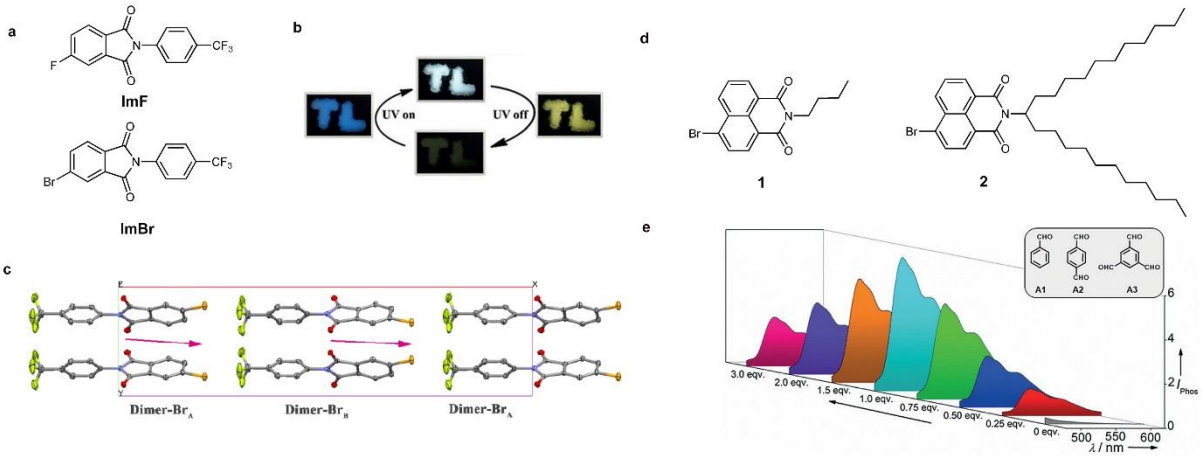

Figure 1-2. a) Molecular structures of **ImF** and **ImBr**. b) Tricolor emission switching of **ImBr**. Reproduced with permission.[50] Copyright 2018, Wiley-VCH. c) Crystal packing mode of **ImBr**. d) Molecular structures of compounds **1** and **2**. e) Phosphorescence spectral changes of **2** with increasing equivalents of A2 at RT in air. Reproduced with permission.[51] Copyright 2019, Wiley-VCH.

introduces strong SOC. In addition, non-centrosymmetric packing and hydrogen bonds, immobilizing the molecular conformations in the crystalline state, reduce nonradiative decay channels (Figure 1-2c). In 2009, Sukumaran *et al.* first reported a solvent-free liquid long alkyl chain-substituted bromonaphthalimide **2** (Figure 1-2d) which exhibit RTP in air.[51] Compound

1 shows phosphorescence lifetimes **of** 6.2 ms at 25 ˚C and 319 ms at -196 ˚C while compound **2** exhibits phosphorescence lifetimes of 5.7 ms at 25 ˚C and 210 ms at 196 ˚C. The solvent-free liquid **2** shows phosphorescence emission at 594 nm at 25 ˚C in air. According to calculations, a small ΔE_{ST} facilitates ISC, leading to RTP from compound **2**. Interestingly, these phosphors can be used as a sensor of carbonyl compounds. The intensity of phosphorescence from **2** is gradually enhanced with increasing amounts of carbonyl up to 1.0 equivalent (Figure 1-2e). The authors proposed that halogen-bonding in the supramolecular system assists in-plane intermolecular interactions which promotes SOC to generate triplet states efficiently. In the same year, Ma et al. designed several purely organic polymers (**PVP–BrHexene**, **PNVCL–BrNpA**, **PVP–BrNpA**, **PVP–BA**, **PNVCL–BrHexene** and **PNVCL–BA**) based on lactams (Figure 1-3a and 1-3b).[52] Except for **PNVCL–BrHexene**, the phosphorescence lifetimes (τ_p) of the polymers vary from 0.13 to 0.94 ms, with phosphorescence quantum yields (Φ_p) ranging from 0.4 to 1.6 %. Lactam groups bearing lone pairs not only provide hydrogen bonds, but also enhance the ISC rate. Furthermore, the polymer matrix provides a rigid environment which restricts molecular motions, resulting in efficient RTP.

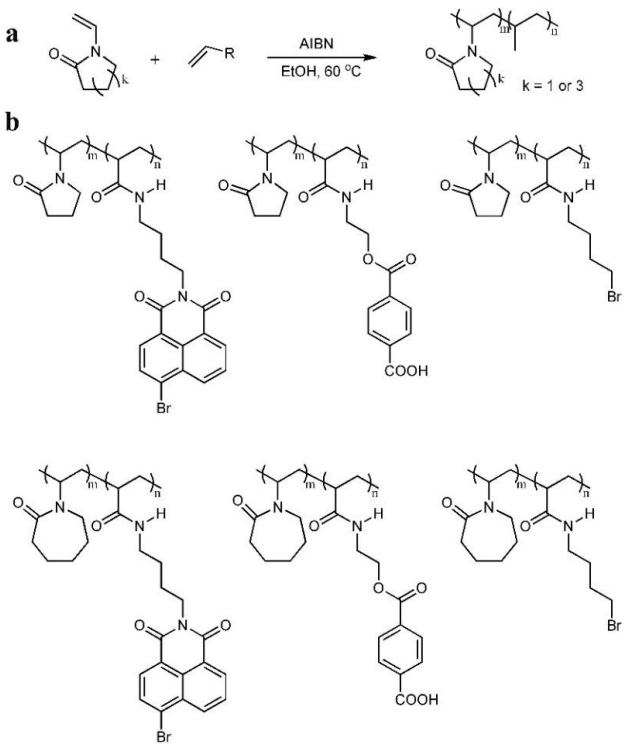

Figure 1-3. a) Method for polymerization. b) Structures of the **PVP–** and **PNVCL–**polymers. Reproduced with permission.[52] Copyright 2019, Wiley-VCH.

In 2020, Bo *et al*. reported two groups of ladder-type organic phosphors (Figure 1-4a).[53] In group B, they utilized the bulky norbornyl (NB) moiety to separate N-methyl phthalimide

groups, achieving persistent RTP for which the phosphorescence lifetime can reach 357.1 ms and quantum yields up to a relatively high value of 2% (Figure 1-4a). By analyzing the crystal structure, they found that a parallel stacking alignment reduces the π-π distances which generate stronger hydrogen to oxygen and π interactions between molecules (Figure 1-4b). This also facilitates the S_1 to T_n transition, thus increasing the phosphorescence efficiency. They also demonstrated an application in the field of dual data encryption which is based on the reversible photochromic properties of **α-PA** (Figure 1-4c and 1-4d). In the solid state, **α-PA** shows no color change under short irradiation times by UV light (254 nm). In contrast, upon irradiation for up to 10 s, the color of the sample changes from achromaticity to yellow. In addition, the blue emission of the sample is quenched. After irradiation with daylight or heating, the sample becomes colorless again.

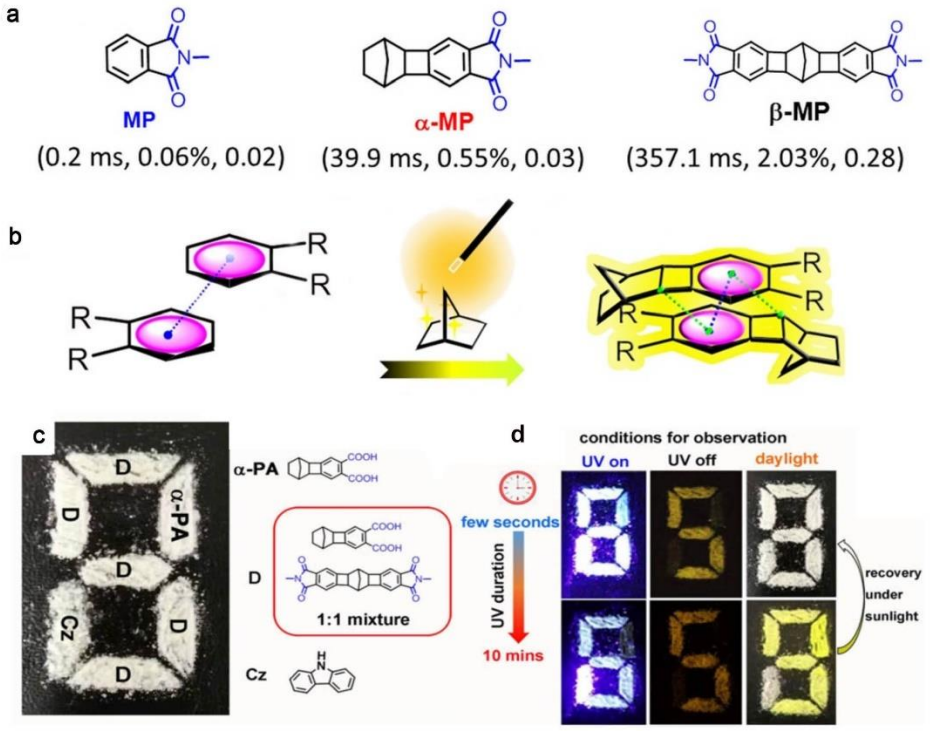

Figure 1-4. a) Molecular structure of the luminophores in the crystalline powder state. b) The vital role NB plays in triggering RTP. c) The different parts of the pattern „8"; d) pictures of the pattern "8" taken after different UV exposure times. Reproduced with permission.[53] Copyright 2020, Wiley-VCH.

1.3.2 Boron-Containing RTP Materials

Boron-containing RTP luminophores have gained considerable interest because of their easy accessibility, low cost, and simple modification. In addition, oxygen atoms in boronic acids and esters can promote intersystem crossing and hydroxy groups in boronic acids can form strong hydrogen bonds. In 2017, Yuasa *et al*. reported the crystalline phenylboronic acid derivatives **PB**, **PDB** and **PDBEG** (Figure 1-5a) in which the phosphorescence lifetime of **PDBEG** reaches

1.6 s.[20] According to the photophysical data obtained in the crystal matrix, they suggested that charge-transfer complexes formed between two neighboring molecules play a major role in persistent RTP. In this complex, ISC is driven by hyperfine-coupling, which is termed HFC-driven. This new phosphorescence mechanism through CT formation provides useful design guidance for new types of photosensitizers. Meanwhile, Li's group designed and synthesized an AIEgen **DPPBO** (Figure 5b; AIE = aggregation-induced emission) stimulated by mechanical forces with dual fluorescence and phosphorescence.[21] Based on analysis of the crystal structure, combined with theoretical studies, they proposed that the polar boron oxygen bond of the ester contributes with the oxygen lone pairs to produce strong intermolecular and intramolecular interactions (Figure 1-5c), but also to the population of triplet states by promoting the spin-forbidden transition of excited states from singlet to triplet via ISC. Li's group also reported that the commercially available **PBA-MeO** (4-methoxyphenyl)boronic acid (Figure 1-5d) exhibits persistent green RTP for which the phosphorescence lifetime can reach 2.24 s.[54] Their findings suggest that the rigidification and interactions between neighbouring molecules in the aggregated state prohibit rapid nonradiative decay. Moreover, the triplet states are stabilized by effective π–π stacking which enhances the ISC process. It is one of the longest lifetimes for an organic molecule with a single component reported so far. In 2019, Su et al. thoroughly investigated the RTP properties of boronic ester-substituted phenoxathiine-based derivatives **i-PXT-BPin**, **PXT-BPin** and **TE-BPin** (Figure 1-5e).[55] However, it is noted that the efficiency of RTP was not always enhanced in the boronic esters examined. Only **PXT-BPin** was found to have a high phosphorescence quantum yield (Φ_p=20%). By analysis of the crystal structure, they found that **PXT-BPin** adopts a more condensed intermolecular packing mode compared to other molecules in the crystalline state and has an (n, π*) transition, which accelerates the ISC process (Figure 1-5f). Moreover, the molecular vibrations and rotations were significantly reduced in crystalline **PXT-BPin**, resulting in the preservation of a high quantum yield. Fukushima's group investigated 19 arylboron compounds and measured their photophysical properties (Figure 1-6a and 1-6b). These compounds displayed lifetimes of up to several seconds at room temperature in air.[56] Theoretical calculations for boronic ester **2** (Figure 1-6a) indicate that the (pinacol)B−C_{ipso} moiety has an out-of-plane distortion in the T_1 state, which may mix σ and π orbitals to accelerate ISC. However, it is not clear how the structural changes influence the RTP in the solid state. They proposed that solid-state molecular packing may have an important effect on the phosphorescence properties, compared to the positions and numbers of boron substituents on the phenyl ring. This exciting finding inspired researchers to use boronic acid and ester moieties to develop new RTP phosphors. Liang's group developed a

highly sensitive oxygen detector (**TBBU)** embedded in PMMA films (Figure 1-6c). The value of Φ_p is as high as 13% and the lifetime is as long as 350 ms under vacuum.[57] **TBBU** is designed as a non-coplanar D-π-A structure without symmetry which uses the boronic ester as the acceptor. It allows intermolecular aromatic rings to adopt a side-by-side packing mode with a head-to-tail arrangement (Figure 1-6d). Therefore, the large pores retained in the solid state increase the sensitivity for oxygen detection. On the one hand, with the addition of O_2, the color of the doped film turns deep blue from pink-blue and enables a visual detection of oxygen (Figure 1-6e). On the other hand, the value of $1/\tau_p$ is positively correlated with the O_2 concentration value, which enables the quantitative detection of oxygen. This method demonstrates a simple and reliable way to detect oxygen by using persistent RTP properties.

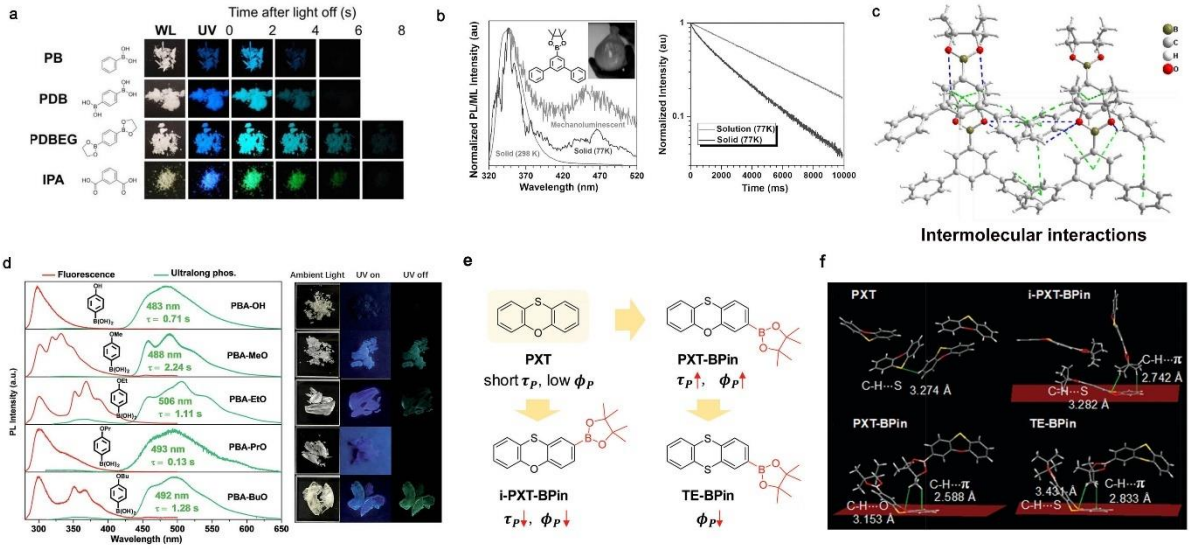

Figure 1-5. a) Chemical structures and afterglow images of **PB**, **PDB**, **PDBEG** and **IPA**. Reproduced with permission.[20] Copyright 2017, Wiley-VCH. b) Photoluminescent and mechanoluminescent spectra of **DPP-BO** at 298 K and 77 K in the solid state. Reproduced with permission. c) The intermolecular C-H···π interactions are displayed in green lines and the C-H···O interactions are displayed in blue lines.[21] Copyright 2017, Wiley-VCH. d) PL spectra of the crystalline **PBA**, and the corresponding RTP photographs taken before and after UV light irradiation. Reproduced with permission.[54] Copyright 2017, The Royal Society of Chemistry. e) Chemical structures of **PXT**, **i-PXT-BPin**, **PXT-BPin** and **TE-BPin**. Reproduced with permission. e) Single crystal structures and intermolecular interactions of **PXT**, **PXT-BPin**, **i-PXT-BPin** and **TE-BPin**.[55] Copyright 2019, The Royal Society of Chemistry.

Compared to boronic acids and esters, triarylborane-based phosphors are easier to modify because of possible substitution at the three phenyl rings.[58-59] In addition, increased π to empty boron p orbital transitions may also accelerate the rate of the ISC process. In 2020, Zhao's group reported a triarylborane-based biphenyl phosphor derivative (**Br_2-BN-BPh**) (Figure 1-7a).[60] The highly twisted biphenyl skeleton separates the HOMO and LUMO, leading to a small value of ΔE_{ST} (Figure 1-7b). Both the small ΔE_{ST} and the bromine heavy atom can

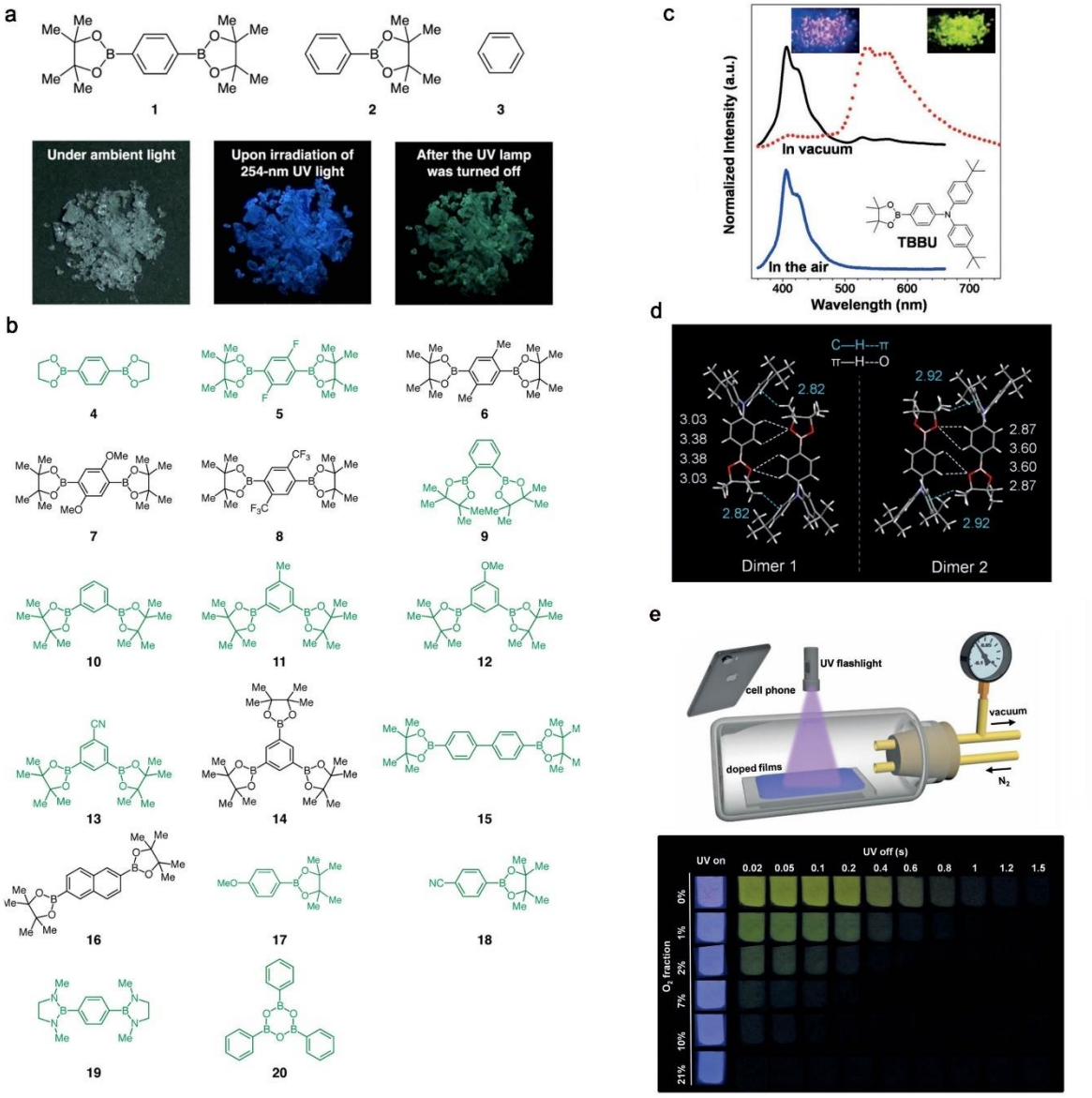

Figure 1-6. a) Molecular structures of **1**-**3**. Afterglow photographs of crystalline **1**. b) Molecular structures of boron compounds in which compounds with RTP are shown in green and the other are black. Reproduced with permission.[56] Copyright 2017, American Chemical Society. c) PL spectra of crystalline **TBBU**. Inset: digital images at room temperature. d) Crystal structure of **TBBU**. e) Oxygen detection with the **TBBU** doped film (top) and persistent RTP images (bottom) of the doped film at different oxygen concentrations. Reproduced with permission.[57] Copyright 2019, Wiley-VCH.

improve the SOC and thus increase the ISC rate. In addition, the rigid backbone of **Br_2-BN-BPh** and the boron to nitrogen and π−π interactions within molecules can suppress nonradiative decay, resulting in a phosphorescence quantum yield as high as 36%. In the same year, our group designed triarylboranes **1**–**4** (Figure 1-7c) with different numbers of -CH_3 moieties on the benzene ring.[22] Interestingly, crystalline **3** (tris(2,6-dimethylphenyl)borane) exhibits long-lived yellow phosphorescence with a lifetime of 0.5 s. Compounds **1** and **3** are the first triarylborane-based phosphors without any lone pairs or heavy atoms which display ultralong RTP under ambient conditions. Theoretical calculations reveal that transitions between (σ, B p)

and (π, B p) can also speed up the rate of ISC (k_{isc}), which is an addition to the normal ISC process, and which is accelerated by transitions between ^{1}(n, π*) and ^{3}(π, π*) (Figure 9d). Moreover, compound **3** has the highest phosphorescence efficiency among the four compounds. By analysis of the crystal structure, we found that there is a void in the unit cell of **3**. It is proposed that the presence of the voids may play an important role, for example enhancing π–π interactions between these aryl rings when excited, which may help to supress nonradiative decay and achieve persistent RTP.

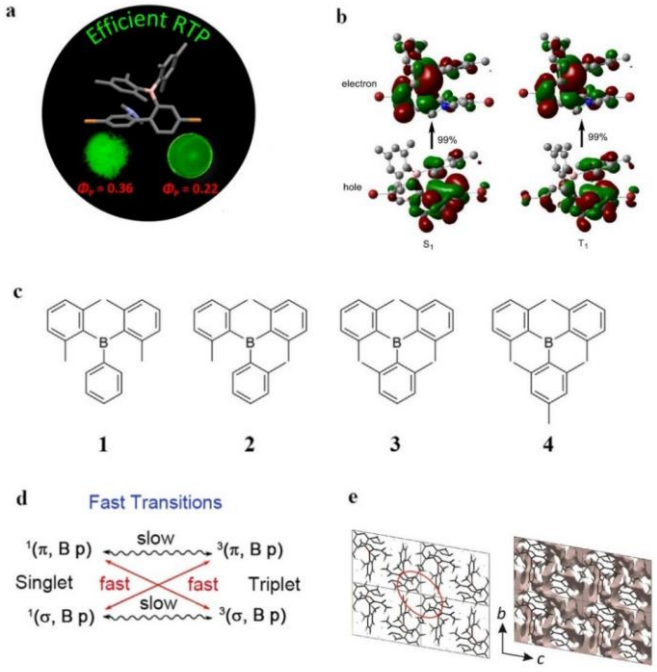

Figure 1-7. a) Chemical structure of **Br$_2$-BN-BPh**. b) Natural transition orbitals for the S_1 and T_1 states of **Br$_2$-BN-BPh**. Reproduced with permission.[60] Copyright 2020, American Chemical Society. c) Molecular structures of compounds **1**–**4**. d) Fast transitions between (σ, B p) and (**π**, B p). e) Crystal structure of compound **3**, and plot of the Hirshfeld surface of the crystal voids (0.002 a.u.). Reproduced with permission.[22] Copyright 2020, Wiley-VCH.

In 2007, Fraser's group reported a single-component, multi-emissive (RTP, delayed fluorescence and fluorescence) difluoride dibenzoylmethane coupled with poly(lactic acid).[61] This multifunctional material is responsive to many factors such as temperature and oxygen (Figure 1-8a). Two years later, they developed a difluoroboron dibenzoylmethane-poly(lactic acid) **BF2dbm(I)PLA** substituted by iodine.[62] By controlling the **PLA** chain length by lactide polymerization, this purely organic phosphor can be used for versatile applications. On the one hand, a low-molecular-weight **P1** film with a dominant phosphorescence and weak fluorescence is a promising ratiometric oxygen sensor. On the other hand, higher molecular weight polymer boron nanoparticles **P2** with balanced fluorescence and phosphorescence

emission can serve as ratiometric tumor hypoxia imaging agents (Figure 1-8b). In 2007, Fu *et al*. developed an organic phosphorescence nanowire laser (Figure 1-8c) using a difluoroboron compound substituted by sulfur.[63] The lone pairs of the nitro group and the sulfur substituent induced an intramolecular charge transfer (ICT) transition leading to highly efficient ISC from S_1 (n,π*) to T_1 (π,π*) (Φ_{ISC} = 100%) which enables organic solid-state laser (OSSL) phosphorescence with an emission peak at 650 nm. This work successfully applied a four-coordinate boron RTP material in practical use as a laser.

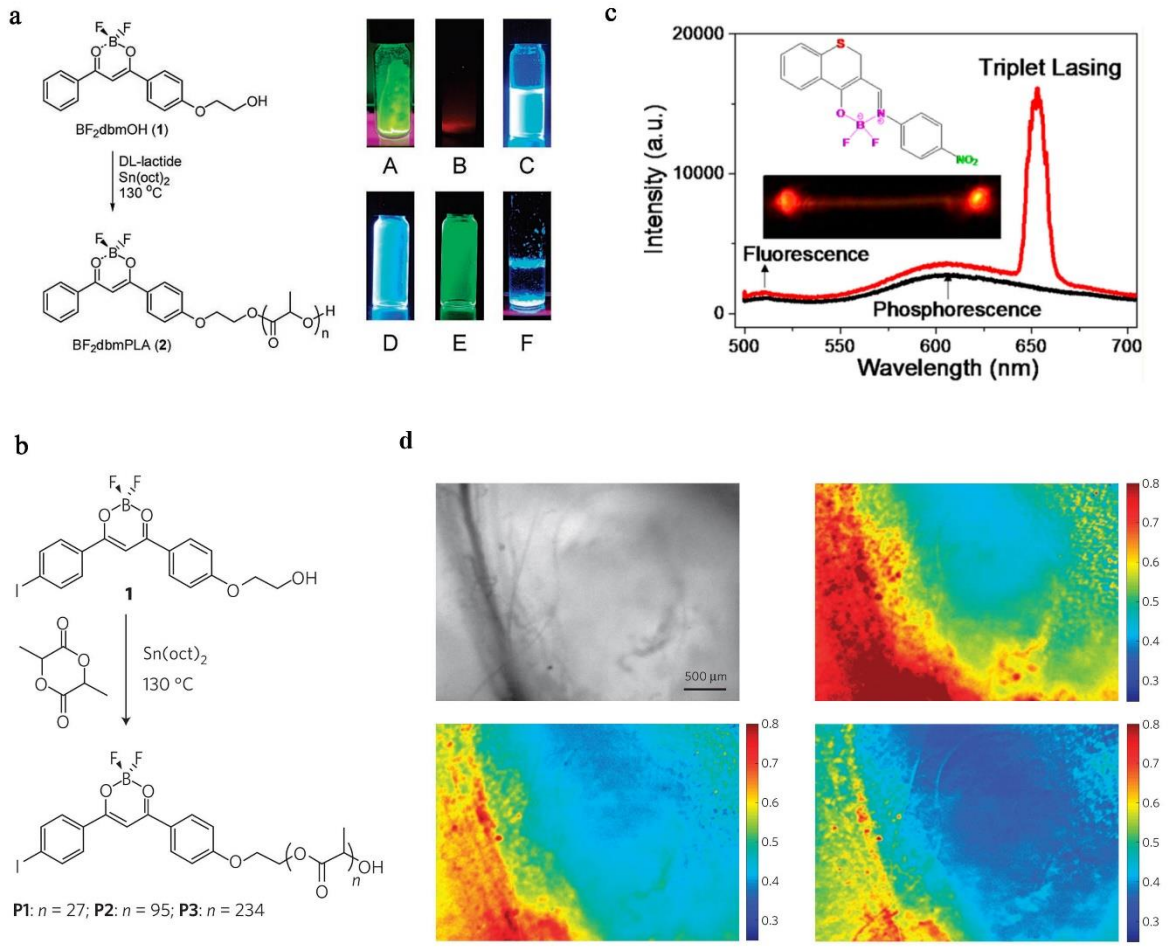

Figure 1-8. a) Synthesis of difluoroboron-based polymer. Insert: luminescent images under 365 nm UV light. BF_2dbmOH: (A) solid state at RT; (B) solid state at 77 K; (C) CH_2Cl_2 solution. **BF_2dbmPLA**: (D) short-lived blue fluorescence and (E) phosphorescence in a thin film under nitrogen; (F) particle suspension in water after 45 days. Reproduced with permission.[61] Copyright 2007, American Chemical Society. b) Polymerization of BF_2dbm(I)PLA (**P1**–**P3**). Reproduced with permission.[62] Copyright 2009, Nature Publishing Group. c) Triplet lasing. Reproduced with permission.[63] Copyright 2017, American Chemical Society. d) Images of tumour hypoxia with **P2** nanoparticles. Reproduced with permission.[42] Copyright 2009, Nature Publishing Group.

1.3.3 Sulfur-Containing RTP Materials

Sulfur is one of the most important elements used in RTP materials. First, the lone pairs of sulfur provide n to π transitions and thus increase intersystem crossing according to El-Sayed's

rule. Moreover, multiple intermolecular interactions between S···H or S···π can suppress nonradiative pathways by restricting molecular rotations and vibrations. In 2020, Wolf et al. reported diarylethene luminophores **1o**, **2o** and **3** containing quinoline moieties (Figure 1-9a).[64] Compound **1o** shows typical diarylethene photocyclization character in CH_2Cl_2 solution when irradiated by 365 nm UV, with its color turning from colorless in the open form to red in the closed form. Phosphor **3** is achieved by methylation of the quinoline nitrogen of **1o**. The emission peak at 575 nm showed a phosphorescence lifetime as long as 1.9 ms at room temperature while the higher energy peak at 540 nm exhibited a much longer lifetime of up to 244 ms at 77 K (Figure 1-9b and 1-9c). Theoretical studies revealed that the HOMO and LUMO are separated to a large extent in the space, which can promote ISC (Figure 1-9d). In addition, charge transfer from the benzothiophene to the quinolinium group may also enhance ISC. Moreover, strong interactions between the DAE (diarylethene) cation and the $[BF_4]^-$ anion prevent amorphous **3** from coming into contact with triplet quenching species and inhibit vibrational relaxation.

Phenothiazine is a good electron donating group which is easily modified by bulky substituents. Therefore, using a phenothiazine unit to construct molecules with D-A-D or D-A structures can generate a spatially well-separated HOMO and LUMO. This produces an ICT state and a small ΔE_{ST}, which can accelerate the ISC process. In 2016, Bryce's group reported a number of phenothiazine based luminophores, in which sterically bulky groups on the phenothiazine ring restrict rotation around the bond of carbon and nitrogen linking the donor and acceptor moieties (Figure 1-10a). In zeonex films, compounds **1** and **6** have obvious TADF. However, with increasing steric hindrance from methyl to *t*-Bu groups on the phenothiazine rings,

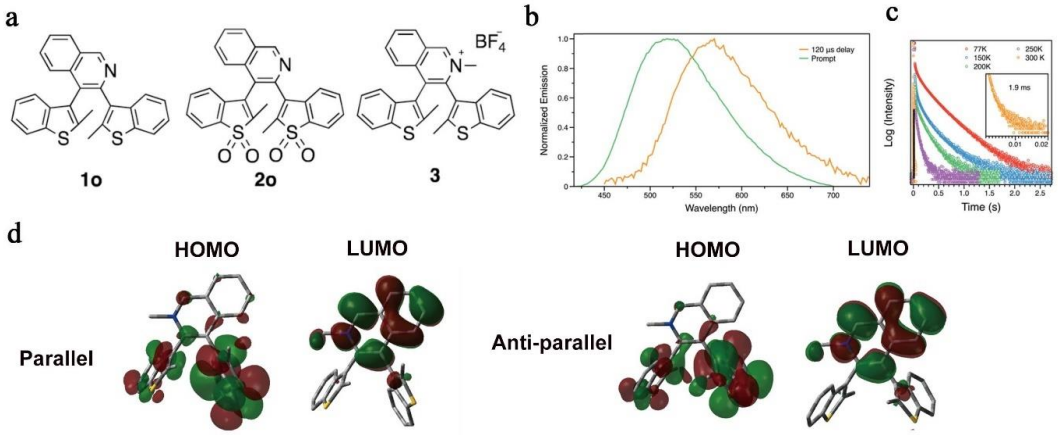

Figure 1-9. a) Molecular structures of **1o**, **2o** and **3** (top). b) and c) PL spectra and decays of **3** in the powder state under air. d) Frontier orbital diagrams of compound **3** in parallel and anti-parallel conformations. Reproduced with permission. [64] Copyright 2020, The Royal Society of Chemistry.

phosphorescence gradually dominates in the solid state emission.[65] They proposed that the motion of bulky, substituted molecules when aggregated is thus restricted and there is less conformational flexibility, such that electron transfer from the ^{1}D–^{1}A states to the ^{1}CT state is prohibited (Figure 1-10b). Moreover, the main non-radiative relaxation that affects T_1 is also restricted, leading to long-lived RTP under ambient conditions. In 2019, they also developed the strategy of using methoxy groups to increase the value of Φ_p in the solid state.[66] As mentioned before, the methoxy groups lead to molecules with rigid D−A−D and D−A structures (Figure 1-10c and 1-10d) which promote efficient RTP properties.

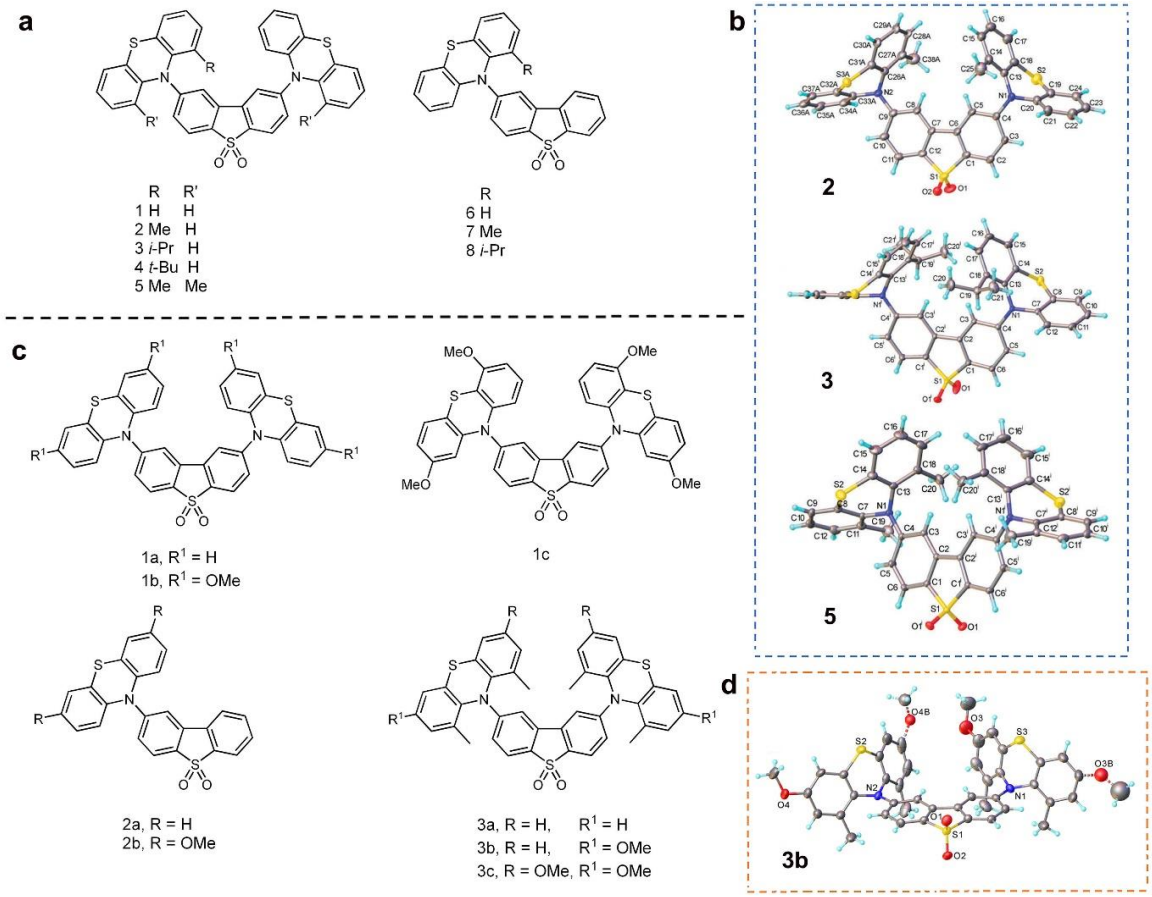

Figure 1-10. a) Structures of D–A–D and D–A molecules **1**-**8**. b) Crystal structure of **2**, **3** and **5**. Reproduced with permission.[65] Copyright 2016, The Royal Society of Chemistry. c) Molecular structures of **1a**-**1c**, **2a**-**2b** and **3a**-**3c**. d) Crystal structure of **3b**. Reproduced with permission.[66] Copyright 2019, American Chemical Society.

In order to promote n–π* transitions and populate triplet states, Li *et al*. developed a number o f phenothiazine-5,5-dioxide derivatives (**CS-CH_3O**, **-CH_3**, **-H**, **-Br**, **-Cl**, and **-F**),[67] all of whi ch displayed RTP properties with lifetimes ranging from 88 to 410 ms (Figure 1-11a). After sy stematic investigation of the calculation results and crystal structures, they suggest that robust π–π interactions between molecules could help in the stabilization of the T_1 state (Figure 1-11 b). In addition, phosphors **CS-Br**, **-Cl**, and **-F**, bearing accepting groups, have more enhanced π–π interactions, compared to those (**CS-CH_3O** and **CS-CH_3**) with donor substituents, resultin g more intense RTP. They demonstrated that phosphor **CS-F** is a good candidate for bioimagi ng applications due to the long phosphorescence lifetime (Figure 1-11c). In 2019, they reporte d the use of an aromatic-substituted phenothiazine-5,5-dioxide with nonaromatic alkyl chains to obtain a series of **CS-C_nH_{2n+1}** phosphors.[68] It is interesting that these organic RTP lumino phores showed an odd-even effect with odd alkyl-substituted compounds exhibited longer pho sphorescence lifetimes than those modified with even ones (Figure 1-11d). They selected **CS-C_3H_7**, which shows the best RTP performance, to investigate its use in in-vivo imaging (Figur e 1-11e). After subcutaneous injection of nanoparticles of **CS-C_3H_7**, persistent phosphorescen

ce was clearly observed in a living mouse with low background noise. Zhang et al. developed thioether-based molecules **DSP** and **DSQ** (Figure 1-12a) which show "turn-on" RTP after trea tment with AcOH or HCl vapor.[69] The emission from the compounds cannot be observed wh en irradiated by 365-nm UV. However, when exposed to acid vapor, **DSPH**$^+$ and **DSQH**$^+$ sho w bright green or yellow emission upon irradiation at RT (Figure 1-12b), which is a good exa mple of the use in acid sensors via RTP "turn-on" properties. Theoretical calculations revealed that the lowest triplet states of **DSP** and **DSQ** are largely localized π–π* transitions. After pro tonation, however, the lowest triplet states are CT transitions, resulting in strong RTP (Figure 1-14c). This "turn-on" organic RTP molecular design has potential applications for acid senso rs. In 2020, Chou *et al*. also reported a sulfur-based photoinduced intramolecular H-bond on/o ff switching RTP system (Figure 1-14d).[70] Interestingly, they observed dual RT phosphoresc ence bands at 550 and 685 nm in **DM-7HIT**. According to the identical lifetimes and calculate d energies of the excited states, they excluded many possibilities for the origin of the 550 nm band such as T−T annihilation, TADF, ESIPT (excited state intramolecular proton transfer) an d a higher T_2 state. Finally, they proposed a hydrogen bond on/off mechanism which incorpor ates one pre-equilibrium involving two states T_1 and T'_1 mainly resulting from n to π* transiti ons (Figure 1-14e), leading to identical phosphorescence lifetimes at 550 and 685 nm in soluti on-phase. This proposed hydrogen bond on/off mechanism broadens the scope for organic RT P.

1.3.4 Quinoxaline Derivative-Based RTP Materials

The design principles for TADF molecules bearing a D-A structure, which require small ΔE_{ST} values and efficient ISC processes, are quite similar to the basic ones used for organic RTP

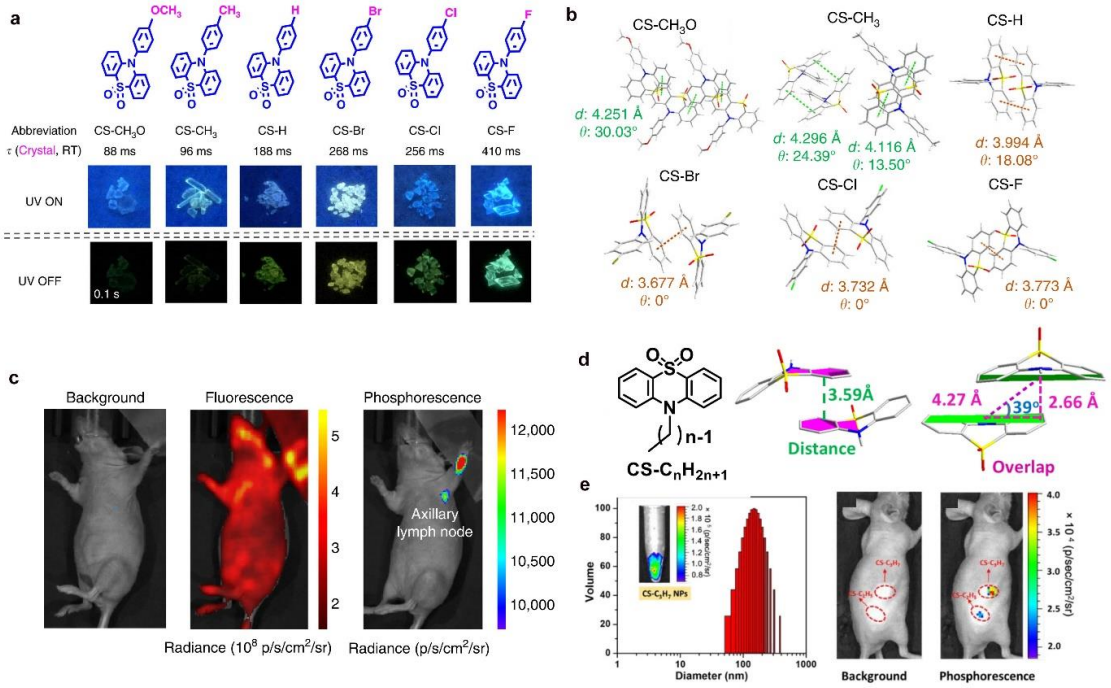

Figure 1-11. a) Molecular structures of the six compounds from **CS-CH₃O** to **CS-F** (top). Afterglow photographs of the six targeted molecules (bottom). b) Crystal structures of six compounds from **CS-CH₃O** to **CS-F.** c) Ultralong phosphorescence and fluorescence imaging of lymph node in living mice 1 h after the intradermal injection of **CS-F** nanoparticles into the forepaw of mice. Reproduced with permission.[67] Copyright 2018, Nature Publishing Group. d) Molecular and crystal structures used in this work. e) The left is the particle size distribution spectrum, insert: in-vitro phosphorescence imaging of **CS-C₃H₇** NPs. At the right is in-vivo phosphorescence imaging pictures of **CS-C₃H₇** and **CS-C₂H₅** NPs. Reproduced with permission.[68] Copyright 2019, The Royal Society of Chemistry.

molecules. In 2017, Yang's group designed a new purely organic luminophor with simultaneous TADF and RTP properties.[71] The quinoxaline group is an electron acceptor while the phenoxazine moiety was chosen as the electron donor. Because of the well separated HOMO and LUMO (Figure 1-13a), ΔE_{ST} of **DBQPXZ** is as low as 0.0863 eV while the corresponding calculated value is 0.0871 eV. In the crystalline state, the band at 564 nm is ascribed to organic phosphorescence of which the lifetime is 3.2 ms at room temperature (Figure 1-13b and 1-13c). Interestingly, when the temperature is below 170 K, the S_1 to T_1 transition dominates the decay process. When the temperature is above 170 K, TADF emission is the main component. Moreover, the external quantum efficiency of a fabricated OLED device can reach up to 16.8%. In 2018, Ma et al. reported an aza-aromatic **DPPZ** based on phenazine (Figure 1-14a), for which the authors found single-molecule white light emission (SMWLE) which they explained with a dual RTP emission, $T_2 \rightarrow S_0$ and $T_1 \rightarrow S_0$.[72] When the time gate is set to 160 μs, the nanosecond lifetime of **DPPZ** disappears completely, and only the long lifetime belonging to dual phosphorescence (T_n and T_1) appeared in the spectrum (Figure 1-14b). In addition, the emission band between 480 and 530 nm is assigned to the T_2 state and almost disappears when the delay timescale reaches 1.4 ms.

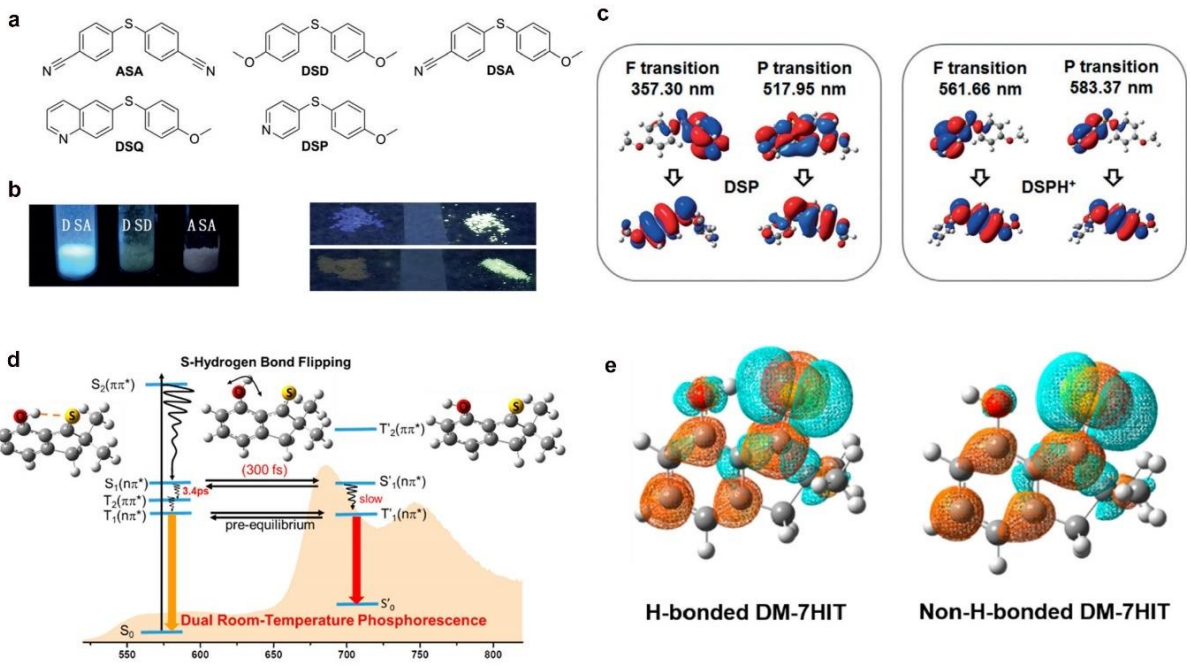

Figure 1-12. a) Molecular structures of **ASA**, **DSD**, **DSA**, **DSQ** and **DSP**. b) PL images of crystalline **DSA**, **DSD** and **ASA** under 365-nm UV light (left). Photographs displaying PL changes of crystalline **DSQ** and **DSP** before and after exposure to acetic acid vapor (right). c) Molecular orbital diagrams showing fluorescence (F, lowest singlet-state) and phosphorescence (P, lowest triplet-state) transitions for DSP/DSPH$^+$ pair. Reproduced with permission. [69] Copyright 2018, Wiley-VCH. d) Schematic energy diagram of the mechanism of H-bond hopping for **DM-7HIT**. e) The calculated HOMO and LUMO of H-bonded and non-H-bonded **DM-7HIT**. Reproduced with permission.[70] Copyright 2019, American Chemical Society.

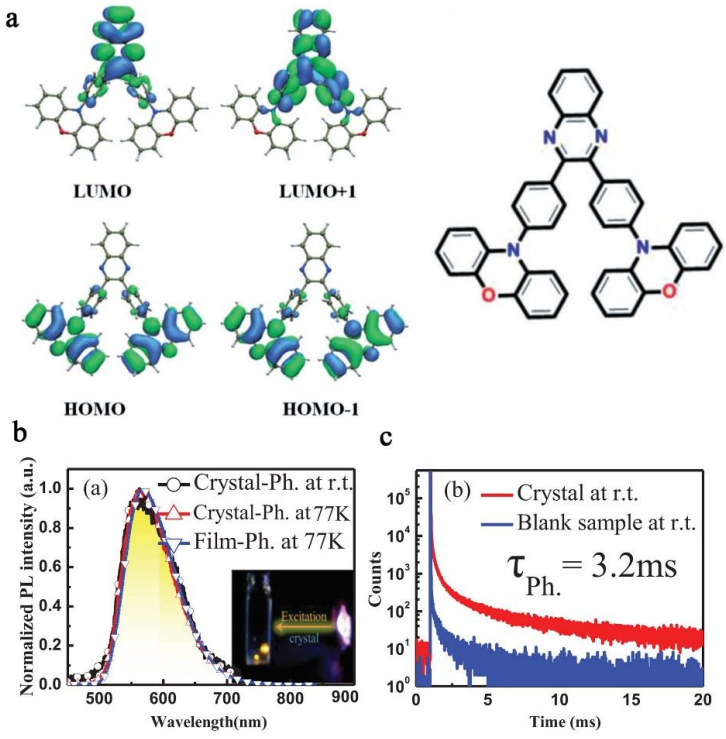

Figure 1-13. a) Molecular structure of **DBQPXZ** and its fronter orbitals. b) Normalized phosphorescence and c) transient PL decay spectra of **DBQPXZ**. Reproduced with permission.[71] Copyright 2017, Wiley-VCH.

1.3.5 Siloxy Group-Induced RTP Materials

While elements such as nitrogen, oxygen and sulfur bearing lone pairs are commonly used in the molecular design of RTP materials, silicon is rarely employed in phosphorescent luminophores. In 2016, Hasobe *et al*. reported siloxy-substituted benzene derivatives **1a-1c** (Figure 1-14c). The phosphorescence lifetimes are ca. 76.0 to 98.3 ms and they show outstanding luminescence quantum yields of 46% to 64%.[73] By crystal structure analysis, they found multiple intermolecular interactions which efficiently reduce intramolecular motion, thereby suppressing nonradiative decay to a large extent. Calculations revealed that the conjugation between silicon to carbon σ-orbitals and the n-orbital of the siloxy moiety can stabilize the T_1 state, which explains the remarkably high RTP performance. According to the proposed mechanism, the positions of silicon and carbon atoms connected to the oxygen atom of the ether do not influence the stabilization of the T_1 state through σ–n conjugation (Figure 1-14d). Therefore, they also investigated a series of silylmethoxy benzene derivatives **2a-2f**.[74] They found that **2a-2f** not only exhibit intense RTP in the crystalline state, but show efficient

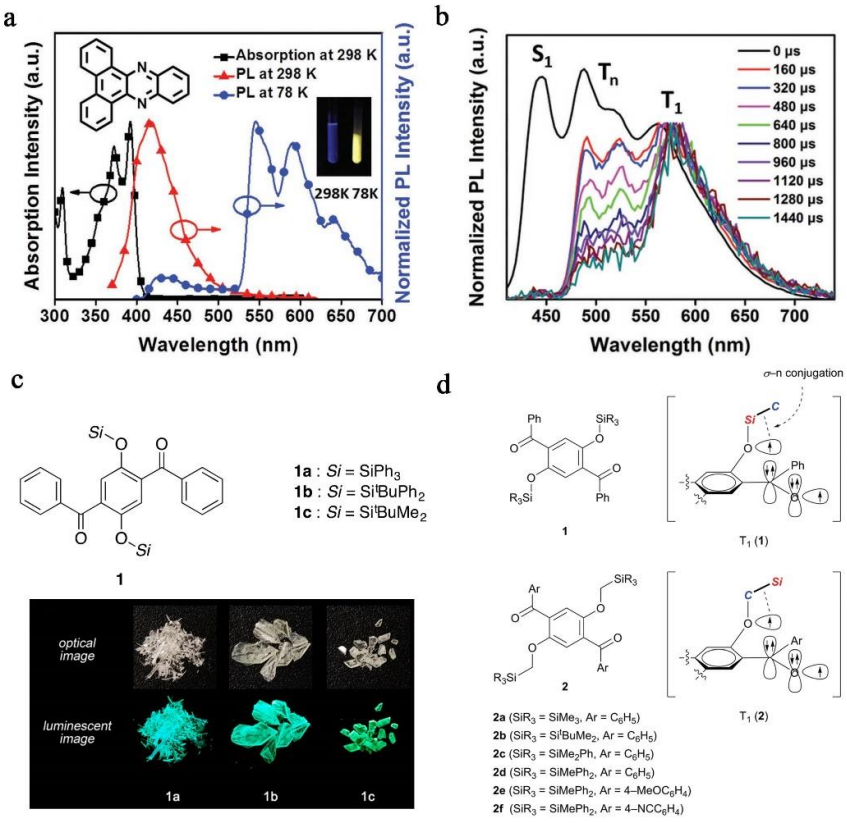

Figure 1-14. a) Chemical structure, absorption, and emission spectra of **DPPZ** in THF solution at 298 and 78 K. b) Normalized PL spectra of **DPPZ** as a neat powder. Reproduced with permission.[72] Copyright 2018, Wiley-VCH. c) Molecular structures of 1,4-dibenzoyl-2,5- bis(siloxy)benzenes **1a**−**1c** (top) and luminescent images of crystals (bottom). Reproduced with permission.[73] Copyright 2016, American Chemical Society. d) Chemical structures and orbital descriptions of the T_1 states of **1** and **2**. Reproduced with permission.[74] Copyright 2018, The Royal Society of Chemistry.

RTP when doped in PMMA films which were prepared and measured under vacuum. Moreover, the phosphorescence of PMMA films of **2** responds quickly to oxygen and is thus a potential candidate for application as an oxygen sensor.

1.3.6 Carbazole-Based RTP Materials

RTP phosphors based on carbazole have been widely investigated in recent years.[75] However, in 2020, Liu et al. proved that the presence of an isomeric impurity in commercial carbazole leads to enhanced RTP even with a concentration of less than 0.5 mol%,[26] as the isomeric impurity can cause obvious differences in the RTP lifetime and quantum yield. Therefore, we suggest that the reported carbazole-based RTP materials which were prepared directly from commercial carbazole should be carefully reexamined. On the other hand, reported research already confirmed that carbazole derivatives tested for purity exhibit RTP. In order to make comparisons with the corresponding carbazole isomer, Tang *et al*. investigated **TCz-F**, **TCz-H**, and **TCz-OH** (Figure 1-15a) which were synthesized from commercial/lab carbazole through S_NAr reactions.[27] This provided insight into the push-pull electronic effect on photophysical behavior. Lab-made **TCz-OH-Lab** only shows fluorescence while **TCz-F-Lab** and **TCz-H-Lab** exhibit obvious RTP in the solid state with a phosphorescence lifetime as long as 48.6 and 29.9 ms and quantum yield up to 0.8% and 0.7%, respectively. The isomer did have a great influence on the RTP properties. On one hand, the phosphorescence emissions of **TCz-F-Lab** and **TCz-H-Lab** were blueshifted by ca. 40 nm compared to corresponding commercial compounds. On the other hand, both the phosphorescence lifetimes and quantum yields were dramatically enhanced, indicating that the effect of the isomer should not be neglected in carbazole-related phosphors. Due to the strong blue fluorescence and efficient RTP of **TCz-F-Cm**, it was successfully applied as an emitter material in an OLED device to generate white-light emission with CIE coordinates of (0.357, 0.317) at a current density of 3.6 mA cm^{-2} (Figure 15b and 15c). Also in 2020, Aakash *et al*. designed carbazole-based phosphor **3a**, functionalized by a phenylmethanone group (Figure 1-16a) which has an ultralong phosphorescence lifetime of over 4.1 s and a high quantum yield up to 11%, by controlling the molecular packing in the crystalline state.[76] In addition to the small ΔE_{ST} to facilitate the ISC process, and intermolecular interactions to suppress nonradiative decay, the existence of dense helical arrays in the aggregated solid of **3a** significantly stabilize the triplet state, resulting in the long phosphorescence lifetime (Figure 1-16b). No helical arrays and only loose packing modes in the crystalline assembly were observed for **1**, **2** and **3b**-**3e**. Therefore, they show weaker RTP than **3a**. Very recently, Li's group also synthesized two carbazole-based RTP

luminophores **PTCz** and **CCz** (Figure 1-16c) substituted by a phthalide (**PT**) moiety and by a typical C=O unit, respectively.[77] The butterfly-like molecule **PTCz** showed a much longer phosphorescence lifetime (τ_p) of 810 ms and quantum yield (Φ_P) of 5.1% while the τ_p value of its corresponding carbonyl-substituted molecule **CCz** is only 12.1 ms. In crystals, the PT unit enabled **PTCz** to adopt the desired strong packing mode which produced intense intermolecular interactions. In addition, the neighboring acceptor (**PT** unit) and donor (**Cz** group) facilitate intermolecular charge transfer (ICT), enabling transitions between the singlet and triplet states (Figure 1-16d). They also provided an example of the application of **PTCz** in anticounterfeiting. Upon turning off the UV light, only "F" made from **PTCz** showed the yellow afterglow in the original pattern "E" (Figure 1-16e).

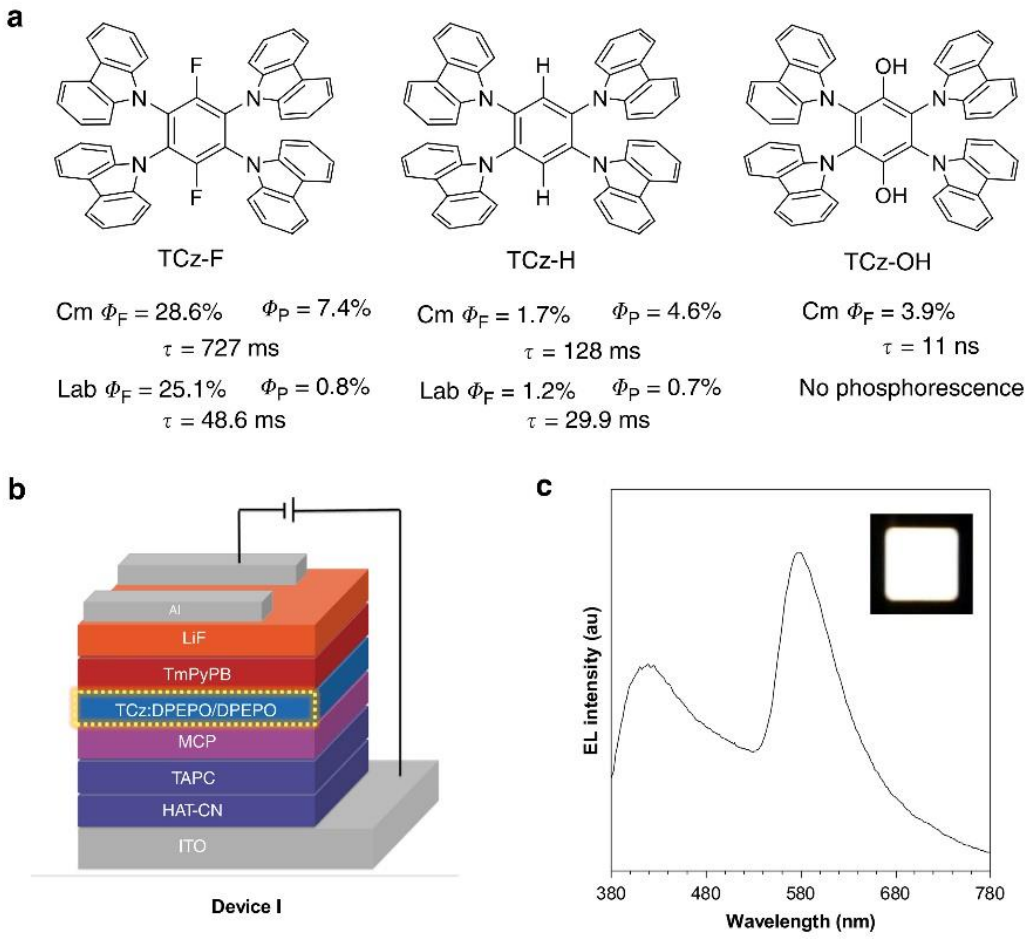

Figure 1-15. a) Molecular structures and photophysical properties. b) Configuration of OLED. c) The EL spectrum of device I at a current density of 3.6 mA cm^{-2}. Reproduced with permission.[27] Copyright 2020, Nature Publishing Group.

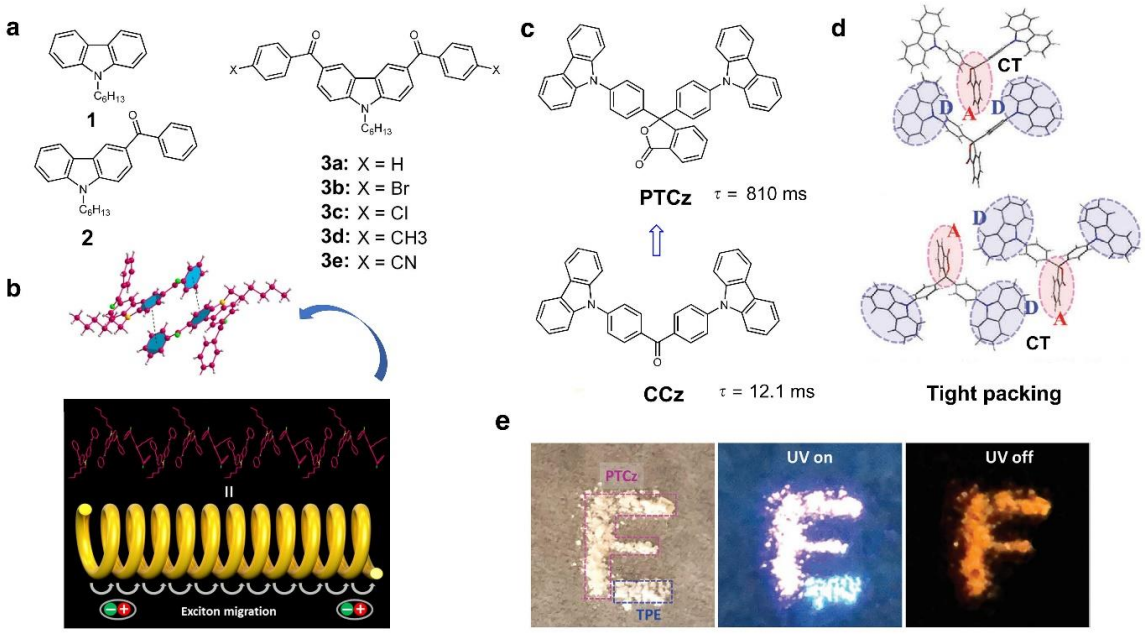

Figure 1-16. a) Chemical structures of compounds **1**, **2** and **3a**-**3e**. b) Schematic of the helical array of **3a** leading to triplet exciton migration, insert: π–π interaction between the adjacent molecules. Reproduced with permission.[76] Copyright 2020, Wiley-VCH c) Molecular structures of **PTCz** and **CCz**. d) Tight packing mode in the crystals. e) Photographs of the letter "E" containing the pattern "F", demonstrating the potential application of the **PTCz** materials in anticounterfeiting. Reproduced with permission.[77] Copyright 2021, Wiley-VCH

1.3.7 Other RTP Materials with Unusual Structures

Quinoxalines, phenothiazines, boronic esters and amides and their derivatives are typically utilized as single-component organic phosphors. However, there are a few RTP materials which are not based on these common structures. Below are a few examples selected for discussion. In 2018, Tang *et al*. designed and synthesized five different heavy halide-substituted organic salts based on phenyl oxazolium (**TPO-I**, **-Br**, **-Cl**, **-F** and **-P**), which are highly emissive under UV light with phosphorescence lifetimes ranging from 48 to 706 μs.[78] Crystal structures and results of calculations indicate that interactions between the negative charge of the halide and positive charge of the aromatic ring improve SOC and increase the ISC rate. These so-called anion–π^+ interactions involving halide atoms represents a new design for RTP luminophores. Among the five phosphors, in the solid state, **TPO-Br** exhibits single-molecule white light emission (SMWLE) with a combination of blue fluorescence and yellow RTP (Figure 1-17a). In addition, the white light color could also be obtained by changing the ratios of components between **TPO-I** and **-Cl** or **TPO-I** and **-P**. They successfully doped **TPO-Br** in PEG and demonstrated its application as a white light display and in 3D printing. In 2019, Bechtold *et al*. reported the non-planar homotruxene phosphor **8** (Figure 1-17b) which was synthesized by dehydrative cyclotrimerization of 1-tetralone at high temperature with $TiCl_4$.[23] The temperature-dependent emission spectrum showed a strong emission at 566 nm. The

phosphorescence lifetime reaches 0.38 s and the value of Φ_p is up to 5.6% under ambient conditions in the solid state. In addition to phosphorescence, there is also a delayed fluorescence peak at 412 nm induced by triplet–triplet annihilation, as indicated by its temperature and concentration dependence. Although there is no heavy atom or heteroatom bearing lone pairs to enhance ISC, calculations suggested that the twist between one central benzene ring and the three outer benzenes of **8** causes a change of angular momentum associated with electronic transitions which is necessary for SOC. In addition, the high triplet energy reduces nonradiative decay pathways. In the same year, Huang' group reported a series of indolo[3,2-b]carbazole analogues (Figure 1-17c). The RTP maxima of the analogues vary from 442 to 623 nm and the related phosphorescence lifetimes range from 2 to 759 ms.[79] Theoretical calculations suggest the absence of an ISC process in the isolated molecule despite the narrow energy gap (Figure 1-17d). When aggregated, T-shaped dimers form hydrogen to π interactions which induce ICT between indolyl and phenyl groups leading to a high radiative decay rate. Furthermore, the calculated orbital coupling element of **Ben-H** for T_1/S_0 (1.25 cm^{-1}) is much larger than that in

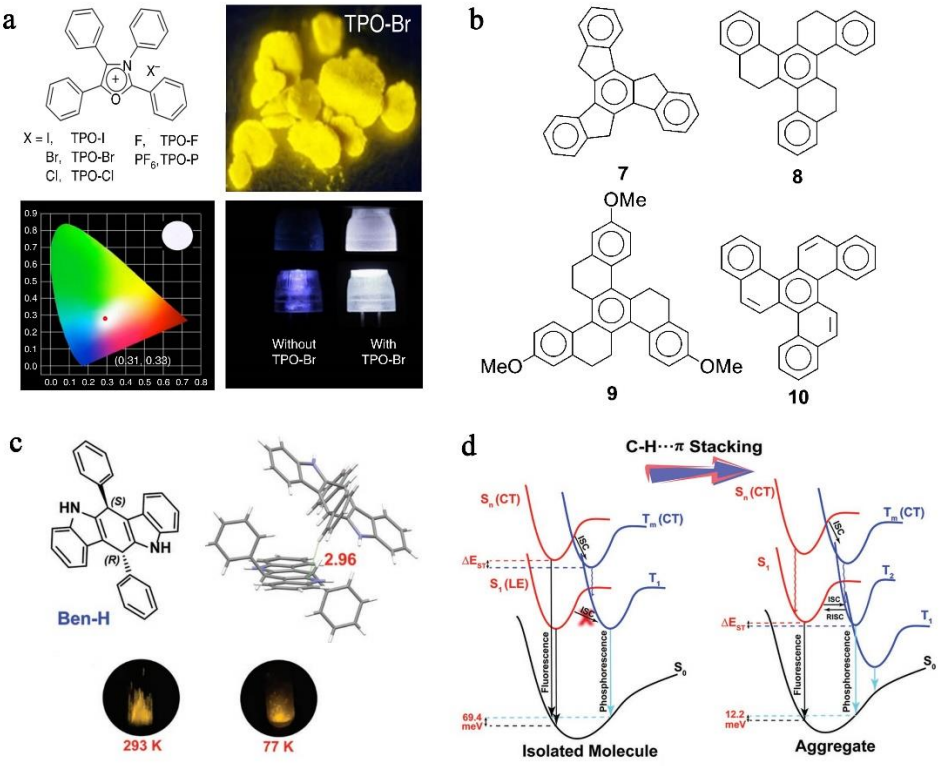

Figure 1-17. a) Chemical structures of **TPO-I**, **-Br**, **-Cl**, **-F**, and **-P** (top left). Photographs of **TPO-Br** under UV light (top right). CIE 1931 coordinates from the **TPO-Br**-based PEG film (2%, m/m, bottom left). Luminescent images of 3D printed lampshades irradiated at 365 nm without and with **TPO-Br** (bottom left). Reproduced with permission.[78] Copyright 2018, Nature Publishing Group. b) Planar and twisted rigidified derivatives of triphenylbenzene. Reproduced with permission.[23] Copyright 2019, Wiley-VCH. c) Molecular structure of **Ben-H** and the C-H···π interaction in **Ben-H**-DMSO. d) The proposed energy level diagrams for **Ben-H** in single molecule and aggregated state. Reproduced with permission.[79] Copyright 2019, Wiley-VCH.

the isolated molecule ($<<10^{-2}$ cm^{-1}) also demonstrating the importance of aggregation. Finally, the influence of C-H···π interactions suppressing molecular thermal rotation and vibration in the crystal cannot be neglected.

1.4 Multi-Component RTP

1.4.1 RTP from Host-Guest Systems

Host–guest systems are one of the most important categories of multi-component RTP phosphors. Among them, a number of host-guest systems are related to the trap/detrap mechanism, which requires efficient photo-induced charge separation and charge recombination processes. In 2017, Adachi's group chose molecule **TMB** (guest) as the donor with a very stable radical cation, and **PPT** (host) as the strong acceptor (Figure 1-18a).[80] When photoexcited, charge-transfer occurs between **TMB** and **PPT**. The radical anions produced diffuse until they encounter a **TMB** radical cation. During the slow recombination process, phosphorescent emission is generated (Figure 1-18b). The phosphorescence duration of a fabricated 1 mol% TMB/PPT film can last for more than 5000 seconds with an excitation time of 180 s at 300 K. In subsegment work,[81] they systematically studied the RTP properties using three different donor molecules (**TMB**, **DMDTB** and **TTB**) and the same acceptor **PPT** (Figure 1-18c). The RTP performance is greatly influenced by the energy gap between ^{1}CT (lowest singlet excited state of the exciplex) and ^3LE_D (the lowest triplet excited state of the donor). They demonstrate that the large energy gap for populating the ^{3}LE excitons, which inhibits the charge-transfer process, leads to a reduced quantum efficiency of phosphorescence.

Organic RTP materials based on carbazole (**Cz**) and its derivatives recently have been widely developed. In 2020, Liu *et al.* successfully isolated and identified the impurity which was an isomer of **Cz**, namely 1H-benzo[f]indole (**Bd**), from a commercially available **Cz** source.[26] Next, they prepared two kinds of **Cz** starting materials. One was from commercially available **Cz** obtained from TCI (Tokyo Chemical Industry, **TCI-Cz**) while the other **Lab-Cz** was prepared from 2-aminobiphenyl (Figure 1-18d). With the two **Cz** sources, they checked two reported RTP phosphors **CPhCz** and **DPhCzT**, and found that although the crystals have the same unit cells, **TCI-CPhCz** and **TCI-DPhCzT** showed RTP, while **Lab-CPhCz** and **Lab-DPhCzT** showed no emission upon turning off the UV light (Figure 1-18e). Interestingly, the impurity **Bd** itself does not exhibit RTP in the crystalline state, so they performed doping experiments with **CPhCz** and **DPhCzT** and their corresponding isomeric impurities **CPhBd** and **DPhBdT** at 0, 0.5, 1,5, 10 and 100 mol%, respectively. All doped systems examined

exhibited obvious RTP with different lifetimes and quantum yields. Even 0.01 mol% **CPhBd** and **DPhBdT** still showed RTP. They proposed that **Cz** and **Bd** have different electron-donating abilities and induce charge-separated states which can act as good triplet energy traps (Figure 1-18f). Importantly, they also speculate that, in addition to carbazole systems, impurity issues may also exist with dibenzothiophene and dibenzofuran derivatives. Very recently, Ma *et al.* also reported RTP induced by trace components.[82] They incorporate two host molecules **1BBI** and **DIB** with seven guest molecules to form bicomponent RTP systems (Figure 1-19). The RTP quantum yield of **1BBI**/**4BBI** is as high as 74.2% while the lifetime of **DIB**/**DMQI** can reach up to 430 ms. This work provides additional insight into the impact of impurities on RTP properties.

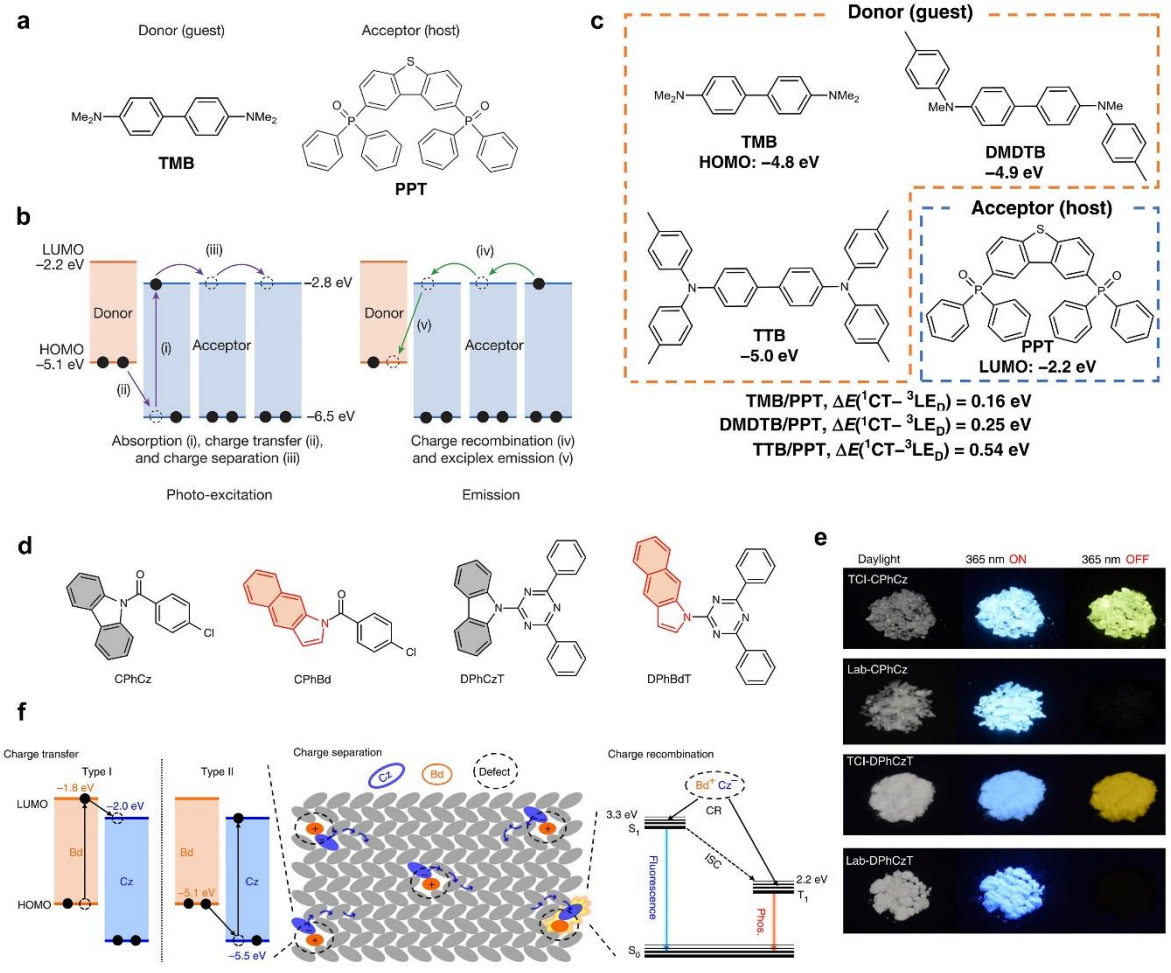

Figure 1-18. a) Chemical structures of **TMB** and **PPT**. b) Proposed mechanism of RTP. Reproduced with permission.[80] Copyright 2017, Nature Publishing Group. c) Chemical structures and HOMO or LUMO energy levels of the three electron donors (**TMB**, **DMDTB**, and **TTB**) and the electron acceptor (**PPT**). Reproduced with permission.[81] Copyright 2020, Nature Publishing Group. d) Molecular structures of **CPhCz**, **CPhBd**, **DPhCzT** and **DPhBdT**. e) Images of TCI- and laboratory synthesized **CPhCz** and **DPhCzT** crystalline powders before and after UV light irradiation. f) Proposed mechanism of RTP. Reproduced with permission.[26] Copyright 2020, Nature Publishing Group.

In addition to bicomponent systems for persistent RTP governed by the trap/detrap mechanism, some unintended discoveries also inspired researchers to explore the reason for their observations. Zhang's group unexpectedly found that a trace amount of side product **X** generated by a side reaction with the DMF solvent could induce persistent RTP when doped in the host **BrBID** (Figure 1-20a).[83] The quantum efficiency of the bicomponent system **X**/**BrBID** is up to 25.4% with a lifetime of 48 ms. After excluding the possibility of a single heavy atom effect, they proposed that in the crystalline matrix, molecule **X** could replace the position of **BrBID** which causes an n–σ* orbital interaction between a Br atom and an NMe_2 group, thus enhancing the spin–orbit coupling (Figure 1-20b). This work not only provides a new view on persistent RTP from bicomponent systems, but also confirms the role of trace

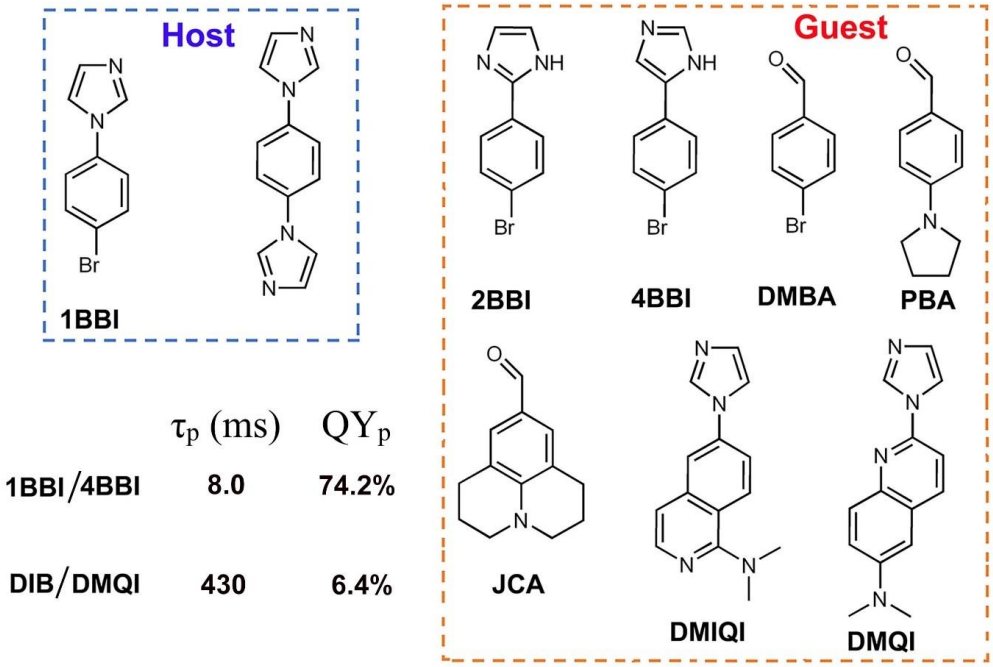

Figure 1-19. Molecular structures of selected host and guest molecules.

impurities and their dramatic influence on the observed RTP phenomenon, which might be mistaken for single molecular behavior. This strategy usually introduces strong intermolecular interactions into designed system, such as hydrogen bonding which could restrict and prevent molecular rotations and vibrations to a large extent, and thus reduce the nonradiative pathways and boost the phosphorescence efficiency. In 2011, Kim *et al*. reported an emitter/host system with ambient phosphorescent quantum yields reaching 55% by combining three concepts: the heavy atom effect, aromatic carbonyls and halogen bonding.[84] The emitter **Br6A** suffered from

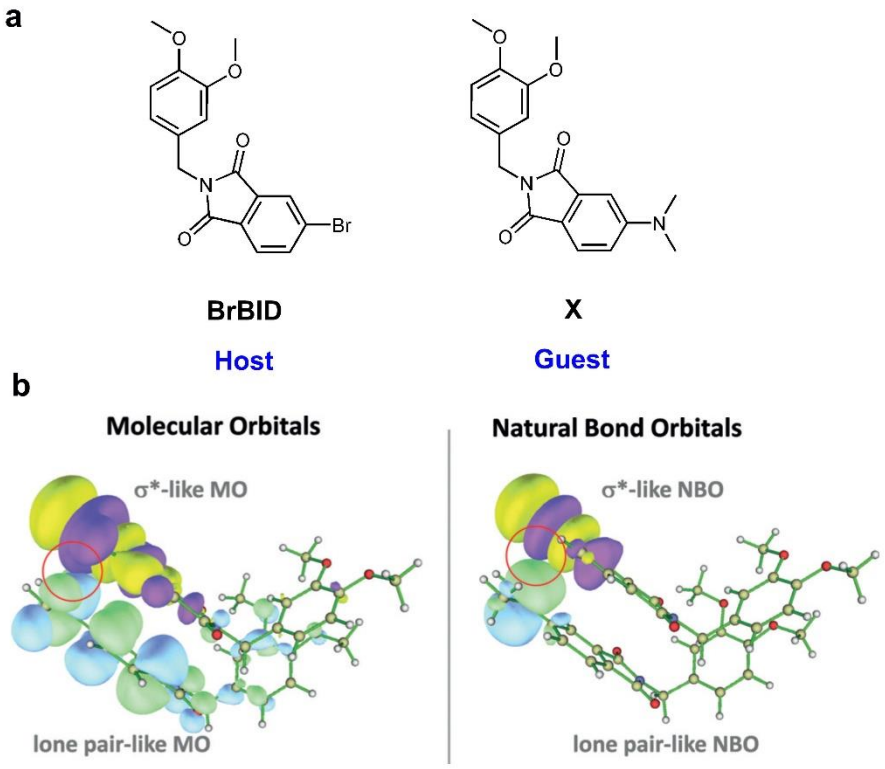

Figure 1-20. a) Molecular structures of **BrBID** and **X**. b) Molecular orbitals and natural bond orbitals of the proposed **BrBID** and **X** model in the crystal. Reproduced with permission.[83] Copyright 2020, Wiley-VCH.

luminescent quenching with moderate phosphorescence upon aggregation (Figure 1-21a and 1-21c). When the emitter, a brominated aromatic aldehyde (**Br6A**), is doped into the host crystal, a dibrominated analogue(**Br6**), self-quenching of the isolated **Br6A** molecules is successfully prevented. Therefore, the overall quantum yield is largely enhanced (Figure 1-21b and 1-21d). As the experiment results indicate, the brominated aromatic aldehyde emitters always show the best RTP performance when doped into a matrix of their dibrominated analogues. Moreover, the aldehyde groups are close to bromine atoms, which promotes the population of triplet states and activates phosphorescence emission. In addition to **Br6A**/**Br6** system, the authors also examined the doping effect of the emitters **Br(5-8)A** and the hosts **Br(5-8).** These systems display phosphorescence quantum yields ranging from 9% to 55% (Figure 1-21e and 1-21f).[85] In 2013, Hirata et al. successfully achieved blue-green-red persistent host–guest RTP materials of which the phosphorescence lifetime is as long as 1 s and the quantum efficiency is as high as 10% under ambient conditions (Figure 1-22a and 1-22b).[86] The secondary amino-substituted highly deuterated aromatic hydrocarbon was the guest while the hydroxy steroid was selected as the host to minimize the triplet quenching rate caused by oxygen permeation and diffusional motion. This is achieved by the introduction of a rigid matrix. According to the

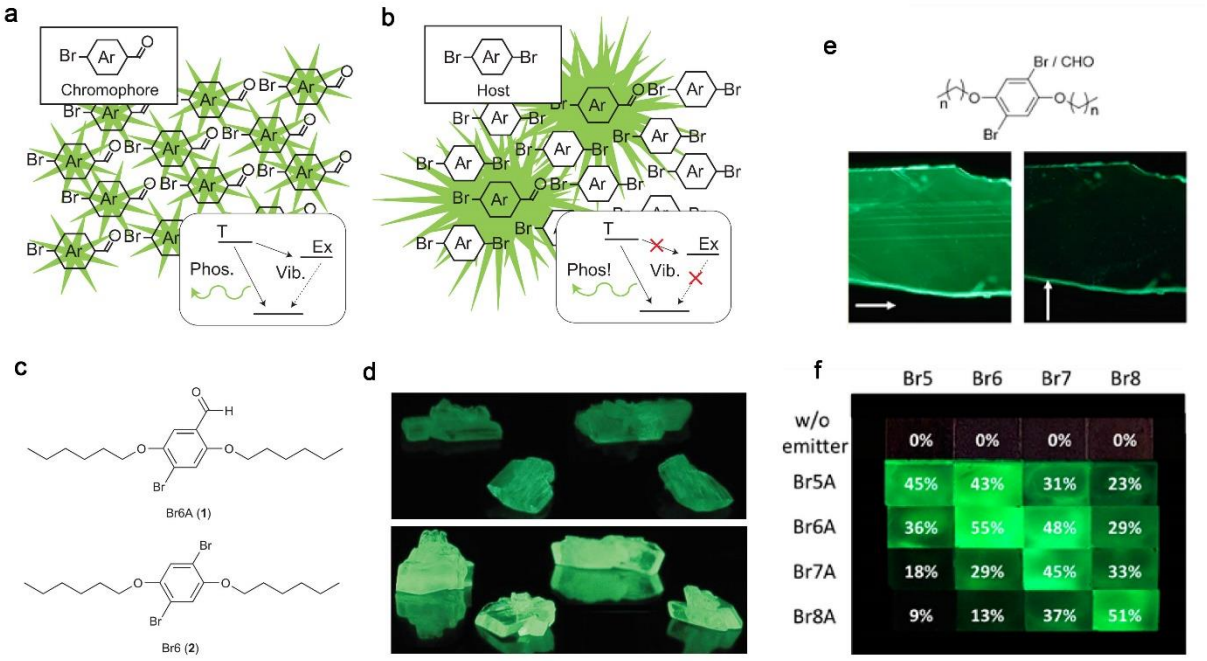

Figure 1-21. a) The chromophore is a brominated aromatic aldehyde. b) The host is a dibrominated analogue of the chromophore. c) Molecular structures of **Br6A** and **Br6**. d) Images of crystalline **Br6A** and **Br6** under 365 nm irradiation. Reproduced with permission.[84] Copyright 2011, Nature Publishing Group. e) Chemical structures of **Br(5-8)A** and **Br(5-8)**. Polarized phosphorescent images from a thin **Br6A**/**Br6** crystal. f) Photograph of drop cast crystals made of host and guest molecules irradiated under 365 nm irradiation. Reproduced with permission.[85] Copyright 2014, American Chemical Society.

design strategy, they also developed a reversible recording material, which responds to heating by utilizing **Dye 1** as the guest, **Cholesterol** as the host matrix and a phenol derivative **THEB** as the dispersant (Figure 1-22c).[87] The recording state was achieved by exposing the host andguest system to UV light. The resulting blue-green phosphorescence can be completely erased by heating the sample to 90 °C for 1 min. Recovery can be achieved by heating the sample to 150 °C. By continuously repeating the process of recording and erasing, a reversible thermal recording material was demonstrated (Figure 1-22d). In 2016, the authors applied the host-guest afterglow system in OLED devices, which gave a maximum external quantum efficiency (ηEQE) of ca. 1%.[88] **CzSte** acts as a host and **DMFLTPD-d36** was selected as an emitter in co-deposited films, achieving persistent RTP (τ_p = 0.61 s) (Figure 1-22e). Using the **DMFLTPD-d36**/**CzSte** system as the emitter layer in OLEDs, the device showed green after glow phosphorescence (τ_p = 0.39 s) (Figure 22f). They proposed that the hydrophobic steroid moiety of **CzSte** provides strong intermolecular interactions and forms a rigid host matrix, prohibiting molecular movements to some extent and suppressing nonradiative pathways of the guest molecules.

In 2016, Wang and coworkers developed a host-guest system with a unique greenish RTP which could last almost 1 s under ambient conditions.[89] They inserted the guest N-phenylnaphthalen-2-amine (**PNA**) into the host 4,4'-dibromobiphenyl (**DBBP**) with a mass ratio of 1:100 (Figure 1-22a). The Φ_{PL} value of the **PNA/DBBP**-doped sample was up to 30%, in which phosphorescence contributes 53% of the total emission, resulting in a very high phosphorescence quantum yield (Φ_p = 17%) (Figure 1-23b). Their study indicates that the host **DBBP** crystal serves as a rigid matrix, which isolates the emitter molecules and avoids emission quenching by efficiently reducing nonradiative decay. In 2018, Fu *et al*. tried doping two β-iminoenamine-BF_2 derivatives as guests (**S-2CN** and **S-2I**) into a 4-iodoaniline host (**I–Ph–NH_2**, Figure 1-23c) realizing bright red RTP emissions under ambient conditions.[90] It was proposed that strong hydrogen bonding in the crystal of the host-guest system contributes to the efficient RTP. Interesting, **S-2I/I–Ph–NH_2** is responsive to HCl vapor. Upon exposure to HCl, the existing hydrogen bonding of **S-2I**···**I–Ph–NH_2** transformed into **I–Ph–NH_2·HCl** and the red RTP emission is turned off. Because a cyano group has a stronger electron-accepting ability,

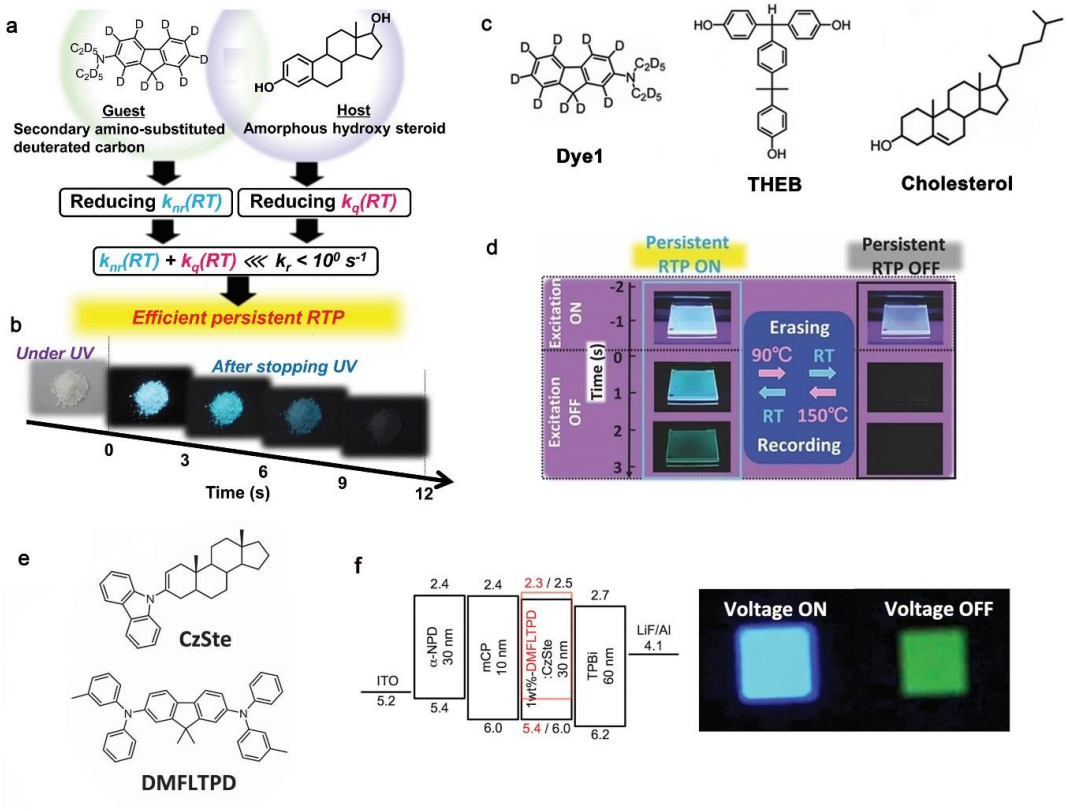

Figure 1-22. a) Material design for guest and host structures. b) After glow photographs. Reproduced with permission.[86] Copyright 2013, Wiley-VCH. c) Chemical structures of compound **1**, **THEB**, and **cholesterol**. d) Reversible thermal recording and erasing using persistent RTP. The recording material was composed of 1.0 wt% **1**, 9.0 wt% **THEB**, and 90 wt% cholesterol. Reproduced with permission.[87] Copyright 2013, Wiley-VCH. e) Chemical structures of **CzSte** and **DMFLTPD**. f) OLED structure showing energy levels in eV (left) and photographs of EL during and after electrical excitation of a device containing **CzSte** as a host (right). Reproduced with permission.[88] Copyright 2016, Wiley-VCH.

S-2CN /I–Ph–NH_2 still retains its bright RTP emission. According to the above observations, the host-guest doped systems are potential candidates for applications in bio-imaging and anti-counterfeiting materials. In the same year, Tian and coworkers designed a host-guest system which exhibits multicolor emission, from yellow to purple and even shows white light emission.[91] The guest is a linear blue-fluorescent **AC** bearing a coumarin moiety while the host is a phosphorescent β-cyclodextrin derivative **BrNp-β-CD** (Figure 1-23d). UV−Vis absorption spectra revealed that the host-guest complex interacted in a 1:1 stoichiometry. When the host-guest complex with varying ratios was excited at different wavelengths, the PL emission and the CIE coordinate values continuously changed. The CIE coordinates (0.29, 0.33) of white-light emission were achieved when the host **BrNp-β-CD** was doped with 0.1 equivalent of **AC** and excited at 295 nm. The coordinate is quite similar to the standard white color value (0.33, 0.33). This work provides a new method in the search for pure white-light emitting materials.

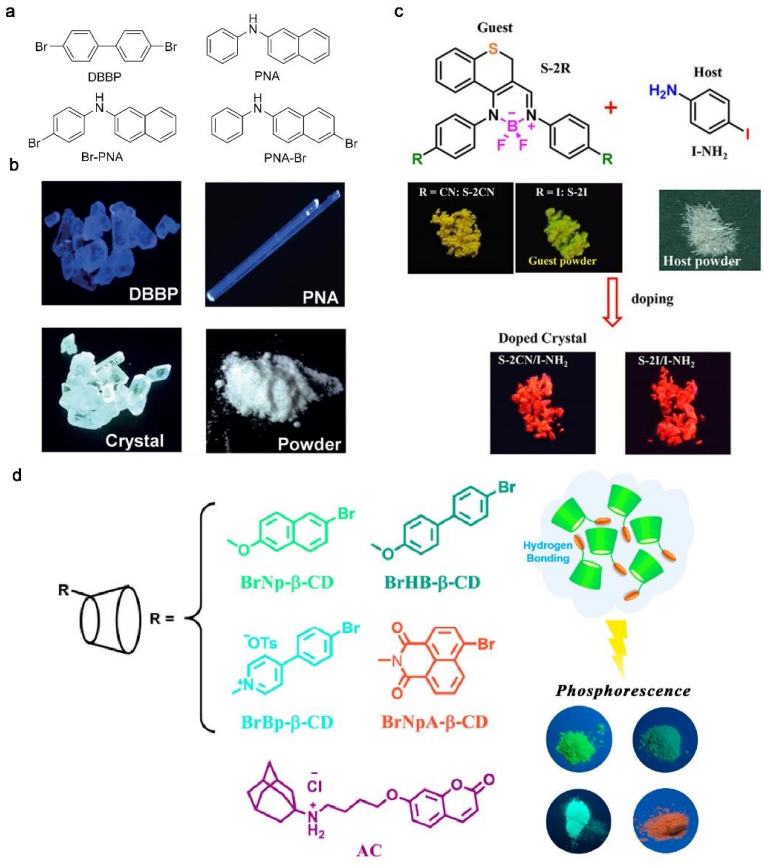

Figure 1-23. a) Molecular structures of host and guest. b) Images of crystalline **DBBP**, **PNA**, **PNA** doped **DBBP** (1 % mass ratio), and **PNA/DBBP** (1 % mass ratio) irradiated at 365 nm. Reproduced with permission.[89] Copyright 2016, Wiley-VCH. c) Chemical structures of **S-2CN**, **S-2I** and **I-Ph-NH2**. Photographs of host powder crystals under ambient light; images of guest powder (top) and doped system (bottom) under 365 nm irradiation. Reproduced with permission.[90] Copyright 2018, Wiley-VCH. d) Molecular structures of RTP emissive **BrNp-**, **BrHB-**, **BrBp-**, and **BrNpA-β-CD** and guest molecule **AC**. Reproduced with permission.[91] Copyright 2018, American Chemical Society.

In 2019, Tang et al. selected **PCP**, **PA**, and 1,2-**DCB** as host matrices while 1,8-naphthalic anhydride **NA** (Figure 1-24a) was used as the guest.[92] Both host and guest molecules are electron-deficient in order to prevent self-quenching from PET (photo-induced electron transfer). The phosphorescence lifetime of the doped system can reach 600 ms with a total quantum yield of over 20%. According to femtosecond transient absorption spectra, a small amount of guest molecules in the mixture can substantially enhance the rate of ISC of the host. Moreover, they proposed that cluster excitons formed by neighboring host and guest molecules produced transient species, which can be experimentally detected and then immediately relax to a stable localized triplet state of the guest (Figure 1-24b).

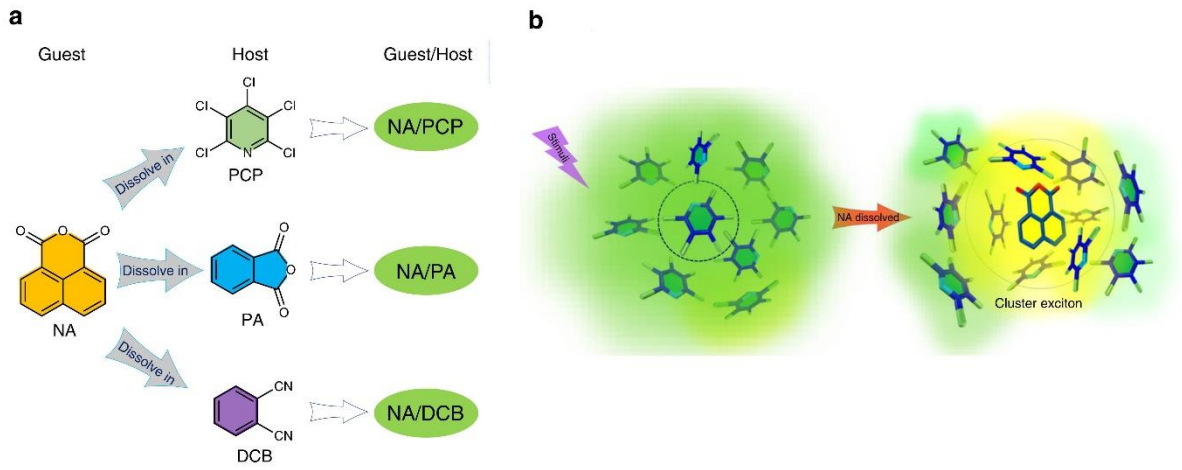

Figure 1-24. a) Chemical structures of **PCP** (pentachloropyridine), **PA** (phthalic anhydride), **DCB** (1,2-dicyanobenzene) and **NA** (1,8-naphthalic anhydride). b) Mechanism and application of the guest/host system. Reproduced with permission.[92] Copyright 2019, Nature Publishing Group.

1.4.2 RTP from Supramolecular Systems

Doping organic materials into polymer films is also a popular method to realize efficient RTP, as the polymer not only provides a rigid environment, but also forms intermolecular interactions with the embedded organic molecules. In 2013, Kim's group reported a temperature sensor by doping purely organic **Br6A** into a PMMA film (Figure 1-25a).[93] In addition, polymer tacticity helps to improve the quantum efficiency of the doped system (Figure 1-25b). Embedding **Br6A** in isotactic PMMA (iPMMA) results in a relatively high phosphorescence quantum yield of 7.5%, that is ten times higher compared to **Br6A** in atactic PMMA (aPMMA) or syndiotactic PMMA (sPMMA) at the same doping level. Moreover, they hypothesized that the quantum yield of the phosphorescence depends on the degree of β-relaxation. Therefore, they explained the tuning of the phosphorescence quantum yield by suppressing the β-relaxation, which should be prone to temperature changes. They then also utilized phosphor **G1** doped into a poly(vinyl

alcohol) (PVA) matrix (Figure 1-25c and 1-25d), which greatly enhanced the phosphorescence efficiency to 24% by the introduction of strong halogen and hydrogen bonds.[94] Interestingly, when the surface of the **G1–PVA** film was treated with water, the green phosphorescence transformed into blue fluorescence, which may be useful for ratiometric water sensing. In 2019, Reineke's group first reported visible-light activated RTP from five hole-transporting materials (Figure 1-25e) dispersed inside a PMMA film with lifetimes up to 700 ms.[95] The doped films can be used for printing of information through straightforward erasing/rewriting processes depending on the concentration of oxygen inside the films (Figure 1-25f). Su's group developed a simple molecule **G**, modified by six benzoic acid moieties and select poly(vinyl alcohol) (PVA) as the polymer matrix (Figure 1-26a).[96] Interestingly, **G**-doped PVA films exhibit RTP lifetimes as long as 0.28 s and quantum efficiencies as high as 2.85%. After irradiation for 65

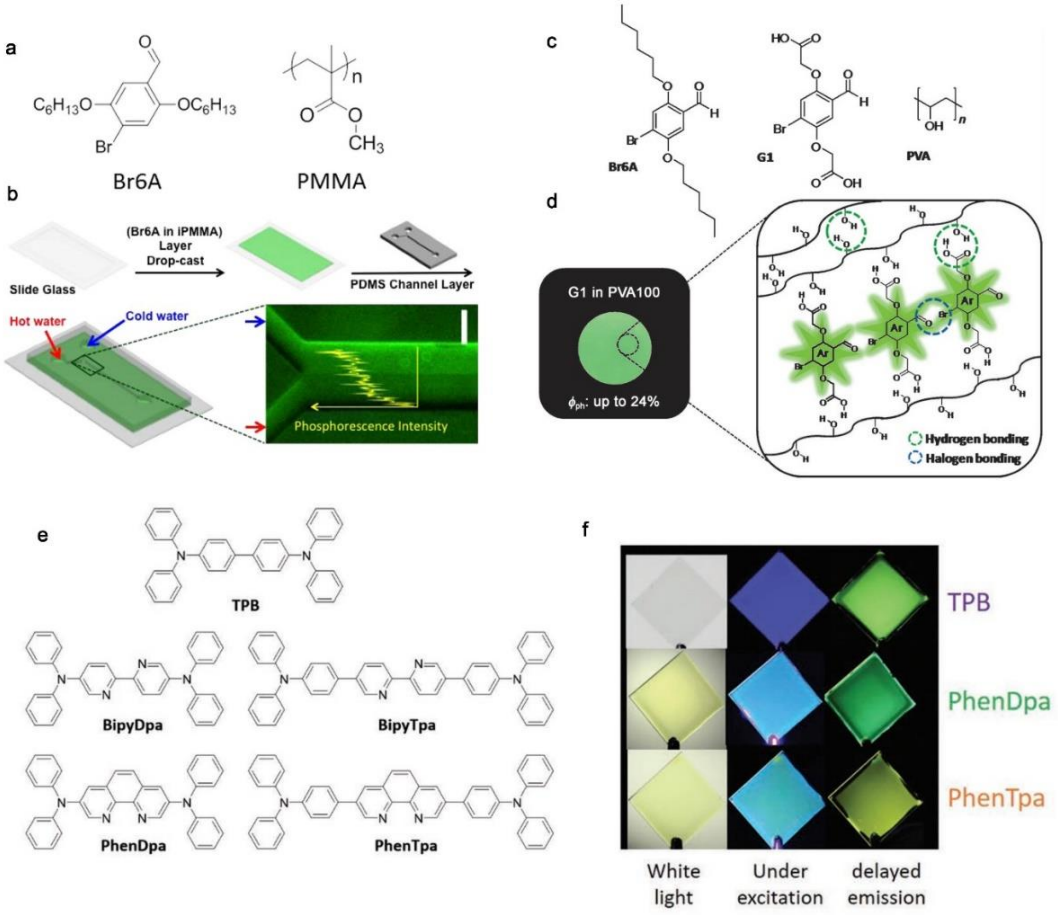

Figure 1-25. a) Structure of **Br6A** and PMMA polymer. b) Fabrication method and the microfluidic device prepared from an emitting layer (**Br6A** in iPMMA) and a PDMS channel layer. Reproduced with permission.[93] Copyright 2013, American Chemical Society. c) Chemical structures of **Br6A**, **G1**, and **PVA**. d) Phosphorescence image of **G1** embedded in **PVA100** under UV light (λ = 365 nm). Reproduced with permission.[94] Copyright 2014, Wiley-VCH. e) Chemical structures of targeted molecules. f) Photographs of targeted molecules under sunlight (left), under excitation (middle) (λ_{ex} = 365 nm for **TPB** and λ_{ex} = 420 nm for **PhenDpa** and **PhenTpa**), and after excitation (right). Reproduced with permission.[95] Copyright 2019, Wiley-VCH.

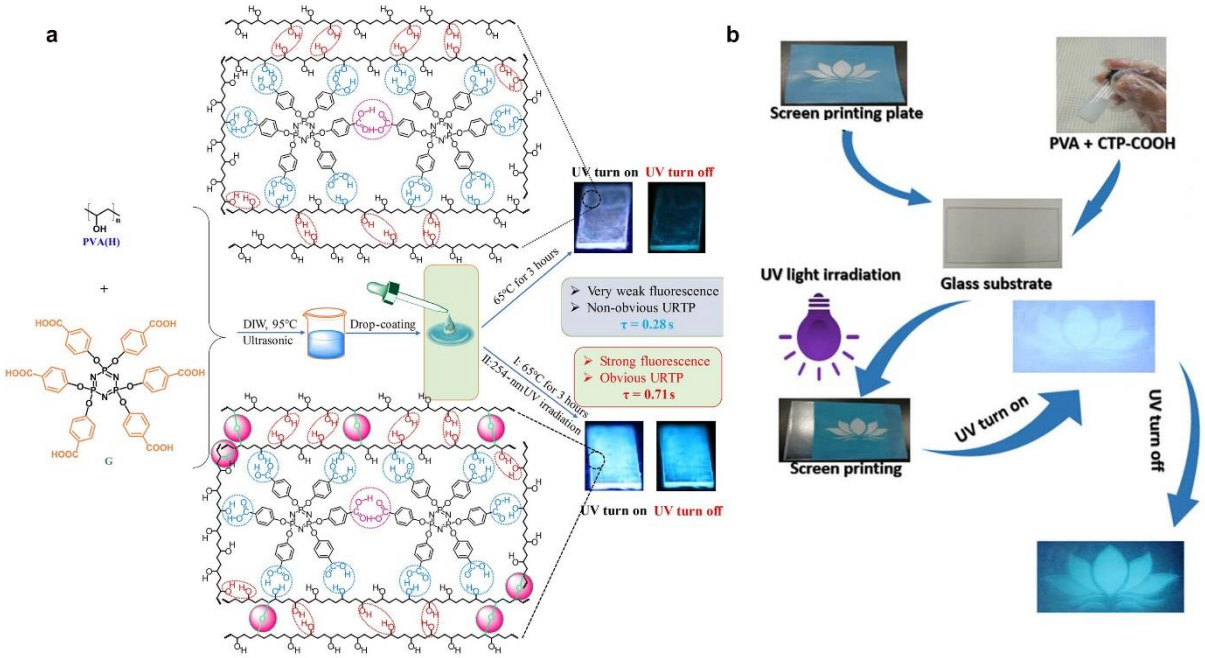

Figure 1-26. a) Molecular structures of **G** and **PVA** and the fabrication method for G-doped **PVA** films for RTP. b) Green screen printing without any inks using the lotus flower screen plate. Reproduced with permission.[96] Copyright 2018, Science Publishing Group.

min with 254 nm light, the corresponding values of τ_p and Φ_p increased to 0.71 s and 11.23%, respectively. They proposed that hydrogen bonds between the PVA matrix and **G** suppress molecular movement and also boost the ISC process. Under UV light, cross-links formed between PVA chains further reduce nonradiative decay in the films. By changing the irradiation time, they successfully utilized a green screen-printing technology in an anti-counterfeiting application without using any inks (Figure 1-26b).

Compared to doping molecules into a polymer matrix, the formation of covalent bonds between polymer and luminophore is a superior way to further restrict nonradiative relaxation pathways because of the more rigid environment. In 2015, Kim *et al*. reported a diene-modified phosphor (**DA1**) connected with the polymer PFMA (Figure 1-27a) by Diels–Alder reaction.[97] The optimized rigid matrix exhibits persistent RTP with the value of Φ_p up to ca. 28%, which is several-times higher than that of the doped system without cross-linking. They also developed an oxygen sensor from core-shell polymer nanoparticles (NPs).[98] They choose polystyrene (**PS**) as the matrix and water soluble and biocompatible poly(2-methyl-2-oxazoline) (**PMeOx**) as the outer shell, connected by a phosphor (Figure 1-27b). The resulting NPs show an oxygen detection limit of 60 nM which can be applied not only in the gas phase but also in aqueous solution (Figure 1-27c). In 2020, Zhao and coworkers developed a series of radical cross-linked

PDBA (Figure 1-27e) by multicomponent copolymerization of acrylic acid, vinyl-functionalized naphthalene, and benzene with different molar feed ratio, initiated by 2-azoisobutyronitrile.[99] Interestingly, when the excitation wavelength is varied from 254 to 370 nm these copolymers show multicolor emissions from blue to yellow (Figure 1-27d). In addition, the phosphorescent lifetime is up to 1.2 s with a maximum value of Φ_p as high as 37.5% under ambient conditions. They proposed that numerous carbonyl and hydroxyl groups, combined with the tight copolymer environment, not only boost the ISC rate but also restrict the nonradiative decay of excited triplet state by forming hydrogen bonds. They demonstrated the use of a copolymer for security printing (Figure 1-27f).

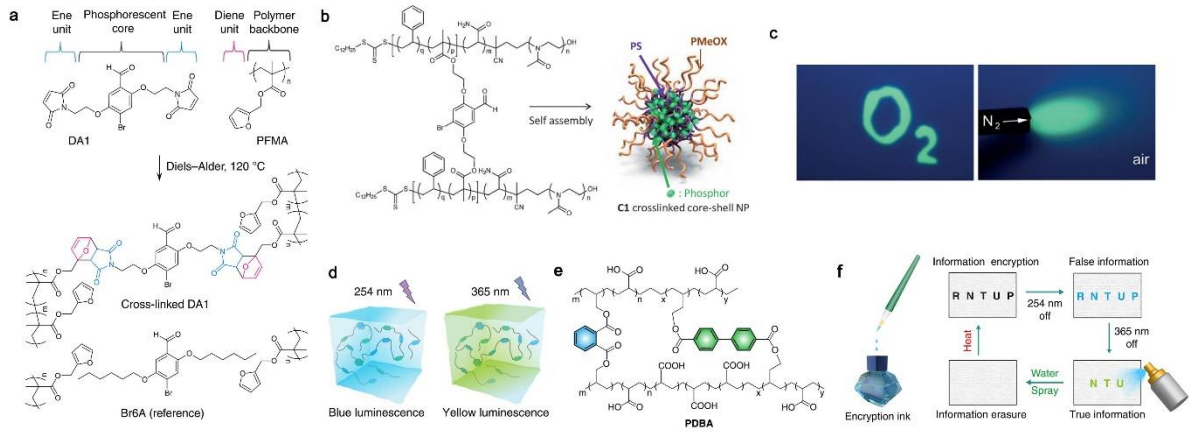

Figure 1-27. a) Chemical structures of **DA1**, **PFMA**, cross-linked **DA1** and **Br6A**. Reproduced with permission.[97] Copyright 2015, Nature Publishing Group. b) Description of **C1**-crosslinked NPs. c) Images upon illumination of the planar optical sensor with the 366 nm line of a UV-lamp. Bright green phosphorescence indicates the areas of the sensor soaked with an anoxic aqueous solution for the left image and the area of the sensor deoxygenated with a flow of nitrogen (bottom image). Reproduced with permission.[98] Copyright 2020, Nature Publishing Group. d) Excitation dependent RTP (λ_{ex} = 254 and 365 nm) of multi-component copolymer under ambient conditions. e) Molecular structure of polymer **PDBA**. f) Process of information encryption by using the multi-component copolymer **PDNA** (NTU) and **PDA** (RP) as encryption ink under ambient conditions. Reproduced with permission.[99] Copyright 2017, Wiley-VCH.

Self-assembly is also a useful approach to build a rigid molecular framework to suppress nonradiative relaxation for RTP. In 2018, Huang's group designed a multi-component supramolecular system (**MA-IPA**) containing aromatic acids and melamine (**MA**) (Figure 1-28a) in aqueous solution by self-assembly.[13] The supermolecule constructed shows a persistent lifetime of 1.91 s and Φ_p of 24.3%. Strong hydrogen bonding between isophthalic acid and melamine molecules help to realize efficient RTP. They successfully printed **MA-IPA** materials on a piece of filter paper to fabricate a QR code which can be recognized when the UV light was turned off (Figure 1-28b). Two years later, Ma et al. constructed the self-

assembled system **TBP-CB[8]** by applying a 1:1 ratio of cucurbit[8]uril **CB[8]** and a triazine derivative **TBP**, and observed a phosphorescence lifetime of 0.190 ms in aqueous solution

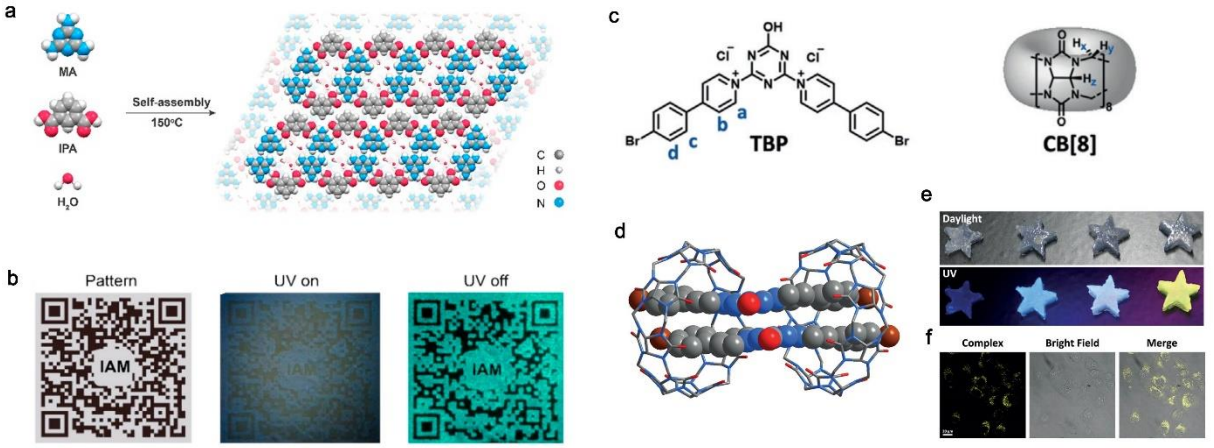

Figure 1-28. a) Design concept of supramolecular architecture. b) Application of ultralong phosphors in a QR code. Reproduced with permission.[13] Copyright 2018, American Chemical Society. c) Structures of **CB[8]** and **TBP**. d) Side view of crystalline structure of the **$(TBP)_2$·CB[8]$_2$** assembly. C, gray; N, blue; O, red; Br, brown. e) Pictures of multicolor hydrogels irradiated by sunlight and 365 nm light. f) Luminescent images of HeLa cells treated with **TBP-CB[8]** complex (left), bright field (middle), and merge (right) confocal . Reproduced with permission.[100] Copyright 2020, Wiley-VCH.

(Figure 1-28c and 1-28d).[100] They proposed that dipole–dipole interactions, hydrophobic interactions and hydrogen bonding in the stacking patterns of **CB[8]** and **TBP** efficiently suppressed the molecular vibrations and rotations. In addition, the photoluminescence emission color of the **TBP** aqueous solution changes upon continuous addition of **CB[8]**. According to this phenomenon, they obtained three different hydrogels which show blue, white, and yellow emission when irradiated by 365 nm light (Figure 1-28e). They also examined bio-imaging applications in HeLa cells.

1.5 RTP from Carbon Dots (CDs)

Because of their low toxicity, chemical stability and eco-friendly advantages, carbon dots (CDs) are used in a variety of applications in bioimaging, LEDs and sensors. However, most research treats CDs as fluorescent nanomaterials, and seldom were their RTP properties considered for applications. In 2016, Yang's group mixed N-doped CDs (NCDs) with melting recrystallization urea and biuret matrices through a one-pot process.[101] The multi-component matrices provide efficient hydrogen bonding and a rigid environment to suppress nonradiative decay (Figure 1-29a). More importantly, they proposed that C=N double bonds at the surface of NCDs could decrease the ΔE_{ST} and boost electronic transitions by creating new energy levels. In 2018, Lin *et al*. first introduced RTP polymer carbon dots (Figure 1-29b) through heating ethylenediamine

and phosphoric acid.[102] The green afterglow can remain for almost 10 s and the phosphorescence lifetime is up to 1.39 s (Figure 1-29c). Heating ethylenediamine and phosphoric acid at 180 °C formed only fluorescent CDs. Upon increasing the temperature to 280 °C, further crosslinking reactions in the F-CDs occurred, resulting in more compact P-CDs. On one hand, the denser structure could effectively restrict vibrations and rotations. On the other hand, the N- and P-doping elements bearing lone pairs provided n→π* transitions to populate triplet states and thus accelerate the rate of ISC. Two years later, in 2020, they also developed TA-CDs (Figure 1-29d) with aggregation-induced RTP properties.[103] Interestingly, they successfully applied TA-CD dispersions as an anti-counterfeiting agent and, in addition, the RTP is responsive to moisture (Figure 1-29e). Shi *et al*. also reported persistent RTP from CDs induced by the presence of water.[104] They proposed that water could build robust networks between CDs and cyanuric acid (CA) via hydrogen bonds (Figure 1-29f). The rigid matrix effectively restricts molecular movement and thus reduces nonradiative decay, resulting in a long phosphorescence lifetime (687 ms). Moreover, multiple C=O bonds in the entire CD-CA system increase transitions of n→π* type and greatly enhance the ISC process. They also applied CD-CA suspensions to detect Fe^{3+} ions in water. The phosphorescence intensity gradually decreased with the addition of Fe^{3+} ions. This method, based on phosphorescence quenching, has a detection limit of 32 μM for Fe^{3+}, making it a good candidate for ion sensor applications. In 2019, Rogach *et al*. developed color-tunable powdered CDs with RTP

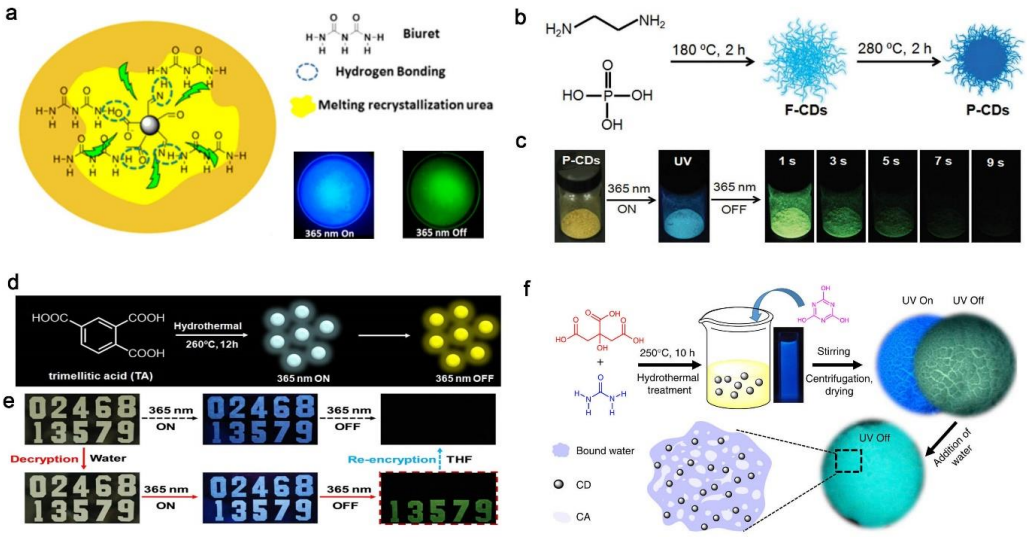

Figure 1-29. a) NCDs are inserted into urea and biuret matrices. Reproduced with permission.[101] Copyright 2016, American Chemical Society. b) Procedures for the preparation of **F-CDs** and **P-CDs**. c) Afterglow images of the **P-CD** powder. Reproduced with permission.[102] Copyright 2018, Wiley-VCH. d) The synthetic method for preparing **TA-CDs**, and RTP photographs irradiated by UV light. e) Information encryption and decryption processes using **TA-CDs** and interference CDs inks. Reproduced with permission.[103] Copyright 2020, Wiley-VCH. f) Preparation method for the CDs and the **CD-CA** system. Reproduced with permission.[104] Copyright 2018, Nature Publishing Group.

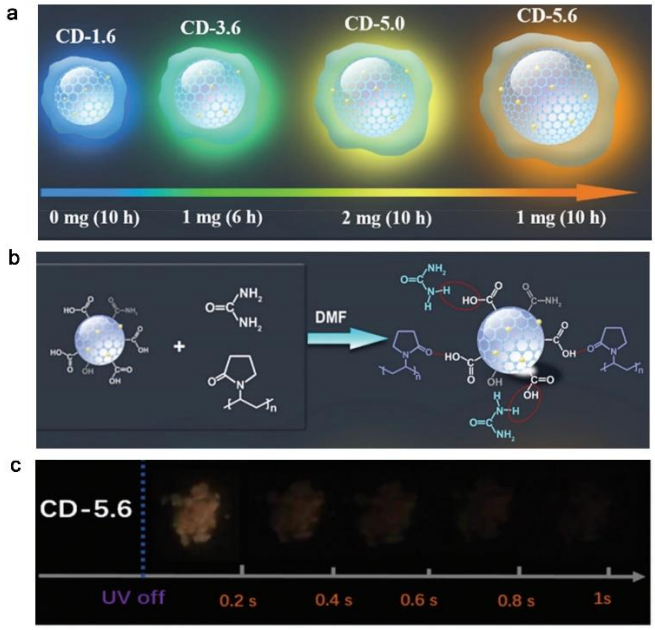

Figure 1-30. a) Four different CD sizes. b) Seeded growth reaction for formation of CDs. c) Afterglow images of the CD-5.6 powders under irradiation at 365 nm. Reproduced with permission.[15] Copyright 2019, Wiley-VCH.

properties by controlling CD growth (Figure 1-30a).[15] The RTP phenomenon is enhanced by a variety of nitrogen-containing moieties on the surface, such as $–NH_2$, C=N and C–N bonds (Figure 1-30b). In addition, the polyvinylpyrrolidone polymer chains protect the CDs from coming into contact with quenching species therefore preventing nonradiative pathways, especially in a CD-5.6 powder with large nanoparticles (Figure 1-30c). Finally, they also showed an example of the utilization of CD-5.6 for data encryption.

1.6 Outlook

In order to achieve persistent RTP materials, much effort has been devoted to diversified molecular design in both single molecule and multi-component systems. Intense study has shown that heteroatoms (N, O and S) or corresponding functional groups are especially useful in realizing efficient RTP.[105] Therefore, carbazole,[106] indoline,[107] quinoline,[108] phenothiazine[109] and their derivatives[110] account for the majority of RTP luminophores. The reason is simple: these atoms and related moieties bear lone pairs which enhance the rate of the ISC process through El-Sayed's rule.[111] In addition, the active sites in these molecules make it easy to fabricate the desired phosphors and the total cost is quite low. We also point out that 3-coordinate boron, with an empty p_z orbital, can also accelerate ISC processes via transitions between (σ, B p) and (π, B p), indicating that introducing lone pairs is only one way to enhance ISC.[22] This new finding makes boron-containing compounds, especially triarylboranes, good candidates for RTP luminophores. Considering the development of efficient RTP materials in

the future, a systematic study of existing systems is essential to help us clearly elucidate the mechanism behind these photoluminescent properties. However, the types of RTP systems with high performance are still quite limited. The discovery of new persistent RTP systems is always inspiring and will also expand our insight into the origin of purely organic phosphorescent phenomena.

The main issue is to enhance the RTP lifetime and efficiency at the same time. Based on our current understanding, there are mainly two strategies to achieve this aim. One is to populate the triplet state by speeding up the ISC process. What we address here are commonly used heavy atoms which can enhance SOC. From the perspective of cost and environmental issues, the synthetic expense of RTP luminophores with heavy atoms is higher and they are not as environmentally friendly. In addition, it is hard to achieve a balance between phosphorescence lifetime and quantum yield, as introducing heavy atoms also boosts radiative decay rates from the triplet state, which shortens the lifetime, therefore, the trend is to omit heavy atoms in the design of RTP systems. Another strategy is to restrict the non-radiative pathways, as RTP performance not only relies on molecular structure, but also depends on the aggregation state. Crystallization methods play a major role in supressing non-radiative decay, which requires rigid paking modes and strong intermolecar interactions in the crystalline matrix.[112] To achieve an ideal crystalline envronment with effficent RTP is quite challenging and currently unpreditable through rational molecular design. It also limits practical use if high performance of RTP is only possible in the crystalline state. At the same time it is crucial to reduce the trap concentration in a crystal which is an important factor for triplet quenching, which can be achieved by using crystals of the highest purity.[113] As an alternative, amorphous RTP materials such as polymers,[114] are more competitive due to their easier processibility and high environmental stability, although the intrinsic mechanism still needs systematic study and further exploration. Another approach is to develop host-guest systems which do not require a strict crystaline enviornment. More importantly, this enables otherwise non-emissive luminophores to emit strong and persistent RTP under ambient conditions, which greatly enlarges the variety of RTP phosphors. Host-guest systems are quite promissing, but the underlying driving force needs further clarification for rational design.

Because of their superior lifetimes, RTP materials are widely used in security printing and bioimaging fileds.[115] Compared to fluorescence, phosphorescence enabling long afterglow which cannot be replicated by fluorescent dyes, and is helpful to remove short-lived background emissions.[109] In order to realize anti-counterfeiting applications of RTP materials in real life,

more effort should be put into industrial development and commercialization. For future developments in bioimaging, it is vital to explore red and NIR RTP phosphores because red light emission provides deeper tissue penetration and less photon scattering. Due to their bright phosphorescence, RTP phosphores have also been applied in OLEDs.[105] Although intense work was conducted on PHOLEDs, deep blue and white light devices based on RTP materials are still a challenge. So far, there have been less applications in sensing compared to other fields. It is necessary to find new candidates and to improve detection limits at the same, for practical use.

Recently, many concerns have been raised regarding impurities in purely organic RTP materials, especially in carbazole-based phosphors. We stress that much work has already proven that confirmed pure carbazole-based luminophors show persistent RTP phenomenon. However, it is necessary to re-examine some of the previously reported examples, as trace impurities greatly influence their photophysical properties. For future work, we suggest that, in purely organic RTP systems, it is critical to re-examine their photophysical properties after further purifications of the sample, such as multiple recrystallizations. While it may not be possible to remove the impurity completely by normal purification methods, its reduction in the sample should result in obvious changes in phosphorescence emission, lifetime and quantum yield. The varying results induced by different amounts of impurities are already indicated in many reports, make this purification step necessary for reliable results.

1.7 Conclusions

Benefiting from the high degree of structural diversity of organic molecules, a variety of room temperature phosphors have been designed and synthesized in the last two decades. Their applications in oxygen sensors, security printing and biological imaging have been widely tested. There are mainly two basic approaches to achieving efficient RTP. The first is to focus on enhancing ISC as equations (2) and (3) indicate that phosphorescence largely depends on the rate of the ISC process. Therefore, elements bearing lone pairs (N, O, S) or their corresponding functional groups are utilized for the realization of room temperature phosphors. The second strategy is to reduce the nonradiative decay rate of the triplet state(s) which has a direct effect on the efficiency of phosphorescence. A popular method is to dope luminophores into a polymer matrix or to construct host-guest systems. More recently, the introduction of carbon dots (CDs) has received much attention due to the advantages of CDs, such as easy modification and chemical stability. However, it is still difficult to develop a universal and

systematic method to predict and prepare RTP materials. In order to broaden the range of practical applications of the organic RTP materials, the mechanism of phosphorescent emission needs to be further explored. Moreover, to develop high performance RTP materials bearing excellent values of τ_p and Φ_p simultaneously remains a formidable challenge as they are mutually influenced. However, new breakthroughs can be expected and new types of organic RTP materials are likely to result. Finally, we note again that extreme care must be taken to assure the purity of all compounds employed, as even trace impurities can give rise to anomalous results. Thus, some of the systems which have been reported probably warrant re-examination by other researchers.

1.8 Reference

[1] H. Chen, X. Yao, X. Ma, H. Tian, *Adv. Opt. Mater.* **2016**, *4*, 1397-1401.

[2] S. Reineke, F. Lindner, G. Schwartz, N. Seidler, K. Walzer, B. Lussem, K. Leo, *Nature* **2009**, *459*, 234-238.

[3] A. Kishimura, T. Yamashita, K. Yamaguchi, T. Aida, *Nat. Mater.* **2005**, *4*, 546-549.

[4] L. Huang, C. Qian, Z. Ma, *Chem. Eur. J.* **2020**, *26*, 11914-11930.

[5] S. Xu, R. Chen, C. Zheng, W. Huang, *Adv. Mater.* **2016**, *28*, 9920-9940.

[6] J. Zhao, W. Wu, J. Sun, S. Guo, *Chem. Soc. Rev.* **2013**, *42*, 5323-5351.

[7] S. Mukherjee, P. Thilagar, *Chem. Commun.* **2015**, *51*, 10988-11003.

[8] X. Ma, J. Wang, H. Tian, *Acc. Chem. Res.* **2019**, *52*, 738-748.

[9] T. Zhang, X. Ma, H. Wu, L. Zhu, Y. Zhao, H. Tian, *Angew. Chem. Int. Ed.* **2020**, *59*, 11206-11216.

[10] J. Wang, C. Wang, Y. Gong, Q. Liao, M. Han, T. Jiang, Q. Dang, Y. Li, Q. Li, Z. Li, *Angew. Chem. Int. Ed.* **2018**, *57*, 16821-16826.

[11] E. Hamzehpoor, D. F. Perepichka, *Angew. Chem. Int. Ed.* **2020**, *59*, 9977-9981.

[12] T. Wang, C. Zhou, X. Zhang, D. Xu, *Poly. Chem.* **2018**, *9*, 1303-1308.

[13] L. Bian, H. Shi, X. Wang, K. Ling, H. Ma, M. Li, Z. Cheng, C. Ma, S. Cai, Q. Wu, N. Gan, X. Xu, Z. An, W. Huang, *J. Am. Chem. Soc.* **2018**, *140*, 10734-10739.

[14] T. Ono, A. Taema, A. Goto, Y. Hisaeda, *Chem. Eur. J.* **2018**, *24*, 17487-17496.

[15] J. Zhu, X. Bai, X. Chen, H. Shao, Y. Zhai, G. Pan, H. Zhang, E. V. Ushakova, Y. Zhang, H. Song, A. L. Rogach, *Adv. Opt. Mater.* **2019**, *7*, 1801599.

[16] T. J. Penfold, E. Gindensperger, C. Daniel, C. M. Marian, *Chem. Rev.* **2018**, *118*, 6975–7025.

[17] H. Matsuoka, M. Retegan, L. Schmitt, S. Hoger, F. Neese, O. Schiemann, *J. Am. Chem. Soc.* **2017**, *139*, 12968-12975.

[18] J. S. Ward, R. S. Nobuyasu, M. A. Fox, A. S. Batsanov, J. Santos, F. B. Dias, M. R. Bryce, *J. Org. Chem.* **2018**, *83*, 14431-14442.

[19] R. Joshi, O. R. Meitei, M. Jadhao, H. Kumar, S. K. Ghosh, *Phys. Chem. Chem. Phys.* **2016**, *18*, 27910-27920.

[20] S. Kuno, T. Kanamori, Z. Yijing, H. Ohtani, H. Yuasa, *ChemPhotoChem* **2017**, *1*, 102-106.

[21] J. Yang, Z. Ren, Z. Xie, Y. Liu, C. Wang, Y. Xie, Q. Peng, B. Xu, W. Tian, F. Zhang, Z. Chi, Q. Li, Z. Li, *Angew. Chem. Int. Ed.* **2017**, *56*, 880-884.

[22] Z. Wu, J. Nitsch, J. Schuster, A. Friedrich, K. Edkins, M. Loebnitz, F. Dinkelbach, V. Stepanenko, F. Wurthner, C. M. Marian, L. Ji, T. B. Marder, *Angew. Chem. Int. Ed.* **2020**, *59*, 17137-17144.

[23] C. A. M. Salla, G. Farias, M. Rouzieres, P. Dechambenoit, F. Durola, H. Bock, B. de Souza, I. H. Bechtold, *Angew. Chem. Int. Ed.* **2019**, *58*, 6982-6986.

[24] H. Yuasa, S. Kuno, *Bull. Chem. Soc. Jpn.* **2018**, *91*, 223–229.

[25] L. Huang, C. Qian, Z. Ma, *Chem. Eur.J.* **2020**, *26*, 11914 –11930.

[26] C. Chen, Z. Chi, K. C. Chong, A. S. Batsanov, Z. Yang, Z. Mao, Z. Yang, B. Liu, *Nat. Mater.* **2020**, *20*, 175-180.

[27] H. T. Feng, J. Zeng, P. A. Yin, X. D. Wang, Q. Peng, Z. Zhao, J. W. Y. Lam, B. Z. Tang, *Nat. Commun.* **2020**, *11*, 2617.

[28] aH. Li, H. Li, W. Wang, Y. Tao, S. Wang, Q. Yang, Y. Jiang, C. Zheng, W. Huang, R. Chen, *Angew Chem Int Ed Engl* **2020**, *59*, 4756-4762; bC. Chen, Z. Chi, K. C. Chong, A. S. Batsanov, Z. Yang, Z. Mao, Z. Yang, B. Liu, *Nat. Mater.* **2020**.

[29] Z. An, C. Zheng, Y. Tao, R. Chen, H. Shi, T. Chen, Z. Wang, H. Li, R. Deng, X. Liu, W. Huang, *Nat. Mater.* **2015**, *14*, 685-690.

[30] Y. Gong, G. Chen, Q. Peng, W. Z. Yuan, Y. Xie, S. Li, Y. Zhang, B. Z. Tang, *Adv. Mater.* **2015**, *27*, 6195-6201.

[31] C. Li, X. Tang, L. Zhang, C. Li, Z. Liu, Z. Bo, Y. Q. Dong, Y.-H. Tian, Y. Dong, B. Z. Tang, *Adv. Opt. Mater.* **2015**, *3*, 1184-1190.

[32] Z. Mao, Z. Yang, Y. Mu, Y. Zhang, Y. F. Wang, Z. Chi, C. C. Lo, S. Liu, A. Lien, J. Xu, *Angew. Chem. Int. Ed.* **2015**, *54*, 6270-6273.

[33] P. Xue, J. Sun, P. Chen, P. Wang, B. Yao, P. Gong, Z. Zhang, R. Lu, *Chem. Commun.* **2015**, *51*, 10381-10384.

[34] Z. Yang, Z. Mao, X. Zhang, D. Ou, Y. Mu, Y. Zhang, C. Zhao, S. Liu, Z. Chi, J. Xu, Y. C. Wu, P. Y. Lu, A. Lien, M. R. Bryce, *Angew. Chem. Int. Ed.* **2016**, *55*, 2181-2185.

[35] S. Cai, H. Shi, J. Li, L. Gu, Y. Ni, Z. Cheng, S. Wang, W. W. Xiong, L. Li, Z. An, W. Huang, *Adv. Mater.* **2017**, *29*, 1701244.

[36] S. M. A. Fateminia, Z. Mao, S. Xu, Z. Yang, Z. Chi, B. Liu, *Angew. Chem. Int. Ed.* **2017**, *56*, 12160-12164.

[37] Y. Xie, Y. Ge, Q. Peng, C. Li, Q. Li, Z. Li, *Adv. Mater.* **2017**, *29*, 1606829.

[38] S. Cai, H. Shi, Z. Zhang, X. Wang, H. Ma, N. Gan, Q. Wu, Z. Cheng, K. Ling, M. Gu, C. Ma, L. Gu, Z. An, W. Huang, *Angew. Chem. Int. Ed.* **2018**, *57*, 4005-4009.

[39] Y. Tao, R. Chen, H. Li, J. Yuan, Y. Wan, H. Jiang, C. Chen, Y. Si, C. Zheng, B. Yang, G. Xing, W. Huang, *Adv. Mater.* **2018**, *30*, 1803856.

[40] Y. Xiong, Z. Zhao, W. J. Zhao, H. L. Ma, Q. Peng, Z. K. He, X. P. Zhang, Y. C. Chen, X. W. He, J. Lam, B. Z. Tang, *Angew. Chem. Int. Ed.* **2018**, *27*, 8129-8133.

[41] L. Xu, G. Li, T. Xu, W. Zhang, S. Zhang, S. Yin, Z. An, G. He, *Chem. Commun.* **2018**, *54*, 9226-9229.

[42] Z. He, H. Gao, S. Zhang, S. Zheng, Y. Wang, Z. Zhao, D. Ding, B. Yang, Y. Zhang, W. Z. Yuan, *Adv. Mater.* **2019**, *31*, 1807222.

[43] L. Huang, L. Liu, X. Li, H. Hu, M. Chen, Q. Yang, Z. Ma, X. Jia, *Angew. Chem. Int. Ed.* **2019**, *58*, 16445-16450.

[44] X. Liang, T. T. Liu, Z. P. Yan, Y. Zhou, J. Su, X. F. Luo, Z. G. Wu, Y. Wang, Y. X. Zheng, J. L. Zuo, *Angew. Chem. Int. Ed.* **2019**, *58*, 17220-17225.

[45] S. Hirata, *Adv. Opt. Mater.* **2017**, *5*, 1700116.

[46] M. Baroncini, G. Bergamini, P. Ceroni, *Chem. Commun.* **2017**, *53*, 2081-2093.

[47] A. P. Demchenko, V. I. Tomin, P. T. Chou, *Chem. Rev.* **2017**, *117*, 13353-13381.

[48] S. Hirata, *J. Mater. Chem. C* **2018**, *6*, 11785-11794.

[49] A. Forni, E. Lucenti, C. Botta, E. Cariati, *J. Mater. Chem. C* **2018**, *6*, 4603-4626.

[50] J. A. Li, J. Zhou, Z. Mao, Z. Xie, Z. Yang, B. Xu, C. Liu, X. Chen, D. Ren, H. Pan, G. Shi, Y. Zhang, Z. Chi, *Angew. Chem. Int. Ed.* **2018**, *57*, 6449-6453.

[51] G., A. Manthanath, V. C. Wakchaure, K. C. Ranjeesh, T. Das, K. Vanka, T. Nakanishi, S. B. Sukumaran, *Angew. Chem. Int. Ed.* **2018**, *131*, 2306-2310.

[52] D. Wang, Z. Yan, M. Shi, J. Dai, Q. Chai, H. Gui, Y. Zhang, X. Ma, *Adv. Opt. Mater.* **2019**, *7*, 1901277.

[53] W. Liu, J. Wang, Y. Gong, Q. Liao, Q. Dang, Z. Li, Z. Bo, *Angew. Chem. Int. Ed.* **2020**, *132*, 20336-20341.

[54] Z. Chai, C. Wang, J. Wang, F. Liu, Y. Xie, Y.-Z. Zhang, J.-R. Li, Q. Li, Z. Li, *Chem. Sci.* **2017**, *8*, 8336-8344.

[55] M. Li, X. Cai, Z. Qiao, K. Liu, W. Xie, L. Wang, N. Zheng, S. J. Su, *Chem. Commun.* **2019**, *55*, 7215-7218.

[56] Y. Shoji, Y. Ikabata, Q. Wang, D. Nemoto, A. Sakamoto, N. Tanaka, J. Seino, H. Nakai, T. Fukushima, *J. Am. Chem. Soc.* **2017**, *139*, 2728-2733.

[57] Y. Zhou, W. Qin, C. Du, H. Gao, F. Zhu, G. Liang, *Angew. Chem. Int. Ed.* **2019**, *58*, 12102-12106.

[58] M. Ferger, S. Berger, F. Rauch, S. Schönitz, J. Rühe, J. Krebs, A. Friedrich, T. B. Marder, *Chem. Eur. J.* **2021**. DOI: 10.1002/chem.202100632.

[59] S. M. Berger, M. Ferger, T. B. Marder, *Chem. Eur. J.* **2021**, *27*, 7043-7058.

[60] J.-L. Ma, H. Liu, S.-Y. Li, Z.-Y. Li, H.-Y. Zhang, Y. Wang, C.-H. Zhao, *Organometallics* **2020**, *39*, 4153−4158.

[61] G. Q. Zhang, J. B. Chen, S. J. Payne, S. E. Kooi, J. N. Demas, C. L. Fraser, *J. Am. Chem. Soc.* **2007**, *129*, 8942-8943.

[62] G. Zhang, G. M. Palmer, M. W. Dewhirst, C. L. Fraser, *Nat. Mater.* **2009**, *8*, 747-751.

[63] Z. Yu, Y. Wu, L. Xiao, J. Chen, Q. Liao, J. Yao, H. Fu, *J. Am. Chem. Soc.* **2017**, *139*, 6376-6381.

[64] Z. Xu, Q. T. Liu, X. Z. Wang, Q. Liu, D. Hean, K. C. Chou, M. O. Wolf, *Chem. Sci.* **2020**, *11*, 2729-2734.

[65] J. S. Ward, R. S. Nobuyasu, A. S. Batsanov, P. Data, A. P. Monkman, F. B. Dias, M. R. Bryce, *Chem. Commun.* **2016**, *52*, 2612-2615.

[66] J. S. Ward, R. S. Nobuyasu, M. A. Fox, J. A. Aguilar, D. Hall, A. S. Batsanov, Z. Ren, F. B. Dias, M. R. Bryce, *J. Org. Chem.* **2019**, *84*, 3801-3816.

[67] J. Yang, X. Zhen, B. Wang, X. Gao, Z. Ren, J. Wang, Y. Xie, J. Li, Q. Peng, K. Pu, Z. Li, *Nat. Commun.* **2018**, *9*, 840-849.

[68] J. Yang, H. Gao, Y. Wang, Y. Yu, Y. Gong, M. Fang, D. Ding, W. Hu, B. Z. Tang, Z. Li, *Mater. Chem. Front.* **2019**, *3*, 1391-1397.

[69] L. K. Huang, B. Chen, X. P. Zhang, C. O. Trindle, F. Liao, Y. C. Wang, H. Miao, Y. Luo, G. Q. Zhang, *Angew. Chem. Int. Ed.* **2018**, *57*, 16046-16050.

[70] Z. Y. Liu, J. W. Hu, C. H. Huang, T. H. Huang, D. G. Chen, S. Y. Ho, K. Y. Chen, E. Y. Li, P. T. Chou, *J. Am. Chem. Soc.* **2019**, *141*, 9885-9894.

[71] L. Yu, Z. Wu, C. Zhong, G. Xie, Z. Zhu, D. Ma, C. Yang, *Adv. Opt. Mater.* **2017**, *5*, 1700588.

[72] C. Zhou, S. Zhang, Y. Gao, H. Liu, T. Shan, X. Liang, B. Yang, Y. Ma, *Adv. Funct. Mater.* **2018**, *28*, 1802407.

[73] M. Shimizu, R. Shigitani, M. Nakatani, K. Kuwabara, Y. Miyake, K. Tajima, H. Sakai, T. Hasobe, *J. Phys. Chem. C* **2016**, *120*, 11631-11639.

[74] M. Shimizu, T. Kinoshita, R. Shigitani, Y. Miyake, K. Tajima, *Mater. Chem. Front.* **2018**, *2*, 347-354.

[75] Q. Li, Z. Li, *Acc Chem Res* **2020**, *53*, 962-973.

[76] A. D. Nidhankar, Goudappagouda, D. S. Mohana Kumari, S. K. Chaubey, R. Nayak, R. G. Gonnade, G. V. P. Kumar, R. Krishnan, S. S. Babu, *Angew. Chem. Int. Ed.* **2020**, *59*, 13079-13085.

[77] Z. Ruan, Q. Liao, Q. Dang, X. Chen, C. Deng, Z. Gao, J. Lin, S. Liu, Y. Chen, Z. Tian, Z. Li, *Adv. Opt. Mater.* **2021**, 2001549.

[78] J. Wang, X. Gu, H. Ma, Q. Peng, X. Huang, X. Zheng, S. H. P. Sung, G. Shan, J. W. Y. Lam, Z. Shuai, B. Z. Tang, *Nat. Commun.* **2018**, *9*, 2963-2971.

[79] F. Li, S. Guo, Y. Qin, Y. Shi, M. Han, Z. An, S. Liu, Q. Zhao, W. Huang, *Adv. Opt. Mater.* **2019**, *7*, 1900511.

[80] R. Kabe, C. Adachi, *Nature* **2017**, *550*, 384-387.

[81] Z. Lin, R. Kabe, K. Wang, C. Adachi, *Nat. Commun.* **2020**, *11*, 191.

[82] B. B. Ding, L. W. Ma, Z. Z Huang, X. Ma, H. Tian, *ChemRxiv*, **2021**, DOI: 10.26434/chemrxiv.13285589.v1.

[83] B. Chen, W. Huang, H. Su, H. Miao, X. Zhang, G. Zhang, *Angew. Chem. Int. Ed.* **2020**, *59*, 10023-10026.

[84] O. Bolton, K. Lee, H. J. Kim, K. Y. Lin, J. Kim, *Nat. Chem.* **2011**, *3*, 205-210.

[85] O. Bolton, D. Lee, J. Jung, J. Kim, *Chem. Mater.* **2014**, *26*, 6644-6649.

[86] S. Hirata, K. Totani, J. Zhang, T. Yamashita, H. Kaji, S. R. Marder, T. Watanabe, C. Adachi, *Adv. Funct. Mater.* **2013**, *23*, 3386-3397.

[87] S. Hirata, K. Totani, H. Kaji, M. Vacha, T. Watanabe, C. Adachi, *Adv. Opt. Mater.* **2013**, *1*, 438-442.

[88] R. Kabe, N. Notsuka, K. Yoshida, C. Adachi, *Adv. Mater.* **2016**, *28*, 655-660.

[89] J. Wei, B. Liang, R. Duan, Z. Cheng, C. Li, T. Zhou, Y. Yi, Y. Wang, *Angew. Chem. Int. Ed.* **2016**, *55*, 15589-15593.

[90] L. Xiao, Y. Wu, Z. Yu, Z. Xu, J. Li, Y. Liu, J. Yao, H. Fu, *Chem. Eur. J.* **2018**, *24*, 1801-1805.

[91] D. Li, F. Lu, J. Wang, W. Hu, X. M. Cao, X. Ma, H. Tian, *J. Am. Chem. Soc.* **2018**, *140*, 1916-1923.

[92] X. Zhang, L. Du, W. Zhao, Z. Zhao, Y. Xiong, X. He, P. F. Gao, P. Alam, C. Wang, Z. Li, J. Leng, J. Liu, C. Zhou, J. W. Y. Lam, D. L. Phillips, G. Zhang, B. Z. Tang, *Nat. Commun.* **2019**, *10*, 5161.

[93] D. Lee, O. Bolton, B. C. Kim, J. H. Youk, S. Takayama, J. Kim, *J. Am. Chem. Soc.* **2013**, *135*, 6325-6329.

[94] M. S. Kwon, D. Lee, S. Seo, J. Jung, J. Kim, *Angew. Chem. Int. Ed.* **2014**, *53*, 11177-11181.

[95] M. Louis, H. Thomas, M. Gmelch, A. Haft, F. Fries, S. Reineke, *Adv. Mater.* **2019**, *31*, 1807887.

[96] Y. Su, S. Z. F. Phua, Y. B. Li, X. J. Zhou, D. B. Jana, G. F. Liu, W. Q. Lim, W. K. Ong, C. L. Yang, Y. l. Zhao, *Sci. Adv.* **2018**, *4*, 9732.

[97] M. S. Kwon, Y. Yu, C. Coburn, A. W. Phillips, K. Chung, A. Shanker, J. Jung, G. Kim, K. Pipe, S. R. Forrest, J. H. Youk, J. Gierschner, J. Kim, *Nat. Commun.* **2015**, *6*, 8947.

[98] Y. Yu, M. S. Kwon, J. Jung, Y. Zeng, M. Kim, K. Chung, J. Gierschner, J. H. Youk, S. M. Borisov, J. Kim, *Angew. Chem. Int. Ed.* **2017**, *56*, 16207-16211.

[99] L. Gu, H. Wu, H. Ma, W. Ye, W. Jia, H. Wang, H. Chen, N. Zhang, D. Wang, C. Qian, Z. An, W. Huang, Y. Zhao, *Nat. Commun.* **2020**, *11*, 944.

[100] J. Wang, Z. Huang, X. Ma, H. Tian, *Angew. Chem. Int. Ed.* **2020**, *59*, 9928-9933.

[101] Q. Li, M. Zhou, Q. Yang, Q. Wu, J. Shi, A. Gong, M. Yang, *Chem. Mater.* **2016**, *28*, 8221-8227.

[102] K. Jiang, Y. Wang, C. Cai, H. Lin, *Adv. Mater.* **2018**, *30*, 1800783.

[103] K. Jiang, X. Gao, X. Feng, Y. Wang, Z. Li, H. Lin, *Angew. Chem. Int. Ed.* **2020**, *59*, 1263-1269.

[104] Q. Li, M. Zhou, M. Yang, Q. Yang, Z. Zhang, J. Shi, *Nat. Commun.* **2018**, *9*, 734.

[105] W. Zhao, Z. He, B. Z. Tang, *Nature Res. Mater.* **2020**, *5*, 869-885.

[106] Q. Peng, H. Ma, Z. Shuai, *Acc. Chem. Res.* **2021**, *54*, 940-949.

[107] M. Singh, K. Liu, S. Qu, H. Ma, H. Shi, Z. An, W. Huang, *Adv. Opt. Mater.* **2021**, 2002197.

[108] L. Xiao, H. Fu, *Chem. Eur. J.* **2019**, *25*, 714-723.

[109] Kenry, C. Chen, B. Liu, *Nat. Commun.* **2019**, *10*, 2111.

[110] A. D. Nidhankar, Goudappagouda, V. C. Wakchaure, S. S. Babu, *Chem. Sci.* **2021**, *12*, 4216-4236.

[111] M.-M. Fang, J. Yang, Z. Li, *Chinese J. Polym. Sci*. **2019**, *37*, 383-393.

[112] J. Yang, Z. Chi, W. Zhu, B. Z. Tang, Z. Li, *Sci. China Chem* **2019**, *62*, 1090-1098.

[113] J. Gierschner, J. Q. Shi, B. M. Medina, D. R. Sanjuán, S. Varghese, S. Y. Park, *Adv. Optical Mater.* **2021**, 2002251.

[114] G. Qu, Y. Zhang, X. Ma, *Chin. Chem. Lett.* **2019**, *30*, 1809-1814.

[115] H. Tian, X. Ma, C. Xu, J. Wang, *Angew. Chem. Int. Ed.* **2018**, *57*, 10854-10858.

CHAPTER TWO

–

PERSISTENT ROOM TEMPERATURE PPHOSPHORESCENCE FROM TRIARYLBORANES: A COMBINED EXPERIMENTAL AND THEORETICAL STUDY

Persistent Room Temperature Phosphorescence from Triarylboranes: A Combined Experimental and Theoretical Study

2.1 Introduction

Luminophores with ultralong room temperature phosphorescence (RTP) have attracted much attention because of a variety of applications in time-gated biological imaging,[1] anti-counterfeiting,[2] watch dials, safety signs and optoelectronic devices.[3] Unlike metal-containing materials, in which the heavy atom effect can efficiently accelerate the intersystem crossing (ISC) process from singlet to triplet excited states,[4] RTP from purely organic molecules is relatively rare because the formation of the triplet states is usually not efficient as ISC is slow. In addition, radiative decay from T_1 to the S_0 ground state is also spin forbidden, and is very slow compared to the non-radiative relaxation from T_1 in an unrestricted environment.[5] Designing purely organic systems showing ultralong RTP is a challenge.[6] Key approaches involve reducing the nonradiative decay rate ($k_{nr}(T_1)$) from T_1 by (1) avoiding collisions with quenching species such as oxygen, and (2) minimizing vibrational relaxation (Figure 2-1a).[7] For example, Tang and coworkers reported purely organic luminophors which phosphoresce in the crystalline state.[8] Huang and colleagues proposed that effective stabilization of triplet excited states via strong coupling in H-aggregated molecules enables their lifetimes to become orders of magnitude longer than those of conventional organic fluorophores.[9] Adachi and co-workers developed efficient persistent RTP materials by minimizing nonradiative decay rates in organic amorphous host-guest materials.[10] Very recently, Wang and co-workers have achieved ultralong RTP from *N*-phenyl-2-naphthylamine by confining it in a crystalline dibromobiphenyl matrix.[11] To increase the population of triplet excitons, heteroatoms with lone pairs are usually introduced into organic systems to enhance spin–orbit coupling (El-Sayed's rule),[12] which is why most RTP phosphors are limited to phenothiazine, carbazole, and naphthylimide derivatives (Figure 2-1b).[1b, 4d, 13] Thus, intersystem crossing usually involves $^1(n, \pi^*) \rightarrow ^3(\pi, \pi^*)$ transitions. Recently, arylboronic acids and esters, which also contain lone pairs on their hydroxy or alkoxy groups, have been reported to show RTP with lifetimes up to several seconds in the solid state.[14] Thus far, ultralong RTP from purely organic phosphors without lone pairs have rarely been reported,[15] as k_{isc} is slow.

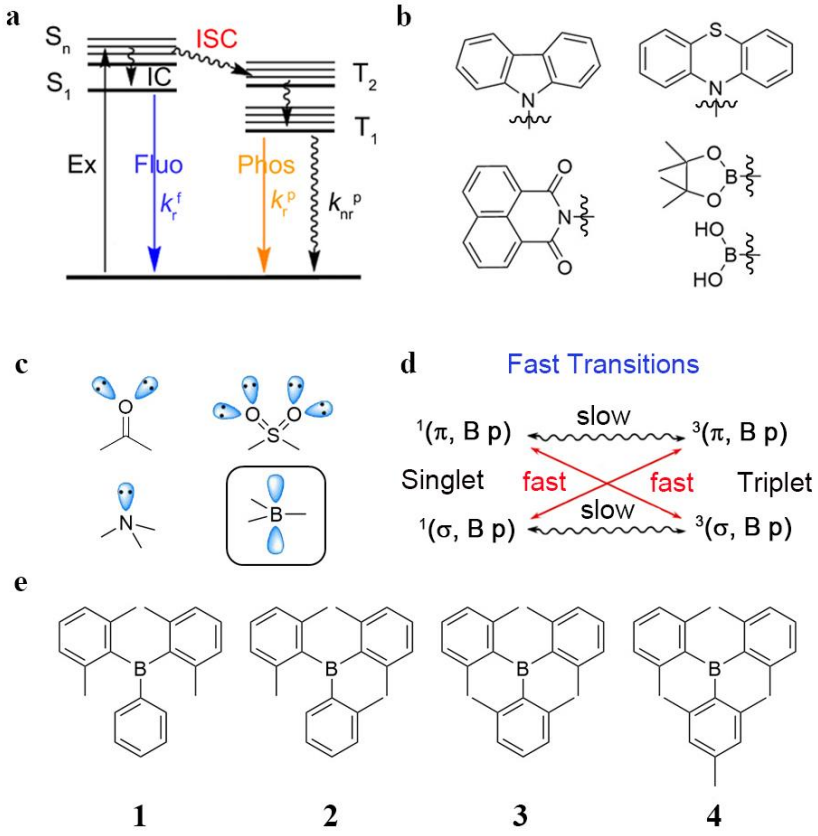

Figure 2-1. (a) Jablonski-diagram; (b) the structural features of reported RTP materials; (c) typical functional groups having lone pairs in organic phosphors, and the empty p_z orbital on three-coordinate boron; (d) fast transitions between (σ, B p) and (π, B p); (e) molecular structures of compounds **1**-**4**.

In fact, organic compounds without lone pairs,[16] such as triarylboranes, can show phosphorescence in a frozen optical glass at 77 K (Figure 2-1c).[17] This indicates that k_{isc} in a photo-excited triarylborane molecule can compete with fluorescence, for which rate constant is usually on the magnitude of 10^7 s^{-1}. Therefore, we propose that k_{isc} can also be accelerated by (σ, B p)→(π, B p) transitions, which would be the inversion of the normally observed ^{1}(n, π*)→^{3}(π, π*) ISC process (Figure 2-1d). However, probably due to the fact that the non-radiative decay rate from T_1 k_{nr}^p at RT is usually much faster than the phosphorescence, RTP from triarylboranes has not been reported. Only if k_{nr}^p is suppressed to a large extent, might we observe RTP from triarylboranes. In 1955, Wittig et al. reported that some triarylboranes, including tris(2-methylphenyl)borane, showed a yellowish-white emission under UV light.[18] However, no lifetimes were reported and when we prepared tris(2-methylphenyl)borane it showed only blue fluorescence, i.e., no phosphorescence at room temperature was detected. Given our interest in the linear and nonlinear optical properties of 3-coordinate organoboron

compounds,[19] we examined the triarylboranes **1**-**4** (Figure 2-1e). Crystalline samples of **3** (tris(2,6-dimethylphenyl)borane) show ultralong (τ_p = 478 ms), intense, yellow phosphorescence under ambient conditions, and it is thus, to the best of our knowledge, the first triarylboron compound without lone pairs to display ultralong RTP.

2.2 Results and Discussion

2.2.1 Photophysical properties combined with theoretical study

The synthesis and characterization of all compounds are given in the Section **2.4** and the photophysical properties of **1**-**4** are summarized in Table 2-1. The important results of our quantum chemical studies are shown in brackets, and complete data are given in Tables 2-13 and 2-15. The UV-Vis absorption and emission spectra were first measured in hexane. Compounds **1**-**4** all show a broad first absorption band between 280-350 nm in hexane, which can be assigned to B← π transitions, i.e. a transition from the aryl ring π-systems to the empty p-orbital on the boron atom (Figure 2-2a). Our calculations reveal that this band is formed by up to five electronic transitions, $S_1 \leftarrow S_0$ to $S_4 \leftarrow S_0$ in the D_3-symmetric compound **3** and $S_1 \leftarrow S_0$ to $S_5 \leftarrow S_0$ in the less symmetric compounds **1**, **2**, and **4** (Figures 2-48 to 2-53). The energies of the absorption maxima decreased in the order **1** > **2** > **3** > **4**. This indicates that introducing each methyl substituent, a weak σ-donor, on the phenyl ring, red shifts the absorption spectra by 6-12 nm (580-1230 cm^{-1}). The fluorescence spectra of the compounds in hexane show the same trend; their maxima red shift 2-7 nm (150-530 cm^{-1}) for each methyl group added to the phenyl ring (Figure 2-2a). However, the emission spectra of crystalline **1**-**4** are not related to their chemical structures in an obvious way (Figure 2-2b). In general, the fluorescence spectra of the solid, crystalline samples of compounds **1**-**4** are all redshifted compared with those in hexane solution. The bathochromic shift of **3** (2060 cm^{-1}) is considerably larger than those of **1**, **2**, and **4**. The bathochromic shifts of **2** (750 cm^{-1}) and **4** (930 cm^{-1}) are smaller than that of **1** (1150 cm^{-1}). This indicates that intermolecular interactions in crystalline **1** and **3** are larger than those in **2** and **4**, which is one possible explanation for the slower nonradiative decay (k_{nr}) from both S_1 and T_1, *vide infra*. In addition, compounds **1** and **3** may also have a higher probability of showing excimer emissions.

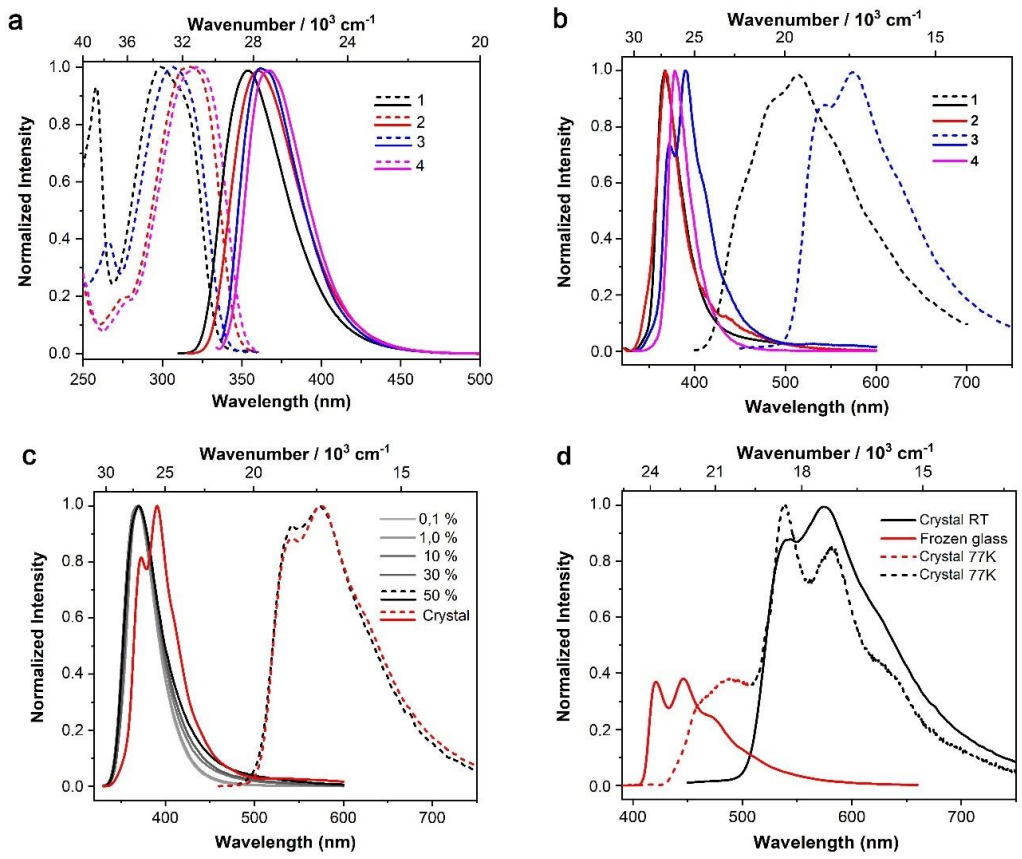

Figure. 2-2 (a) Normalized UV/Vis absorption (dashed lines) and fluorescence emission (solid lines) spectra of **1**-**4** in hexane solution at room temperature (λ_{exc} = 290 nm); (b) PL emission spectra (solid lines) of crystalline **1**-**4**, and time-gated phosphorescence emission (dashed lines) spectra at room temperature (λ_{exc} = 305 nm); (c) total PL emission (solid lines) and time-gated phosphorescence emission (dashed lines) spectra of **3** at 0.1, 1.0, 10, 30 and 50 % loadings in PMMA films and in the crystalline state at room temperature (λ_{exc} = 305 nm); (d) Time-gated phosphorescence emission spectra of compound **3** in the crystalline state at room temperature (solid black), frozen methylcylohexane glass matrix (solid red), and crystalline state (dashed line) at 77 K.

We noticed that, upon exposure to a hand-held UV-lamp (λ = 365 nm), crystalline **3** showed violet fluorescence which disappears immediately when the lamp is turned off. Persistent greenish-yellow phosphorescence emission was then observed, which is visible to the naked eye for almost 4 s (Figure 2-3). Time-gated emission spectroscopy revealed long-lived (τ = 478 ms) phosphorescence from crystalline **3**, with an emission maximum at 575 nm and a shoulder at 540 nm (Figures 2-2b). To the best of our knowledge, this is the first triarylborane to show long-lived RTP, and one of the rare examples where free electron pairs are absent. However, in 1955, Wittig reported a yellowish-white emission from some triarylboranes including tris(2-methylphenyl)borane under UV light.[18] We prepared pure tris(2-methylphenyl)borane, as a white solid, and our sample shows only blue fluorescence

Table 2-1. Experimental and calculated (in brackets) photophysical properties of compounds **1**-**4** in hexane and the crystalline state at RT, and in a frozen methylcyclohexane glass at 77 K.

	State	λ_f /nm	Φ_f %	k_r^f /10^7 s^{-1}	k_{nr}^f /10^8 s^{-1}	k_{isc}^f /s^{-1}	λ_p /nm	Φ_p %	τ_p /s
1	Crystalline[a]	369	3.4	2	6.0		524	0.3	0.09 (21%), 0.68 (79%)
	Crystalline[b]	368					471, 502, 541		2.27
	Frozen glass[b]	349 {383}				{1*10^7}	404, 427 {425, 597}		1.45 {8}
2	Crystalline[a]	369	6.9	4	5.8		nd[c]		nd
	Crystalline[b]	352, 366					426, 449		0.22 (39%), 1.22 (61%)
	Frozen glass[b]	373 {391}				{6*10^6}	417, 442 {448, 476}		1.57 {8}
3	Crystalline[a]	371, 390	17.0	10	5.9		540, 575	1.2	0.48
	Crystalline[b]	372, 392, 415					488, 538, 582, 630		0.52 (23%), 1.64 (77%)
	Frozen glass[b]	375 {404}				{5*10^7}	421, 446 {456, 486}		1.48 {7}
4	Crystalline[a]	381	6.3	4	6.2		nd[c]		nd
	Crystalline[b]	370					456,485		0.08 (32%), 1.32 (68%)
	Frozen glass[b]	374 {430}				{3*10^7}	425, 452 {458, 489}		1.36 {5}

[a] measured at RT; [b] measured at 77 K; [c] not detected (nd).

with an emission maximum at 377 nm (Figure 2-6). No phosphorescence was detected in solution or in the solid state at room temperature, while it does show phosphorescence at 435 nm with lifetime of ca. 2 s in a frozen methylcyclohexane glass at 77 K (Figure 2-7). In addition to the RTP from **3**, RTP was also observed from crystalline **1**, with a phosphorescence emission maximum at 515 nm and a lifetime of τ = 680 ms. Compared to compound **3**, the phosphorescence quantum yield (Φ_P) of **1** is 0.26 %, which is lower than that of **3** (1.14 %). We did not observe any phosphorescence from compounds **2** and **4** at room temperature.

Interestingly, we found that the photoluminescence behaviors of **3** largely depend on its aggregation state. We investigated two different kinds of aggregation states, crystals (sample **A**) and ball-milled powder (sample **B**). SEM pictures and powder X-ray diffraction (pXRD) patterns clearly revealed the difference between the samples. In the ball-milled powder, we can see smaller size particles with a larger surface area (Figure 2-13). However, the powder X-ray diffraction pattern of the ball-milled sample shows a diffraction pattern which is broader compared to the pattern obtained from the

crystalline sample **A** (Figure 2-21), and this indicates that the powder sample **B** still contains some small crystals. We find that the emission maxima differ by 25 nm (1760

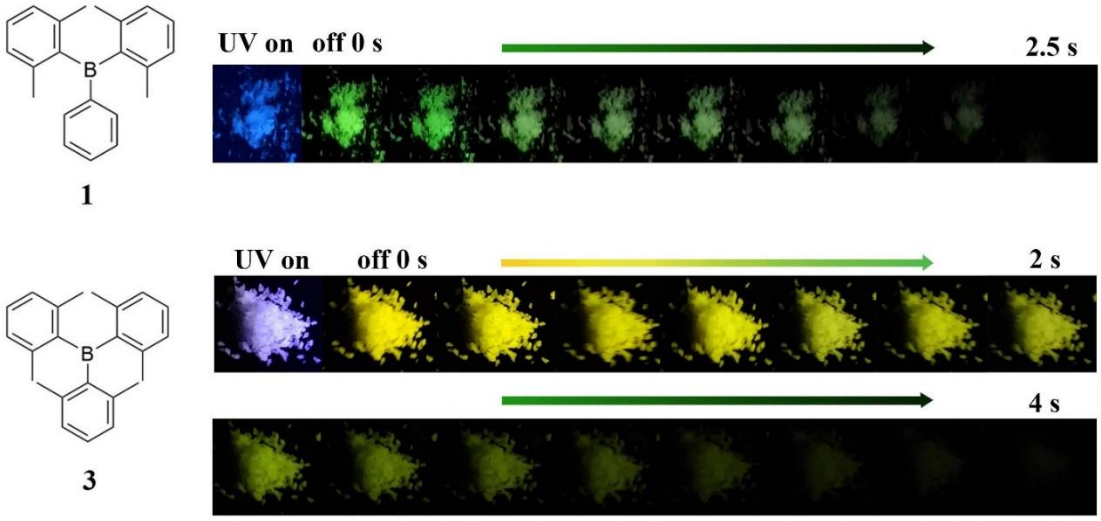

Figure. 3 Photographs of crystalline **1** and **3** taken during and after irradiation (365 nm) under ambient conditions.

cm^{-1}) and that the peak at 350 nm in the excitation spectrum of sample **A** decreases in intensity as the crystalline domains increase (Figures 2-15 to 2-16). Although the fluorescence lifetime and the time-gated phosphorescence emission spectra remained the same, the phosphorescence lifetime and quantum yield decreased significantly for the ball-milled sample **B** compared with crystalline **A**, from 478 to 340 ms and 1.12 % to 0.2 %, respectively. In the ball-milled powder, the exposed surface area is much larger, and phosphorescence is more sensitive to oxygen quenching, compared to the crystalline state. This hypothesis is supported by phosphorescence lifetime measurements under argon, for which the difference between the two samples disappears (Figures 2-18 and 2-19).

To understand further the relationship between molecular structure and phosphorescence, we measured the emission spectra of **1-4** in a frozen methylcyclohexane optical glass at 77 K (Figures 2-22 and 2-23), where we can assume that there are no intermolecular interactions present ($c < 10^{-5}$ mol/L). All four compounds show two well-separated emission bands. We observed phosphorescence emissions (400-600 nm), which are all hypsochromically shifted in comparison to the emission from the solid at room temperature (by 5230-5670 cm^{-1}). All compounds show

similar vibrational fine structures except compound **1**, because **1** has low-frequency vibrational modes according to our calculations, which broaden the emission bands. In addition, there are high energy fluorescence emission bands (330-400 nm), which show less vibrational fine structure (Figure 2-22).

We further noticed that the RTP emission in crystalline samples of **3** is noticeable red shifted by 5230 cm^{-1} when compared to that in the frozen glass (Figure 2-2d). Such a large shift makes it unlikely that it results from the suppression of the internal conversion (temperature effect) in the excited state, or by a less polar environment (environment effect) in the frozen glass. To examine how temperature influences the luminescent behavior of crystalline samples, we also measured the emission spectra of crystalline **1**-**4** at 77 K (Figure 2-25). In crystalline **3**, a sharp fluorescence peak appears at 415 nm at 77 K, which is almost identical to the fluorescence in the frozen glass. However, a very broad phosphorescent emission ranging from 430 to 720 nm (Figure 2d) is observed, which we assign to two phosphorescence bands, one at 488 nm and a second ranging from 500 to 720 nm. We noticed that the band at 488 nm is only visible at low temperature and is most likely not a vibrational band of the 500-720 nm emission, for which the range is identical to the spectrum at room temperature (Figure 2-2d). We observe two lifetimes, one of 1.64 s, and a second of 0.52 s, which further support the existence of two independent triplet states. We note that the longer lifetime is almost identical to the lifetime in the frozen glass, in which we can assume the absence of any intermolecular interaction except with solvent matrix molecules. We assume that the band at 488 nm is phosphorescence which is caused by the population of the T_1 state of the triarylboranes and which is only visible when the non-radiative decay is suppressed. Therefore, it cannot be observed at higher temperatures, at which $k_{np}(T_1)$ dominate. This emission is also found in the frozen glass in which it is shifted by 67 nm (3260 cm^{-1}), which is a reasonable shift if one considers the different environments of the frozen glass matrix and the crystalline sample. The emission between 500 – 720 nm, however, is the real RTP emission which is an aggregation induced phenomenon, in contrast to the phosphorescence at 488 nm. It is important to note that this emission is absent in the dilute frozen glass, in which we can assume that the emission resembles that of the isolated molecules. Furthermore, when **3** is embedded in a poly(methyl methacrylate) (PMMA) matrix, RTP is only observed in very highly doped films (≥ 50 wt%, Figure

2-2c), further confirming the critical role of aggregation for this emission (Figures 2-8 to 2-12).

2.2.2 Theoretical study

The maxima of the computed emission spectra (Figures 2-55 and 2-58) are red shifted (by 1220-1820 cm^{-1}) with respect to the experimental spectra in a frozen glass while the energies of the 0-0 transitions agree well. The red shifts of the maxima are partially attributed to the harmonic oscillator approximation, which overestimates the intensities at the long wavelength tail of the emission spectrum that stems from electric dipole transitions between the vibrational ground state of the electronically excited state and vibrationally excited levels of the electronic ground state. The calculated values for k_{isc} of **1**-**4** are ca. 10^7 s^{-1}, thus ISC can compete with fluorescence. Noticeably, the major components of the phosphorescence lifetimes of all four compounds are similar, with a value of ca. 1.5 s (Figure 2-24). Up to six triplet states are located energetically below or very close to the S_1 state as shown in Figures 2-53 and 2-54. Some of the triplet potential energy surfaces cross the S_1 energy profile along the linear interpolated path connecting the Franck-Condon point with the minimum of the S_1 state. ISC is nevertheless fastest for a transition between S_1 and T_2 in **1**, **2**, **3** and **4**. To understand the origin of the non-negligible spin–orbit coupling (SOC) between these states, we computed and plotted the differences of the electron densities between the ground and excited-state wave functions. S_1 and T_1 of compound **3**, for example (Figure 2-4), result from similar (π, B p) excitations, with T_1 showing additional contributions from local (π, π*) excitations on xylyl ring a. For this transition,[12] the SOC is very small. Comparing the difference densities of S_1 and T_2 instead, we see two major differences. First, in T_2, most of the electron density has been transferred from the other two xylyl rings b and c. As the largest SOCs result from one-center terms, excitations from different π systems to the same boron orbital yield negligible interaction matrix elements. This evidence clearly demonstrates that k_{isc} can also be accelerated by (σ, B p)→(π, B p) and (π, B p)→(σ, B p) transitions.

The second, and more important, difference with regard to SOC is a contribution to the T_2 wave function in which charge is transferred from a σ-type orbital connecting xylyl ring a with boron. The change of orbital angular momentum on this carbon atom leads to stronger SOC than expected in the absence of (n, π*) excitations. An electronic

matrix element $|<T_2|H_{SO}|S_1>| \approx 1\ cm^{-1}$ is sufficient for ISC to proceed at a rate of $\approx 10^7\ s^{-1}$ (for more details, see Tables 2-13 and 2-14). As the calculated fluorescence and ISC rate constants are of the same order of magnitude, the competition between the two processes is easily explained. Although triplet formation is likely to occur in all compounds, no phosphorescence was detected in solution at room temperature, likely due to rapid nonradiative decay $k_{np}(T_1)$ compared to slow k_p. Our data indicate that triplet excited states are formed in all compounds **1**-**4** after excitation.

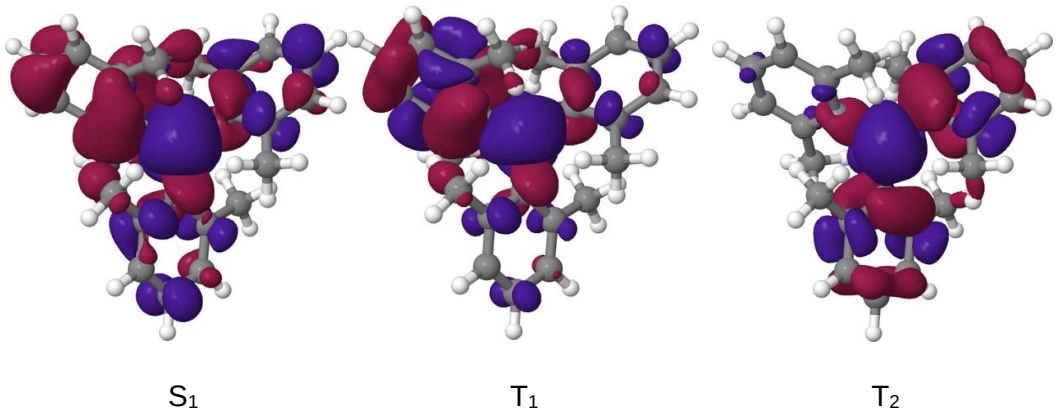

Figure 2-4. Difference densities (|isovalue| = 0.001 [e Å^{-3}]^{½}) of low-lying excited states of compound **3** at the TDDFT-optimized geometry of the S_1 state. A loss of electron density with respect to the S_0 state is indicated in red, a gain in blue.

2.2.3 Crystal Structure Analysis

To understand the effect of the solid-state structures and the intermolecular packing on the luminescence properties, the crystal structures of compounds **1**-**4** were obtained via single-crystal X-ray diffraction (Figures 2-31 to 2-34). If we compare the molecular geometries of compounds **1**-**4** in their crystal structures, we can observe the influence of additional methyl groups on the phenyl rings close to the central boron atom. While the B–C bond distances lie in a similar range for the bulkier m-xylyl and mesityl groups (1.576 – 1.587 Å), the B–C (aryl) distances to the o-tolyl group (B–C = 1.570(2) Å in compound **2**) and the phenyl ring (B–C = 1.569(2) Å in compound **1**) are slightly shorter (Table 2-4). The effect of the bulkiness of the substituent and, hence, repulsion between methyl groups is further observed in the torsion angles between the aryl groups and the BC3 planes. While the torsion angles are in a similar range (50.0 – 54.9°) for the m-xylyl and mesityl groups in compounds **3** and **4**, a significantly smaller torsion angle

(41.9°) is observed for the o-tolyl group in compound **2**, and a very small torsion angle of only 16.1° is observed for the phenyl group in compound **1**. These smaller torsion angles are compensated by larger torsion angles (56.7 – 65.3°) for the m-xylyl groups in compounds **1** and **2** compared to those of compounds **3** and **4** (Table 2-4).

Calculated minimum energy structures of the S_1 and T_1 states reveal opposite trends of the B–C bond lengths. In the S_1 state, the bond connecting boron and the aryl group from which electron density is transferred to boron (B-R2 in Table 2-15) is elongated upon excitation while the other two B–C bonds shorten with respect to the electronic ground-state structure. In the T_1 state, which exhibits more local (π, π^*) contributions to the excitations than S_1, the first B–C bond shortens and the other two are elongated (Figures 2-57 and 2-58). In compounds **3** and **4**, with methyl groups in the ortho positions of all aryl rings, the dihedral angles change by 10° at most in the S_1 state, and by less than 7° in T_1. Corresponding displacements of the minimum dihedral angles in compound **1** reach values up to 15° and 17°, respectively, and up to 14° and 13°, respectively, in compound **2**.

In order to compare and classify the types and magnitudes of the intermolecular interactions within single crystals of these four triarylboranes, which organize in a complex three-dimensional arrangement, the concept of Hirshfeld surface analysis was applied.[20] The Hirshfeld surface is a special isosurface defined by the weighting function $w(\mathbf{r}) = 0.5$ for a particular molecule. This means that the Hirshfeld surface envelops the volume within which the particular molecule contributes more than half of the electron density. Hence, it also includes information on the nearest neighbors and closest contacts to the molecule. The molecules are most densely packed in compound **2**, as is clear from both the crystal packing coefficient c_k, which corresponds to the ratio of volume occupied by all molecules in the unit cell to the unit cell volume, and the surface of the crystal's void per formula unit, which is obtained from the Hirshfeld analysis (Table 2-5).[21] Interestingly, compounds **1** and **3** show similar, intermediate packing densities, while compound **4** seems to have the loosest packing. While the surfaces of the voids seem to be spread well throughout the unit cells of compounds **1**, **2**, and **4**, a larger solvent-accessible void of 9 $Å^3$ is present in compound **3** around the origin of the unit cell (Figure 2-5). From comparison of the fluorescence emissions of compounds **1**-**4**, we can conclude that the RTP is not correlated with the packing density, as compound **2** is the densest packed compound. A deeper insight into the

intermolecular interactions is required in order to provide an interpretation of the observed differences in emission behavior. Fingerprint analysis of the Hirshfeld surface and its breakdown into the individual relative contributions in crystals of **1**-**4**,[22] exhibited a strong contribution of H···H interactions (75 – 83 %), followed by a significant amount of C···H interactions (17 – 25 %) in all four compounds (Figures 2-35 to 2-26). Only a very weak contribution of C···C interactions is observed for compound **3** (0.2 %). While this analysis shows the relative contributions of the

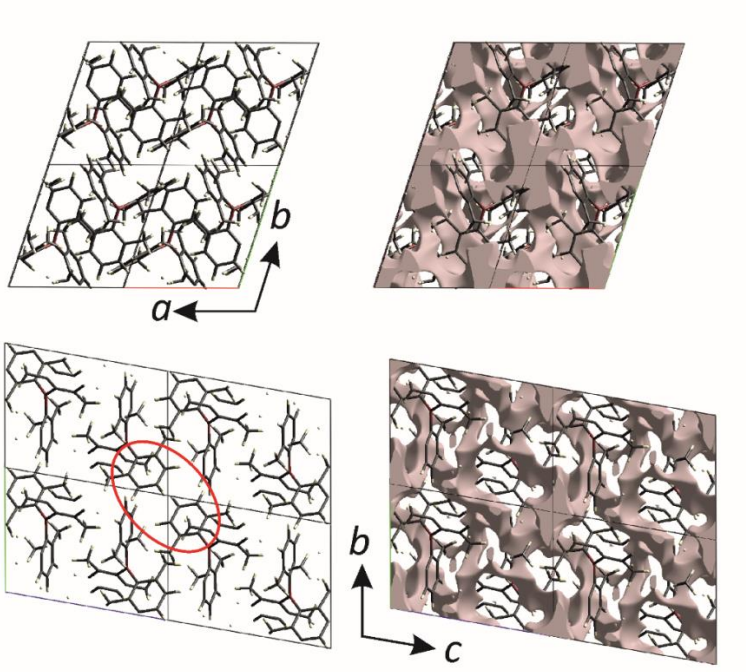

Figure 2-5. Crystal structure of compound **3** (left) projected along the *c* axis (top) and along the *a* axis (bottom), and plot of the surface of the crystal voids (0.002 au) from the Hirshfeld analysis (right). Four unit cells are shown in each case. Note the larger voids around the origin of the unit cell, as best observed in the centers of the drawings. The red ellipse encloses the aryl rings that are involved in a weak π···π interaction.

different types of intermolecular interactions, we are now interested in their strengths in the individual crystal structures. Compounds **1** and **3** exhibit several significant intermolecular C−H···C interactions, including strong, nearly linear interactions (C···H = 2.835 – 2.841 Å, C−H···C = 164 – 168°, Table 2-6). In addition, compound **1** has a short H···H contact (2.241 Å) between two aryl rings, which is also demonstrated by the spike in the bottom left corner of its fingerprint plot (Figure 2-36).

Compound **2**, although more densely packed than **1** and **3**, shows significantly fewer and weaker intermolecular C−H···C interactions. In addition, it shows a nearly linear, weak C−H···π interaction towards the centroid of an m-xylyl ring (H···π = 2.907 Å)

and two close C···C contacts (C···C = 3.334 and 3.384 Å), a strong one between two aryl rings, and a weak one between the same aryl and a methyl group (Table 2-6). These results are consistent with our analysis of the fluorescence emission in the crystalline states, wherein compounds **1** and **2** have the same emission maxima although one more methyl group is introduced to the phenyl ring in compound **2**. This may be explained by the presence of more and stronger interactions in **1** than in **2**. In crystals of compound **4**, intermolecular interactions are the weakest (Table 2-6). This is in agreement with the loosest packing mode. In addition to the strong C−H···C interactions, compound **3** also has a strong C···C interaction (C6···C6 = 3.319 Å) between two aryl rings with an approximately parallel alignment of their planes. This is the shortest nearest-neighbor (nn) C···C distance in all of the compounds. The interplanar separation between the aryl planes is only 2.980 Å; however, the offset shift is large (4.221 Å), resulting in a centroid-to-centroid distance of 5.167 Å, the latter two values being too large for a typical offset face-to-face π···π stacking interaction between two arenes (Table 2-7), which typically have values ranging from 3.3–3.8 Å for the interplanar separation, < 4.0 Å for the offset, and < 5.0 Å for the centroid-to-centroid distance.[23] There exists another arrangement of nearly parallel aryl rings, which has a longer C···C distance (3.495 Å) and interplanar separation (3.397 Å), but a smaller shift (3.493 Å) and, hence, a smaller centroid-to-centroid distance of 4.872 Å, all of those values being within the typical range of weak π···π interactions. The aryl rings, and hence the π···π interaction, are situated close to the voids, which are around the origin (Figure 2-5). It is proposed that, on compression of the crystal structure, the voids may shrink and, hence, the offset may also be reduced, enhancing the π···π interaction between these aryl rings. On the other hand, expansion of the molecule may also bring the rings closer together and enhance the π···π interaction. We assume that the aggregation of molecules forming C−H···C and π···π interactions is important for effective RTP in compounds **1** and **3**. A C···C offset aryl-aryl interaction is also present in both compounds **2** and **4** (Table 2-7); however, the C−H···C interactions are much weaker in these compounds. In summary, the presence of both strong C−H···C and C···C contacts as well as weak π···π interactions in compound **3**, together with the void accumulation at the origin of the unit cell (Figure 2-5) may be the reason for the strong redshift and persistence of the aggregation-induced phosphorescence emission of these crystals at room temperature and in highly doped PMMA-films.

2.3 Conclusion

We have prepared triarylboranes without lone pairs which exhibit long-lived room-temperature phosphorescence in the crystalline state and in highly doped PMMA films. Theoretical calculations revealed that the ISC process can be accelerated by transitions between local sigma and π excitation, which is consistent with photophysical studies of the isolated molecules in a frozen glass and is an extension of El-Sayed's rule. Moreover, the phosphorescent compounds **1** and **3** have the strongest interactions, especially when considering C−H···C interactions, which appear to play an important role in achieving persistent RTP and, at the same time, suppressing nonradiative decay. However, compounds **2** and **4** have fewer and weaker contacts in their crystalline states, and their nonradiative decay is fast, even though compound **2** has the densest packing. Thus, we do not observe RTP from crystals of compounds **2** and **4**. This study on triarylboranes provides an interesting example of how to expand the scope of purely organic phosphorescent materials.

2.4 Experimental details and characterization data

2.4.1 General information details

Compounds **1**-**4** were prepared according to reported literature procedures.[24] All starting materials were purchased from commercial sources and were used without further purification. The organic solvents for synthetic reactions and for photophysical measurements were HPLC grade, further treated to remove trace water using an Innovative Technology Inc. Pure-Solv Solvent Purification System and deoxygenated using the freeze-pump-thaw method. All synthetic reactions were performed in an Innovative Technology Inc. glovebox or under an argon atmosphere using standard Schlenk techniques. ^{1}H, ^{13}C and ^{11}B NMR spectra were measured on a Bruker Avance 500 MHz (^{1}H, 500 MHz; ^{13}C, 126 MHz; ^{11}B, 160 MHz), Bruker Avance III 400 MHz (^{1}H, 400 MHz; ^{13}C, 101 MHz; ^{11}B, 128 MHz) or a Bruker Avance III HD 300 MHz (^{11}B, 96 MHz) NMR spectrometer. Mass spectra were recorded on Agilent 7890A/5975C Inert GC/MSD systems operating in EI mode. High resolution mass spectra were obtained using a Thermo Fisher Scientific Exactive™ Plus Orbitrap MS System with an Atmospheric Solids Analysis Probe (ASAP^{+}). Elemental analyses were performed on a Leco CHNS-932 Elemental Analyser.

General photophysical measurements. All measurements were performed in standard quartz cuvettes (1 cm × 1 cm cross-section) except for amorphous powder samples. They were prepared on 1 x 5 cm quartz plate (under air) or in a sealed cuvette (under argon atmosphere). The emission signal showed no decrease in intensity or shape even after continuous irradiation over a period of 4 h. The samples could be recovered after each measurement and show the same photophysical properties when measured again. We therefore did not find any evidence for (photo)decomposition of our samples. UV-visible absorption spectra were recorded using an S6 Agilent 8453 diode array UV-visible spectrophotometer. The molar extinction coefficients were calculated from three independently prepared samples in hexane solution. The emission spectra were recorded using an Edinburgh Instruments FLSP920 or FLSP980 spectrometer equipped with a double monochromator for both excitation and emission, operating in right angle geometry mode, and all spectra were fully corrected for the spectral response of the instrument. All solutions used in photophysical measurements had a concentration lower than 10^{-5} M to minimize inner filter effects during fluorescence measurements.

Quantum yield measurements. The photoluminescent quantum yields were measured using a calibrated integrating sphere (inner diameter: 150 mm) from Edinburgh Instruments combined with the FLSP920 spectrometer described above. For solution-state measurements, the longest-wavelength absorption maximum of the compound in the hexane was chosen as the excitation wavelength. For solid-state measurements, the excitation wavelength was 305 nm. The phosphorescence quantum yield of compounds **1** and **3** were obtained using the equation:

$$\boldsymbol{\Phi}_{\mathrm{P}} = \frac{B}{A} \times \boldsymbol{\Phi}_{\mathrm{PL}}$$

Where A and B represent the integrated areas of the total photoluminescence and phosphorescence spectra, respectively. For the phosphorescence quantum yields, the phosphorescence componentwas separated from the total photoluminescence (PL) spectrum based on the phosphorescence spectrumobtained separately. $\boldsymbol{\Phi}_{\mathrm{PL}}$ represents the absolute photoluminescence quantum yields of compounds in solid state.

Lifetime measurements. Fluorescence lifetimes were recorded using the time-correlated single-photon counting (TCSPC) method using an Edinburgh Instruments FLSP920 spectrometer equipped with a high-speed photomultiplier tube positioned

after a single emission monochromator. Measurements were made in right-angle geometry mode, and the emission was collected through a polarizer set to the magic angle. Solutions were excited with a pulsed diode laser at a wavelength of 316 nm at repetition rates of 10 or 20 MHz. The instrument response functions (IRF) were *ca.* 230 ps FWHM. The phosphorescence lifetimes were measured using a μF920 pulsed 60 W Xenon microsecond flashlamp, with a repetition rate of 0.2 Hz at room temperature and 0.1 Hz at 77 K. Decays were recorded to 10000 counts in the peak channel with a record length of at least 2000 channels. Iterative reconvolution of the IRF with one decay function and non-linear least-squares analysis were used to analyze the data. The quality of all decay fits was judged to be satisfactory, based on the calculated values of the reduced χ^2 and Durbin-Watson parameters and visual inspection of the weighted residuals.

Scanning Electron Microscopy SEM images were recorded using a Zeiss Ultra Plus field emission scanning electron microscope equipped with GEMINI e-Beam column operated at 1-3 kV with an aperture size set to 10 or 30 μm to avoid excessive charging and radiation damage of the areas imaged.

Powder X-ray diffraction and Phase analysis Compound **3** was ground into a powder until hardly any room-temperature phosphorescence was observed. Powder X-ray diffraction patterns were collected from two parts of the powder sample in reflection geometry on a Bruker D8 Discover powder diffractometer with Da Vinci design and linear Lynx-Eye detector. X-ray radiation (Cu-Kα_1; λ = 1.5406 Å) was focused with a Goebel mirror and Cu-Kα_2 radiation was eliminated by a Ni-absorber. Data were collected from 5 – 60° 2θ in steps of 0.025° at ambient temperature. They were corrected for an offset in 2θ and exported using the Bruker AXS Diffrac-Suite. The diffraction patterns were then converted using CMPR software[25] for further processing with the GSAS program[26] Cell parameters, background, scaling factor, zero shift and profile parameters were refined using the LeBail method. The starting values for the refinement were taken from the single-crystal structure refinement at 100 K.

Crystal structure determination Crystals suitable for single-crystal X-ray diffraction were selected, coated in perfluoropolyether oil, and mounted on MiTeGen sample holders. For the data collection at room temperature, a crystal was glued onto the holder. Diffraction data were collected on a Rigaku XTALAB Synergy S diffractometer with

a semiconductor HPA-detector (HyPix-6000) using Cu-Kα radiation monochromated by multi-layer focusing mirrors or Bruker X8 Apex II 4-circle diffractometers with CCD area detectors using Mo-Kα radiation monochromated by graphite or multi-layer focusing mirrors. The crystals were cooled using an Oxford Cryostream low-temperature device. Data for compounds **1**, **2**, **3**, and **4** were collected at 100 K. Additional data for compound **3** were collected at 293, 240, 180, 120, and 83 K. The images were processed and corrected for Lorentz-polarization effects and absorption as implemented in the Bruker software packages. The structures were solved using the intrinsic phasing method (SHELXT)[27] and Fourier expansion technique. All non-hydrogen atoms were refined in anisotropic approximation, with hydrogen atoms 'riding' in idealized positions, by full-matrix least squares against F^2 of all data, using SHELXL[28] software and the SHELXLE graphical user interface[29]. Diamond[30] software was used for graphical representation. Other structural information was extracted using Mercury[31] and OLEX2[32] software. Hirshfeld surfaces were calculated and analyzed using the Crystal Explorer[33] program.

2.4.2 Synthesis

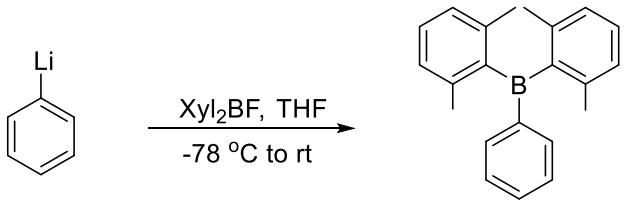

1

Bis(2,6-dimethylphenyl)(phenyl)borane (1): To a solution of bis(2,6-dimethylphenyl)-fluoroborane[34] (720 mg, 3.0 mmol) in anhydrous THF (20 mL) a hexane solution of PhLi (1.9 mL, 1.6 M, 3.1 mmol) was added dropwise by syringe at -78 °C. The reaction mixture was warmed to room temperature and stirred overnight. The reaction was quenched with a saturated solution of NaCl and the aqueous layer was extracted with Et_2O. The combined organic layer was dried over anhydrous Na_2SO_4, filtered, and concentrated under reduced pressure. The resulting crude material was subjected to silica gel column chromatography using *n*-hexane as eluent to afford 518 mg (1.74 mmol, 58%) of **1** as a white solid.

^{1}H NMR (400 MHz, $CDCl_3$, r.t., ppm): δ 7.53-7.47 (m, 3H), 7.38-7.34 (m, 2H), 7.24 (t, J = 8 Hz, 2H), 6.99 (d, J = 8 Hz, 4H), 2.05 (s, 12H);

^{13}C NMR (126 MHz, $CDCl_3$, r.t., ppm): δ 145.4 (br), 144.5 (br), 140.7, 136.5, 132.3, 129.0, 128.1, 127.3, 23.6;

^{11}B NMR (160 MHz, $CDCl_3$, r.t., ppm): δ 75 (br);

MS (EI^+) m/z: 298 $[M]^+$;

HRMS ($ASAP^+$): m/z calcd for $[C_{22}H_{23}B]$: 298.1887; found: 298.1882 (|Δ| = 1.68 ppm);

Elem. Anal. Calcd (%) for $C_{22}H_{23}B$: C, 88.60; H 7.77; Found: C, 88.71; H, 7.92.

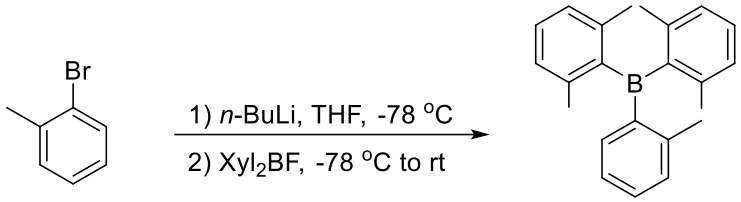

2

Bis(2,6-dimethylphenyl)(o-tolyl)borane (2) : To a solution of 1-bromo- 2-methylbenzene (462 mg, 2.7 mmol) in anhydrous THF (20 mL) a hexane solution of *n*-BuLi (1.7 mL, 1.6 M, 2.7 mmol) was added dropwise by syringe at -78 °C. The mixture was stirred at the same temperature for 1 h. A solution of bis(2,6-dimethylphenyl)fluoroborane (624 mg, 2.6 mmol) in anhydrous THF (5 mL) was added to the reaction mixture via syringe. The reaction mixture was warmed to room temperature and stirred overnight. The reaction was quenched with saturated solution of NaCl and the aqueous layer was extracted with Et_2O. The combined organic layer was dried over anhydrous Na_2SO_4, filtered, and concentrated under reduced pressure. The resulting crude material was subjected to silica gel column chromatography using *n*-hexane as eluent to afford 508 mg (1.63 mmol, 64%) of **2** as a white solid.

^{1}H NMR (500 MHz, $CDCl_3$, r.t., ppm): δ 7.33-7.29 (t, *J* = 8 Hz, 1H), 7.21 (d, *J* = 8 Hz, 1H), 7.18-7.14 (m, 4H), 6.94 (d, *J* = 8 Hz, 4H), 2.08 (s, 3H), 2.02 (s, 12H);

^{13}C{^{1}H} NMR (126 MHz, $CDCl_3$, r.t., ppm): δ 147.4 (br), 146.0 (br), 142.7, 140.3, 135.0, 131.2, 130.0, 129.3, 127.5, 125.7, 23.2, 22.5;

^{11}B NMR (160 MHz, $CDCl_3$, r.t., ppm): δ 76 (br);

MS (EI^+) m/z: 312 $[M]^+$.

HRMS ($ASAP^+$): m/z calcd for [$C_{23}H_{25}B$]: 312.2158; found: 312.2145 (|Δ| = 4.16 ppm);

Elem. Anal. Calcd (%) for $C_{23}H_{25}B$: C, 88.47; H, 8.07; Found: C, 88.72; H, 8.23.

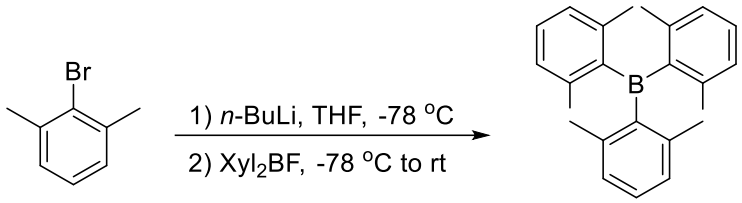

3

Tris(2,6-dimethylphenyl)borane (3): A solution of 2-bromo-m-xylene (1.1 mL, 8.3 mmol) in THF (10 mL) was treated with *t*-BuLi (1.7 M in pentane, 8.8 mL, 15 mmol) under argon at –78 °C. Then it was stirred at RT for 3 h before a solution of Xyl_2BF (1.8 g, 7.5 mmol) in THF (5 mL) was added at –78 °C and the reaction was allowed to warm to room temperature and stirred overnight. After 16 h, the reaction was quenched by adding 1 mL of water under argon. After removing the solvent and recrystallisation of the yellow solid from EtOH, the title compound was obtained as a white crystalline material (1.6 g, 64 %).

^{1}H NMR (500 MHz, $CDCl_3$, r.t., ppm): δ 7.14 (t, *J* = 8 Hz, 3H), 6.91 (d, *J* = 8 Hz, 6H), 2.02 (s, 18H);

^{13}C{^{1}H} NMR (75 MHz, $CDCl_3$) δ 147.2 (br), 140.9, 130.0, 128.2, 23.3;

^{11}B NMR (160 MHz, $CDCl_3$, r.t., ppm): δ 77 (br);

MS (EI) m/z: 326;

HRMS ($ASAP^+$): m/z calcd for [$C_{24}H_{27}B$]: 326.2200; found: 326.2194 (|Δ| = 1.84 ppm);

Elem. Anal. calcd for $C_{24}H_{27}B$: C, 88.35; H, 8.34; Found C 88.51, H 7.86.

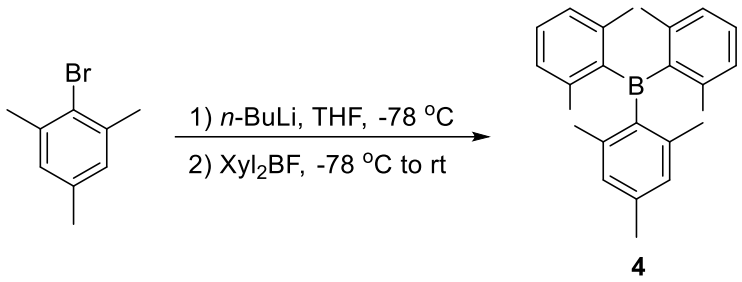

4

Bis(2,6-dimethylphenyl)(mesityl)borane (4): To a solution of 2-bromo-1,3,5-trimethylbenzene (617 mg, 3.1 mmol) in anhydrous THF (20 mL) a hexane solution of *n*-BuLi (1.9 mL, 1.6 M, 3.1 mmol) was added dropwise by syringe at -78 ˚C. The mixture was stirred at the same temperature for 1 h. A solution of bis(2,6-dimethylphenyl)fluoroborane (720 mg, 3.0 mmol) in anhydrous THF (5 mL) was added to the reaction mixture via syringe. The reaction mixture was warmed to room temperature and stirred overnight. The reaction was quenched with saturated solution of NaCl and the aqueous layer was extracted with Et_2O. The combined organic layer was dried over anhydrous Na_2SO_4, filtered, and concentrated under reduced pressure. The resulting crude material was subjected to silica gel column chromatography using *n*-hexane as eluent to afford 715 mg (2.1 mmol) of **4** in 71% yield as a white solid.

^{1}H NMR (400 MHz, $CDCl_3$, r.t., ppm): δ 7.13 (t, *J* = 8 Hz, 2H), 6.91 (s, 2H), 6.90 (s, 2H), 6.75 (d, *J* = 1 Hz, 2H), 2.27 (s, 3H), 2.03 (s, 6H), 2.01 (s, 6H), 1.98 (s, 6H).

^{13}C{^{1}H} NMR (126 MHz, $CDCl_3$, r.t., ppm): δ 147.2 (br), 143.9 (br), 140.9, 140.5, 140.4, 139.6, 129.4, 128.8, 127.8, 127.8, 23.1, 22.9, 22.9, 21.4 ppm.

^{11}B NMR (160 MHz, $CDCl_3$, r.t., ppm): δ 78 (br).

MS (EI^+) m/z: 340 $[M]^+$.

HRMS ($ASAP^+$): m/z calcd for $[C_{25}H_{29}B]$: 340.2357; found: 340.2350 (|Δ| = 2.06 ppm);

Elem. Anal. Calcd (%) for $C_{25}H_{29}B$: C, 88.23; H, 8.59; Found: C, 87.90; H, 8.74.

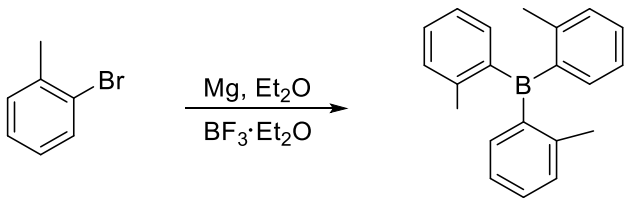

Tris(2-methylphenyl)borane: In a 200-mL, three-necked, round-bottomed flask maintained under argon and equipped with a reflux condenser, whose top was connected to an argon inlet and a pressure-equalizing dropping funnel, were placed 0.14 g (5.8 mmol) of magnesium turnings. With stirring, 50 mL of 3 g (17.5 mmol) of 1-bromo-2-methylbenzene anhydrous ether solution was added in one portion. The mixture was warmed to initiate the reaction and was then heated under reflux for another 2 h. Subsequently, 0.72 ml (5.8 mmol) $BF_3 \cdot Et_2O$ was added to the mixture. After 24 h, 150 mL of dry ether was added, while maintaining an argon atmosphere. The mixture was filtered and the filtrate was evaporated to dryness. The crude material was crystallized from pentane at –35 °C to afford 1.26 g (4.4 mmol, 76 %) of tris(2-methylphenyl)borane as white solids.

^{1}H NMR (500 MHz, $CDCl_3$, r.t., ppm): δ 7.34 (m, 3H), 7.18 (m, 9H), 2.10 (s, 9H);

^{13}C{^{1}H} NMR (126 MHz, $CDCl_3$, r.t., ppm): δ 146.3 (br.), 142.4, 134.8, 130.4, 129.8, 125.0, 23.1;

^{11}B NMR (160 MHz, $CDCl_3$, r.t., ppm): δ 73 (br);

HRMS ($ASAP^+$): m/z calcd for $[C_{22}H_{21}B]$: 284.1731; found: 284.1723 (|Δ| = 2.82 ppm);

Elem. Anal. Calcd (%) for $C_{22}H_{21}B$: C, 88.75; H, 7.45; Found: C, 88.51; H, 7.45.

2.4.3 Photophysical data

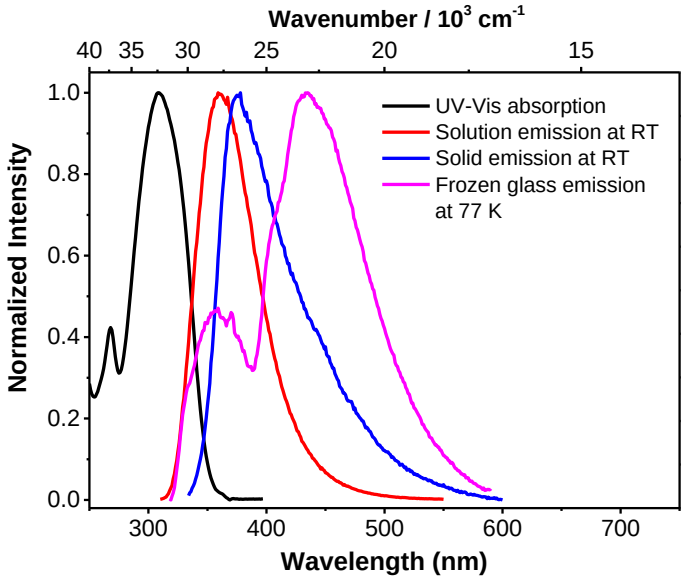

Figure 2-6. Normalized absorption and emission spectra of tris(2-methylphenyl)borane (E_x = 305 nm) in hexane.

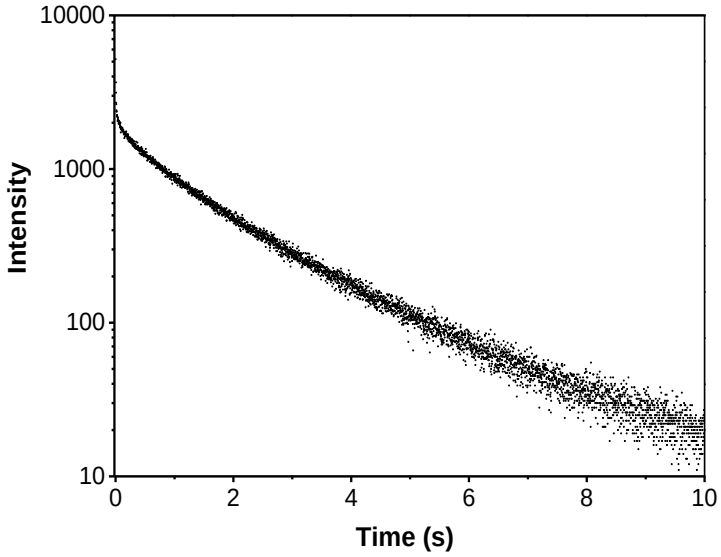

Figure 2-7. Decay of the 450 nm emission from tris(2-methylphenyl)borane in a frozen methylcyclohexane glass at 77 K.

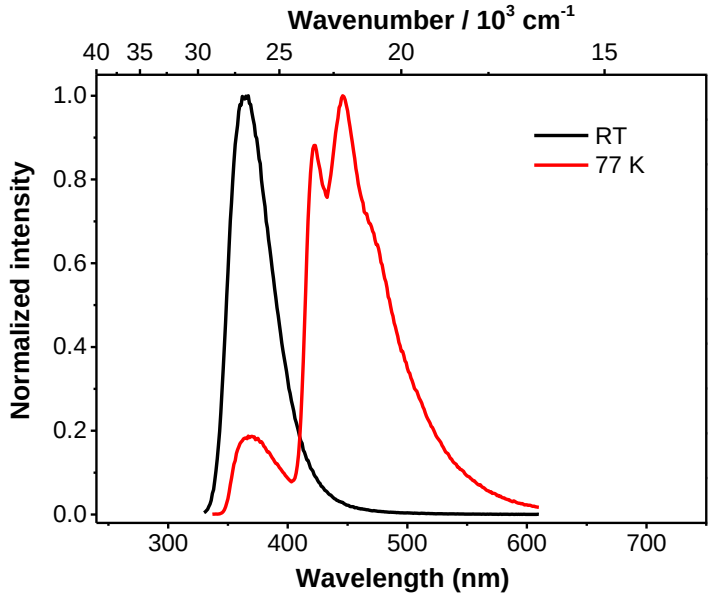

Figure 2-8. Normalized emission spectra of **3** in a PMMA film (1 %) at room temperature and 77 K (E_x = 305

nm).

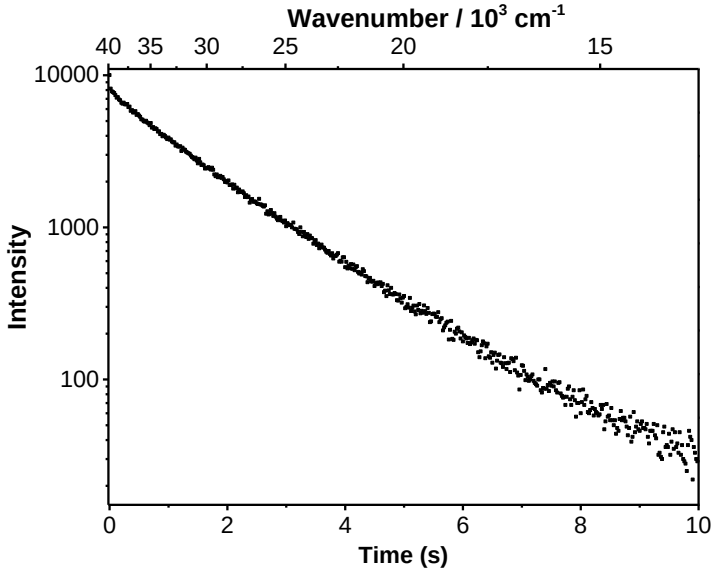

Figure 2-9. Decay of the 450 nm emission from **3** in a PMMA film (1 %) at 77 K.

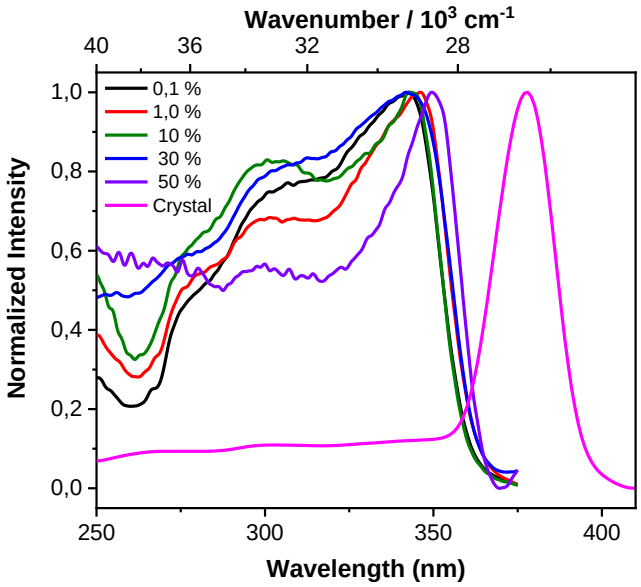

Figure 2-10. Normalized excitation spectra of compound **3** in 0.1, 1.0, 10, 30 and 50 % PMMA film and the crystalline state.

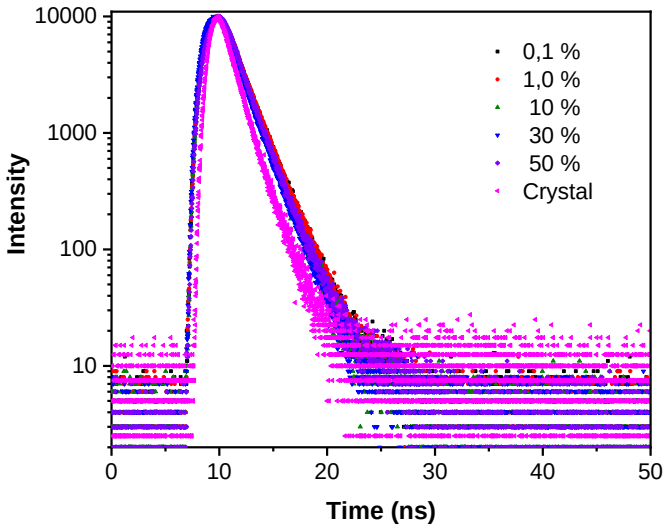

Figure 2-11. Decays of fluorescence at maximum emission wavelength of compound **3** in 0.1, 1.0, 10, 30 and 50 % PMMA film and the crystalline state.

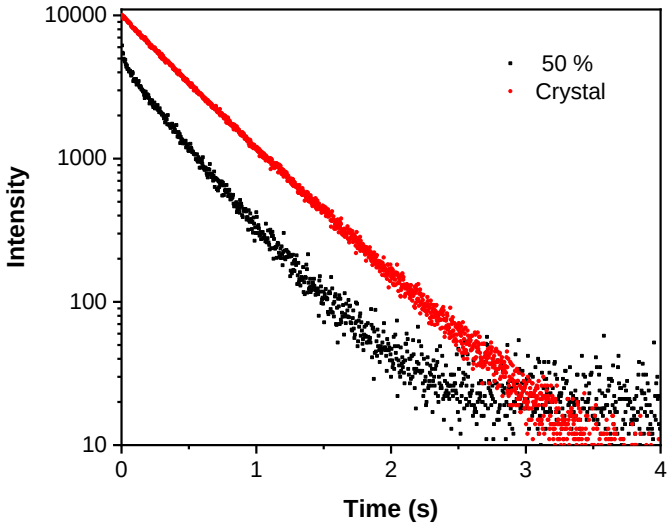

Figure 2-12. Decays of phosphorescence emission at 550 nm of compound **3** in 50 % PMMA film (407 ms) and the crystalline state (478 ms) at room temperature under air.

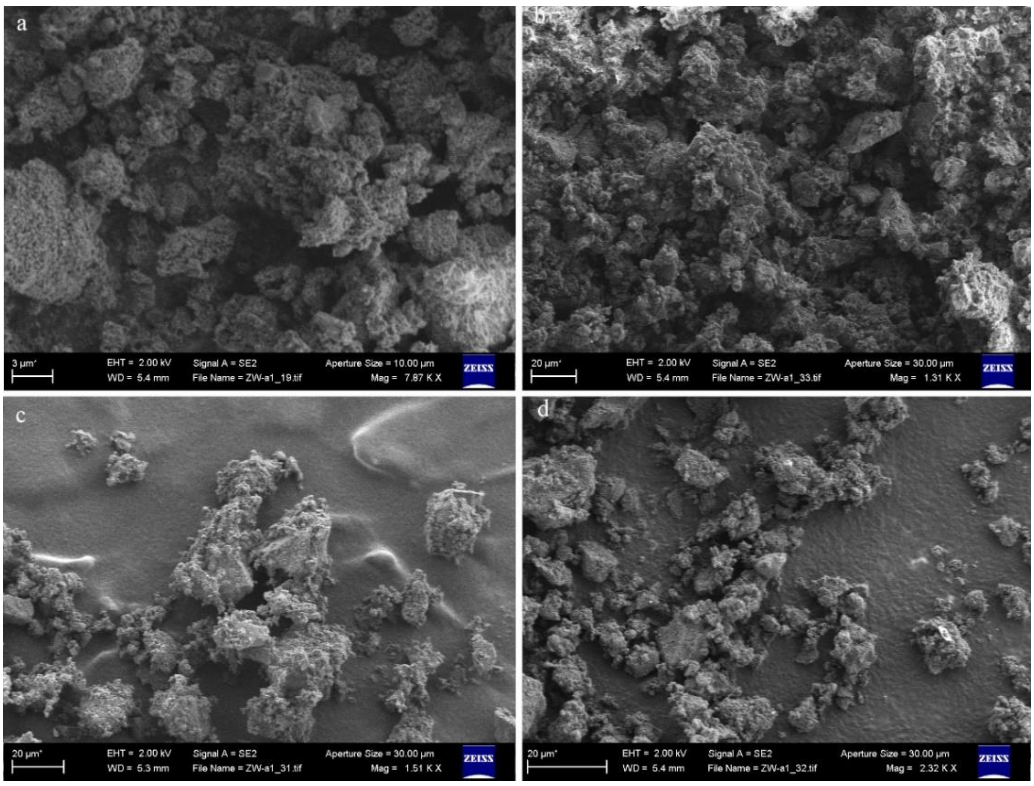

Figure 2-13. (a)-(d) SEM pictures of **3** in ball-milled powder state.

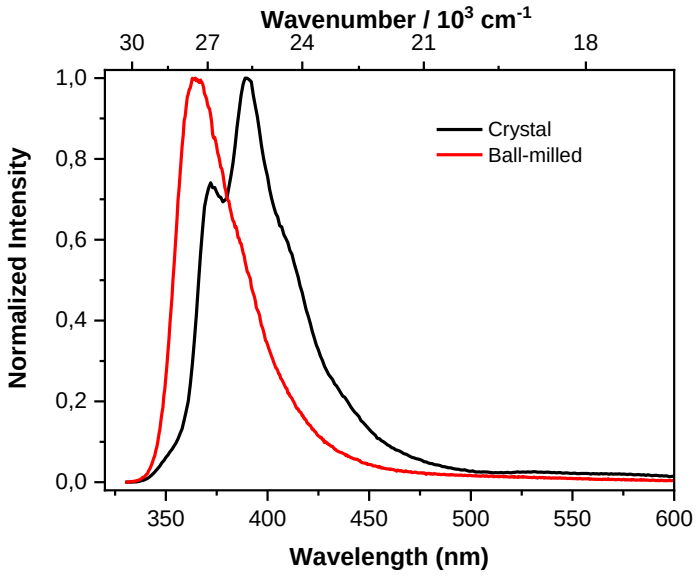

Figure 2-14. Normalized PL emission spectra of **3** in **the** crystalline state and ball-milled powder state at room temperature (E_x = 305 nm).

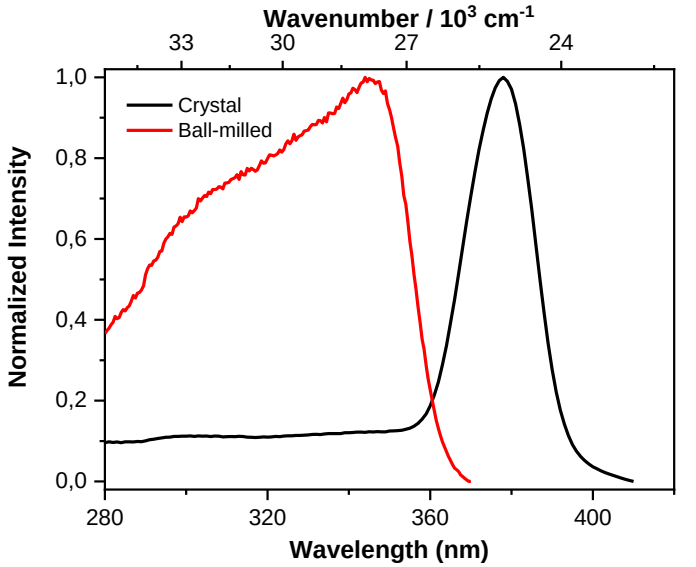

Figure 2-15. Normalized excitation spectra of **3** in **the** crystalline state and ball-milled powder state at room temperature.

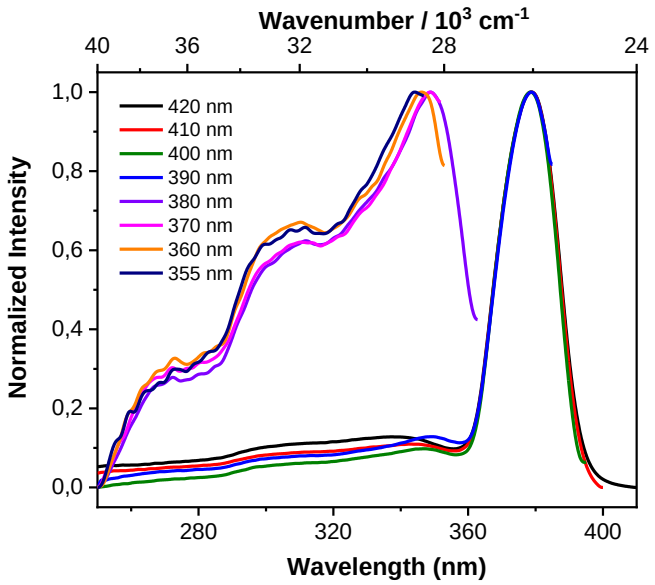

Figure 2-16. Normalized emission dependent excitation spectra of compound **3** in the crystalline state from 420 to 355 nm.

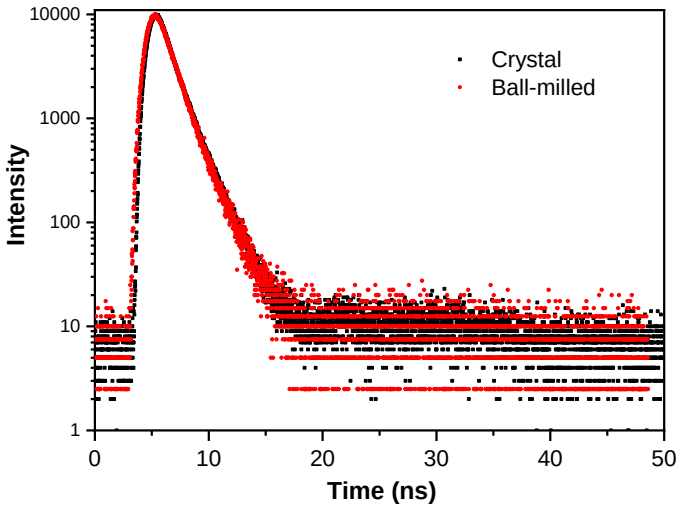

Figure 2-17. Fluorescence decay of **3** in **the** crystalline state and ball-milled powder state at room temperature.

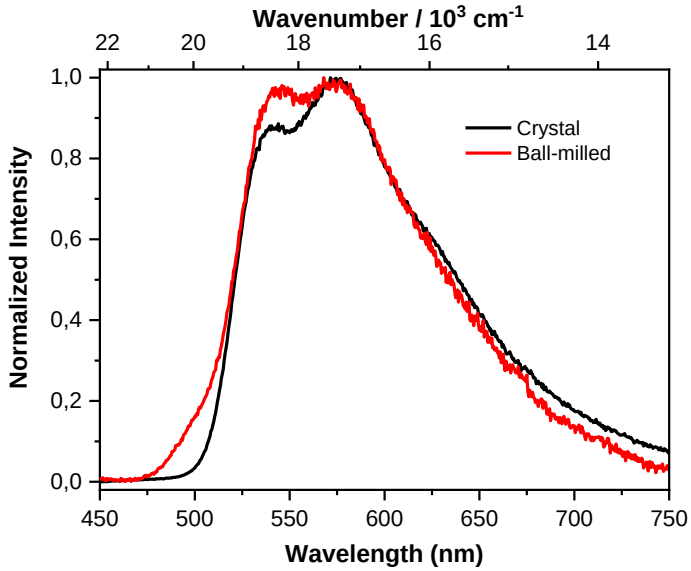

Figure 2-18. Normalized time-gated phosphorescence emission spectra of **3** in **the** crystalline state and ball-milled powder state at room temperature (E_x = 305 nm).

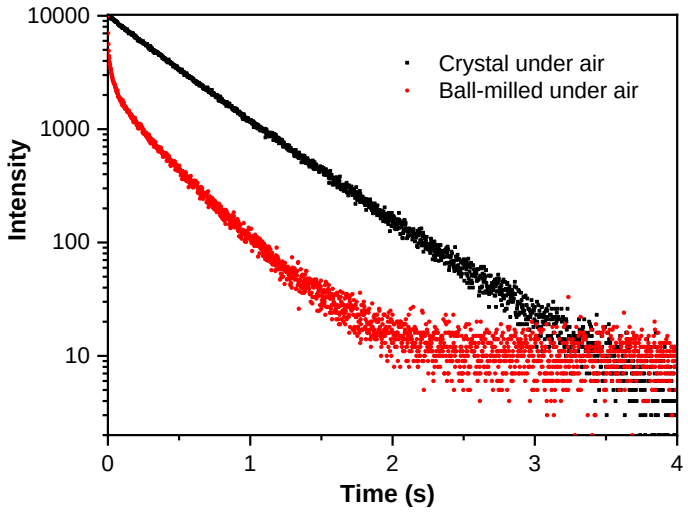

Figure 2-19. Phosphorescence decay of **3** in the crystalline state (470 ms) and ball-milled powder state (340 ms) at room temperature under air.

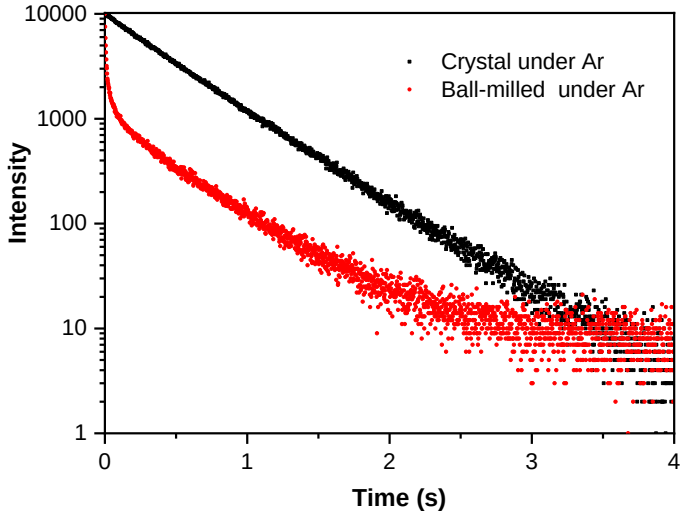

Figure 2-20. Phosphorescence decay of **3** in the crystalline state (478 ms) and ball-milled powder state (481 ms) at room temperature under argon.

Table 2-2. Unit cell parameters of **3** obtained from the LeBail refinement of powder X-ray diffraction data at room temperature. Ball-milled samples were made by putting compound 3 in a stainless-steel vial (2 ml) and ground with five steel balls (3 mm) for five minutes at a frequency of 15 Hz in a Lab Wizz LMLW 320/2 ball mill

Data	**# Ball-milled**
λ / Å, radiation	1.5406, Cu-Kα_1
2θ range / °	5 – 60
a / Å	8.6437(9)
b / Å	9.7390(9)
c / Å	12.3531(14)
α / °	98.497(8)
β / °	90.908(7)
γ / °	107.648(5)
Volume / Å^3	978.0(2)
R_p	0.0264
wR_p	0.0387

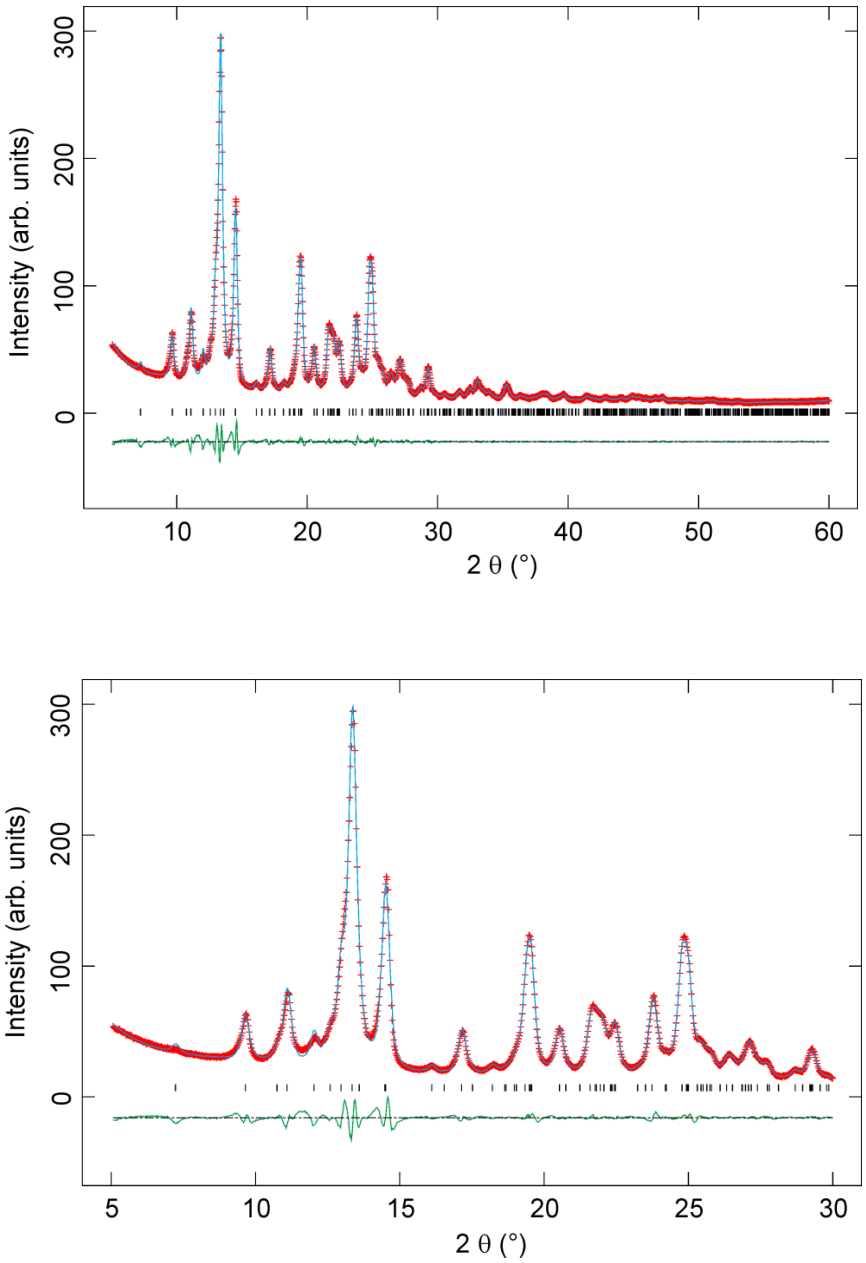

Figure 2-21. Powder diffraction patterns (ball-milled sample **B**) of compound **3** in the full range from 5 – 60° 2θ (top) and in the range from 5 – 30° 2θ (bottom). Red crosses represent the experimental values. The continuous blue line shows the results of the Le Bail fit to the data. The difference between experimental data and LeBail fit is represented by the green line at the bottom of the plot. Vertical bars show the positions of the Bragg reflections of compound **3**.

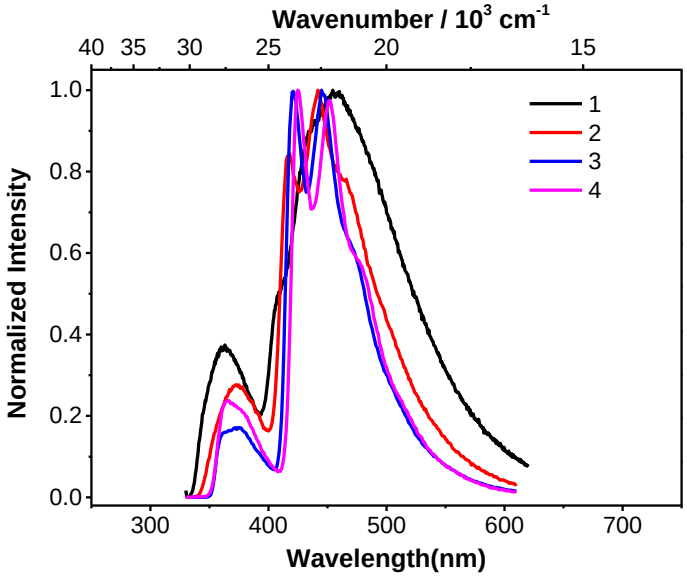

Figure 2-22. Normalized photoluminescence emission spectra of **1-4** in a frozen methylcyclohexane glass at 77 K (E_x = 305 nm).

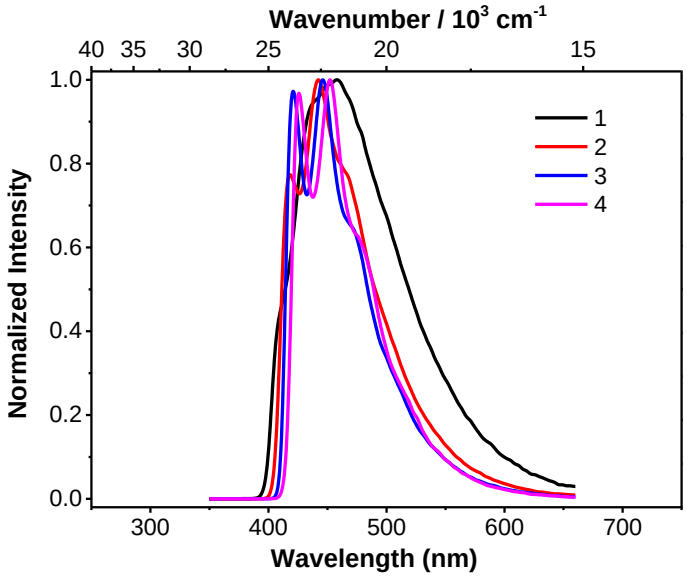

Figure 2-23. Normalized time-gated phosphorescence emission spectra of compounds **1-4** in a frozen methylcyclohexane glass at 77 K (E_x = 305 nm).

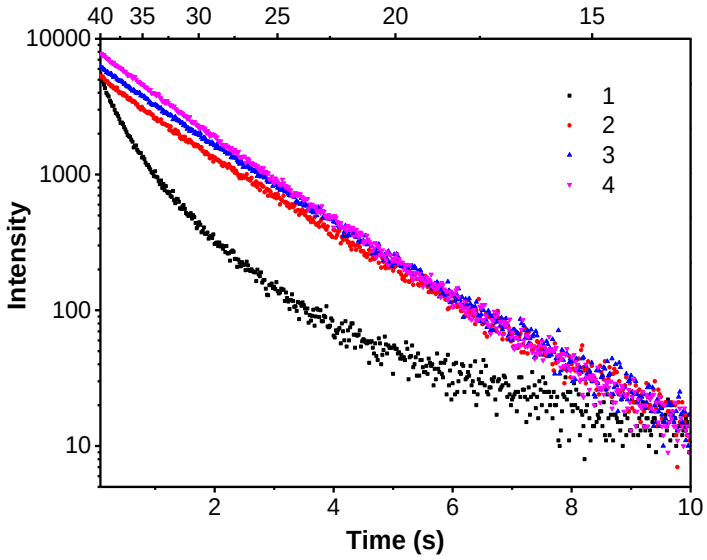

Figure 2-24. Decays of the phosphorescent emissions of **1-4** in a frozen methylcyclohexane glass at 77 K.

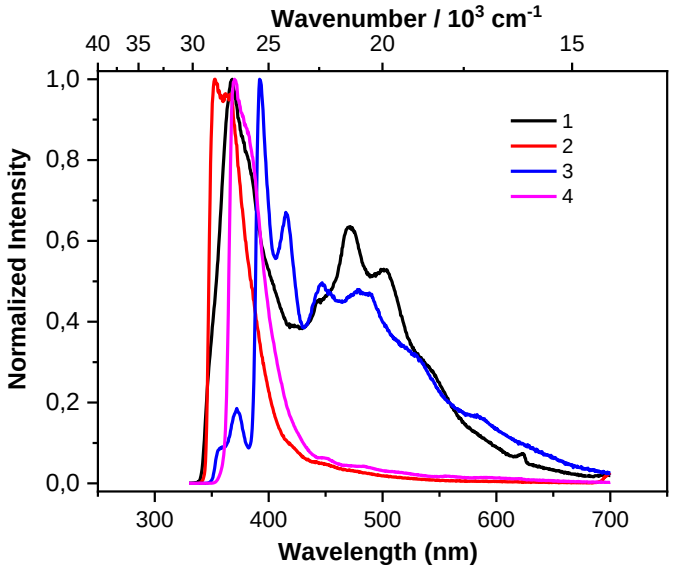

Figure 2-25. Normalized photoluminescent emission spectra of crystalline **1-4** at 77 K (E_x = 305 nm).

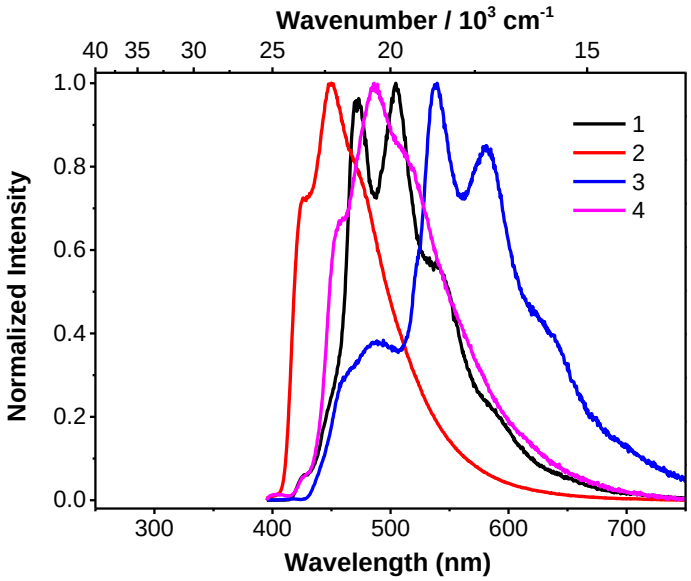

Figure 2-26. Normalized time-gated phosphorescence emission spectra of crystalline **1-4** at 77 K (E_x = 305 nm).

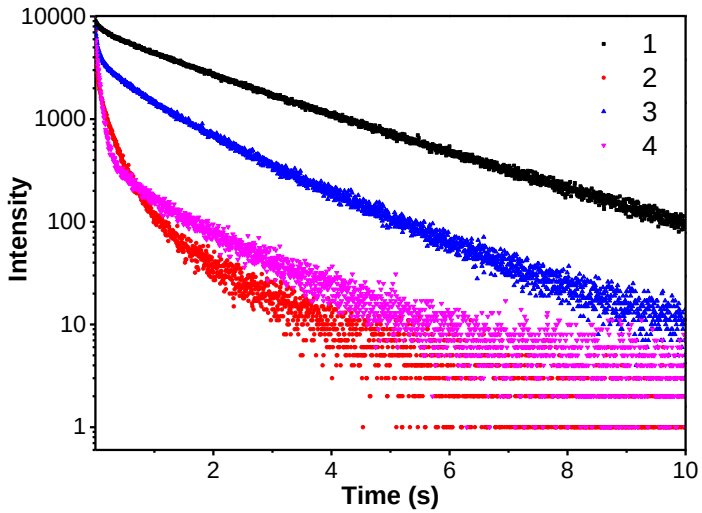

Figure 2-27. Decays of the maximum phosphorescent emissions of crystalline **1-4** at 77 K.

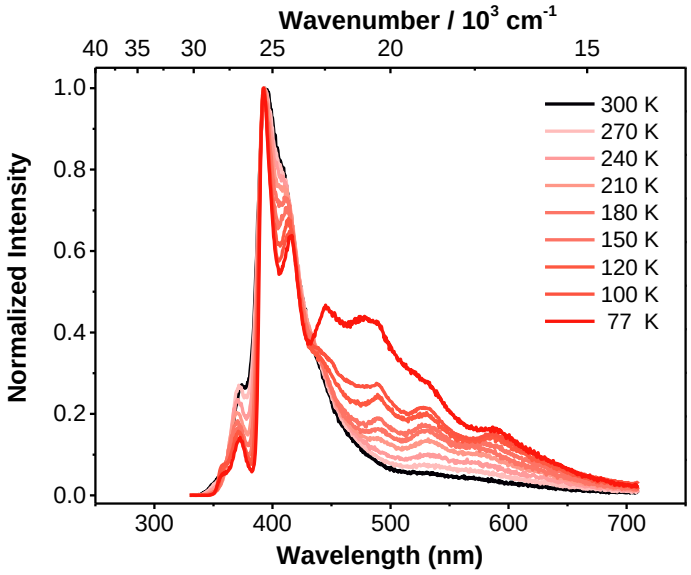

Figure 2-28. Normalized photoluminescent emission spectra of crystalline **3** at different temperatures (E_x = 305 nm).

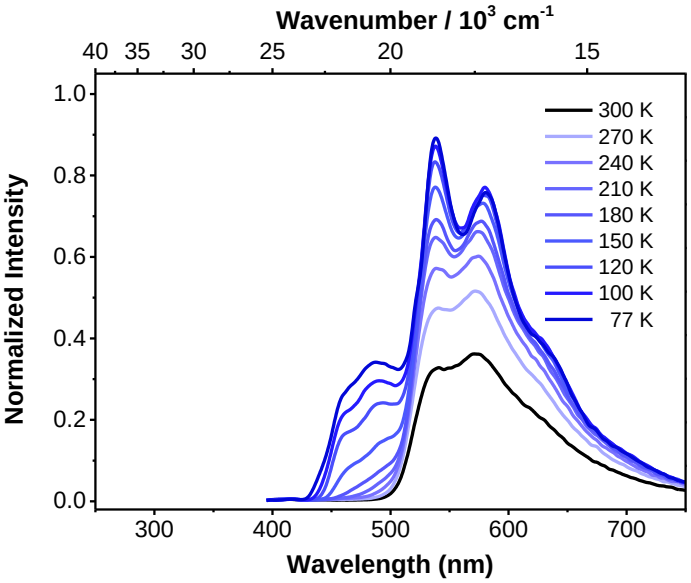

Figure 2-29. Normalized time-gated phosphorescence emission spectra of crystalline **3** at different temperatures (E_x = 305 nm).

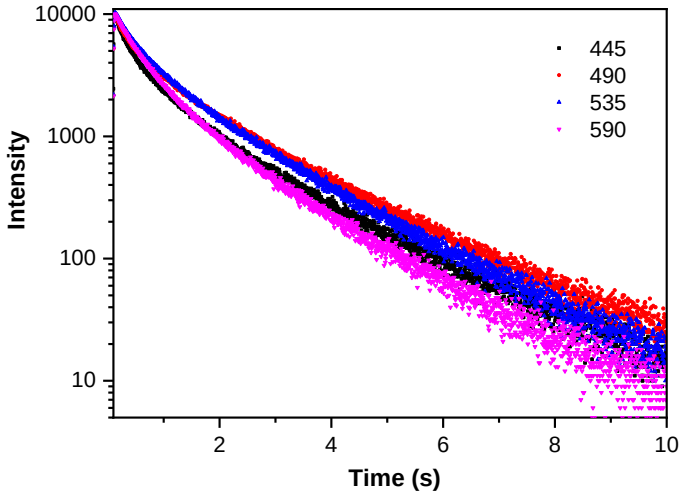

Figure 2-30. Decays of the phosphorescent emission of crystalline **3** at 445, 490, 535 and 590 nm at 77 K.

2.4.4 Solid crystal structure data

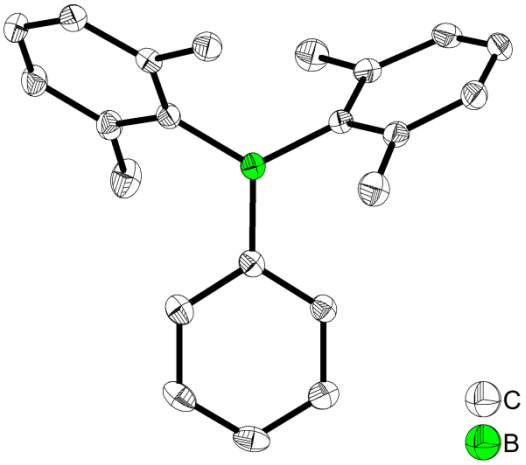

Figure 2-31. The solid-state molecular structure of **1** determined by single-crystal X-ray diffraction at 100 K. All ellipsoids are drawn at the 50% probability level, and H atoms are omitted for clarity.

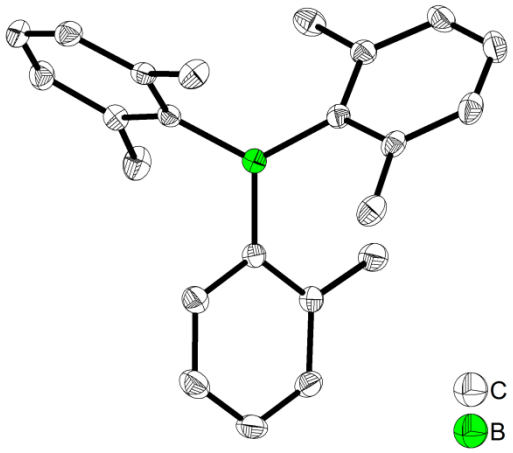

Figure 2-32. The solid-state molecular structure of **2** determined by single-crystal X-ray diffraction at 100 K. All ellipsoids are drawn at the 50% probability level, and H atoms are omitted for clarity.

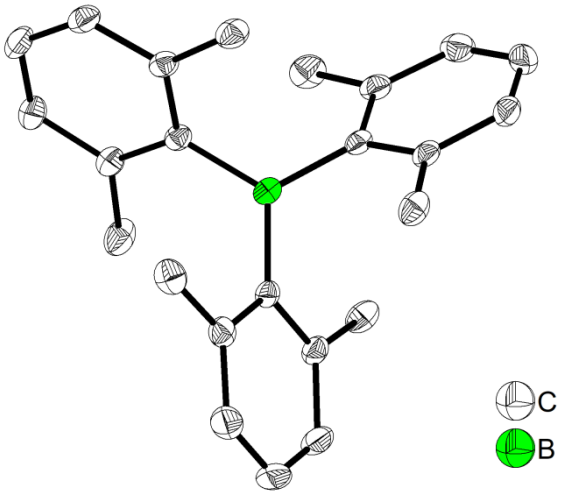

Figure 2-33. The solid-state molecular structure of **3** determined by single-crystal X-ray diffraction at 100 K. All ellipsoids are drawn at the 50% probability level, and H atoms are omitted for clarity.

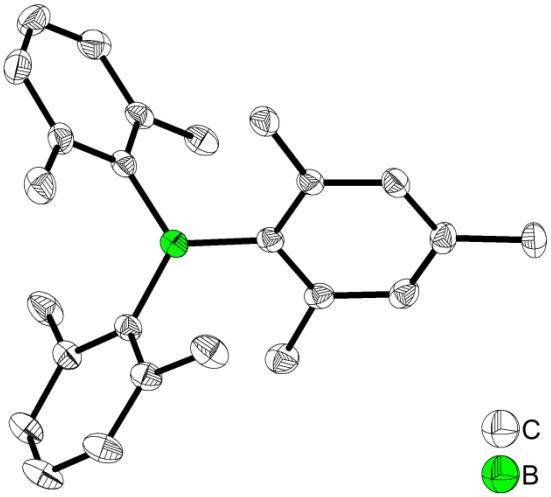

Figure 2-34. The solid-state molecular structure of **4** determined by single-crystal X-ray diffraction at 100 K. All ellipsoids are drawn at the 50% probability level, and H atoms are omitted for clarity. The major structural conformation with a refined occupancy of 0.809(4) is shown here.

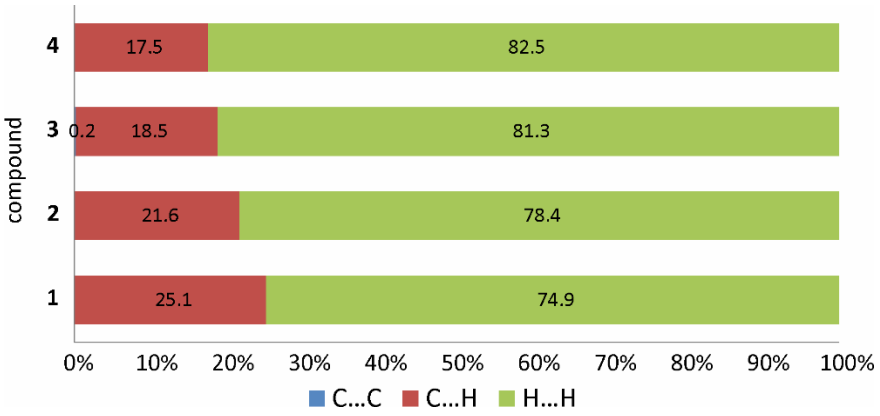

Figure 2-35. Percentage contributions to the Hirshfeld surface area for the various close intermolecular contacts in compounds **1**, **2**, **3**, and **4** at 100 K.

Table 2-3. Single-crystal X-ray diffraction data and structure refinements of **1**, **2**, **3**, and **4**.

Data	**1**	**2**	**3**	**4**
CCDC number	1940099	1940100	1940101	1940107
Empirical formula	$C_{22}H_{23}B$	$C_{23}H_{25}B$	$C_{24}H_{27}B$	$C_{25}H_{29}B$
Formula weight / $g \cdot mol^{-1}$	298.21	312.24	326.26	340.29
T / K	100(2)	100(2)	100(2)	100(2)
radiation, λ / Å	MoKα 0.71073	MoKα 0.71073	MoKα 0.71073	MoKα 0.71073
Crystal size / mm^3	0.23×0.29×0.78	0.28×0.35×0.41	0.23×0.36×0.41	0.12×0.42×0.48
Crystal color, habit	colorless block	colorless block	colorless block	colorless plate
μ / mm^{-1}	0.063	0.064	0.063	0.063
Crystal system	Monoclinic	Monoclinic	Triclinic	Triclinic
Space group	$P2_1/c$	$P2_1/n$	$P\bar{1}$	$P\bar{1}$
a / Å	8.148(6)	8.138(5)	8.511(4)	8.445(3)
b / Å	10.828(3)	18.060(10)	9.675(2)	9.647(3)
c / Å	19.832(9)	12.161(7)	12.241(4)	12.890(5)
α / °	90	90	99.28(2)	99.166(15)
β / °	97.06(4)	90.293(11)	90.87(4)	91.49(3)
γ / °	90	90	107.44(2)	105.371(15)
Volume / $Å^3$	1736.5(16)	1787.4(17)	946.9(6)	997.1(6)
Z	4	4	2	2
ρ_{calc} / $g \cdot cm^{-3}$	1.141	1.160	1.144	1.133
$F(000)$	640	672	352	368
θ range / °	2.069 - 28.310	2.019 - 28.338	2.514 - 26.732	1.604 - 28.441
Reflections collected	19166	19909	16834	24532
Unique reflections	4300	4440	4009	5019
Parameters / restraints	212 / 0	222 / 0	232 / 0	253 / 0
GooF on F^2	1.054	1.029	1.035	1.050
R_1 [I>2σ(I)]	0.0469	0.0501	0.0437	0.0480
wR^2 (all data)	0.1256	0.1350	0.1174	0.1316
Max. / min. residual electron density / $e \cdot Å^{-3}$	0.364 / –0.236	0.382 / –0.207	0.365 / –0.230	0.366 / –0.244

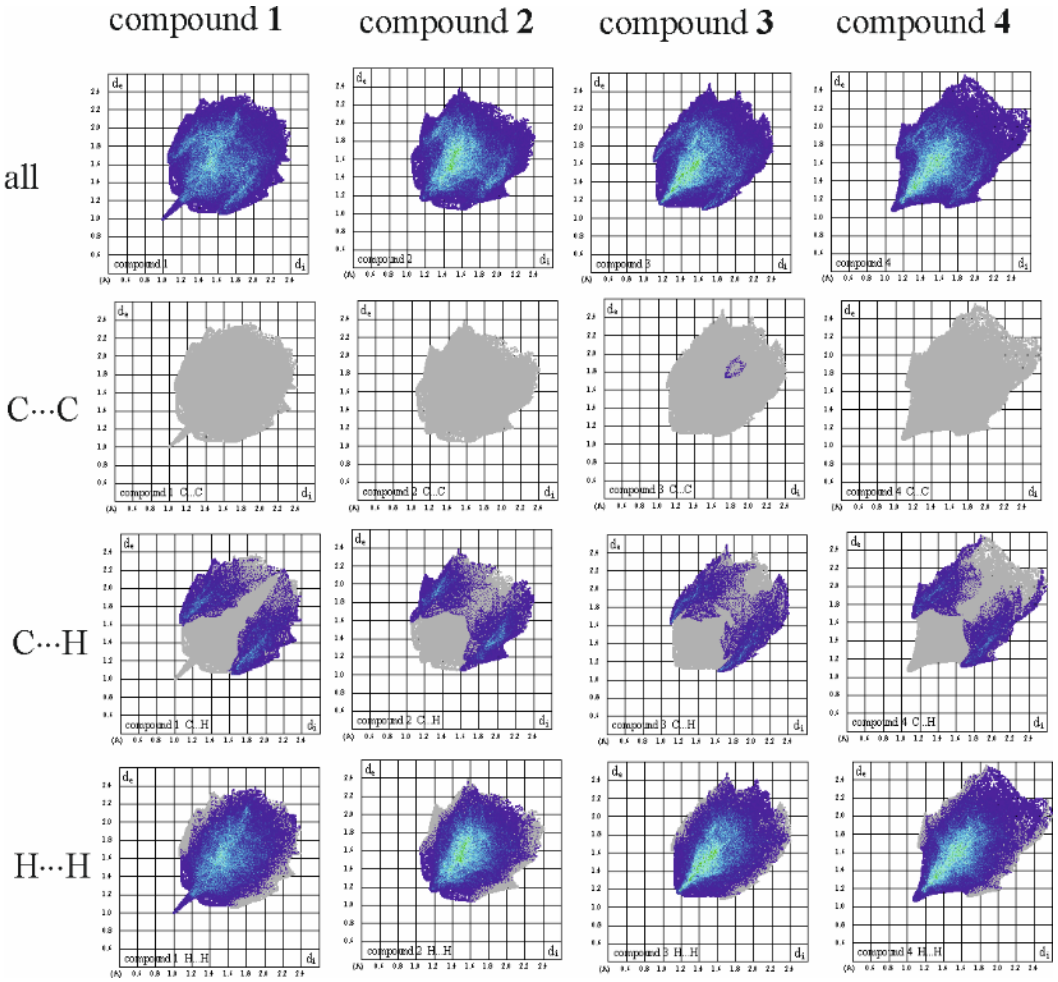

Figure 2-36. Two-dimensional fingerprint plots of molecules **1**, **2**, **3**, and **4** calculated from the Hirshfeld surfaces. The top row shows the complete fingerprint plots, while the other plots indicate the contributions of the individual intermolecular interactions (C···C, C···H, and H···H from top to bottom) within the grey area of all contributions.

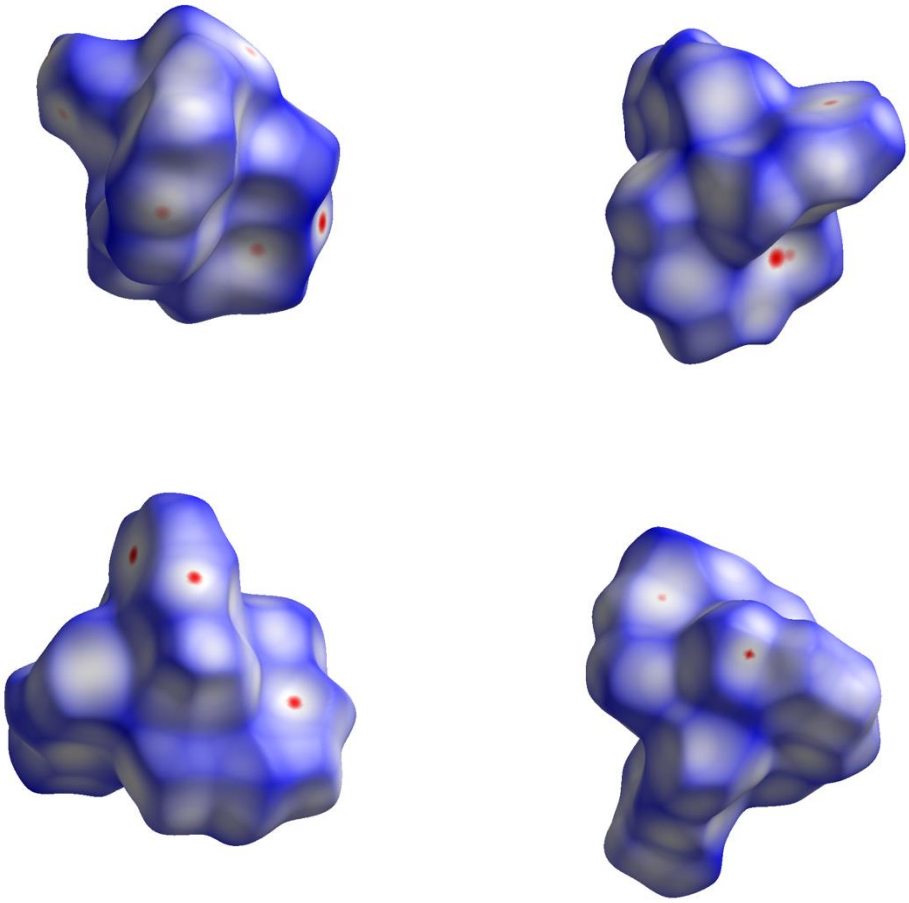

Figure 2-37. Hirshfeld surfaces of compounds **1** (top left), **2** (top right), **3** (bottom left), and **4** (bottom right) at 100 K mapped with d_{norm} over the range -0.16 to 1.40. Close contacts are shown red on the surface.

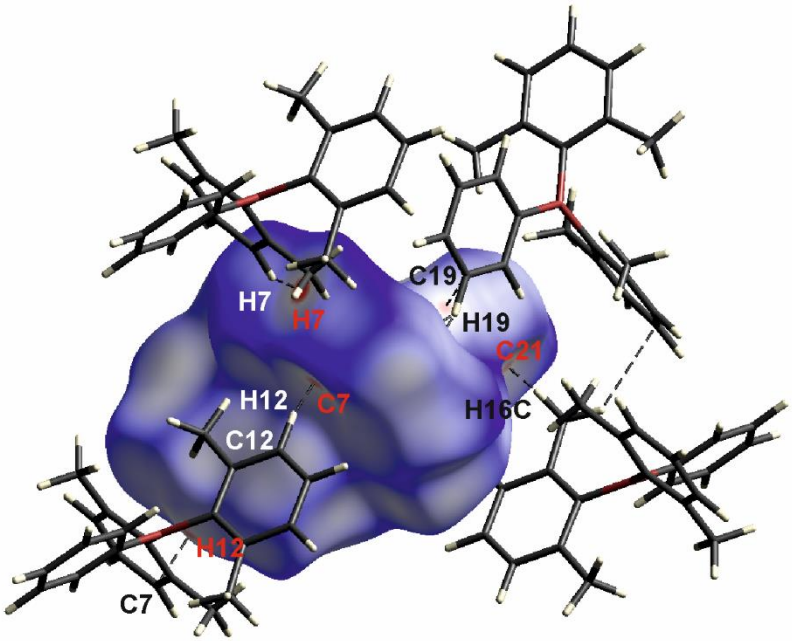

Figure 2-38. Hirshfeld surface of compound **1** mapped with d_{norm} over the range -0.16 to 1.40 at 100 K. Neighbouring molecules associated with close contacts are shown.

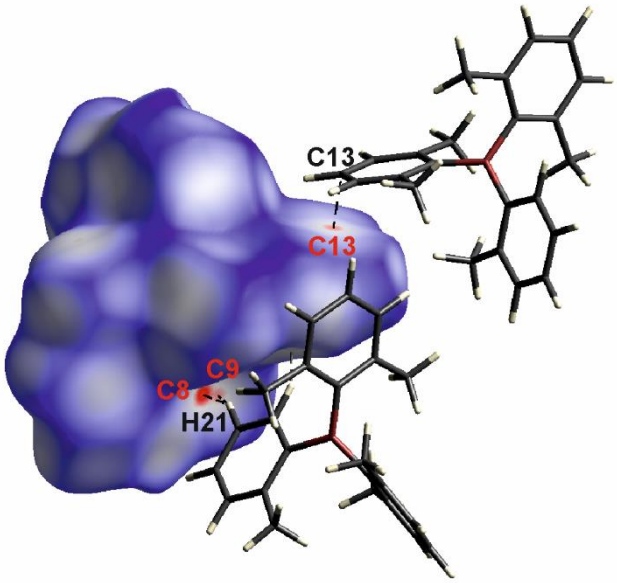

Figure 2-39. Hirshfeld surface of compound **2** mapped with d_{norm} over the range -0.16 to 1.40 at 100 K. Neighbouring molecules associated with close contacts are shown.

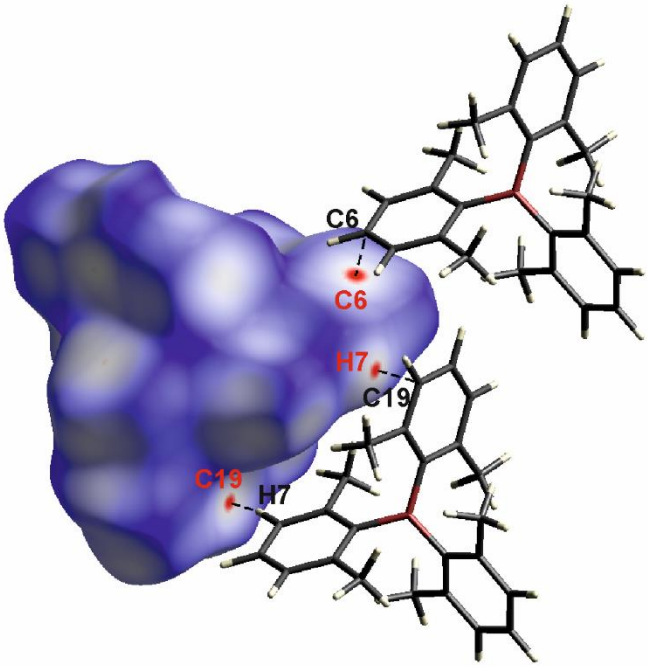

Figure 2-40. Hirshfeld surface of compound **3** mapped with d_{norm} over the range -0.16 to 1.40 at 100 K. Neighbouring molecules associated with close contacts are shown.

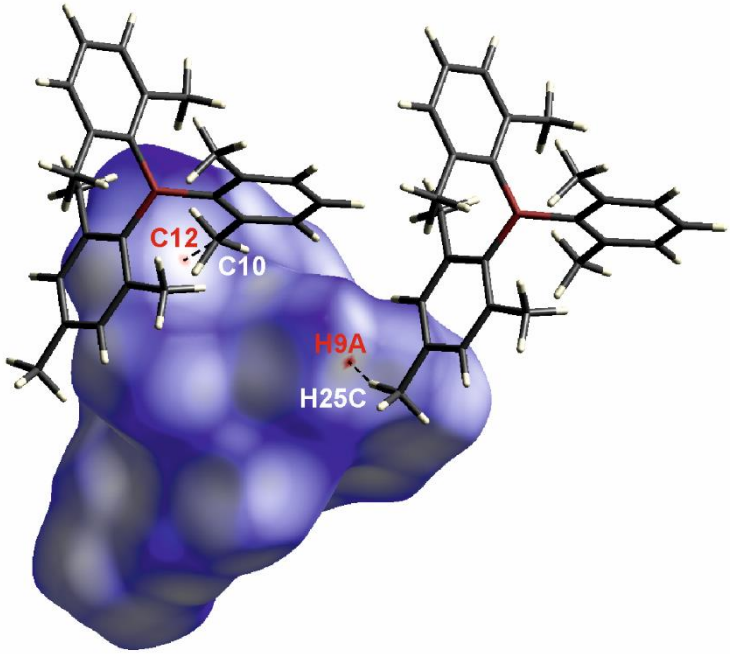

Figure 2-41. Hirshfeld surface of compound **4** mapped with d_{norm} over the range -0.16 to 1.40 at 100 K. Neighbouring molecules associated with close contacts are shown.

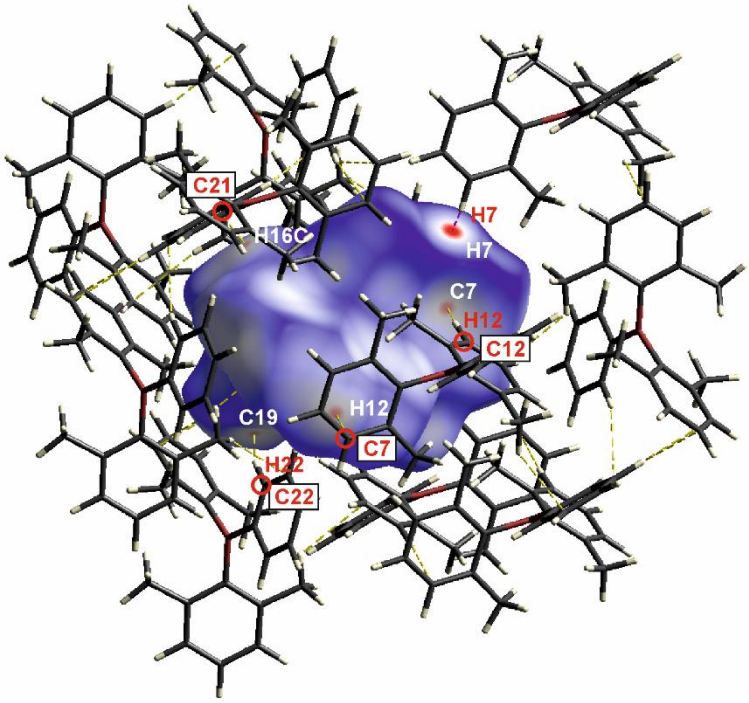

Figure 2-42. Hirshfeld surface of compound **1** mapped with d_{norm} over the range -0.16 to 1.40 at 100 K. Neighbouring molecules associated with close contacts are shown. Closest contacts are labelled.

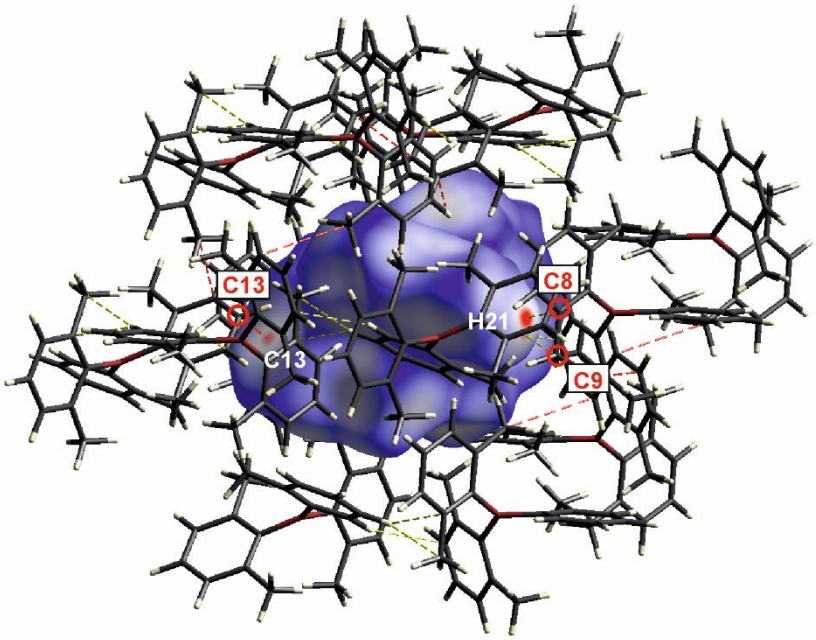

Figure 2-43. Hirshfeld surface of compound **2** mapped with d_{norm} over the range -0.16 to 1.40. Neighbouring molecules associated with close contacts are shown. Closest contacts are labelled.

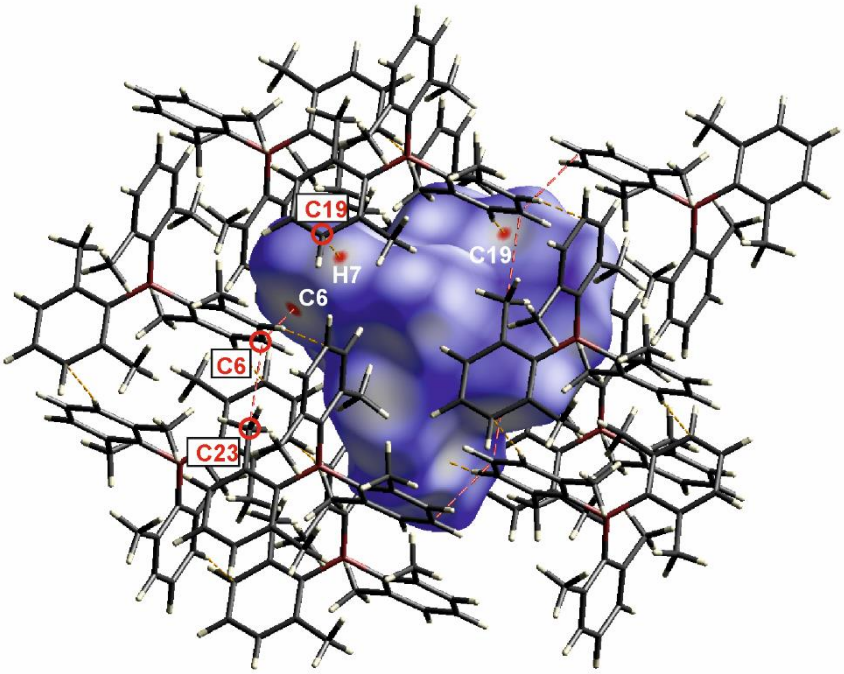

Figure 2-44. Hirshfeld surface of compound **3** mapped with d_{norm} over the range -0.16 to 1.40 at 100 K. Neighbouring molecules associated with close contacts are shown. Closest contacts are labelled.

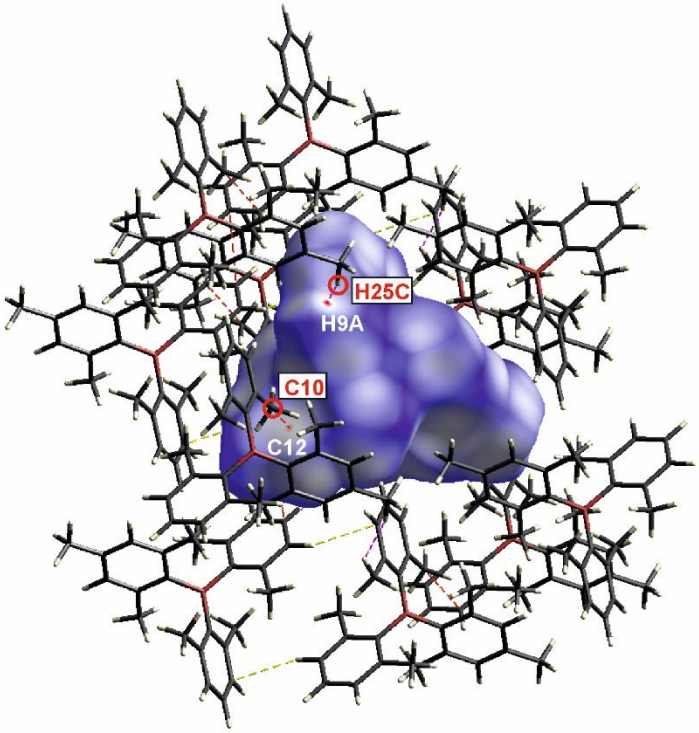

Figure 2-45. Hirshfeld surface of compound **4** mapped with d_{norm} over the range -0.16 to 1.40 at 100 K. Neighbouring molecules associated with close contacts are shown. Closest contacts are labelled.

Table 2-4. Selected bond lengths (Å) and angles (°) of compounds **1**, **2**, **3**, and **4** at 100 K**.**

	1	**2**	**3**	**4**[a]
Sum ∠ CBC	360.0(1)	359.9(1)	360.0(1)	360.0(1)
B–C	1.5867(18) 1.5819(18) 1.5686(19)	1.583(2) 1.581(2) 1.570(2)	1.5795(19) 1.5826(18) 1.5858(18)	1.5848(18) 1.5794(18) 1.5763(18)
∠ BC3 – aryl	65.28(6) 57.45(6) 16.09(9)	60.53(5) 56.67(6) 41.91(6)	53.52(7) 52.91(7) 53.92(6)	49.96(5) 54.85(6) 51.15(6)

[a] The mesityl group is disordered with one of the m-xylyl groups.

Table 2-5. Properties of crystals of compounds **1**, **2**, **3**, and **4** at 100 K: Volume within van der Waals (V_m), Hirshfeld (V_H), and surface of the crystal voids (V_v), crystal packing coefficient (c_k), solvent accessible volume (V_{solv}), and percentage of intermolecular contacts.

	1	**2**	**3**	**4** [a]
V_m / Å³	283.36	298.60	312.20	323.94
V_H / Å³	427.11	440.18	466.68	491.63
V_v / Å³	211.86	169.00	103.82	111.40
V_v / Å³ per formula unit	52.97	42.25	51.91	55.70
c_k	0.654	0.668	0.659	0.650
V_{solv} / Å³	0.0	0.0	9.0	0.0
C···C / %	0.0	0.0	0.2	0.0
C···H / %	25.1	21.6	18.5	17.5
H···H / %	74.9	78.4	81.3	82.5

[a] The mesityl group is disordered with one of the m-xylyl groups. The configuration with the major occupancy (80%) is considered in this comparison.

Table 2-6. Intermolecular C−H···C(π), C···C, and H···H interaction distances (Å) and angles (°) in compounds **1**, **2**, **3**, and **4** at 100 K. Distances and angles of strong interactions are in bold type.

Compound	C−H···C	H···C/H	C···C	∠(CHC)
1	H7···H7	**2.241**		
	C12−H12···C7	**2.835**	**3.769**	**168.04**
	C19−H19···C5	**2.839**	**3.767**	**166.01**
	C19−H19···C6	2.887	3.650	138.19
	C22−H22···C19	2.856	3.761	159.93
	C16(methyl)−H16C···C21	2.792	3.634	144.47
	C16(methyl)−H16B···C13	2.851	3.532	127.27
2	C21−H21···C8	2.752	3.572	145.00
	C21−H21···C9(methyl)	2.859	3.742	155.05
	C22−H22···C12	2.877	3.756	154.27
	C10(methyl)−H10B···C14	2.861	3.384	114.33
	C12-H12···π (centroid of aryl#1)	2.907	3.830	168.10
	C13···C13		3.334	
	C10(methyl)···C14		3.384	
3	C7−H7···C19	**2.841**	**3.765**	**164.41**
	C14−H14···C21	2.871	3.815	**171.96**
	C5−H5···C12	2.897	3.832	168.18
	C6···C6		**3.319**	
	C6···C23(methyl)		3.392	
4	H9A(methyl)···H25C (methyl)	2.311		
	C14−H14···C7	2.893	3.745	149.84
	C13A···C13A		3.392	
	C10(methyl)···C12		3.378	

Table 2-7. Aryl···aryl (π···π) distances (Å) and angles (°) in crystals of **1**, **2**, **3**, and **4** at 100 K: nearest-neighbour (nn) C···C distances, centroid-centroid distances, interplanar separations, shifts, and slip angles. Aryl rings are numbered 1, 2, or 3 according to the C1, C2, or C3 atom being present and bonding to the boron atom, respectively. The closest interactions are in bold type.

Compound	Aryl···Aryl	nn C···C	Centroid-centroid distance	Interplanar separation	Shift	Slip angle
1	#1···#1	3.857(5)	6.123(3)	2.513(6)	5.583(4)	65.7
	#2···#2	4.315(5)	6.275(3)	3.507(5)	5.203(5)	56.0
	#1···#2	4.526(4)	6.587(3)	3.886(5) / 2.982(6)	5.319(5) / 5.874(4)	53.8/ 63.1
2	#2···#2	**3.3338(17)**	**5.000(2)**	**3.1607(13)**	**3.8745(19)**	**50.8**
	#3···#3	3.5833(12)	5.489(2)	3.0270(15)	4.578(3)	56.5
	#1···#1	4.1070(16)	6.348(3)	3.0521(15)	5.566(3)	61.3
3	#1···#1	**3.319(3)**	**5.1671(17)**	**2.980(3)**	**4.221(3)**	**54.8**
	#2···#2	**3.495(3)**	**4.8718(16)**	**3.397(3)**	**3.493(3)**	**45.8**
4	#2···#2	**3.392(3)**	**5.1873(18)**	**3.096(3)**	**4.162(2)**	**53.4**
	#3···#3	3.768(3)	5.2472(18)	3.550(3)	3.864(3)	47.4
	#2···#2	4.396(3)	6.077(2)	3.613(3)	4.887(3)	53.5

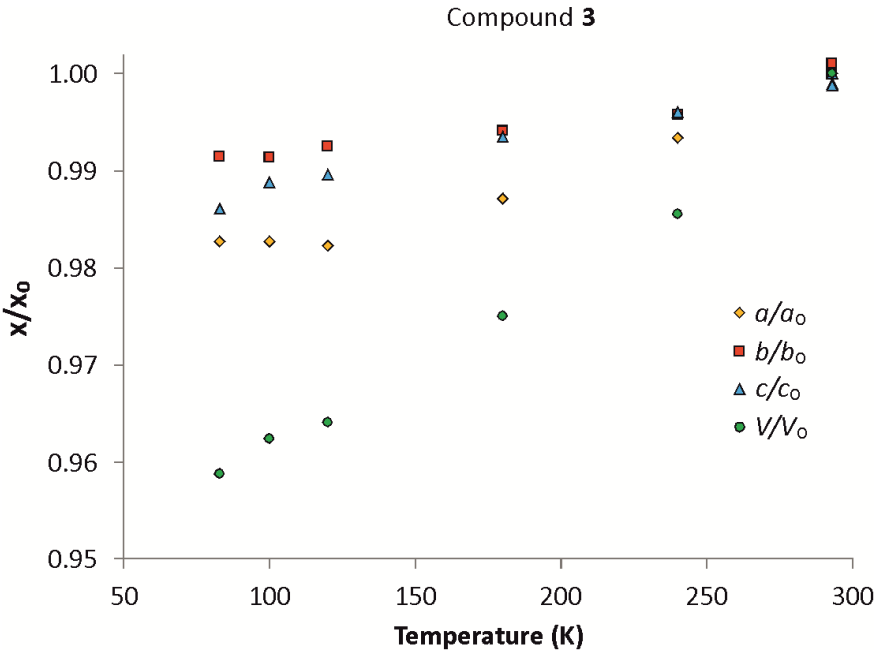

Figure 2-46. Temperature dependence of the normalized unit cell lengths and volume of compound **3**.

Table 2-8. Temperature-dependent single-crystal X-ray diffraction data and structure refinements of **3**, $C_{24}H_{27}B$. Formula weight = 326.26 g·mol^{-1}; F(000) = 352; Z = 2.

T / K	293(2)	240(2)	180(2)	120(2)	83(2)
CCDC number	1940102	1940103	1940104	1940105	1940106
λ / Å, radiation	0.71073, MoKα				
Crystal color, habit	Colorless, block				
Crystal size / mm³	0.28×0.40×0.48	0.27×033×0.34	0.27×033×0.34	0.27×033×0.34	0.27×033×0.34
Crystal system	Triclinic				
Space group	$P\ \bar{1}$				
a / Å	8.661(2)	8.604(2)	8.549(2)	8.507(3)	8.511(3)
b / Å	9.7587(15)	9.718(2)	9.7014(13)	9.6857(13)	9.6752(16)
c / Å	12.379(2)	12.330(3)	12.2995(16)	12.2513(17)	12.207(2)
α / °	98.602(7)	98.854(7)	99.073(6)	99.278(7)	99.373(8)
β / °	90.91(2)	90.760(13)	90.765(12)	90.929(18)	91.212(19)
γ / °	107.622(7)	107.483(16)	107.392(18)	107.37(2)	107.48(3)
Volume / Å^3	983.9(3)	969.6(4)	959.3(3)	948.6(4)	943.4(4)
ρ_{calc} / g·cm^{-3}	1.101	1.117	1.130	1.142	1.149
μ / mm^{-1}	0.061	0.062	0.062	0.063	0.063
θ range / °	2.473 – 26.022	2.487 – 26.020	2.502 – 26.021	2.810 – 26.022	2.516 – 26.011
Reflections collected	14499	16739	16620	16349	16202
Unique reflections	3876	3811	3773	3726	3710
Parameters / restraints	232 / 0	232 / 0	232 / 0	307 / 0	307 / 0
GooF on F^2	1.027	1.047	1.028	1.029	1.057
R_1 [I>2σ(I)]	0.0525	0.0549	0.0513	0.0465	0.0448
wR^2 (all data)	0.1519	0.1542	0.1377	0.1247	0.1149
Max. / min. residual electron density / e·Å^{-3}	0.215 / –0.147	0.211 / –0.163	0.225 / –0.178	0.213 / –0.202	0.268 / –0.209

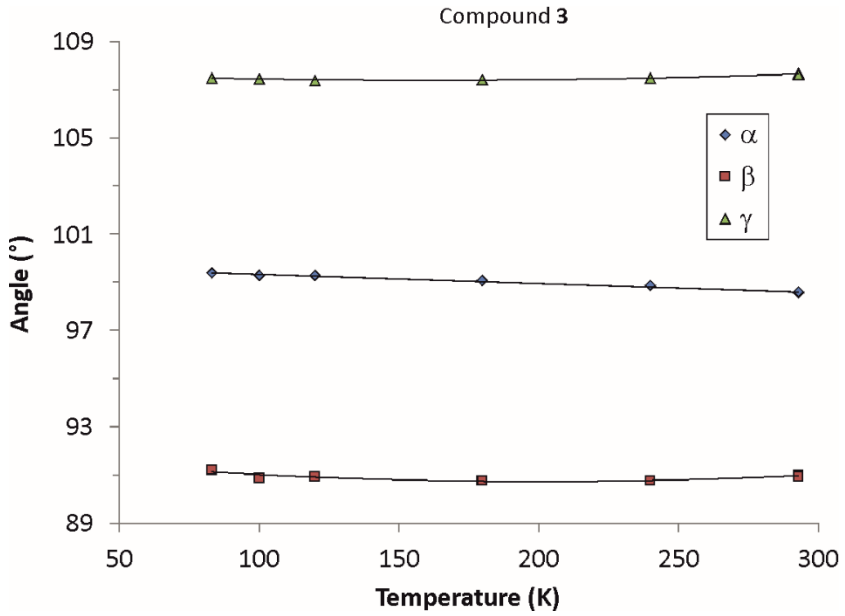

Figure 2-47. Temperature dependence of the unit cell angles (°) of compound **3**.

Table 2-9. Temperature dependence of **s**elected bond lengths (Å) and angles (°) of compound **3.**

T (K)	**293**	**240**	**180**	**120**	**100**	**83**
Sum ∠ CBC	360.0(2)	360.0(2)	360.0(2)	360.0(1)	360.0(1)	360.0(1)
B–C	1.577(3) 1.579(3) 1.587(3)	1.574(3) 1.583(3) 1.585(3)	1.576(3) 1.581(3) 1.590(3)	1.579(2) 1.584(2) 1.589(2)	1.5795(19) 1.5826(18) 1.5858(18)	1.579(2) 1.584(2) 1.588(2)
∠ BC3 – aryl	53.68(9) 53.06(8) 52.74(6)	53.66(9) 53.07(8) 53.15(6)	53.57(8) 52.91(7) 53.69(5)	53.46(7) 52.89(7) 53.91(5)	53.52(7) 52.91(7) 53.92(6)	53.30(7) 53.01(6) 53.86(5)

Table 2-10. Temperature dependence of the properties of crystals of compound **3**: Volume within van der Waals (V_m), Hirshfeld (V_H), and surface of the crystal voids (V_v), crystal packing coefficient (c_k), solvent accessible volume (V_{solv}), and percentage of intermolecular contacts. pfu…per formula unit.

T (K)	**293**	**240**	**180**	**120**	**100**	**83**
V_m / Å³	309.49	309.73	311.79	312.64	312.20	312.92
V_H / Å³	485.16	478.07	472.87	467.55	466.68	464.92
V_v / Å³	140.13	126.45	115.58	104.17	103.82	98.90
V_v / Å³ pfu	70.07	63.23	57.79	52.09	51.91	49.45
c_k	0.629	0.639	0.650	0.659	0.659	0.663
V_{solv} / Å³	11.0	10.9	9.1	9.0	9.0	9.0
C···C / %	0.2	0.2	0.2	0.3	0.2	0.2
C···H / %	17.0	17.6	18.1	18.6	18.5	18.8
H···H / %	82.8	82.2	81.7	81.1	81.3	81.0

Table 2-11. Temperature dependence of the intermolecular C−H···C and C···C interaction distances (Å) and angles (°) in compound **3**.

T (K)	**293**	**240**	**180**	**120**	**100**	**83**
H7···C19	2.924	2.881	2.860	2.80(2)	2.841	2.815(2)
C7···C19	3.816	3.787	3.779	3.768(3)	3.765	3.771(2)
∠(C7-H7-C19)	161.3	162.0	163.1	162(1)	164.41	162(1)
H14···C21	2.971	2.929	2.897	2.86(2)	2.871	2.85(2)
C14···C21	3.897	3.865	3.842	3.823(3)	3.815	3.815(2)
∠(C14-H14-C21)	174.1	173.7	172.9	169(1)	171.96	170(1)
H5···C12	3.028	2.982	2.934	2.85(2)	2.897	2.88(2)
C5···C12	3.943	3.907	3.870	3.831(3)	3.832	3.817(3)
∠(C5-H5-C12	168.4	168.5	168.5	170(1)	168.18	167(1)
C6···C6	3.421	3.376	3.343	3.324(2)	3.319	3.318(2)
C6···C23(methyl)	3.487	3.460	3.430	3.402(2)	3.392	3.376(2)

Table 2-12. Temperature dependence of the aryl···aryl (π···π) distances (Å) and angles (°) in crystals of **3**: nearest-neighbour (nn) C···C distances, centroid-centroid distances, interplanar separations, shifts, and slip angles. Aryl rings are numbered 1, 2, or 3 according to the C1, C2, or C3 atom being present and bonding to the boron atom, respectively.

T (K)	Aryl···Aryl	nn C···C	Centroid-centroid distance	Interplanar separation	Shift	Slip angle
293	#1···#1	3.421(5)	5.3311(19)	2.996(4)	4.409(3)	55.8
	#2···#2	3.633(6)	4.9301(19)	3.523(4)	3.449(4)	44.4
240	#1···#1	3.375(4)	5.2606(19)	2.995(4)	4.325(3)	55.3
	#2···#2	3.587(5)	4.9088(19)	3.479(4)	3.463(4)	44.9
180	#1···#1	3.343(4)	5.2075(16)	2.991(4)	4.263(3)	54.9
	#2···#2	3.544(4)	4.8973(16)	3.440(4)	3.486(3)	45.4
120	#1···#1	3.3239(7)	5.1722(6)	2.9827(9)	4.2255(10)	54.8
	#2···#2	3.4938(8)	4.8779(5)	3.3963(9)	3.5013(10)	45.9
100	#1···#1	3.319(3)	5.1671(17)	2.980(3)	4.221(3)	54.8
	#2···#2	3.495(3)	4.8718(16)	3.397(3)	3.493(3)	45.8
83	#1···#1	3.318(3)	5.1715(14)	2.973(3)	4.231(2)	54.9
	#2···#2	3.469(3)	4.8633(14)	3.375(3)	3.502(3)	46.1

6.5.1 Theoretical calculation details

The Turbomole program package was used for all geometry optimizations.[35] The equilibrium geometry of the electronic ground state was optimized with Kohn-Sham density functional theory (DFT)[36] employing the B3-LYP functional.[37] For the singlet excited state geometries, full linear response time dependent DFT (TDDFT)[38] calculations were performed whereas the Tamm-Dancoff approximation was employed for the triplet states. Atomic orbitals were represented by split-valence basis sets with polarization functions (SVP) from the Turbomole basis set library.[39] Electronic excitation energies and transition dipole moments were calculated with a redesigned variant of the DFT/MRCI[40] method. DFT/MRCI is a semi-empirical multireference configuration interaction approach based on Kohn-Sham orbitals and orbital energies of a closed shell BH-LYP[27b, 41] functional determinant. To avoid double counting of electron correlation, high-lying configurations with energies more than 1 E_h above the highest root in the reference space are discarded. The reference space was determined iteratively, starting with single and double excitations of 12 electrons within an active window of 12 frontier orbitals. At all geometries, 11 singlet and 10 triplet roots were

determined. Absorption line spectra were broadened with Gaussians of 1000 cm^{-1} full width at half maximum (FWHM). Electronic spin–orbit coupling matrix elements (SOCMEs) and phosphorescence lifetimes were obtained with the SPOCK program.[42] Harmonic vibrational frequencies were determined numerically at the TDDFT or TDA level using the SNF code.[43] The FC profiles of the emission spectra were obtained using the Fourier transform approach implemented in the Vibes program.[44] Herein, a time interval of 300 fs and a grid of 16384 points were chosen. The correlation function was damped with a Gaussian function of 200 cm^{-1} FWHM and the temperature was set to 77 K. All spectra were normalized to one. Rate constants for intersystem crossing (ISC) of the respective S_1 states to the T_1 states of all compounds and a few other triplet states were computed for a temperature of 300 K in Condon approximation. For the integration of the time correlation function in the VIBES program a time interval of 250 fs, an integration grid of 1000 points and smaller damping of width 0.3 cm^{-1} were chosen. The electronic SOCME is largest for the ISC from S_1 to T_2, but harmonic vibrational wavefunctions of the latter state could unfortunately not be determined due to (near) degeneracy of the T_1 and T_2 potentials at the T_2 minimum. For that reason, we used the modes of the T_1 (compounds **1** and **2**) or T_3 potentials (compounds **3** and **4**) to estimate the vibrational density of final states at the energies of the initial singlet states which are required in addition to the sum over squared SOCMEs to determine the ISC rate constants in Condon approximation.[45]

Table 2-13. Spin–orbit coupling matrix elements (absolute values, cm^{-1}) of the S_1, T_1, and T_2 states at the respective S_1 minimum geometry.

SOCME	x	y	z	$(x^2 + y^2 + z^2)$
		Compound 1		
$\langle T_1 \vert \hat{H}_{SO} \vert S_1 \rangle$	0.039	0.149	0.232	0.078
$\langle T_2 \vert \hat{H}_{SO} \vert S_1 \rangle$	0.524	0.999	0.022	1.273
		Compound 2		
$\langle T_1 \vert \hat{H}_{SO} \vert S_1 \rangle$	0.154	0.167	0.147	0.073
$\langle T_2 \vert \hat{H}_{SO} \vert S_1 \rangle$	0.403	0.883	0.159	0.967
		Compound 3		
$\langle T_1 \vert \hat{H}_{SO} \vert S_1 \rangle$	0.024	0.039	0.002	0.002
$\langle T_2 \vert \hat{H}_{SO} \vert S_1 \rangle$	0.005	1.270	0.038	1.614
		Compound 4		
$\langle T_1 \vert \hat{H}_{SO} \vert S_1 \rangle$	0.048	0.060	0.030	0.007
$\langle T_2 \vert \hat{H}_{SO} \vert S_1 \rangle$	0.317	1.067	0.706	1.737

Table 2-14. Photophysical properties of compounds **1**-**4** in vacuum as obtained from quantum chemical calculations.

Compound	λ_{abs} /nm [a]	k_{isc} /s^{-1} [b]	λ_f /nm [c]	k_f/ s^{-1}	τ_f /ns [d]	λ_p /nm [c]	k_p / s^{-1}	τ_p /s [d]
1	303	≈$1*10^7$	(335), 383	$2*10^7$	45	(425), 597	0.13	8
2	308	≈$6*10^6$	368, 391	$2*10^7$	45	448, 476	0.13	8
3	314	≈$5*10^7$	367, 404	$3*10^7$	38	456, 486	0.14	7
4	316	≈$3*10^7$	381, 430	$4*10^7$	25	458, 489	0.20	5

[a] Absorption maximum of line spectrum broadened by Gaussian function of 1000 cm^{-1} full width at half maximum; [b] rate constant for the fastest of the open ISC channels; [c] maximum of 0-0 band, maximum of Franck-Condon spectrum at 77 K, entries given in parentheses indicate the position of a shoulder; [d] pure radiative lifetime assuming a quantum yield of **1**

Table 2-15. Selected bond lengths (Å) and angles (°) of the isolated compounds **1**, **2**, **3**, and **4** as obtained from geometry optimizations of the S_0, S_1, and T_1 states. The electronic excitation in the S_1 and T_1 states mainly involves residue R2.

1: R1=phenyl, R2=R3=xylyl; **2**: R1=tolyl, R2=R3=xylyl
3: R1=R2=R3=xylyl; **4**: R1=R3=xylyl, R2=mesityl

Compound **1**	S_0	S_1	T_1
B-R1	1.574	1.532	1.568
B-R2	1.589	1.620	1.567
B-R3	1.589	1.592	1.602
∠R1(C)-B-(C-C)R2	55.3	70.5	38.4
∠R2(C)-B-(C-C)R3	55.4	49.8	61.5
∠R3(C)-B-(C-C)R1	28.3	20.3	20.6
∠R2(C)-B-(C-C)R1	28.3	13.2	25.5
∠R3(C)-B-(C-C)R2	55.5	67.1	43.4
∠R1(C)-B-(C-C)R3	55.2	48.4	62.0
Compound **2**	S_0	S_1	T_1
B-R1	1.580	1.546	1.574
B-R2	1.588	1.610	1.562
B-R3	1.591	1.597	1.605
∠R1(C)-B-(C-C)R2	51.9	59.2	39.0
∠R2(C)-B-(C-C)R3	53.0	46.8	55.5
∠R3(C)-B-(C-C)R1	38.1	25.3	31.5
∠R2(C)-B-(C-C)R1	38.7	24.2	36.9
∠R3(C)-B-(C-C)R2	54.2	60.9	44.1
∠R1(C)-B-(C-C)R3	55.4	51.6	58.5
Compound **3**	S_0	S_1	T_1
B-R1	1.590	1.581	1.596
B-R2	1.590	1.611	1.557
B-R3	1.590	1.579	1.595
∠R1(C)-B-(C-C)R2	50.1	56.4	43.4
∠R2(C)-B-(C-C)R3	49.9	38.9	48.8
∠R3(C)-B-(C-C)R1	49.8	43.6	47.8
∠R2(C)-B-(C-C)R1	49.9	40.3	49.2
∠R3(C)-B-(C-C)R2	50.3	56.8	43.6
∠R1(C)-B-(C-C)R3	49.6	42.3	47.5
Compound **4**	S_0	S_1	T_1
B-R1	1.591	1.575	1.593
B-R2	1.587	1.619	1.564
B-R3	1.591	1.577	1.596
∠R1(C)-B-(C-C)R2	49.4	58.9	43.9
∠R2(C)-B-(C-C)R3	49.6	39.3	48.1
∠R3(C)-B-(C-C)R1	49.8	42.2	46.1
∠R2(C)-B-(C-C)R1	49.9	38.6	47.1
∠R3(C)-B-(C-C)R2	49.4	59.0	44.3
∠R1(C)-B-(C-C)R3	49.7	42.8	47.6

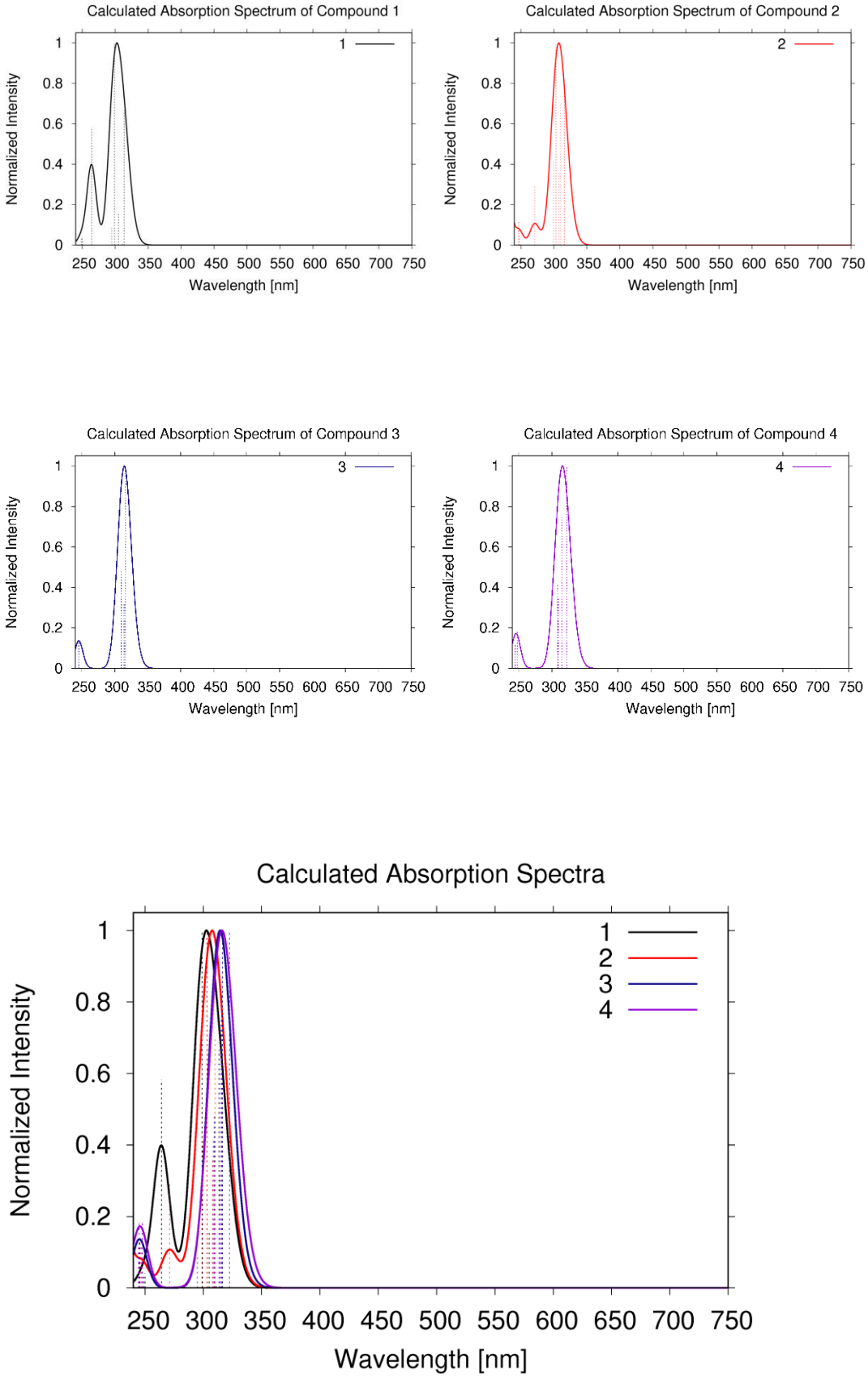

Figure 2-48. Calculated absorption spectra of the isolated compounds **1**, **2**, **3**, and **4**.

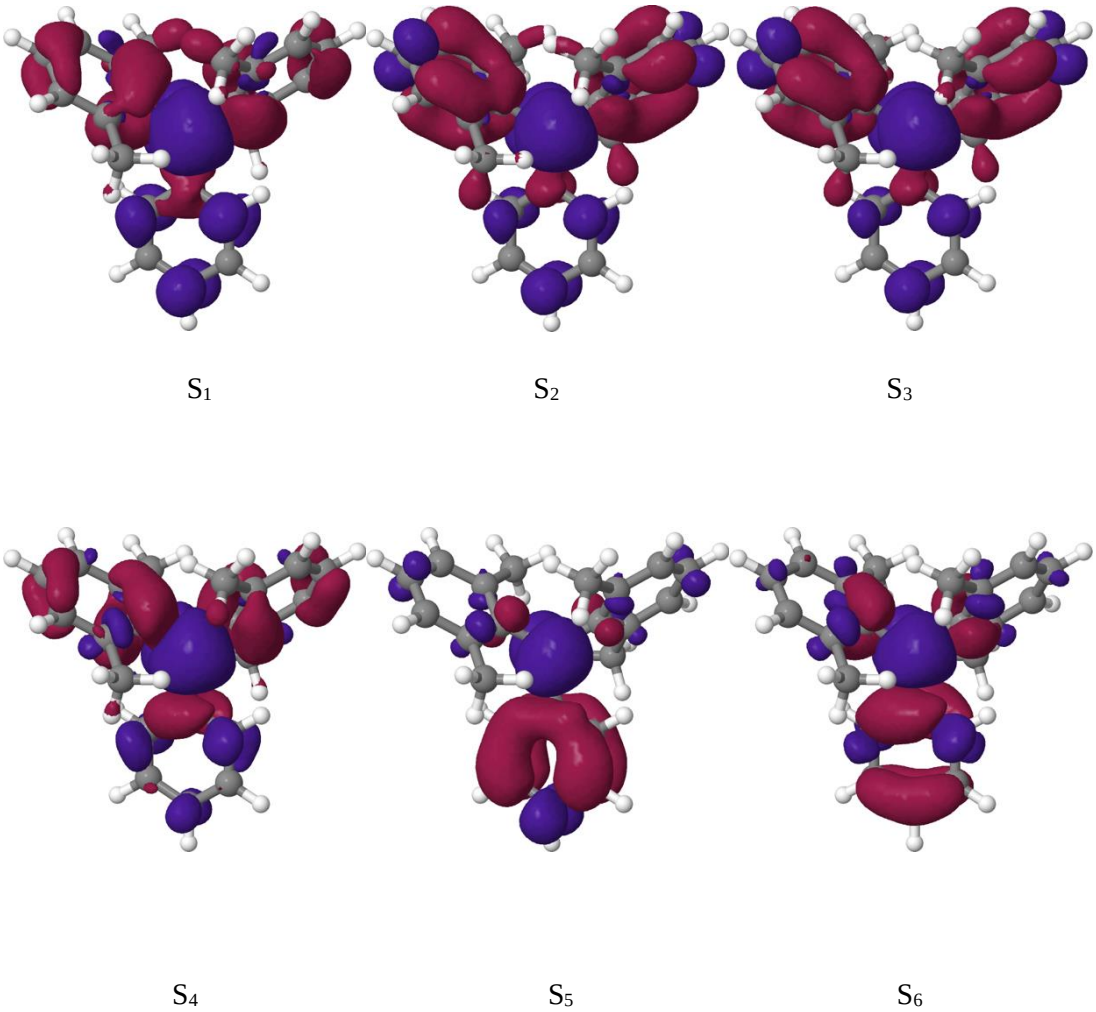

Figure 2-49. Difference densities (|isovalue| = 0.001) of low-lying singlet excited states of compound **1** at the DFT-optimized ground-state geometry. A loss of electron density with respect to the S_0 state is indicated in red, a gain in blue.

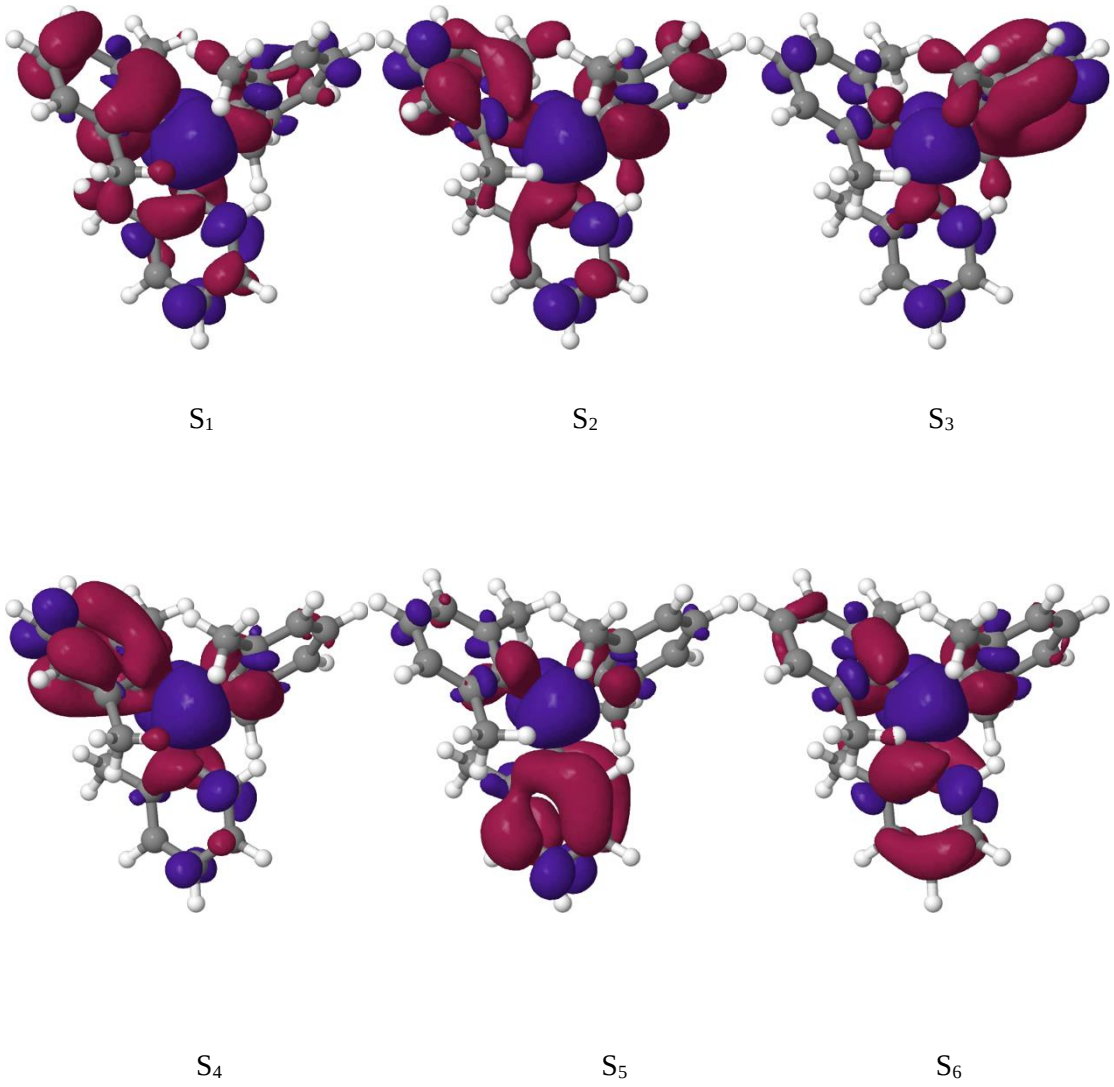

Figure 2-50. Difference densities (|isovalue| = 0.001) of low-lying singlet excited states of compound **2** at the DFT-optimized ground-state geometry. A loss of electron density with respect to the S_0 state is indicated in red, a gain in blue.

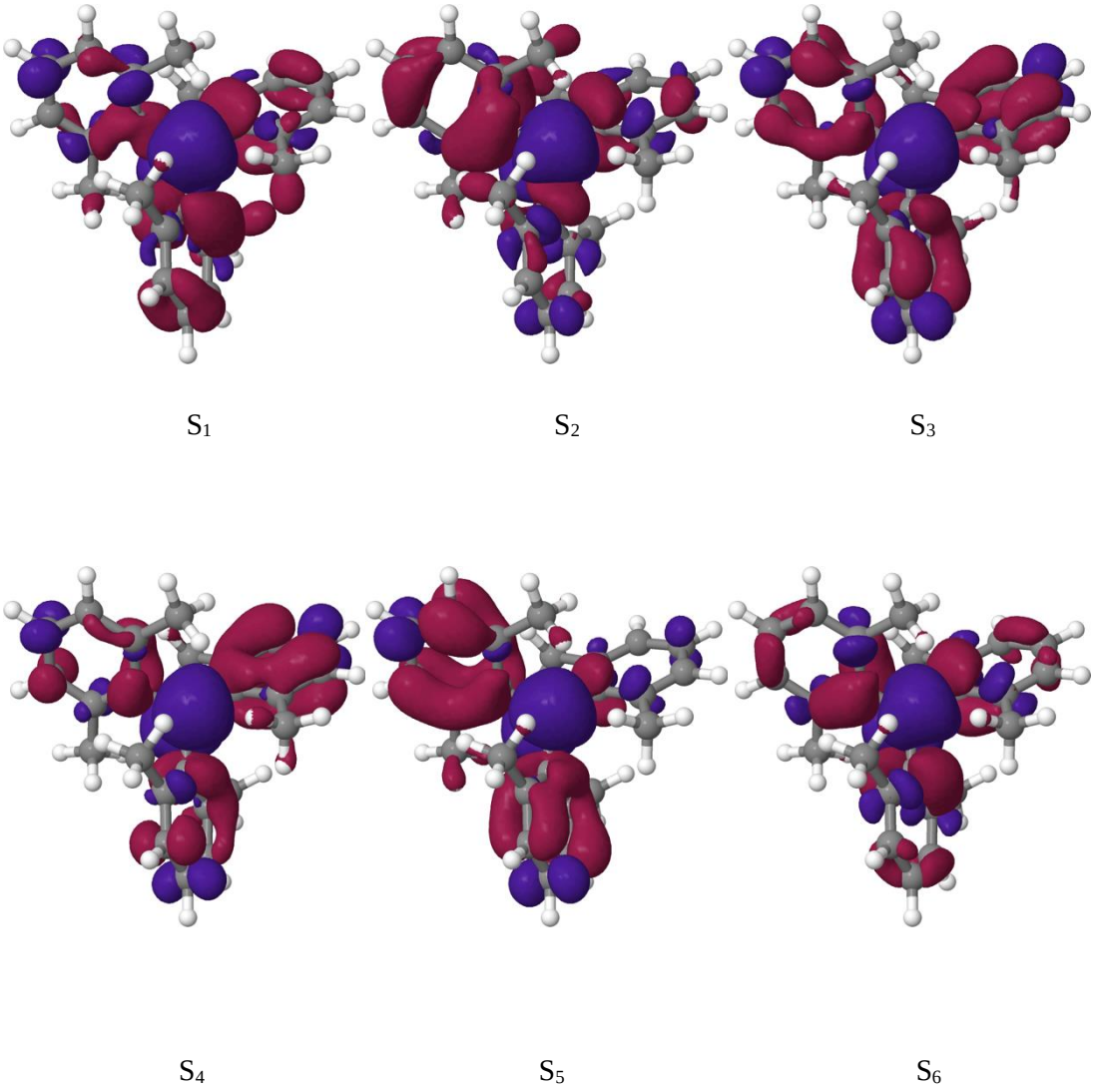

Figure 2-51. Difference densities (|isovalue| = 0.001) of low-lying singlet excited states of compound **3** at the DFT-optimized ground-state geometry. A loss of electron density with respect to the S_0 state is indicated in red, a gain in blue.

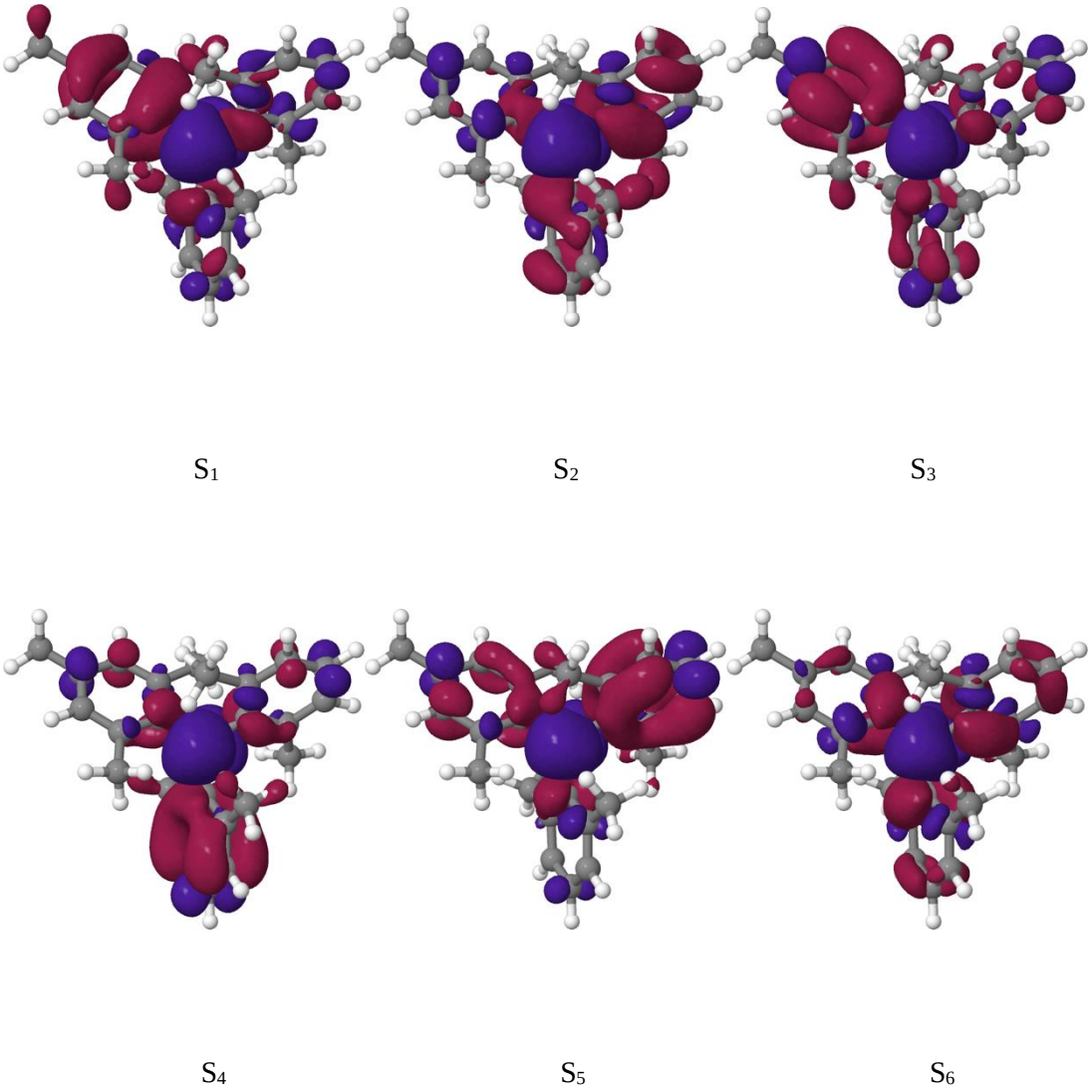

Figure 2-52. Difference densities (|isovalue| = 0.001) of low-lying singlet excited states of compound **4** at the DFT-optimized ground-state geometry. A loss of electron density with respect to the S_0 state is indicated in red, a gain in blue.

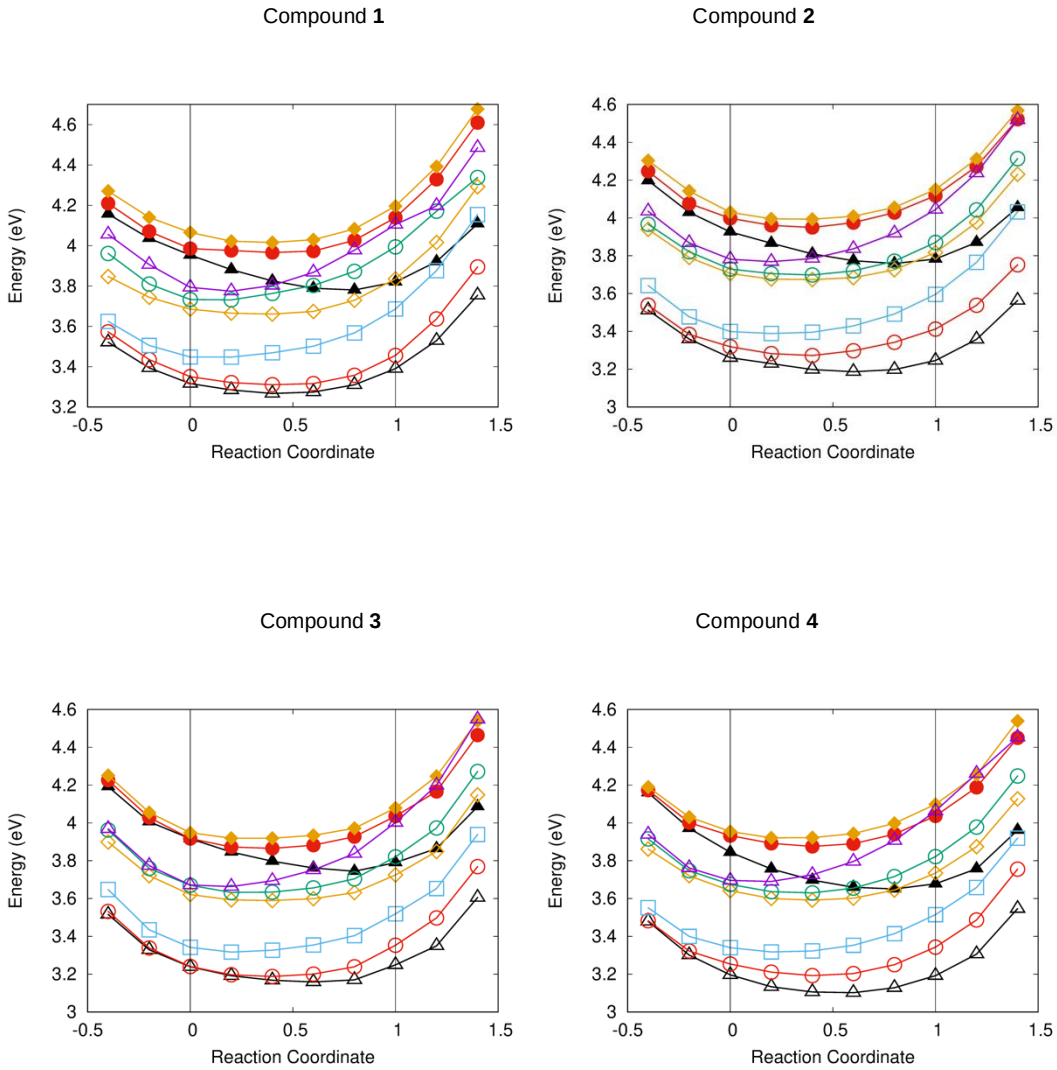

Figure 2-53. DFT/MRCI potential energy profiles of low-lying singlet (filled symbols) and triplet (open symbols) states of compounds **1**, **2**, **3**, and **4**. The reaction coordinate connects the DFT-optimized S_0 geometry (RC = 0) and the TDDFT-optimized geometry of the first excited singlet state S_1 (RC = 1) and is extrapolated on both sides. Potential energy curve crossings are observed between the S_1 state (full black triangles) and excited triplet states along the relaxation path from the Franck-Condon geometry.

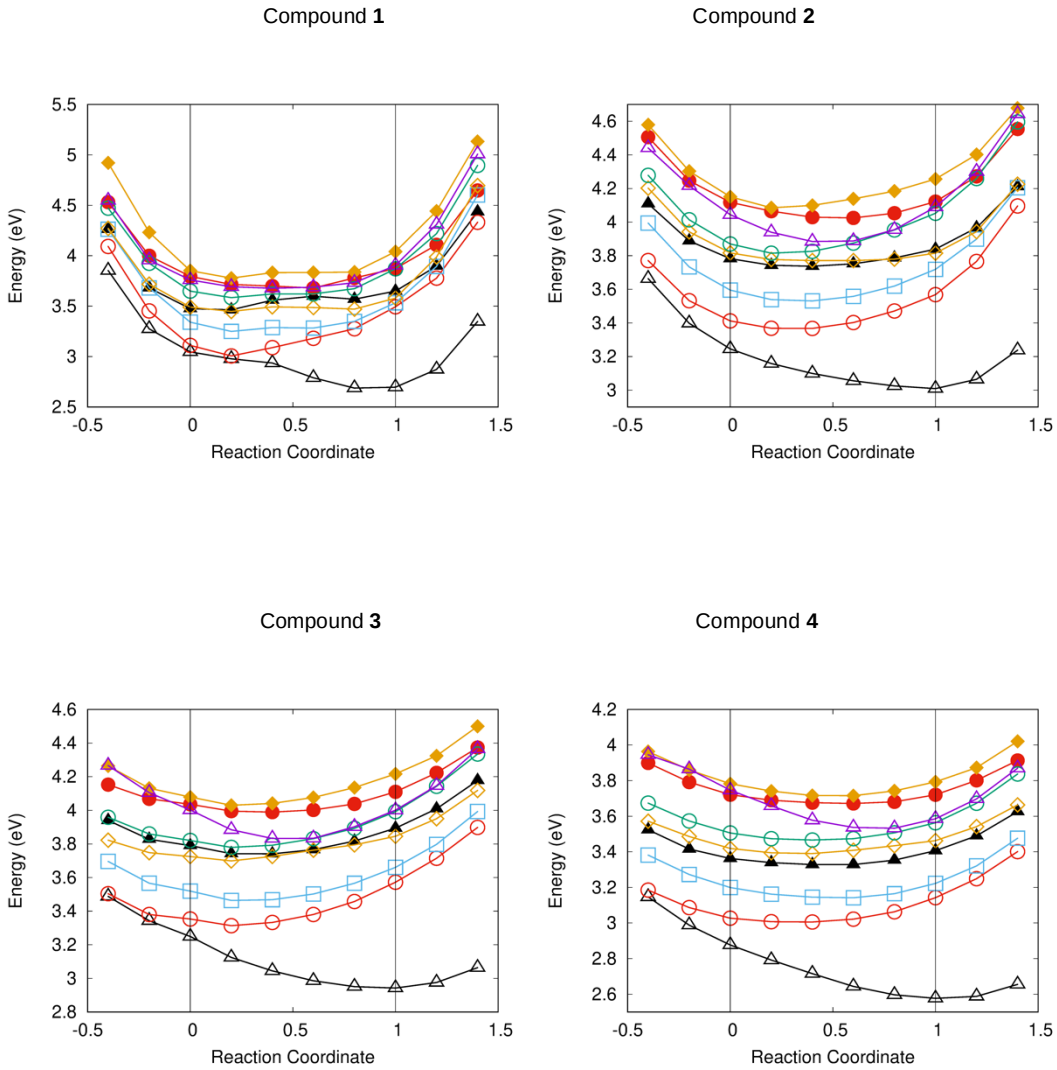

Figure 2-54. DFT/MRCI potential energy profiles of low-lying singlet (filled symbols) and triplet (open symbols) states of compounds **1**, **2**, **3**, and **4**. The reaction coordinate connects the TDDFT-optimized geometries of the S_1 (RC = 0) and T_1 (RC = 1) states and is extrapolated on both sides.

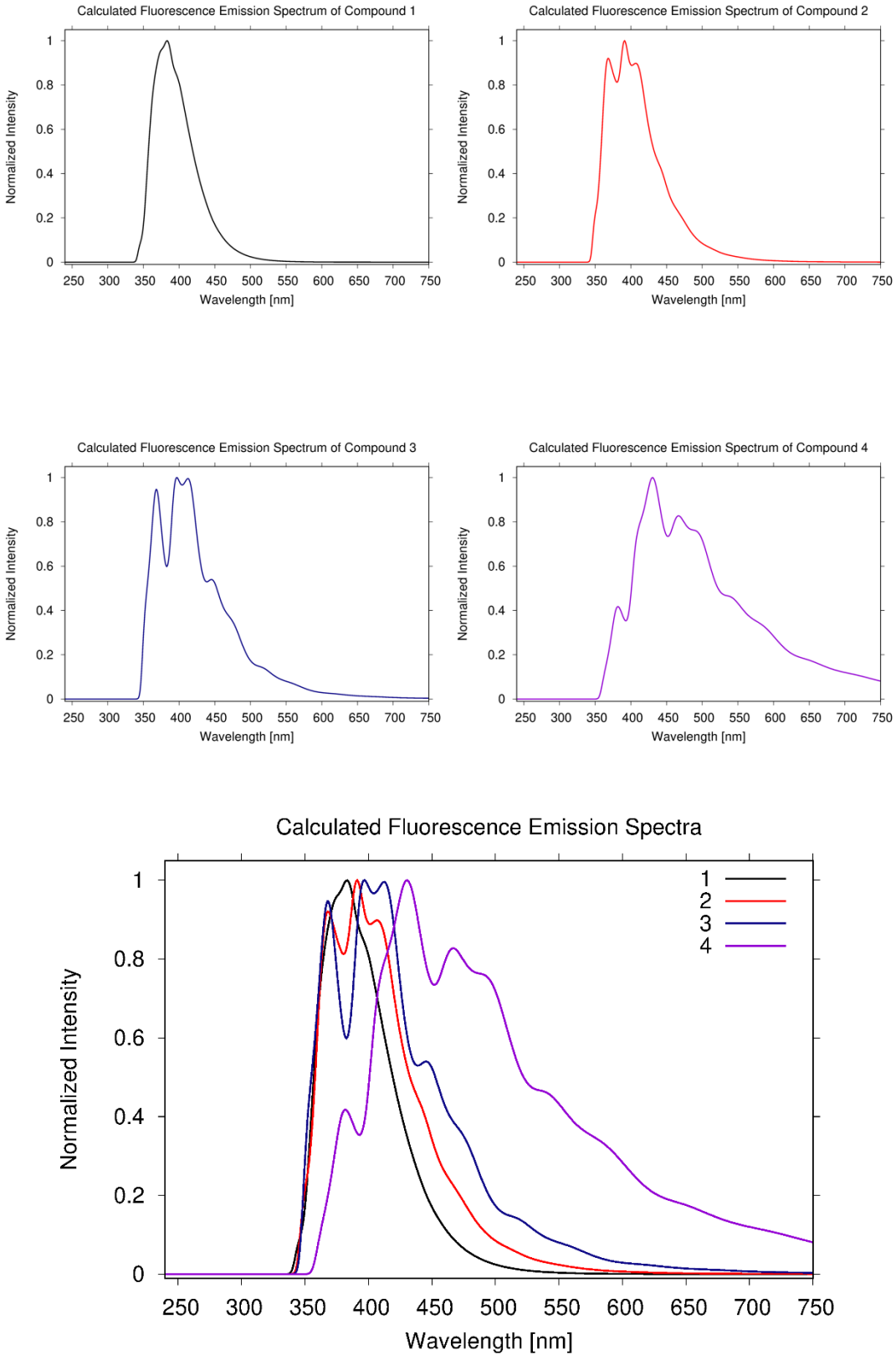

Figure 2-55. Calculated fluorescence spectra of the isolated compounds **1**, **2**, **3**, and **4** at 77 K.

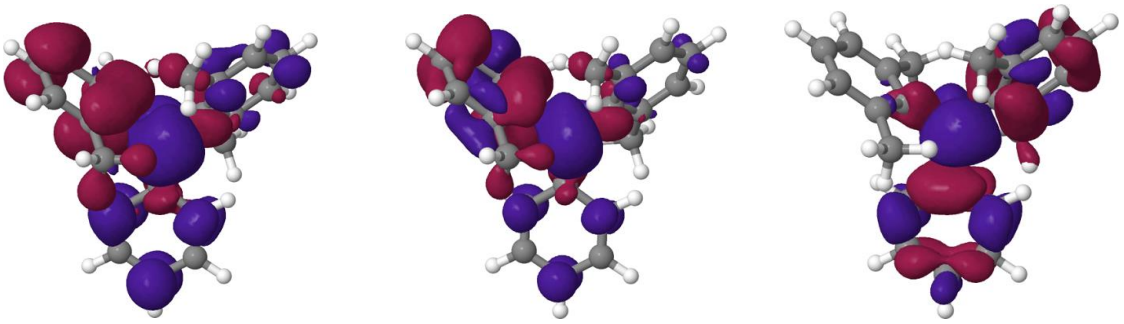

Compound **1** S_1 T_1 T_2

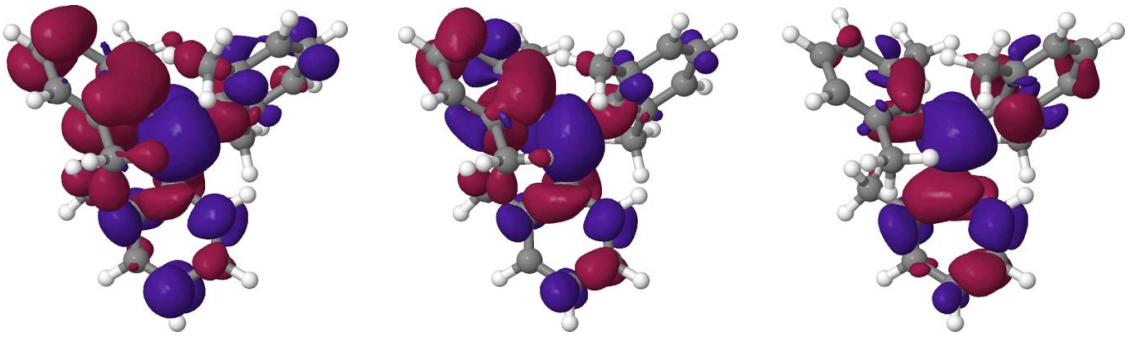

Compound **2** S_1 T_1 T_2

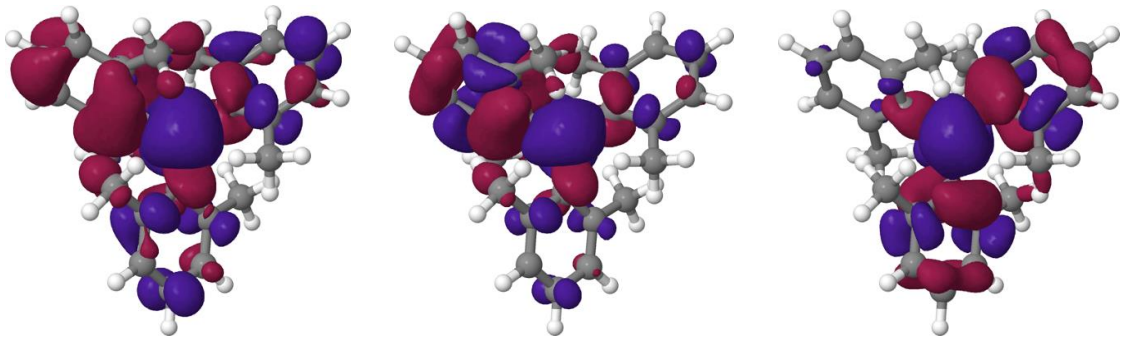

Compound **3** S_1 T_1 T_2

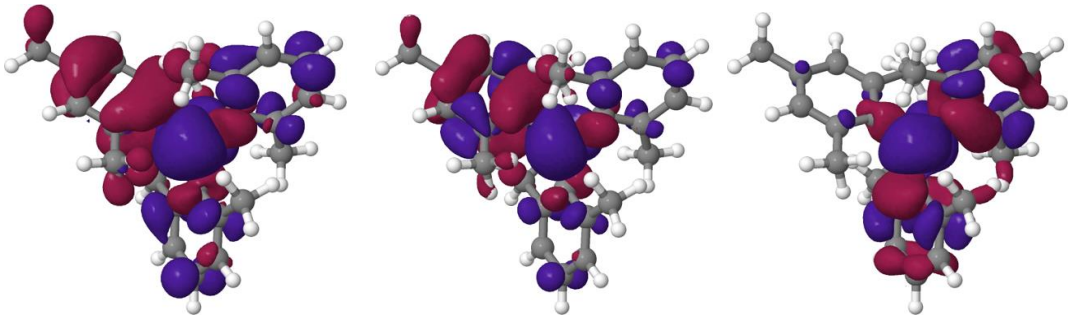

Compound **4** S_1 T_1 T_2

Figure 2-56. Difference densities (|isovalue| = 0.001) of low-lying excited states of compounds **1**, **2**, **3**, and **4** at the TDDFT-optimized geometry of the S_1 state. A loss of electron density with respect to the S_0 state is indicated in red, a gain in blue.

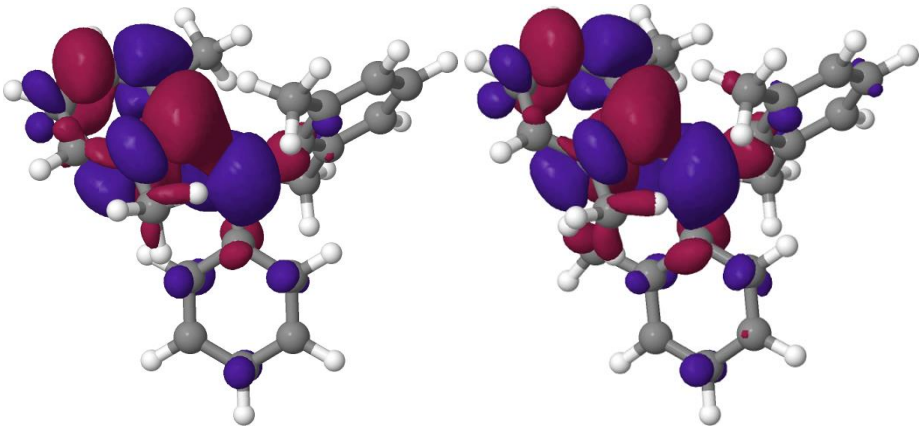

Compound **1** T_1 Compound **2** T_1

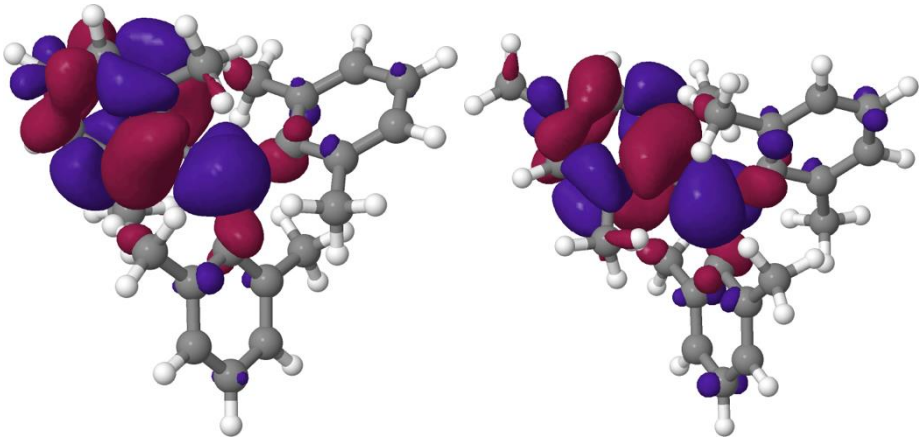

Compound **3** T_1 Compound **4** T_1

Figure 2-57. Difference densities (|isovalue| = 0.001) of the T_1 state of compounds **1**, **2**, **3**, and **4** at its TDDFT-TDA-optimized minimum geometry. A loss of electron density with respect to the S_0 state is indicated in red, a gain in blue.

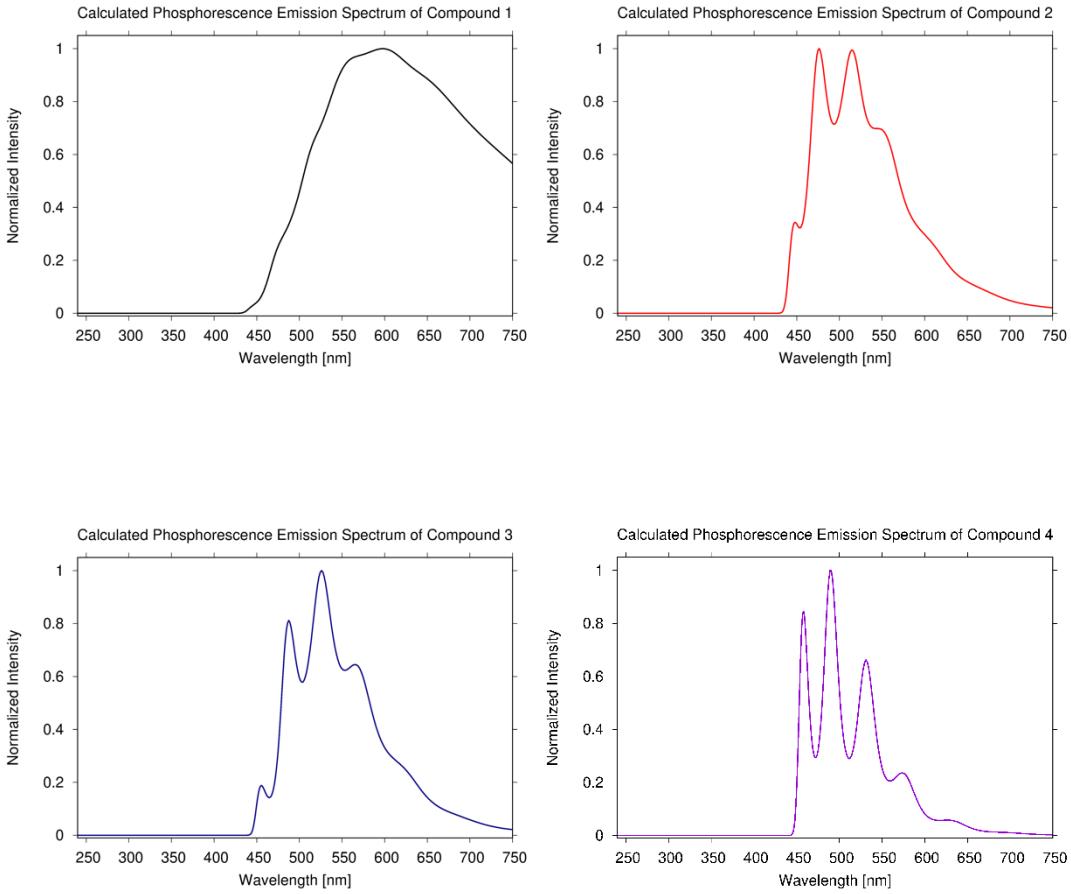

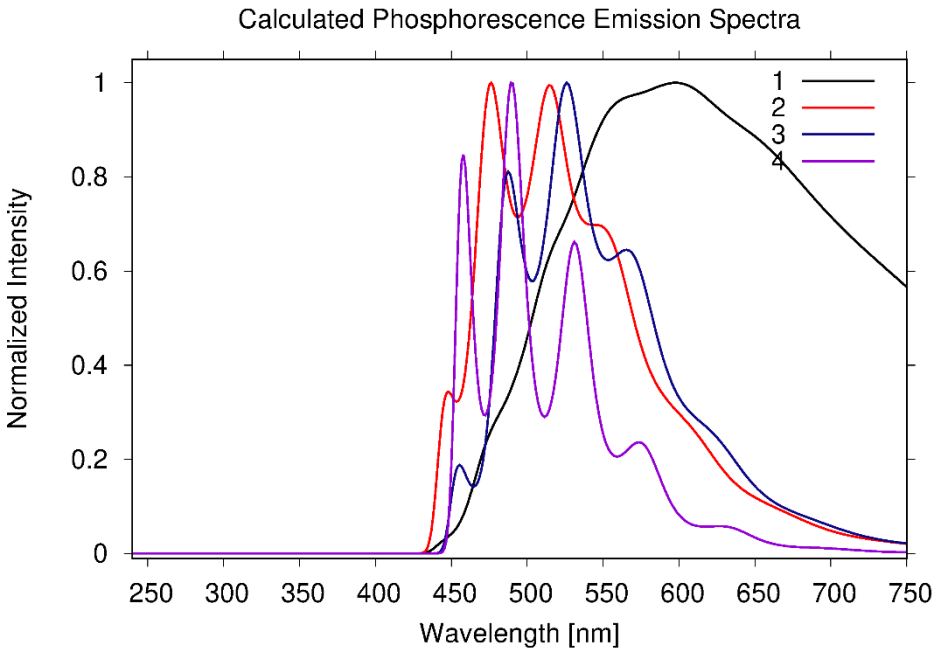

Figure 2-58. Calculated phosphorescence spectra of the isolated compounds **1**, **2**, **3**, and **4** at 77 K.

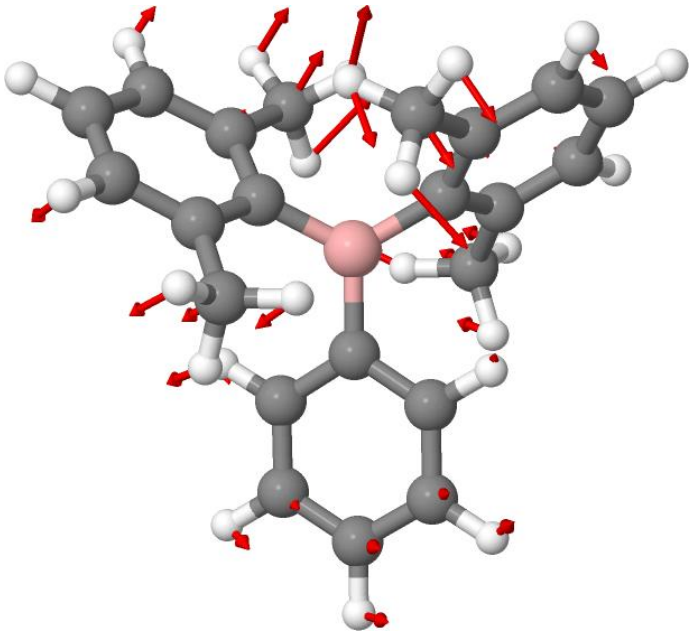

Figure 2-59. Low-frequency vibrational mode in the S_0 state of compound **1** showing the largest displacement with respect to the corresponding mode in the T_1 state. Excitation of this mode causes the extraordinary breadth of the phosphorescence emission of this compound. One methyl group in ortho-position of residue R3 is sufficient to prevent similar large-amplitude motions along in compound **2**.

2.5 Reference

[1] a) T. Maldiney, A. Lecointre, B. Viana, A. Bessiere, M. Bessodes, D. Gourier, C. Richard, D. Scherman, *J. Am. Chem. Soc.* **2011**, *133*, 11810-11815; b) J. Yang, X. Zhen, B. Wang, X. Gao, Z. Ren, J. Wang, Y. Xie, J. Li, Q. Peng, K. Pu, Z. Li, *Nat. Commun.* **2018**, *9*, 840-849; c) G. Zhang, G. M. Palmer, M. W. Dewhirst, C. L. Fraser, *Nat. Mater.* **2009**, *8*, 747-751; d) K. Y. Zhang, Q. Yu, H. Wei, S. Liu, Q. Zhao, W. Huang, *Chem. Rev.* **2018**, *118*, 1770-1839; e) X. F. Wang, H. Y. Xiao, P. Z. Chen, Q. Z. Yang, B. Chen, C. H. Tung, Y. Z. Chen, L. Z. Wu, *J. Am. Chem. Soc.* **2019**, *141*, 5045-5050.

[2] a) M. Baroncini, G. Bergamini, P. Ceroni, *Chem. Commun.* **2017**, *53*, 2081-2093; b) S. Cai, H. Shi, J. Li, L. Gu, Y. Ni, Z. Cheng, S. Wang, W. W. Xiong, L. Li, Z. F. An, W. Huang, *Adv. Mater.* **2017**, *29*, 1701244; c) C. Li, X. Tang, L. Zhang, C. Li, Z. Liu, Z. Bo, Y. Q. Dong, Y. H. Tian, Y. Dong, B. Z. Tang, *Adv. Opt. Mater.* **2015**, *3*, 1184-1190.

[3] L. Dou, J. You, Z. Hong, Z. Xu, G. Li, R. A. Street, Y. Yang, *Adv. Mater.* **2013**, *25*, 6642-6671.

[4] a) A. Fermi, G. Bergamini, M. Roy, M. Gingras, P. Ceroni, *J. Am. Chem. Soc.* **2014**, *136*, 6395-6400; b) T. J. Penfold, E. Gindensperger, C. Daniel, C. M. Marian, *Chem. Rev.* **2018**, *118*,

6975-7025; c) J. Zhao, W. Wu, J. Sun, S. Guo, *Chem. Soc. Rev.* **2013**, *42*, 5323-5351; d) S. Xu, R. Chen, C. Zheng, W. Huang, *Adv. Mater.* **2016**, *28*, 9920-9940.

[5] a) O. Bolton, D. Lee, J. Jung, J. Kim, *Chem. Mater.* **2014**, *26*, 6644-6649; b) S. Cai, H. Shi, Z. Zhang, X. Wang, H. Ma, N. Gan, Q. Wu, Z. Cheng, K. Ling, M. Gu, C. Ma, L. Gu, Z. An, W. Huang, *Angew. Chem. Int. Ed.* **2018**, *57*, 4005-4009; *Angew. Chem.* **2018**, *130*, 4069-4073; c) P. Ceroni, *Chem* **2016**, *1*, 524-526; d) M. A. El-Sayed, *J. Chem. Phys.* **1963**, *38*, 2834-2838; e) R. M. Hochstrasser, *J. Chem. Phys.* **1963**, *39*, 3153-3154; f) R. Joshi, O. R. Meitei, M. Jadhao, H. Kumar, S. K. Ghosh, *Phys. Chem. Chem. Phys.* **2016**, *18*, 27910-27920; g) H. Matsuoka, M. Retegan, L. Schmitt, S. Hoger, F. Neese, O. Schiemann, *J. Am. Chem. Soc.* **2017**, *139*, 12968-12975; h) G. Q. Zhang, J. B. Chen, S. J. Payne, S. E. Kooi, J. N. Demas, C. L. Fraser, *J. Am. Chem. Soc.* **2007**, *129*, 8942-8943.

[6] a) S. M. A. Fateminia, Z. Mao, S. Xu, Z. Yang, Z. Chi, B. Liu, *Angew. Chem. Int. Ed.* **2017**, *56*, 12160-12164; *Angew. Chem.* **2017**, *129*, 12328-12332; b) K. Jiang, Y. Wang, C. Cai, H. Lin, *Adv. Mater.* **2018**, *30*, 1800783; c) Y. Katsurada, S. Hirata, K. Totani, T. Watanabe, M. Vacha, *Adv. Opt. Mater.* **2015**, *3*, 1726-1737; d) M. S. Kwon, D. Lee, S. Seo, J. Jung, J. Kim, *Angew. Chem. Int. Ed.* **2014**, *53*, 11177-11181; *Angew. Chem.* **2014**, *126*, 11359-11363; e) Q. Li, M. Zhou, Q. Yang, Q. Wu, J. Shi, A. Gong, M. Yang, *Chem. Mater.* **2016**, *28*, 8221-8227; f) S. Mukherjee, P. Thilagar, *Chem. Commun.* **2015**, *51*, 10988-11003; g) M. Shimizu, R. Shigitani, M. Nakatani, K. Kuwabara, Y. Miyake, K. Tajima, H. Sakai, T. Hasobe, *J. Phys. Chem. C* **2016**, *120*, 11631-11639; h) Y. Yu, M. S. Kwon, J. Jung, Y. Zeng, M. Kim, K. Chung, J. Gierschner, J. H. Youk, S. M. Borisov, J. Kim, *Angew. Chem. Int. Ed.* **2017**, *56*, 16207-16211; *Angew. Chem.* **2017**, *129*, 16425-16429; i) Z. Xu, Q. T. Liu, X. Z. Wang, Q. Liu, D. Hean, K. C. Chou, M. O. Wolf, *Chem. Sci.* **2020**, *11*, 2729-2734.

[7] a) M. S. Kwon, Y. Yu, C. Coburn, A. W. Phillips, K. Chung, A. Shanker, J. Jung, G. Kim, K. Pipe, S. R. Forrest, J. H. Youk, J. Gierschner, J. Kim, *Nat. Commun.* **2015**, *6*, 8947; b) D. Lee, O. Bolton, B. C. Kim, J. H. Youk, S. Takayama, J. Kim, *J. Am. Chem. Soc.* **2013**, *135*, 6325-6329; c) H. Shi, Z. An, P. Z. Li, J. Yin, G. Xing, T. He, H. Chen, J. Wang, H. Sun, W. Huang, Y. Zhao, *Cryst. Growth Des.* **2016**, *16*, 808-813; d) X. G. Wu, C.Y. Huan, D. G. Chen, D. H. Liu, C. C. Wu, K. J. Chou, B. Zhang, Y. F. Wang, Y. Liu, E. Y. Li, W. G. Zhu, P. T. Chou, *Nat. Commun*. **2020**, *11*, 2145; e) J. F. Wang, Z. F. Chai, J. Q. Wang, C. Wang, M. M. Han, Q. Y. Liao, A. R. Huang, P. X. Lin, C. G. Li, Q. Q. Li, Z. Li, *Angew. Chem. Int. Ed.* **2019**, *58*, 17297-17302; *Angew. Chem.* **2019**, *58*,17457-17462.

[8] a) Y. Gong, G. Chen, Q. Peng, W. Z. Yuan, Y. Xie, S. Li, Y. Zhang, B. Z. Tang, *Adv. Mater.* **2015**, *27*, 6195-6201; b) Y. Gong, L. Zhao, Q. Peng, D. Fan, W. Z. Yuan, Y. Zhang, B. Z. Tang, *Chem. Sci.* **2015**, *6*, 4438-4444; c) Z. He, W. Zhao, J. W. Y. Lam, Q. Peng, H. Ma, G. Liang, Z. Shuai, B. Z. Tang, *Nat. Commun.* **2017**, *8*, 416; d) W. Zhao, Z. He, Jacky W. Y. Lam, Q. Peng, H. Ma, Z. Shuai, G. Bai, J. Hao, B. Z. Tang, *Chem* **2016**, *1*, 592-602.

[9] Z. F. An, C. Zheng, Y. Tao, R. Chen, H. Shi, T. Chen, Z. Wang, H. Li, R. Deng, X. Liu, W. Huang, *Nat. Mater.* **2015**, *14*, 685-690.

[10] S. Hirata, K. Totani, J. Zhang, T. Yamashita, H. Kaji, S. R. Marder, T. Watanabe, C. Adachi, *Adv. Funct. Mater.* **2013**, *23*, 3386-3397.

[11] J. Wei, B. Liang, R. Duan, Z. Cheng, C. Li, T. Zhou, Y. Yi, Y. Wang, *Angew. Chem. Int. Ed.* **2016**, *55*, 15589-15593; *Angew. Chem.* **2016**, *128*, 15818-15822.

[12] M. A. El-sayed, *Nature* **1963**, *197*, 481-482.

[13] a) X. F. Chen, C. Xu, T. Wang, C. Zhou, X. P. Zhang, J. N. Demas, C. O. Trindle, G. Q. Zhang, *Angew. Chem. Int. Ed.* **2016**, *55*, 9872-9876; *Angew. Chem.* **2016**, *55*, 9872-9876; b) S. Hirata, *Adv. Opt. Mater.* **2017**, *5*, 1700116; c) D. Li, F. Lu, J. Wang, W. Hu, X. M. Cao, X. Ma, H. Tian, *J. Am. Chem. Soc.* **2018**, *140*, 1916-1923; d) P. K. Samanta, D. Kim, V. Coropceanu, J. L. Bredas, *J. Am. Chem. Soc.* **2017**, *139*, 4042-4051; e) Y. Xiong, Z. Zhao, W. J. Zhao, H. L. Ma, Q. Peng, Z. K. He, X. P. Zhang, Y. C. Chen, X. W. He, J. Lam, B. Z. Tang, *Angew. Chem. Int. Ed.* **2018**, *57*, 7997-8001; *Angew. Chem.* **2018**, *130*, 8129-8133; f) J. Yang, X. Gao, Z. Xie, Y. Gong, M. Fang, Q. Peng, Z. Chi, Z. Li, *Angew. Chem. Int. Ed.* **2017**, *56*, 15299-15303; *Angew. Chem.* **2017**, *129*, 15501-15505; g) Z. Yang, Z. Mao, X. Zhang, D. Ou, Y. Mu, Y. Zhang, C. Zhao, S. Liu, Z. Chi, J. Xu, Y. C. Wu, P. Y. Lu, A. Lien, M. R. Bryce, *Angew. Chem. Int. Ed.* **2016**, *55*, 2181-2185; *Angew. Chem.* **2016**, *128*, 2221-2225.

[14] a) Z. Chai, C. Wang, J. Wang, F. Liu, Y. Xie, Y. Z. Zhang, J. R. Li, Q. Li, Z. Li, *Chem. Sci.* **2017**, *8*, 8336-8344; b) S. Kuno, T. Kanamori, Z. Yijing, H. Ohtani, H. Yuasa, *ChemPhotoChem* **2017**, *1*, 102-106; c) Y. Shoji, Y. Ikabata, Q. Wang, D. Nemoto, A. Sakamoto, N. Tanaka, J. Seino, H. Nakai, T. Fukushima, *J. Am. Chem. Soc.* **2017**, *139*, 2728-2733; d) Q. Sun, L. Tang, Z. Zhang, K. Zhang, Z. Xie, Z. Chi, H. Zhang, W. Yang, *Chem. Commun.* **2017**, *54*, 94-97; e) J. Yang, Z. Ren, Z. Xie, Y. Liu, C. Wang, Y. Xie, Q. Peng, B. Xu, W. Tian, F. Zhang, Z. Chi, Q. Li, Z. Li, *Angew. Chem. Int. Ed.* **2017**, *56*, 880-884; *Angew. Chem.* **2017**, *129*, 898-902.

[15] a) M. Zander, *Naturwissenschaften* **1962**, *49*, 7; b) D. B. Clapp, *J. Am. Chem. Soc.* **1939**, *61*, 523-524; c) C. A. M. Salla, G. Farias, M. Rouzieres, P. Dechambenoit, F. Durola, H. Bock, B. de Souza, I. H. Bechtold, *Angew. Chem. Int. Ed.* **2019**, *58*, 6982-6986; *Angew. Chem.* **2019**, *131*, 7056-7060.

[16] a) C. Dou, S. Saito, S. Yamaguchi, *J. Am. Chem. Soc.* **2013**, *135*, 9346-9349; b) Z. M. Hudson, S. Wang, *Acc. Chem. Res.* **2009**, *42*, 1584-1596; c) F. Jakle, *Chem. Rev.* **2010**, *110*, 3985-4022; d) W. L. Jia, D. T. Song, S. N. Wang, *J. Org. Chem.* **2003**, *68*, 701-705; e) C. Reus, S. Weidlich, M. Bolte, H. W. Lerner, M. Wagner, *J. Am. Chem. Soc.* **2013**, *135*, 12892-12907; f) S. Saito, K. Matsuo, S. Yamaguchi, *J. Am. Chem. Soc.* **2012**, *134*, 9130-9133; g) C. R. Wade, A. E. J. Broomsgrove, S. Aldridge, F. P. Gabbai, *Chem. Rev.* **2010**, *110*, 3985-4022; h) S. Yamaguchi, A. Wakamiya, *Pure. Appl. Chem.* **2006**, *78*, 1413-1424.

[17] a) X. Wang, S. L. Gong, D. Song, Z. H. Lu, S. Wang, *Adv. Funct. Mater.* **2014**, *24*, 7257-7271; b) Z. L. Zhang, R. M. Edkins, N. Jörn, K. Fucke, A. Steffen, L. E. Longobardi, D. W. Stephan, C. Lambert, T. B. Marder, *Chem. Sci.* **2015**, *6*, 308-321.

[18] G. Wittig, W. Herwig, *Chem. Ber.* **1955**, *88*, 962-976.

[19] a) C. D. Entwistle, T. B. Marder, *Chem. Mater.* **2004**, *16*, 4574-4585; b) L. Ji, S. Griesbeck, T. B. Marder, *Chem. Sci.* **2017**, *8*, 846-863.

[20] a) J. J. McKinnon, A. S. Mitchell, M. A. Spackman, *Chem. Eur. J.* **1998**, *4*, 2136-2141; b) J. J. McKinnon, M. A. Spackman, A. S. Mitchell, *Acta Crystallogr. B* **2004**, *60*, 627-668; c) M. A. Spackman, D. Jayatilaka, *CrystEngComm* **2009**, *11*, 19-32; d) M. A. Spackman, P. G. Byrom, *Chem. Phys. Lett.* **1997**, *267*, 215-220.

[21] M. J. Turner, J. J. McKinnon, D. Jayatilaka, M. A. Spackman, *CrystEngComm* **2011**, *13*, 1804-1813.

[22] a) J. J. McKinnon, D. Jayatilaka, M. A. Spackman, *Chem. Commun.* **2007**, 3814-3816; b) A. Parkin, G. Barr, W. Dong, C. J. Gilmore, D. Jayatilaka, J. J. McKinnon, M. A. Spackman, C.

C. Wilson, *CrystEngComm* **2007**, *9*, 648-652; c) M. A. Spackman, J. J. McKinnon, *CrystEngComm* **2002**, *4*, 378-392.

[23] a) T. Dahl, *Acta Chem. Scand.* **1994**, *48*, 95-106; b) C. A. Hunter, J. K. M. Sanders, *J. Am. Chem. Soc.* **1990**, *112*, 5525-5534; c) M. O. Sinnokrot, C. D. Sherrill, *J. Phys. Chem. A* **2004**, *108*, 10200-10207; d) M. O. Sinnokrot, E. F. Valeev, C. D. Sherrill, *J. Am. Chem. Soc.* **2002**, *124*, 10887-10893; e) L. Loots, L. J. Barbour, *John Wiley & Sons*, Chichester, UK, **2012**, 109-124.

[24] H. Pan, G. L. Fu, Y. H. Zhao, C. H. Zhao, *Org. Lett.* **2011**, *13*, 4830-4833.

[25] B. H. Toby, *J. Appl. Crystallogr.* **2005**, *38*, 1040-1041.

[26] A. C. Larson, R. B. Von Dreele, Los Alamos National Laboratory Report LAUR, **2004**, pp. 86-748.

[27] G. M. Sheldrick, *Acta. Crystallogr. A Found. Adv.* **2015**, *71*, 3-8.

[28] G. M. Sheldrick, *Acta. Crystallogr. A Found. Adv.* **2008**, *64*, 112-122.

[29] C. B. Hübschle, G. M. Sheldrick, B. Dittrich, *J. Appl. Crystallogr.* **2011**, *44*, 1281-1284.

[30] K. D. Brandenburg, Crystal and Molecular Structure Visualization, Crystal Impact H. Putz & K. Brandenburg GbR, Bonn (Germany), **2017**.

[31] C. F. Macrae, I. J. Bruno, J. A. Chisholm, P. R. Edgington, P. McCabe, E. Pidcock, L. R. Monge, R. Taylor, J. van de Streek, P. A. Wood, *J. Appl. Crystallogr.* **2008**, *41*, 466-470.

[32] O. V. Dolomanov, L. J. Bourhis, R. J. Gildea, J. A. K. Howard, H. Puschmann, *J. Appl. Crystallogr.* **2009**, *42*, 339-341.

[33] M. J. Turner, J. J. McKinnon, S. K. Wolff, D. J. Grimwood, P. R. Spackman, D. Jayatilaka, M. A. Spackman, CrystalExplorer17 (2017), University of Western Australia, http://hirshfeldsurface.net.

[34] I. R. Morgan, A. E. J. Broomsgrove, P. Fitzpatrick, D. Vidovic, A. L. Thompson, I. A. Fallis, S. Aldridge, *Organometallics* **2010**, *29*, 4762-4765.

[35] TURBOMOLE V7.0, a development of University of Karlsruhe and Forschungszentrum Karlsruhe GmbH, 1989-2007; TURBOMOLE GmbH, since 2007; available from **http://www.turbomole.com.**

[36] M. von Arnim, R. Ahlrichs, *J. Comput. Chem.* **1998**, *19*, 1746-1757.

[37] a) A. D. Becke, *J. Chem. Phys.* **1993**, *98*, 5648-5652; b) C. Lee, W. Yang, R. G. Parr, *Phys. Rev. B: Condens. Matter Mater. Phys.* **1988**, *37*, 785-789; c) P. J. Stephens, F. J. Devlin, C. F. Chabalowski, M. J. Frisch, *J. Phys. Chem. A* **1994**, *98*, 11623-11627.

[38] G. Scalmani, M. J. Frisch, B. Mennucci, J. Tomasi, R. Cammi, V. Barone, *J. Chem. Phys.* **2006**, *124*, 94107.

[39] A. Schäfer, H. Horn, R. J. Ahlrichs, *J. Chem. Phys.* **1992**, *97*, 2571-2577.

[40] I. Lyskov, M. Kleinschmidt, C. M. Marian, *J. Chem. Phys.* **2016**, *144*, 034104.

[41] A. D. Becke, *J. Chem. Phys.* **2014**, *140*, 1372.

[42] a) M. Kleinschmidt, C. M. Marian, *Chem. Phys.* **2005**, *311*, 71-79; b) M. Kleinschmidt, J. Tatchen, C. M. Marian, *J. Comput. Chem.* **2002**, *23*, 824-833; c) M. Kleinschmidt, J. Tatchen, C. M. Marian, *J. Chem. Phys.* **2006**, *124*, 124101.

[43] J. Neugebauer, M. Reiher, C. Kind, B. A. Hess, *J. Comput. Chem.* **2002**, *23*, 895-910.

[44] a) M. Etinski, J. Tatchen, C. M. Marian, *J. Chem. Phys.* **2011**, *134*, 154105; b) M. Etinski, J. Tatchen, C. M. Marian, *Phys. Chem. Chem. Phys.* **2014**, *16*, 4740-4751.

[45] T. J. Penfold, E. Gindensperger, C. Daniel, C. M. Marian, *Chem. Rev.* **2018**, *118*, 6975-7025.

[46] a) J. J. McKinnon, A. S. Mitchell, M. A. Spackman, *Chem. Eur. J.* **1998**, *4*, 2136-2141; b) J. J. McKinnon, M. A. Spackman, A. S. Mitchell, *Acta Crystallogr. B* **2004**, *60*, 627-668; c) M. A. Spackman, D. Jayatilaka, *CrystEngComm* **2009**, *11*, 19-32; d) M. A. Spackman, P. G. Byrom, *Chem. Phys. Lett.* **1997**, *267*, 215-220.

[47] M. J. Turner, J. J. McKinnon, D. Jayatilaka, M. A. Spackman, *CrystEngComm* **2011**, *13*, 1804-1813.

[48] a) J. J. McKinnon, D. Jayatilaka, M. A. Spackman, *Chem. Commun.* **2007**, *0*, 3814–3816; b) A. Parkin, G. Barr, W. Dong, C. J. Gilmore, D. Jayatilaka, J. J. McKinnon, M. A. Spackman, C. C. Wilson, *CrystEngComm* **2007**, *9*; c) M. A. Spackman, J. J. McKinnon, *CrystEngComm* **2002**, *4*, 378-392.

[49] a) T. Dahl, *Acta Chem. Scand.* **1994**, *48*, 95-106; b) C. A. Hunter, J. K. M. Sanders, *J. Am. Chem. Soc.* **1990**, *112*, 5525-5534; c) M. O. Sinnokrot, C. D. Sherrill, *J. Phys. Chem. A* **2004**, *108*, 10200-10207; d) M. O. Sinnokrot, E. F. Valeev, C. D. Sherrill, *J. Am. Chem. Soc.* **2002**, *124*, 10887-10893; e) L. Loots, L. J. Barbour, *John Wiley & Sons*, Chichester, UK, **2012**, 109-124.

CHAPTER THREE

–

AGGREGATION-INDUCED DUAL PHOSPHORESCENCE FROM (O-BROMOPHENYL)BORANE AT ROOM TEMPERATURE

Aggregation-induced dual phosphorescence from (o-bromophenyl)-bis(2,6-dimethylphenyl)borane at room temperature

3.1 Introduction

Purely organic phosphors have received considerable research interest in optoelectronic devices,[1] bioimaging,[2] molecular sensing[3] and security printing[4] due to efficient utilization of their triplet states. So far, most luminophores displaying room temperature phosphorescence (RTP) are restricted to inorganics containing noble transition metals such as iridium (Ir) and platinum (Pt), as transition-metal complexes are characterized by strong spin–orbit coupling (SOC) induced by heavy metal

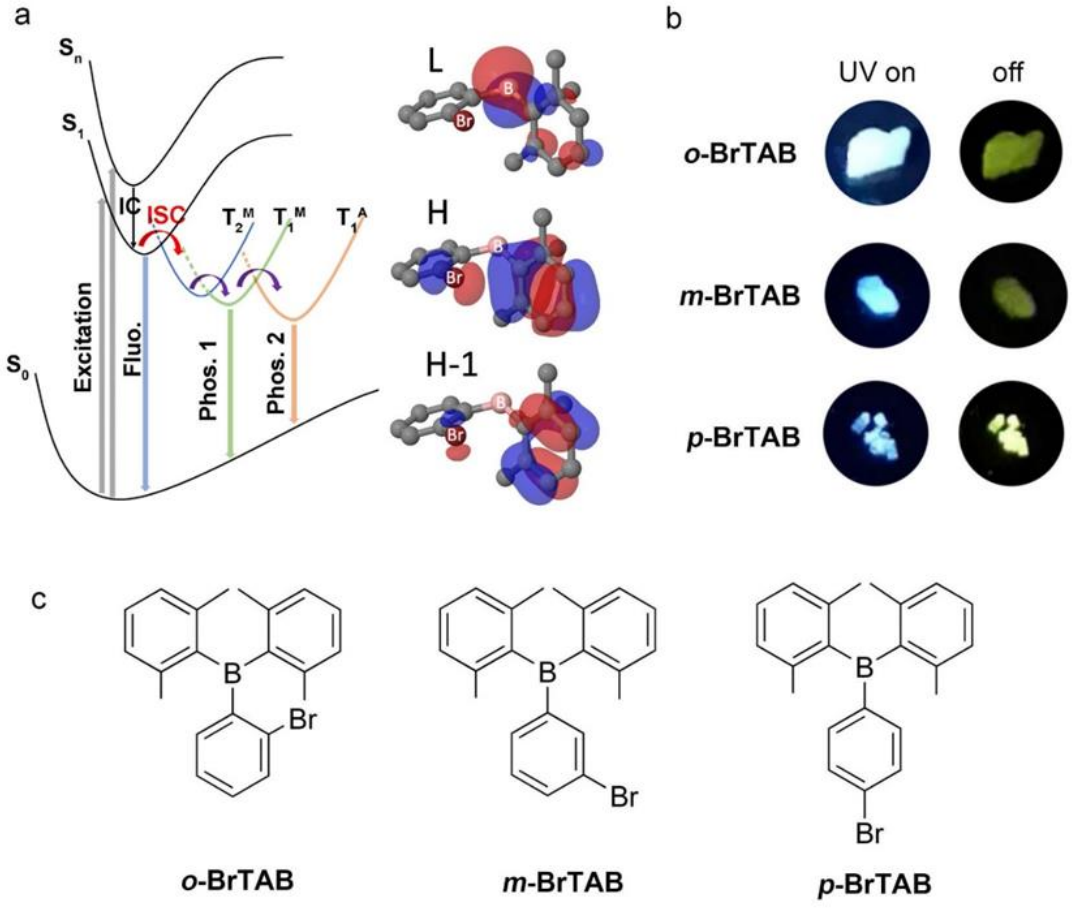

Figure 3-1. (a) Proposed mechanism of the dual phosphorescent emission in ***o*-BrTAB** and essential parts of the molecular orbitals involved in the transitions; T_1^M, and T_2^M represent monomer states, T_1^A an aggregate state (b) afterglow photographs taken before and after irradiation (λ_{ex} = 365 nm) under ambient conditions; (c) molecular structures of the three isomeric compounds described in the paper.

ions and an intrinsic conformational rigidity which can theoretically harvest 100% of the electrically generated singlet and triplet excitons.[5] In addition, the phosphorescence emission spectra and quantum efficiencies can be tuned by modification of the ligand system. On the other hand, purely organic phosphors generally show inefficient intersystem crossing (ISC) and slow radiative decay rates from the lowest triplet state (T_1) to the ground singlet state (S_0).[6] In addition, the long-lived triplet excitons in metal-free luminophores can interact with environmental quenchers such as O_2, which quench the phosphorescence to a great extent.[7] In order to achieve RTP, one prerequisite is to enhance SOC to accelerate the ISC process, typically by utilizing heteroatoms, heavy atoms, or particular functional groups containing heteroatoms with lone pairs such as C=O, C=S or NR_2.[8] At the same time, it is also important to suppress nonradiative pathways and to isolate the chromophores from oxygen by host−guest doping,[9] crystallization,[10] or incorporation in a polymer matrix or on carbon dots.[11] Unlike trapped organic phosphors which emit only single component phosphorescence,[12] dual phosphorescence emission results from two different triplet states and was observed previously in a frozen glass matrix at low temperature.[13] More recently, dual room temperature phosphorescence (DRTP) in aggregated states was reported by several groups. For example, Tang''s group developed a single-molecule white light phosphor which emits from both T_1 and T_2 states at room temperature.[14] Huang *et al*. reported a series of indole derivatives which show DRTP via inter-/intramolecular charge transfer.[15] Zhang *et al*. designed a number of D–sp^3–linker–A-type triphenylamine (TPA) luminophores, which showed a TPA-localized triplet state T_1^L and an acceptor centered triplet state T_1^H simultaneously in a PMMA film.[16] Ma's group observed dual phosphorescence from pyridine-modified carbazole derivatives originating from T_1 and T_1* states.[17] Although several DRTP luminophores have been reported, research on this topic and the types of DRTP systems are still quite limited,[18] and there is no reliable design concept and strategy to achieve DRTP luminophores with high performance.

Based on our long standing interest in 3-coordinate organoboron materials[19] and their optical and electronic properties,[20] we successfully designed persistent triarylboron phosphors with efficient ISC via (σ, B p)→(π, B p) transitions.[21] However, it seemed likely that the SOC and, thus, the ISC rate constant could be improved. It is proposed that introducing heavy atoms (Br or I) into existing persistent RTP luminophores to enhance the SOC may greatly improve the performance of RTP

phosphors. Br or I atoms can also provide multiple efficient intermolecular interactions to restrict nonradiative pathways, which is crucial to stabilize triplet states.[22] More importantly, the dense crystalline matrix provides a favorable environment for delocalization of the excitation and the formation of energy dispersed band structures.[23] Herein, we introduced the heavy atom Br into phenyl-bis(2,6-dimethylphenyl)borane at different positions on the phenyl ring to obtain 3 isomers (***o***-, ***m***- and ***p***-**BrTAB**, Figure 3-1c). Interestingly, (2-bromophenyl)bis(2,6-dimethylphenyl)borane (***o***-**BrTAB**) exhibits DRTP in the crystalline state under ambient conditions (Figure 3-1b). The faster, higher energy phosphorescence ranging from 430 to 490 nm with a short lifetime of 0.8 ms is ascribed to the T_1^M state of the monomer while the long-lived, lower energy phosphorescence emission in the range of 490-700 nm with a lifetime of up to 234 ms is attributed to the T_1^A state of an aggregate in the crystalline material.

3.2 Results and Discussion

3.2.1 Photophysical properties

The compound ***o***-**BrTAB** was synthesized[24] by reaction of the Grignard reagent (2,6-Me_2-C_6H_3)MgBr with *o*-Br-$C_6H_4BF_3K$, whereas ***m***- and ***p***-**BrTAB** were prepared by the reaction of bis(2,6-dimethylphenyl)fluoroborane with the respective aryllithium species generated by mono lithium–halogen exchange of *m*- or *p*-dibromobenzene with *n*-BuLi**.** All three compounds showed absorption bands between 270 and 350 nm in hexane which are attributed to B←π transitions with extinction coefficients of ε = 10000–16000 $_M{}^{-1}cm^{-1}$ (Figure 3-2a and Table 3-1). Placement of the Br atoms at the *ortho*, *meta* and *para* positions of the phenyl group had no obvious effect on the molecular energy levels of the three triarylboranes.

The spectra are composed of two absorption bands, where the lower energy band, around 300 nm, is more intense than the one at 260-270 nm. DFT/MRCI (multireference configuration interaction) calculations (Figure 3-17) show that the band at 300 nm is an overlay of the $S_0 \rightarrow S_1$ and $S_0 \rightarrow S_4$ absorptions, while the band at higher energy arises from the $S_0 \rightarrow S_6$ absorption. They also reveal that

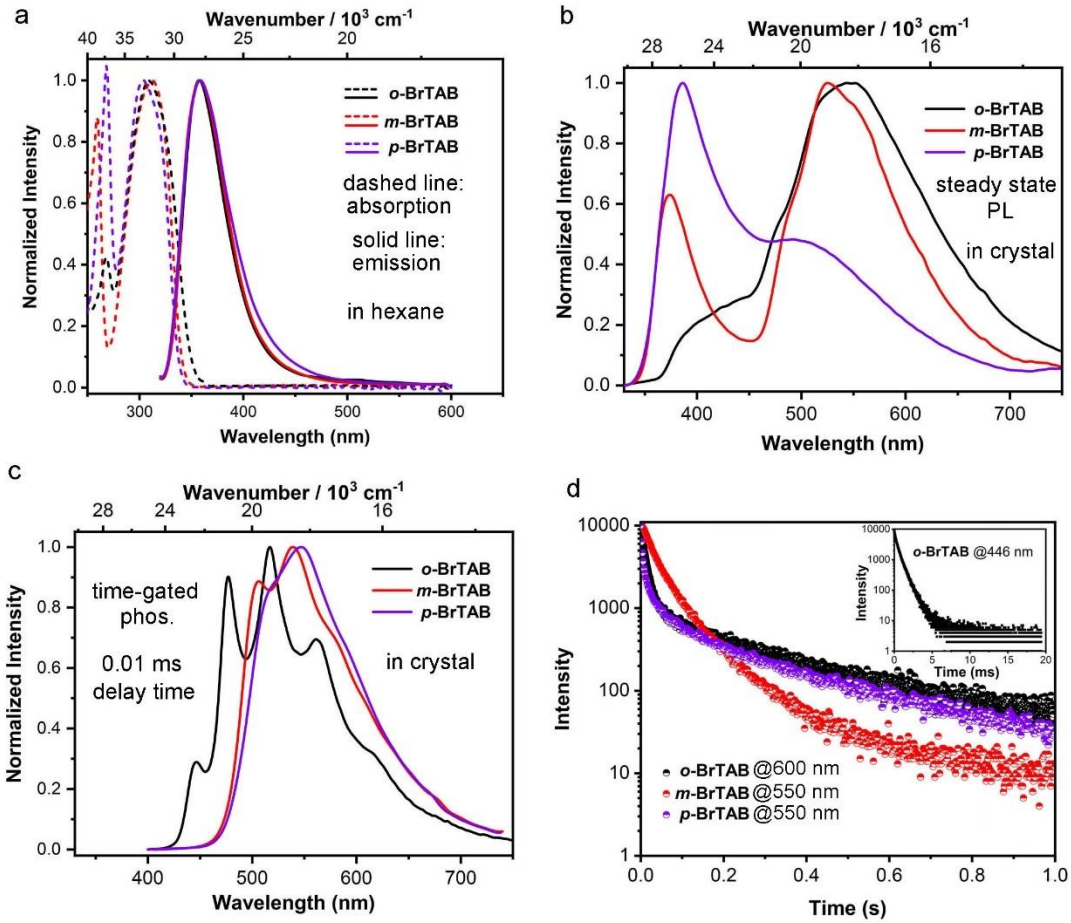

Figure 3-2. Normalized (a) UV/Vis absorption and fluorescence in hexane, (b) PL and (c) time-gated (0.01 ms delay) phosphorescence spectra of crystalline ***o*-**, ***m*-** and ***p*-BrTAB** (λ_{ex} = 305 nm). (d) Decays of the phosphorescence (600 nm for ***o*-BrTAB** and 550 nm for ***m*-** and ***p*-BrTAB**) in the crystalline state. Insert: decay of the phosphorescence (446 nm) of crystalline ***o*-BrTAB**. All above measurements were conducted at room temperature in air.

irradiation of the compounds with UV light in the 310-320 nm wavelength regime predominantly populates the S_1 state. The experimental fluorescence spectra of the 3 isomers in solution almost overlap with emission maxima at 358 nm. Our calculations show the onsets of the fluorescence to occur at 348 nm for ***o*-BrTAB**, 328 nm for ***m*-BrTAB** and 324 nm for ***p*-BrTAB**, while experimentally, the onset is located at 328 nm for all three compounds. The computed fluorescence rate constants for ***o*-**, ***m*-**, and ***p*-BrTAB** are 1×10^7, 2×10^7 and 2×10^7 s^{-1}, respectively, (Table 3-4) while their corresponding experimental fluorescence rate constants are 1×10^7, 6×10^6 and 1×10^7 s^{-1}, respectively, showing good agreement between calculated and experimental values (Table 3-1 and Table 3-4).

Table 3-1. Photophysical properties of ***o***-, ***m***- and ***p*-BrTAB** in hexane and the crystalline state at RT, and in frozen methylcyclohexane and in the crystalline state at 77 K.

Compound	State (T)	λ_{abs} nm	ε $_M^{-1}cm^{-1}$	Φ_{PL} %	λ_f nm	Φ_f %	τ_f ns	τ_0^f ns	k_r^f s^{-1}	λ_p nm	Φ_p %	τ_p (T_1^M) ms	τ_p (T_1^A) ms
***o*-BrTAB**	Solution (RT)[a]	312	10900	3.5	358	3.5	2.8	80	$1*10^7$	nd[b]		nd	nd
	Crystalline (RT)[c]			1.5	-	0.2	3.2	$8*10^3$	$1*10^5$	446, 477, 517, 562[d]	1.3	0.3 (34%), 0.8 (66%)	13 (22%), 234 (78%)
	Crystalline (77 K)	-		-	-		-	-		431, 455		0.3 (28%), 2.1 (72%)	161 (42%), 453 (58%)
	Frozen glass (77 K)[e]	-		-	-					457		23 (57%), 92 (43%)	-
***m*-BrTAB**	Solution (RT)[a]	310	11300	1.4	358	1.4	2.3	164	$6*10^6$	nd		-	nd
	Crystalline (RT)[c]	-		3.8	374	0.7	6.0	$3*10^3$	$3*10^5$	506, 539	3.1	-	64 (67%), 215 (33 %)
	Crystalline (77 K)			-	374		-	-		430, 458, 483, 510		51 (54 %), 153 (45%)	45 (28%), 512 (72 %)
	Frozen glass (77 K)[e]	-		-	-		-	-		438		154 (55%), 486 (45 %)	-
***p*-BrTAB**	Solution (RT)[a]	304	15200	1.2	358	1.2	1.7	77	$1*10^7$	nd		-	nd
	Crystalline (RT)[c]	-		4.4	386	2.4	2.9	121	$8*10^6$	547	2.0	-	90 (30%), 378 (70 %)
	Crystalline (77 K)	-		-	386			-		427, 458, 510		18 (69 %), 59 (31%)	166 (19%), 581 (81 %)
	Frozen glass (77 K)[e]	-		-	367		-	-		438		53 (48%), 201 (52 %)	-

[a] Measured in hexane at room temperature (RT); [b] not detected (nd); [c] measured in the crystalline state at RT; [d] The maximum fluorescence emission wavelength of ***o*-BrTAB** is estimated to occur at ca. 400-405 nm, but cannot be more accurately determined due to the overlap of fluorescence and phosphorescence; [e] 446 and 477 nm are ascribed to $\mathbf{T_1^M}$ and 517 and 562 nm are ascribed to $\mathbf{T_1^A}$; [f] measured in frozen methylcyclohexane at 77 K. For the phosphorescence lifetimes, the value given in % in parentheses is the larger of two contributions to a bi-exponential fit of the decay.

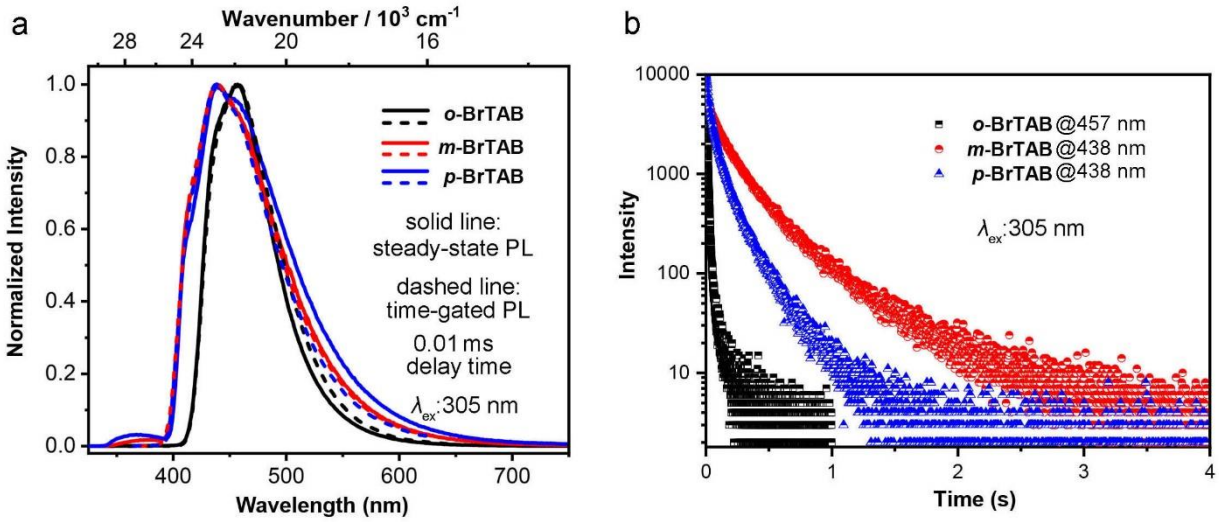

Figure 3-3. (a) Normalized photoluminescence (solid line) and time-gate phosphorescence (dashed line) spectra and (b) decays of the phosphorescence of ***o***-, ***m***- and ***p*-BrTAB** at their maximum emission wavelength in a frozen methylcyclohexane glass at 77 K (λ_{ex} = 305 nm).

We also measured the PL emission spectra in a frozen methylcyclohexane optical glass at 77 K (Figure 3-3). Compared to ***m***- and ***p*-BrTAB**, which still show some residual fluorescence at higher energies (330-400 nm), only phosphorescence with a lifetime of 23 ms (57 %) was observed in the spectrum of ***o*-BrTAB**, which indicates that ISC is very efficient and the phosphoresce quantum yield is much higher than that of fluorescence. Note that, as indicated in the footnote to Table 3-1, % values in parentheses are the larger of two contributions to a bi-exponential fit of the decays. Comparison of both experimental and computedfluorescence rate constants (*ca*. 10^7 s^{-1}) with the fastest ISC rate constants for ***o***-, ***m***-, and ***p*-BrTAB** obtained from our theoretical calculations (*vide infra*) of 1×10^{10}, 9×10^8 and 3×10^8 s^{-1} (Table 3-4), respectively, supports the above observations at 77 K in the frozen matrices. Thus, in the bromo-substituted triarylboranes, most of the excited state population is transferred to the triplet manifold, especially in ***o*-BrTAB**. The heavy atom effect of Br on the monomer phosphorescence radiative lifetimes is in the order ***o*-BrTAB** > ***p*-BrTAB** > ***m*-BrTAB** (Table 3-4), in agreement with the experimental trends listed in Table 3-1. The absence of DRTP in the frozen glass at 77 K suggests that the longer-lived phosphorescence component must originate from an aggregated state.

However, the photoluminescence spectra at room temperature in the crystalline state are much different from the results in solution (Figure 3-2b). First, in addition to the fluorescence peaks attributed to the monomer excited state at short wavelength, broad peaks between 450 and 750 nm result from phosphorescence. The longer-lived (phosphorescence) emission lifetimes

measured for ***o***-, ***m***- and ***p*-BrTAB** at room temperature are 234 (78 %), 64 (67%) and 378 (70 %) ms, respectively, where the percentages given are those of the larger component of a bi-exponential fit to the decay curves (Figure 3-2d). Second, the fluorescence emissions from crystalline samples of ***o***-, ***m***- and ***p*-BrTAB** are all redshifted compared with those in hexane solution. The bathochromic shift of ***p*-BrTAB** (2026 cm^{-1}) is approximately twice that of ***m*-BrTAB** (1194 cm^{-1}). Third, ***o*-BrTAB** has a larger ratio of phosphorescence to fluorescence

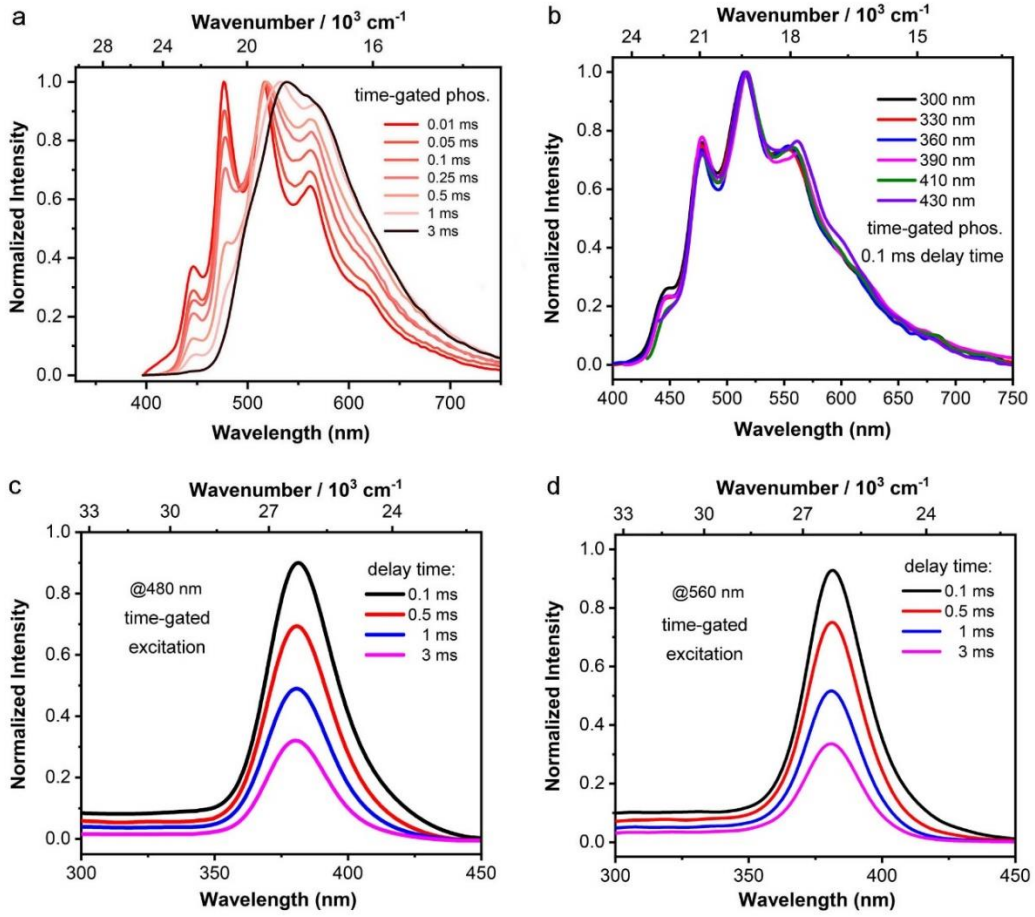

Figure 3-4. Normalized time-gated phosphorescence spectra of crystalline ***o*-BrTAB** (a) with different delay times and (b) with 0.1 ms delay at different excitation wavelength. Time-gated excitation spectra (c, 480 nm) and (d, 560 nm) of crystalline ***o*-BrTAB** at different delay times at room temperature.

intensity, indicating that ISC in ***o*-BrTAB** is the most efficient of the three isomers. The time-gated phosphorescence spectrum of crystalline ***o*-BrTAB** at room temperature shows four fine structured bands at 446, 477, 517 and 562 nm, respectively (Figure 3-2c). The vibrational fine structure is also present in the computed Franck-Condon (FC) spectrum of the T_1^M emission, though less pronounced. We attribute it to a progression of a vibrational mode with a frequency

of 1673 cm^{-1} in the electronic ground state which corresponds to an asymmetric C-C stretching motion of the xylyl ring closest to the Br atom.

The aggregation state of ***o*-BrTAB** has a large influence on the photoluminescence behavior. A ground solid sample of ***o*-BrTAB** exhibited multiple small size particles with increased surface area as observed by SEM (Figure 3-2). The powder X-ray diffraction pattern of the ground ***o*-BrTAB** sample shows its crystalline nature (Figure 3-10). In the ground sample, the exposed surface area is much larger than in the single crystal and, as slower phosphorescence is more sensitive to oxygen quenching, the ratio of phosphorescence to fluorescence dramatically decreased (Figure 3-9). The longer phosphorescence lifetime decreases significantly from 234 to 191 ms and the quantum yield is too small to be measured. The shorter phosphorescence lifetime also drops slightly to 0.7 ms, further indicating the important role of the aggregation state in the photoluminescence behavior. In addition, ***o*-BrTAB** was embedded in a poly(methyl methacrylate) (PMMA) matrix at different loading levels. In a highly doped film (40 wt%, Figure 3-11), the time-gated phosphorescence emission blueshifts (*ca*. 600 cm^{-1}) compared to that in the crystalline state, and only the short lifetime (0.8 ms) component was detected, while in an even more concentrated PMMA film (60 wt%, Figure 3-12), the long lifetime (226 ms) component emerged. The experimental results clearly indicate that longer-lived component of the the DRTP is induced by aggregation.

The DRTP was confirmed by time-gated phosphorescence spectroscopy of ***o*-BrTAB** at room temperature (Figure 3-4a). Upon increasing the delay time, the intensity of peaks of the shorter wavelength emission components at 446 and 477 nm decreased gradually. When the delay time was set at 3 ms, the short-lived monomer T_1^M emission of ***o*-BrTAB** almost disappeared, and the remaining long lifetime component is ascribed to phosphorescence from the T_1^A state of an aggregate. We performed time-gated excitation spectroscopy of crystalline ***o*-BrTAB** at 480 and 560 nm, respectively (Figures 3-4c and 3-4d). The two spectra are identical in the range of 300 to 450 nm, which indicates that one absorption leads to all exited states. We also measured time-gated phosphorescence spectra at different excitation wavelengths (Figure 3-4b). The two triplet excited states always appear at the same time which further proves that T_1^M and T_1^A originate from the same absorption ($S_0 \rightarrow S_1$ and $S_0 \rightarrow S_n$). Therefore, we propose that first, the single molecule of ***o*-BrTAB** is excited into its S_1^M or S_n^M state. Then it undergoes ISC to T_2^M

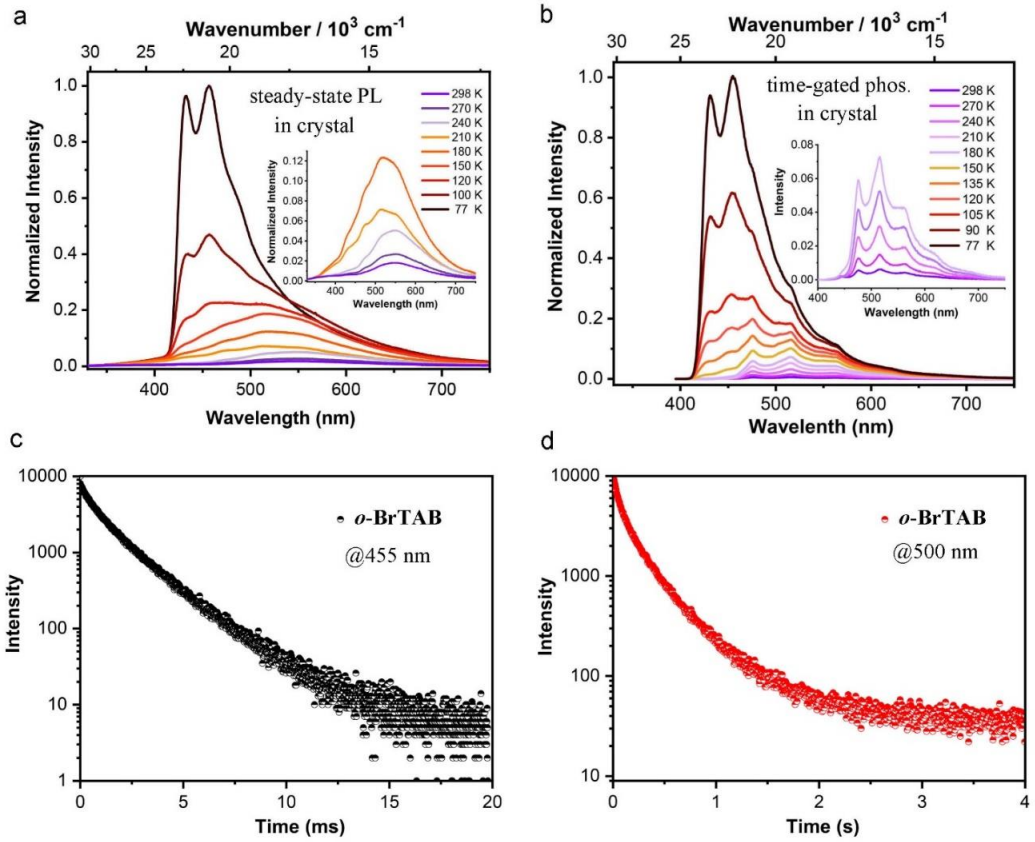

Figure 3-5. (a) Steady-state photoluminescence and (b) time-gated (delay time 0.01 ms) phosphorescence spectra of crystalline ***o*-BrTAB** at different temperatures (λ_{ex} = 305 nm). Decays of the phosphorescence emission (c) (λ_{em} = 455 nm) and (d) (λ_{em} = 500 nm) of crystalline ***o*-BrTAB** at 77 K.

which undergoes IC to a short-lived T_1^M state. At the same time, T_1^A evolves into a T_1^M state, emitting more slowly and at lower energy. The process going from T_1^M to T_1^A was confirmed by temperature-dependent, time-gated spectroscopic study of crystalline ***o*-BrTAB** (Figure 3-5b). Upon decreasing the temperature from 298 to 77 K, the phosphorescence peaks belonging to T_1^M at 446 and 477 nm blueshift to *ca*. 431 and 455 nm, respectively, which become dominant at 77 K with a lifetime *ca*. 2.1 ms. At 77 K, the long-lived T_1^A emission at longer wavelength still exists with a lifetime of *ca*. 453 ms (58 %), but in a much lower ratio compared to the short-lived component. Thus, there is a thermal barrier for the conversion of T_1^M to T_1^A, and lowering the temperature makes it harder to cross the barrier.

For crystalline ***m***- and ***p*-BrTAB**, we did not observe dual phosphorescence at room temperature, but only at low temperature. At 77 K, new emission peaks at 431 and 455 nm appeared in the time-gated spectra with the phosphorescence lifetimes of crystalline ***m***- and ***p*-BrTAB** of 51 (54 %) and 18 (69 %) ms, respectively, being much shorter than the lifetimes 512 (72 %) and 581 (81 %) ms of the longer-wavelength emissions (Figure 3-13 to 3-16). As

the strength of intermolecular interactions is especially distinct between the three compounds at room temperature, only ***o*-BrTAB** exhibits strong intermolecular interactions, effectively suppressing the nonradiative decay rate k_{nr}, which plays an important role in stabilizing the triplet states. Hence, a nonradiative decay channel is opened for ***m*-** and ***p*-BrTAB** going from 77K to RT. In ***o*-BrTAB**, the radiative channel can compete with the nonradiative one even at RT. This may be the reason that dual phosphorescence is only observed in ***o*-BrTAB** at room temperature and a detailed discussion of intermolecular interactions is provided in the crystal structure analysis section (*vide infra*).

3.2.2 Theoretical study

Recently, Sarkar and Hendrickson et al. reported on the three isomeric *o*-, *m*-, and *p*-bromobenzaldehydes.[25] When Br is *ortho* to the aldehyde, SOC is greatly enhanced, consistent with our observations. Looking at Table 3-4, the heavy Br atom effect leads to efficient ISC for all three compounds. However, while the fluorescence rate constant has the same order of magnitude (10^7 s^{-1}) for all three isomers, the ISC rate constants decrease in the order ***o*-** > ***m*-** > ***p*-BrTAB**. For ***p*-BrTAB** and ***m*-BrTAB**, ISC is 15 and 45 times faster, respectively, than fluorescence, so that residual fluorescence might be expected from those 2 isomers. For ***o*-BrTAB**, however, ISC is 1000 times faster than fluorescence, so nearly all excited molecules rapidly form triplet states. As can be seen in the difference densities in Figures 3-20 to 3-22, bromine is involved the stronger in the excitation the closer it is located to the boron center. Following El-Sayed,[26] a change in orbital character is required for a fast ISC process. This orbital change is visible in all three isomers, but most dominant in the ***o*-BrTAB** compound, where the Br p-orbital changes its orientation moving from the S_1 to the T_2 state (Figure 3-6) causing the squared SOCME to increase markedly to 18640 cm^{-2}. Despite the similarity of the electron distributions in both states (Figure 3-6), even the S_1^M and T_1^M states experience substantial mutual SOC in ***o*-BrTAB**. With a squared sum of SOCMEs of 25 cm^{-2}, the $S_1^M \rightarrow T_1^M$ transition is significantly faster (k_{ISC} = 2×10^9 s^{-1}) than in the unsubstituted compound. Nevertheless, with a rate constant of *ca*. 1×10^{10} s^{-1}, the $S_1^M \rightarrow T_2^M$ ISC is five times faster than the direct $S_1^M \rightarrow T_1^M$ ISC. Besides ISC, internal conversion (IC) plays an important role for the population of the emissive T_1 state from higher triplet states. In ***o*-BrTAB**, we found a conical intersection allowing a very efficient population transfer from T_2 to T_1 without the necessity to surmount a large energy barrier in the process.

In ***m*-BrTAB**, the largest SOCMEs arise between the $S_1^M \rightarrow T_2^M$ and $S_1^M \rightarrow T_3^M$ pair of states. Both target states are similar in character except that the bromine involvement is more pronounced in the T_3^M state, yielding a rate constant of 9×10^8 s^{-1} for the $S_1^M \rightarrow T_3^M$ ISC in this isomer. In ***p*-BrTAB**, the bromine substitution primarily enhances the probabilities of the $S_1^M \rightarrow T_1^M$ and $S_1^M \rightarrow T_3^M$ ISCs. Here we find the T_2^M state to be more similar in character to the S_1^M state than the T_1^M state. The fastest ISC is found for the $S_1^M \rightarrow T_3^M$ channel with k_{ISC} = 3×10^8 s^{-1}. A comparison of the ISC rate constants with the fluorescence rate constants of *ca*. 10^7 s^{-1} (Table 3-4) suggests that the fluorescence quantum yield is low and that most of the excited state population is transferred to the triplet manifold in the bromo-substituted triarylboranes, in particular in the ***o*-BrTAB** isomer, which is consistent with the low fluorescence intensities observed in a frozen glass at 77 K.

The phosphorescence rate constant of T_1 depends essentially on three factors: the magnitude of the SOC matrix element (SOCME) between T_1 and singlet states S_n, the energy difference between T_1 and S_n, and the brightness of the S_n-S_0 transition. Interference effects aside, the larger the T_1-S_n SOC, the smaller the T_1-S_n energy difference, and the larger the S_n-S_0 transition dipole, the larger the phosphorescence probability.[27] Because of the large T_1-S_2 SOC and T_1-S_4 SOC, ***o*-BrTAB** can borrow substantial intensity from the spin-allowed bright transitions (S_2-S_0 and S_4-S_0, respectively). In ***m*-BrTAB** and ***p*-BrTAB**, SOC between T_1 and the low-lying singlet states is small and, therefore, the intensity borrowing is not very efficient. Hence, ***o*-BrTAB** is the only compound with a phosphorescence rate constant in the millisecond regime; the other two have rate constants of 5 s (***m*-BrTAB**) and 1 s (***p*-BrTAB**) according to the calculations.

To explain the experimentally observed dual phosphorescence, we first searched for the most probable pathways from the singlet to the triplet states of the monomer. For the unsubstituted compound phenyl-bis(2,6-dimethylphenyl)borane, we have already shown that the $S_1 \rightarrow T_1$ transition is slower than $S_1 \rightarrow T_2$.[21] This can be rationalized by the stronger change in orbital character when moving from S_1 to T_2 and thus, following El Sayed's rule,[26] the SOCMEs between S_1 and T_2 are much larger than those for $S_1 \rightarrow T_1$. The bromine substitution increases the SOCMEs in general with respect to those of the unsubstituted compound. As may be expected, the heavy-atom effect is strongest for the *ortho*-substituted compound. Even in this case, the change in excitation character is larger for the $S_1^M \rightarrow T_2^M$ transition. In particular, the p orbital hole at the Br atom changes orientation (*vide supra*) as required for an El-Sayed

allowed transition.[26] Very close to the T_2^M minimum, however, the T_2^M and T_1^M states of ***o*-BrTAB** undergo a conical intersection without the necessity to surmount a substantial energy barrier. Therefore, the population is not trapped in the T_2^M state but is rapidly transferred to the T_1^M state. The possibility that the dual phosphorescence originates from T_2^M and T_1^M states can be ruled out.

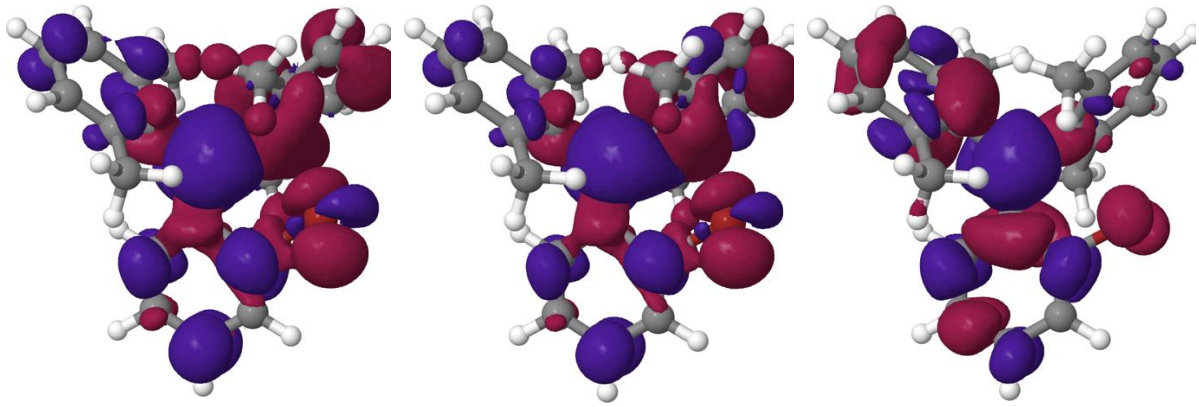

Figure 3-6. Difference of electron density distributions in the S_1^M, T_1^M and T_2^M states of the ***o*-BrTAB** monomer with regard to the electronic ground state, S_0^M, at the S_1^M geometry. Red areas indicate a loss of electron density upon excitation, blue areas a gain.

3.2.3 Crystal structure analysis

To understand the effect of the solid-state structures and the intermolecular packing on the luminescence properties, the structures of ***o*-**, ***m*-** and ***p*-BrTAB** were obtained at low temperature (100 K) and at ambient temperature (290 K for ***o*-BrTAB**, 296 K for ***m*-BrTAB**, and 300 K for ***p*-BrTAB**) using single-crystal X-ray diffraction (Figure 3-7). Comparison of the molecular geometries of ***o*-**, ***m*-** and ***p*-BrTAB** in their crystal structures shows only a small effect of the Br atom position on the bond lengths and angles. All but one of the B–C bond distances are similar within 3 esd's (1.574(3)–1.585(2) Å at 100 K). Only the B–C bond to the Br-substituted aryl ring in ***p*-BrTAB** is significantly shorter (1.563(2) and 1.561(2) Å for the two non-symmetry equivalent molecules at 100 K, Table 3-13). The BC_3 moiety is planar in all three compounds with the sum of C–B–C angles being 360° within the standard uncertainties. The individual angles are in the range 118.0(2)–122.9(2)° except for the C1–B–C7 angle in ***o*-BrTAB** which is significantly smaller (116.3(2)° at 100 K, Table 3-13). This is the angle between the Br-substituted aryl ring R1 and the m-xylyl group R2 arranged on the

opposite side with respect to the Br–C2 bond. Another interesting feature is that the B–C1–C2 angle (127.2(2)°) to the C2 carbon atom to which the Br atom is bonded in ***o*-BrTAB** is

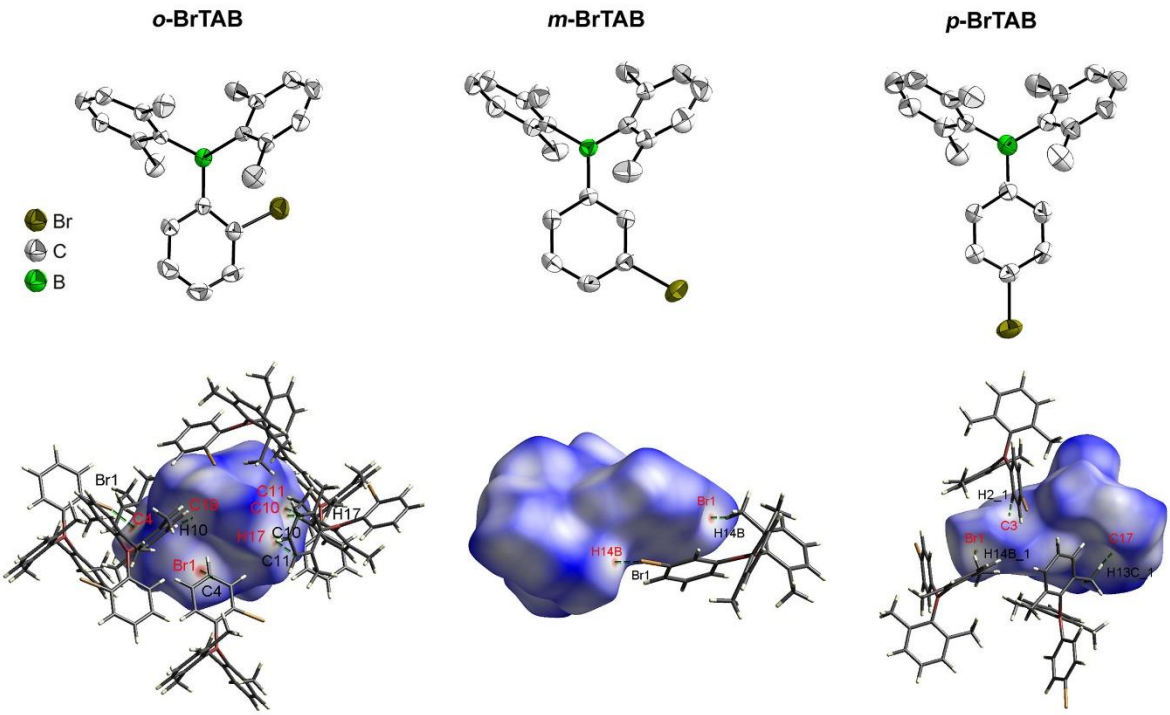

Figure 3-7. The solid-state molecular structure of ***o*-BrTAB**, ***m*-BrTAB** and ***p*-BrTAB** (top left to right) determined by single-crystal X-ray diffraction at room temperature. Ellipsoids are drawn at the 50% probability level, and H atoms are omitted for clarity. Hirshfeld surfaces of ***o*-BrTAB**, ***m*-BrTAB** and ***p*-BrTAB** (bottom left to right) mapped with d_{norm} over the range -0.12 to 1.50 at room temperature. Neighboring molecules associated with close contacts are shown.

significantly larger than all other B–C–C angles in ***o*-**, ***m*-** and ***p*-BrTAB** which are in the range 117.5(2)–122.9(1)° at 100 K (Table 3-13), and the B–C1–C6 angle (117.7(2)°) to the other side of the R1 aryl ring is rather small. The larger B–C1–C2 angle in ***o*-BrTAB** is attributed to the bulkiness of the long Br–C bond at the *ortho* position of the R1 ring and the Br atom being close to the central B atom and the C atom of the next-nearest m-xylyl group R3 with intramolecular Br···B (3.345(2) Å) and Br···C15 (3.298(2) Å) distances below the sum of van der Waals radii[28] (3.75 Å for Br···B and 3.53 Å for Br···C). The effect of the bulkiness of the substituents and, hence, repulsion between methyl groups and also the Br atom, is further observed in the torsion angles between the aryl groups and the BC_3 planes. While the torsion angles are in a similar range (50.1 – 68.6°) for the m-xylyl groups, a significantly smaller torsion angle (41.9°) is observed for the Br-substituted phenyl rings. Here, the Br *ortho*-substituted phenyl ring shows a larger torsion angle (38.6(1)°) in ***o*-BrTAB** than the Br *meta*- and *para*-substituted phenyl rings (20.1–24.8°) in ***m*-** and ***p*-BrTAB** due to repulsion effects

(Table 3-13). The molecular geometries in the solid state of ***o***-, ***m***- and ***p***-**BrTAB** at 290 K, 296 K and 300 K, respectively, are very similar to those at 100 K (Table 3-12).

The molecules are similarly densely packed in the three compounds as is obvious from the crystal packing coefficients (Table 3-17). The molecular volumes and molecular surface areas are also very similar. However, the volume of the solvent accessible voids in the unit cells, as calculated with the OLEX2 program,[29] is increased in ***p***-**BrTAB** (2.7 % at 300 K) and in ***m***-**BrTAB** (4.4 % at 296 K) at ambient temperature, compared to ***o***-**BrTAB** (1.7% at 290 K) and to the low-temperature crystal structures at 100 K (0–1.8 % in the three compounds). This indicates a looser packing mode in ***p***-**BrTAB** and ***m***-**BrTAB** than in ***o***-**BrTAB** at room temperature.

A Hirshfeld surface analysis based on the crystal structures was performed in order to quantify the nature and type of intermolecular interactions.[30] The Hirshfeld surface is a special isosurface defined by the weighting function w(**r**) = 0.5 for a particular molecule. This means that the Hirshfeld surface envelops the volume within which the particular molecule contributes more than half of the electron density. Hence, it also includes information on the nearest neighbors and closest contacts to the molecule (Figure 3-7). The similarity of the amounts and types of interactions in the three compounds is demonstrated in the two-dimensional fingerprint plots and their breakdown to the individual relative contributions (Figures 3-32 and 3-33, 100 K).[31] At 100 K, major contributions are from H···H interactions (61 – 67%), followed by a significant amount from C···H (19 – 25%) and Br···H (10 – 15%) interactions. Minor contributions (0.2 – 1.8%) are Br···C, C···C, and Br···Br interactions with C···C interactions being dominant in ***m***-**BrTAB**, Br···Br interactions in one of the symmetry-independent molecules (no. 2) of ***p***-**BrTAB**, and Br···C interactions in both ***o***-**BrTAB** and ***p***-**BrTAB** (Figure 3-32, Table 3-17). Relative contributions to intermolecular interactions are very similar for the room temperature structures.

At 100 K, the C−H···C interactions are strongest in ***o***-**BrTAB**, with C···H distances in the range 2.735(2)–2.812(2) Å, and two nearly linear interactions with C−H···C = 165.82(15)° and 175.45(15)° (Table 3-14). C−H···C interactions are weaker in ***p***-**BrTAB** (C···H = 2.810(2)–2.865(2) Å, C−H···C = 131.16(11)–162.62(11)°) although of similar number as in ***o***-**BrTAB** and, significantly, weakest in ***m***-**BrTAB** (C···H = 2.836(2)–2.888(3) Å, C−H···C = 143.96(15)–166.26(15)°) as well as being fewer in number. While there are close Br···H contacts (2.9425(12) – 3.1001(3) Å) in all three compounds, ***o***-**BrTAB** exhibits the closest

Br···C contact of 3.354(2) Å. Another close Br···C contact (3.480(2) Å) is found in ***p*-BrTAB**. In addition, ***o*-BrTAB** has a short C···C contact (3.361(3) Å) between an aryl ring and a methyl group, and ***p*-BrTAB** shows two close H···H contacts (2.266 and 2.363 Å) between two aryl rings (Table 3-14). Interestingly, ***m*-BrTAB** is the only compound, in which two weak intermolecular π···π interactions between aryl rings can be found (Table 3-16). One involves the Br-substituted phenyl rings with an interplanar separation of 3.640(3) Å and an offset shift of 2.261(4) Å. The nearest-neighbor C···C distance is 3.698(5) Å. The other one involves the R3 xylyl rings with a slightly smaller interplanar separation of 3.544(4) Å, but a larger offset shift of 3.457(4) Å, and a nearest-neighbor C···C distance of 3.637(5) Å.

At room temperature (290 K), there are still a significant number of intermolecular C−H···C interactions (C···H = 2.846(4)–2.873(4) Å, C−H···C = 136.4(2)–177.2(3)°) and a close Br···C contact of 3.432(5) Å present in ***o*-BrTAB** (Table 3-15). However, in ***m*-BrTAB** C···H contacts are long and weak, and the π···π interactions are also insignificant due to large interplanar separations of 3.812(4) Å and 3.645(6) Å with shifts of 2.305(6) Å and 3.437(6) Å, respectively, at 296 K (Table 3-15). Only a close Br···H interaction (2.9857(8) Å) with a methyl group is still significant. In ***p*-BrTAB**, two intermolecular C−H···C interactions remain (C···H = 2.870(2) Å and 2.887(2) Å, C−H···C = 145.18(15)° and 132.78(13)°) at 300 K, a close H···H interaction with 2.393(1) Å, and close Br···H interaction (2.9648(4) Å) with a methyl group only (Table 3-15). Thus, only ***o*-BrTAB** exhibits strong intermolecular interactions and, especially, a close Br···C contact at room temperature, which may be the reason that dual phosphorescence is only observed in ***o*-BrTAB** at room temperature.

In summary, the presence of multiple C−H···C and C−H···Br interactions between molecules in the crystals effectively suppresses the nonradiative decay rate k_{nr}, which plays an important role in stabilizing the triplet states and achieving RTP. As the strength of intermolecular interactions is especially distinct between the three compounds at room temperature, and is strongest for ***o*-BrTAB**, this effect may be the reason that we observe DRTP in crystalline ***o*-BrTAB** at room temperature, but only at low temperature for ***m*-BrTAB** and ***p*-BrTAB**.

3.3 Conclusions

We reported three bromo-substituted triarylboron isomers which show persistent room temperature phosphorescence (RTP). Among them, (2-bromophenyl)bis(2,6-dimethylphenyl)borane (***o*-BrTAB**) exhibits rare dual room temperature phosphorescence

(DRTP) with lifetimes of 0.8 ms (short wavelength component) and 234 ms (long wavelength component), respectively, in the crystalline state. Single-crystal structure analysis shows that multiple molecular C−H···C and C−H···Br contacts in the crystals suppress the nonradiative decay rate k_{nr} and stabilize the triplet states. In addition, the rigid crystalline matrix provides a favorable environment for realizing dual phosphorescence at room temperature.

3.4 Experimental details and characterization data

3.4.1 General information details

All starting materials were purchased from commercial sources and were used without further purification. The organic solvents for synthetic reactions and for photophysical measurements were HPLC grade, further treated to remove trace water using an Innovative Technology Inc. Pure-Solv Solvent Purification System and deoxygenated using the freeze-pump-thaw method. All synthetic reactions were performed in an Innovative Technology Inc. glovebox or under an argon atmosphere using standard Schlenk techniques. ^{1}H, ^{13}C and ^{11}B NMR spectra were measured on a Bruker Avance 500 MHz (^{1}H, 500 MHz; ^{13}C, 126 MHz; ^{11}B, 160 MHz) NMR spectrometer. Mass spectra were recorded on Agilent 7890A/5975C Inert GC/MSD systems operating in EI mode. High resolution mass spectra were obtained using a Thermo Fisher Scientific Exactive™ Plus Orbitrap MS System with an Atmospheric Solids Analysis Probe ($ASAP^{+}$). Elemental analyses were performed on a Leco CHNS-932 Elemental Analyser.

General photophysical measurements. All measurements were performed in standard quartz cuvettes (1 cm × 1 cm cross-section). UV-visible absorption spectra were recorded using an Agilent 8453 diode array UV-visible spectrophotometer. The molar extinction coefficients were calculated from three independently prepared samples in hexane solution. The emission spectra were recorded using an Edinburgh Instruments FLSP920 spectrometer equipped with a double monochromator for both excitation and emission, operating in right angle geometry mode, and all spectra were fully corrected for the spectral response of the instrument. All solutions used in photophysical measurements had a concentration lower than 10^{-5} M to minimize inner filter effects during fluorescence measurements.

Quantum yield measurements. The photoluminescent quantum yields were measured using a calibrated integrating sphere (inner diameter: 150 mm) from Edinburgh Instruments combined with the FLSP920 spectrometer described above. For solution-state measurements, the longest-wavelength absorption maximum of the compound in hexane was chosen as the

excitation wavelength. For solid-state measurements, the excitation wavelength was 305 nm. The phosphorescence quantum yield of compounds ***o***-, ***m***- and ***p***-**BrTAB** were obtained using the equation:

$$\boldsymbol{\Phi}_{\mathrm{P}} = \frac{B}{A} \times \boldsymbol{\Phi}_{\mathrm{PL}}$$

where A and B represent the integrated area of the total photoluminescence and phosphorescence spectra, respectively. The phosphorescence component was separated from total photoluminescence (PL) based on the phosphorescence spectrum for phosphorescence quantum yields. Φ_{PL} represents the absolute photoluminescence quantum yields of the compounds in the solid state.

Lifetime measurements. Fluorescence lifetimes were recorded using the time-correlated single-photon counting (TCSPC) method on an Edinburgh Instruments FLSP920 spectrometer equipped with a high-speed photomultiplier tube positioned after a single emission monochromator. Measurements were made in right-angle geometry mode, and the emission was collected through a polarizer set to the magic angle. Solutions were excited with a pulsed diode laser at a wavelength of 316 nm at repetition rates of 5-10 MHz. The instrument response functions (IRF) were *ca.* 230 ps FWHM. The phosphorescence lifetimes were measured using a μF920 pulsed 60 W Xenon microsecond flashlamp, with a repetition rate of 0.2 or 50 Hz at room temperature and 0.1 Hz at 77 K. Decays were recorded to 10000 counts in the peak channel with a record length of at least 2000 channels. Iterative reconvolution of the IRF with double exponential function and non-linear least-squares analysis were used to analyze the data. The quality of all decay fits was judged to be satisfactory, based on the calculated values of the reduced χ^2 and Durbin-Watson parameters and visual inspection of the weighted residuals. Time-gating was used to measure the emission following a specific delay time the range of 0.01-3 ms.

Powder X-ray diffraction and Phase analysis The compound ***o***-**BrTAB** was ground into a powder using an agate mortar until hardly any room-temperature phosphorescence was observed. The powder X-ray diffraction pattern was collected in reflection geometry on a Bruker D8 Discover powder diffractometer with Da Vinci design and linear Lynx-Eye detector. X-ray radiation (Cu-Kα_1; λ = 1.5406 Å) was focused with a Goebel mirror and Cu-Kα_2 radiation was eliminated by a Ni-absorber. Data were collected from 2θ = 2 – 60° in steps of

0.025° at ambient temperature. They were corrected for an offset in 2θ and exported using the Bruker AXS Diffrac-Suite. The diffraction patterns were then converted using CMPR software[32] for further processing with the GSAS program.[33] Cell parameters, background, scaling factor, zero shift and profile parameters were refined using the LeBail method. The data range 2θ = 2 – 5° was excluded from refinement as no reflection was either observed or predicted in this range and due to high background signal at low angles. The starting values for the refinement were taken from the single-crystal structure refinement at 100 K.

Scanning Electron Microscopy SEM images were recorded using a Zeiss Ultra Plus field emission scanning electron microscope equipped with GEMINI e-Beam column operated at 1-3 kV with an aperture size set to 10 or 30 μm to avoid excessive charging and radiation damage of the areas imaged.

Quantum chemical calculations All geometries were obtained using the Turbomole[34] and Gaussian[35] program packages utilizing Kohn–Sham density functional theory (DFT) in combination with the PBE0[36-38] functional. For excited state optimizations, linear response time-dependent DFT (TDDFT) was employed, and, for triplet states, the Tamm–Dancoff approximation (TDDFT-TDA) was additionally used. Vibrational frequency calculations were carried out with the Gaussian program package. In all computations, the def2-SVP[39] basis set was utilized on all atoms except for bromine, for which a cc-pVTZ-PP[40] basis set in combination with the defpp-ecp[41] pseudopotential was employed. Energies and multi reference configuration interaction (MRCI) wavefunctions of the lowest ten excited states of singlet and triplet spin multiplicity, respectively, were optimized with the DFT/MRCI[41-42] method applying the redesigned R2016 Hamiltonian[43] and an initial active space of 12 electrons in 12 frontier orbitals. The orbital basis for the DFT/MRCI calculations is obtained from DFT utilizing the BH-LYP[44-45] functional. Absorption spectra were obtained by broadening the corresponding DFT/MRCI line spectra with Gaussian functions of 1000 cm^{-1} full width at half maximum (FWHM). The SPOCK[46-48] program package was employed to compute spin–orbit coupling matrix elements (SOCMEs) and phosphorescence rate constants from spin–orbit coupled wavefunctions obtained with the MRSOCI procedure. Franck–Condon (FC) emission spectra and intersystem crossing (ISC) rate constants were obtained utilizing a time evolution approach implemented in the VIBES[49-50] program. Here an integration grid of 16384 points over 300 fs time period and a Gaussian damping function of 200 cm^{-1} FWHM was employed for FC spectra. For ISC rate constants, a grid of 1000 points

over a 250 fs time period and a Gaussian damping function of 0.3 cm^{-1} FWHM was used. Temperature effects of the population of the vibrational modes were accounted for by a Boltzmann distribution in the initial electronic state.

Crystal structure determinations Crystals suitable for single-crystal X-ray diffraction were selected, coated in perfluoropolyether oil, and mounted on MiTeGen sample holders. Diffraction data were collected on Bruker X8 Apex II 4-circle diffractometers with CCD area detectors using Mo-K_α radiation monochromated by graphite or multi-layer focusing mirrors or on a Bruker D8-Quest diffractometer with a CPA area detector and multi-layer mirror monochromated Mo-Kα radiation. Data were collected at ambient temperature and at 100 K. The crystals were cooled using an Oxford Cryostream low-temperature device. The images were processed and corrected for Lorentz-polarization effects and absorption as implemented in the Bruker software packages. The structures were solved using the intrinsic phasing method (SHELXT)[51] and Fourier expansion technique. All non-hydrogen atoms were refined in anisotropic approximation, with hydrogen atoms 'riding' in idealized positions, by full-matrix least squares against F^2 of all data, using SHELXL[52] software and the SHELXLE graphical user interface.[53] Diamond[54] software was used for graphical representation. Other structural information was extracted using Mercury[55] and OLEX2[56] software. Hirshfeld surfaces were calculated and analyzed using the Crystal Explorer[57] program. Crystal data and experimental details are listed in Table 3-3; full structural information has been deposited with Cambridge Crystallographic Data Centre. CCDC-2085814 (***o*-BrTAB** at 100 K), CCDC-2085815 (***m*-BrTAB** at 100 K), CCDC-2085816 (***p*-BrTAB** at 100 K), CCDC-2089473 (***o*-BrTAB** at 290 K), CCDC-2118234 (***m*-BrTAB** at 296 K) and CCDC-2118235 (***p*-BrTAB** at 300 K).

3.4.2 Synthesis

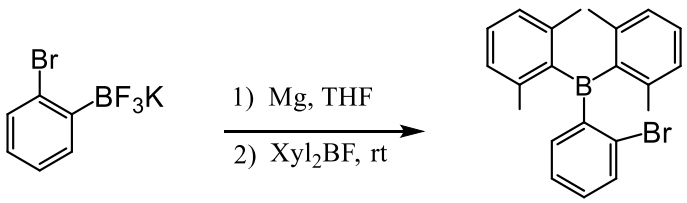

(2-bromophenyl)bis(2,6-dimethylphenyl)borane (*o*-BrTAB) : A 250 mL three-necked round bottom flask, equipped with a dropping funnel and water-cooled condenser, was used. In a typical preparation, an anhydrous THF solution of 2-bromo-1,3-dimethylbenzene (896 mg,

4.5 mmol) was added dropwise to the flask containing magnesium (120 mg, 5.0 mmol) and 100 mL of anhydrous THF. The solution was refluxed during the addition period, which required approximately 3 h, and then allowed to cool to room temperature. To this solution (2-bromophenyl)trifluoroborane potassium salt[58] (789 mg, 3.0 mmol) in anhydrous THF was added and the reaction was stirred overnight. The resulting mixture was subjected to silica gel column chromatography eluting with *n*-hexane to afford ***o*-BrTAB** (722 mg,1.92 mmol) in 64% yield as white a solid: ^{1}H NMR (500 MHz, CD_2Cl_2, rt, ppm): δ 7.58–7.55 (m, 1H), 7.30–7.27 (m, 2H), 7.20–7.16 (m, 3H), 6.95 (d, *J* = 8 Hz, 4H), δ 2.03 (s, 12H). ^{13}C NMR (126 MHz, CD_2Cl_2, rt, ppm): 149.5 (br), 145.5 (br), 141.0, 136.1, 133.1, 132.3, 130.0, 128.4, 127.8, 127.4, 23.2. ^{11}B NMR (160 MHz, CD_2Cl_2, r.t., ppm): 76 (br). MS (EI^+) m/z: 376 $[M]^+$. HRMS ($ASAP^+$): m/z calcd for 376.0992 $[M]^+$; found: 376.0990 [*M*] (|Δ| = 0.53 ppm). Elem. Anal. Calcd (%) for $C_{22}H_{22}BBr$: C, 70.07; H, 5.88; Found: C, 69.91; H, 6.07.

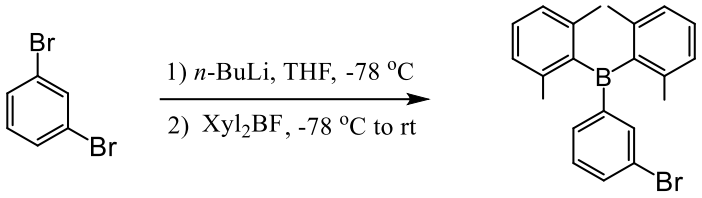

(3-bromophenyl)bis(2,6-dimethylphenyl)borane (*m*-BrTAB) : To a solution of 1,3-dibromobenzene (402 mg, 1.7 mmol) in anhydrous THF (20 mL) was added a hexane solution of *n*-BuLi (1.2 mL, 1.6 M, 1.9 mmol) dropwise by syringe at -78 °C. The mixture was stirred at the same temperature for 1 h. A solution of bis(2,6-dimethylphenyl)fluoroborane[59] (408 mg, 1.7 mmol) in anhydrous THF (5 mL) was added to the reaction mixture via syringe. The reaction mixture was warmed to room temperature and stirred overnight. The reaction was quenched with a saturated solution of NaCl and the aqueous layer was extracted with Et_2O. The combined organic layer was dried over anhydrous Na_2SO_4, filtered, and concentrated under reduced pressure. The resulting mixture was subjected to silica gel column chromatography eluting with *n*-hexane to afford ***m*-BrTAB (**498 mg, 1.3 mmol) in 78% yield as a white solid: ^{1}H NMR (500 MHz, CD_2Cl_2, rt, ppm): δ 7.68 (ddd, J = 8, 2 and 1 Hz, 1H), 7.65–7.63 (m, 1H), 7.46 (dt, J = 7, 1 Hz, 1H), 7.35–7.28 (m, 1H), 7.25 (t, J = 8 Hz, 2H), 7.08–7.02 (m, 4H), 2.07 (s, 12H). ^{13}C{^{1}H} NMR (126 MHz, CD_2Cl_2, rt, ppm): 148.1 (br), 143.9 (br), 140.6, 138.3, 134.8, 134.6, 130.0, 129.4, 127.4, 122.9, 23.3. ^{11}B NMR (160 MHz, CD_2Cl_2, rt, ppm): 75 (br). MS (EI^+) m/z: 376 $[M]^+$. HRMS ($ASAP^+$): m/z calcd for $[M]^+$: 376.0930; found: 376.0937[*M*] (|Δ| = 1.86 ppm). Elem. Anal. Calcd (%) for $C_{22}H_{22}BBr$: C, 70.07; H, 5.88; Found: C, 69.98; H, 6.07.

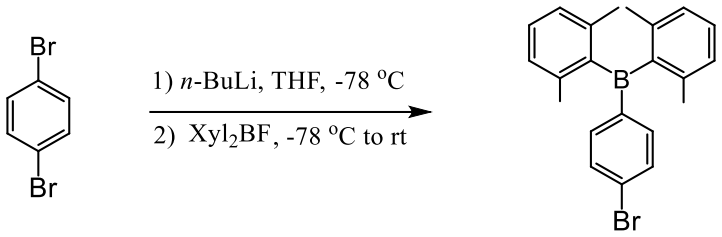

(4-bromophenyl)bis(2,6-dimethylphenyl)borane (*p*-BrTAB) : To a solution of 1,4-dibromobenzene (402 mg, 1.7 mmol) in anhydrous THF (20 mL) was added a hexane solution of *n*-BuLi (1.2 mL, 1.6 M, 1.9 mmol) dropwise by syringe at -78 °C. The mixture was stirred at the same temperature for 1 h. A solution of bis(2,6-dimethylphenyl)fluoroborane[59] (408 mg, 1.7 mmol) in anhydrous THF (5 mL) was added to the reaction mixture via syringe. The reaction mixture was warmed to room temperature and stirred overnight. The reaction was quenched with a saturated solution of NaCl and the aqueous layer was extracted with Et_2O. The combined organic layer was dried over anhydrous Na_2SO_4, filtered, and concentrated under reduced pressure. The resulting mixture was subjected to silica gel column chromatography eluting with *n*-hexane to afford ***p*-BrTAB (**537 mg, 1.4 mmol) in 84% yield as a white solid: ^{1}H NMR (500 MHz, CD_2Cl_2, rt, ppm): δ 7.55–7.51 (m, 2H), 7.39–7.35 (m, 2H), 7.20 (t, J = 8 Hz, 2H), 7.03–6.98 (m, 4H), 2.03 (s, 12H). ^{13}C{^{1}H} NMR (126 MHz, $CDCl_3$, rt, ppm): 144.2 (br), 144.0 (br.), 140.8, 138.1, 131.6, 129.4, 127.9, 127.5, 23.7. ^{11}B NMR (160 MHz, CD_2Cl_2, rt, ppm): 74 (br). MS (EI^+) m/z: 376 $[M]^+$. HRMS ($ASAP^+$): m/z calcd for $[M]^+$: 376.0992; found: 376.0993 [*M*] (|Δ| = 0.27 ppm). Elem. Anal. Calcd (%) for $C_{22}H_{22}BBr$: C, 70.07; H, 5.88; Found: C, 70.04; H, 6.02.

3.4.3 SEM

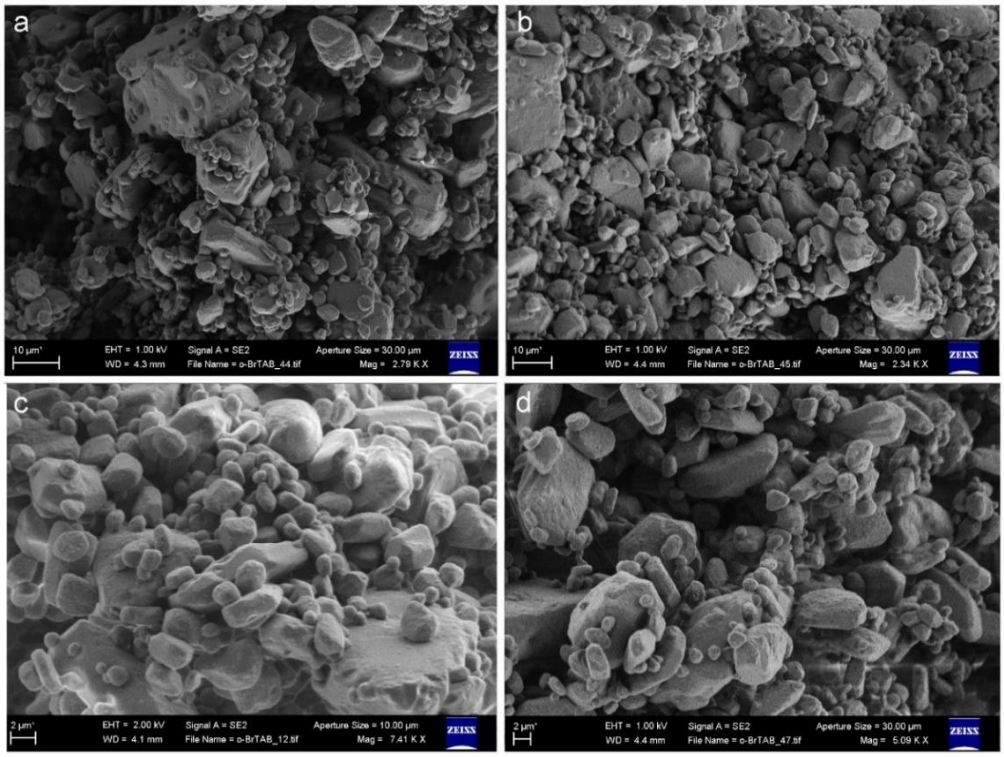

Figure 3-8. (a)-(d) SEM pictures of ***o*-BrTAB** as a ground powder.

3.4.4 Photophysical spectra

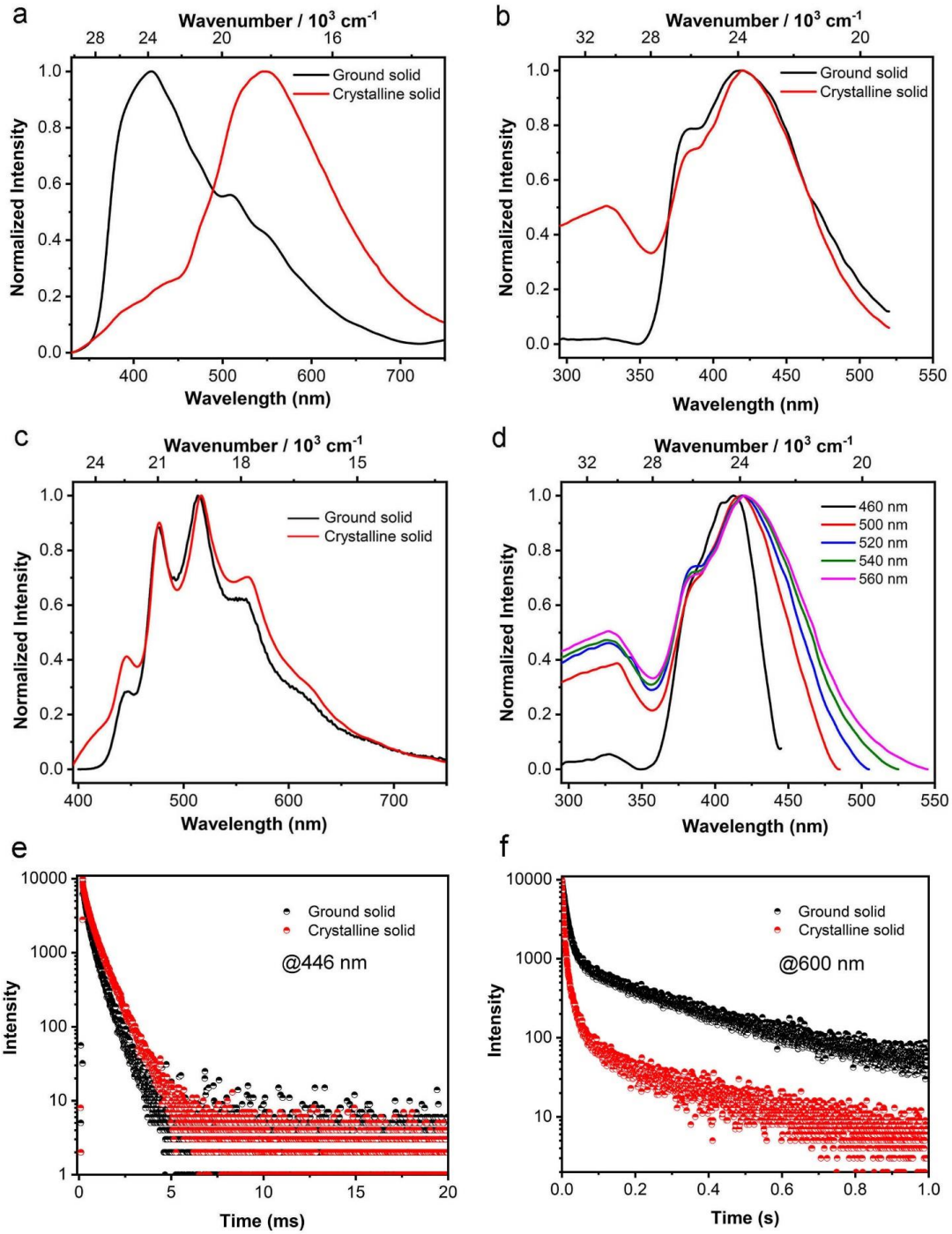

Figure 3-9. Normalized (a) photoluminescence emission, (b) excitation and (c) time-gated (delay time 0.01 ms) phosphorescence emission of ***o*-BrTAB** in the crystalline state and ground powder at room temperature in air (λ_{ex} = 305 nm). (d) Normalized wavelength-dependent excitation spectra of ***o*-BrTAB** in the crystalline state from λ_{ex} = 460 to 560 nm. (e) Phosphorescence decay (λ_{em} = 446 nm) of ***o*-BrTAB** in the crystalline state (τ_p= 0.8 ms) and

ground powder (τ_p = 0.7 ms) at room temperature in air. (f) Phosphorescence decay (λ_{em} = 600 nm) of ***o*-BrTAB** in the crystalline state (τ_p = 234 ms) and ground powder (τ_p = 191 ms) at room temperature under air.

Table 3-2. Unit cell parameters of ***o*-BrTAB** obtained from the LeBail refinement of powder X-ray diffraction data at room temperature.

Data	***o*-BrTAB**
λ / Å, radiation	1.5406, Cu-Kα_1
θ range / °	5 – 60
a / Å	8.2022(5)
b / Å	12.1584(5)
c / Å	18.8797(6)
α / °	90.0
β / °	93.312(4)
γ / °	90.0
Volume / Å^3	1879.7(1)
R_p	0.0495
wR_p	0.0798

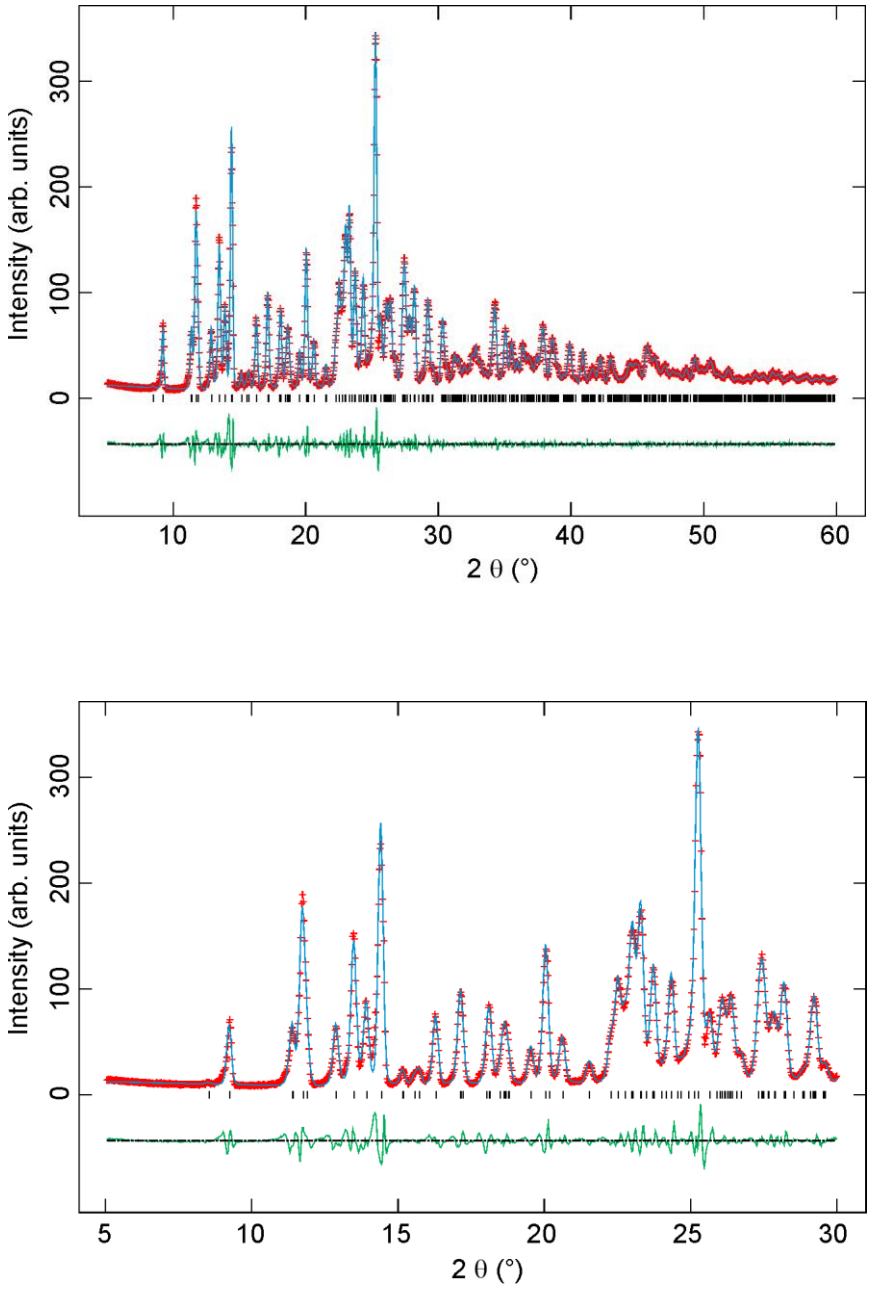

Figure 3-10. Powder X-ray diffraction patterns of compound ***o*-BrTAB** after grinding crystals in an agate mortar (top) in the full range 5 – 60° and (bottom) in the selected range 2θ = 5 – 30°. Red crosses represent the experimental values. The continuous blue lines show the results of the Le Bail fit to the data. The difference between experimental data and LeBail fit is represented by the green lines at the bottom of the plots. Vertical bars show the positions of the Bragg reflections of ***o*-BrTAB**.

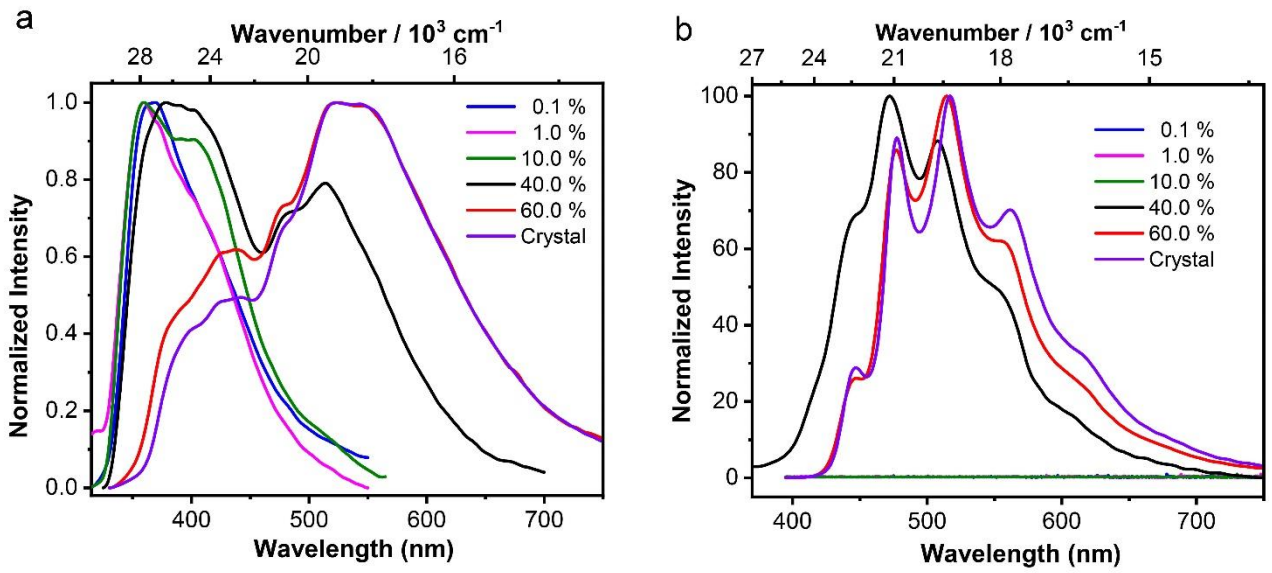

Figure 3-11. Normalized (a) PL emission and (b) time-gated phosphorescence emission spectra (delay time 0.01 ms) spectra of ***o*-BrTAB** in 0.1, 1.0, 10, 40 and 60 % PMMA film and the crystalline state (λ_{ex} = 305 nm).

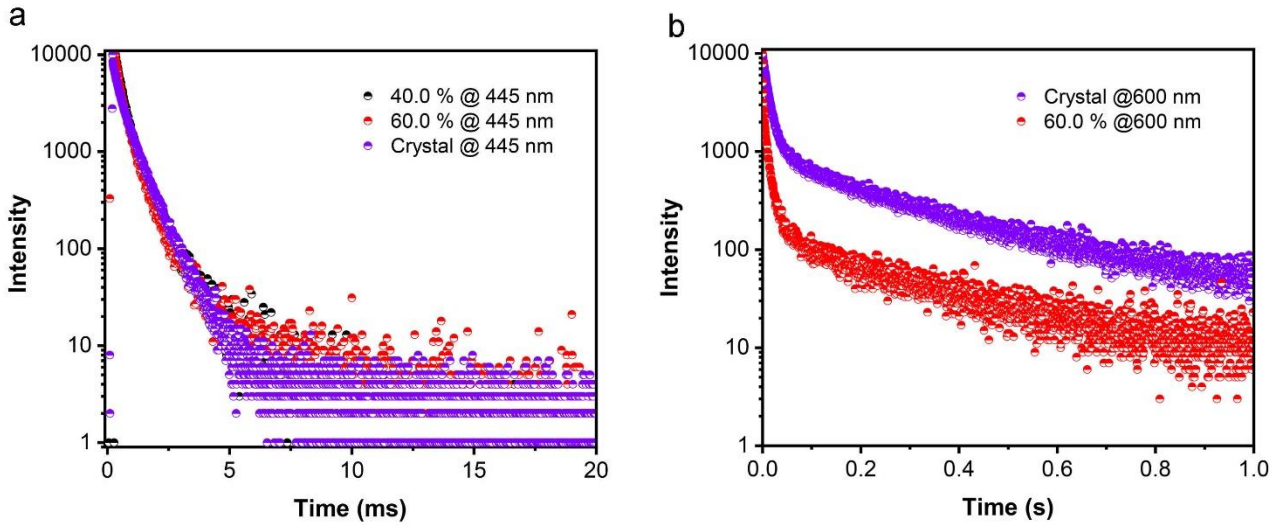

Figure 3-12. (a) Decays of phosphorescence emission (λ_{em} = 446 nm, τ_p = 0.8 ms) of ***o*-BrTAB** in 40 % PMMA film, 60 % PMMA film and the crystalline state at room temperature in air. (b) Decays of phosphorescence emission at 600 nm of ***o*-BrTAB** in 60 % PMMA film (τ_p = 226 ms) and the crystalline state (τ_p = 234 ms) at room temperature in air.

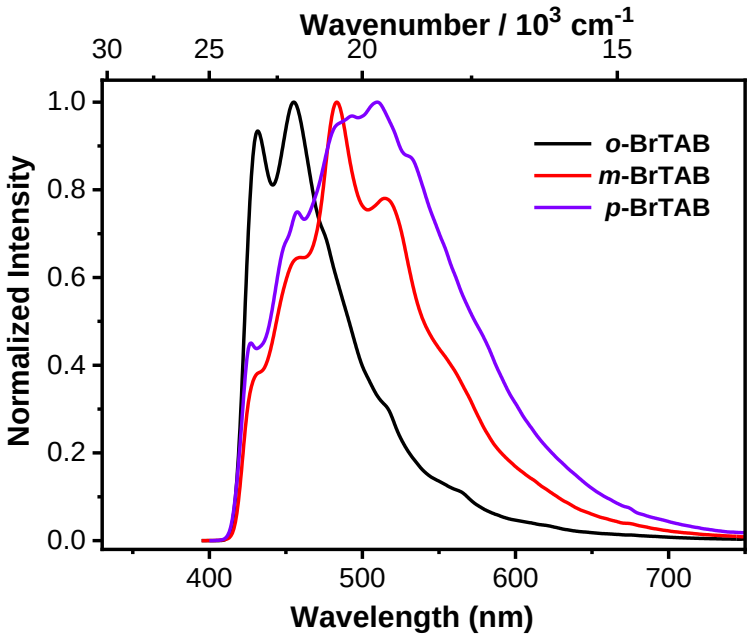

Figure 3-13. Normalized time-gated (delay time 0.01 ms) phosphorescence emission spectra of crystalline ***o***-, ***m***- and ***p*-BrTAB** at 77 K.

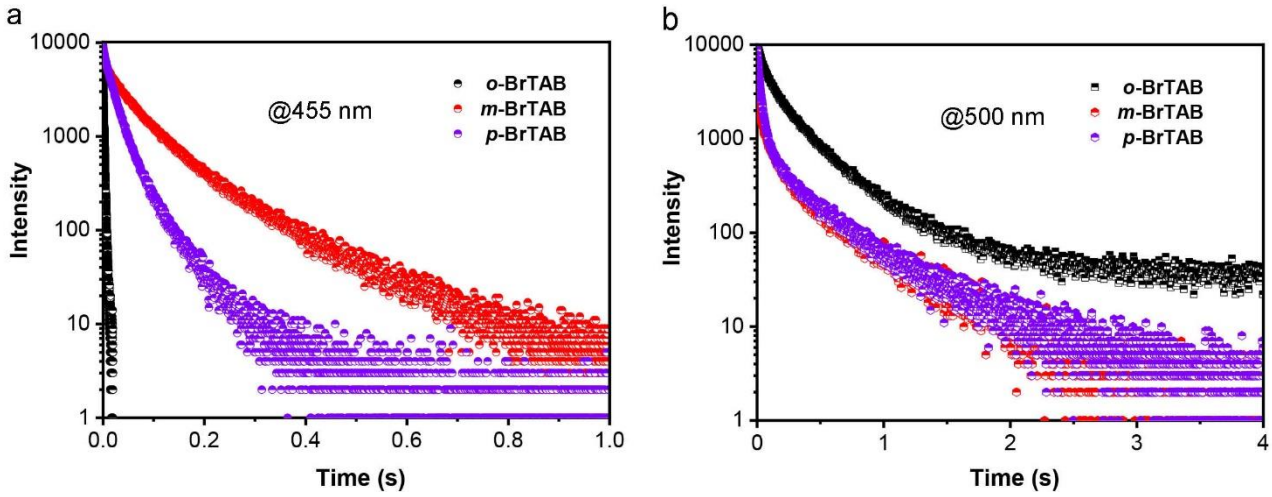

Figure 3-14. Decays of the phosphorescence emission (a) (λ_{em} = 455 nm) and (b) (λ_{em} = 500 nm) of crystalline ***o***-, ***m***- and ***p*-BrTAB** at 77 K.

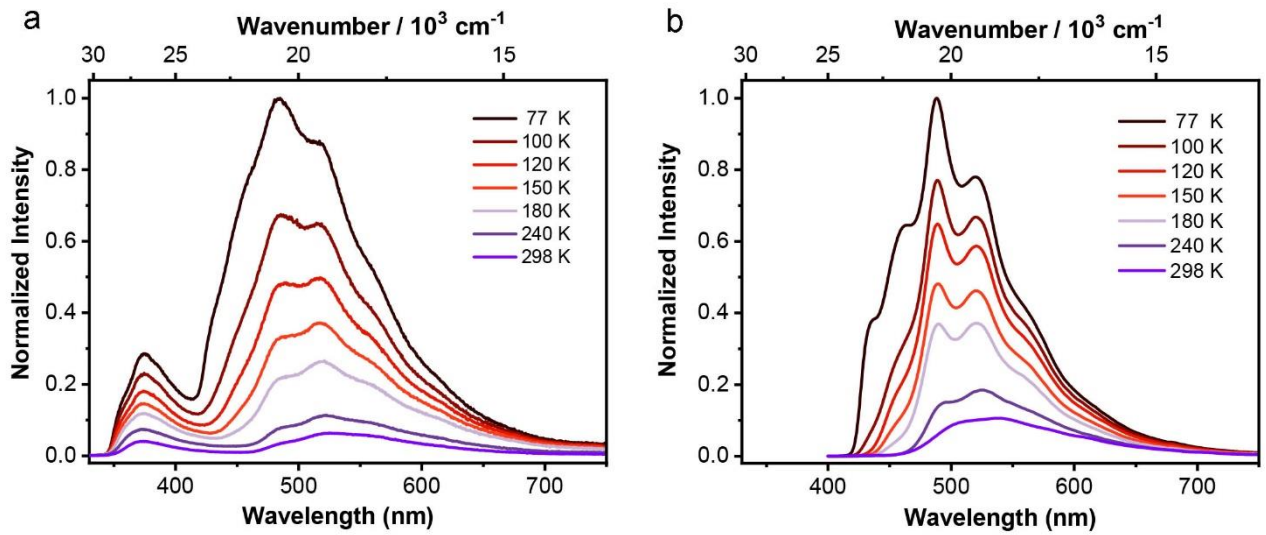

Figure 3-15. (a) Photoluminescence emission and (b) time-gated (delay time 0.01 ms) phosphorescence emission spectra of crystalline ***m*-BrTAB** at different temperatures (λ_{ex} = 305 nm).

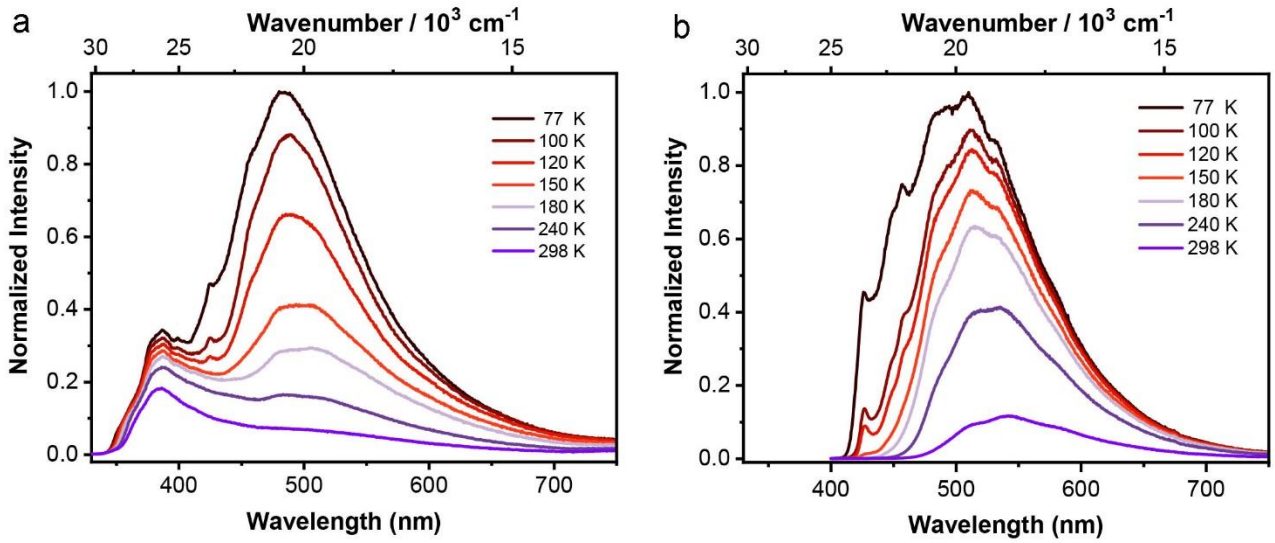

Figure 3-16. (a) Photoluminescence emission and (b) time-gated (delay time 0.01 ms) phosphorescence emission spectra of crystalline ***p*-BrTAB** at different temperatures (λ_{ex} = 305 nm).

3.4.5 Theoretical calculation details

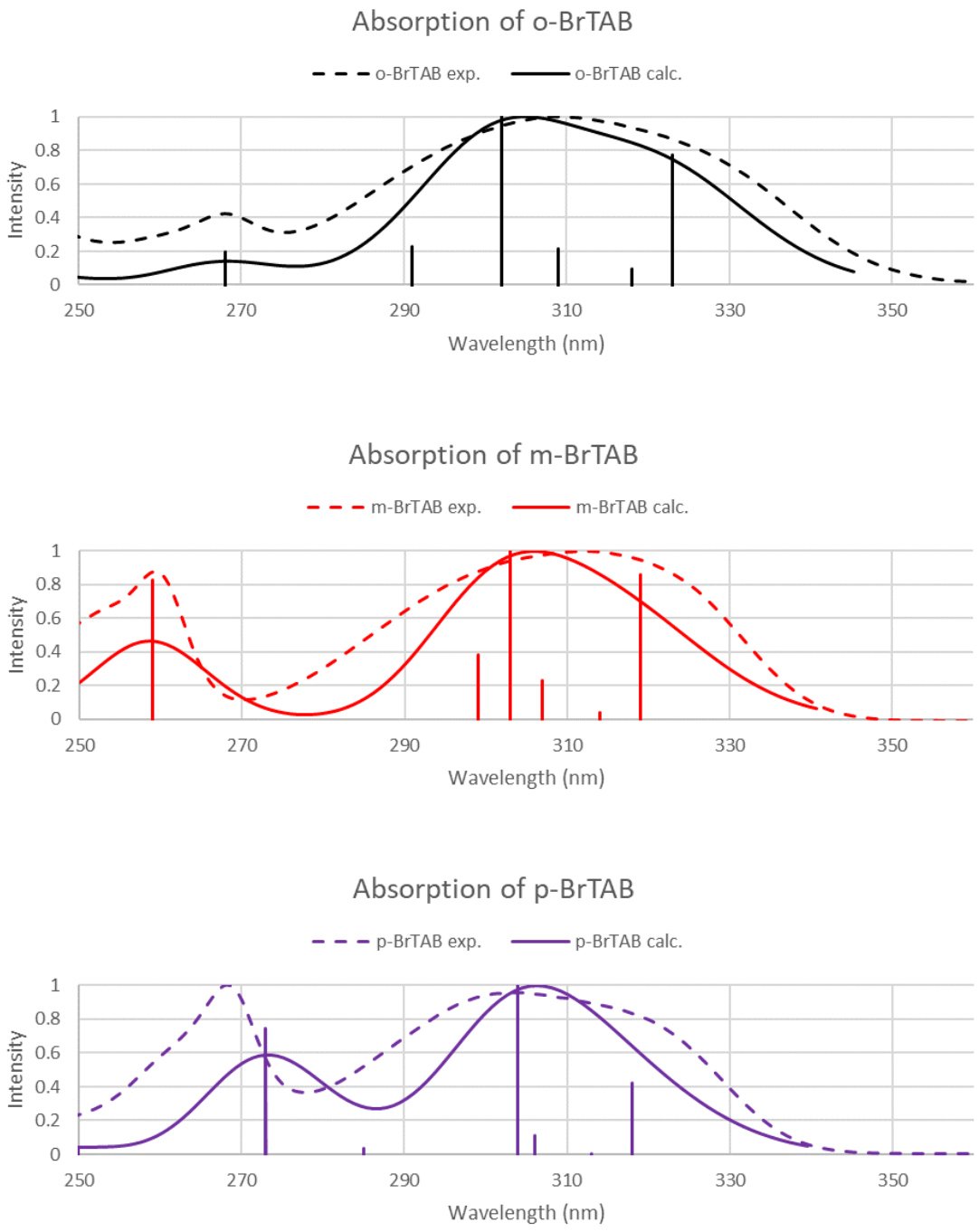

Figure 3-17. Calculated absorption spectra of **o-BrTAB**, **m-BrTAB** and **p-BrTAB** compared to experimental spectra.

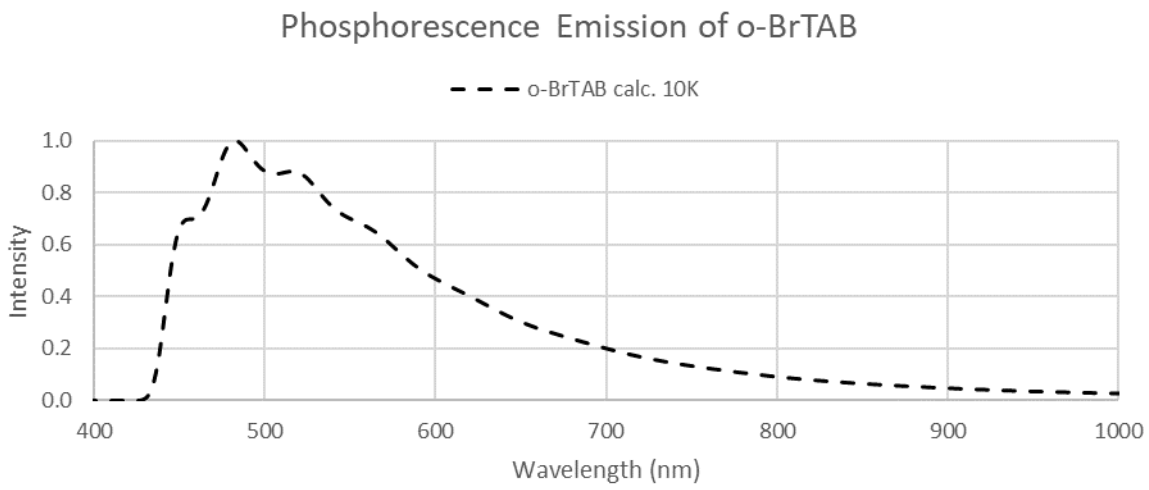

Figure 3-18. Calculated phosphorescence spectrum of the monomeric **o-BrTAB** at 10 K.

Table 3-3: Spin–orbit coupling matrix elements (absolute values, cm^{-1}) of S_1^M, T_1^M, T_2^M and T_3^M states at the respective S_1^M minimum.

SOCME	**x**	**y**	**z**	**$(x^2 + y^2 + z^2)$**
		***o*-BrTAB**		
$\langle T_1^M \lvert \hat{H}_{SO} \rvert S_1^M \rangle$	4.792	1.299	0.833	25.348
$\langle T_2^M \lvert \hat{H}_{SO} \rvert S_1^M \rangle$	122.773	44.841	39.445	18639.878*
		***m*-BrTAB**		
$\langle T_1^M \lvert \hat{H}_{SO} \rvert S_1^M \rangle$	0.117	0.165	0.106	0.052
$\langle T_2^M \lvert \hat{H}_{SO} \rvert S_1^M \rangle$	7.238	0.901	2.988	62.133
$\langle T_3^M \lvert \hat{H}_{SO} \rvert S_1^M \rangle$	9.894	3.037	3.934	122.585*
		***p*-BrTAB**		
$\langle T_1^M \lvert \hat{H}_{SO} \rvert S_1^M \rangle$	0.263	0.140	2.740	7.594*
$\langle T_2^M \lvert \hat{H}_{SO} \rvert S_1^M \rangle$	0.390	0.055	0.374	0.295
$\langle T_3^M \lvert \hat{H}_{SO} \rvert S_1^M \rangle$	0.353	1.055	1.805	4.497*

* marks the fastest ISC channel of the low lying singlet and triplet states.

Table 3-4. Photophysical properties of compounds **o-BrTAB**, **m-BrTAB** and **p-BrTAB** *in vacuo* as obtained from quantum chemical calculations.

	λ_{abs} **nm** [a]	k_{isc} s^{-1} [b]	λ_f **nm** [c]	k_f s^{-1}	τ_f **ns** [d]	λ_p **nm** [c]	k_p s^{-1}	τ_p **s** [d]
o-BrTAB	305	$\approx 1 \cdot 10^{10}$	500	$1 \cdot 10^7$	81	451, 488, 515, 563	515	0.002
o-Dimer				$1 \cdot 10^7$	96	-	1041	0.001
m-BrTAB	306	$\approx 9 \cdot 10^8$	412	$2 \cdot 10^7$	49	-	0.202	4.94
p-BrTAB	306	$\approx 3 \cdot 10^8$	385	$2 \cdot 10^7$	45	-	1.03	0.97

[a] Absorption maximum of line spectrum broadened by Gaussian function; [b] rate constant for the fastest of the open ISC channels (***o*-BrTAB**: $S_1^M \rightarrow T_2^M$, ***m*-BrTAB**: $S_1^M \rightarrow T_3^M$ and ***p*-BrTAB**: $S_1^M \rightarrow T_1^M/T_3^M$); [c] maximum of 0-0 band, maximum of Franck-Condon spectrum at 10 K; [d] radiative lifetime assuming a quantum yield of 100 %.

Table 3-5. Calculated phosphorescence lifetimes of the lowest monomer triplet components.

τ_p **[s]**	T_α	T_β	T_γ	$T_{average}$	$T_{exp,\ short}$ [a]	$T_{exp,\ long}$ [a]
o-BrTAB	0.0007	0.0367	0.0070	0.0019	0.8077	174.2307
o-dimer	0.0003	0.0200	0.0297	0.0010		
m-BrTAB	2.3030	8.4451	18.3713	4.2161	5.6667	56.8889
m-dimer	3.6310	0.3058	4.1039	0.7918		
p-BrTAB	1.6762	17.2833	0.4107	0.9712	0.9000	29.0500
p-dimer	0.2339	3.5239	0.6741	0.4965		

[a] Radiative phosphorescence lifetime (τ_p/Φ_p) obtained from the experimental lifetime (τ_p) measured in the crystal at RT and the phosphorescence quantum yield (Φ_p).

Table 3-6. Vertical and adiabatic energies of the low-lying excited singlet and triplet states in the monomers. Adiabatic energies are marked in grey.

Energies [eV]	**@S_0^M**	**@S_1^M**	**@T_1^M**	**@T_2^M**	**@T_3^M**
			***o*-BrTAB**		
S_1^M	3.85	3.56	3.64	3.86[a]	
T_1^M	3.26	3.25	2.98	3.17[a]	
T_2^M	3.39	3.80	3.66	3.26[a]	
T_3^M	3.53	3.98	3.79	3.63[a]	
			***m*-BrTAB**		
S_1^M	3.89	3.78	3.96	3.94	3.91
T_1^M	3.32	3.39	3.03	3.83	3.27
T_2^M	3.38	3.52	3.86	3.01	3.38
T_3^M	3.49	3.71	3.95	3.94	3.42
			***p*-BrTAB**		
S_1^M	3.91	3.82	3.99	3.99	3.90
T_1^M	3.32	3.48	2.99	3.93	3.15
T_2^M	3.32	3.41	3.51	3.04	3.29
T_3^M	3.43	4.71	3.61	3.88	3.34

[a] Obtained at the crossing point between T_1 and T_2.

Table 3-7. Adiabatic energy gaps including vibrational zero-point energies.

Energies [eV]	***o*-BrTAB**	***m*-BrTAB**	***p*-BrTAB**
$S_1^M - S_0^M$	3.48	3.66	3.71
$T_1^M - S_0^M$	2.89	2.91	2.93
$S_1^M - T_1^M$	0.60	0.75	0.83
$S_1^M - T_2^M$		0.76	0.78
$S_1^M - T_3^M$		0.26	0.41

Table 3-8. Vertical and adiabatic energies of the low-lying excited singlet and triplet states in the dimers. Adiabatic energies are marked in grey.

Energies [eV]	**@S_0^D**	**@S_1^D**	**@T_1^D**
		***o*-BrTAB**	
S_1^D	3.65	3.41	3.51
T_1^D	3.07	3.11	2.93
T_2^D	3.07	3.61	3.52
T_3^D	3.21	3.78	3.54
T_4^D	3.21	3.83	3.71
		***m*-BrTAB**	
S_1^D	3.75	3.64	3.68
T_1^D	3.26	3.33	2.93
T_2^D	3.26	3.54	3.63
T_3^D	3.30	3.80	3.72
T_4^D	3.30	3.81	3.79
		***p*-BrTAB**	
S_1^D	3.79	3.65	3.81
T_1^D	3.20	3.23	3.02
T_2^D	3.24	3.41	3.48
T_3^D	3.25	3.66	3.63
T_4^D	3.37	3.71	3.64

Table 3-9: Selected bond lengths and angles of the isolated compounds **o-BrTAB**, **m-BrTAB** and **p-BrTAB** as obtained from geometry optimizations of the S_0^M, S_1^M, T_1^M, T_2^M and T_3^M states. R1 = bromo- xylyl, R2 = R3 = xylyl

***o*-BrTAB**	**@S_0^M**	**@S_1^M**	**@T_1^M**		
B-R1	1.581	1.532	1.566		
B-R2	1.578	1.614	1.560		
B-R3	1.582	1.584	1.587		
C-Br	1.896	1.912	1.902		
∠ R1(C)-B-(C-C)R2	49.4	67.2	49.2		
∠ R2(C)-B-(C-C)R3	51.7	47.4	49.7		
∠ R3(C)-B-(C-C)R1	42.4	23.1	31.3		
∠ R2(C)-B-(C-C)R1	44.2	19.3	33.3		
∠ R3(C)-B-(C-C)R2	52.3	58.1	46.3		
∠ R1(C)-B-(C-C)R3	55.3	49.8	51.1		
***m*-BrTAB**	**@S_0^M**	**@S_1^M**	**@T_1^M**	**@T_2^M**	**@T_3^M**
B-R1	1.574	1.531	1.568	1.568	1.553
B-R2	1.581	1.586	1.594	1.560	1.589
B-R3	1.582	1.606	1.559	1.595	1.587
C-Br	1.891	1.900	1.893	1.894	1.873
∠ R1(C)-B-(C-C)R2	54.5	48.4	62.5	36.1	-51.9
∠ R2(C)-B-(C-C)R3	55.0	65.6	42.1	61.7	-55.7
∠ R3(C)-B-(C-C)R1	27.8	13.2	25.6	20.1	-20.1
∠ R2(C)-B-(C-C)R1	27.9	19.6	20.3	25.3	-22.2
∠ R3(C)-B-(C-C)R2	54.6	49.1	61.6	41.9	-51.2
∠ R1(C)-B-(C-C)R3	54.9	69.8	36.4	62.7	-55.7
***p*-BrTAB**	**@S_0^M**	**@S_1^M**	**@T_1^M**	**@T_2^M**	**@T_3^M**
B-R1	1.571	1.530	1.543	1.566	1.561
B-R2	1.583	1.606	1.588	1.559	1.584
B-R3	1.583	1.586	1.588	1.595	1.584
C-Br	1.887	1.890	1.854	1.887	1.872
∠ R1(C)-B-(C-C)R2	55.1	69.5	52.4	35.2	53.4
∠ R2(C)-B-(C-C)R3	55.0	49.1	52.3	63.5	53.1
∠ R3(C)-B-(C-C)R1	27.2	19.8	21.8	19.2	26.4
∠ R2(C)-B-(C-C)R1	27.2	13.2	21.8	24.9	26.4
∠ R3(C)-B-(C-C)R2	55.0	65.5	51.6	41.0	53.1
∠ R1(C)-B-(C-C)R3	55.0	48.4	52.9	63.9	53.4

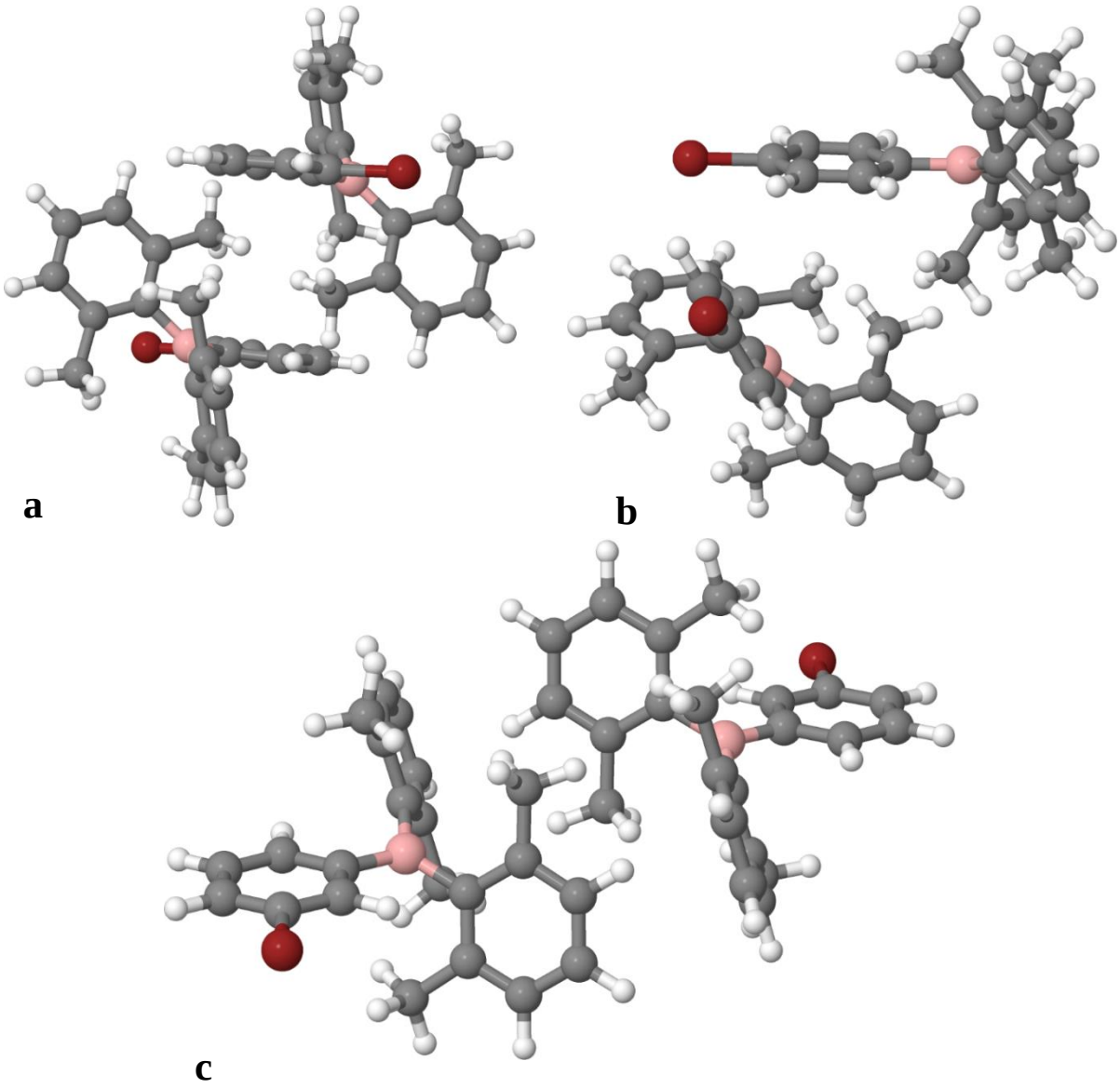

Figure 3-19. Dimer geometries of **o-BrTAB** (a), **p-BrTAB** (b) and **m-BrTAB** (c).

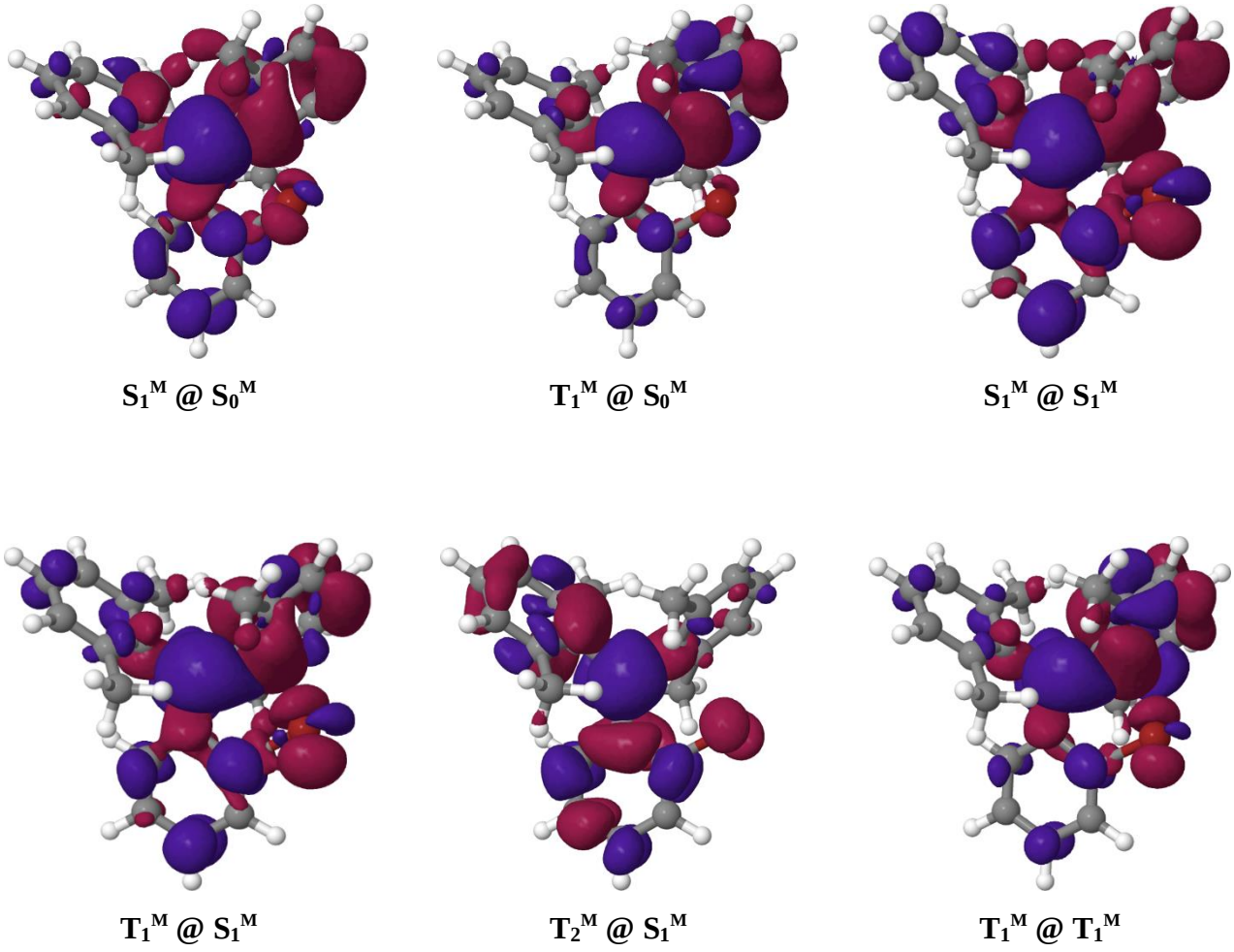

Figure 3-20. Difference densities of the S_1^M, T_1^M, and T_2^M states of **o-BrTAB** at various molecular geometries. Red areas indicate a loss of electron density upon excitation from the electronic ground state, and blue areas a gain.

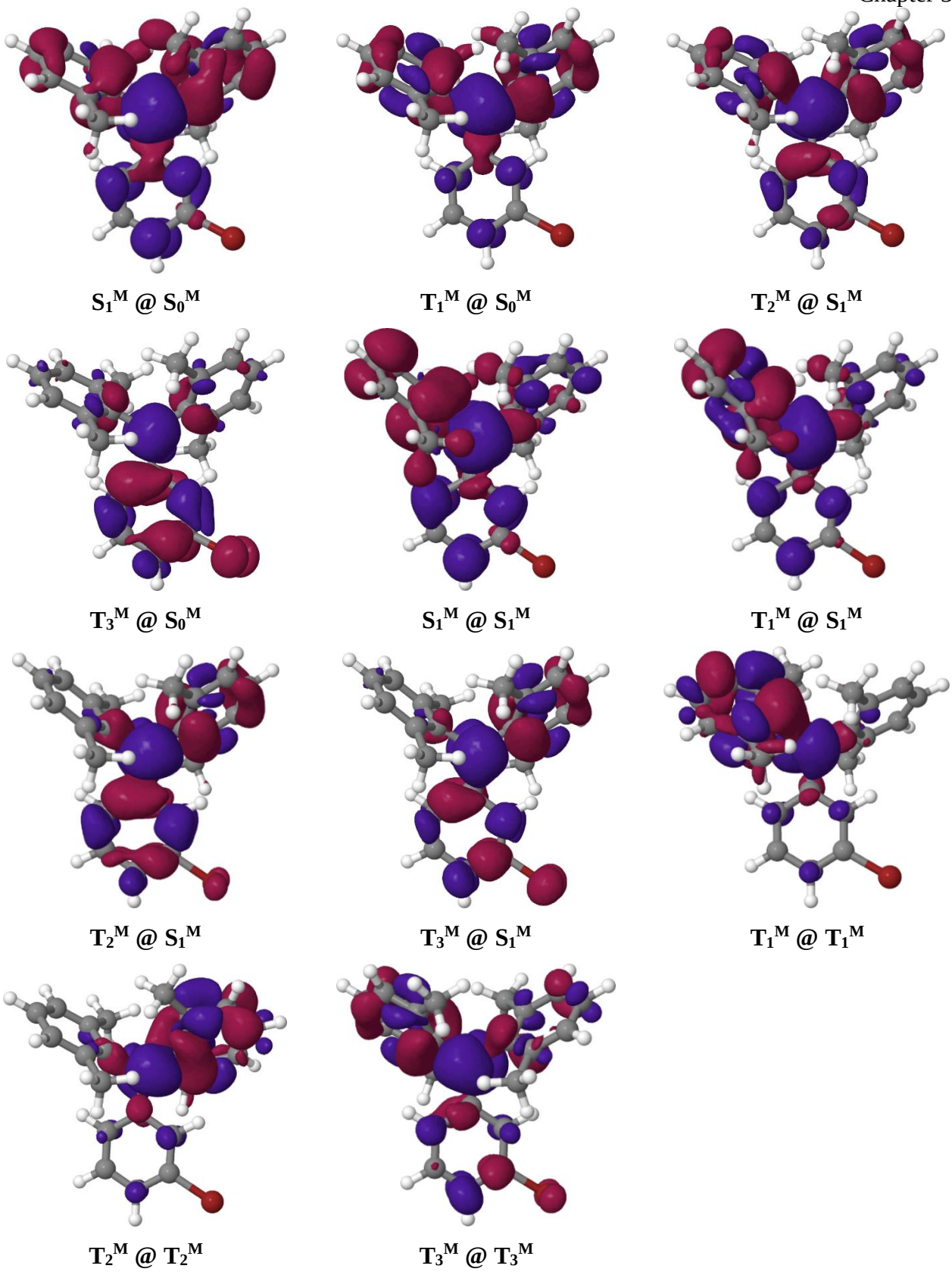

Figure 3-21. Difference densities of the S_1^M, T_1^M, T_2^M and T_3^M states of **m-BrTAB**. For color codes, see above.

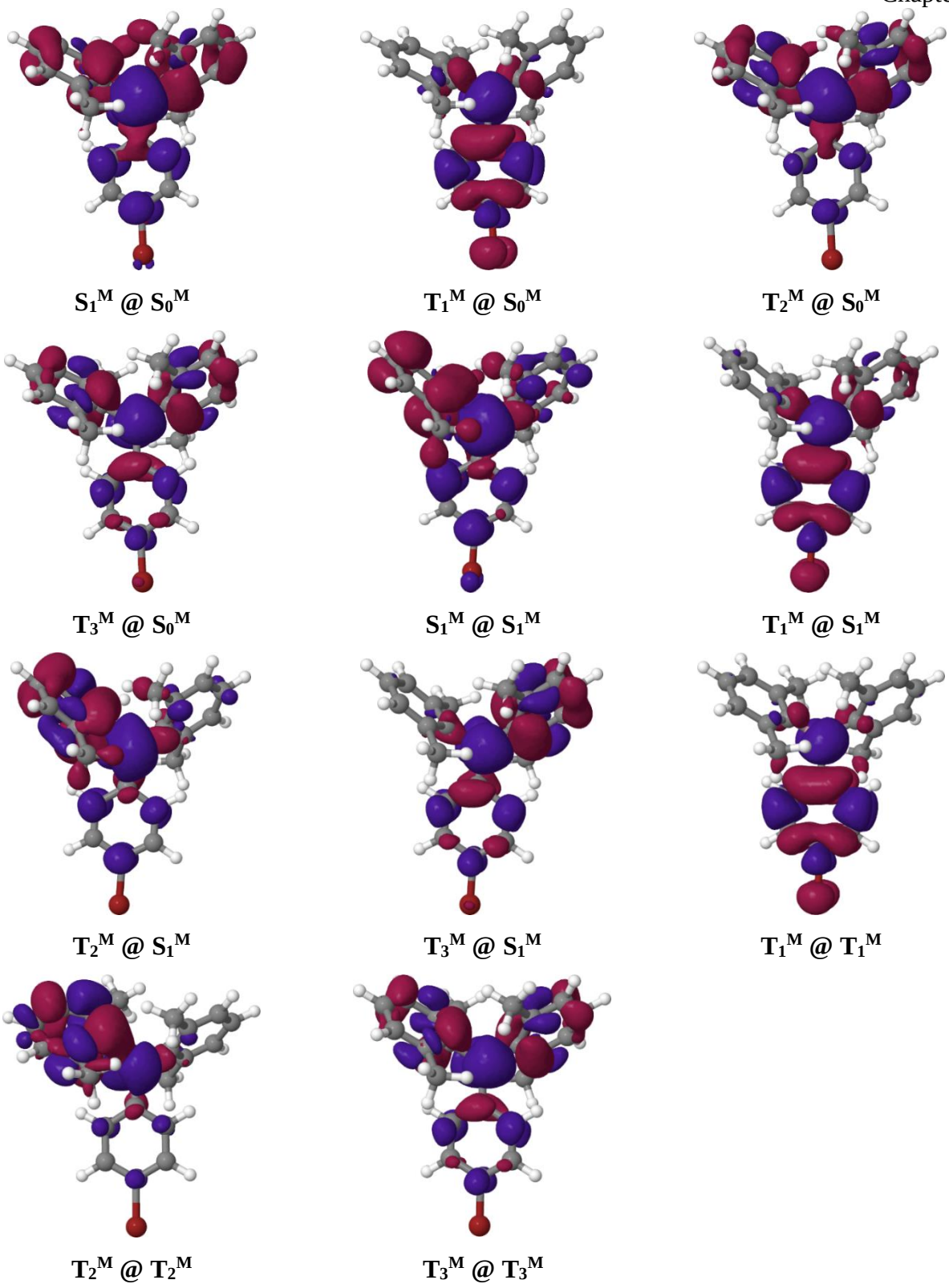

Figure 3-22. Difference densities of the S_1^M, T_1^M, T_2^M and T_3^M states of **p-BrTAB**. For color codes, see above

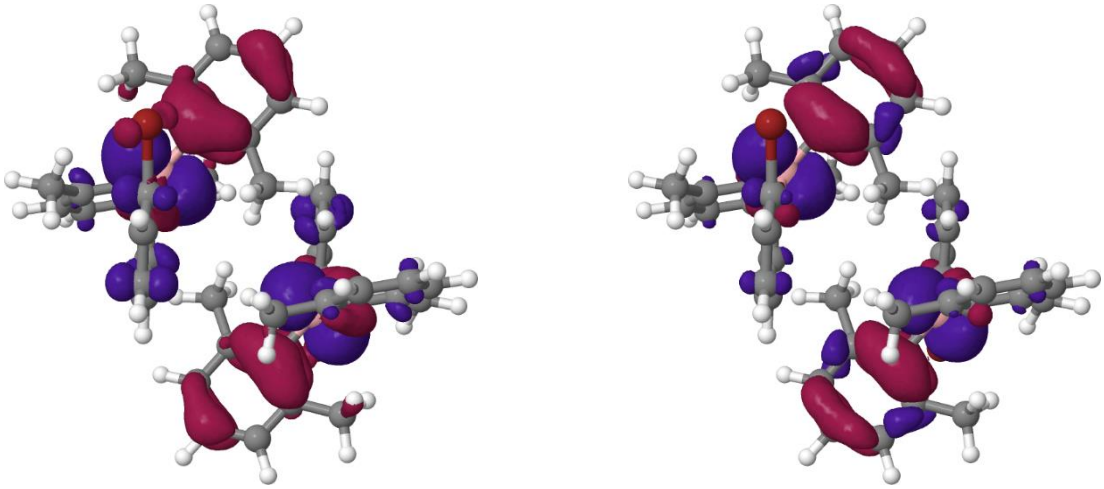

S_1^D @ S_0^D **T_1^D @ S_0^D**

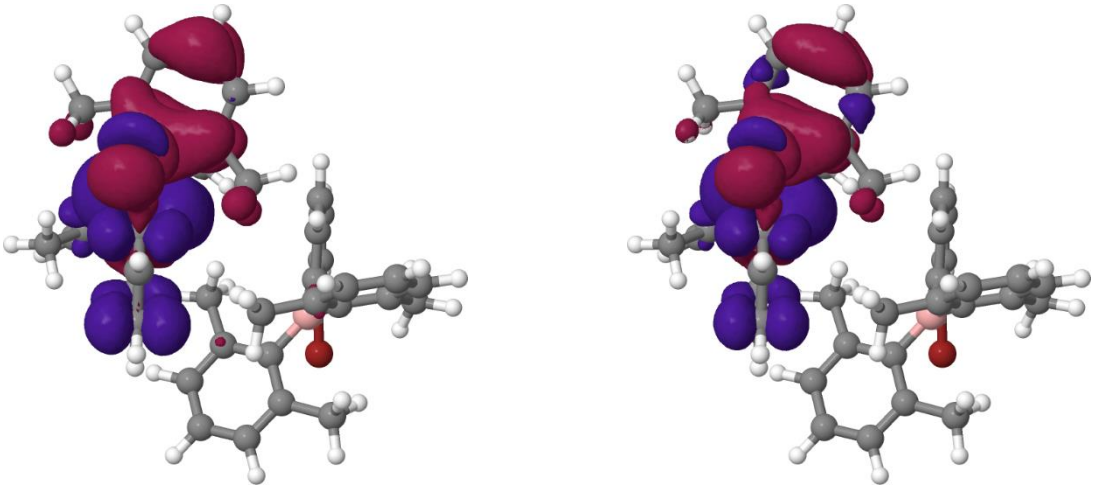

S_1^D @ S_1^D **T_1^D @ S_1^D**

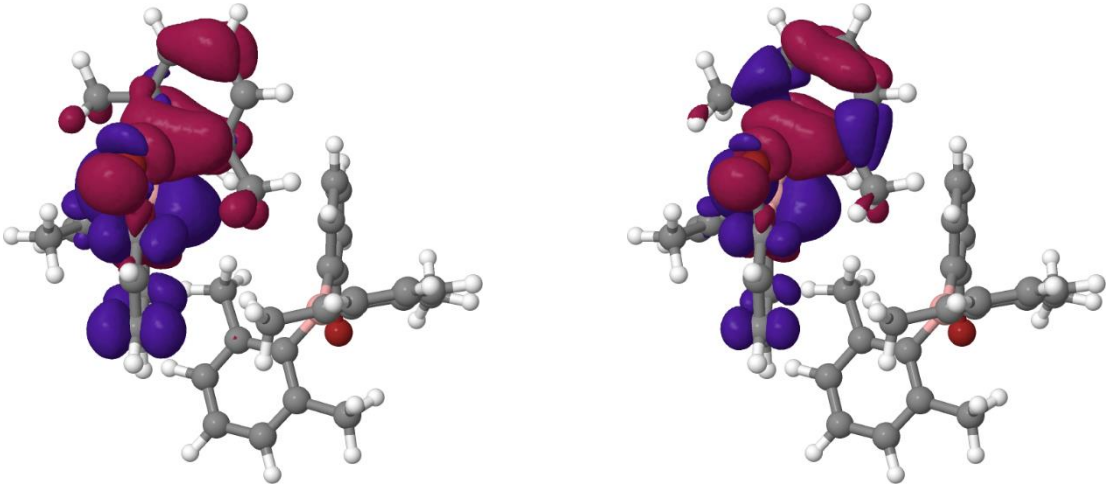

S_1^D @ T_1^D **T_1^D @ T_1^D**

Figure 3-23. Difference densities of the S_1^D and T_1^D states of the **o-BrTAB** dimer. For color codes, see above.

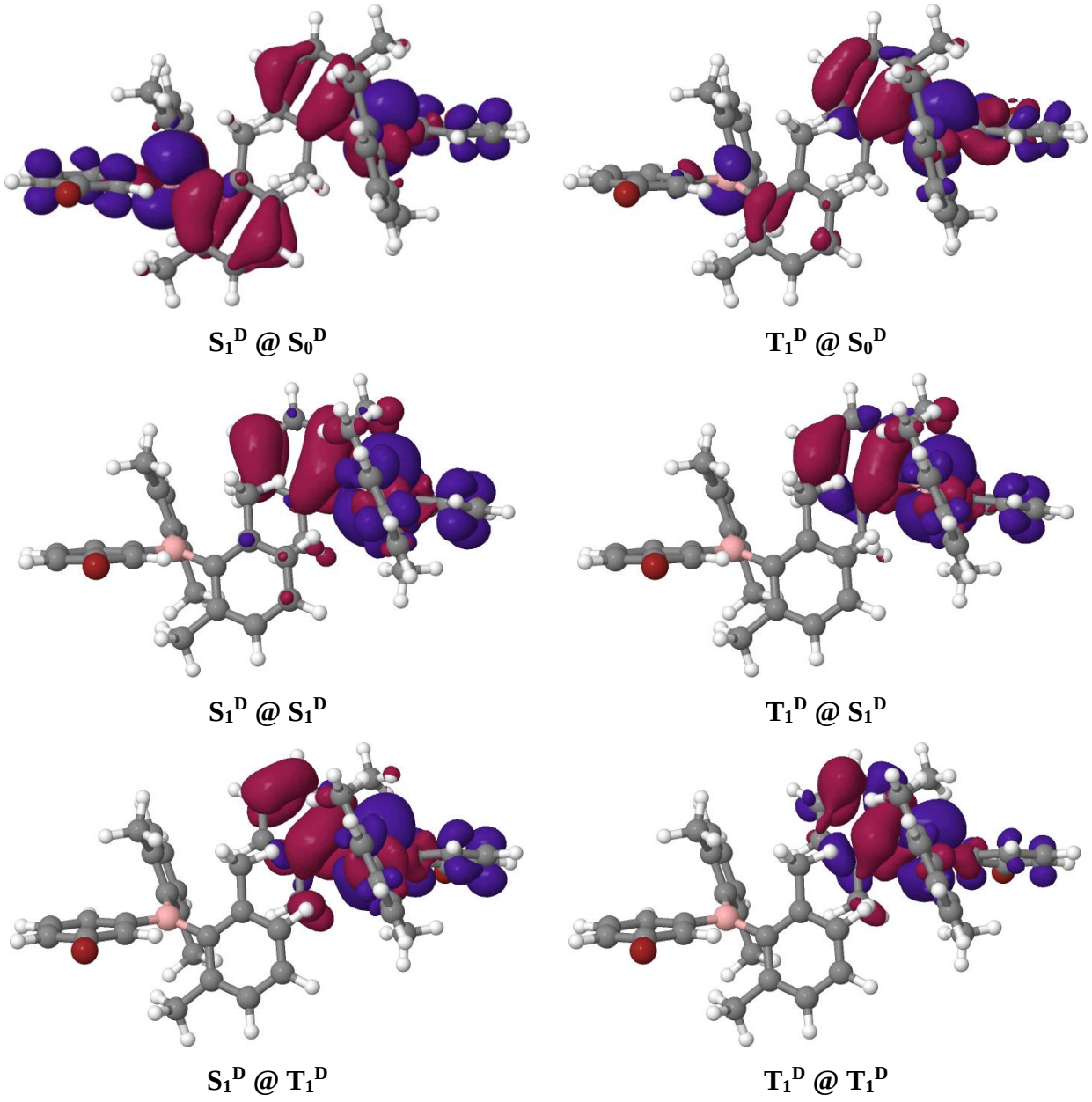

Figure 3-24. Difference densities of the S_1^D and T_1^D states of the **m-BrTAB** dimer. For color codes, see above.

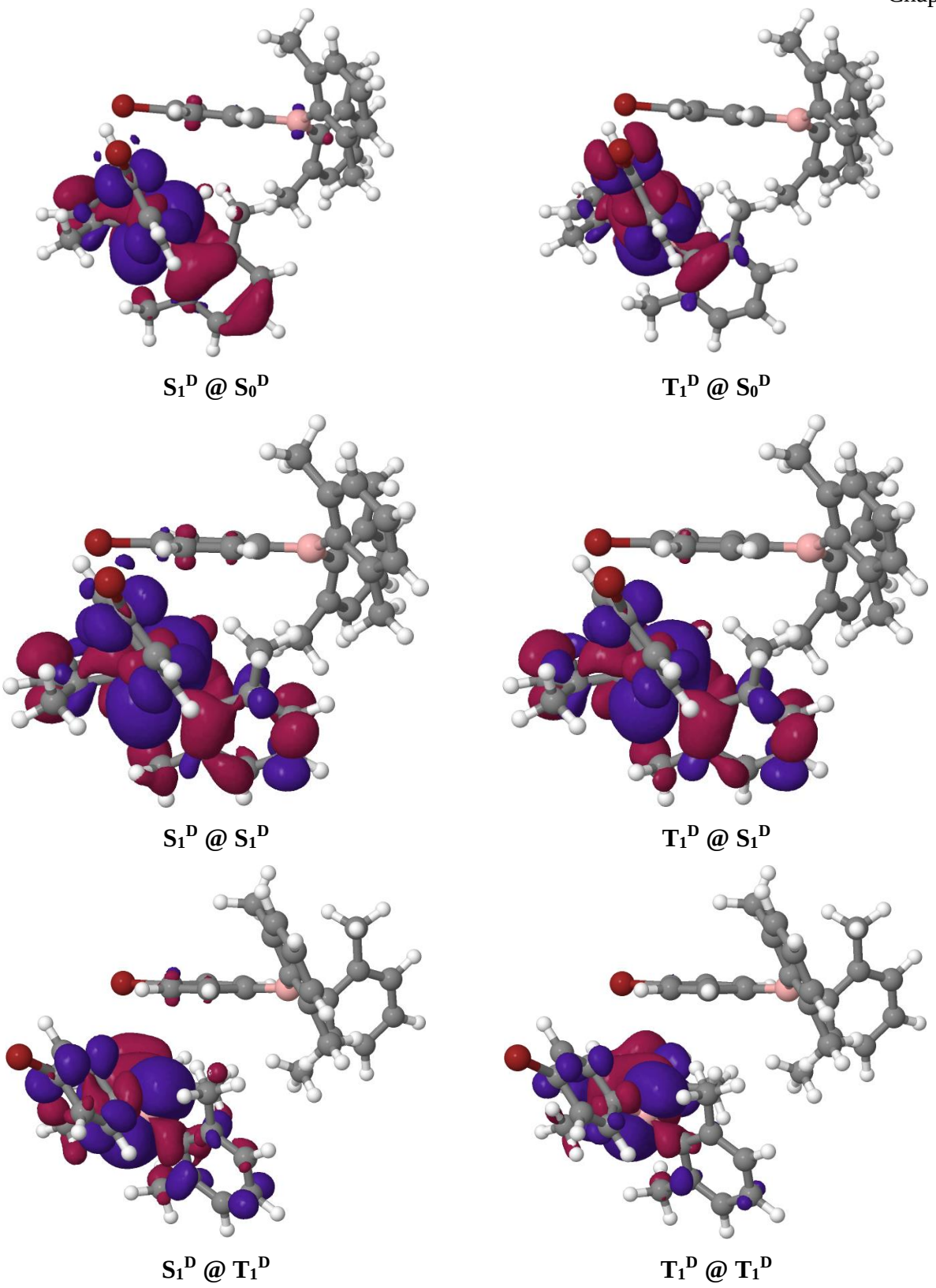

Figure 3-25. Difference densities of the S_1^D and T_1^D states of the **p-BrTAB** dimer. For color codes, see above.

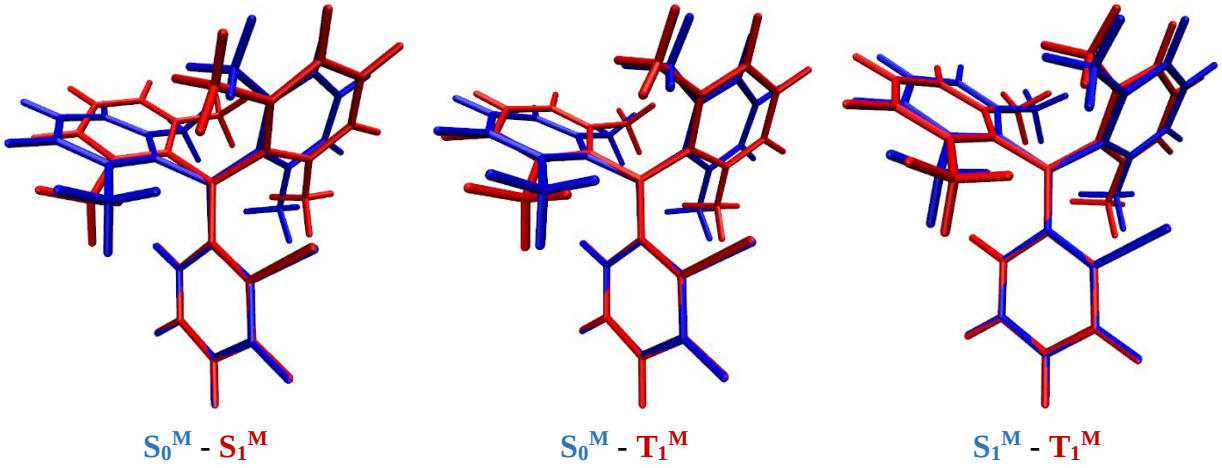

Figure 3-26. Structure overlays of **o-BrTAB**.

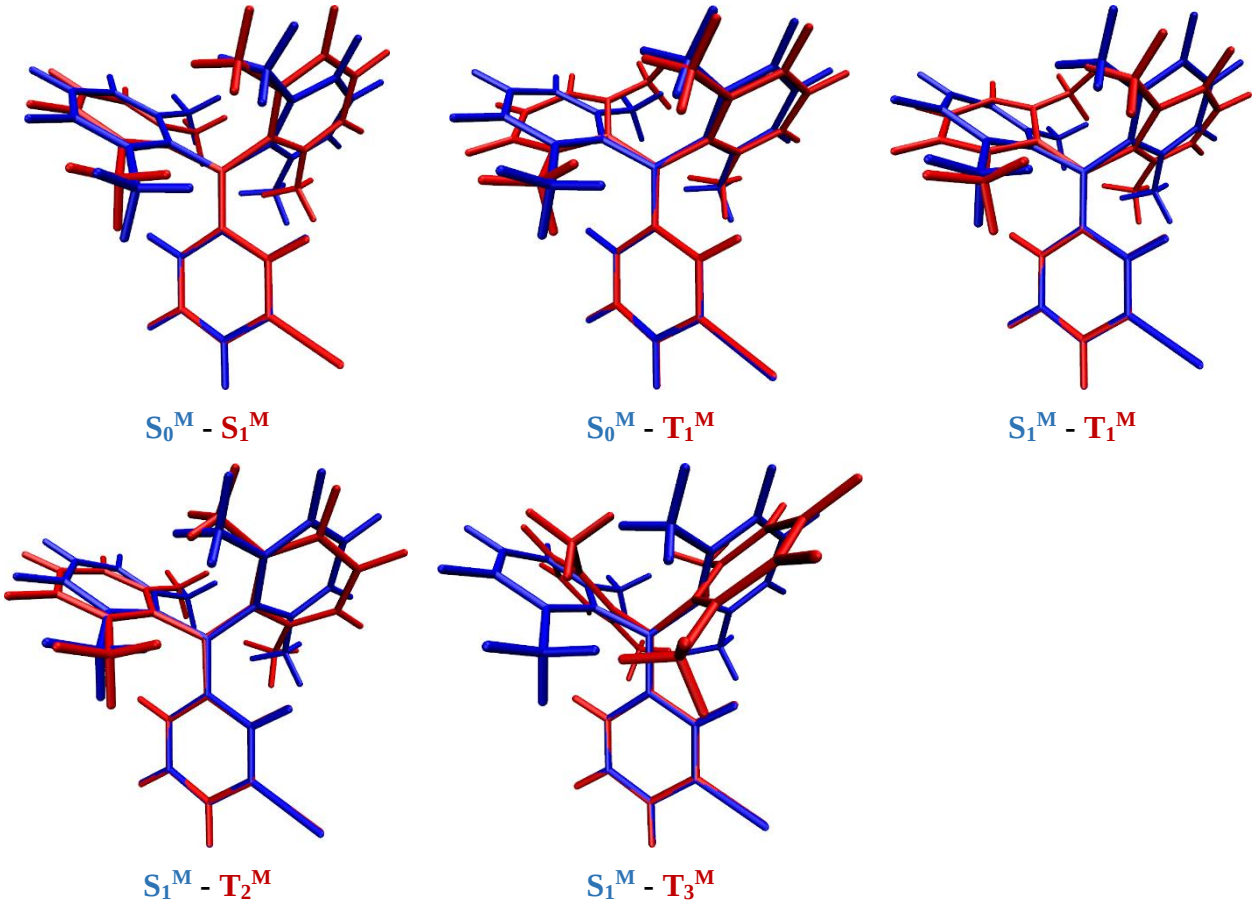

Figure 3-27. Structure overlays of **m-BrTAB**.

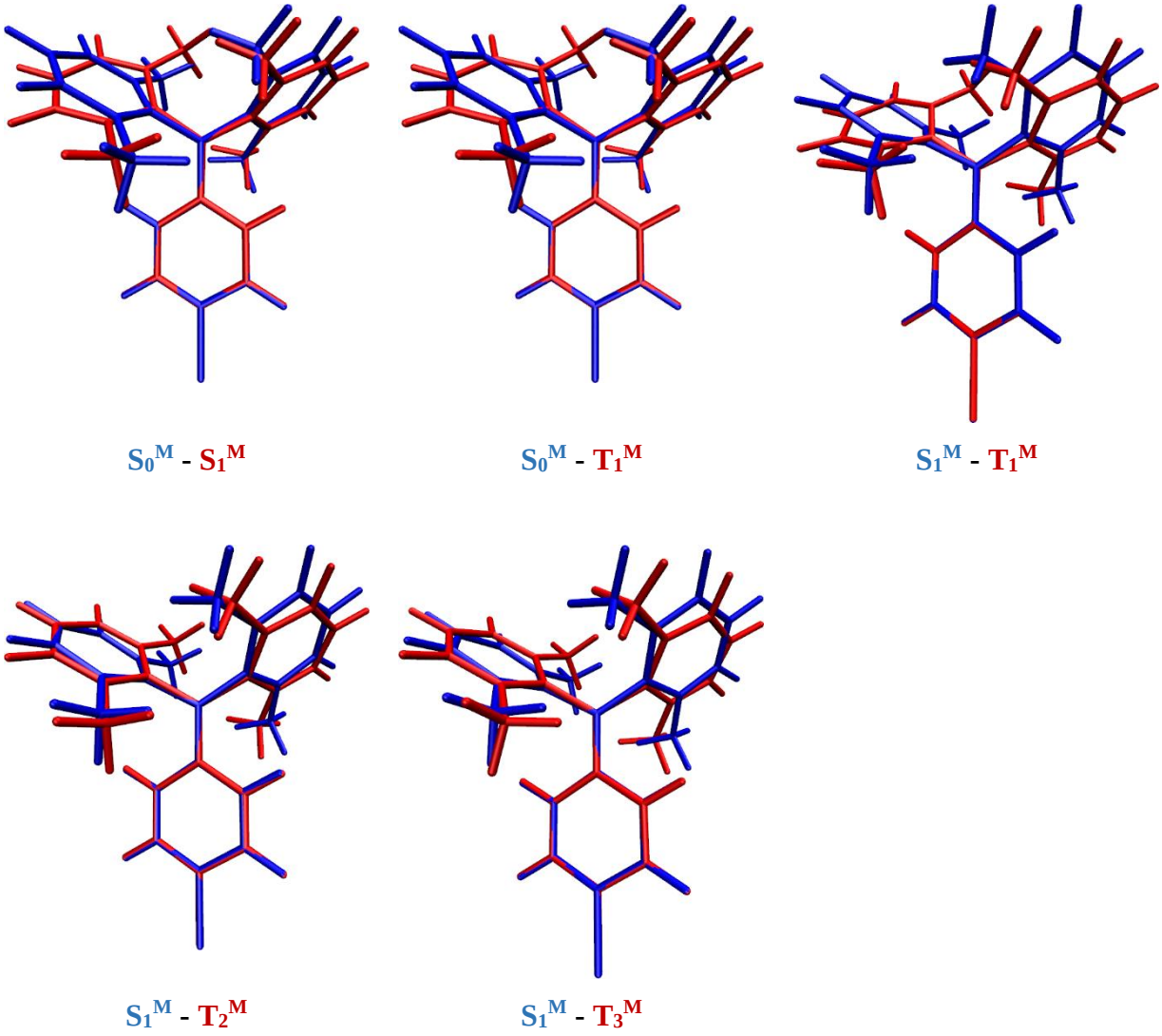

Figure 3-28. Structure overlays of **p-BrTAB**.

3.4.6 Solid crystal structure data

Table 3-10. Single-crystal X-ray diffraction data and structure refinements of ***o*-BrTAB**, ***m*-BrTAB** and ***p*-BrTAB** at 100 K.

Data	***o*-BrTAB**	***m*-BrTAB**	***p*-BrTAB**
CCDC number	2085814	2085815	2085816
Empirical formula	$C_{22}H_{22}BBr$	$C_{22}H_{22}BBr$	$C_{22}H_{22}BBr$
Formula weight / $g \cdot mol^{-1}$	377.11	377.11	377.11
T / K	100(2)	100(2)	100(2)
Radiation, λ / Å	Mo-Kα 0.71073	Mo-Kα 0.71073	Mo-Kα 0.71073
Crystal size / mm^3	0.42×0.29×0.22	0.34×0.21×0.09	0.32×0.30×0.25
Crystal color, habit	colorless block	colorless plate	colorless block
μ / mm^{-1}	2.235	2.230	2.213
Crystal system	Monoclinic	Triclinic	Monoclinic
Space group	$P2_1/n$	$P\ \bar{1}$	$C2/c$
a / Å	8.1374(6)	7.559(3)	21.837(7)
b / Å	12.0614(9)	8.296(3)	18.956(5)
c / Å	18.7609(14)	15.372(6)	17.946(8)
α / °	90	102.84(3)	90
β / °	93.027(2)	94.23(2)	90.31(4)
γ / °	90	99.364(18)	90
Volume / $Å^3$	1838.8(2)	921.3(6)	7429(5)
Z	4	2	16
ρ_{calc} / $g \cdot cm^{-3}$	1.362	1.359	1.349
F(000)	776	388	3104
θ range / °	2.008 - 27.481	2.562 - 29.575	2.149 - 29.574
Reflections collected	36785	25129	95509
Unique reflections	4221	5190	10416
Parameters / restraints	221 / 0	221 / 0	441 / 0
GooF on F^2	1.060	1.059	1.019
R_1 [I>2σ(I)]	0.0350	0.0422	0.0306
wR^2 (all data)	0.0973	0.1117	0.0776
Max. / min. residual electron density / $e \cdot Å^{-3}$	1.278 / –0.548	2.049 / –0.380	0.439 / –0.594

Table 3-11. Single-crystal X-ray diffraction data and structure refinements of of ***o*-BrTAB**, ***m*-BrTAB** and ***p*-BrTAB** at ambient temperature. Formula weight = 377.11 g·mol^{-1}.

Data	***o*-BrTAB**	***m*-BrTAB**	***p*-BrTAB**
CCDC number	2089473	2118234	2118235
Empirical formula	$C_{22}H_{22}BBr$	$C_{22}H_{22}BBr$	$C_{22}H_{22}BBr$
T / K	290(2)	296(2)	300(2)
Radiation, λ / Å	Mo-Kα 0.71073	Mo-Kα 0.71073	Mo-Kα 0.71073
Crystal size / mm³	0.10×0.22×0.31	0.33×0.28×0.07	0.37×0.32×0.20
Crystal color, habit	Colorless block	Colorless plate	Colorless block
μ / mm^{-1}	2.178	2.162	2.213
Crystal system	Monoclinic	Triclinic	Monoclinic
Space group	$P2_1/n$	$P\ \bar{1}$	$C2/c$
a / Å	8.200(6)	7.6560(17)	21.9758(5)
b / Å	12.164(6)	8.3568(9)	19.2403(5)
c / Å	18.944(8)	15.496(3)	18.2089(3)
α / °	90	102.709(10)	90
β / °	93.277(7)	94.76(3)	91.0120(10)
γ / °	90	98.290(19)	90
Volume / Å^3	1886.4(17)	950.3(3)	7697.9(3)
Z	4	2	16
ρ_{calc} / g·cm^{-3}	1.328	1.318	1.302
F(000)	776	388	3104
θ range / °	1.991 - 26.372	1.357 – 26.370	2.394 – 26.371
Reflections collected	27916	25227	50647
Unique reflections	3859	3891	7870
Parameters / restraints	221 / 0	221 / 0	441 / 0
GooF on F^2	1.120	1.059	1.054
R_1 [I>2σ(I)]	0.0476	0.0489	0.0349
wR^2 (all data)	0.1197	0.1212	0.0990
Max. / min. residual electron density / e·Å^{-3}	0.373 / –0.579	0.590 / –0.512	0.412 / –0.716

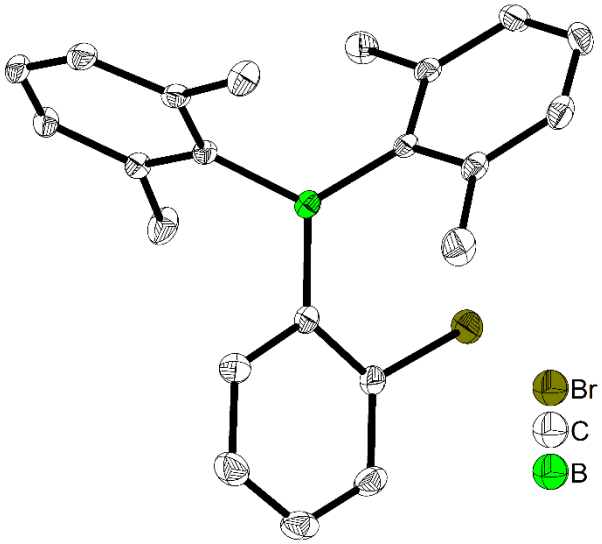

Figure 3-29. The solid-state molecular structure of ***o*-BrTAB** determined by single-crystal X-ray diffraction at 100 K. Ellipsoids are drawn at the 50% probability level, and H atoms are omitted for clarity.

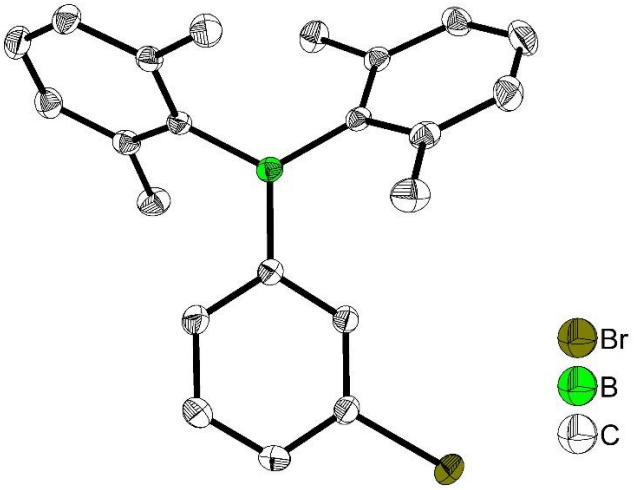

Figure 3-30. The solid-state molecular structure of ***m*-BrTAB** determined by single-crystal X-ray diffraction at 100 K. Ellipsoids are drawn at the 50% probability level, and H atoms are omitted for clarity.

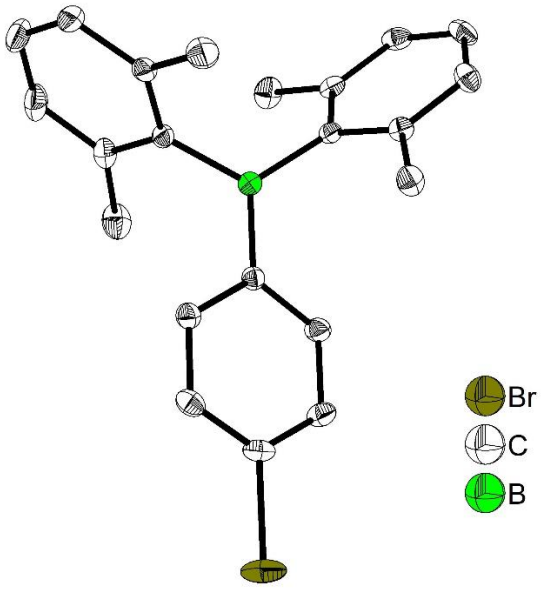

Figure 3-31. The solid-state molecular structure of ***p*-BrTAB** determined by single-crystal X-ray diffraction at 100 K. Ellipsoids are drawn at the 50% probability level, and H atoms are omitted for clarity. Only one of two non-symmetry-equivalent molecules is shown here.

Table 3-12. Selected bond lengths (Å) and angles (°) as well as intramolecular contacts (Å) of ***o*-BrTAB**, ***m*-BrTAB** and ***p*-BrTAB** at 100 K. Aryl rings are numbered R1, R2, or R3 according to the C1, C7, or C15 atom being present and bonded to the boron atom, respectively.

	***o*-BrTAB**	***m*-BrTAB**	***p*-BrTAB**	
			Molecule 1	Molecule 2
C–Br	1.906(2)	1.899(2)	1.8982(16)	1.9007(17)
∠ C1–B–C15	121.38(18)	119.06(18)	119.58(14)	119.46(13)
∠ C1–B–C7	**116.28(18)**	118.00(18)	119.16(13)	122.29(13)
∠ C7–B–C15	122.15(19)	122.92(18)	121.26(13)	118.22(13)
Sum ∠ CBC	359.8(2)	360.0(2)	360.0(1)	360.0(1)
B–C1	1.578(3)	1.577(3)	**1.563(2)**	**1.561(2)**
B–C7	1.583(3)	1.579(3)	1.583(2)	1.585(2)
B–C15	1.574(3)	1.575(3)	1.581(2)	1.580(2)
∠ BC3 – aryl R1	38.61(9)	21.33(12)	20.06(8)	24.77(7)
∠ BC3 – aryl R2	61.02(6)	59.69(9)	63.38(7)	53.47(7)
∠ BC3 – aryl R3	55.21(9)	50.09(9)	57.88(7)	68.62(7)
∠ B–C1–C2	**127.2(2)**	121.18(18)	121.27(13)	122.85(14)
∠ B–C1–C6	**117.74(19)**	**117.47(19)**	121.34(14)	119.98(13)
∠ B–C15–C16	120.81(19)	121.33(18)	121.27(14)	120.93(14)
∠ B–C15–C20	120.93(19)	120.69(19)	120.78(14)	120.37(14)
∠ B–C7–C12	121.59(19)	121.47(18)	120.36(13)	120.77(13)
∠ B–C7–C8	119.71(19)	120.22(19)	120.88(14)	121.32(13)
Shortest B–Br contact	3.345(2)			
Shortest C15–Br contact	3.298(2)			

Table 3-13. Selected bond lengths (Å) and angles (°) as well as intramolecular contacts (Å) of ***o*-BrTAB**, ***m*-BrTAB** and ***p*-BrTAB** at ambient temperature. Aryl rings are numbered R1, R2, or R3 according to the C1, C7, or C15 atom being present and bonded to the boron atom, respectively.

	***o*-BrTAB**	***m*-BrTAB**	***p*-BrTAB**	
T (K)	290(2)	296(2)	300(2)	
			Molecule 1	Molecule 2
C–Br	1.905(4)	1.896(3)	1.896(2)	1.899(2)
∠ C1–B–C15	121.3(4)	119.3(2)	119.35(18)	119.57(17)
∠ C1–B–C7	**116.1(3)**	117.4(3)	118.66(17)	121.78(17)
∠ C7–B–C15	122.4(3)	123.3(3)	121.99(18)	118.63(16)
Sum ∠ CBC	359.8(3)	360.0(3)	360.0(1)	360.0(2)
B–C1	1.578(5)	1.575(4)	**1.561(3)**	**1.560(3)**
B–C7	1.581(5)	1.584(4)	1.581(3)	1.587(3)
B–C15	**1.565(5)**	1.572(4)	1.583(3)	1.579(3)
∠ BC3 – aryl R1	39.27(2)	22.30(12)	22.15(8)	27.05(8)
∠ BC3 – aryl R2	60.38(1)	60.46(12)	63.22(8)	53.57(8)
∠ BC3 – aryl R3	54.78(2)	49.85(12)	57.06(8)	66.37(8)
∠ B–C1–C2	**127.2(3)**	121.5(3)	121.44(17)	122.74(17)
∠ B–C1–C6	**118.0(3)**	**117.4(3)**	121.83(17)	120.54(17)
∠ B–C15–C16	120.8(3)	121.3(3)	121.20(19)	120.93(18)
∠ B–C15–C20	121.6(3)	121.0(3)	120.83(18)	120.17(18)
∠ B–C7–C12	121.4(3)	121.3(3)	120.77(19)	121.04(17)
∠ B–C7–C8	120.2(3)	119.8(3)	120.5(2)	121.03(17)
Shortest B–Br contact	3.350(4)			
Shortest C15–Br contact	3.304(4)			

Table 3-14. Intermolecular C−H···C/Br, C···C/Br, and H···H interaction distances (Å) and angles (°) in ***o*-BrTAB**, ***m*-BrTAB** and ***p*-BrTAB** at 100 K.

Compound	C−H···C(Br)	H··· C(Br,H)	C···C(Br)	∠ (CHC(Br))
***o*-BrTAB**	C4−H4···Br1	**3.1001(3)**	**3.354(2)**	97.16(15)
	C5−H5···C9	2.802(2)	3.618(3)	144.62(15)
	C19−H19···C3	2.802(2)	3.730(3)	165.82(15)
	C10−H10···C19	**2.753(2)**	3.488(3)	134.74(14)
	C17−H17···C10	2.800(2)	3.652(3)	149.78(15)
	C17−H17···C11	2.821(2)	3.768(3)	175.45(15)
	C14···C18 (methyl)		3.361(3)	
***m*-BrTAB**	C22(methyl)−H22B···C18	2.836(2)	3.676(4)	144.13(17)
	C9−H9···C16	2.861(2)	3.790(3)	166.26(15)
	C17−H17···C9	2.888(3)	3.699(4)	143.96(15)
	C14(methyl)−H14B···Br1	**2.9425(12)**	3.898(3)	165.05(14)
	C10−H10···Br1	**3.0346(13)**	3.736(3)	131.85(15)
***p*-BrTAB**	H11_1··· H11_1	2.3628(10)		
	H10_1··· H17_1	2.2659(5)		
	C2−H2_1···C4	2.8390(17)	3.752(2)	161.38(10)
	C3−H3···C9_1	2.821(2)	3.520(3)	131.16(11)
	C3−H3···C10_1	2.820(2)	3.686(3)	152.03(11)
	C9−H9···C16	2.8655(18)	3.783(3)	162.62(11)
	C13(methyl)−H13C_1···C17	2.8102(18)	3.653(3)	144.58(10)
	C3_1···Br1		**3.480(2)**	
	C14(methyl)−H14B_1···Br1	**2.9635(11)**	3.594(2)	123.11(10)

Table 3-15. Intermolecular C−H···C/Br, C···C/Br, and H···H interaction distances (Å) and angles (°) in ***o*-BrTAB**, ***m*-BrTAB** and ***p*-BrTAB** at ambient temperature. Significant intermolecular contacts as calculated below the sum of van der Waals radii using the Mercury program are given in black color, while farther contacts, which do not play a significant role, are given in red for comparison with the close contacts at 100 K given in Table S13.

Compound	C−H···C(Br)	H··· C(Br,H)	C···C(Br)	∠ (CHC(Br))
***o*-BrTAB 290(2) K**	C4−H4···Br1	3.1579(9)	**3.432(5)**	99.2(3)
	C5−H5···C9	**2.855(4)**	3.658(5)	145.3(2)
	C19−H19···C3	2.907(5)	3.809(6)	163.8(3)
	C10−H10···C19	**2.846(4)**	3.577(6)	136.4(2)
	C17−H17···C10	**2.873(4)**	3.709(6)	150.4(3)
	C17−H17···C11	**2.873(4)**	3.802(6)	177.2(3)
	C14···C18 (methyl)		3.426(6)	
***m*-BrTAB 296(2) K**	C22(methyl)−H22B···C18	2.981(4)	3.759(6)	139.0(3)
	C9−H9···C16	2.946(3)	3.858(4)	167.2(2)
	C17−H17···C9	2.980(3)	3.779(5)	144.9(2)
	C14(methyl)−H14B···Br1	**2.9857(8)**	3.927(3)	166.77(18)
	C10−H10···Br1	3.1583(6)	3.846(4)	132.3(3)
***p*-BrTAB 300(2) K**	H11_1··· H11_1	2.480(1)		
	H10_1··· H17_1	**2.393(1)**		
	C2−H2_1···C4	2.9083(19)	3.792(3)	159.20(14)
	C3−H3···C9_1	**2.887(2)**	3.585(3)	132.78(13)
	C3−H3···C10_1	2.913(2)	3.763(3)	152.60(13)
	C9−H9···C16	2.982(2)	3.879(4)	162.38(17)
	C9–H9···C17	2.935(2)	3.819(3)	159.24(16)
	C13(methyl)−H13C_1···C17	**2.870(2)**	3.699(3)	145.18(15)
	C3_1···Br1		3.611(3)	
	C14(methyl)−H14B_1···Br1	**2.9648(4)**	3.635(3)	127.98(15)

Table 3-16. Aryl···aryl (π···π) distances (Å) and angles (°) in crystals of ***m*-BrTAB** at 100 K and 296 K: nearest-neighbour (nn) C···C distances, centroid-centroid distances, interplanar separations, shifts, and slip angles. Aryl rings are numbered R1 or R3 according to the C1 or C15 atom being present and bonding to the boron atom, respectively.

Compound	Aryl···Aryl	nn C···C	Centroid-centroid distance	Interplanar separation	Shift	Slip angle
***m*-BrTAB 100 K**	R1···R1	3.698(5)	4.285(2)	3.640(3)	2.261(4)	31.8
	R3···R3	3.637(5)	4.951(3)	3.544(4)	3.457(4)	44.3
***m*-BrTAB 296 K**	R1···R1	3.871(8)	4.455(3)	3.812(4)	2.305(6)	31.2
	R3···R3	3.750(7)	5.034(3)	3.645(6)	3.473(6)	43.6

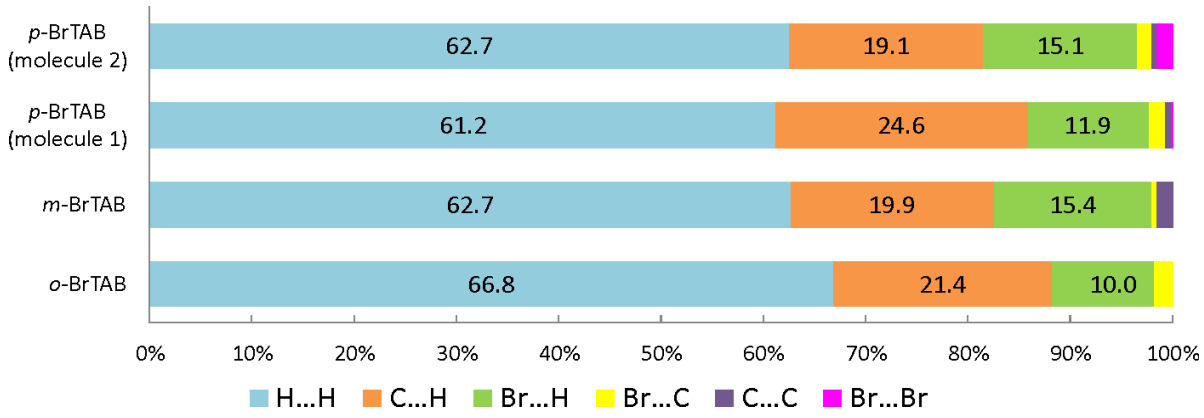

Figure. 3-32. Percentage contributions to the Hirshfeld surface area for the various close intermolecular contacts in ***o*-BrTAB**, ***m*-BrTAB**, and ***p*-BrTAB** at 100 K. In ***p*-BrTAB**, two symmetrically non-equivalent molecules are distinguished by slightly different contributions.

Table 3-17. Properties of crystals of ***o*-BrTAB**, ***m*-BrTAB** and ***p*-BrTAB** at ambient temperature and at 100 K: Volume of the molecule within van der Waals (V_m), Hirshfeld (V_H), and of the surface of the crystal voids (V_v), surface area of the molecule within van der Waals (SA_m), Hirshfeld (SA_H), and void surface area (SA_v), crystal packing coefficient (c_k), solvent accessible volume (V_{solv}), and percentage of intermolecular contacts. pfu…per formula unit; van der Waals radii used: C 1.7 Å, H: 1.09 Å, B: 2 Å, Br: 1.85 Å.

	***o*-BrTAB**		***m*-BrTAB**		***p*-BrTAB**			
T (K)	**290**	**100**	**296**	**100**	**Mol. 1 300 K**	**Mol. 2 300 K**	**Mol. 1 100 K**	**Mol. 2 100 K**
V_m / Å³	299.75	302.60	300.52	303.08	300.13	300.93	302.56	303.09
SA_m / Å²	344.28	347.42	345.67	348.27	346.83	346.31	350.12	348.78
V_H / Å³	464.68	452.75	467.53	453.02	472.65	474.25	455.65	457.64
SA_H / Å²	**367.41**	**364.05**	382.95	378.28	382.30	386.48	376.05	380.28
V_v / Å³	263.15	218.07	130.42	104.28	1174.41		912.57	
V_v / Å³ pfu	65.79	54.52	65.21	52.14	**73.40**		57.04	
SA_v / Å²	752.74	644.85	387.91	323.83	3275.62		2820.38	
SA_v / Å² pfu	**188.19**	161.21	193.96	161.92	204.73		176.27	
c_k	0.635	0.658	0.633	0.658	0.624		0.653	
V_{solv} / Å³	**31.9 (1.7%)**	0.0 (0%)	**41.9 (4.4%)**	16.2 (1.8%)	**209.2 (2.7%)**		39.3 (0.5%)	
Br···Br /%	0	0	0	0	0.3	1.8	0.2	1.6
Br···C / %	1.7	1.8	0.4	0.5	1.4	1.4	1.5	1.4
Br···H / %	10.2	10.0	15.6	15.4	12.1	15.5	11.9	15.1
C···C / %	0	0	**1.4**	**1.6**	0.4	0.4	0.6	0.5
C···H / %	20.4	21.4	18.9	19.9	23.5	18.1	24.6	19.1
H···H / %	**67.7**	**66.8**	63.6	62.7	62.4	62.8	61.2	62.3

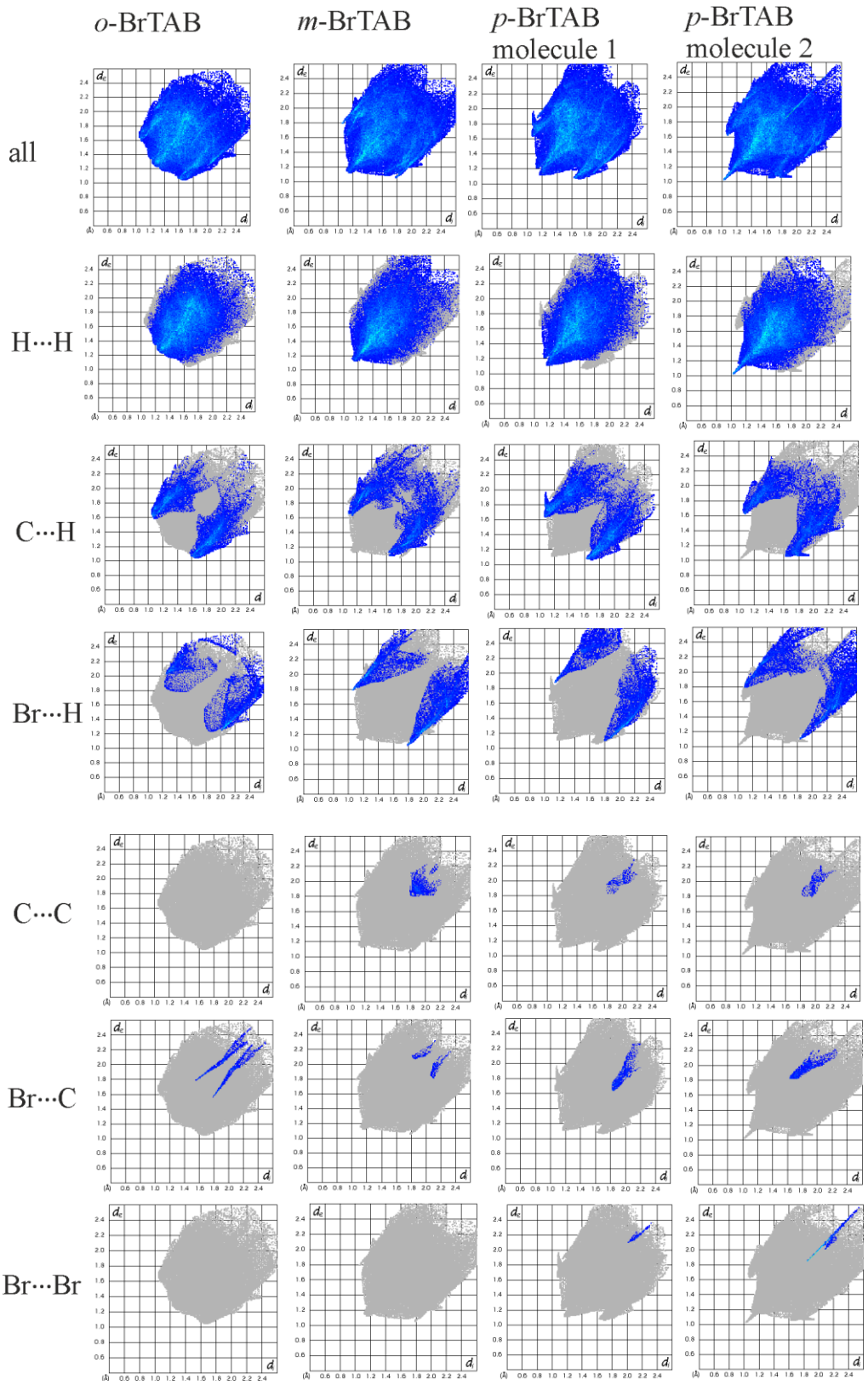

Figure 3-33. Two-dimensional fingerprint plots of molecules ***o*-BrTAB**, ***m*-BrTAB**, and ***p*-BrTAB** at 100 K calculated from the Hirshfeld surfaces. In ***p*-BrTAB**, two non-equivalent molecules are distinguished. The top row shows the complete fingerprint plots, while the other plots indicate the contributions of the individual intermolecular interactions (H···H, C···H, Br···H, C···C, Br···C, and Br···Br from top to bottom) within the grey area of all contributions.

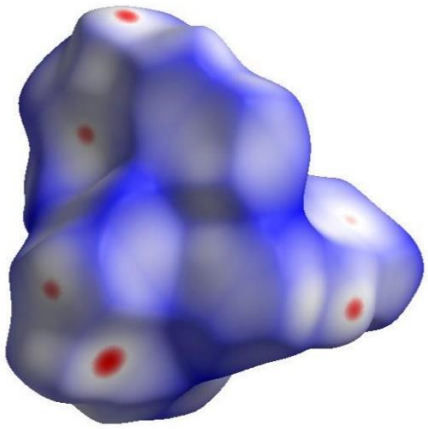

Figure 3-34. Hirshfeld surface of ***o*-BrTAB** at 100 K mapped with d_{norm} over the range -0.113 to 1.476. Close contacts are shown in red on the surface.

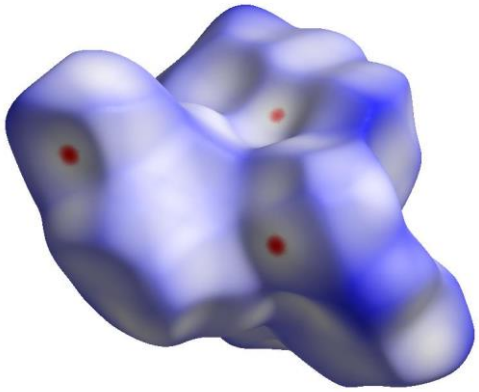

Figure 3-35. Hirshfeld surface of ***m*-BrTAB** at 100 K mapped with d_{norm} over the range -0.113 to 1.476. Close contacts are shown in red on the surface.

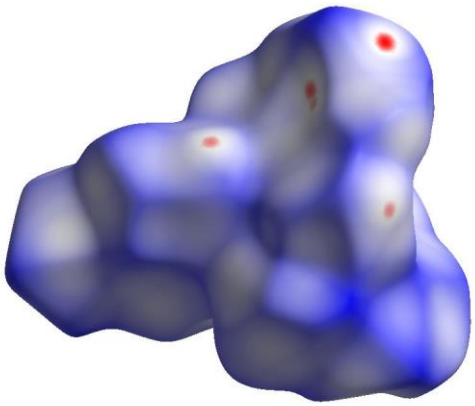

Figure 3-36. Hirshfeld surface of ***p*-BrTAB** at 100 K mapped with d_{norm} over the range -0.102 to 1.532. Close contacts are shown in red on the surface.

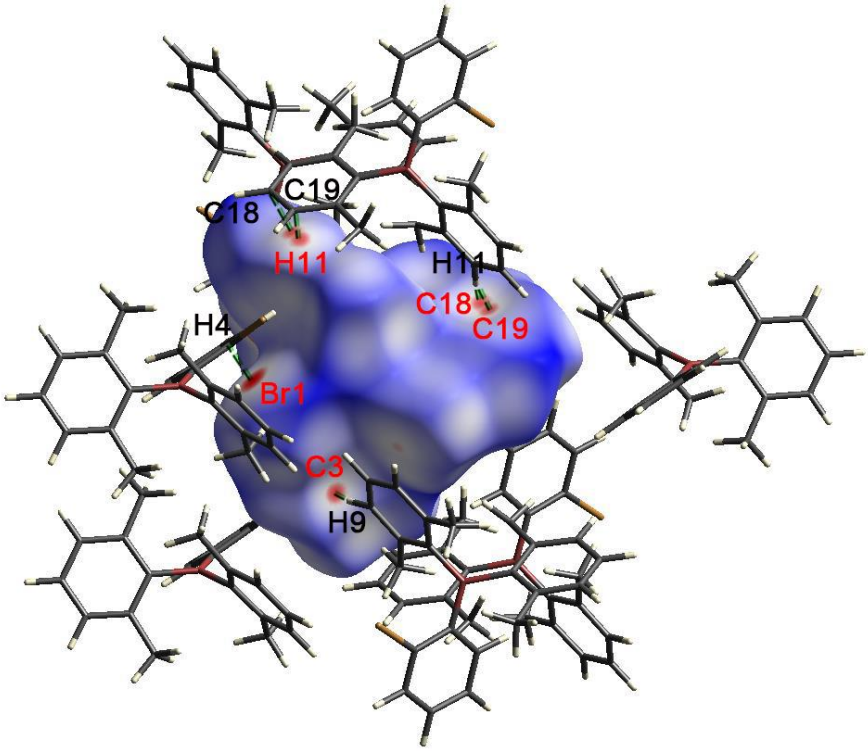

Figure 3-37. Hirshfeld surface of ***o*-BrTAB** mapped with d_{norm} over the range -0.113 to 1.476 at 100 K. Neighboring molecules associated with close contacts are shown.

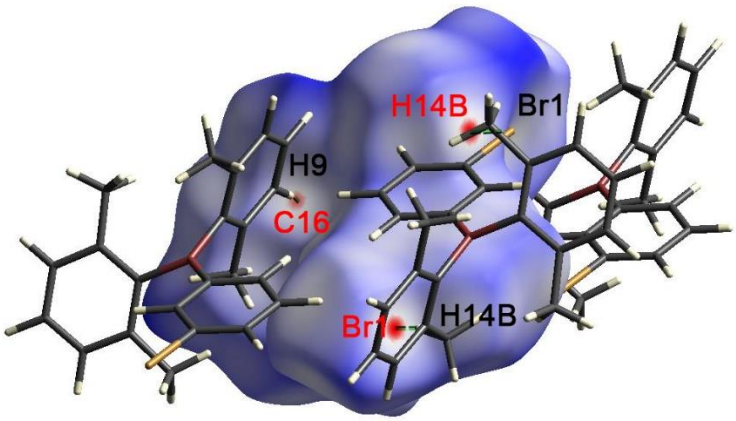

Figure 3-38. Hirshfeld surface of ***m*-BrTAB** mapped with d_{norm} over the range -0.113 to 1.476 at 100 K. Neighboring molecules associated with close contacts are shown.

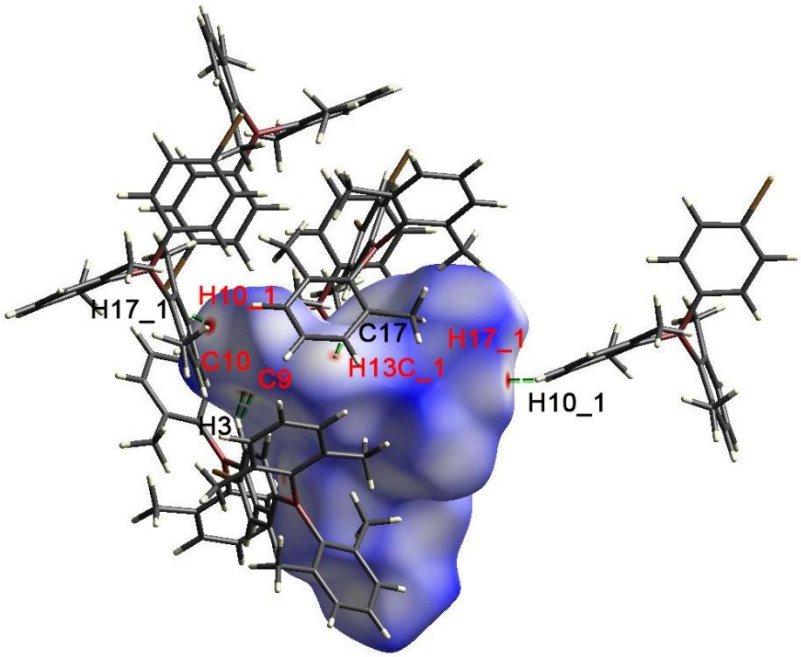

Figure 3-39. Hirshfeld surface of ***p*-BrTAB** mapped with d_{norm} over the range -0.102 to 1.532 at 100 K. Neighboring molecules associated with close contacts are shown.

3.5 Reference

[1] a) S. Hirata, K. Totani, J. Zhang, T. Yamashita, H. Kaji, S. R. Marder, T. Watanabe, C. Adachi, *Adv. Funct. Mater*. **2013**, *23*, 3386-3397; b) L. Dou, J. You, Z. Hong, Z. Xu, G. Li, R. A. Street, Y. Yang, *Adv. Mater*. **2013**, *25*, 6642-6671; c) S. Reineke, F. Lindner, G. Schwartz, N. Seidler, K. Walzer, B. Lussem, K. Leo, *Nature* **2009**, 459, 234-238; d) S. Hirata, K. Totani, H. Kaji, M. Vacha, T. Watanabe, C. Adachi, *Adv. Opt. Mater.* **2013**, *1*, 438-442.

[2] a) L. Huang, C. Qian, Z. Ma, *Chem. Eur. J*. **2020**, *26*, 11914-11930; b) J. Yang, X. Zhen, B. Wang, X. Gao, Z. Ren, J. Wang, Y. Xie, J. Li, Q. Peng, K. Pu, Z. Li, *Nat. Commun*. **2018**, *9*, 840-849; c) S. Xu, R. Chen, C. Zheng, W. Huang, *Adv. Mater.* **2016**, *28*, 9920-9940; d) J. Zhao, W. Wu, J. Sun, S. Guo, *Chem. Soc. Rev*. **2013**, *42*, 5323-5351; e) H. T. Feng, J. Zeng, P. A. Yin, X. D. Wang, Q. Peng, Z. Zhao, J. W. Y. Lam, B. Z. Tang, *Nat. Commun.* **2020**, *11*, 2617.

[3] a) Z. He, H. Gao, S. Zhang, S. Zheng, Y. Wang, Z. Zhao, D. Ding, B. Yang, Y. Zhang, W. Z. Yuan, *Adv. Mater.* **2019**, *31*, 1807222; b) T. Maldiney, A. Lecointre, B. Viana, A. Bessiere, M. Bessodes, D. Gourier, C. Richard, D. Scherman, *J. Am. Chem. Soc.* **2011**, *133*, 11810-11815; c) X. F. Wang, H. Y. Xiao, P. Z. Chen, Q. Z. Yang, B. Chen, C. H. Tung, Y. Z. Chen, L. Z. Wu, *J. Am. Chem. Soc.* **2019**, *141*, 5045-5050; d) G. Zhang, G. M. Palmer, M. W. Dewhirst, C. L. Fraser, *Nat. Mater.* **2009**, *8*, 747-751; e) K. Y. Zhang, Q. Yu, H. Wei, S. Liu, Q. Zhao, W. Huang, *Chem. Rev.* **2018**, *118*, 1770-1839.

[4] a) P. Long, Y. Feng, C. Cao, Y. Li, J. Han, S. Li, C. Peng, Z. Li, W. Feng, *Adv. Funct. Mater.* **2018**, *28*, 1800791; b) Y. Tao, R. Chen, H. Li, J. Yuan, Y. Wan, H. Jiang, C. Chen, Y. Si, C. Zheng, B. Yang, G. Xing, W. Huang, *Adv. Mater.* **2018**, *30*, 1803856; c) B. Zhou, D. P. Yan, *Adv. Funct. Mater.* **2019**, *29*, 1807599.

[5] a) M. C. Tang, M. Y. Leung, S. L. Lai, M. Ng, M. Y. Chan, V. W. W. Yam, *J. Am. Chem. Soc.* **2018**, *140*, 13115-13124; b) O. S. Wenger, *J. Am. Chem. Soc.* **2018**, *140*, 13522-13533; c) K. Y. Zhang, P. Gao, G. Sun, T. Zhang, X. Li, S. Liu, Q. Zhao, K. K. Lo, W. Huang, *J. Am. Chem. Soc.* **2018**, *140*, 7827-7834; d) W. Liu, J. Wang, Y. Gong, Q. Liao, Q. Dang, Z. Li, Z. Bo, *Angew. Chem. Int. Ed*. **2020**, *59*, 20161-20166; *Angew. Chem*. **2020**, *132*, 20336-20341.

[6] a) C. J. Chen, R. J. Huang, A. S. Batsanov, P. Pander, Y. T. Hsu, Z. G. Chi, F. B. Dias, M. R. Bryce, *Angew. Chem. Int. Ed.* **2018**, *57*, 16407-16411; *Angew. Chem*. **2018**, *130*, 16645-16649; b) L. K. Huang, B. Chen, X. P. Zhang, C. O. Trindle, Y. C. Wang, H. Miao, Y. Luo, G. Q. Zhang, *Angew. Chem. Int. Ed.* **2018**, *57*, 16046-16050; *Angew. Chem*. **2018**, *130*, 16278-16282; c) S. M. A. Fateminia, Z. Mao, S. Xu, Z. Yang, Z. Chi, B. Liu, *Angew. Chem. Int. Ed.* **2017**, *56*, 12160-12164; *Angew. Chem*. **2017**, *129*, 12328-12332; d) K. Jiang, Y. Wang, C. Cai, H. Lin, *Adv. Mater.* **2018**, *30*, 1800783; e) L. Favereau, C. Quinton, C. Poriel, T. Roisnel, D. Jacquemin, J. Crassous, *J. Phys. Chem. Lett.* **2020**, *11*, 6426-6434; f) E. Januszewski, A. Lorbach, R. Grewal, M. Bolte, J. W. Bats, H. W. Lerner, M. Wagner, *Chem. Eur. J.* **2011**, *17*, 12696-12705; g) T. Kushida, C. Camacho, A. Shuto, S. Irle, M. Muramatsu, T. Katayama, S. Ito, Y. Nagasawa, H. Miyasaka, E. Sakuda, N. Kitamura, Z. Zhou, A. Wakamiya, S. Yamaguchi, *Chem. Sci*. **2014**, *5*, 1296-1304.

[7] a) J. Wang, Z. Huang, X. Ma, H. Tian, *Angew. Chem. Int. Ed*. **2020**, *59*, 9928-9933; *Angew. Chem*. **2020**, *132*, 10014-10019; b) L. Bian, H. Shi, X. Wang, K. Ling, H. Ma, M. Li, Z. Cheng, C. Ma, S. Cai, Q. Wu, N. Gan, X. Xu, Z. An, W. Huang, *J. Am. Chem. Soc*. **2018**, *140*, 10734-10739; c) W. Zhao, Z. He, B. Z. Tang, *Nature Res. Mater*. **2020**, *5*, 869-885; d) W. Ratzke, L. Schmitt, H. Matsuoka, C. Bannwarth, M. Retegan, S. Bange, P. Klemm, F. Neese, S. Grimme, O. Schiemann, J. M. Lupton, S. Hoger, *J. Phys. Chem. Lett.* **2016**, **7**, 4802-4808; e) E. Lucenti, A. Forni, C. Botta, L. Carlucci, C. Giannini, D. Marinotto, A. Previtali, S. Righetto, E. Cariati, *J. Phys. Chem. Lett.* **2017**, *8*, 1894-1898; f) W. L. Jia, D. T. Song, S. N. Wang, *J. Org. Chem*. **2003**, *68*, 701-705.

[8] a) M. Louis, H. Thomas, M. Gmelch, A. Haft, F. Fries, S. Reineke, *Adv. Mater.* **2019**, *31*, 1807887; b) H. Shi, Z. An, P. Z. Li, J. Yin, G. Xing, T. He, H. Chen, J. Wang, H. Sun, W. Huang, Y. Zhao, *Cryst. Growth Des.* **2016**, *16*, 808-813; c) H. Tian, X. Ma, C. Xu, J. Wang, *Angew. Chem. Int. Ed.* **2018**, *57*, 10854-10858; *Angew. Chem*. **2018**, *130*, 11020-11024; d) J. Wang, C. Wang, Y. Gong, Q. Liao, M. Han, T. Jiang, Q. Dang, Y. Li, Q. Li, Z. Li, *Angew. Chem. Int. Ed.* **2018**, *57*, 16821-16826; *Angew. Chem*. **2018**, *130*, 17063-17068;e) Z. Y. Zhang, Y. Chen, Y. Liu, *Angew. Chem. Int. Ed.* **2019**, *58*, 6028-6032; *Angew. Cheme*. **2019**, *131*, 6089-6093; f) J. L. Ma, H. Liu, S. Y. Li, Z. Y. Li, H. Y. Zhang, Y. Wang, C. H. Zhao,

Organometallics **2020**, *39*, 4153-4158; g) J. Gierschner, J. Q. Shi, B. M. Medina, Sanjuán, S. Varghese, S. Y. Park, *Adv. Opt. Mater.* **2021**, 2002251; h) H. Yuasa, S. Kuno, *Bull. Chem. Soc. Jpn*. **2018**, *91*, 223–229.

[9] a) R. Kabe, C. Adachi, *Nature* **2017**, *550*, 384-387; b) D. Li, F. Lu, J. Wang, W. Hu, X. M. Cao, X. Ma, H. Tian, *J. Am. Chem. Soc.* **2018**, *140*, 1916-1923; c) J. Wei, B. Liang, R. Duan, Z. Cheng, C. Li, T. Zhou, Y. Yi, Y. Wang, *Angew. Chem. Int. Ed.* **2016**, *55*, 15589-15593; *Angew. Chem*. **2016**, *128*, 15818-15822; d) Z. Lin, R. Kabe, K. Wang, C. Adachi, *Nat. Commun.* **2020**, *11*, 191; e) B. Chen, W. Huang, H. Su, H. Miao, X. Zhang, G. Zhang, *Angew. Chem. Int. Ed*. **2020**, *59*, 10023-10026; *Angew. Chem*. **2020**, *132*, 10109-10112; f) O. Bolton, K. Lee, H. J. Kim, K. Y. Lin, J. Kim, *Nat. Chem.* **2011**, *3*, 205-210; g) C. Chen, Z. Chi, K. C. Chong, A. S. Batsanov, Z. Yang, Z. Mao, Z. Yang, B. Liu, *Nat. Mater.* **2020**, *20*, 175-180.

[10] a) Y. Gong, G. Chen, Q. Peng, W. Z. Yuan, Y. Xie, S. Li, Y. Zhang, B. Z. Tang, *Adv. Mater.* **2015**, *27*, 6195-6201; b) Y. Gong, L. Zhao, Q. Peng, D. Fan, W. Z. Yuan, Y. Zhang, B. Z. Tang, *Chem. Sci.* **2015**, *6*, 4438-4444; c) D. C. Green, M. A. Holden, M. A. Levenstein, S. Zhang, B. R. G. Johnson, J. Gala de Pablo, A. Ward, S. W. Botchway, F. C. Meldrum, *Nat. Commun.* **2019**, *10*, 206; d) K. Narushima, Y. Kiyota, T. Mori, S. Hirata, M. Vacha, *Adv. Mater.* **2019**, *31*, 1807268.

[11] a) Q. Li, M. Zhou, M. Yang, Q. Yang, Z. Zhang, J. Shi, *Nat. Commun.* **2018**, *9*, 734; b) H. W. Wu, W. J. Chi, Z. Chen, A. K. Bindra, G. B. Yang, X. G. Liu, Y. L. Zhao, *Adv. Funct. Mater.* **2019**, *29*, 1807243; c) A. D. Nidhankar, Goudappagouda, D. S. Mohana Kumari, S. K. Chaubey, R. Nayak, R. G. Gonnade, G. V. P. Kumar, R. Krishnan, S. S. Babu, *Angew. Chem. Int. Ed.* **2020**, *59*, 13079-13085; *Angew. Chem*. **2020**, *132*, 13179-13185.

[12] a) Z. Chai, C. Wang, J. Wang, F. Liu, Y. Xie, Y. Z. Zhang, J. R. Li, Q. Li, Z. Li, *Chem. Sci.* **2017**, *8*, 8336-8344; b) X. F. Chen, C. Xu, T. Wang, C. Zhou, X. P. Zhang, J. N. Demas, C. O. Trindle, G. Q. Zhang, *Angew. Chem. Int. Ed.* **2016**, *55*, 9872-9876; *Angew. Chem*. **2016**, *128*, 10026-10030; c) P. K. Samanta, D. Kim, V. Coropceanu, J. L. Bredas, *J. Am. Chem. Soc.* **2017**, *139*, 4042-4051; d) Y. Shoji, Y. Ikabata, Q. Wang, D. Nemoto, A. Sakamoto, N. Tanaka, J. Seino, H. Nakai, T. Fukushima, *J. Am. Chem. Soc.* **2017**, *139*, 2728-2733; e) J. Yang, X. Gao, Z. Xie, Y. Gong, M. Fang, Q. Peng, Z. Chi, Z. Li, *Angew. Chem. Int. Ed.* **2017**,

56, 15299-15303; *Angew. Chem*. **2017**, *129*, 15501-15505; f) E. Hamzehpoor, D. F. Perepichka, *Angew. Chem. Int. Ed.* **2016**, *59*, 9977-9981; *Angew. Chem*. **2016**, *132*, 10063-10067.

[13] a) S. A. Bagnicha, N. N. Khropika, V. N. Knykshtoa, A. L. Mikhalchuk, *Chem. Phys.* **2001**, *274*, 29-35; b) S. Bhattacharyya, L. R. Sousa, S. Ghosh, *Chem. Phys. Lett.* **1997**, *269*, 314-320; c) T. Itoh, *J. Chem. Phys.* **1987**, *87*, 4361-4367; d) T. Itoh, *J. Lumin.* **2004**, *109*, 221-225; e) T. Nakayama, K. Sakurai, K. Ushida, K. Kawatsura, K. Hamanoue, *Chem. Phys. Lett.* **1989**, *164*, 557-561; f) S. Samanta, M. B. Roy, M. Chatterjee, S. Ghosh, *J. Lumin.* **2007**, *126*, 230-238.

[14] Z. He, W. Zhao, J. W. Y. Lam, Q. Peng, H. Ma, G. Liang, Z. Shuai, B. Z. Tang, *Nat. Commun.* **2017**, *8*, 416.

[15] F. Y. Li, S.Guo, Y. Y. Qin, Y. X. Shi, M. P. Han, Z. F. An, S. J. Liu, Q. Zhao, W. Huang, *Adv. Opt. Mater*. **2019**, *7*, 1900511.

[16] T. Wang, Z. B. Hu, X. C. Nie, L. K. Huang, M. Hui, X. Sun, G. Q. Zhang, *Nat. Commun.* **2021**, *12*, 1364.

[17] Y. Liu, Z. M. Ma, J. W. Liu, M. X. Chen, Z. Y. Ma, X. R. Jia, *Adv. Opt. Mater.* **2021**, *9*, 2001685.

[18] a) S. J. Woo, Y. H. Kim, J. J. Kim, *Chem. Mater.* **2021**, *33*, 5618−5630; b) T. Wang, Xi. G. Su, X. P. Zhang, X. C. Nie, L. K. Huang, X. Y. Zhang, X. Sun, Y. Luo, G. Q. Zhang, *Adv. Mater*. **2019**, *31*, 1904273; c) C. Zhou, S. Zhang, Y. Gao, H. Liu, T. Shan, X. Liang, B. Yang, Y. Ma, *Adv. Funct. Mater.* **2018**, *28*, 1802407; d) S. K. Behera, S. Y. Park, J. Gierschner, *Angew. Chem. Int. Ed*. **2021**, *60*, 22624–22638; *Angew. Chem*. **2021**, *133*, 22804-22820.

[19] a) A. Fukazawa and S. Yamaguchi, *Chem. Asian J.* **2009**, *4*, 1386-1400; b) X. Wang, S. L. Gong, D. T. Song, Z. H. Lu, S. N. Wang, *Adv. Funct. Mater*. **2014**, *24*, 7257-7271; c) M. Hirai, N. Tanaka, M. Sakai, and S. Yamaguchi, *Chem. Rev.* **2019**, *119*, 8291-8331; d) Z. M. Hudson, S. N. Wang, *Acc. Chem. Res*. **2009**, *42*, 1584-1596; e) S. Yamaguchi, A. Wakamiya, *Pure Appl. Chem.* **2006**, *78*, 1413-1424; f) F. Jäkle, *Chem. Rev*. **2010**, *110*, 3985-4022; g) E. Grotthuss, A. John, T. Kaese, M. Wagner, *Asian J. Org. Chem.* **2018**, *7*, 37-53; h) R. J. Kahan, W. Hirunpinyopas, J. Cid, M. J. Ingleson, R. A. W. Dryfe, *Chem. Mater*. **2019**, *31*,

1891−1898; i) S. S. Kothavale, J. Y. Lee, *Adv. Opt. Mater*. **2020**, *8*, 2000922; j) M. Gon, K. Tanaka, Y. Chujo, *Bull. Chem. Soc. Jpn*. **2019**, *92*, 7-18; k) G. Turkoglu, M. E. Cinar, T. Ozturk, *Molecules* **2017**, *22*, 1522; l) H. H. Hackney, D. F. Perepichka, *Aggregate* **2021**, e123; m) H. E. Hackney, D. G. Hall, *ChemPhotoChem* **2022**, e202100219.

[20] a) Z. Yuan, N. J. Taylor, T. B. Marder, I. D. Williams, S. K. Kurtz, L.-T. Cheng, *J. Chem. Soc., Chem. Commun*. **1990**, 1489-1492; b) C. D. Entwistle, T. B Marder, *Angew. Chem. Int. Ed*. **2002**, *41*, 2927-2931; *Angew. Chem*. **2002**, *114*, 3051-3056; c) C. D. Entwistle, T. B. Marder, *Chem. Mater*. **2004**, *16*, 4574-4585; d) L. Ji, S. Griesbeck, T. B. Marder, *Chem. Sci.* **2017**, *8*, 846-863; e) J. He, F. Rauch, M. Finze, T. B. Marder, *Chem. Sci.* **2021**, *12*, 128-147; f) S. M. Berger, T. B. Marder, *Mater. Horiz.* **2022**, *9*, 112-120; g) Z. Wu, J. C. Roldao, F. Rauch, A. Friedrich, M. Ferger, F. Würthner, J. Gierschner, T. B. Marder, *Angew. Chem. Int. Ed*. **2022**, https://doi.org/10.1002/anie.202200599.

[21] a) Z. Wu, J. Nitsch, J. Schuster, A. Friedrich, K. Edkins, M. Loebnitz, F. Dinkelbach, V. Stepanenko, F. Würthner, C. M. Marian, L. Ji, T. B. Marder, *Angew. Chem. Int. Ed.* **2020**, *59*, 17137-17144; *Angew. Chem*. **2020**, *132*, 17285-17292; b) Z. Wu, J. Nitsch, T. B. Marder, *Adv. Opt. Mater.* **2021**, 2100411.

[22] a) Q. Peng, H. Ma, Z. Shuai, *Acc. Chem. Res*. **2021**, *54*, 940-949; b) A. D. Nidhankar, Goudappagouda, V. C. Wakchaure, S. S. Babu, *Chem. Sci.* **2021**, *12*, 4216-4236.

[23] a) V. Stehr, R. F. Fink, B. Engels, J. Pflaum, C. Deibel, *J. Chem. Theory Comput.* **2014**, *10*, 1242-1255; b) M. Tabachnyk, B. Ehrler, S. Bayliss, R. H. Friend, N. C. Greenham, *Appl. Phys. Lett.* **2013**, *103*, 153302.

[24] S. M Berger, M. Ferger, F. Rauch, T. B Marder, *Chem. Eur. J.* **2021**, *27*, 9094-9101.

[25] S. Sarkar, H. P. Hendrickson, D. Lee, F. Devine, J. Jung, E. Geva, J. Kim and B. D. Dunietz, *J. Phys. Chem. C*, **2017**, *121*, 3771-3777.

[26] a) El-Sayed, *M. A. Acc. Chem. Res*. **1968**, *1*, 8–16; b) C. M. Marian, *Annu. Rev. Phys. Chem*. **2021**, *72*, 617-640.

[27] C. M. Marian, Spin-Orbit Coupling in Molecules. In Reviews in Computational Chemistry (eds K.B. Lipkowitz and D.B. Boyd), **2001**. https://doi.org/10.1002/0471224413.ch3.

[28] M. Mantina, A. C. Chamberlin, R. Valero, C. J. Cramer, D. G. Truhlar, *J. Phys. Chem. A* **2009**, *113*, 5806-5812.

[29] O. V. Dolomanov, L. J. Bourhis, R. J. Gildea, J. A. K. Howard, H. Puschmann, *J. Appl. Crystallogr.* **2009**, *42*, 339-341.

[30] a) J. J. McKinnon, A. S. Mitchell, M. A. Spackman, *Chem. Eur. J.* **1998**, *4*, 2136-2141; b) J. J. McKinnon, M. A. Spackman, A. S. Mitchell, *Acta Crystallogr. B* **2004**, *60*, 627-668; c) M. A. Spackman, P. G. Byrom, *Chem. Phys. Lett.* **1997**, *267*, 215-220; d) M. A. Spackman, D. Jayatilaka, *CrystEngComm* **2009**, *11*, 19-32.

[31] a) J. J. McKinnon, D. Jayatilaka, M. A. Spackman, *Chem. Commun.* **2007**, 3814-3816; b) A. Parkin, G. Barr, W. Dong, C. J. Gilmore, D. Jayatilaka, J. J. McKinnon, M. A. Spackman, C. C. Wilson, *CrystEngComm* **2007**, *9*, 648-652; c) M. A. Spackman, J. J. McKinnon, *CrystEngComm* **2002**, *4*, 378-392.

[32] B. H. Toby, *J. Appl. Crystallogr.* **2005**, *38*, 1040-1041.

[33] A. C. Larson, R. B. Von Dreele, Los Alamos National Laboratory Report LAUR, **2004**, pp. 86-748.

[34] TURBOMOLE V7.0 2015, A development of University of Karlsruhe and Forschungszentrum Karlsruhe GmbH, 1989-2007, TURBOMOLE GmbH, since 2007, available from http://www.turbomole.com.

[35] Gaussian 98 g09, Revision E.01, M. J. Frisch, G. W. Trucks, H. B. Schlegel, G. E. Scuseria, M. A. Robb, J. R. Cheeseman, G. Scalmani, V. Barone, B. Mennucci, G. A. Petersson, H. Nakatsuji, M. Caricato, X. Li, H. P. Hratchian, A. F. Izmaylov, J. Bloino, G. Zheng, J. L. Sonnenberg, M. Hada, M. Ehara, K. Toyota, R. Fukuda, J. Hasegawa, M. Ishida, T. Nakajima, Y. Honda, O. Kitao, H. Nakai, T. Vreven, J. A. Montgomery, Jr., J. E. Peralta, F. Ogliaro, M. Bearpark, J. J. Heyd, E. Brothers, K. N. Kudin, V. N. Staroverov, T. Keith, R. Kobayashi, J. Normand, K. Raghavachari, A. Rendell, J. C. Burant, S. S. Iyengar, J. Tomasi, M. Cossi, N. Rega, J. M. Millam, M. Klene, J. E. Knox, J. B. Cross, V. Bakken, C. Adamo, J. Jaramillo, R. Gomperts, R. E. Stratmann, O. Yazyev, A. J. Austin, R. Cammi, C. Pomelli, J. W. Ochterski, R. L. Martin, K. Morokuma, V. G. Zakrzewski, G. A. Voth, P. Salvador, J. J. Dannenberg, S.

Dapprich, A. D. Daniels, O. Farkas, J. B. Foresman, J. V. Ortiz, J. Cioslowski, and D. J. Fox, Gaussian, Inc., Wallingford CT, 2013.

[36] J. P. Perdew, M. Ernzerhof and K. Burke, *J. Chem. Phys*. **1996**, *105*, 9982–9985.

[37] J. P. Perdew, K. Burke and M. Ernzerhof, *Phys. Rev. Lett*. **1996**, *77*, 3865–3868.

[38] C. Adamo and V. Barone, *J. Chem. Phys.* **1999**, *110*, 6158–6170.

[39] K. Eichkorn, F. Weigend, O. Treutler, R. Ahlrichs, *Theor. Chem. Acc.*, **1997**, 97, 119.

[40] K.A. Peterson, D. Figgen, E. Goll, H. Stoll and M. Dolg, *J. Chem. Phys.*, **2003**, 119, 11113.

[41] S. Grimme, Mirko Waletzke, J. Chem. Phys. **1999**, 111, 5645-5655.

[42] C. M. Marian, A. Heil and M. Kleinschmidt, *WIREs Comput. Mol. Sci*. **2019**, 9, e1394.

[43] I. Lyskov, M. Kleinschmidt, C. M. Marian, *J. Chem., Phys.*, **2016**, 144, 034104

[44] A. D. Becke, *J. Chem. Phys.*, **1993**, 98, 1372.

[45] C. Lee, W. Yang, and R. G. Parr, *Phys. Rev. B* **1988**, 37, 785.

[46] M. Kleinscmidt, J. Tatchen and C. M. Marian, *J. Chem. Phys*. **2006**, *124*, 124101.

[47] M. Kleinschmidt and C. M. Marian, *Chem. Phys.* **2005**, *311*, 71-79.

[48] M. Kleinschmidt, J. Tatchen and C. M. Marian, *J. Comput. Chem*. **2002**, *23*, 824-833.

[49] M. Etinski, J. Tatchen and C. M. Marian, *J. Chem. Phys*. **2011**, *134*, 154105.

[50] M. Etinski, J. Tatchen and C. M. Marian, *Phys. Chem. Chem. Phys*. **2014**, *16*, 4740-4751.

[51] G. M. Sheldrick, *Acta Crystallogr. A Found Adv.* **2015**, *71*, 3-8.

[52] G. M. Sheldrick, *Acta Crystallogr. A* **2008**, *64*, 112-122.

[53] C. B. Hübschle, G. M. Sheldrick, B. Dittrich, *J. Appl. Crystallogr.* **2011**, *44*, 1281-1284.

[54] K. D. Brandenburg, Crystal and Molecular Structure Visualization, Crystal Impact, H. Putz & K. Brandenburg GbR, Bonn (Germany), 2017.

[55] C. F. Macrae, I. J. Bruno, J. A. Chisholm, P. R. Edgington, P. McCabe, E. Pidcock, L. Rodriguez-Monge, R. Taylor, J. van de Streek, P. A. Wood, *J. Appl. Crystallogr.* **2008**, *41*, 466-470.

[56] O. V. Dolomanov, L. J. Bourhis, R. J. Gildea, J. A. K. Howard, H. Puschmann, *J. Appl. Crystallogr.* **2009**, *42*, 339-341.

[57] P. R. Spackman, M. J. Turner, J. J. McKinnon, S. K. Wolff, D. J. Grimwood, D. Jayatilaka, M. A. Spackman, CrystalExplorer21 (2021), University of Western Australia, http://crystalexplorer.net.

[58] Y. A. Cho, D. S. Kim, H. R. Ahn, B. Canturk, G. A. Molander, J. Ham, *Org. Lett*. **2009**, *11*, 4330-4333.

[59] a) M. Ferger, S. M. Berger, F. Rauch, M. Schonitz, J. Ruhe, J. Krebs, A. Friedrich, T. B. Marder, *Chem. Eur. J*. **2021**, *27*, 9094-9101; b) Z. Wu, J. Nitsch, J. Schuster, A. Friedrich, K. Edkins, M. Loebnitz, F. Dinkelbach, V. Stepanenko, F. Würthner, C. M. Marian, L. Ji, T. B. Marder, *Angew. Chem. Int. Ed*. **2020**, *59*, 17137-17144.

CHAPTER FOUR

–

PURE BORIC ACID DOES NOT SHOW ROOM TEMPERATURE PHOSPHORESCENCE (RTP)

Pure Boric Acid Does Not Show Room Temperature Phosphorescence (RTP)

4.1 Introduction

Boric acid (BA) made from borax was first reported in 1832.[1] In the following 100 years, reactions of BA with other inorganic salts were continuously investigated.[2] Since 1920, researchers have been using BA as a glass matrix for optical materials, and have reported that pure BA does not luminesce.[3] Because of its high electron affinity, BA is a suitable matrix material for radical cations of aromatics such as naphthalene and anthracene to study their absorption spectra.[4] With its high degree of rigidity to suppress vibration- and rotation-assisted nonradiative decay,[5] delayed fluorescence[6] and phosphorescence[7] of aromatic hydrocarbons doped into a BA glass matrix can be realized even at room temperature. Due to these advantages, BA glass has become one of the most convenient and attractive media for studying the photophysical behavior of aromatic hydrocarbons.[8] In the last two decades, purely organic materials which display persistent room temperature phosphorescence (RTP) have received tremendous interest because of their low cost, easy fabrication, and high biological compatibility,[9] which led to a wide variety of applications in biological imaging,[10] organic light-emitting diodes (OLEDs),[11] and security printing technology.[12] Unlike for metal complexes, with strong spin-orbit coupling (SOC), intersystem crossing (ISC) in organic compounds, which plays an important role in phosphorescence emission, is typically less effective.[13] In addition, under ambient conditions, nonradiative deactivation by ISC and consecutive thermal relaxation as well as quenching by species such as O_2, rapidly deactivate the triplet excitons.[14] Therefore, on the one hand, introducing heavy atoms to enhance the SOC and incorporating non-metal heavy atoms or carbonyl groups with lone pairs[14] are useful approaches to develop RTP systems with high performance.[15] On the other hand, suppressing the nonradiative decay path through vibrational-assisted relaxation and avoiding collisions with O_2 by crystallization or polymerization are also key to realizing persistent afterglow.[5, 16] A variety of organic RTP materials were developed by utilizing the above strategies. However, concern for the existence of impurities and their role in contributing to the observed phosphorescence has been discussed since the 1920s.[3b, 17] Organic crystal impurities and their luminescence sensitization have been intensively analyzed in the following decades in solid state

physics;[17] however, this was largely overlooked in the materials science community, and has been raised again only recently.[18] For example, Liu's group identified and isolated a carbazole isomer which is responsible for many carbazole-related phosphors made from commercial carbazole sources[19] and Ma and co-workers designed a number of trace impurity-induced bicomponent RTP systems based on derivatives.[20] Zhang's group reported that a side product produced by reaction with the DMF solvent resulted in red RTP when doped into phthalimide hosts.[21] All of the above results show that even trace impurities can dramatically influence the photophysical properties of organic systems.

Figure 4-1 a) Synthesis of boric acid from $B(OMe)_3$. b) Photographs of BA as a ground powder and as crystals, taken under daylight. The ground powder retains crystallinity.

In 2021, P. Wu and co-workers reported that 'pure' BA exhibits RTP with a lifetime of up to 0.6 s in the crystalline state when irradiated at 280 nm under ambient conditions.[22] Based on our experience in research on 3-coordinate boron-containing optical materials,[23] and that of other leading research groups,[24] and increasing numbers of reports on so-called "unconventional" luminescence phenomena,[25] as well as the history noted above, we were suspicious of the reported phenomenon. Therefore, we synthesized pure BA from $B(OMe)_3$ to examine its optical properties, including any possible RTP, as crystals and ground powder (Figure 4-1a), noting that the ground powder retains crystallinity, i.e., it is not amorphous. When exposed to 254 nm UV light, in contrast to the previous report[22] there is no emission observed from either crystalline or powdered BA prepared as noted above. Upon turning off the UV light, the pure BA solid samples do not show any afterglow, indicating that the recently reported RTP from BA was induced by an unknown impurity in their

sample. Importantly, and in contrast, a commercial sample of BA of the type employed in the previous study[22] does show RTP in our spectrophotometers, as well as a very broad absorption starting at ca. 375 nm, which must be due to an impurity. In addition, our experimental and theoretical investigations suggest that there is no possibility of pure BA to show RTP at the excitation wavelength of 280 nm employed in reference [22], as the pure material has no absorption in that region of the spectrum (200-450 nm).

4.2 Results and Discussion

4.2.1 Photophysical Study

We synthesized and purified a sample of BA starting from $B(OMe)_3$, and obtained clean ^{11}B NMR spectra of our sample, both in solution and in the solid state. We then measured the absorption spectra of BA in methanol, isopropanol, and water solutions at concentrations of 10^{-5} M (Figure 4-2a). The cut-off wavelengths of methanol and isopropanol are 205 nm. There was no absorption peak observed at wavelengths longer than 205 nm, which indicates that aromatic species are not present in our sample of BA. The cut-off wavelength of water is 190 nm. There is also no absorption peak observed in the spectrum at >200 nm. Even upon increasing the concentration of BA in methanol to 10^{-4} or 10^{-3} M, no absorbance at >205 nm was observed (Figure 4-5). Solid state absorption spectra were then recorded on a Varian Cary 5 UV-vis-NIR spectrophotometer using a 'praying mantis diffuse reflectance' assembly that allowed us to record absorption spectra to 200 nm. Absorption and excitation spectra of anthracene in the solid state were also recorded as a reference (Figures 4-6 and 4-7). What is clear is that the spectrum of pure BA does not show any absorption in the region between 200 and 485 nm. In contrast, commercial BA (Sigma-Aldrich: 99.999% trace metals basis, the commercial material employed by Wu et al. with the highest purity as specified by the manufacturer) shows a broad absorption band with an onset at ca. 380 nm (Figure 4-2b), indicating the presence of impurities.

According to the study published by Wu et al.,[22] upon changing the excitation wavelength from 280 to 365 nm, the phosphorescence intensity continuously decreased. Therefore, we measured the photoluminescent (PL) emission and time-gated (1 ms) phosphorescence emission spectra of BA as

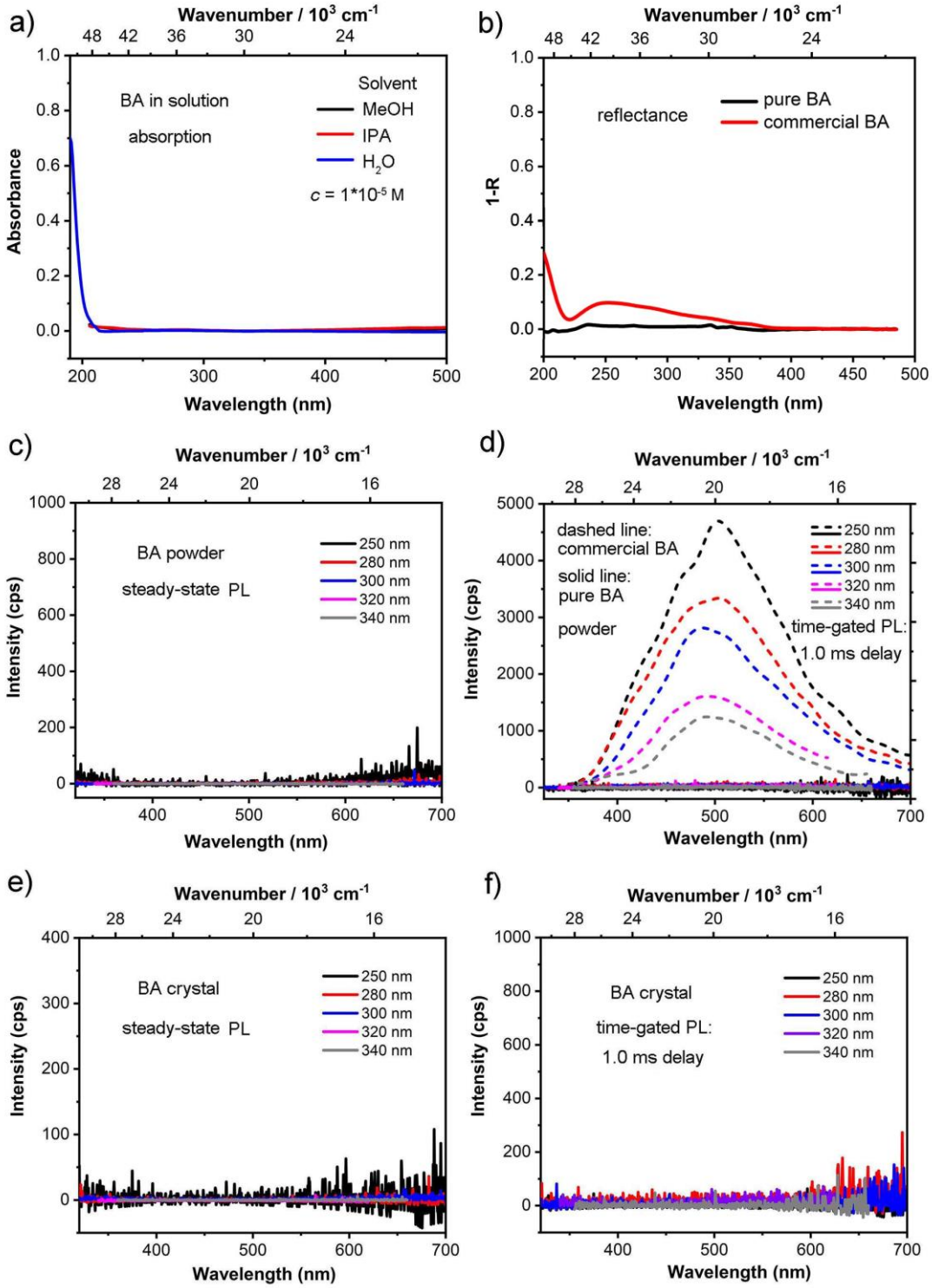

Figure 4-2 a) UV-vis absorption spectra of **pure BA** in MeOH, isopropanol and H_2O solutions (c = 10^{-5} mol/L). The onset of absorption at *ca.* 205 nm is due to the solvent cut-off. b) UV-vis absorption spectra (R = Reflectance) of solid samples of **pure, crystalline BA** (black) and **commercial BA** (red). Steady-state photoluminescence (PL) (c) and time-gated PL: 1.0 ms delay (d) spectra of **commercial BA** (dashed line) and **pure BA** (solid line) as a ground powder (not amorphous) at different excitation wavelengths under the same conditions. Photoluminescence (e) and time-gated (1.0 ms delay) emission (f) spectra of **pure, crystalline BA** at different excitation wavelengths.

both crystals and as a ground powder, again, noting that the powder retains crystallinity, with varied excitation wavelengths from 250 to 400 nm (Figures 4-2c to 4-2f and Figures 4-8 to 4-13). However, as expected, neither the PL nor the time-gated phosphorescence spectra of our pure BA show emission bands, either as a ground powder or as crystals. As a control experiment, we measured PL spectra of the commercial BA sample under the same experimental conditions; indeed, in this case a faint PL signal at room temperature was detected (see dashed lines in Figures 4-2d, and 4-15); the PL spectra are similar but somewhat redshifted[26] and with a similar small blue shift upon going from room temperature to 77 K to that reported in Ref. [22]. It is further noted that the onset of PL (at ca. 370 nm) matches well with the absorption onset (at ca. 380 nm) of commercial BA (Figure 4-2b); this further indicates that the PL originates from the impurity which gives rise to these absorption features. Thus, our comparison of the absorption and PL features of pure and commercial BA undoubtedly proves that even trace impurity levels in commercial BA are sufficient to lead to RTP.

As in Ref. [22], we examined the commercial BA sample by both ^{1}H NMR (using D_2O, CD_3OD, CD_2Cl_2, and THF-d_8 as solvents) and HRMS, but did not obtain evidence for impurity levels larger than the detection limit. Nonetheless, it is clear that the commercial BA sample must contain some form of impurity which gives rise to the absorption and emission observed both in Ref. [22] and by us. We stress, in this context, that even trace amounts of luminescent impurities are easily detected by PL spectroscopy due to the exceptional sensitivity of the method. The nature and amount of this impurity remain unknown; however, we point out again that our synthesis of pure BA is based on $B(OMe)_3$, while industrial synthesis routes usually rely on reaction of boron-containing minerals with sulfuric acid.[27]

4.2.2 Crystal structure analysis

Next, we obtained crystals of pure BA from methanol and collected single-crystal X-ray diffraction data both at 100 K and at room temperature (Table 4-2). The crystal structures obtained are consistent with the published crystal structure of BA (ICSD-61354),[28] which belongs to the triclinic crystal system (space group $P\bar{1}$). The BA molecules are arranged in layers which are perpendicular to the *c* axis. Within one layer, they interact via strong hydrogen bonds with H···O distances in the range of

1.858 – 1.873 Å and O–H···O angles of 172.2 – 174.8° at 100 K, forming six-membered rings (Figures 4-3a and 4-22). The layers weakly interact via relatively short interplanar B···O contacts (3.031(2) and 3.064(2) Å at 100 K, Figure 4-3b). Unit-cell parameters determined at 100 K and room temperature are similar. The direction of the largest thermal expansion upon temperature increase is along the *c* axis, which is the stacking direction of the weakly interacting layers (B···O = 3.153(3) and 3.190(3) Å at 296 K). This results in an overall unit-cell volume expansion from 262.97(3) at 100 K to 273.50(19) $Å^3$ at room temperature upon temperature increase.

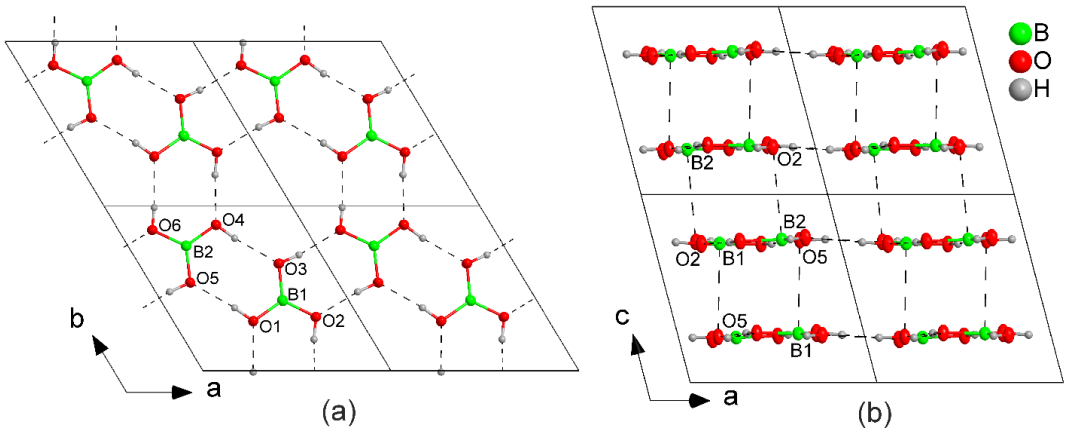

Figure 4-3 (a) One sheet of hydrogen-bonded BA molecules perpendicular to the *c* axis at 100 K. Four unit cells are shown within the (001) plane. (b) Four unit cells (2×1×2) of the crystal structure of BA projected along the *b* axis at 100 K. The closest interplanar B···O contacts (Å) are illustrated by dashed lines: B1···O5 = 3.064(2), B2···O2 = 3.031(2).

It needs to be noted here that the authors in Ref. [22] did not determine the crystal structure of their BA sample, but used the structural model of a trigonal boric acid polymorph, which can be found in the CCDC database (CCDC-1500066) and refers to the report from Kurakevych and Solozhenko,[29] for discussion in their paper. This is the only crystal structure of BA deposited in the CCDC database, while all other crystal structures of BA are deposited in the ICSD database (e.g., ICSD-61354 for the triclinic polymorph). However, Kurakevych and Solozhenko[29] used the structural model of Shuvalov and Burns[30] for a rare polymorph of BA, H_3BO_3-3*T*, in order to interpret their multiphase powder X-ray diffraction pattern obtained from a high-pressure, high-temperature synthesis of a boron subnitride. The H_3BO_3-3*T* polymorph has trigonal symmetry (space group $P3_2$, ICSD-281322) and was characterized by Shuvalov and Burns[30] as an unexpected product crystallizing in addition to the triclinic H_3BO_3-2*A* polymorph in an attempt to synthesize new sodium uranyl borate compounds. The authors in Ref. [22] mentioned a good match of the powder X-ray diffraction pattern

obtained from their boric acid sample with the structural model of trigonal H_3BO_3-3*T* (see Figure 4-9 in Wu et al.[22]). However, the trigonal model does not describe all observed reflections of the diffraction pattern. Instead, the diffraction pattern can be nicely interpreted as the crystal structure of triclinic H_3BO_3-2*A*, as is obvious from a simulation of the powder X-ray diffraction patterns of both polymorphs (Figure 4-24). Hence, we conclude that the BA sample in Ref. [22] was indeed the same triclinic polymorph of BA as that in our own study.

4.2.3 Theoretical study

Further negative evidence for an intrinsic cause of the appearance of RTP in solid BA arises from quantum-chemical calculations. This was in fact done in Ref. [22], based on time-dependent density functional theory (TD-DFT); however, the results were interpreted in an erroneous way. In fact, the authors focused on the natural transition orbital (NTO) topologies, which indicated some through-space interactions for BA clusters in the (110) plane. Furthermore, they showed how the TD-DFT calculated absorption spectra experience a bathochromic shift upon clustering. Nevertheless, the authors failed to discuss that the fact that their calculated maximum absorption wavelength of the BA clusters still resides in the far UV (reaching just 140 nm); under no circumstances can this be the source of their observed RTP in the visible range.[31]

In any case, as the calculated cluster sizes were not very large in the previous calculations, and one may argue that the results could depend on the functional employed, we calculated herein larger clusters, and extended them along the crystallographic *c* axis (see Figure 4-4; for DFT calculated natural transition orbitals (NTOs), see Figure 4-19). In this case, the B3LYP functional was employed, which tends to underestimate electronic transition energies,[32] and thus may define a lower limit for the appearance of BA cluster absorption. As shown in Figure 4-4, clustering of boric acid units in fact generally leads to a bathochromic shift of the electronic S_1 and T_1 transition energies; the shift becomes particular large if the clusters are extended in the *c*-direction. However, a rapid saturation is observed, so that the maximum shift of the clusters vs. the monomer amounts to ca. 0.65 eV for T_1 and 0.95 eV for S_1. Although the shift is considerable, we emphasize that the absorption remains in the deep UV (above 7 eV; 177 nm), in good agreement with our experimental results.

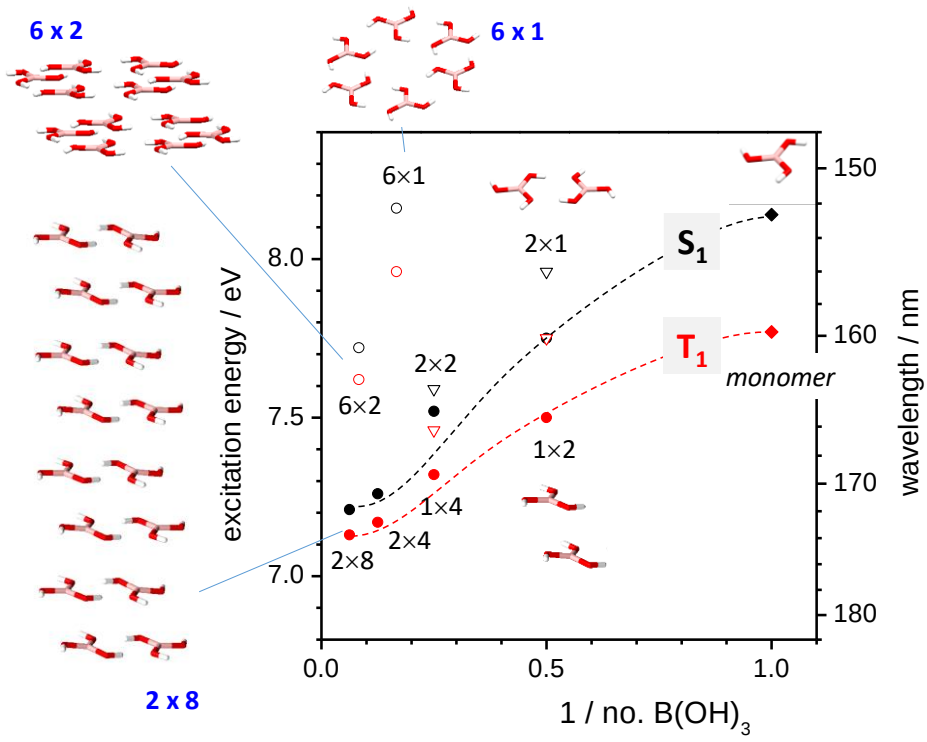

Figure 4-4 Vertical transition energies for the lowest excited singlet and triplet states (S_1, T_1) of BA and clusters thereof, as calculated by TD-DFT; dashed lines are guides for the eyes.

Our study has clearly shown that carefully purified BA, synthesized from $B(OMe)_3$, does not show any intrinsic phosphorescence in the solid state, in particular, in the visible range; TD-DFT calculations fully support our experimental results. In contrast, commercial BA evidently contains traces of (unknown) luminescent impurities, giving rise to blue-colored RTP. Impurity sources could well be side products from synthesis, including impurities in any solvents used, sample contamination, or photoproducts. Such (luminescent) trap states in molecular solids[33] can be directly excited if the concentration and absorption coefficient of the impurities are sufficiently high, which is in fact the case for commercial BA, as demonstrated in the current work (see Figure 4-2b).

Nevertheless, we emphasize that trap luminescence in molecular solids can also be observed if the trap absorption is very low (i.e., below the detection limit) but absorption of the host (i.e. the bulk material) is sufficiently high, as the traps may then very efficiently be reached by exciton migration,[34, 35, 36] down to molar ratios as low as 10^{-8}.[5, 37, 38] We emphasize that a whole generation of solid state physicists was engaged to clarify PL phenomena in organic solids and to disentangle pristine PL of a specific material from dopant/impurity-related PL.[17b, 39] This has been achieved for

materials, e.g., naphthalene and perylene, by sophisticated purification techniques such as zone refinement by the Bridgman method,[40] but obviously has remained unnoticed by many in the currently active community of chemists working on related phenomena. If the host is non-luminescent, exclusive sensitized PL is observed; otherwise dual PL will be perceived.[33c] These sensitizer concentrations can be so low that an unambiguous proof for the absence of trap states by standard analytical methods is not possible; instead, only a negative proof can be given. This type of 'falsification procedure' (negative proof) was successfully followed in the current work; such proof is tedious, but of tremendous importance as it gives a clear, general warning for reports on uncommon luminescence phenomena. In fact, as stated earlier,[5] it seems likely that many reports on so-called 'unconventional luminescence' from solid-state samples of non-conjugated chromophores,[25] may suffer from impurity problems as reported here for commercial BA.

4.3 Conclusions

Boric acid (BA) can be used as an excellent glass matrix, which, when pure, does not display any fluorescence or phosphorescence in the solid state. Our absorption spectra, measured both in solution and in the solid state, clearly show that it is not possible for BA to be excited at wavelengths longer than 200 nm. Our theoretical studies further suggest that the excitation of BA cannot occur at wavelengths longer than 175 nm. Our emission measurements also prove that there is no luminescence from pure BA in the visible region of the spectrum. All above results prove that the reported RTP from commercial BA must have been induced by unknown impurities. We are indeed of the opinion that such 'falsification procedures' to explore all possible avenues for 'negative proof' should be attempted in all original research, especially on systems which display unusual luminescence properties, for example, and for which there is no reason to expect such properties, as this represents good scientific practice. In addition, as we show by discussion of the ca. 100-year history of the use of BA glasses as hosts for RTP systems, it is incumbent upon researchers to search and read the literature carefully, and to cite an appropriate list of relevant publications.

4.4 Experimental details and characterization data

4.4.1 General information details

The starting material, trimethyl borate, was purchased from Alfa Aesar and was used without further purification. Organic solvents for synthetic reactions were HPLC grade, further treated to remove trace water using an Innovative Technology Inc. Pure-Solv Solvent Purification System and deoxygenated using the freeze-pump-thaw method. The synthetic reaction was performed in air at room temperature. The solution ^{11}B NMR spectrum was measured on a Bruker Avance III HD 300 MHz (^{11}B, 96 MHz) NMR spectrometer. The $^{11}B\{^{1}H\}$ RSHE/MAS (Rotor Synchronized Hahn Echo/Magic Angle Spinning) solid-state NMR spectra were recorded on a Bruker Avance Neo WB 400 MHz spectrometer operating at 128.38 MHz for ^{11}B and 400.13 MHz for ^{1}H, using a 4 mm (o.d.) ZrO_2 rotor spinning at 14.8 KHz. The spectra were obtained using a new Bruker 4 mm CP/MAS ATM BBO/^{1}H&^{19}F iProbe. The selective 90° ^{11}B low power pulse was calibrated to 25 ms, to irradiate only the central transition. The acquisition time was 25 ms and the relaxation delay was set to 20 s. Chemical shifts were calibrated externally to the low field shift of adamantane (38.48 ppm). The ^{11}B solid-state spectra were simulated using the software package SOLA.[41]

General photophysical measurements. All measurements were performed in standard quartz cuvettes (1 cm × 1 cm cross-section). UV-visible absorption spectra were recorded using a Perkin Elmer LAMBDA 465 UV/Vis spectrophotometer. Solid state UV-vis absorption (reflectance) spectra were recorded using a Praying Mantis Diffuse Reflectance Accessory on a Varian Cary 5 UV-vis-NIR spectrophotometer with deuterium (UV) and quartz-iodide (vis) lamps as light sources, and PMT (UV-vis) and lead sulfide photocell (NIR) detectors. $BaSO_4$ was used as the reference. To ensure the reliability of the measurement of the boric acid sample, we recorded the reflectance and excitation spectra of anthracene, which shows excellent agreement between the two methods (Figures 4-6 and 4-7). Note the inverted relationship of the vibronic fine structure between the reflectance and excitation spectra of anthracene, a result of 'inner-filter' effects, which can become dramatic for solid samples due to their extremely high concentrations. See footnote 200 in reference 42. The emission spectra were recorded using an Edinburgh Instruments FLSP920 spectrometer equipped with a double monochromator, operating in right angle geometry mode. The time-gated (delay time 1.0 ms) phosphorescence spectra were measured using a μF920 pulsed 60 W Xenon microsecond flashlamp, with a repetition rate of 100 Hz at room temperature. All spectra were fully corrected for the spectral

response of the instrument. For comparison, additional spectra were recorded on an Edinburgh Instruments FLSP980 spectrometer, and are labelled as such below.

Single crystal growth: $B(OH)_3$ (62 mg, 1 mmol) was dissolved in 10 mL of MeOH in a test tube which was placed in a fumehood at room temperature in air, and the solvent was allowed to evaporate slowly. Colorless crystals suitable for single-crystal X-ray diffraction formed after *ca*. 24 h.

Crystal structure determinations Crystals suitable for single-crystal X-ray diffraction were selected, coated in perfluoropolyether oil, and mounted on polyimide microloops. Diffraction data of boric acid at 100 K were collected on a Rigaku XTALAB Synergy S diffractometer with a semiconductor HPA-detector (HyPix-6000) using Cu-Kα radiation monochromated by multi-layer focusing mirrors. The crystal was cooled using an Oxford Cryostreams 800 low-temperature device. Diffraction data at ambient temperature (296 K) were collected on a BRUKER X8-APEX II diffractometer with a CCD area detector and multi-layer mirror monochromated Mo-Kα radiation. The images were processed and corrected for Lorentz-polarization effects and absorption as implemented in the Rigaku and Bruker software packages, respectively. The crystal structure was solved using the intrinsic phasing method (SHELXT)[43] and Fourier expansion technique. All non-hydrogen atoms were refined in anisotropic approximation, with hydrogen atoms 'riding' in idealized positions, by full-matrix least squares against F^2 of all data, using SHELXL[44] software and the SHELXLE graphical user interface.[45] The crystal structure was transformed to the non-standard setting reported for orthoboric acid by Gajhede *et al*.[46] Diamond[47] software was used for graphical representation. Other structural information was extracted using Mercury[48] and OLEX2[49] software. Crystal data and experimental details are listed in Table 4-1; full structural information has been deposited with Cambridge Crystallographic Data Centre. CCDC-2122545 ($B(OH)_3$ – 100 K) and 2122546 ($B(OH)_3$ – 296 K).

Computational Treatment. The ground state (S_0) geometry of boric acid was optimized by density functional theory (DFT) in vacuum, constrained to C_{3h} symmetry. Vertical transition energies for singlet and triplet states (S_n, T_n) were obtained by single point calculations on the S_0 geometry using time-dependent (TD) DFT. Implicit solvent effects were considered via the polarizable continuum model (PCM) using water as a solvent. Adiabatic energies were obtained by excited state geometry

optimization of the S_1 state. For the cluster calculations, molecular structures from the X-ray crystallographic analysis were replaced by DFT-optimized ones, while intermolecular separations were retained from the experimental data. To obtain fully optimized S_0 and S_1 geometries in the crystal, quantum Mechanics/Molecular Mechanics (QM/MM) calculations were performed, using the ONIOM approach.[50] For this, the MM atoms were frozen in their experimental crystal structure positions and treated with the Dreiding force field. The atoms in the QM region were treated at the DFT level. Optimized geometries and their normal coordinates were only obtained for the QM region; for details, see Refs. [51, 52]. For all calculations, the B3LYP functional and 6-311g(d) basis set were used as defined in the Gaussian 09 program package.[53] CASSCF (complete active space self-consistent field) optimization of BA in the S_0 and S_1 states were performed using the OpenMolcas package[54,55] including all $\pi\pi^*$ orbitals[56] and applying the ANO-RCC-VTZP basis-set.[57]

4.4.2 Synthesis

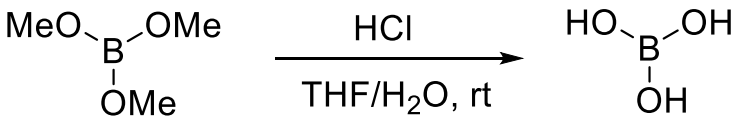

Trimethyl borate (0.9 mL, 8.0 mmol) was stirred in 65 mL of a 4:1 mixture of THF and water for 30 min, at which time aqueous hydrochloric acid (1N, 5.6 mL, 5.6 mmol) was added to the suspension. The reaction mixture was stirred at ambient temperature for overnight. The reaction mixture was diluted with water (30 mL) and extracted with ethyl acetate (3 x 60 mL). The combined extracts were washed with water (2 x 30 mL) and brine (30 mL), dried over sodium sulfate, filtered, and concentrated to dryness by rotary evaporation. The residue was washed with small portions of hexane, to give a colorless, solid product. The solid $B(OH)_3$ was dissolved in methanol at room temperature. Then the solution was transferred to a refrigerator and recrystallized at least 3 times at -25 °C until pure material was obtained as indicated by ^{11}B NMR spectroscopy. Importantly, even the crude material prior to recrystallization did not show RTP.

Solution ^{11}B NMR (96 Hz, 298 K, D_2O): δ = 19.49 ppm.

Simulation parameters of the ^{11}B RSHE/MAS of lab-made $B(OH)_3$ (Figure S14): δ_{iso} = 20.1 ± 0.1 ppm (isotropic chemical shift), C_Q = 2506 ± 10 kHz (quadrupole coupling constant), ηQuad = 0.04 ± 0.02 (quadrupolar asymmetry parameter), LB = 80 Hz (line broadening parameter).

Simulation parameters of the ^{11}B RSHE/MAS of commercial $B(OH)_3$ (Figure S15): δ_{iso} = 20.2 ± 0.1 ppm (isotropic chemical shift), C_Q = 2510 ± 10 kHz (quadrupole coupling constant), ηQuad = 0.03 ± 0.02 (quadrupolar asymmetry parameter), LB = 110 Hz (line broadening parameter).

4.4.3 Photophysical data

All emission and excitation spectra were recorded on an Edinburgh Instruments FLS920 spectrophotometer unless otherwise indicated. Comparison spectra recorded on an Edinburgh Instruments FLS980 spectrophotometer are labelled as such.

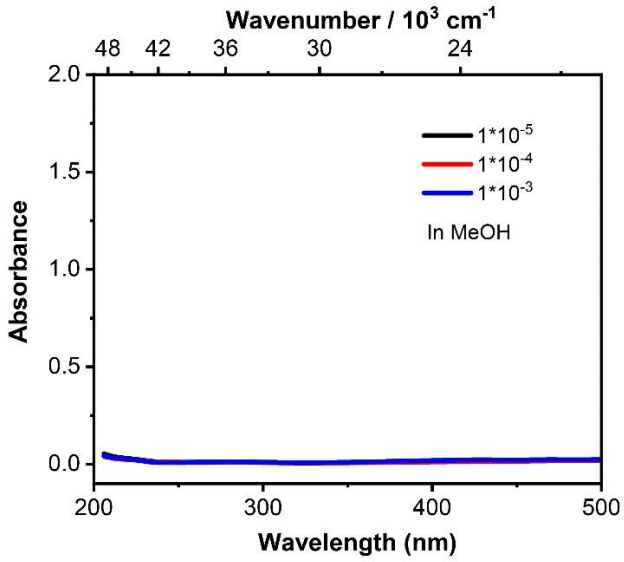

Figure 4-6. Absorption spectra of $B(OH)_3$ in MeOH solutions with varied concentration (c = 10^{-5}, 10^{-4} and 10^{-3} mol/L).

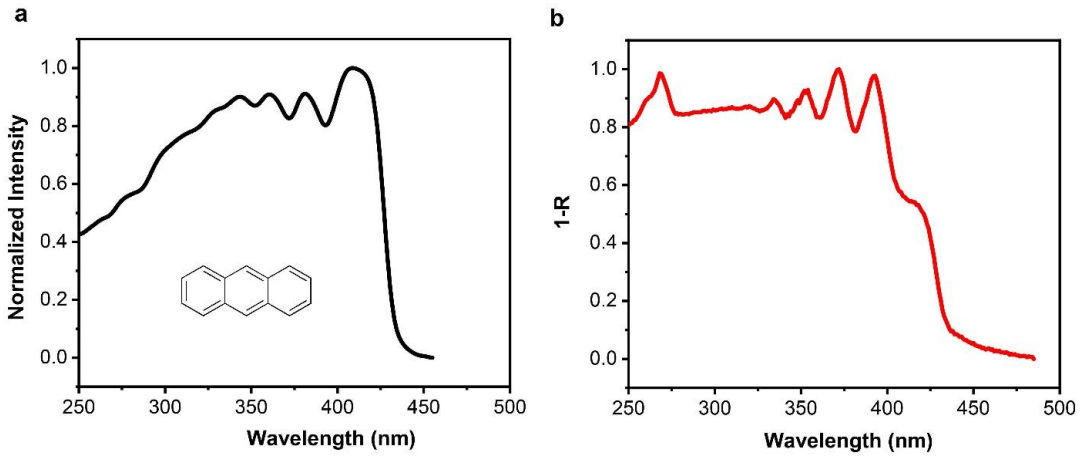

Figure 4-7. Excitation (a) and absorption (b) spectra of anthracene in the crystalline state at room temperature in air (R = Reflectance).

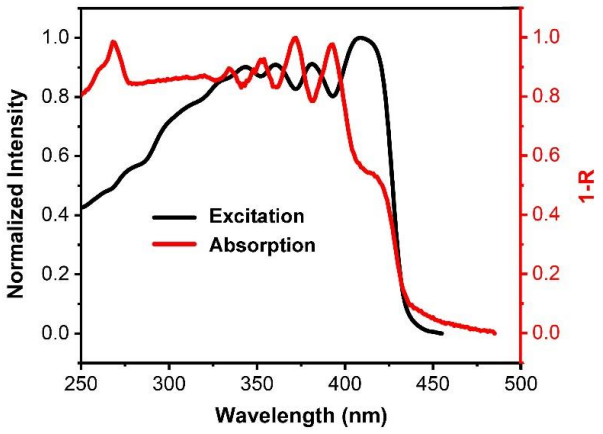

Figure 4-8. Comparison of excitation and absorption spectra of anthracene in the crystalline state at room temperature in air (R = Reflectance).

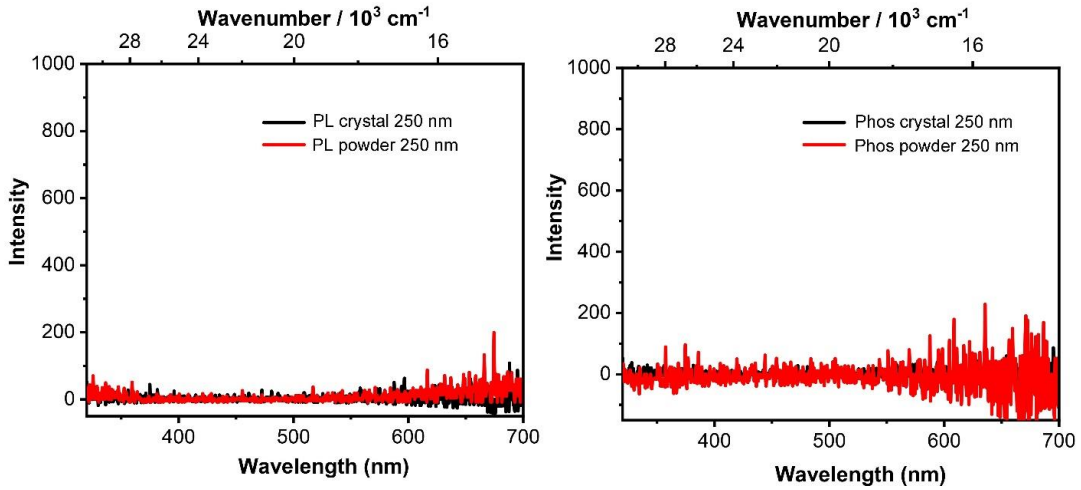

Figure 4-9. Photoluminescent emission (left) and time-gated (delay time = 1 ms) phosphorescence emission (right) spectra of $B(OH)_3$ in the crystal and powder states excited at 250 nm.

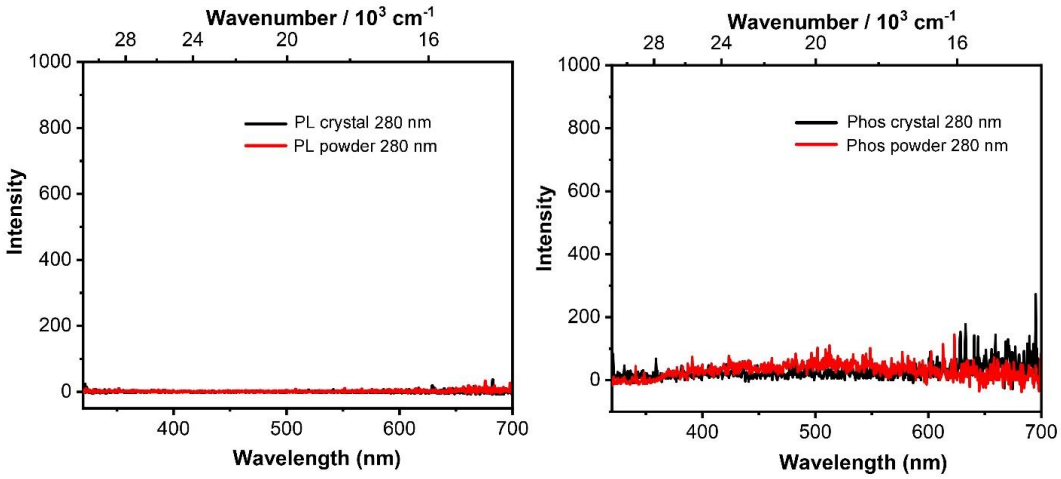

Figure 4-10. Photoluminescent emission (left) and time-gated (delay time = 1 ms) phosphorescence emission (right) spectra of $B(OH)_3$ in the crystal and powder states excited at 280 nm.

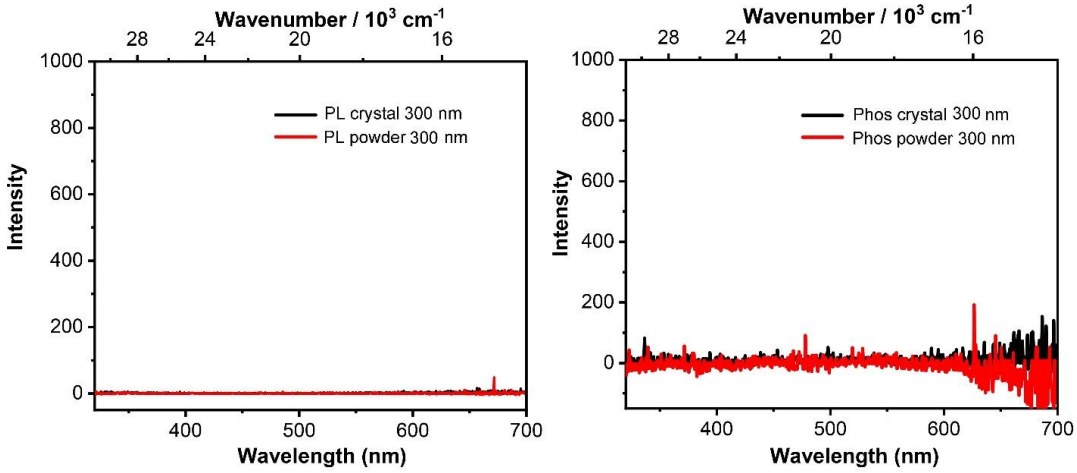

Figure 4-11. Photoluminescent emission (left) and time-gated (delay time = 1 ms) phosphorescence emission (right) spectra of $B(OH)_3$ in the crystal and powder states excited at 300 nm.

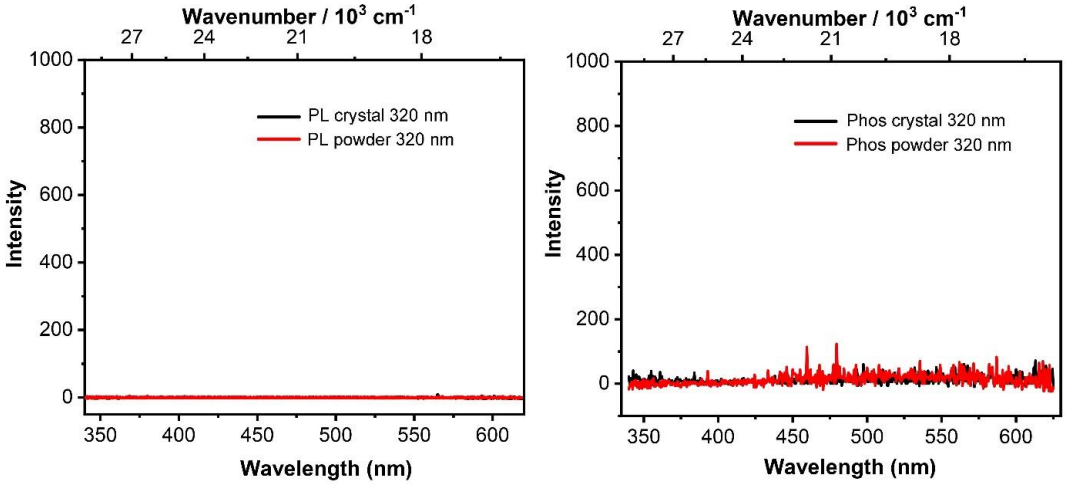

Figure 4-12. Photoluminescent emission (left) and time-gated (delay time = 1 ms) phosphorescence emission (right) spectra of $B(OH)_3$ in the crystal and powder states excited at 320 nm.

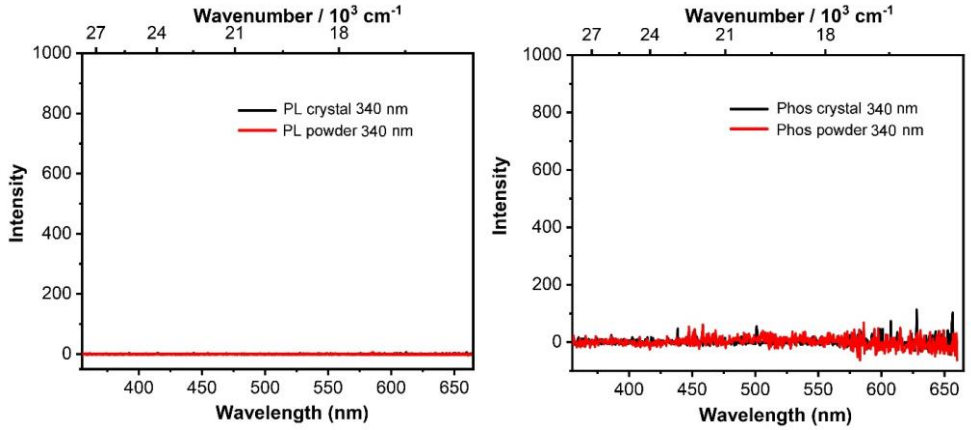

Figure 4-13. Photoluminescent emission (left) and time-gated (delay time 1 ms) phosphorescence emission (right) spectra of $B(OH)_3$ in the crystal and powder state excited at 340 nm.

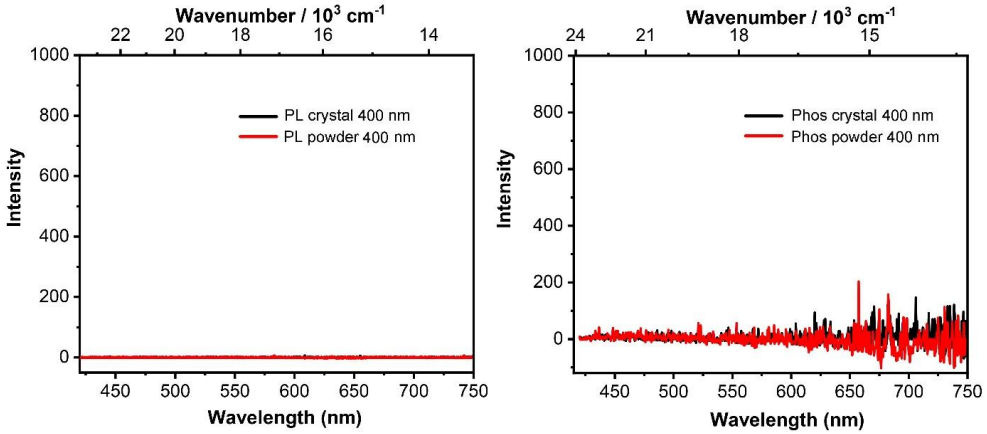

Figure 4-14. Photoluminescent emission (left) and time-gated (delay time = 1 ms) phosphorescence emission (right) spectra of $B(OH)_3$ in the crystal and powder states excited at 400 nm.

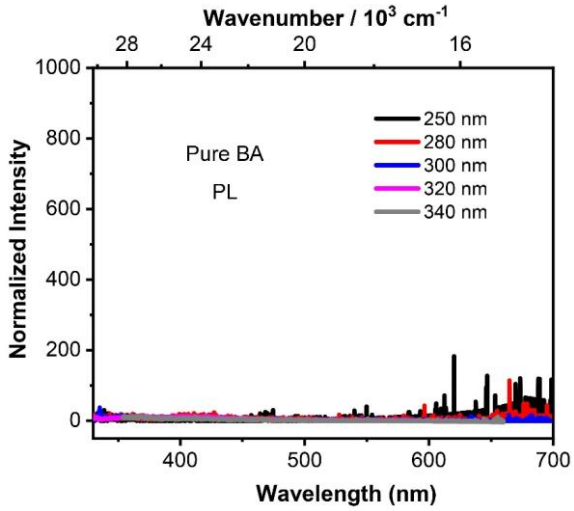

Figure 4-15. Normalized photoluminescence spectra of pure BA in crystalline state at different excitation wavelengths at room temperature on a different spectrophotometer (Edinburgh Instruments FLS980).

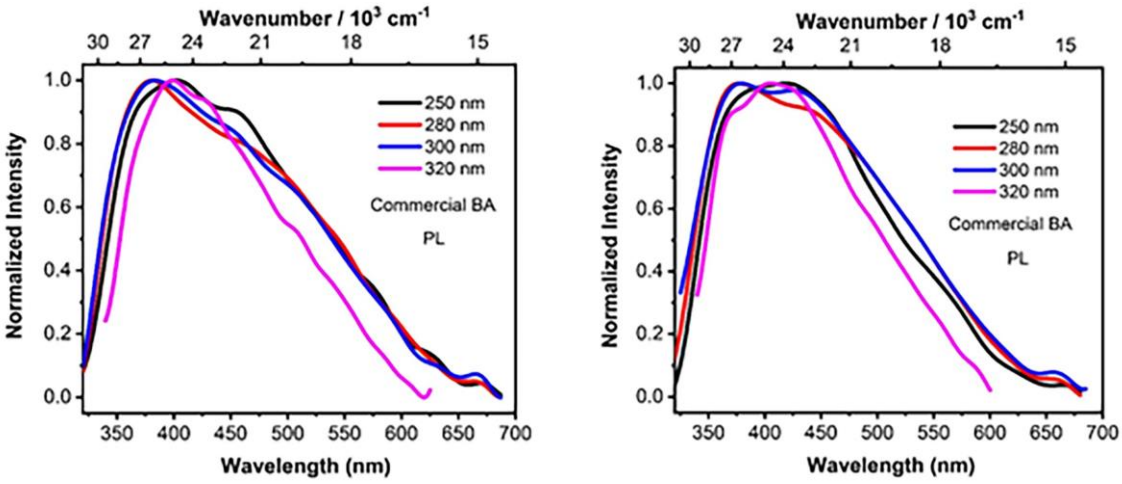

Figure 4-16. Normalized photoluminescence spectra of commercial BA (Sigma-Aldrich: 99.999%) at different excitation wavelengths at room temperature on two different spectrophotometers (left: Edinburgh Instruments FLS920; right Edinburgh Instruments FLS980).

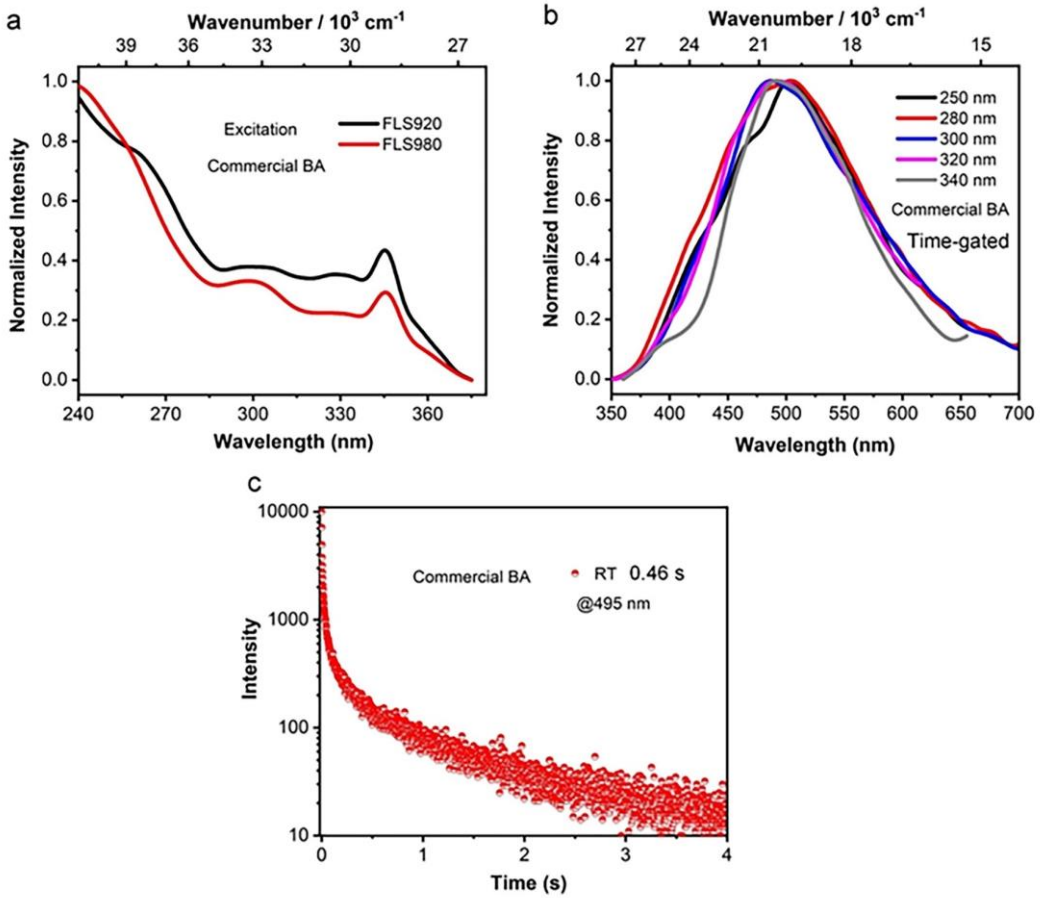

Figure 4-17. Normalized (a) excitation (390 nm) recorded on Edinburgh Instruments FLS920 and FLS980 spectrophotometers, (b) time-gated (delay time: 1 ms) phosphorescence at different excitation wavelengths (FLS920), and (c) phosphorescence decay (495 nm, λ_{ex} = 280 nm, FLS920) of commercial BA (Sigma-Aldrich: 99.999%) at room temperature.

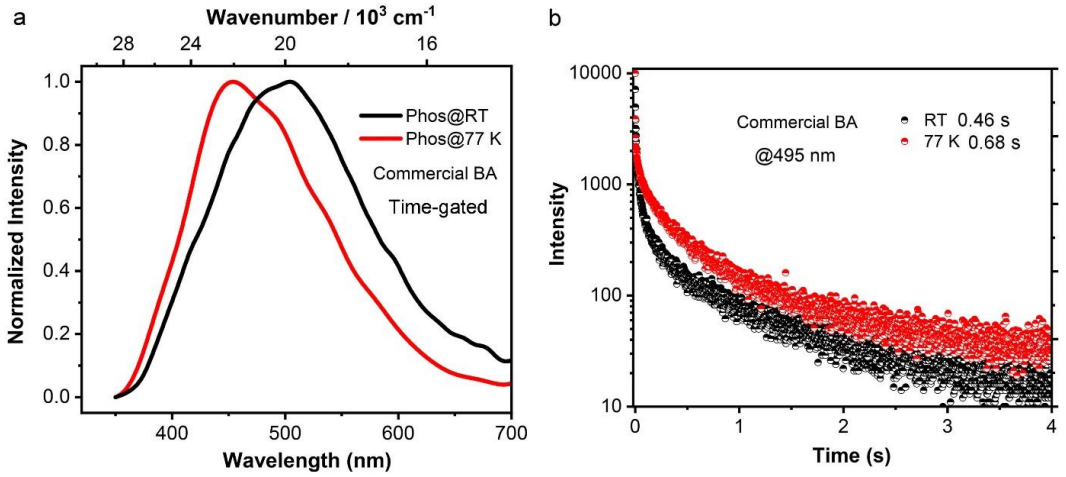

Figure 4-18. (a) Normalized time-gated (delay time: 1 ms) phosphorescence spectra of commercial BA (Sigma-Aldrich: 99.999%) at room temperature and 77 K, (b) Decays of phosphorescence (495 nm) at room temperature and 77 K (λ_{ex} = 280 nm). Recorded on the FLS920 spectrophotometer.

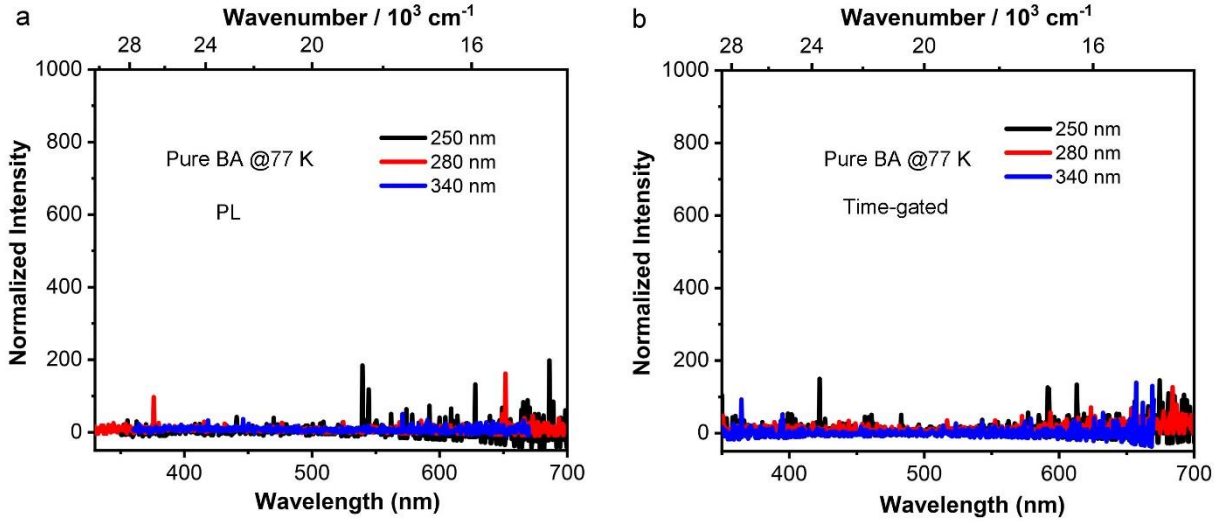

Figure 4-19. Photoluminescence (a) and time-gated (delay time = 1 ms) emission (b) spectra of pure BA in the crystalline state at different excitation wavelengths at 77 K. Recorded on the FLS920 spectrophotometer.

4.4.4 Solid crystal structure data

Table 4-1. Single-crystal X-ray diffraction data and refinement details of $B(OH)_3$ at 100 K and 296 K in comparison with literature data at 105 K.

Data	$B(OH)_3$	$B(OH)_3$	$B(OH)_3$ (reported)
CCDC number	2122545	2122546	ICSD number: 61354
Empirical formula	BH_3O_3	BH_3O_3	BH_3O_3
Formula weight / g·mol^{-1}	61.83	61.83	61.83
T / K	100(2)	296(2)	105
Radiation, λ / Å	Cu-K$_\alpha$ 1.54184	Mo-K$_\alpha$, 0.71073	Mo-K$_\alpha$, 0.71073
Crystal size / mm³	0.021×0.104×0.202	0.416×0.309×0.302	0.15×0.10×0.08
Crystal color, habit	colourless plate	colourless block	- [a]
μ / mm^{-1}	1.453	0.155	1.51
Crystal system	triclinic	triclinic	triclinic
Space group	$P\bar{1}$	$P\bar{1}$	$P\bar{1}$
a / Å	7.0181(3)	7.032(2)	7.0187 (14)
b / Å	7.0360(4)	7.045(4)	7.035 (2)
c / Å	6.3469(5)	6.5737(19)	6.5472 (12)
α / °	92.481(5)	92.51(3)	92.49 (12)
β / °	101.423(5)	101.19(2)	101.46 (2)
γ / °	119.759(5)	119.814(17)	119.76 (2)
Volume / Å^3	262.97(3)	273.4(2)	271.19 (1)
Z	4	4	4
ρ_{calc} / g·cm^{-3}	1.562	1.502	1.562
F(000)	128	128	128
θ range / °	7.219 – 74.402	3.203 – 26.368	up to 55.53
Reflections collected	5615	4287	15761
Unique reflections	1063	1100	1673 [I>2σ(I)] 34.65 < θ < 55.53
Parameters / restraints	79 / 0	79 / 0	73 / 0
GooF on F^2	1.067	1.247	1.004
R_1 [I>2σ(I)]	0.0426	0.0471	0.042
wR_2 (all data)	0.1252	0.1577	0.040 (wR)
Max. / min. residual electron density / e·Å^{-3}	0.276 / –0.395	0.224 / –0.223	0.70 / -0.70

[a] The corresponding information is not provided in the published reference.

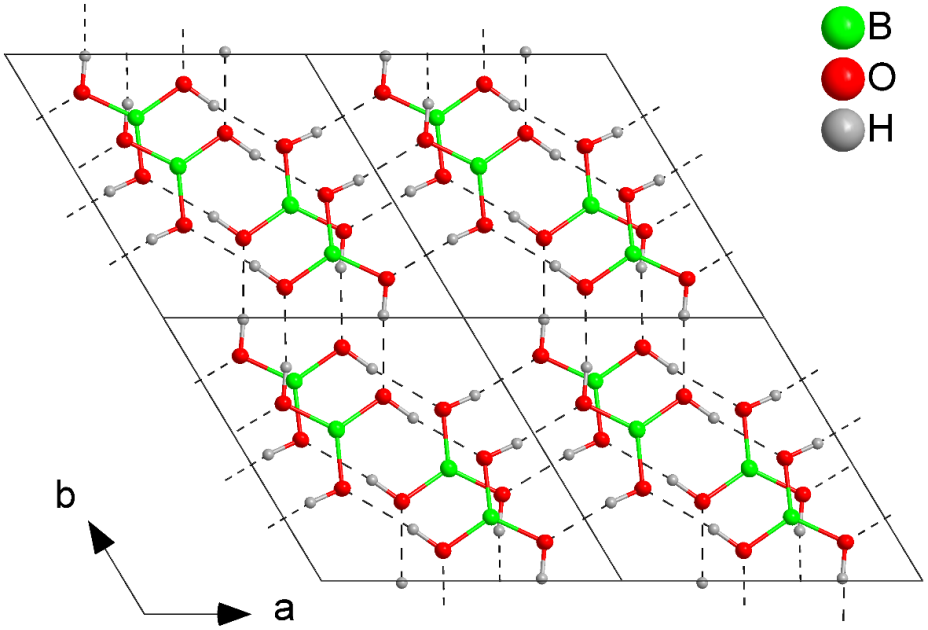

Figure 4-20. Eight unit cells (2×2×2) of the crystal structure of boric acid showing the hydrogen-bonding network within the sheets at 100 K.

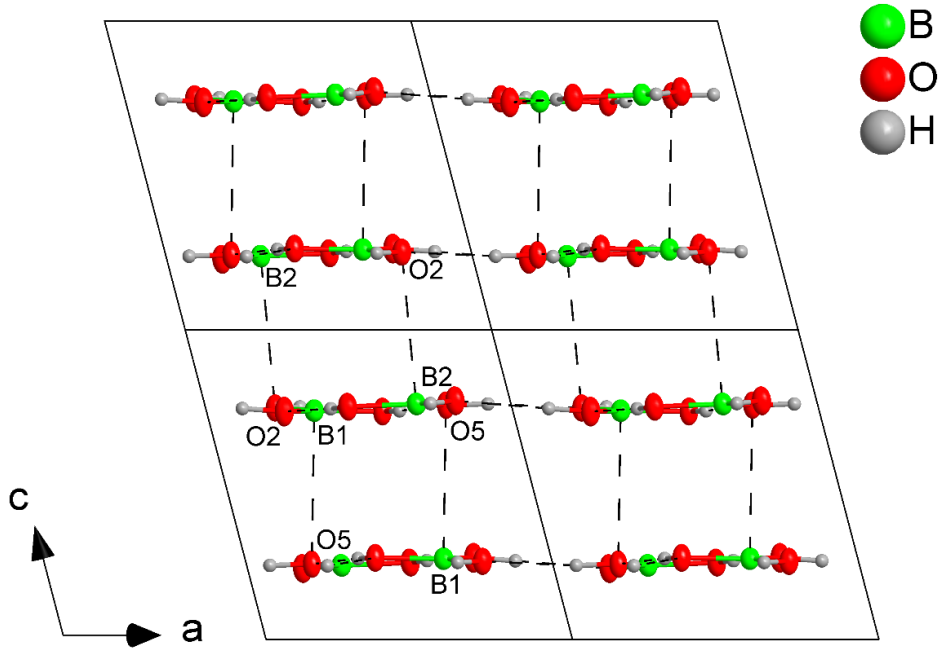

Figure 4-21. Four unit cells (2×1×2) of the crystal structure of boric acid projected along the *b* axis at 100 K. The closest interplanar B–O contacts (Å) are illustrated by dashed lines: B1–O5 = 3.064(2), B2–O2 = 3.031(2).

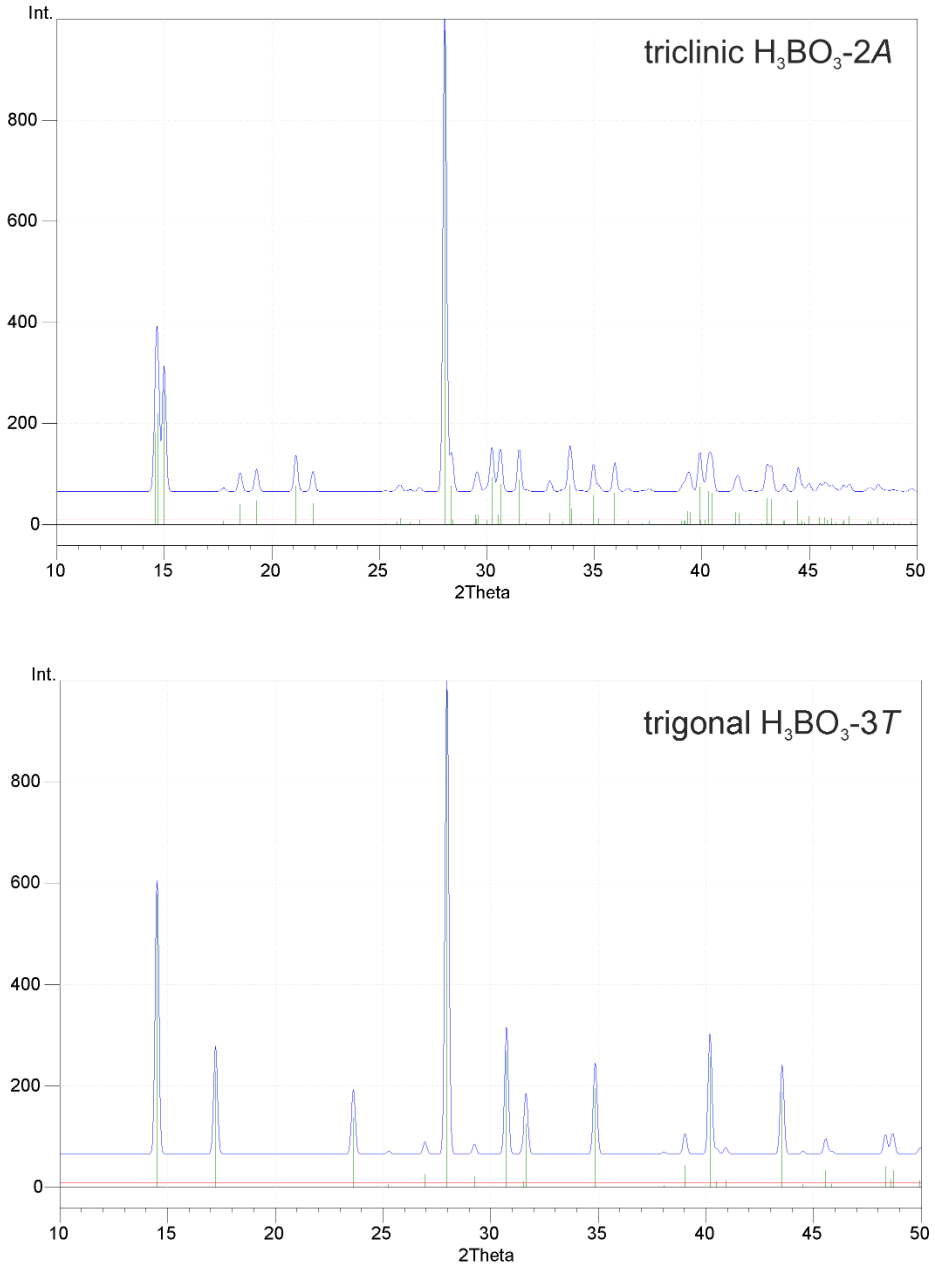

Figure 4-22. Simulated powder X-ray diffraction patterns (blue lines) and reflection positions (green lines) of the room temperature structures of triclinic boric acid, H_3BO_3-2*A* (top, our study) and trigonal boric acid, H_3BO_3-3*T* (bottom, ICSD-281322). Simulations were performed for Cu-Kα_1 radiation with a wavelength λ = 1.5406 Å using the Diamond program.

4.4.5 Theoretical calculation details

Table 4-2. Lowest excited singlet and triplet states (S_1, T_1) as calculated by TD-DFT, presenting vertical transition energies E_{vert} (and wavelength λ_{vert}), oscillator strength and composition (H = HOMO, L = LUMO).

	State	E_{vert} / eV	λ_{vert} / nm	Osc. Streng.	Main CI contribution
1x1	S_1	8.14	152	0.0000	H→L (88%)
	T_1	7.77	160	-	H→L (76%)
1x2	S_1	7.96	156	0.0000	H→L (90%)
	T_1	7.75	160	-	H→L (79%)
2x2	S_1	7.59	163	0.0006	H→L (91%)
	T_1	7.46	166	-	H→L (71%)
4x2	S_1	7.26	171	0.0004	H→L (91%)
	T_1	7.17	173	-	H→L (85%)
8x2	S_1	7.21	172	0.0013	H→L (80%)
	T_1	7.13	174	-	H→L (73%)
2x1	S_1	7.75	160	0.0008	H→L (94%)
	T_1	7.50	165	-	H→L (86%)
4x1	S_1	7.52	165	0.0004	H→L (82%)
	T_1	7.32	169	-	H→L (75%)
8x1	S_1	7.46	166	0.0005	H→L (69%)
	T_1	7.28	170	-	H→L (59%)
16x1	S_1	7.38	168	0.0013	H→L (45%)
					H→L+2 (28%)
	T_1	7.19	173	-	H→L (36%)
					H→L+2 (26%)

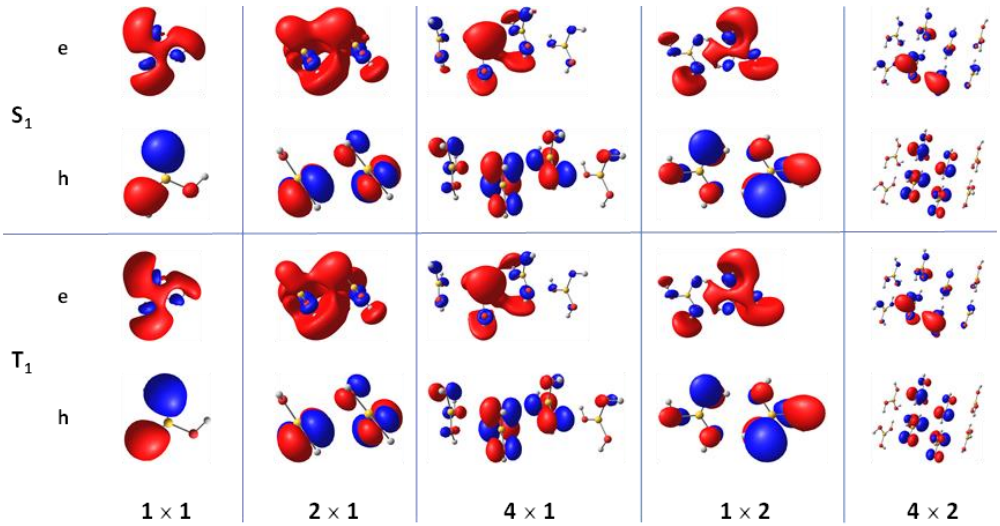

Figure 4-23. DFT calculated natural transition orbitals (NTOs) for the S_1 and T_1 states of $B(OH)_3$ and its clusters, representing holes (h) and electrons (e).

Excited State Relaxation. In Figure S19 of the Supporting Information of Ref. [58], the authors present calculations of the relaxed excited states for BA_x (x = 1,2,6) in the gas phase, being about 6 eV lower than the vertical absorption; this was, however, not further discussed by the authors. We thus repeated the calculations, optimizing the S_1 state of BA in the gas phase at the TD-DFT level; this indeed gives an adiabatic energy of only $E_{ad}(S_0 \leftrightarrow S_1)$ = 2.39 eV, compared with a vertical absorption of $E_{vert}(S_0 \rightarrow S_1)$ = 8.14 eV. However, closer inspection of the optimized S_1 geometry shows a considerable, partial heterolytic dissociation of one O···H bond as supported by the Mulliken charges analysis; a non-bonding distance of 1.747 Å was obtained (compared with 0.962 Å in S_0), while the respective B–O bond length is not significantly shortened. This photo*chemical* reaction is the reason for the very low energy of S_1, unnoticed in Ref. [58]. The same result was obtained by implicit solvent inclusion via PCM. Furthermore, in order to exclude a methodological failure, we performed CASSCF (complete active space self-consistent field) calculations, which confirmed the partial dissociation in S_1. We note that deprotonated BA species were indeed experimentally observed in the gas phase (by negative ion mass spectrometry),[59] as well as in crystalline Brønsted base conjugates.[60] Therefore, in a further step, we investigated whether such photochemical reaction is a possible pathway also in solid state BA; this, however, requires the explicit inclusion of the crystal environment. For this, we performed QM/MM (quantum mechanics/molecular mechanics) calculations of crystalline (and amorphous) BA. Which, in fact, also predicts the partial dissociation of BA in the S_1 state. We emphasize, however, that this (potential) photochemical path can only be activated by irradiation of the sample in the far UV (> 7 eV), and not in the 250-370 nm range; in fact, in the near/middle UV, pure BA does not absorb and, consequently, does not emit, as unambiguously demonstrated by the combined experimental and computational work of the present paper.

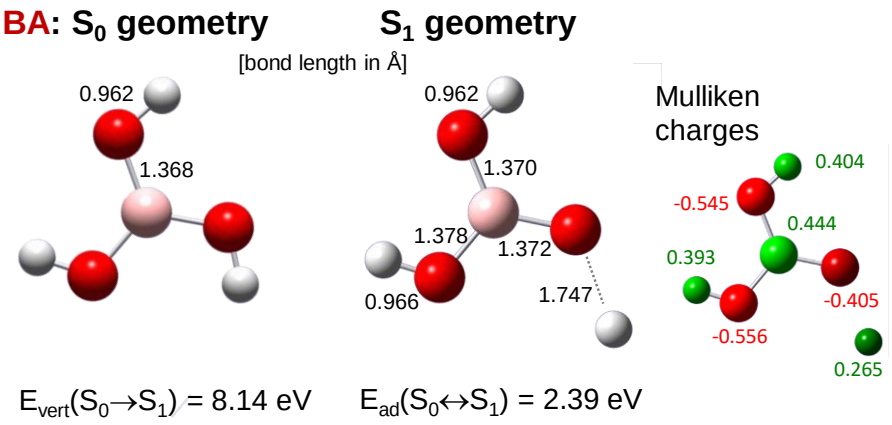

Figure 4-24. (TD)DFT-optimized geometries of BA in the gas phase for the ground state (S_0) and first excited singlet state (S_1) with bond lengths (in Å); Mulliken charges in S_1, vertical absorption energy E_{vert} and adiabatic energy E_{ad}.

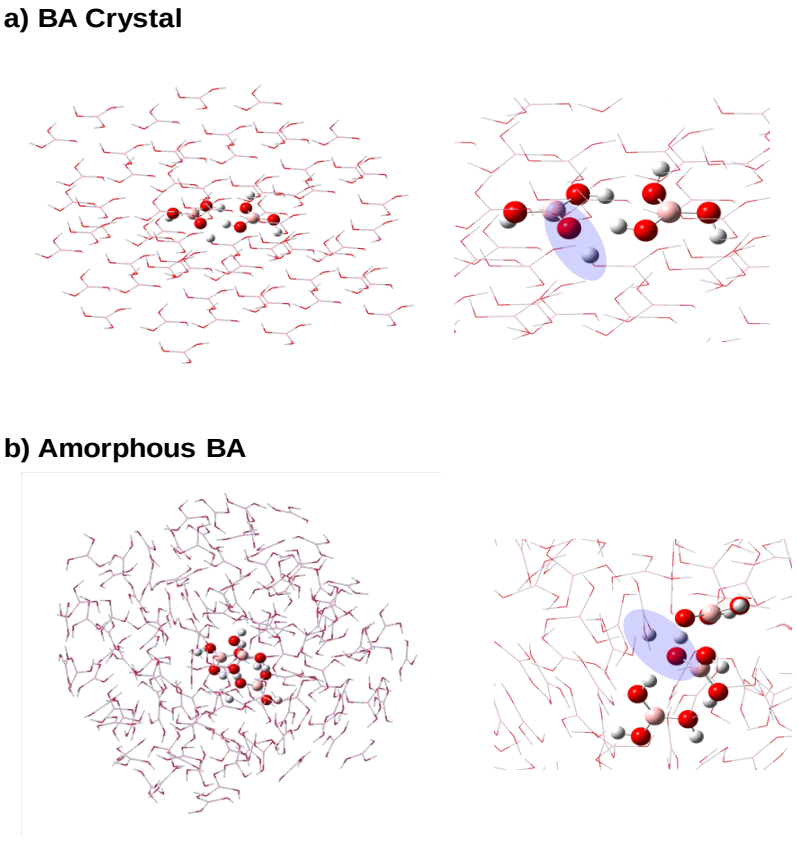

Figure 4-25. Optimized S_1 geometries of BA by QM/MM calculations; a) BA crystal, b) amorphous BA; partially dissociated bonds are highlighted in the zoom-in on the right.

4.5 Reference

[1] A. Duflos, *Chem. Zentbl.* **1832**, *3*, 382-384.

[2] a) H. Rost, *Chem. Zentbl.* **1851**, *22*, 636-638; b) D. Klein, *Chem. Zentbl.* **1880**, *51*, 666; c) O. Schneider, *Chem. Zentbl.* **1891**, *67*, 878-879.

[3] a) E. Tiede, *Ber. Dtsch. Chem. Ges.* **1920**, *53*, 2214-2216; b) E. Tiede, P. Wulff, *Ber. Dtsch. Chem. Ges.* **1922**, *55*, 588-597; c) Note the following statement in G. N. Lewis, D. Lipkin, T. T. Magel, *J. Am. Chem. Soc.* **1941**, *63*, 3005-3018, in which boric acid glass was used as a host material to examine the luminescence of fluorescein: "A glass prepared from the boric acid alone was found to have a faint blue phosphorescence of its own. However, the intensity of this light was found to be less than 1% of that emitted by the fluorescein." These authors did not specify the origin of the boric acid sample and they provided no indications of any attempts to purify it.

[4] a) F. Hughes, R. D. Kirk, F. W. Patten, *J. Chem. Phys.* **1963**, *50*, 872-876; b) Z. H. Zaidi, B. N. Khanna, *J. Chem. Phys.* **1967**, *50*, 3291-3296; c) T. C. Wen, L. C. Hwang, W. Y. Li, C. H. Chen, C. H. Wu, *Chem. Phys.* **2003**, *286*, 293-302.

[5] J. Gierschner, J. Shi, D. Roca-Sanjuán, B. Milián-Medina, S. Varghese, S. Y. Park, *Adv. Opt. Mater.* **2021**, *9*, 2002251.

[6] a) J. Grzywacz, *Nature* **1967**, *213*, 385-386; b) B. P. Singh, G. R. Kumar, K. K. Sharma, *Chem. Phys. Lett.* **1995**, *237*, 485-492; c) H. G. Wang, Z. Zhang, Q. Q. Yan, C. Y. Zhang, Y. F. Xing, Y. Xiong, F. Zhang, Z. G. Wang, *Chem. Phys. Lett.* **2020**, *5*, 13969-13973.

[7] a) M. Kasha, *J. Opt. Soc. Am.* **1948**, *38*, 1068-1073; b) G. N. Lewis, M. Calvin, M. Kasha, *J. Chem. Phys.* **1949**, *17*, 804-812; c) A. N. Russu, E. Vauthey, C. J. Wei, U. P. Wild, *J. Phys. Chem.* **1991**, *95*, 10496-10503.

[8] a) I. H. Munro, T. D. S. Hamilton, J. P. Ray, G. F. Moore, *Phys. Lett.* **1966**, *20*, 386-387; b) S. J. Payne, G. Q. Zhang, J. N. Demas, C. L. Fraser, B. A. Degraff, *J. Opt. Soc. Am.* **2011**, *65*, 1321-1324.

[9] a) S. Mukherjee, P. Thilagar, *Chem. Commun.* **2015**, *51*, 10988-11003; b) T. Zhang, X. Ma, H. Wu, L. Zhu, Y. Zhao, H. Tian, *Angew. Chem. Int. Ed.* **2020**, *59*, 11206-11216; *Angew. Chem.* **2020**, *132*, 11302-11312; d) Z. Wu, J. Nitsch, T. B. Marder, *Adv. Opt. Mater.* **2021**, 2100411; e) H. E. Hackney, D. F. Perepichka, *Aggregate*, **2021**, https://doi.org/10.1002/agt2.123.

[10] a) G. Zhang, G. M. Palmer, M. W. Dewhirst, C. L. Fraser, *Nat. Mater.* **2009**, *8*, 747-751; b) R. Kabe, N. Notsuka, K. Yoshida, C. Adachi, *Adv. Mater.* **2016**, *28*, 655-660; c) X. F. Wang, H. Y. Xiao, P. Z. Chen, Q. Z. Yang, B. Chen, C. H. Tung, Y. Z. Chen, L. Z. Wu, *J. Am. Chem. Soc.* **2019**, *141*, 5045-5050.

[11] a) S. Hirata, *Adv. Opt. Mater.* **2017**, *5*, 1700116; b) Q. Li, Z. Li, *Acc. Chem. Res.* **2020**, *53*, 962-973.

[12] a) L. Bian, H. Shi, X. Wang, K. Ling, H. Ma, M. Li, Z. Cheng, C. Ma, S. Cai, Q. Wu, N. Gan, X. Xu, Z. An, W. Huang, *J. Am. Chem. Soc.* **2018**, *140*, 10734-10739; b) H. Thomas, D. L. Pastoetter, M. Gmelch, T. Achenbach, A. Schlogl, M. Louis, X. Feng, S. Reineke, *Adv. Mater*. **2020**, *32*, e2000880.

[13] a) D. Li, F. Lu, J. Wang, W. Hu, X. M. Cao, X. Ma, H. Tian, *J. Am. Chem. Soc.* **2018**, *140*, 1916-1923; b) F. Li, S. Guo, Y. Qin, Y. Shi, M. Han, Z. An, S. Liu, Q. Zhao, W. Huang, *Adv. Opt. Mater.* **2019**, *7*, 1900511.

[14] N. J. Turro, V. Ramamurthy, J. C. Scaiano, Modern Molecular Photochemistry of Organic Molecules, University Science Books, Sausalito, CA, 2010, Chapter 5.

[15] Y. Yu, M. S. Kwon, J. Jung, Y. Zeng, M. Kim, K. Chung, J. Gierschner, J. H. Youk, S. M. Borisov, J. Kim, *Angew. Chem. Int. Ed.* **2017**, *56*, 16207-16211; *Angew. Chem*. **2017**, *129*, 16425-16429.

[16] a) M. S. Kwon, Y. Yu, C. Coburn, A. W. Phillips, K. Chung, A. Shanker, J. Jung, G. Kim, K. Pipe, S. R. Forrest, J. H. Youk, J. Gierschner, J. Kim, *Nat. Commun.* **2015**, *6*, 8947; b) M. Baroncini, G. Bergamini, P. Ceroni, *Chem. Commun.* **2017**, *53*, 2081-2093.

[17] a) M. Schwoerer, H. C. Wolf, Organic Molecular Solids, Wiley-VCH, Weinheim, Germany, 2007; b) K. W. Benz, H. C. Wolf, *Z. Naturforschg*. **1964**, *19a*, 177-181; c) N. Karl, *J. Cryst. Growth* **1990**, *99*, 1009-1016; d) N. Karl, *J. Cryst. Growth* **1981**, *51*, 509-517.

[18] a) A. D. Nidhankar, Goudappagouda, D. S. Mohana Kumari, S. K. Chaubey, R. Nayak, R. G. Gonnade, G. V. P. Kumar, R. Krishnan, S. S. Babu, *Angew. Chem. Int. Ed*. **2020**, *59*, 13079-13085; *Angew. Chem*. **2020**, *132*, 13179-13185; b) A. D. Nidhankar, Goudappagouda, V. C. Wakchaure, S. S. Babu, *Chem. Sci*. **2021**, *12*, 4216-4236.

[19] C. Chen, Z. Chi, K. C. Chong, A. S. Batsanov, Z. Yang, Z. Mao, Z. Yang, B. Liu, *Nat. Mater.* **2020**, *20*, 175-180.

[20] B. Ding, L. Ma, Z. Huang, X. Ma, H. Tian, *Sci. Adv.* **2021**, *7*, eabf9668.

[21] B. Chen, W. Huang, X. Nie, F. Liao, H. Miao, X. Zhang, G. Zhang, *Angew. Chem. Int. Ed.* **2021**, *60*, 16970-16973; *Angew. Chem*. **2021**, *133*, 17107-17110.

[22] H. Zheng, P. Cao, Y. Wang, X. Lu, P. Wu, *Angew. Chem. Int. Ed.* **2021**, *60*, 9500-9506; *Angew. Chem*. **2021**, *133*, 9586-9592.

[23] a) Z. Yuan, N. J. Taylor, T. B. Marder, I. D. Williams, S. K. Kurtz, L.-T. Cheng, *J. Chem. Soc., Chem. Commun*. **1990**, 1489-1492; b) C. D. Entwistle, T. B Marder, *Angew. Chem. Int. Ed*. **2002**, *41*, 2927-2931; *Angew. Chem*. **2002**, *114*, 3051-3056; c) C. D. Entwistle, T. B. Marder, *Chem. Mater*. **2004**, *16*, 4574-4585; d) L. Ji, S. Griesbeck, T. B. Marder, *Chem. Sci.* **2017**, *8*, 846-863; e) Z. Wu, J. Nitsch, J. Schuster, A. Friedrich, K. Edkins, M. Loebnitz, F. Dinkelbach, V. Stepanenko, F. Würthner, C. M. Marian, L. Ji, T. B. Marder, *Angew. Chem. Int. Ed.* **2020**, *59*, 17137-17144; *Angew. Chem*. **2020**, *132*, 17285-17292; f) J. He, F. Rauch, M. Finze, T. B. Marder, *Chem. Sci.* **2021**, *12*, 128-147; g) S. M. Berger, T. B. Marder, *Mater. Horiz.* **2022**, *9*, 112-120.

[24] a) A. Fukazawa and S. Yamaguchi, *Chem. Asian J.* **2009**, *4*, 1386-1400; b) X. Wang, S. L. Gong, D. T. Song, Z. H. Lu, S. N. Wang, *Adv. Funct. Mater*. **2014**, *24*, 7257-7271; c) M. Hirai, N. Tanaka, M. Sakai, and S. Yamaguchi, *Chem. Rev.* **2019**, *119*, 8291-8331; d) Z. M. Hudson, S. N. Wang, *Acc. Chem. Res*. **2009**, *42*, 1584-1596; e) S. Yamaguchi, A. Wakamiya, *Pure Appl. Chem.* **2006**, *78*, 1413-1424; f) F. Jäkle, *Chem. Rev*. **2010**, *110*, 3985-4022; g) E. Grotthuss, A. John, T. Kaese, M. Wagner, *Asian J. Org. Chem.* **2018**, *7*, 37-53; h) R. J. Kahan, W. Hirunpinyopas, J. Cid, M. J. Ingleson, R. A. W. Dryfe, *Chem. Mater*. **2019**, *31*, 1891−1898; i) S. S. Kothavale, J. Y. Lee, *Adv. Opt. Mater*. **2020**, *8*, 2000922; j) M. Gon, K. Tanaka, Y. Chujo, *Bull. Chem. Soc. Jpn*. **2019**, *92*, 7-18; k) G. Turkoglu, M. E. Cinar, T. Ozturk, *Molecules* **2017**, *22*, 1522; l) S. Y. Li, Z. B. Sun, C. H. Zhao, *Inorg. Chem.* **2017**, *56*, 8705-8717.

[25] a) Y. Wang, Z. Zhao, W. Z. Yuan, *ChemPlusChem* **2020**, *85*, 1065–1080; b) N. Jiang, D. Zhu, Z. Su, M. R. Bryce, *Mater. Chem. Front*. **2021**, *5*, 60-75.

[26] A possible reason for the observed discrepancy is that the PL spectra in Ref. [22] may not have been corrected for the (very pronounced) wavelength sensitivity of the photomultiplier (PMT) tube, as such a correction was not mentioned in the experimental part of their paper. It is further stressed that the companies' spectrometer presetting usually does not autocorrect PL spectra for the PMT sensitivity.

[27] D. M. Schubert, Boric Oxide, Boric Acid, and Borates. In Ullmann's Encyclopedia of Industrial Chemistry, Wiley-VCH: Weinheim, Germany, online Feb. 10, 2015; pp 1−32. DOI: 10.1002/ 14356007.a04_263.pub2.

[28] M. Gajhede, S. Larsen, S. Rettrup, *Acta Crystallogr.* **1986**, *B42*, 545-552.

[29] O. O. Kurakevych, V. L. Solozhenko, *Acta Crystallogr.* **2007**, *C63*, i80-i82.

[30] R. R. Shuvalov, P. C. Burns, *Acta Crystallogr.* **2003**, *C59*, i47-i49.

[31] In contrast, in Figure S19 of Ref. [22], the authors present calculations of the relaxed excited states for BA_x (x = 1, 2, 6) in the gas phase, being about 6 eV lower than the vertical absorption; this was, however, not further discussed by the authors. We thus repeated the calculations, giving very similar results. However, closer inspection of the optimized S_1 gas phase BA geometry reveals a considerable, partial dissociation of one O-H bond as the reason for the low energy of S_1 (see the SI for further discussion); this was double checked with other methods (inter alia CASSF), which qualitatively confirmed the results. We emphasize however, that this (potential) photochemical path can only be activated by excitation in the far UV (> 7 eV), and not in the 250-370 nm range; in fact, in the near/middle UV, pure BA does not absorb, and, consequently, does not emit as unambiguously demonstrated in the present work.

[32] M. Wykes, B. Milián-Medina, J. Gierschner, *Front. Chem.* **2013**, *1*, 35.

[33] a) T. Dutta, K. B. Woody, S. R. Parkin, M. D. Watson, J. Gierschner, *J. Am. Chem. Soc.* **2009**, *131*, 17321-17327; b) N. N. M. Y. Chan, A. Idris, Z. H. Z. Abidin, H. A. Tajuddin, Z. Abdullah, *RSC Adv.* **2021**, *11*, 13409-13445; c) S. K. Behera, S. Y. Park, J. Gierschner, *Angew. Chem. Int. Ed.* **2021**, *60*, 22624-22638; *Angew. Chem.* **2021**, *133*, 22804-22820.

[34] a) G. D. Scholes, *Faraday Discuss*. **2020**, *221*, 265-280; b) O. V. Mikhnenko, P. W. M. Blom, T.-Q. Nguyen, *Energy Environm. Sci.* **2015**, *8*, 1867-1888; c) T. Brixner, R. Hildner, J. Köhler, C. Lambert, F. Würthner, *Adv. Energy Mater*. **2017**, *7*, 1700236;

[35] a) A. Ito, T. J. Meyer, *Phys. Chem. Chem. Phys*. **2012**, *14*, 13731-13745; b) D. Beljonne, C. Curutchet, G. D. Scholes, R. J. Silbey, *J. Phys. Chem. B* **2009**, *113*, 6583–6599.

[36] a) J. Gierschner, *Phys. Chem. Chem. Phys.* **2012**, *14*, 13146-13153; b) D. A. Dexter, *J. Chem. Phys.* **1953**, *21*, 836-850.

[37] a) R. M. Hochstrasser, *J. Chem. Phys*. **1963**, *39*, 3153-3154; b) V. P. Golovchenko, V. G. Roskolod'ko, N. S. Sivak, A. N. Faidysh, *Sov. Phys. J.* **1968**, *11*, 83-86.

[38] Exciton migration is either described by Förster-type or Dexter-type transfer,[5, 35] for singlet and triplet excitons, respectively. Singlet excitons are known to diffuse effectively in molecular solids;[5, 33c, 36] triplet excitons can, however, travel over even larger distances due to the very long triplet lifetimes.[5, 17a] Sensitized PL is then perceived if luminescent traps can act as effective energy acceptors. The high efficiency of this process was, in fact, already realized by Dexter in his seminal theoretical work in 1953, revealingly called "A Theory of Sensitized Luminescence in Solids", see Ref. [36b].

[39] a) E. J. Bowen, E. Mikiewicz, F. W. Smith, *Proc. Phys. Soc. A* **1949**, *62*, 26-31; b) H. Haken, G. Strobl, *Z. Phys.* **1973**, *262*, 135-148; c) R. C. Powell, Z. G. Soos, *J. Lumin.* **1975**, *11*, 1-45; d) R. Silbey, Ann. *Rev. Phys. Chem.* **1976**, *27*, 203-223; e) C. W. Tang, S. A. VanSlyke, C. H. Chen. *J. Appl. Phys*. **1989**, *65*, 3610-3616.

[40] W. Warta, R. Stehle, N. Karl, *Appl. Phys. A* **1985**, *36*, 163-170.

[41] J. Rohonczy, SOLA – Solid Lineshape Analysis Version 2.2.4, Bruker Biospin, Rheinstetten, Germany 2013.

[42] J. Gierschner, J. Shi, B. Milián-Medina, D. Roca-Sanjuán, S. Varghese, S.-Y. Park, *Adv. Opt. Mater*. **2021**, *9*, 20002251.

[43] G. M. Sheldrick, *Acta Crystallogr. A Found Adv.* **2015**, *71*, 3-8.

[44] G. M. Sheldrick, *Acta Crystallogr. A* **2008**, *64*, 112-122.

[45] C. B. Hübschle, G. M. Sheldrick, B. Dittrich, *J. Appl. Crystallogr.* **2011**, *44*, 1281-1284.

[46] M. Gajhede, S. Larsen, S. Rettrup, *Acta Crystallogr.* **1986**, *B42*, 545–552.

[47] K. D. Brandenburg, Crystal and Molecular Structure Visualization, Crystal Impact, H. Putz & K. Brandenburg GbR, Bonn (Germany), 2017.

[48] C. F. Macrae, I. J. Bruno, J. A. Chisholm, P. R. Edgington, P. McCabe, E. Pidcock, L. Rodriguez-Monge, R. Taylor, J. van de Streek, P. A. Wood, *J. Appl. Crystallogr.* **2008**, *41*, 466-470.

[49] O. V. Dolomanov, L. J. Bourhis, R. J. Gildea, J. A. K. Howard, H. Puschmann, *J. Appl. Cryst allogr.* **2009**, *42*, 339-341.

[50] S. Dapprich, I. Komáromi, K. S. Byun, K. Morokuma, M. J. Frisch, A new ONIOM Implementation in Gaussian98. Part I. The Calculation of Energies, Gradients, Vibrational Frequencies and Electric Field Derivatives. *J. Mol. Struct.: THEOCHEM* **1999**, *461-462*, 1-21.

[51] M. Wykes, R. Parambil Mangattu, D. Beljonne, J. Gierschner, *J. Chem. Phys.* **2015**, *143*, 114116.

[52] M. Wykes, S. K. Park, S. Bhattacharyya, S. Varghese, J. E. Kwon, D. R. Whang, I. Cho, R. Wannemacher, L. Lüer, S. Y. Park, J. Gierschner, *J. Phys. Chem. Lett.* **2015**, *6*, 3682–3687.

[53] Gaussian 09, Revision D.01, M. J. Frisch, G. W. Trucks, H. B. Schlegel, G. E. Scuseria, M. A. Robb, J. R. Cheeseman, G. Scalmani, V. Barone, B. Mennucci, G. A. Petersson, H. Nakatsuji, M. Caricato, X. Li, H. P. Hratchian, A. F. Izmaylov, J. Bloino, G. Zheng, J. L. Sonnenberg, M. Hada, M. Ehara, K. Toyota, R. Fukuda, J. Hasegawa, M. Ishida, T. Nakajima, Y. Honda, O. Kitao, H. Nakai, T. Vreven, J. A. Montgomery, Jr., J. E. Peralta, F. Ogliaro, M. Bearpark, J. J. Heyd, E. Brothers, K. N. Kudin, V. N. Staroverov, T. Keith, R. Kobayashi, J. Normand, K. Raghavachari, A. Rendell, J. C. Burant, S. S. Iyengar, J. Tomasi, M. Cossi, N. Rega, J. M. Millam, M. Klene, J. E. Knox, J. B. Cross, V. Bakken, C. Adamo, J. Jaramillo, R. Gomperts, R. E. Stratmann, O. Yazyev, A. J. Austin, R. Cammi, C. Pomelli, J. W. Ochterski, R. L. Martin, K. Morokuma, V. G. Zakrzewski, G. A. Voth, P. Salvador, J. J. Dannenberg, S. Dapprich, A. D. Daniels, O. Farkas, J. B. Foresman, J. V. Ortiz, J. Cioslowski, and D. J. Fox, Gaussian, Inc., Wallingford CT, **2013**.

[54] I. Fdez. Galván, M. Vacher, A. Alavi, C. Angeli, F. Aquilante, J. Autschbach, J. J. Bao, S. I. Bokarev, N. A. Bogdanov, R. K. Carlson, L. F. Chibotaru, J. Creutzberg, N. Dattani, M. G.

Delcey, S. S. Dong, A. Dreuw, L. Freitag, L. M. Frutos, L. Gagliardi, F. Gendron, A. Giussani, L. González, G. Grell, M. Guo, C. E. Hoyer, M. Johansson, S. Keller, S. Knecht, G. Kovačević, E. Källman, G. Li Manni, M. Lundberg, Y. Ma, S. Mai, J. P. Malhado, P. Å. Malmqvist, P. Marquetand, S. A. Mewes, J. Norell, M. Olivucci, M. Oppel, Q. M. Phung, K. Pierloot, F. Plasser, M. Reiher, A. M. Sand, I. Schapiro, P. Sharma, C. J. Stein, L. K. Sørensen, D. G. Truhlar, M. Ugandi, L. Ungur, A. Valentini, S. Vancoillie, V. Veryazov, O. Weser, T. A. Wesołowski, P. O. Widmark, S. Wouters, A. Zech, J. P. Zobel, and R. Lindh, *J. Chem. Theory Comput.* **2019**, *15*, 5925.

[55] F. Aquilante, J. Autschbach, A. Baiardi, S. Battaglia, V. A. Borin, L. F. Chibotaru, I. Conti, L. De Vico, M. Delcey, I. F. Galván, N. Ferré, L. Freitag, M. Garavelli, X. Gong, S. Knecht, E. D. Larsson, R. Lindh, M. Lundberg, P. Å. Malmqvist, A. Nenov, J. Norell, M. Odelius, M. Olivucci, T. B. Pedersen, L. Pedraza-González, Q. M. Phung, K. Pierloot, M. Reiher, I. Schapiro, J. Segarra-Martí, F. Segatta, L. Seijo, S. Sen, D. C. Sergentu, C. J. Stein, L. Ungur, M. Vacher, A. Valentini, and V. Veryazov, *J. Chem. Phys.* **2020**, *152*, 214117.

[56] P. Å. Malmqvist and B. O. Roos, *Chem. Phys. Lett.* **1989**, *155*, 189.

[57] J. P. Zobel, P. O. Widmark, and V. Veryazov, *J. Chem. Theory Comput.* **2020**, *16*, 278.

[58] H. Zheng, P. Cao, Y. Wang, X. Lu, P. Wu, *Angew. Chem. Int. Ed.* **2021**, *60*, 9500-9506; *Angew. Chem.* **2021**, *133*, 9586-9592.

[59] M. Attinà, F. Cacace, G. Occhiucci, A. Ricci, *Inorg. Chem.* **1992**, *31*, 3114-3117.

[60] C. C. Freyhardt, M. Wiebcke, *J. Chem. Soc., Chem. Commun.*, **1994**, 1675-1676.

CHAPTER FIVE

-

SUMMARY / ZUSAMMENFASSUNG

5 Summary/Zusammenfassung

5.1 Summary

5.1.1 Chapter 1

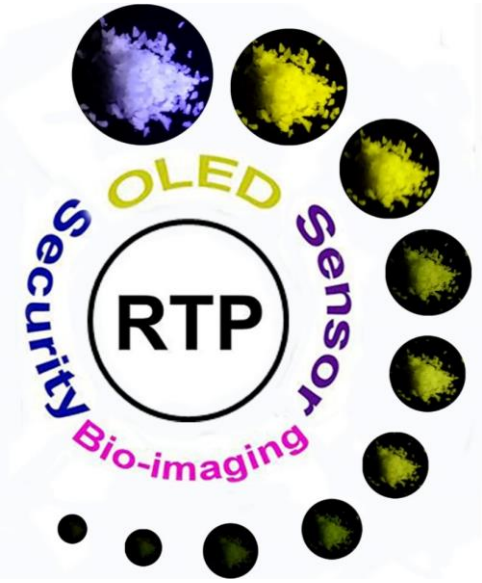

Recently, luminophores showing efficient room-temperature phosphorescence (RTP) have gained tremendous interest due to their numerous applications. However, most phosphors are derived from transition metal complexes because of their intrinsic fast inter-system crossing (ISC) induced by strong spin–orbit coupling (SOC) constants of the heavy metal. Metal-free RTP materials are rare and have become a promising field, because they are inexpensive and environmentally friendly. This review summarizes organic molecular materials with long triplet lifetimes at room temperature from the perspective of whether they stem from a molecular or multi-component system. Among purely organic phosphors, heteroatoms are usually introduced into the backbone in order to boost the singlet-triplet ISC rate constant. In multi-component systems, useful strategies such as host-guest, polymer matrix, copolymerization, and supramolecular assembly provide a rigid matrix to restrict nonradiative pathways thus realizing ultralong RTP.

This chapter is structured as follows. In Section 2, the photophysical parameters (Φ_{isc}, Φ_p, τ_p) required for RTP are presented. In Section 3, purely organic room temperature phosphors are classified according to their categories of functional groups which include amide derivatives, boron- and sulfur-

containing compounds, quinoxaline derivatives, siloxy group-induced and carbazole-based phosphors. In the last part of Section 3, several nonclassical RTP materials are also introduced. Section 4 provides a summary of multi-component RTP systems, and popular, current strategies to construct multi-component RTP materials are presented, host-guest systems, and supramolecular. As it is hard to distinguish whether carbon dots (CDs) are purely organic or multicomponent systems in some cases, we introduce them in Section 5. In the last two sections, we give future perspectives and conclusion.

5.1.2 Chapter 2

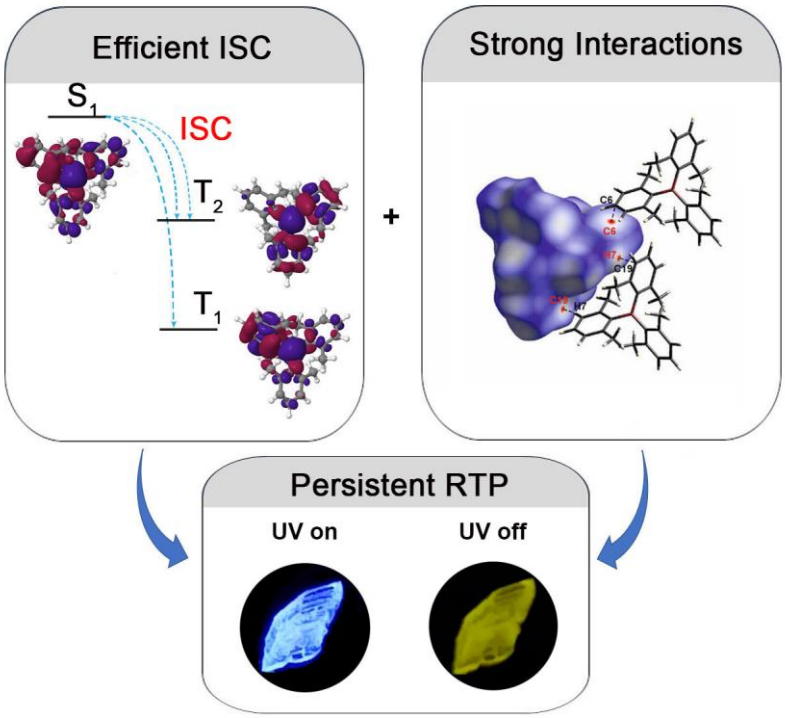

Achieving highly efficient phosphorescence in purely organic luminophors at room temperature remains a major challenge due to slow intersystem crossing (ISC) rates in combination with effective non-radiative processes in those systems. Most room temperature phosphorescent (RTP) organic materials have O- or N-lone pairs leading to low lying (n, π*) and (π, π*) excited states which accelerate k_{isc} through El-Sayed's rule. Herein, we report the first persistent RTP with lifetimes up to 0.5 s from simple triarylboranes which have no lone pairs. RTP is only observed in the crystalline state and in highly doped PMMA films which are indicative of aggregation induced emission (AIE). Detailed crystal structure analysis suggested that intermolecular interactions are important for efficient RTP. Furthermore, photophysical studies of the isolated molecules in a frozen glass, in combination with DFT/MRCI calculations, show that (σ, B p)→(π, B p) transitions accelerate the ISC process. This work provides a new approach for the design of RTP materials without (n, π*) transitions.

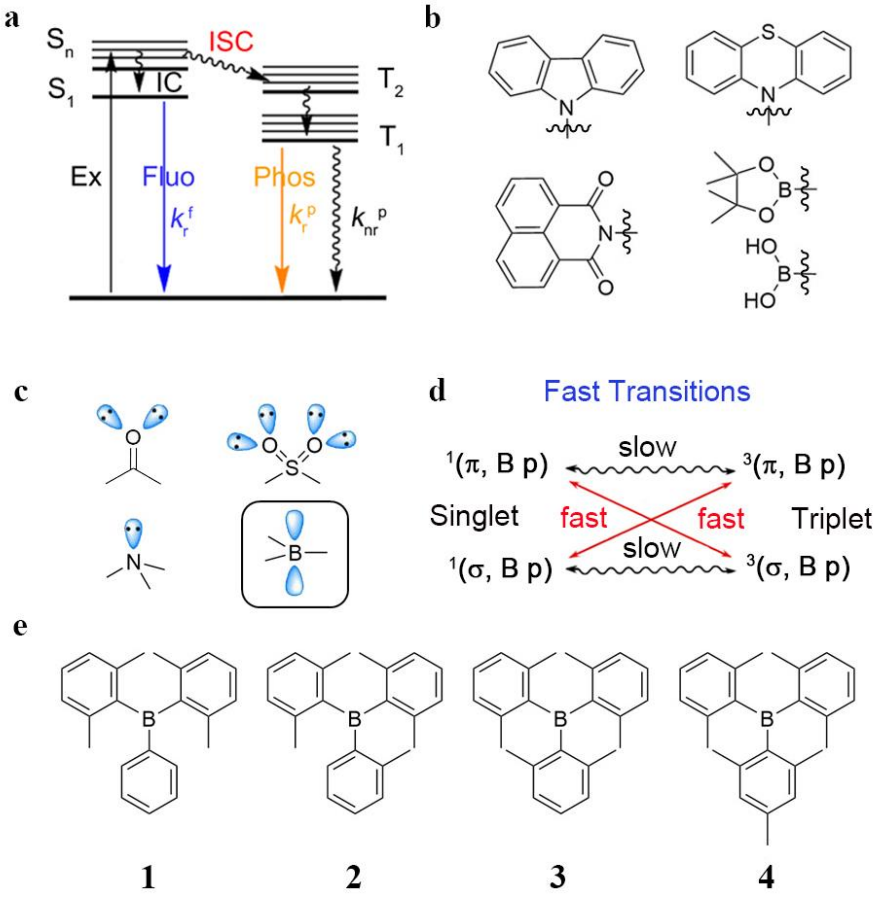

Figure 5-1. (a) Jablonski-diagram; (b) the structural features of reported RTP materials; (c) typical functional groups having lone pairs in organic phosphors, and the empty p_z orbital on three-coordinate boron; (d) fast transitions between (σ, B p) and (π, B p); (e) molecular structures of compounds **1**-**4**.

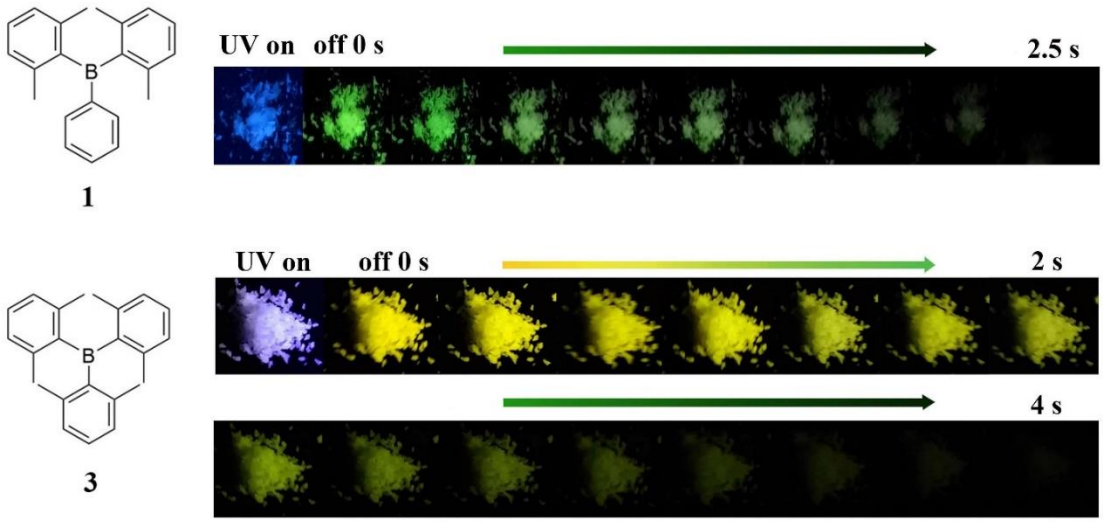

Figure. 5-2 Photographs of crystalline **1** and **3** taken during and after irradiation (365 nm) under ambient conditions.

Key approaches to accelerate the intersystem crossing (ISC) process from singlet to triplet excited states involve reducing the nonradiative decay rate ($k_{nr}(T_1)$) from T_1 by (1) avoiding collisions with quenching species such as oxygen, and (2) minimizing vibrational relaxation (Figure 5-1a). To increase the population of triplet excitons, heteroatoms with lone pairs are usually introduced into organic systems to enhance spin–orbit coupling (El-Sayed's rule), which is why most RTP phosphors are limited to phenothiazine, carbazole, and naphthylimide derivatives (Figure 5-1b). Thus, intersystem crossing usually involves $^1(n, \pi^*) \rightarrow ^3(\pi, \pi^*)$ transitions. In fact, organic compounds without lone pairs, such as triarylboranes, can show phosphorescence in a frozen optical glass at 77 K (Figure 5-1c). Therefore, we propose that k_{isc} can also be accelerated by $(\sigma, B\ p) \rightarrow (\pi, B\ p)$ transitions, which would be the inversion of the normally observed $^1(n, \pi^*) \rightarrow ^3(\pi, \pi^*)$ ISC process (Figure 5-1d). We examined the triarylboranes **1**-**4** (Figure 5-1e). Crystalline samples of **3** (tris(2,6-dimethylphenyl)borane) show ultralong (τ_p = 478 ms), intense, yellow phosphorescence under ambient conditions, and it is thus, to the best of our knowledge, the first triarylboron compound without lone pairs to display ultralong RTP.

5.1.3 Chapter 3

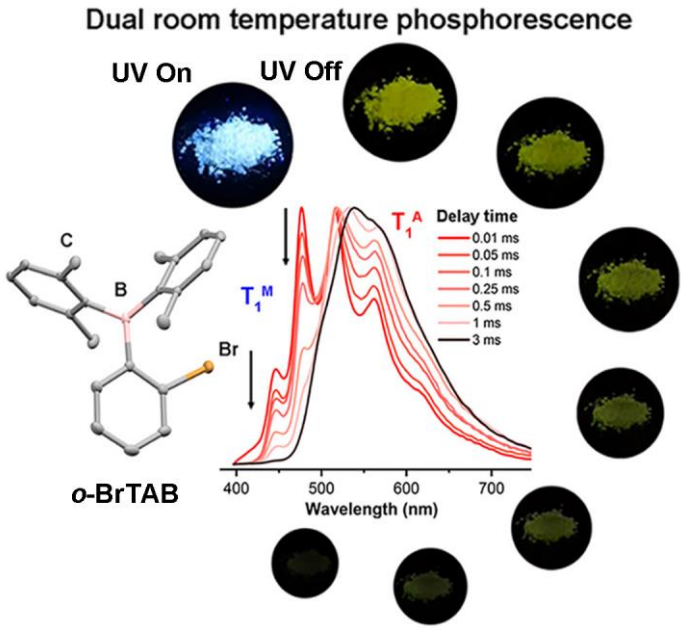

Designing highly efficient purely organic phosphors at room temperature remains a challenge because of fast non-radiative processes and slow intersystem crossing (ISC) rates. The majority of them emit only single component phosphorescence. Herein, we have prepared 3 isomeric (*o*, *m*, *p*-bromophenyl)-bis(2,6-dimethylphenyl)boranes. Among the 3 isomers (***o***-, ***m***- and ***p*-BrTAB**) synthesized, the *ortho*-one is the only one which shows dual phosphorescence, with a short lifetime of 0.8 ms and a long lifetime of 234 ms in the crystalline state at room temperature. It is the first reported DRTP (dual room temperature phosphorescence) from triarylboron compounds. Based on theoretical calculations and crystal structure analysis of ***o*-BrTAB**, the short lifetime component is ascribed to the T_1^M state of the monomer which emits the higher energy phosphorescence. The long-lived, lower energy phosphorescence emission is attributed to the T_1^A state of an aggregate as multiple intermolecular interactions existing in the crystalline ***o*-BrTAB** prohibit nonradiative decay and stabilize the triplet states efficiently.

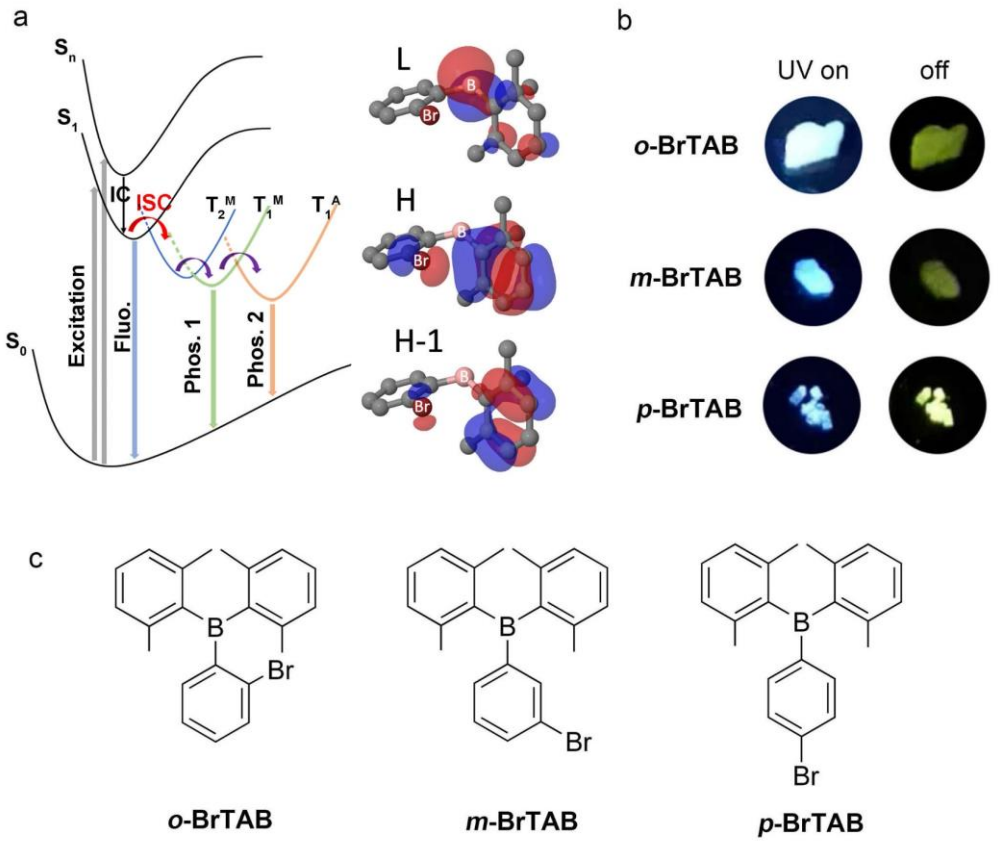

Figure 5-3. (a) Proposed mechanism of the dual phosphorescent emission in ***o*-BrTAB** and essential parts of the molecular orbitals involved in the transitions; T_1^M and T_2^M represent monomer states, T_1^A an aggregate state (b) afterglow photographs taken before and after irradiation (λ_{ex} = 365 nm) under ambient conditions; (c) molecular structures of the three isomeric compounds described in the paper.

It is proposed that introducing heavy atoms (Br or I) into existing persistent RTP luminophores to enhance the SOC may greatly improve the performance of RTP phosphors. We introduced the heavy atom Br into phenyl-bis(2,6-dimethylphenyl)borane at different positions on the phenyl ring to obtain 3 isomers (***o*-**, ***m*-** and ***p*-BrTAB**). Interestingly, (2-bromophenyl)bis(2,6-dimethylphenyl)borane (***o*-BrTAB**) exhibits DRTP in the crystalline state under ambient conditions (Figure 5-3b and 5-3c). The faster, higher energy phosphorescence ranging from 430 to 490 nm with a short lifetime of 0.8 ms is ascribed to the T_1^M state of the monomer while the long-lived, lower energy phosphorescence emission in the range of 490-700 nm with a lifetime of up to 234 ms is attributed to the T_1^A state of an aggregate in the crystalline material (Figure 5-3a).

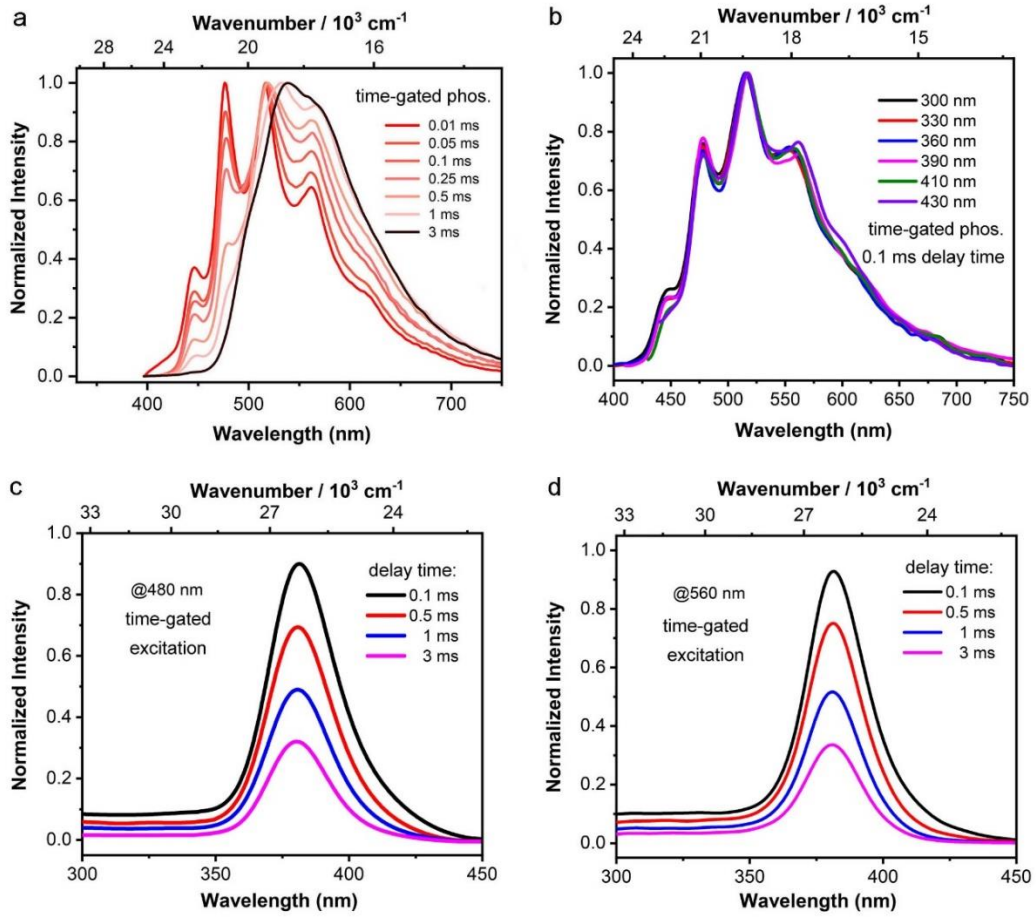

Figure 5-4. Normalized time-gated phosphorescence spectra of crystalline ***o*-BrTAB** (a) with different delay times and (b) with 0.1 ms delay at different excitation wavelength. Time-gated excitation spectra (c, λ_{em} = 480 nm) and (d, λ_{em} = 560 nm) of crystalline ***o*-BrTAB** at different delay times at room temperature.

The DRTP was confirmed by time-gated phosphorescence spectroscopy of ***o*-BrTAB** at room temperature (Figure 5-4a). Upon increasing the delay time, the intensity of peaks of the shorter wavelength emission components at 446 and 477 nm decreased gradually. When the delay time was set at 3 ms, the short-lived monomer T_1^M emission of ***o*-BrTAB** almost disappeared, and the remaining long lifetime component is ascribed to phosphorescence from the T_1^A state of an aggregate. We performed time-gated excitation spectroscopy of crystalline ***o*-BrTAB** at 480 and 560 nm, respectively (Figures 5-4c and 5-4d). The two spectra are identical in the range of 300 to 450 nm, which indicates that one absorption leads to all exited states. We also measured time-gated phosphorescence spectra at different excitation wavelengths (Figure 5-4b). The two triplet excited states always appear at the same time which further proves that T_1^M and T_1^A originate from the same absorption ($S_0 \rightarrow S_1$ and $S_0 \rightarrow S_n$). Therefore, we propose that first, the single molecule of ***o*-BrTAB** is

excited into its S_1^M or S_n^M state. Then it undergoes ISC to T_2^M which undergoes IC to a short-lived T_1^M state. At the same time, T_1^M evolves into a T_1^A state, emitting more slowly and at lower energy. The process going from T_1^M to T_1^A was confirmed by temperature-dependent, time-gated spectroscopic study of crystalline ***o*-BrTAB** (Figure 5-5b). Upon decreasing the temperature from 298 to 77 K, the phosphorescence peaks belonging to T_1^M at 446 and 477 nm blueshift to *ca*. 431 and 455 nm, respectively, which become dominant at 77 K with a lifetime *ca.* 2.1 ms. At 77 K, the long-lived T_1^A emission at longer wavelength still exists with a lifetime of *ca*. 453 ms (58 %), but in a much lower ratio compared to the short-lived component. Thus, there is a thermal barrier for the conversion of T_1^M to T_1^A, and lowering the temperature makes it harder to cross the barrier.

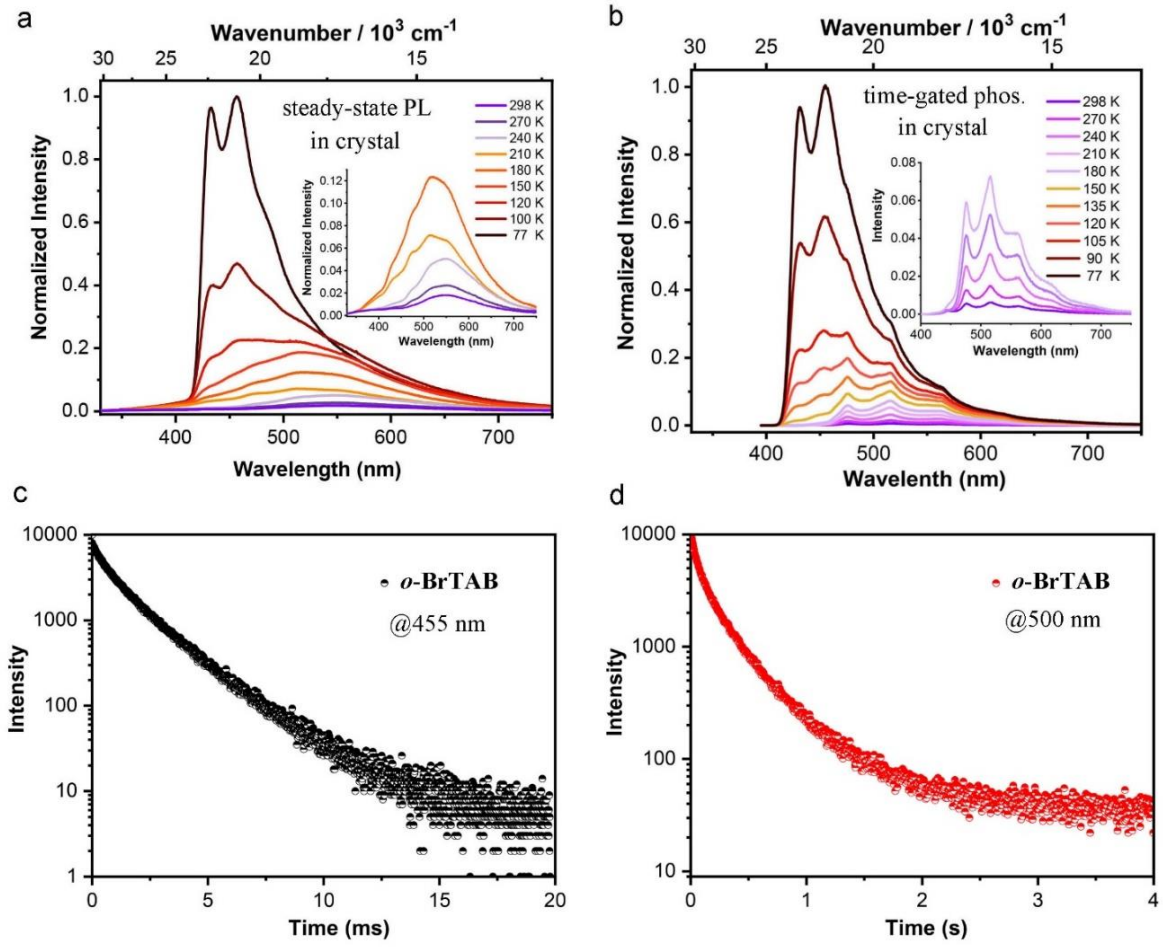

Figure 5-5. (a) Steady-state photoluminescence and (b) time-gated (delay time 0.01 ms) phosphorescence spectra of crystalline ***o*-BrTAB** at different temperatures (λ_{ex} = 305 nm). Decays of the phosphorescence emission (c) (λ_{em} = 455 nm) and (d) (λ_{em} = 500 nm) of crystalline ***o*-BrTAB** at 77 K.

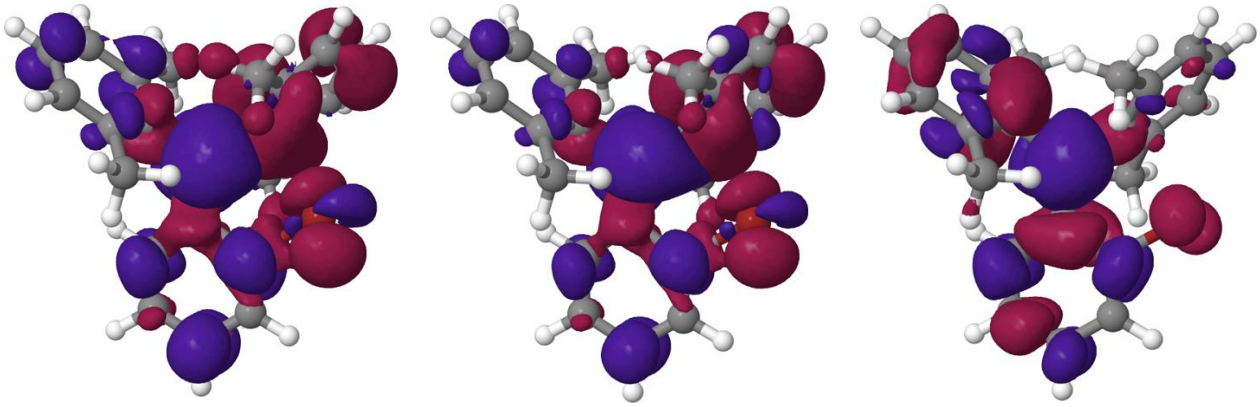

Figure 5-6. Difference of electron density distributions in the S_1^M, T_1^M and T_2^M states of the ***o*-BrTAB** monomer with regard to the electronic ground state, S_0^M, at the S_1^M geometry. Red areas indicate a loss of electron density upon excitation, blue areas a gain.

To explain the experimentally observed dual phosphorescence, we searched for the most probable pathways from the singlet to the triplet states of the monomer. The bromine substitution increases the SOCMEs in general with respect to that of the unsubstituted compound. As may be expected, the heavy-atom effect is strongest for the *ortho*-substituted compound. Despite the similarity of the electron distributions in both states (Figure 5-6), the S_1^M and T_1^M states experience substantial mutual SOC. With a squared sum of SOCMEs of 25 cm^{-2}, the $S_1^M \rightarrow T_1^M$ transition of ***o*-BrTAB** is significantly faster than in the unsubstituted compound. Even in this case, the change in excitation character is larger for the $S_1^M \rightarrow T_2^M$ transition. Nevertheless, with a rate constant of *ca*. 1×10^{10} s^{-1}, the $S_1^M \rightarrow T_2^M$ ISC is five times faster than the direct $S_1^M \rightarrow T_1^M$ ISC. Very close to the T_2^M minimum, the T_2^M and T_1^M states of ***o*-BrTAB** undergo a conical intersection without the necessity to surmount a substantial energy barrier. Therefore, the population is not trapped in the T_2^M state but is rapidly transferred to the T_1^M state. The possibility that the dual phosphorescence originates from T_2^M and T_1^M states can be ruled out.

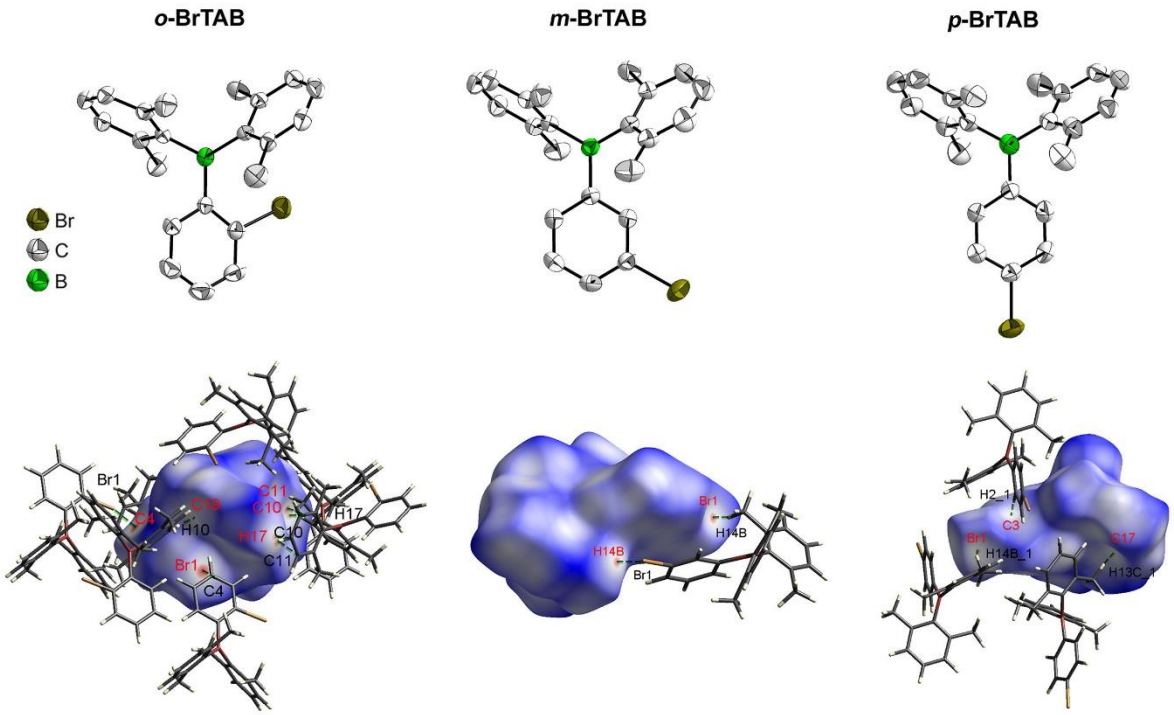

Figure 5-7. The solid-state molecular structure of ***o*-BrTAB**, ***m*-BrTAB** and ***p*-BrTAB** (top left to right) determined by single-crystal X-ray diffraction at room temperature. Ellipsoids are drawn at the 50% probability level, and H atoms are omitted for clarity. Hirshfeld surfaces of ***o*-BrTAB**, ***m*-BrTAB** and ***p*-BrTAB** (bottom left to right) mapped with d_{norm} over the range -0.12 to 1.50 at room temperature. Neighboring molecules associated with close contacts are shown.

The presence of multiple C−H···C and C−H···Br interactions between molecules in the crystals effectively suppresses the nonradiative decay rate k_{nr}, which plays an important role in stabilizing the triplet states and achieving RTP. As the strength of intermolecular interactions is especially distinct between the three compounds at room temperature, and is strongest for ***o*-BrTAB**, this effect may be the reason that we observe DRTP in crystalline ***o*-BrTAB** at room temperature, but only at low temperature for ***m*-BrTAB** and ***p*-BrTAB**.

5.1.4 Chapter 4

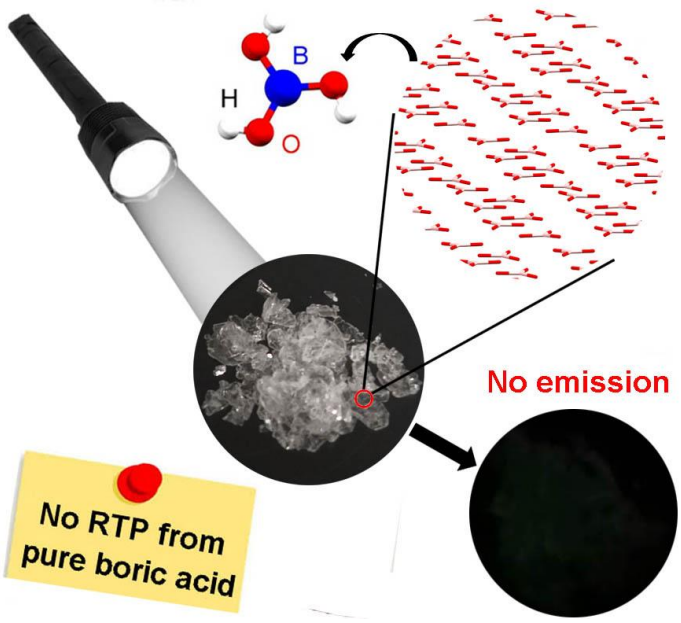

Boric acid (BA) has been used as an excellent glass matrix for optical materials for over 100 years because of its superior qualities including the low temperature required for glass formation, and its easy fabrication. As we show, pure BA itself does not display any fluorescence or phosphorescence in the solid state. However, in 2021, Peng Wu and co-workers, at Sichuan University, reported apparent room temperature phosphorescence (RTP) from BA in the crystalline and powder states when irradiated at 280 nm under ambient conditions. Based on our extensive research and understanding of boron-containing optical materials, we suspected that this apparent RTP from their BA sample was induced by an unidentified impurity. Our own experimental results reveal that pure BA synthesized from trimethylborate, $B(OMe)_3$, does not exhibit any luminescence in the solid state when irradiated with light in the wavelength range 250-400 nm. Our theoretical calculations show that neither individual BA molecules nor (larger) aggregates would absorb light at wavelengths >175 nm, and we observe no absorption of solid BA experimentally at wavelengths >200 nm. Therefore, it is not possible for pure BA to be excited at 250 nm or longer wavelengths even in the solid state as described by Wu. All of our results prove that pure BA does not display RTP.

Figure 5-8 a) Synthesis of boric acid from $B(OMe)_3$. b) Photographs of BA as a ground powder and as crystals, taken under daylight. The ground powder retains crystallinity.

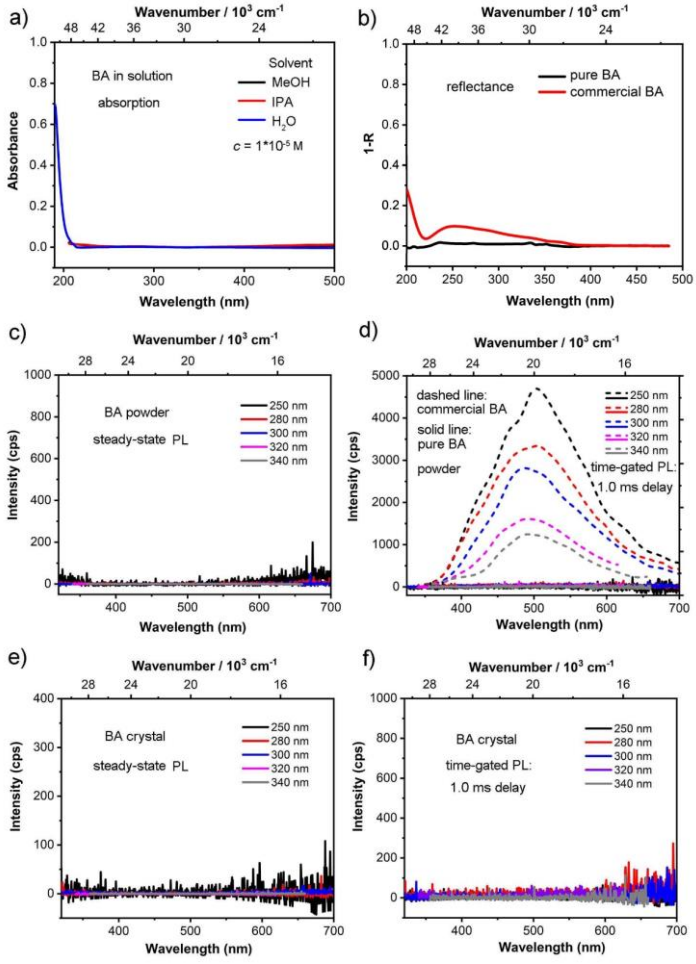

Figure 5-9 a) UV-vis absorption spectra of **pure BA** in MeOH, isopropanol and H_2O solutions (c = 10^{-5} M). The onset of absorption at *ca.* 205 nm is due to the solvent cut-off. b) UV-vis absorption spectra (R = Reflectance) of solid samples of **pure, crystalline BA** (black) and **commercial BA** (red). Steady-state photoluminescence (PL) (c) and time-gated PL: 1.0 ms delay (d) spectra of **commercial BA** (dashed line) and **pure BA** (solid line) as a ground powder (not amorphous) at different excitation wavelengths under the same conditions. Photoluminescence (e) and time-gated (1.0 ms delay) emission (f) spectra of **pure, crystalline BA** at different excitation wavelengths.

We synthesized and purified a sample of BA (Figure 5-8). We then measured the absorption spectra of BA in methanol, isopropanol, and water solutions at concentrations of 10^{-5} mol/L (Figure 5-9a). The cut-off wavelengths of methanol and isopropanol are 205 nm. There was no absorption peak observed at wavelengths longer than 205 nm, which indicates that aromatic species are not present in our sample of BA. The cut-off wavelength of water is 190 nm. There is also no absorption peak observed in the spectrum at >200 nm. Even upon increasing the concentration of BA in methanol to 10^{-4} or 10^{-3} mol/L, no absorbance at >205 nm was observed. What is clear is that the solid-state absorption spectrum of BA does not show any absorption in the region between 200 and 485 nm (Figure 5-9b). We measured the photoluminescent (PL) emission and time-gated (1.0 ms) phosphorescence emission spectra of BA as both crystals and as a ground powder, noting that the powder retains crystallinity, with varied excitation wavelength from 250 to 400 nm (Figures 5-9c to 5-9f). However, as expected, neither the PL nor the time-gated phosphorescence spectra of BA show emission bands, either as a ground powder or as crystals.

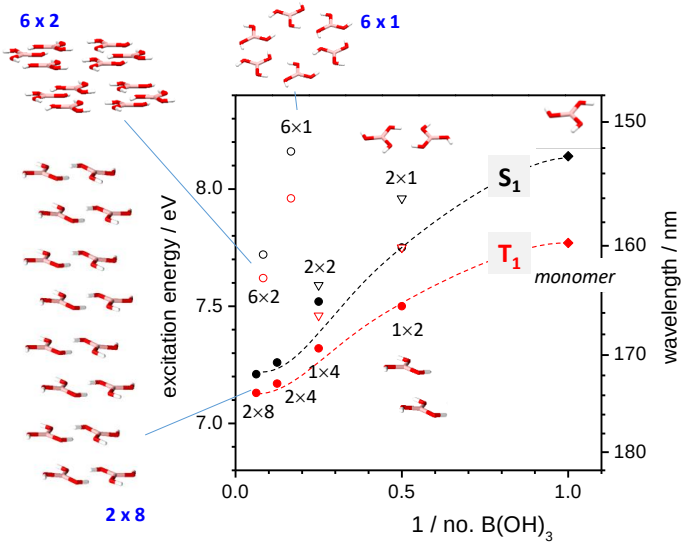

Figure 5-10. Vertical transition energies for the lowest excited singlet and triplet states (S_1, T_1) of BA and clusters thereof, as calculated by TD-DFT; dashed lines are guides for the eyes.

We calculated larger clusters, and extended them along the crystallographic *c* axis (Figure 5-10). In this case, the B3LYP functional was employed, which tends to underestimate electronic transition energies, and thus may define a lower limit for the appearance of BA cluster absorption. As shown

in Figure 5-10, clustering of boric acid units in fact generally leads to a bathochromic shift of the electronic S_1 and T_1 transition energies; the shift becomes particular large if the clusters are extended in the c-direction. However, a rapid saturation is observed, so that the maximum shift of the clusters vs. the monomer amounts to ca. 0.65 eV for T_1 and 0.95 eV for S_1 Although the shift is considerable, we emphasize that the transitions remain in the deep UV (above 7 eV; 177 nm), in good agreement with our experimental results. Our study has clearly shown that carefully purified BA, synthesized from $B(OMe)_3$, does not show any intrinsic phosphorescence in the solid state, in particular, in the visible range; TD-DFT calculations fully support our experimental results. In contrast, commercial BA evidently contains traces of (unknown) luminescent impurities, giving rise to blue-colored RTP. Impurity sources could well be side products from synthesis, including impurities in any solvents used, sample contamination, or photoproducts. Such (luminescent) trap states in molecular solids can be directly excited if the concentration and absorption coefficient of the impurities are sufficiently high, which is in fact the case for commercial BA, as demonstrated in the current work (see Figure 5-9b).

5.2 Zusammenfassung

5.2.1 Kapitel 1

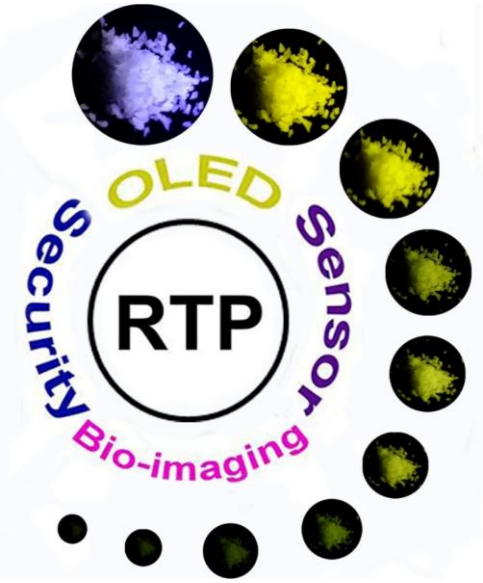

In letzter Zeit haben Luminophore, die eine effiziente Raumtemperatur-Phosphoreszenz (RTP) zeigen, aufgrund ihrer zahlreichen Anwendungen enormes Interesse gefunden. Die meisten phosphoreszierenden Materialien leiten sich jedoch von Übergangsmetallkomplexen ab, da ihr intrinsisches schnelles Intersystem Crossing (ISC) durch die starke Spin Bahn Kopplung (SOC) des Schwermetalls induziert wird. Metallfreie RTP Materialien sind selten und haben sich zu einem vielversprechenden Gebiet entwickelt, da sie kostengünstig und umweltfreundlich sind. Dieses Kapitel fasst organische molekulare Materialien mit langen Triplett Lebensdauern bei Raumtemperatur aus der Perspektive zusammen, ob sie aus einem molekularen oder Mehrkomponentensystem stammen. Bei rein organischen phosphoreszierenden Materialien werden üblicherweise Heteroatome in das Rückgrat eingeführt, um die Singulett Triplett ISC Geschwindigkeitskonstante zu erhöhen. In Mehrkomponentensystemen wird durch nützliche Strategien wie Wirt-Gast, Polymermatrix, Copolymerisation und supramolekulare Anordnung eine starre Matrixanordnung erreicht, durch die nichtstrahlende Pfade eingeschränkt und so ultralange RTP realisiert wird.

Dieses Kapitel ist wie folgt aufgebaut. In Abschnitt 2 werden die für RTP erforderlichen photophysikalischen Parameter (Φ_{isc}, Φ_p, τ_p) vorgestellt. In Abschnitt 3 werden rein organische bei

Raumtemperatur phosphoreszierende Materialien nach ihren jeweiligen funktionellen Gruppen klassifiziert, nämlich Amidderivate, bor- und schwefelhaltige Verbindungen, Chinoxalinderivate, durch Siloxygruppen induzierte und auf Carbazol basierende phosphoreszierenden Materialien. Im letzten Teil von Abschnitt 3 werden auch einige nicht-klassische RTP Materialien vorgestellt. Abschnitt 4 bietet eine Zusammenfassung von Mehrkomponenten RTP Systemen, und es werden beliebte, aktuelle Strategien zum Aufbau von Mehrkomponenten RTP Materialien, Wirt-Gast Systemen und supramolekularen Systemen vorgestellt. Da es teilweise schwer zu unterscheiden ist, ob Carbon Dots (CDs) rein organische oder Mehrkomponentensysteme sind, stellen wir sie in Abschnitt 5 vor. In den letzten beiden Abschnitten geben wir unsere Zukunftsperspektiven und Schlussfolgerungen.

5.2.2 Kapitel 2

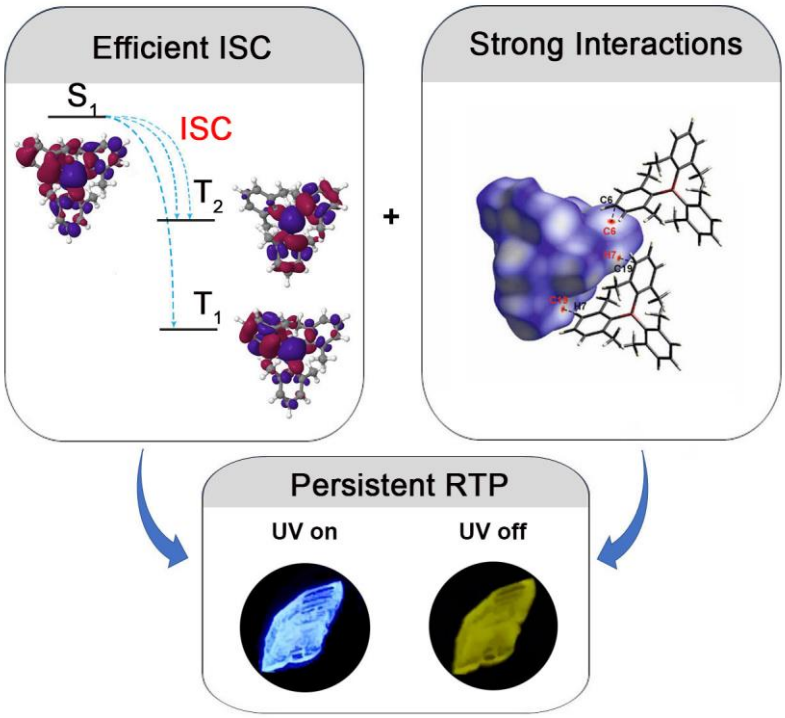

Die Erzielung einer hocheffizienten Phosphoreszenz in rein organischen Luminophoren bei Raumtemperatur bleibt aufgrund der langsamen Intersystem-Crossing (ISC) Raten in Kombination mit effektiven strahlungslosen Prozessen in diesen Systemen eine große Herausforderung. Die meisten bei Raumtemperatur phosphoreszierenden (RTP) organischen Materialien haben O- oder N-Atome mit freien Elektronenpaaren, die zu tiefliegenden (n, π*) und (π, π*) angeregten Zuständen führen, die k_{isc} durch die El-Sayed Regel beschleunigen. Hier berichten wir über die erste persistente RTP mit Lebensdauern von bis zu 0.5 s aus einfachen Triarylboranen, die keine freien Elektronenpaare haben. RTP wird nur im kristallinen Zustand und in hochdotierten PMMA Filmen beobachtet, die auf aggregationsinduzierte Emission (AIE) hinweisen. Detaillierte Kristallstrukturanalysen legten nahe, dass intermolekulare Wechselwirkungen für eine effiziente RTP wichtig sind. Darüber hinaus zeigen photophysikalische Studien der isolierten Moleküle in einem gefrorenen Glas in Kombination mit DFT/MRCI Rechnungen, dass (σ, B p)→(π, B p)-Übergänge den ISC Prozess beschleunigen. Diese Arbeit bietet einen neuen Ansatz für das Design von RTP Materialien ohne (n, π*)-Übergänge.

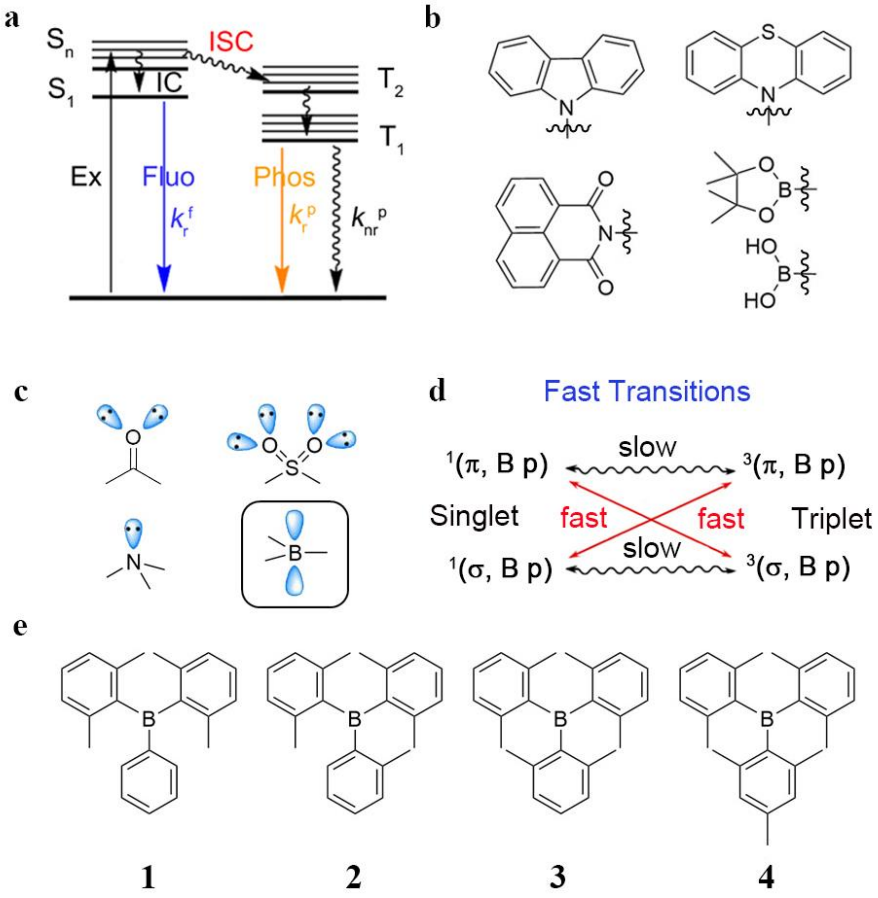

Abbildung 5-1. (a) Jablonski-Diagramm; (b) die strukturellen Merkmale der vorgestellten RTP Materialien; (c) typische funktionelle Gruppen mit freien Elektronenpaaren in organischen Leuchtstoffen und das leere p_z Orbital am dreifach koordinierten Bor; (d) schnelle Übergänge zwischen (σ, B p) und (π, B p); (e) Molekülstrukturen der Verbindungen **1**-**4**.

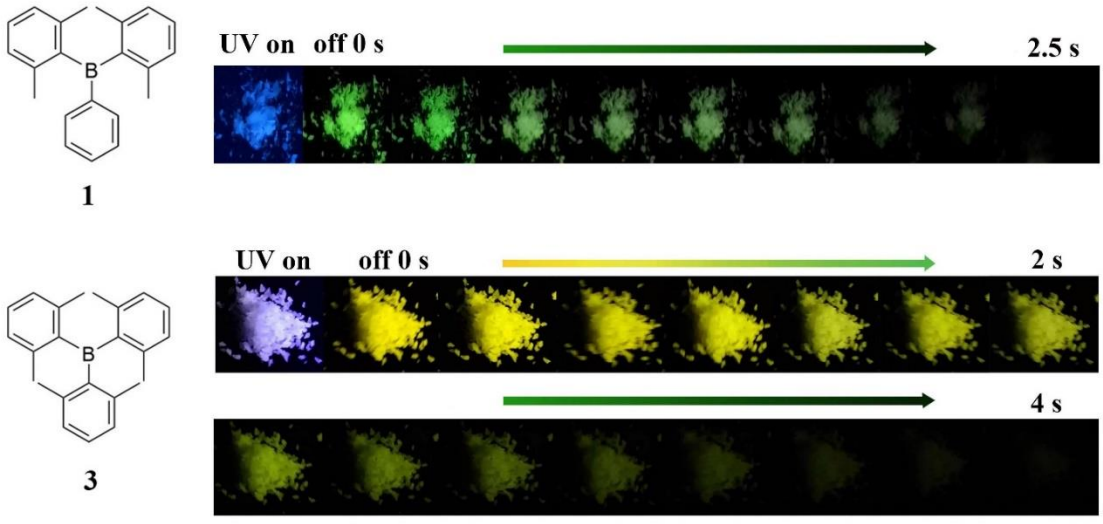

Abbildung 5-2. Fotografien von kristallinem **1** und **3**, aufgenommen während und nach der Bestrahlung (365 nm) unter Umgebungsbedingungen.

Zu den wichtigsten Ansätzen zur Beschleunigung des Intersystem Crossing (ISC) Prozesses von angeregten Singulett- zu Triplett-Zuständen gehört die Reduzierung der strahlungslosen Zerfallsrate ($k_{nr}(T_1)$) von T_1 durch (1) Vermeidung von Kollisionen mit Quenching-Spezies wie Sauerstoff und (2) Minimierung von Schwingungs-Relaxation (Abbildung 5-1a). Um die Population von Triplett-Exzitonen zu erhöhen, werden gewöhnlich Heteroatome mit freien Elektronenpaaren in organische Systeme eingeführt, um die Spin-Bahn-Kopplung zu verbessern (El-Sayed-Regel), weshalb die meisten RTP Leuchtstoffe auf Phenothiazin-, Carbazol- und Naphthylimid-Derivate beschränkt sind (Abbildung 5-1b). Somit beinhaltet Intersystem Crossing normalerweise $^1(n, \pi^*) \rightarrow {}^3(\pi, \pi^*)$ Übergänge. Tatsächlich können organische Verbindungen ohne freie Elektronenpaare, wie Triarylborane, in einem gefrorenen optischen Glas bei 77 K phosphoreszieren (Abbildung 5-1c). Daher schlagen wir vor, dass k_{isc} auch durch $(\sigma, B\ p) \rightarrow (\pi, B\ p)$-Übergänge beschleunigt werden kann, was die Umkehrung des normalerweise beobachteten $^1(n, \pi^*) \rightarrow {}^3(\pi, \pi^*)$ ISC-Prozesses wäre (Abbildung 5-1d). Wir haben die Triarylborane **1**-**4** untersucht (Abbildung 5-1e). Kristalline Proben von **3** (Tris(2,6-dimethylphenyl)boran) zeigen unter Umgebungsbedingungen eine ultralange (τ_p = 478 ms), intensive, gelbe Phosphoreszenz und somit ist **3** nach unserem Wissen die erste Triarylborverbindung ohne freie Elektronenpaare, die ultralange RTP zeigt.

5.2.3 Kapitel 3

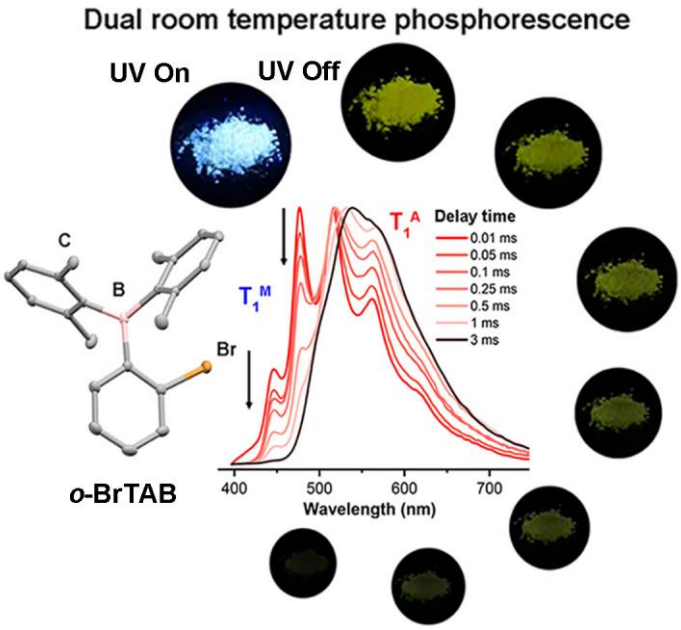

Die Entwicklung hocheffizienter rein organischer phosphoresierender Materialien bei Raumtemperatur bleibt aufgrund schneller strahlungsloser Prozesse und langsamer Intersystem-Crossing (ISC) Raten eine Herausforderung, wobei die meisten nur Einkomponenten-Phosphoreszenz emittieren. Für die Untersuchungen in diesem Kapitel haben wir drei Isomere (*o*, *m*, *p*-Bromphenyl)-bis(2,6-dimethylphenyl)borane hergestellt. Unter den drei synthetisierten Isomeren (***o***-, ***m***- und ***p*-BrTAB**) ist das ortho-Isomer das einzige, das duale Phosphoreszenz zeigt, mit einer kurzen Lebensdauer von 0.8 ms und einer langen Lebensdauer von 234 ms im kristallinen Zustand bei Raum Temperatur. Es ist die erste Triarylborverbindungen, die DRTP (Dual Room Temperature Phosphorescence) zeigt. Basierend auf theoretischen Berechnungen und Kristallstrukturanalysen von ***o*-BrTAB** wird die Komponente mit kurzer Lebensdauer dem T_1^M Zustand des Monomers zugeschrieben, welches die Phosphoreszenz mit höherer Energie emittiert. Die langlebige, niederenergetische Phosphoreszenzemission wird dem T_1^A Zustand eines Aggregats zugeschrieben, da multiple intermolekulare Wechselwirkungen, die im kristallinen ***o*-BrTAB** existieren, den strahlungslosen Zerfall verhindern und die Triplettzustände effizient stabilisieren.

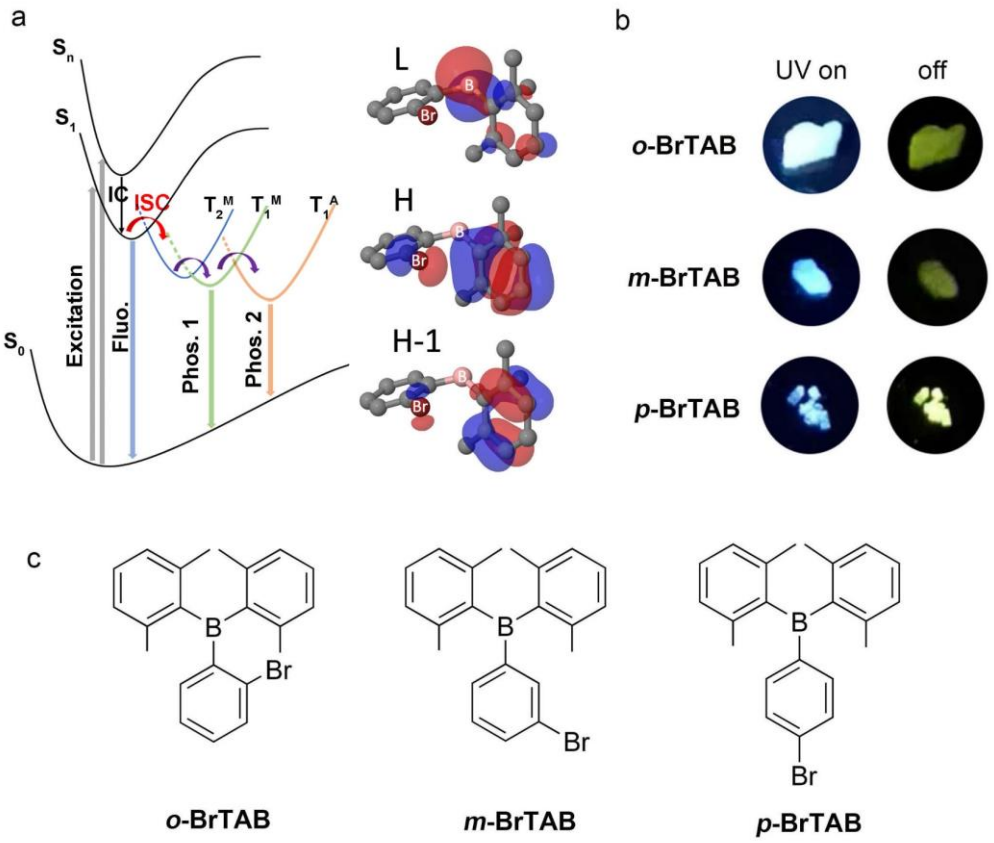

Abbildung 5-3. (a) Vorgeschlagener Mechanismus der dualen phosphoreszierenden Emission in ***o*-BrTAB** und wesentlichen Teilen der an den Übergängen beteiligten Molekülorbitale; T_1^M und T_2^M stellen Monomerzustände dar, T_1^A einen Aggregatzustand (b) Nachleucht-Aufnahmen vor und nach der Bestrahlung (λ_{ex} = 365 nm) unter Umgebungsbedingungen; (c) molekulare Strukturen der drei in der Veröffentlichung beschriebenen isomeren Verbindungen.

Es wird vorgeschlagen, dass die Einführung von Schweratomen (Br oder I) in bestehende persistente RTP Luminophore zur Verbesserung des SOC die Leistung von RTP-Luminophoren stark verbessern kann. Wir führten das Schweratom Br in Phenyl-bis(2,6-dimethylphenyl)boran an verschiedenen Positionen am Phenylring ein, um 3 Isomere (***o***-, ***m***- und ***p*-BrTAB**) zu erhalten. Interessanterweise zeigt (2-Bromphenyl)bis(2,6-dimethylphenyl)boran (***o*-BrTAB**) im kristallinen Zustand unter Umgebungsbedingungen DRTP (Abbildung 5-3b und 5-3c). Die schnellere, energiereichere Phosphoreszenz im Bereich von 430 bis 490 nm mit einer kurzen Lebensdauer von 0,8 ms wird dem T_1^M Zustand des Monomers zugeschrieben, während die langlebige, energieärmere Phosphoreszenzemission im Bereich von 490-700 nm mit einer Lebensdauer von bis zu 234 ms dem T_1^A Zustand eines Aggregats im kristallinen Material zugeschrieben werden (Abbildung 5-3a).

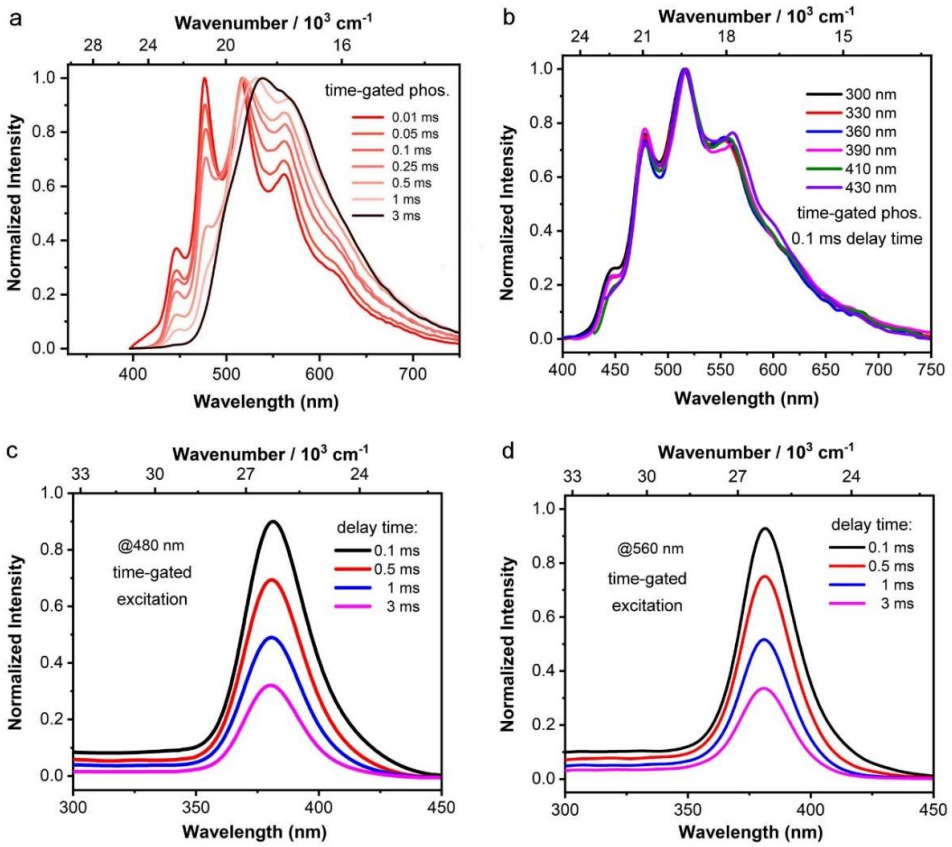

Abbildung 5-4. Normalisierte zeitgesteuerte Phosphoreszenzspektren von kristallinem ***o*-BrTAB** (a) mit unterschiedlichen Verzögerungszeiten und (b) mit 0,1 ms Verzögerung bei unterschiedlicher Anregungswellenlänge. Zeitgesteuerte Anregungsspektren (c, 480 nm) und (d, 560 nm) von kristallinem ***o*-BrTAB** bei unterschiedlichen Verzögerungszeiten bei Raumtemperatur.

Die DRTP wurde durch zeitgesteuerte Phosphoreszenzspektroskopie von ***o*-BrTAB** bei Raumtemperatur bestätigt (Abbildung 5-4a). Beim Erhöhen der Verzögerungszeit nahm die Intensität der Peaks der kürzerwelligen Emissionskomponenten bei 446 und 477 nm allmählich ab. Wenn die Verzögerungszeit auf 3 ms eingestellt wurde, verschwand die kurzlebige Monomer-T_1^M-Emission von ***o*-BrTAB** fast, und die verbleibende Komponente mit langer Lebensdauer wird der Phosphoreszenz aus dem T_1^A-Zustand eines Aggregats zugeschrieben. Wir führten zeitgesteuerte Anregungsspektroskopie von kristallinem ***o*-BrTAB** bei 480 bzw. 560 nm durch (Abbildungen 5-4c und 5-4d). Die beiden Spektren sind im Bereich von 300 bis 450 nm identisch, was darauf hindeutet, dass eine Absorption zu allen angeregten Zuständen führt. Wir haben auch zeitgesteuerte Phosphoreszenzspektren bei verschiedenen Anregungswellenlängen gemessen (Abbildung 5-4b). Die beiden angeregten Triplettzustände treten immer gleichzeitig auf, was weiter beweist, dass T_1^M und T_1^A von derselben Absorption stammen ($S_0 \rightarrow S_1$ und $S_0 \rightarrow S_n$). Daher schlagen wir vor, dass

zuerst das einzelne Molekül von ***o*-BrTAB** in seinen S_1^M- oder S_n^M-Zustand angeregt wird. Dann wird es ISC zu T_2^M unterzogen, das IC zu einem kurzlebigen T_1^M-Zustand unterzogen wird. Gleichzeitig entwickelt sich T_1^A in einen T_1^M-Zustand, der langsamer und mit geringerer Energie emittiert. Der Prozess von T_1^M zu T_1^A wurde durch temperaturabhängige, zeitgesteuerte spektroskopische Untersuchung von kristallinem ***o*-BrTAB** bestätigt (Abbildung 5-5b). Beim Absenken der Temperatur von 298 auf 77 K verschieben sich die zu T_1^M gehörenden Phosphoreszenzpeaks bei 446 und 477 nm zu ca. 431 bzw. 455 nm, die bei 77 K mit einer Lebensdauer von *ca.* 2,1 ms. Bei 77 K existiert noch die langlebige T_1^A-Emission bei längerer Wellenlänge mit einer Lebensdauer von ca. 453 ms (58 %), jedoch in einem deutlich geringeren Verhältnis im Vergleich zur kurzlebigen Komponente. Somit gibt es eine thermische Barriere für die Umwandlung von T_1^M in T_1^A, und eine Senkung der Temperatur macht es schwieriger, die Barriere zu überwinden.

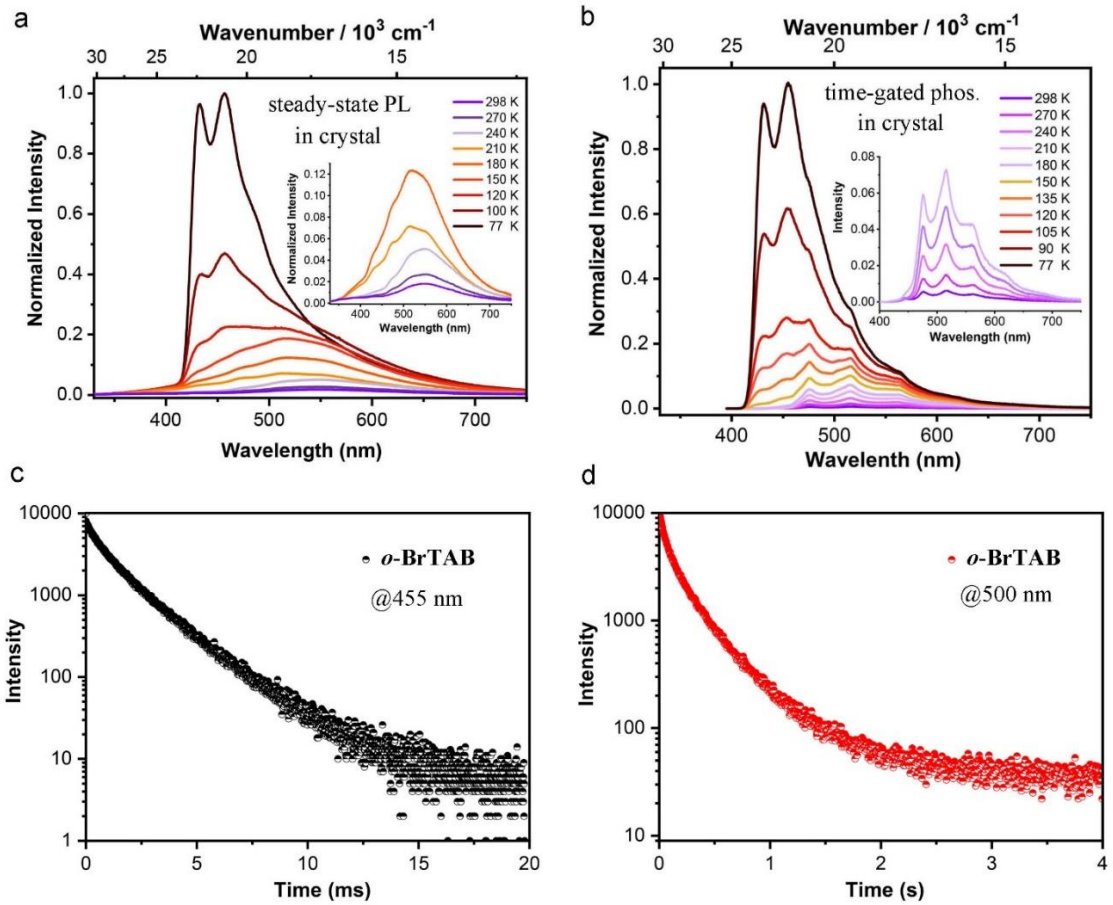

Abbildung 5-5. (a) Steady-State-Photolumineszenz und (b) zeitgesteuerte (Verzögerungszeit 0.01 ms) Phosphoreszenzspektren von kristallinem ***o*-BrTAB** bei verschiedenen Temperaturen (λ_{ex} = 305 nm). Abklingzeiten der Phosphoreszenzemission (c) (λ_{em} = 455 nm) und (d) (λ_{em} = 500 nm) von kristallinem ***o*-BrTAB** bei 77 K.

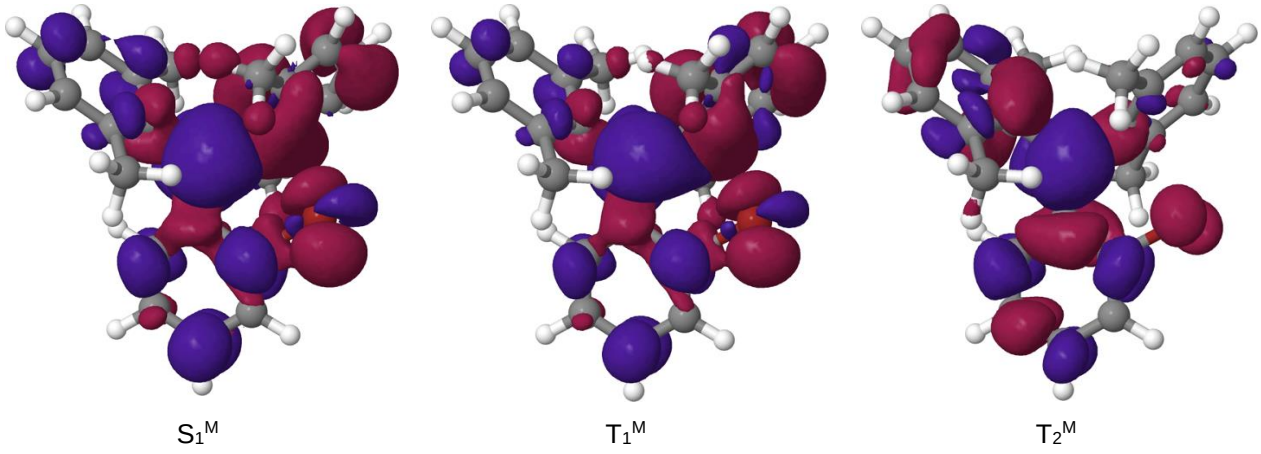

Abbildung 5-6. Unterschied der Elektronendichteverteilungen in den S_1^M, T_1^M und T_2^M Zuständen des ***o*-BrTAB** Monomers in Bezug auf den elektronischen Grundzustand S_0^M bei der S_1^M Geometrie. Rote Flächen bedeuten einen Verlust an Elektronendichte bei Anregung, blaue Flächen eine Verstärkung.

Um die experimentell beobachtete duale Phosphoreszenz zu erklären, suchten wir nach den wahrscheinlichsten Wegen vom Singulett zum Triplettzustand des Monomers. Die Bromsubstitution erhöht die SOCME im Allgemeinen in Bezug auf die der unsubstituierten Verbindung. Erwartungsgemäß ist der Schweratomeffekt für die ortho-substituierte Verbindung am stärksten. Trotz der Ähnlichkeit der Elektronenverteilungen in beiden Zuständen (Abbildung 5-6) erfahren die S_1^M und T_1^M Zustände einen erheblichen gegenseitigen SOC. Mit einer quadrierten Summe der SOCMEs von 25 cm^{-2} ist der $S_1^M \rightarrow T_1^M$ Übergang von ***o*-BrTAB** signifikant schneller als in der unsubstituierten Verbindung. Auch in diesem Fall ist die Änderung des Anregungscharakters beim Übergang $S_1^M \rightarrow T_2^M$ größer. Mit einer Geschwindigkeitskonstante von ca. $1*10^{10}$ s^{-1} ist die $S_1^M \rightarrow T_2^M$ ISC fünfmal schneller als die direkte $S_1^M \rightarrow T_1^M$ ISC. Sehr nahe am T_2^M Minimum durchlaufen die T_2^M und T_1^M Zustände von ***o*-BrTAB** einen konischen Schnittpunkt, ohne dass eine wesentliche Energiebarriere überwunden werden muss. Daher ist die Population nicht im T_2^M Zustand gefangen, sondern wird schnell in den T_1^M Zustand überführt. Die Möglichkeit, dass die duale Phosphoreszenz von T_2^M und T_1^M Zuständen herrührt, kann ausgeschlossen werden.

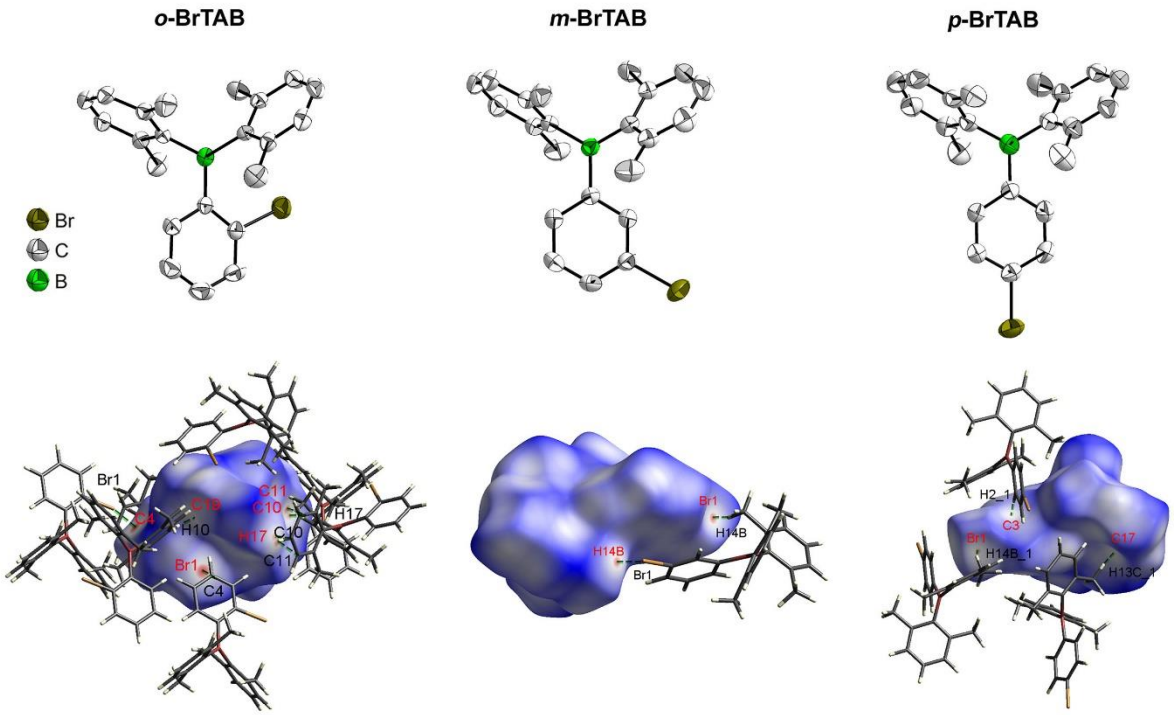

Abbildung 5-7. Die Festkörper-Molekülstruktur von ***o*-BrTAB**, ***m*-BrTAB** und ***p*-BrTAB** (oben von links nach rechts) bestimmt durch Einkristall-Röntgenbeugung bei Raumtemperatur. Ellipsoide sind mit einer Wahrscheinlichkeit von 50 % gezeichnet und H-Atome wurden der Übersichtlichkeit halber weggelassen. Hirshfeld-Oberflächen von ***o*-BrTAB**, ***m*-BrTAB** und ***p*-BrTAB** (unten von links nach rechts) kartiert mit dnorm über den Bereich –0,12 bis 1,50 bei Raumtemperatur. Benachbarte Moleküle mit engen Kontakten sind gezeigt.

Das Vorhandensein mehrerer C−H···C und C−H···Br Wechselwirkungen zwischen Molekülen in den Kristallen unterdrückt effektiv die strahlungslose Zerfallsrate k_{nr}, die eine wichtige Rolle bei der Stabilisierung der Triplettzustände und dem Erreichen von RTP spielt. Da die Stärke der intermolekularen Wechselwirkungen zwischen den drei Verbindungen bei Raumtemperatur besonders ausgeprägt ist und für ***o*-BrTAB** am stärksten ist, kann dieser Effekt der Grund dafür sein, dass wir DRTP in kristallinem ***o*-BrTAB** bei Raumtemperatur beobachten, jedoch nur bei niedriger Temperatur für ***m*-BrTAB** and ***p*-BrTAB**.

5.2.4 Kapitel 4

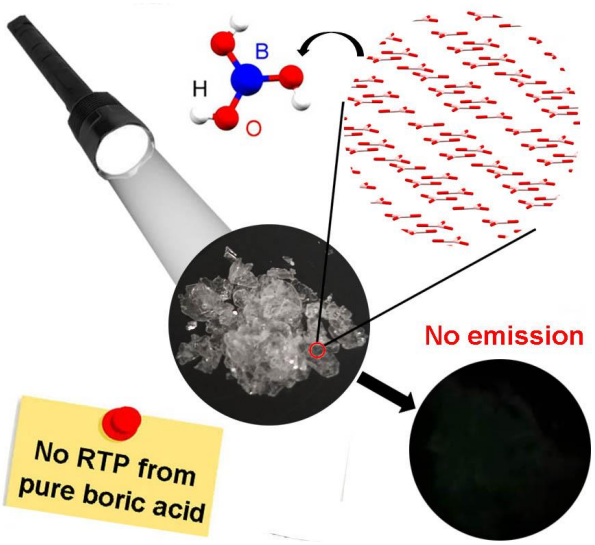

Borsäure (BA) wird seit über 100 Jahren als hervorragende Glasmatrix für optische Materialien aufgrund ihrer überlegenen Eigenschaften, einschließlich der für die Glasbildung erforderlichen niedrigen Temperatur, und ihrer einfachen Herstellung verwendet.Wie wir zeigen, weist reines BA selbst keine auf Fluoreszenz oder Phosphoreszenz im Festkörper. Im Jahr 2021 berichteten Peng Wu und Mitarbeiter von der Sichuan University jedoch über eine scheinbare Raumtemperatur-Phosphoreszenz (RTP) von BA im kristallinen und pulverförmigen Zustand bei Bestrahlung mit 280 nm unter Umgebungsbedingungen. Basierend auf unserer umfangreichen Untersuchung und unserem Verständnis von borhaltigen optischen Materialien vermuteten wir, dass diese scheinbare RTP aus ihrer BA-Probe durch eine nicht identifizierte Verunreinigung induziert wurde. Unsere eigenen experimentellen Ergebnisse zeigen, dass reines BA, synthetisiert aus Trimethylborat, $B(OMe)_3$, im Festkörper bei Bestrahlung mit Licht im Wellenlängenbereich von 250–400 nm keine Lumineszenz zeigt. Unsere theoretischen Berechnungen zeigen, dass weder einzelne BA-Moleküle noch (größere) Aggregate Licht bei Wellenlängen >175 nm absorbieren würden, und wir beobachten experimentell keine Absorption von festem BA bei Wellenlängen >200 nm. Daher ist es selbst im Festkörper nicht möglich, reines BA bei 250 nm oder längeren Wellenlängen anzuregen, wie von Wu beschrieben. Alle unsere Ergebnisse beweisen, dass reines BA kein RTP anzeigt.

Abbildung 5-8. a) Synthese von Borsäure aus $B(OMe)_3$. b) Fotografien von BA als gemahlenes Pulver und als Kristalle, aufgenommen bei Tageslicht. Das gemahlene Pulver behält die Kristallinität.

Wir synthetisierten und reinigten eine Probe von BA (Abbildung 5-8). Anschließend maßen wir die Absorptionsspektren von BA in Methanol, Isopropanol und Wasserlösungen bei Konzentrationen von 10^{-5} mol/L (Abbildung 5-9a). Der Selbstabsorptionsbereich von Methanol und Isopropanol reicht bis 205 nm. Bei Wellenlängen über 205 nm wurde keine Absorption mehrbeobachtet, was darauf hindeutet, dass in unserer BA-Probe keine aromatischen Spezies vorhanden sind. Der Selbstabsorptionsbereich von Wasser reicht bis 190 nm. Es wird ebenfalls kein Absorptionspeak im Spektrum bei >200 nm beobachtet. Selbst bei Erhöhung der BA-Konzentration in Methanol auf 10^{-4} oder 10^{-3} mol/L wurde keine Absorption bei >205 nm beobachtet. Es steht fest, dass das Festkörper-Absorptionsspektrum von BA im Bereich zwischen 200 und 485 nm keine Absorption zeigt (Abbildung 5-9b). Wir haben die Photolumineszenz (PL) Emissionsspektren und die zeitgesteuerten (1.0 ms) Phosphoreszenz-Emissionsspektren von BA sowohl als Kristalle als auch als gemahlenes Pulver gemessen (5-9c bis 5-9f). Wie erwartet, zeigen jedoch weder die PL noch die zeitgesteuerten Phosphoreszenzspektren von BA Emissionsbanden, weder als gemahlenes Pulver noch als Kristalle.

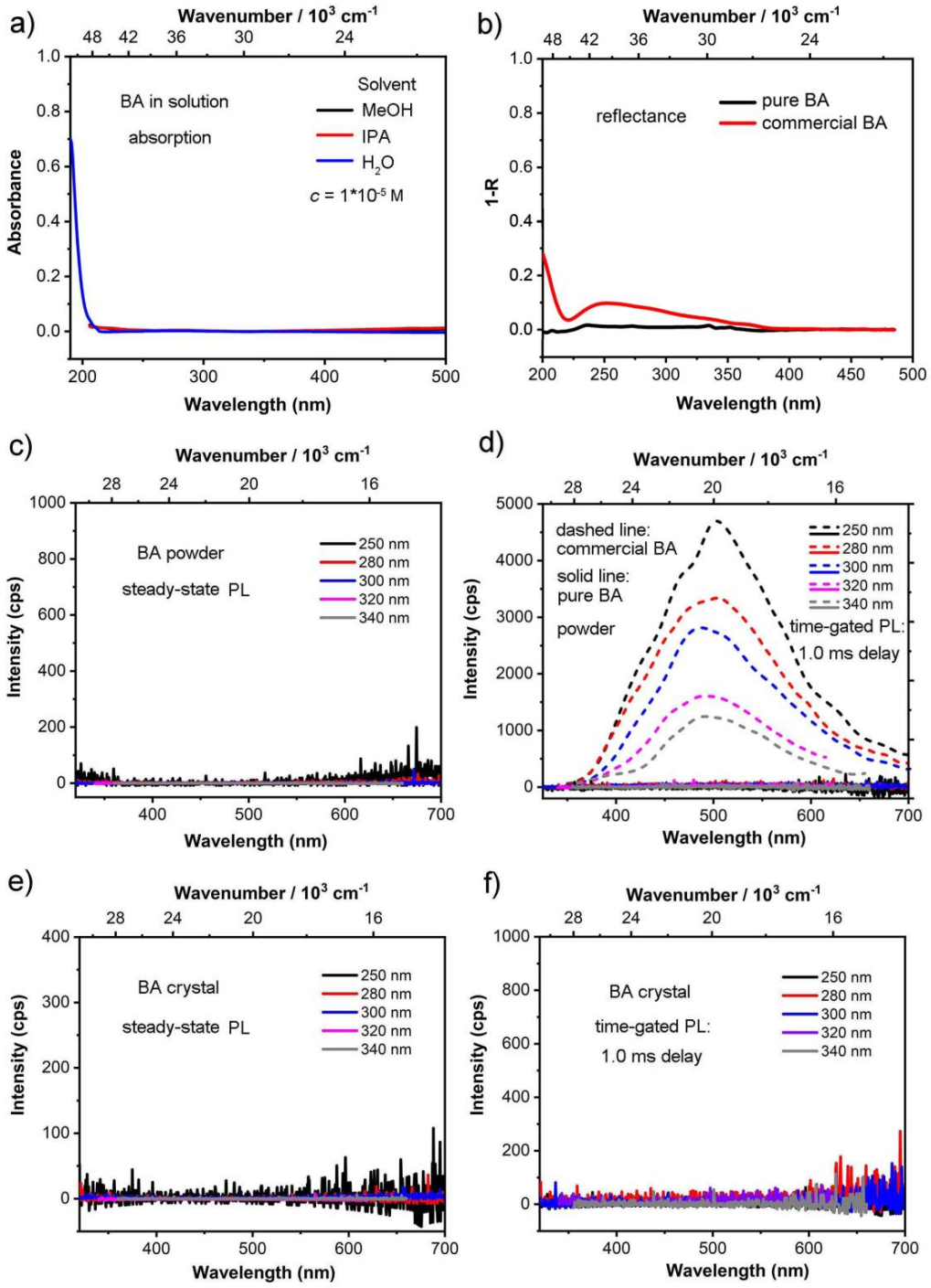

Abbildung 5-9 a) UV-vis-Absorptionsspektren von BA in MeOH, Isopropanol und H_2O Lösungen (c = 10^{-5} M). Der Resorptionsbeginn bei *ca*. 205 nm ist auf den Lösungsmittel- cutoff zurückzuführen. b) UV-Vis-Absorptionsspektren (R = Reflexion) von festen Proben von **reinem**, **kristallinem BA** (schwarz) und **kommerziellem BA** (rot). Gleichgewichtszustand photolumineszenz- (c) und zeitgesteuerter PL: 1.0 ms Verzögerung (d) Spektren von **kommerziellem BA** (gestrichelte Linie) und **reinem BA** (durchgezogene Linie) als gemahlenes Pulver (nicht amorph) bei verschiedenen Anregungswellenlängen unter den gleichen Bedingungen. Photolumineszenz- (e) und zeitgesteuerte (1.0 ms Verzögerung) Emissionsspektren (f) von **reinem**, **kristallinem BA** bei verschiedenen Anregungswellenlängen.

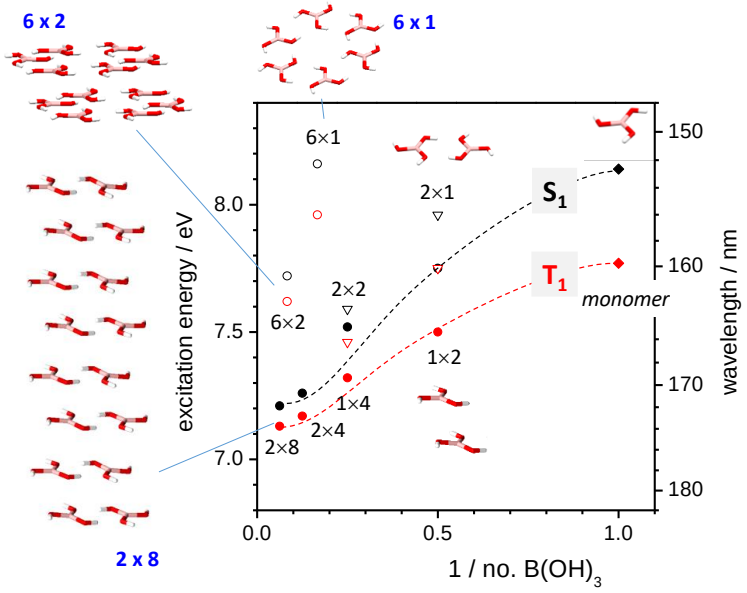

Abbildung 5-10 Vertikale Übergangsenergien für die niedrigsten angeregten Singulett- und Triplettzustände (S_1, T_1) von BA und Clustern davon, berechnet durch TD-DFT; gestrichelte Linien sind Orientierungshilfen.

Wir berechneten größere Cluster und erweiterten sie entlang der kristallographischen c-Achse (Abbildung 5-10). In diesem Fall wurde das B3LYP-Funktional verwendet, welches dazu neigt, die elektronischen Übergangsenergien zu unterschätzen und somit eine untere Grenze für das Auftreten von BA-Clusterabsorption definieren könnte. Wie in Abbildung 5-10 gezeigt, führt die Clusterbildung von Borsäureeinheiten tatsächlich im Allgemeinen zu einer bathochromen Verschiebung der elektronischen S_1 und T_1 Übergangsenergien; die Verschiebung wird besonders groß, wenn die Cluster in c-Richtung verlängert werden. Allerdings wird eine schnelle Sättigung beobachtet, so dass die maximale Verschiebung der Cluster gegenüber dem Monomer ca. 0.65 eV für T_1 und 0.95 eV für S_1 beträgt. Obwohl die Verschiebung beträchtlich ist, betonen wir, dass die Übergänge im tiefen UV-Bereich (über 7 eV; 177 nm) verbleiben, in guter Übereinstimmung mit unseren experimentellen Ergebnissen. Unsere Studie hat eindeutig gezeigt, dass sorgfältig gereinigtes BA, synthetisiert aus $B(OMe)_3$, keine intrinsische Phosphoreszenz im Festkörper zeigt, insbesondere im sichtbaren Bereich; TD-DFT-Berechnungen unterstützen unsere experimentellen Ergebnisse vollständig. Im Gegensatz dazu enthält kommerzielles BA offensichtlich Spuren von (unbekannten) lumineszierenden Verunreinigungen, was zu blau gefärbtem RTP führt. Verunreinigungsquellen können durchaus Nebenprodukte aus der Synthese sein, einschließlich Verunreinigungen in verwendeten Lösungsmitteln, Probenverunreinigungen oder Fotoprodukte. Solche

(lumineszierenden) gefangenen Zustände in molekularen Festkörpern können direkt angeregt werden, wenn die Konzentration und der Absorptionskoeffizient der Verunreinigungen ausreichend hoch sind, was für kommerzielles BA tatsächlich der Fall ist, wie in der aktuellen Arbeit gezeigt wird (siehe Abbildung 5-9b).

CHAPTER SIX

-

APPENDIX

6 Appendix

6.1 NMR and Mass Spectra

6.1.1 Chapter 2

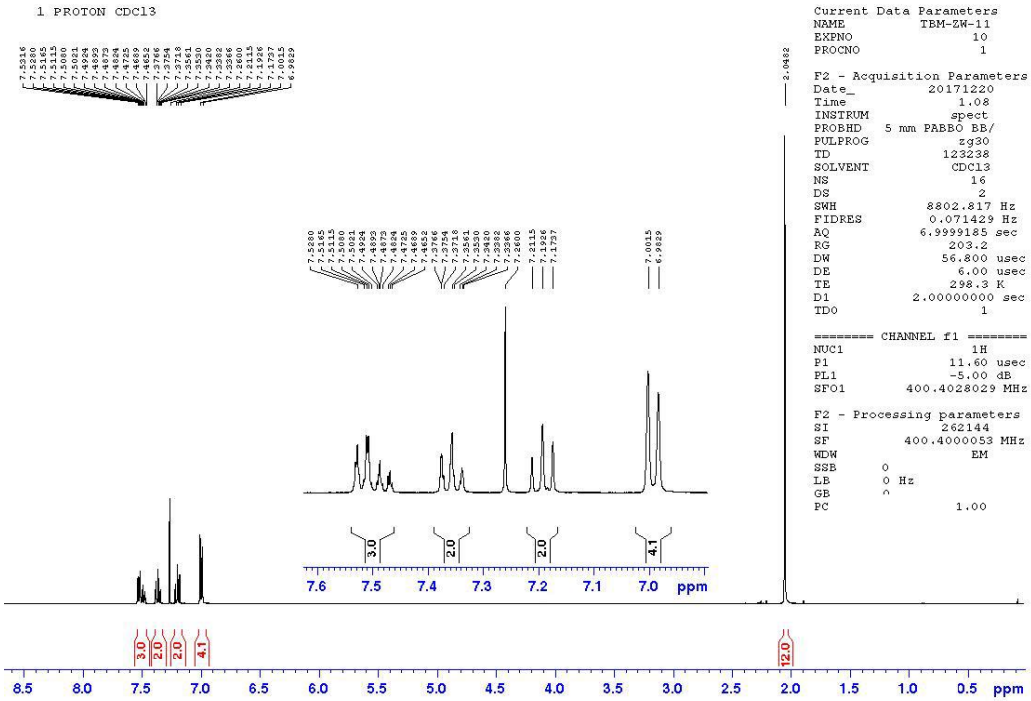

Figure 6-1 ^{1}H NMR spectrum (400 MHz, $CDCl_3$) of **1**.

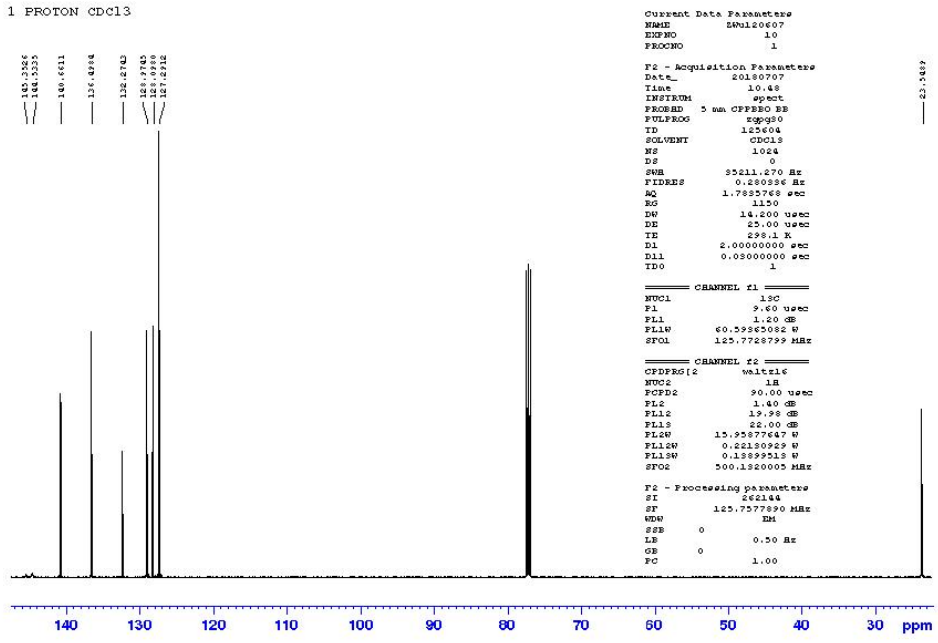

Figure 6-2. $^{13}C\{^{1}H\}$ NMR spectrum (126 MHz, $CDCl_3$) of **1**.

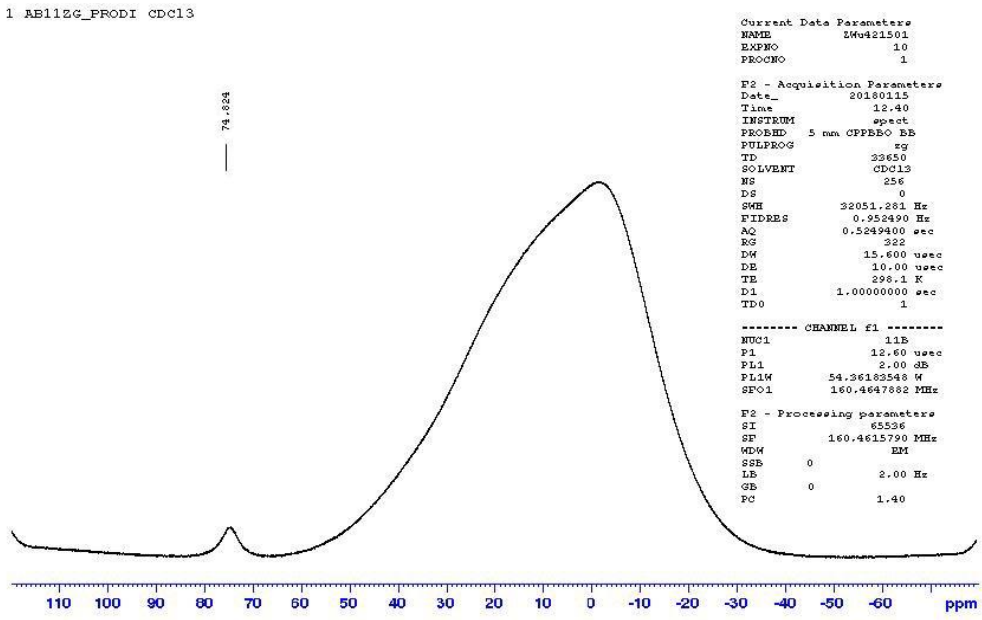

Figure 6-3. ^{11}B NMR spectrum (160 MHz, $CDCl_3$) of **1**.

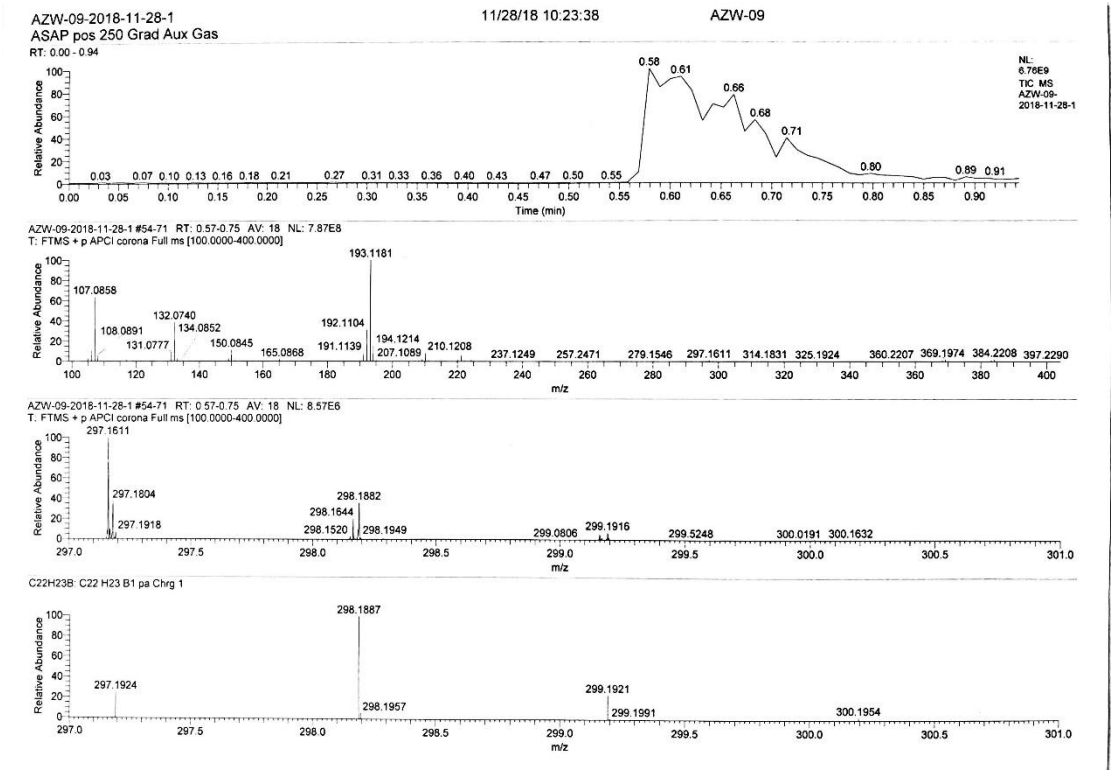

Figure 6-4. HR-ESI-MS spectrum of **1**.

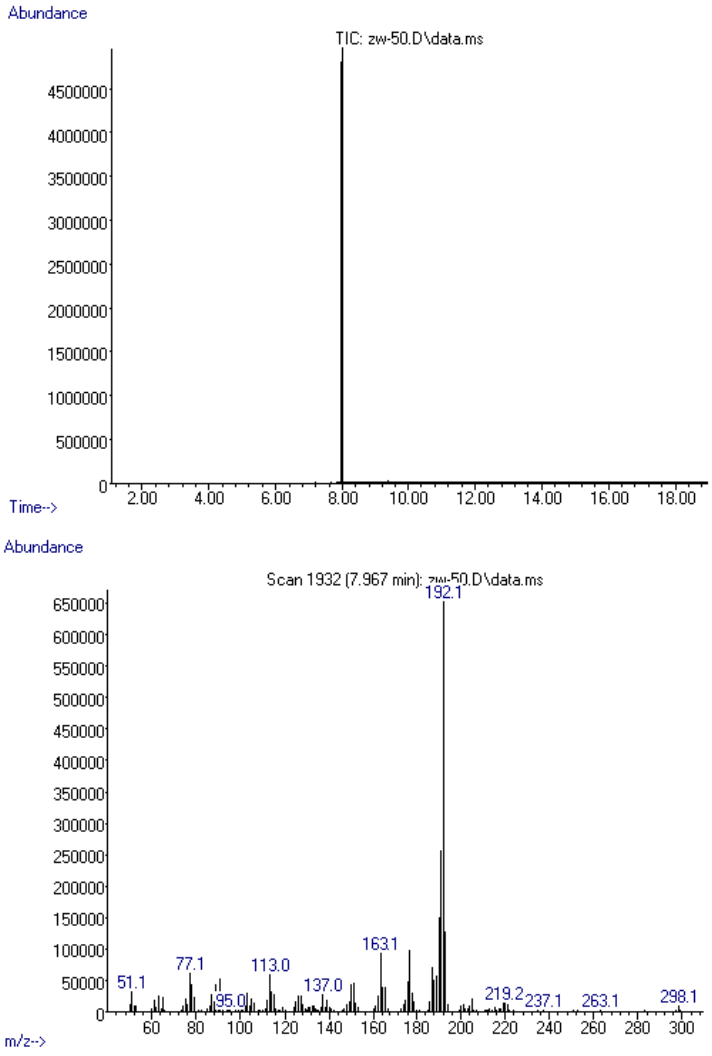

Figure 6-5. GC-MS total ion chromatogram^{TIC} and MS $(EI)_{m/z}$ of **1**.

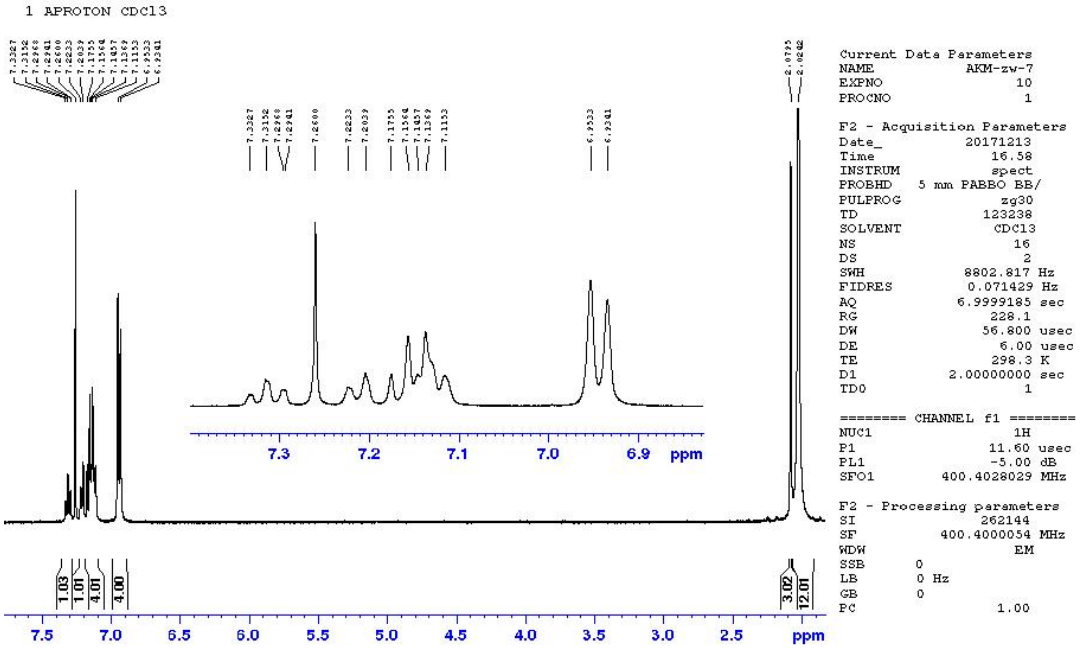

Figure 6-6. ^{1}H NMR spectrum (400 MHz, $CDCl_3$) of **2**.

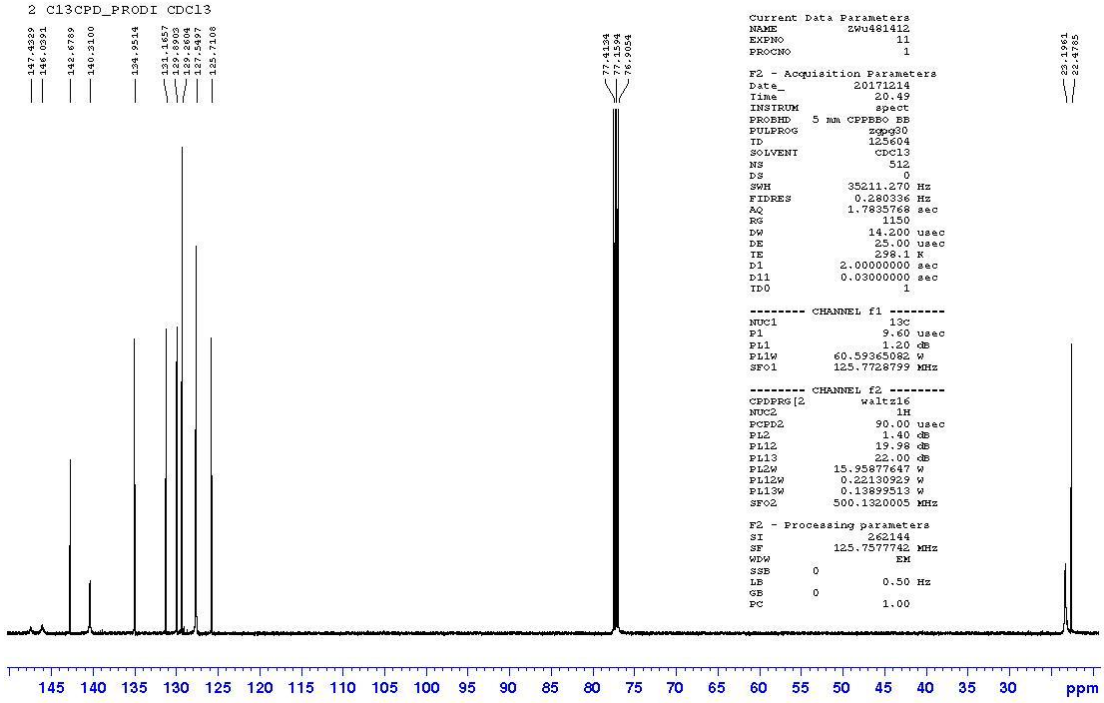

Figure 6-7. $^{13}C\{^{1}H\}$ NMR spectrum (126 MHz, $CDCl_3$) of **2**.

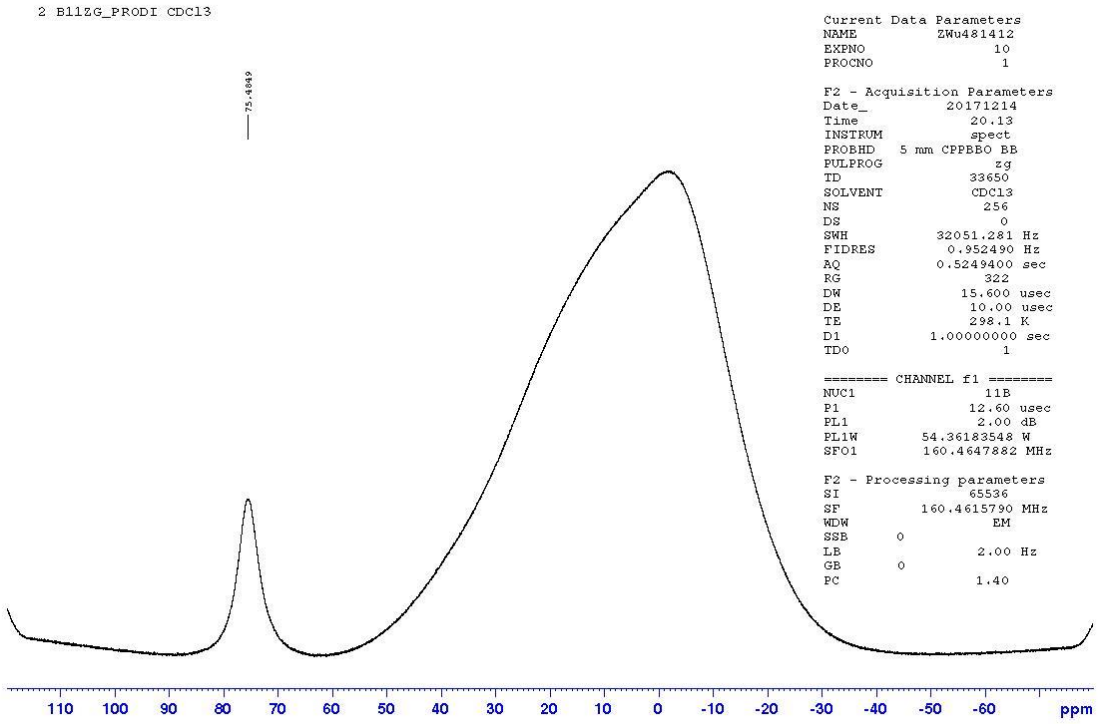

Figure 6-8. ^{11}B NMR spectrum (160 MHz, $CDCl_3$) of **2**.

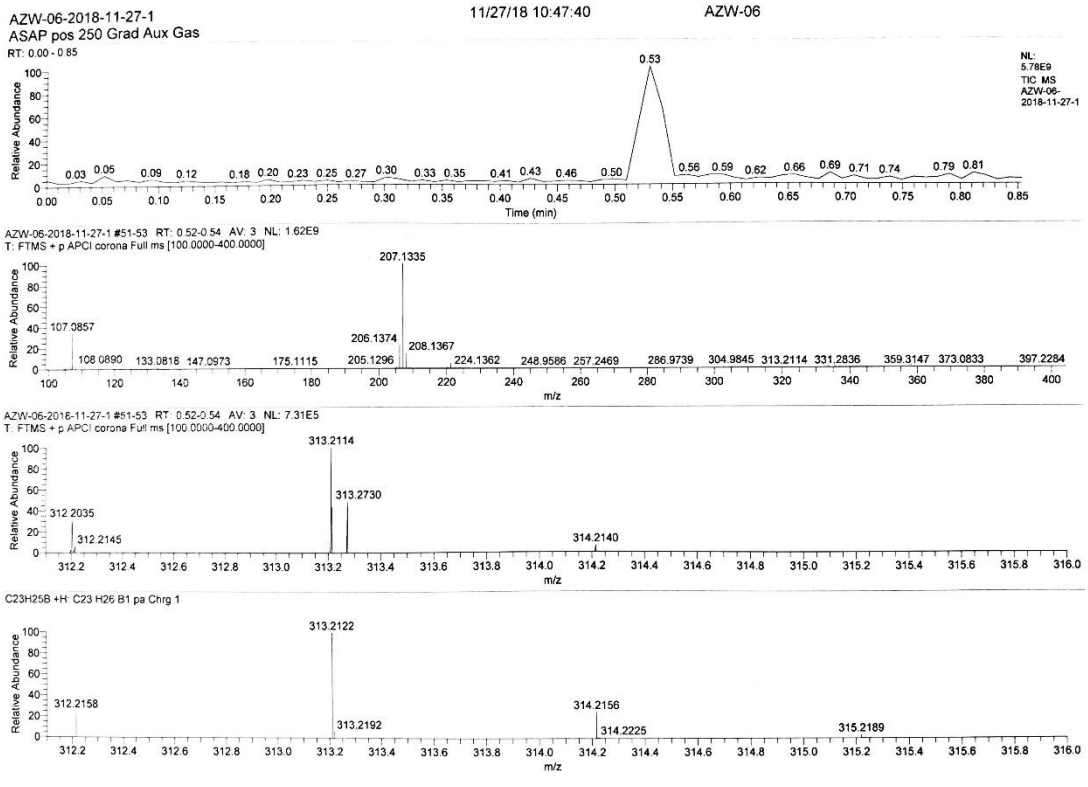

Figure 6-9. HR-ESI-MS spectrum of **2**.

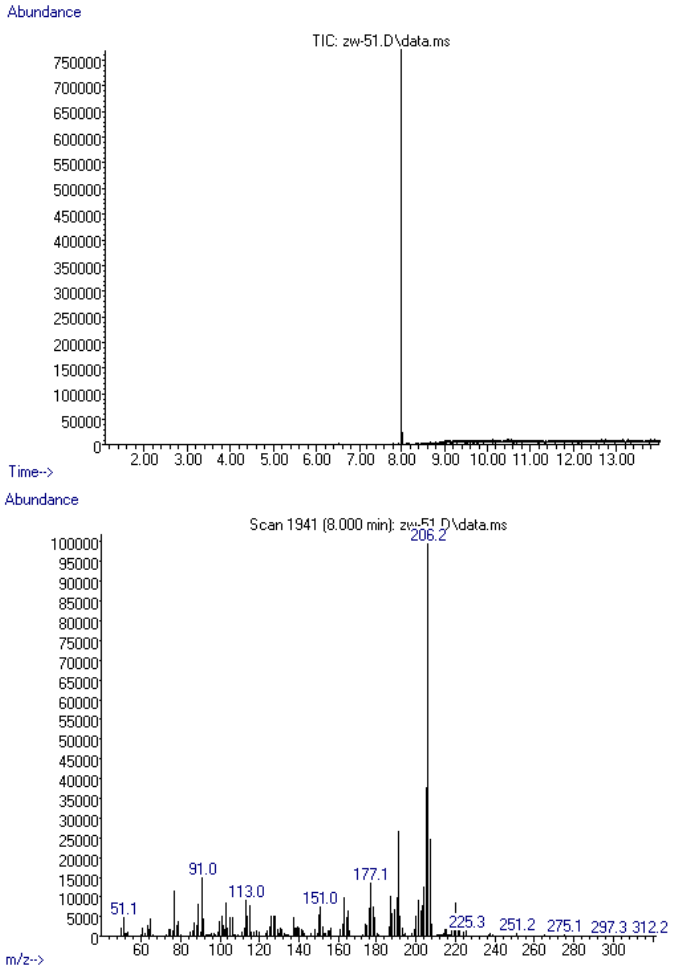

Figure 6-10. GC-MS total ion chromatogram^{TIC} and MS $(EI)_{m/z}$ of **2**.

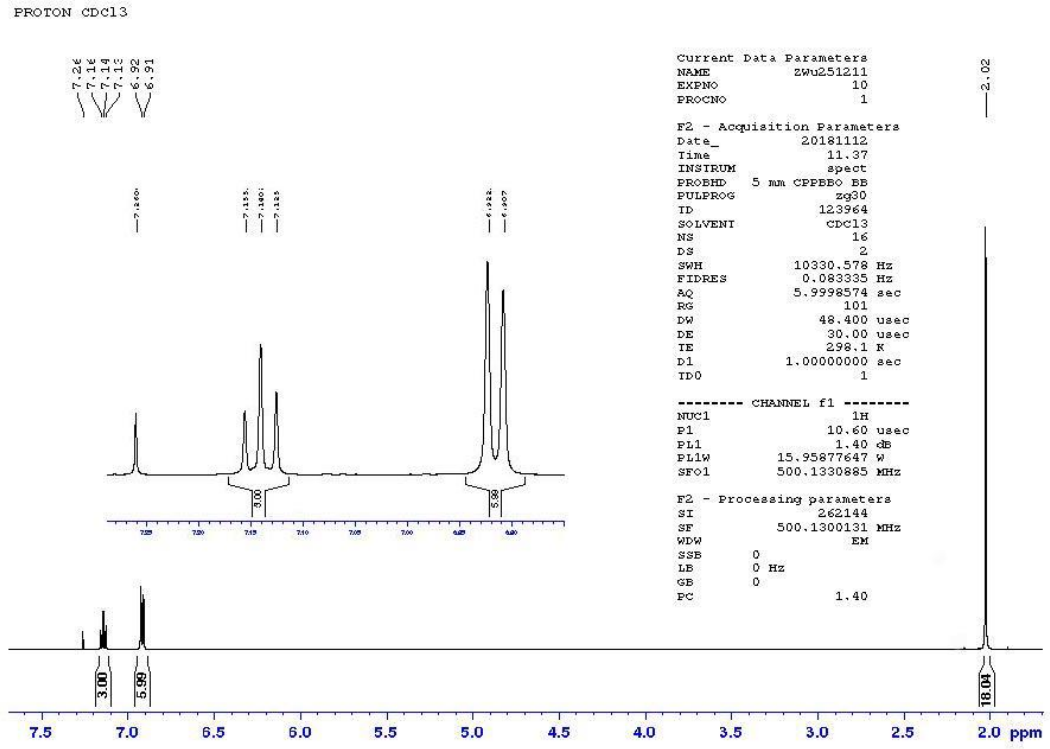

Figure 6-11. ^{1}H NMR spectrum (500 MHz, $CDCl_3$) of **3**.

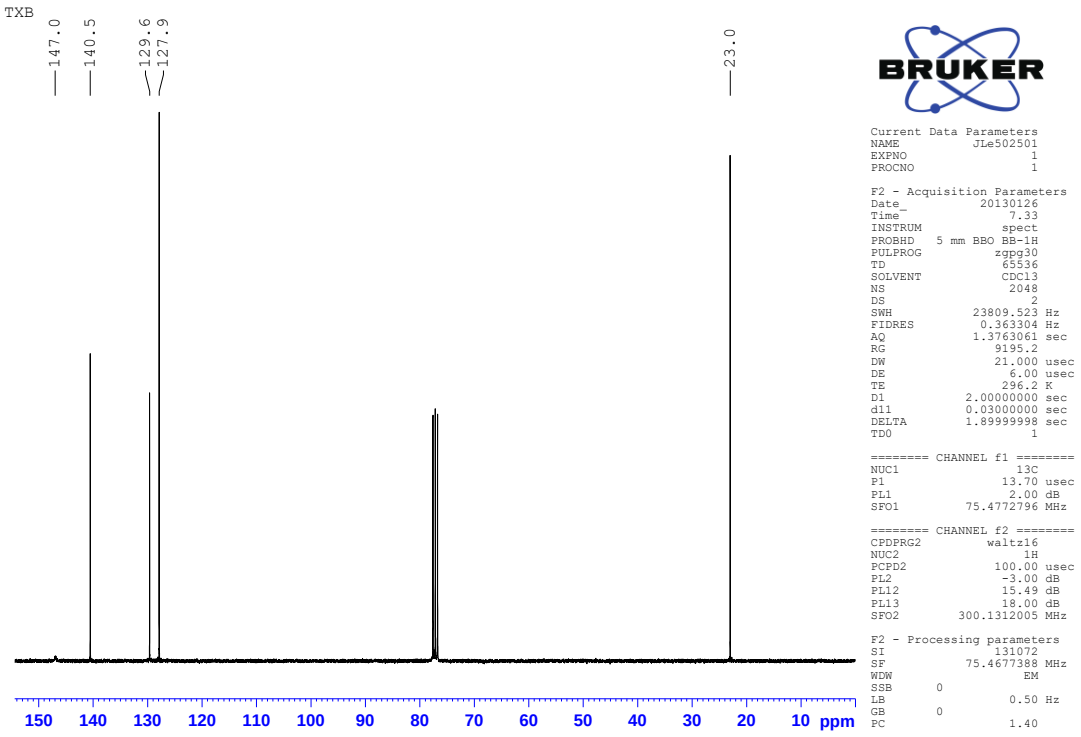

Figure 6-12. $^{13}C\{^{1}H\}$ NMR spectrum (126 MHz, $CDCl_3$) of **3**.

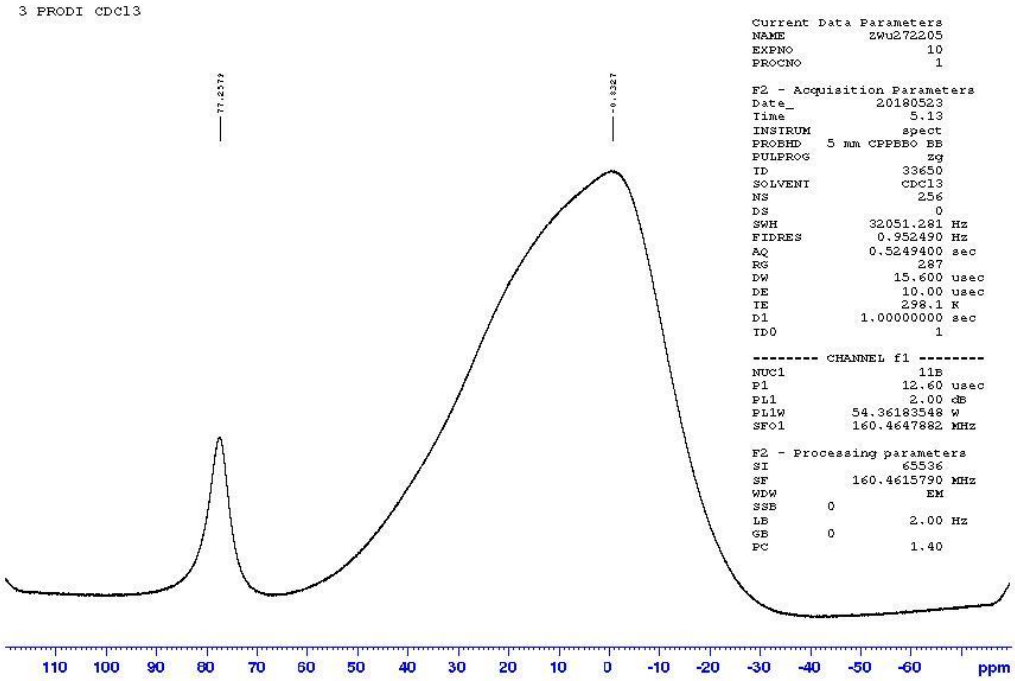

Figure 6-13. ^{11}B NMR spectrum (160 MHz, $CDCl_3$) of **3**.

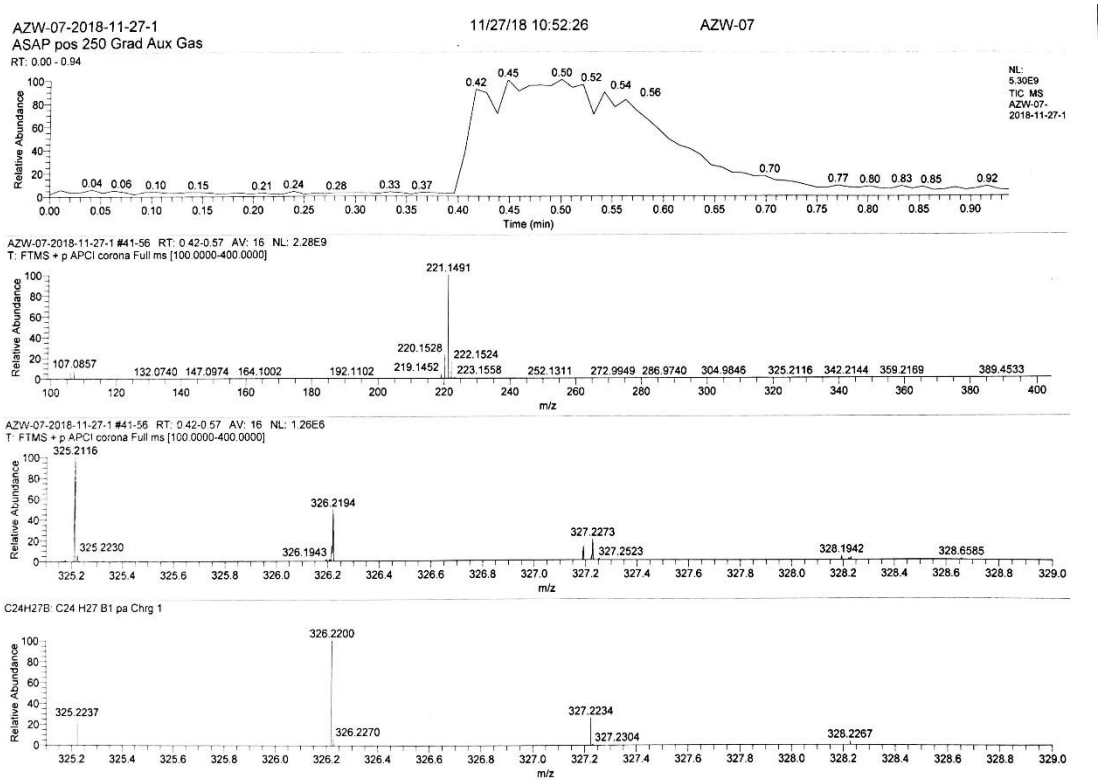

Figure 6-14. HR-ESI-MS spectrum of **3**.

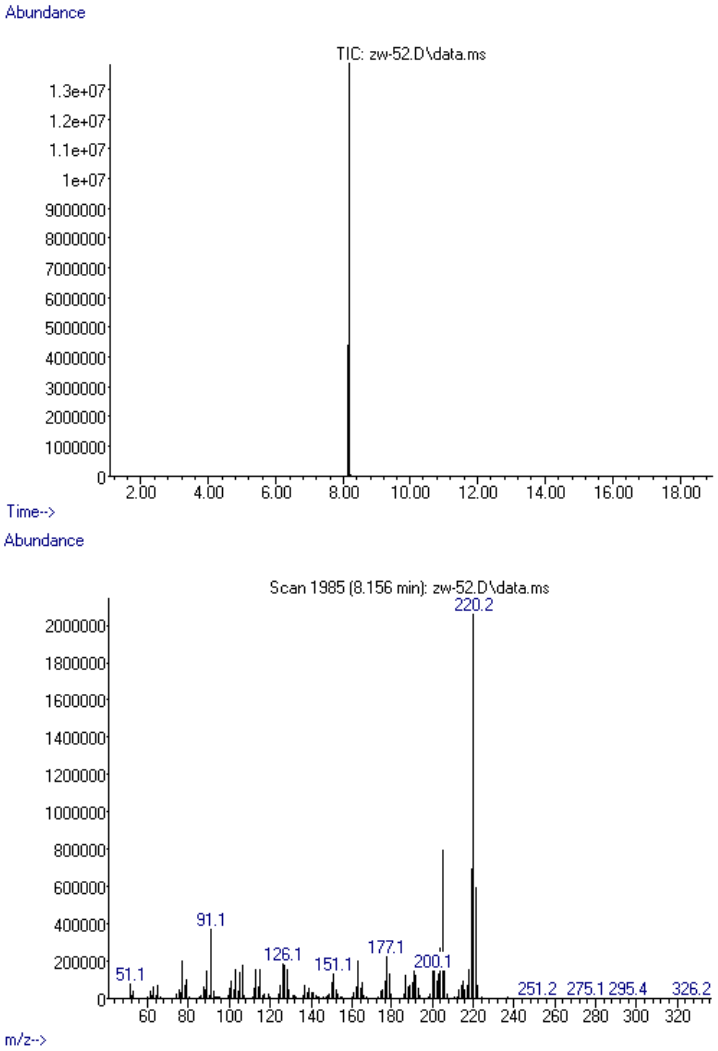

Figure 6-15. GC-MS total ion chromatogram^{TIC} and MS $(EI)_{m/z}$ of **3**.

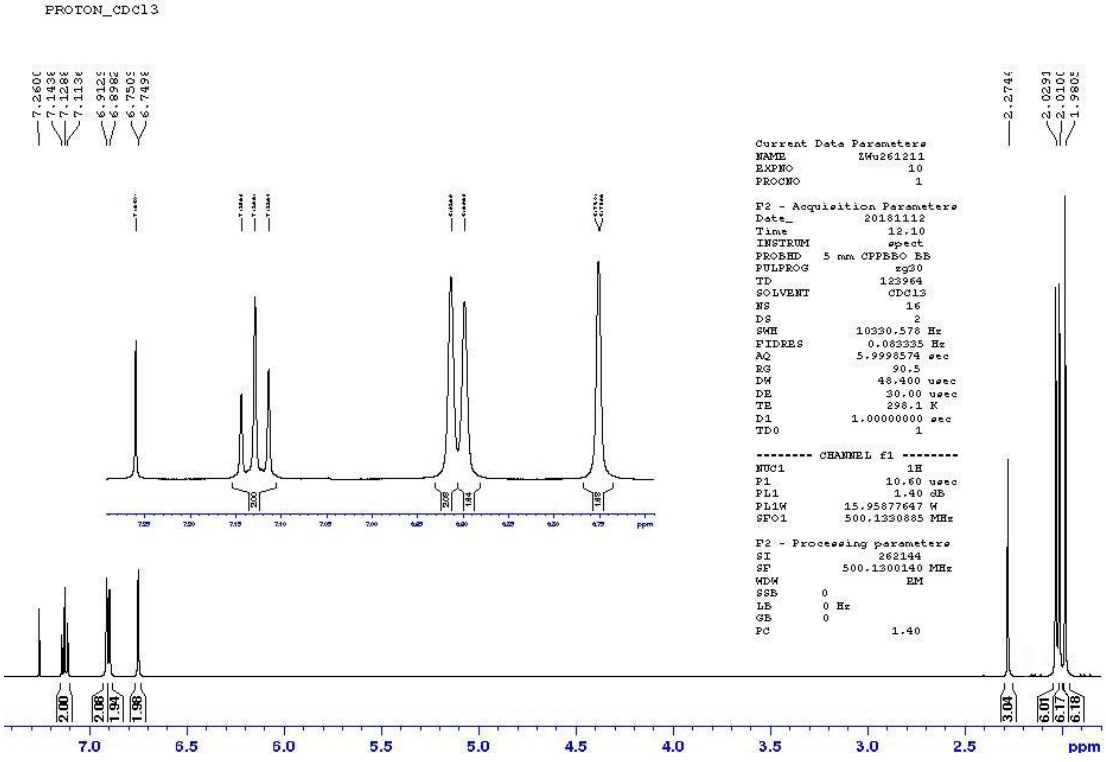

Figure 6-16. ^{1}H NMR spectrum (500 MHz, $CDCl_3$) of **4**.

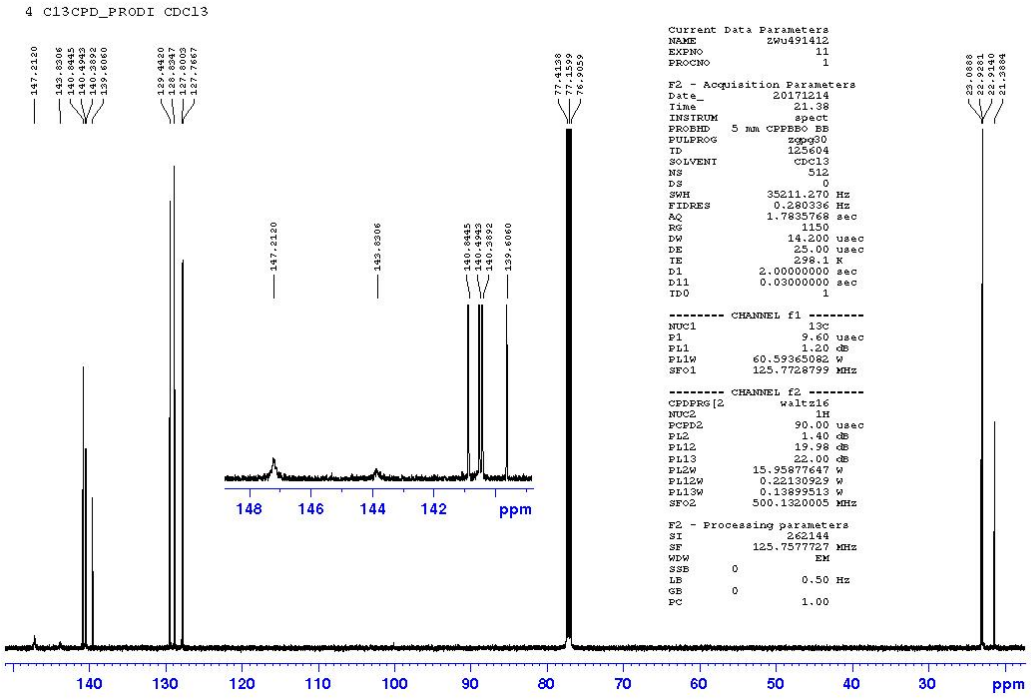

Figure 6-17. $^{13}C\{^{1}H\}$ NMR spectrum (126 MHz, $CDCl_3$) of **4**.

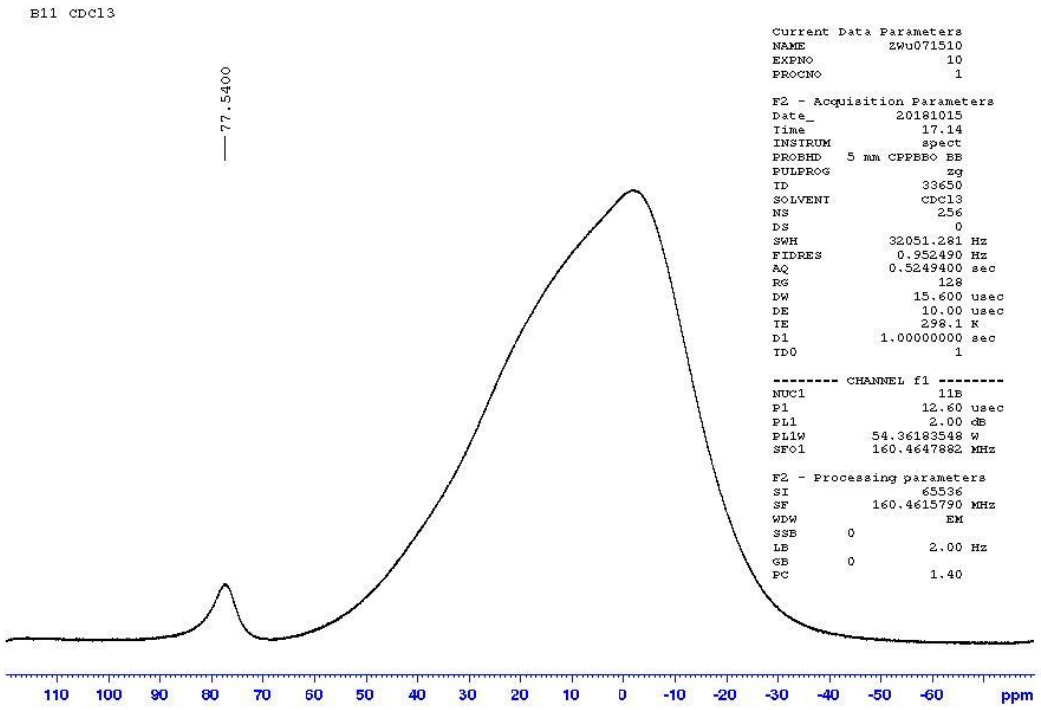

Figure 6-18. ^{11}B NMR spectrum (160 MHz, $CDCl_3$) of **4**.

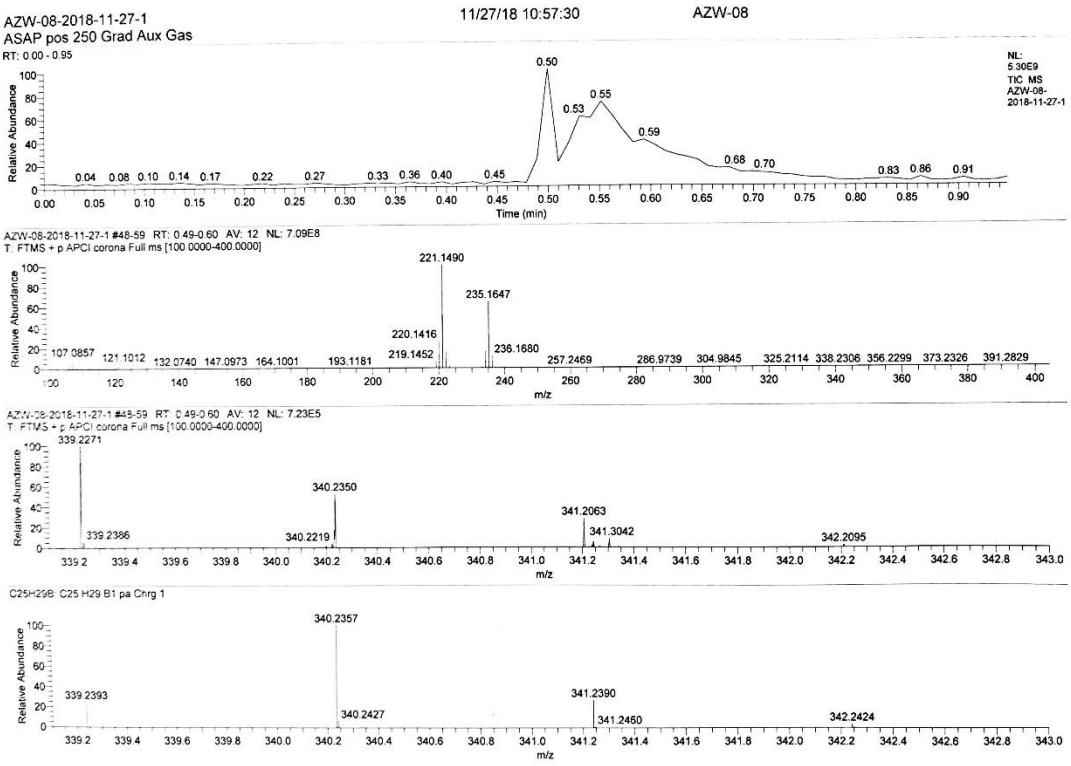

Figure 6-19. HR-ESI-MS spectrum of **4**.

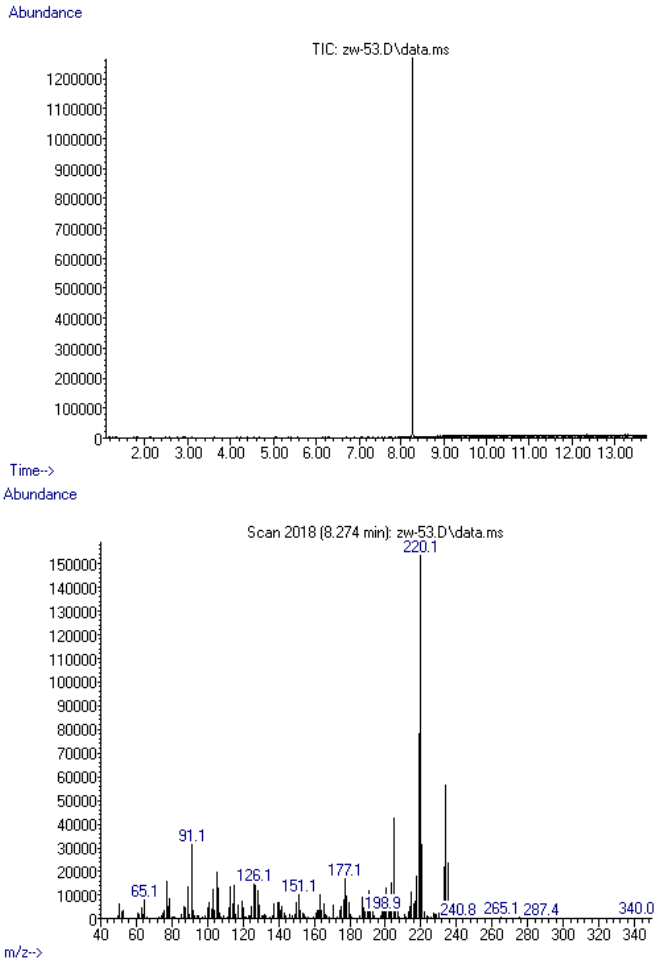

Figure 6-20. GC-MS total ion chromatogram^{TIC} and MS $(EI)_{m/z}$ of **4**.

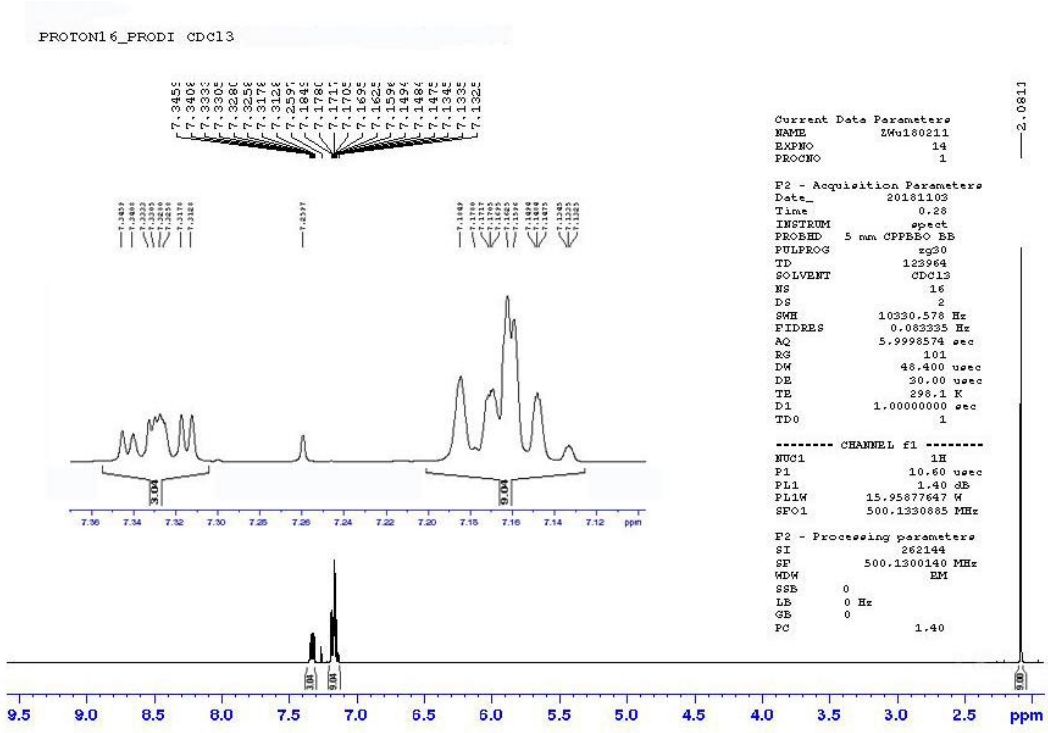

Figure 6-21. ^{1}H NMR spectrum (500 MHz, $CDCl_3$) of **tris(2-methylphenyl)borane**.

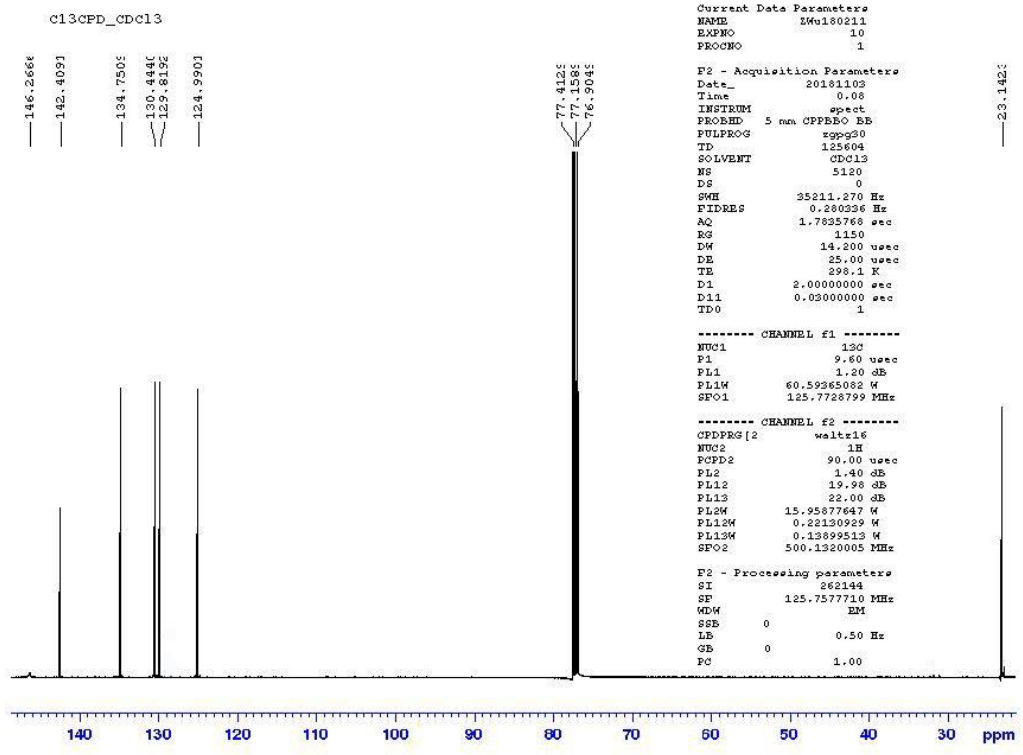

Figure 6-22. $^{13}C\{^{1}H\}$ NMR spectrum (126 MHz, $CDCl_3$) of **tris(2-methylphenyl)borane**.

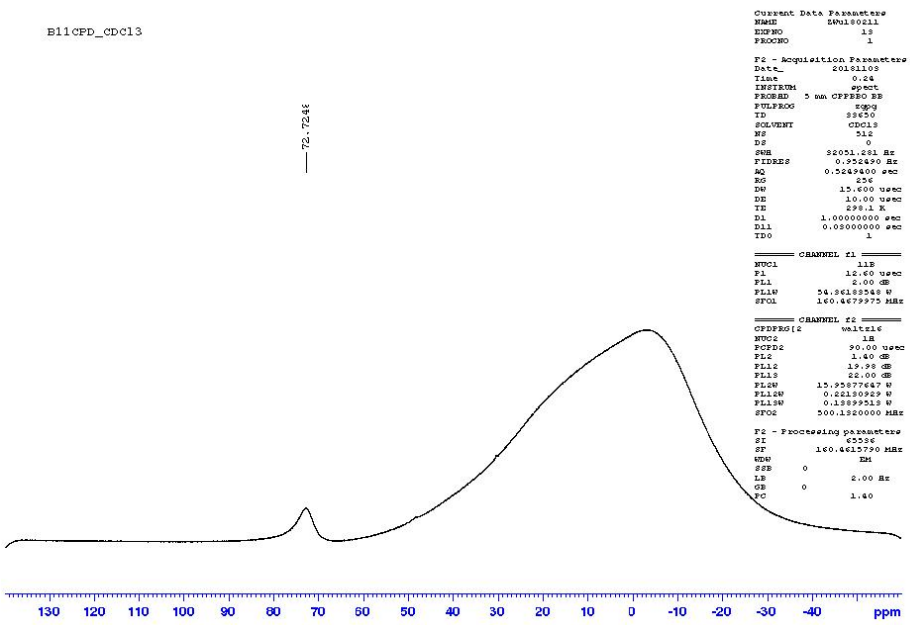

Figure 6-23. ^{11}B NMR spectrum (160 MHz, $CDCl_3$) of **tris(2-methylphenyl)borane**.

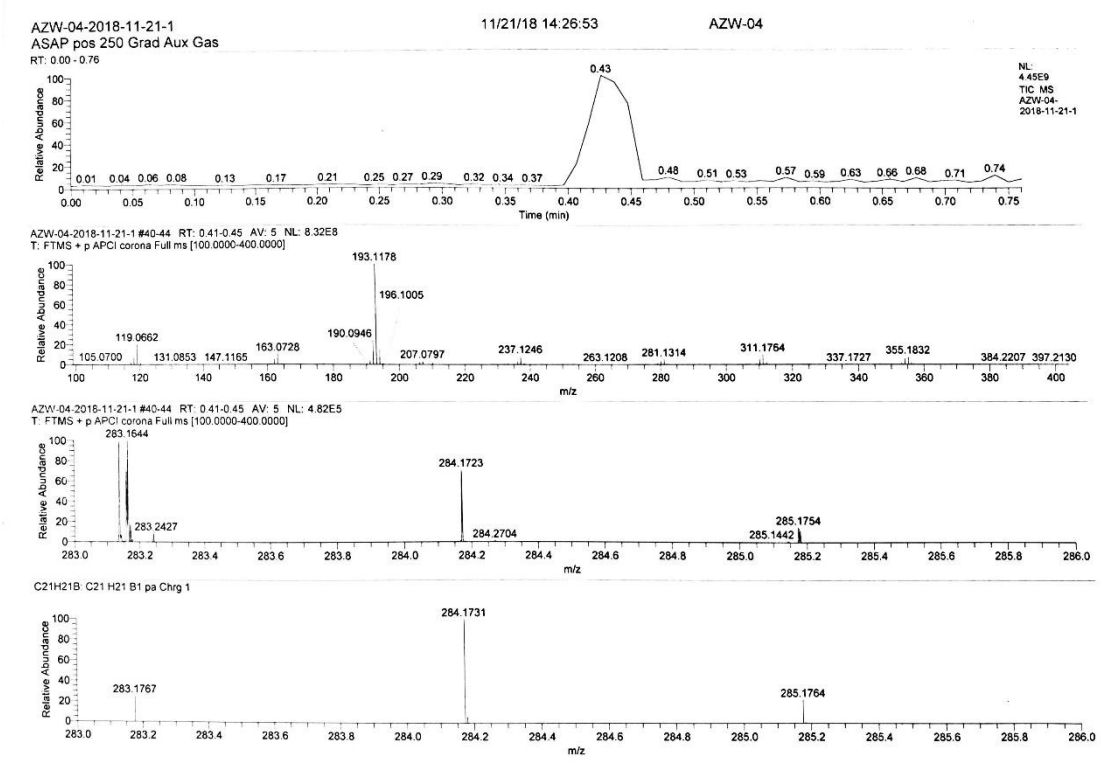

Figure 6-24. HR-ESI-MS spectrum of **tris(2-methylphenyl)borane**.

8.1.2 Chapter 3

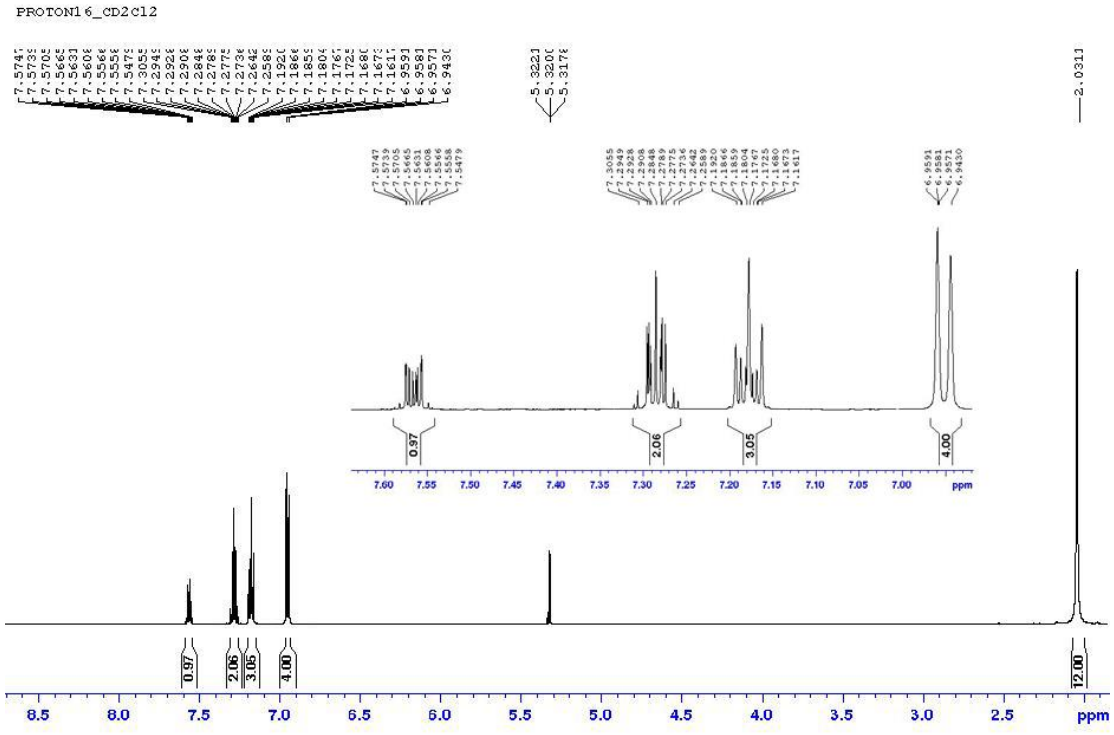

Figure 6-25. ^{1}H NMR spectrum (500 MHz, CD_2Cl_2) of ***o*-BrTAB**.

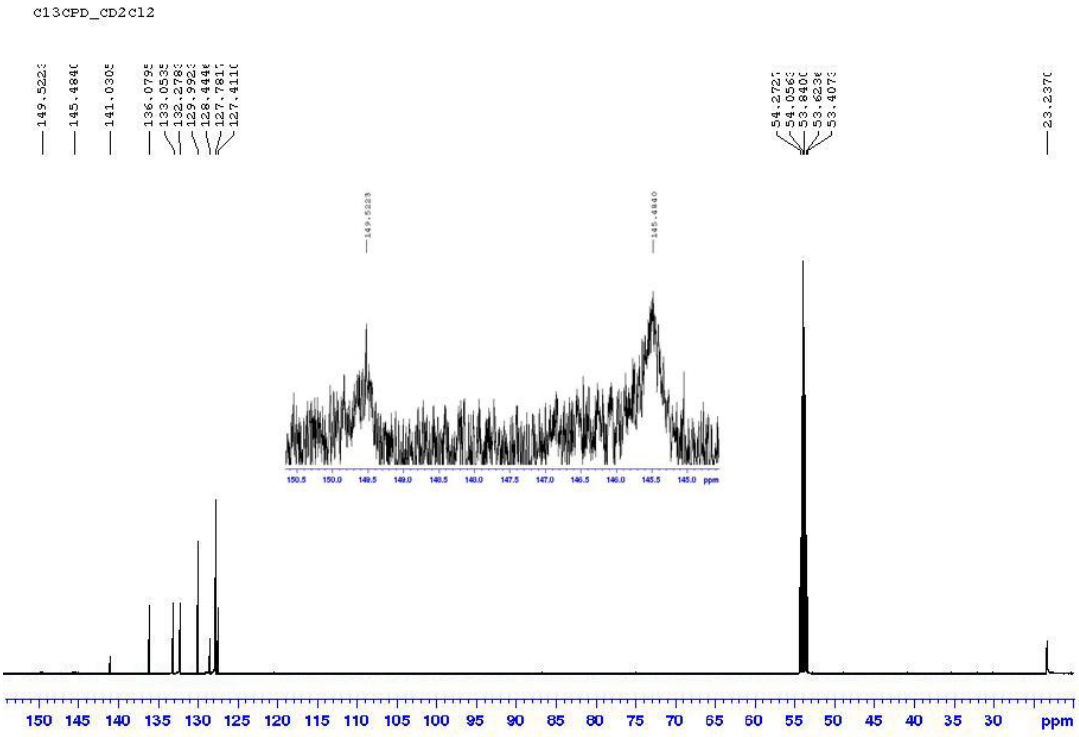

Figure 6-26. $^{13}C\{^{1}H\}$ NMR spectrum (126 MHz, CD_2Cl_2) of ***o*-BrTAB**.

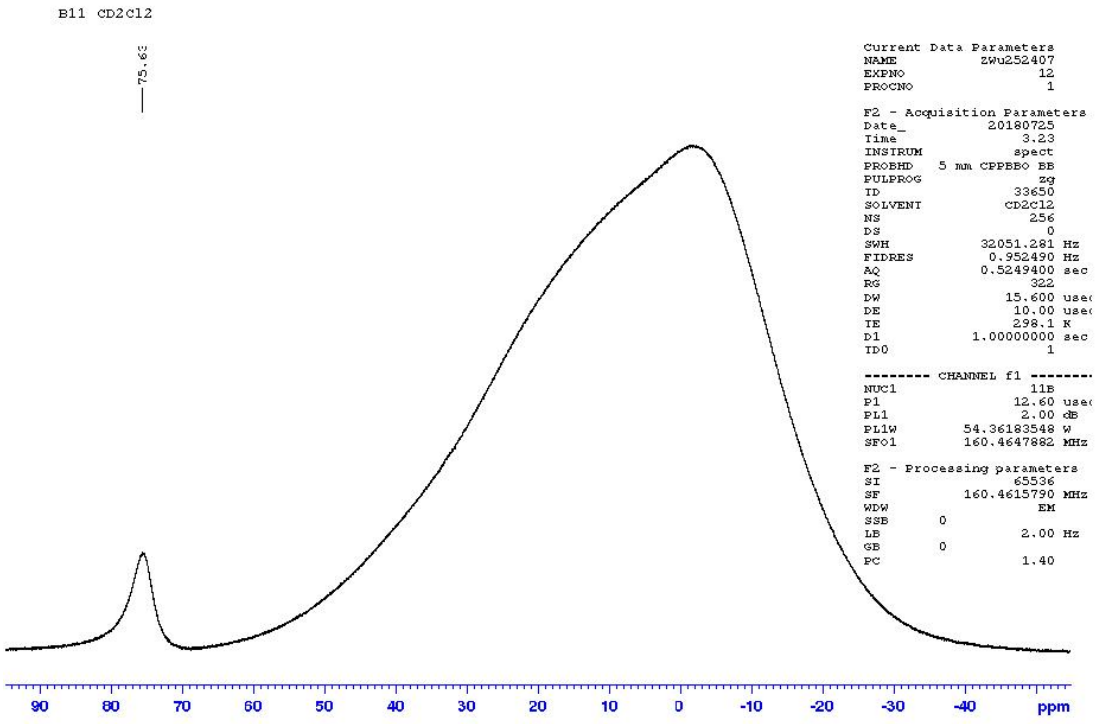

Figure 6-27. ^{11}B NMR spectrum (160 MHz, CD_2Cl_2) of ***o*-BrTAB**.

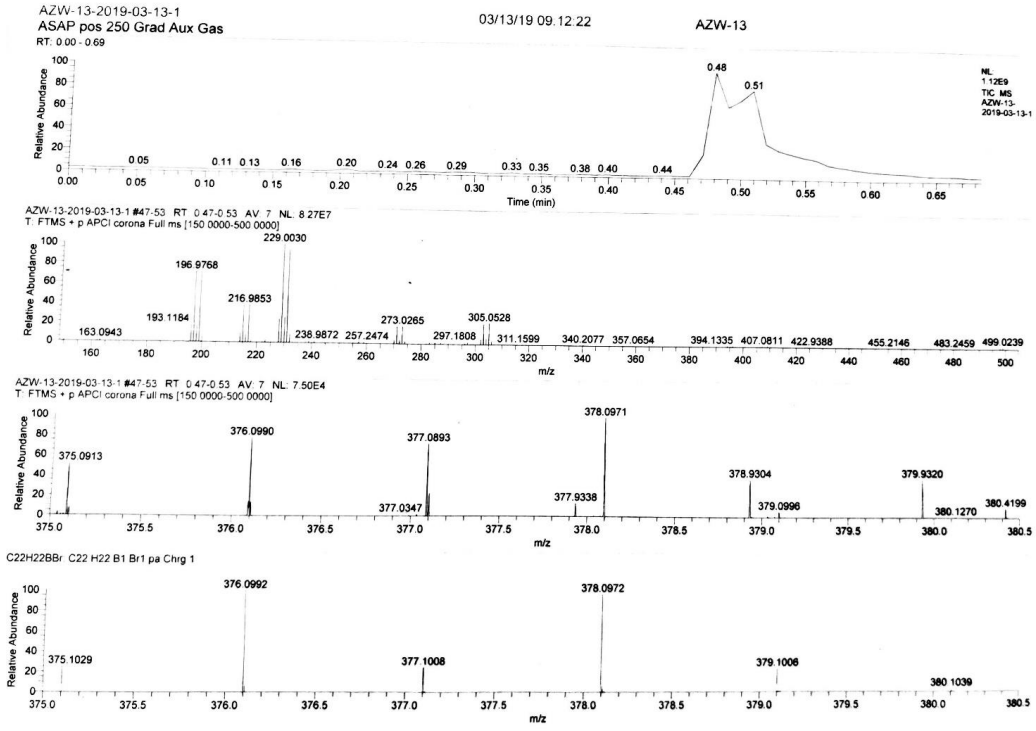

Figure 6-28. HR-ESI-MS spectrum of ***o*-BrTAB**.

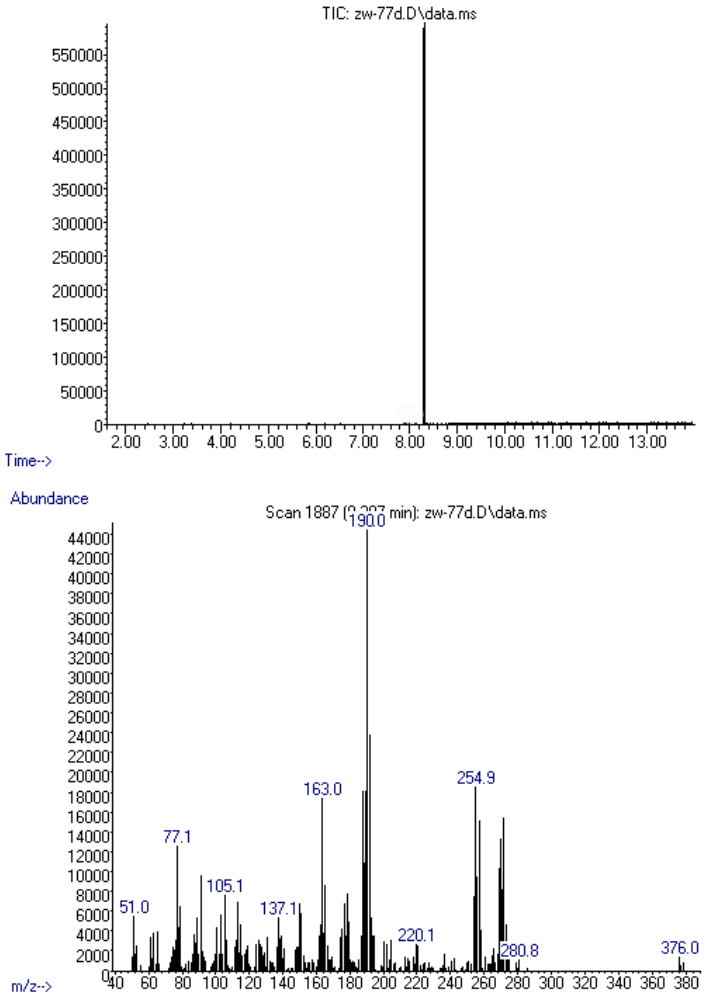

Figure 6-29. GC-MS total ion chromatogram^{TIC} and MS $(EI)_{m/z}$ of ***o*-BrTAB**.

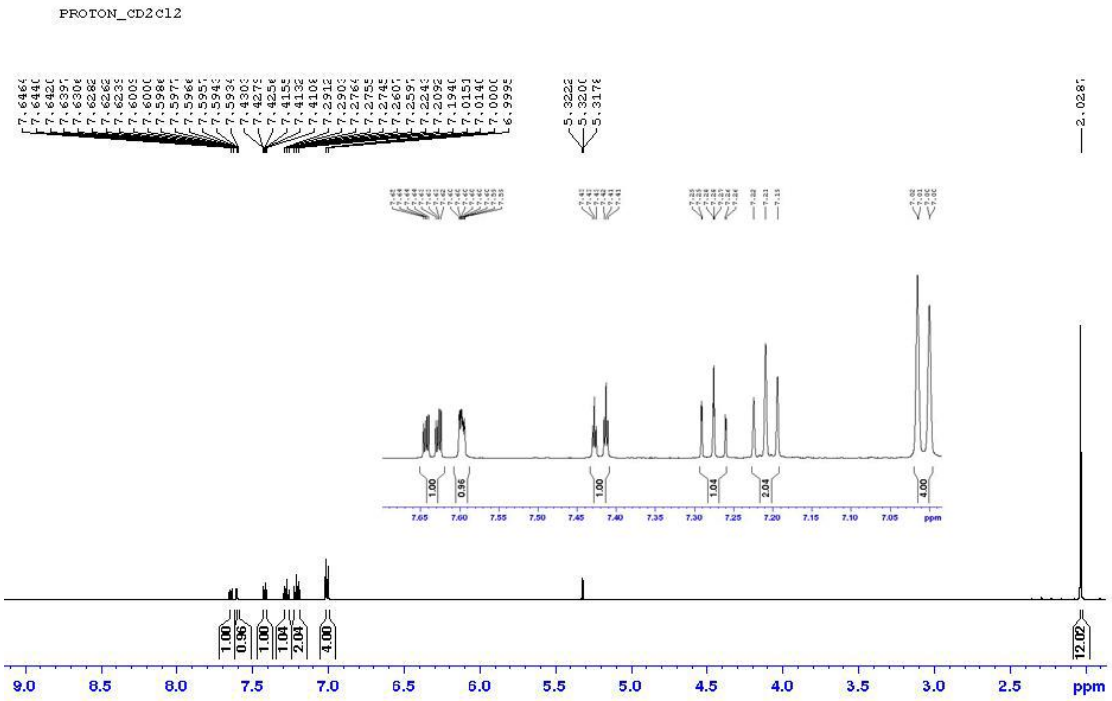

Figure 6-30. ^{1}H NMR spectrum (500 MHz, CD_2Cl_2) of ***m*-BrTAB**.

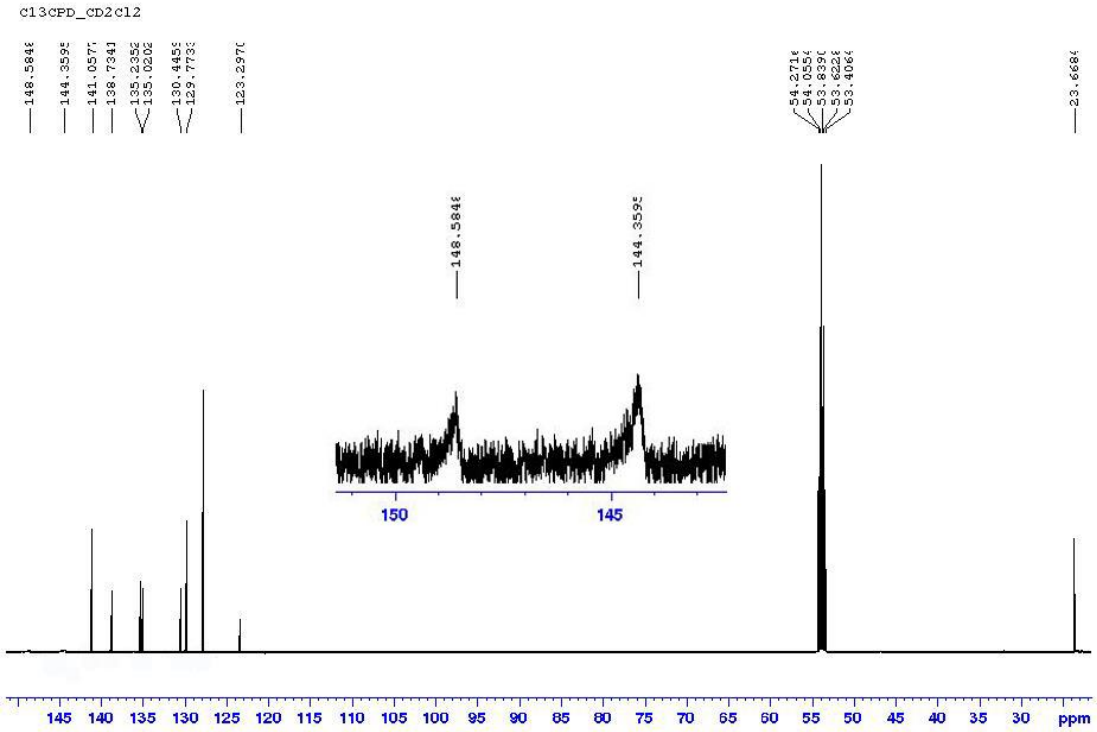

Figure 6-31. $^{13}C\{^{1}H\}$ NMR spectrum (126 MHz, CD_2Cl_2) of ***m*-BrTAB**.

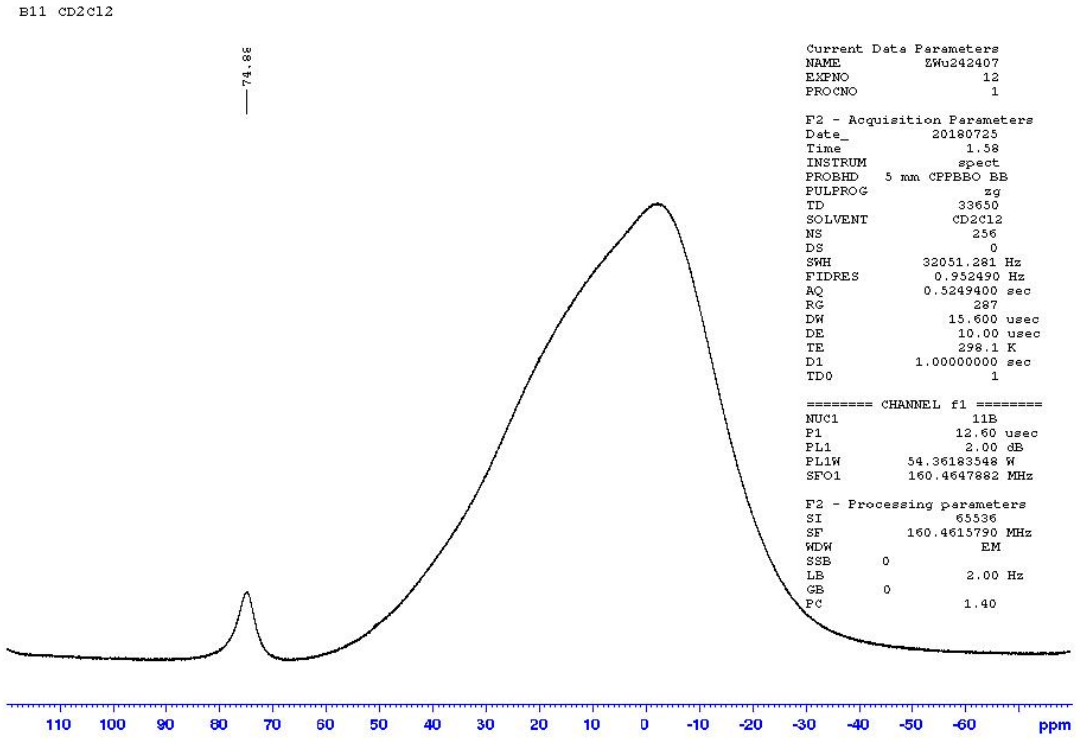

Figure 6-32. ^{11}B NMR spectrum (160 MHz, CD_2Cl_2) of ***m*-BrTAB**.

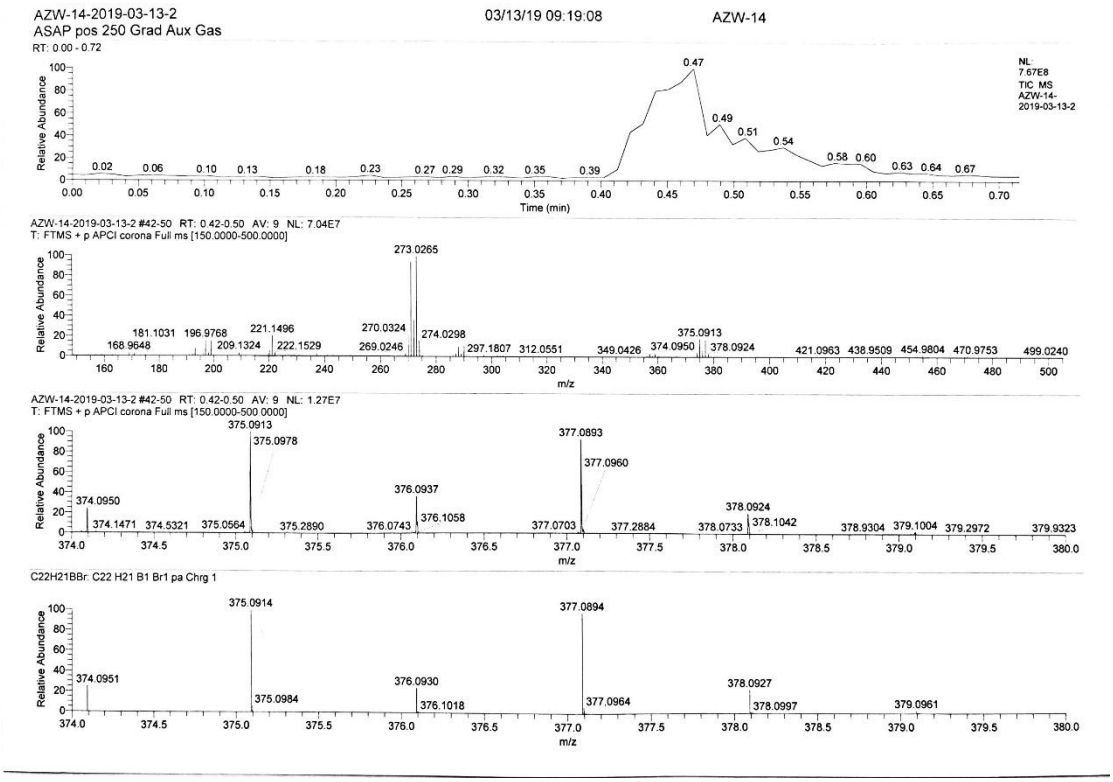

Figure 6-33. HR-ESI-MS spectrum of ***m*-BrTAB**.

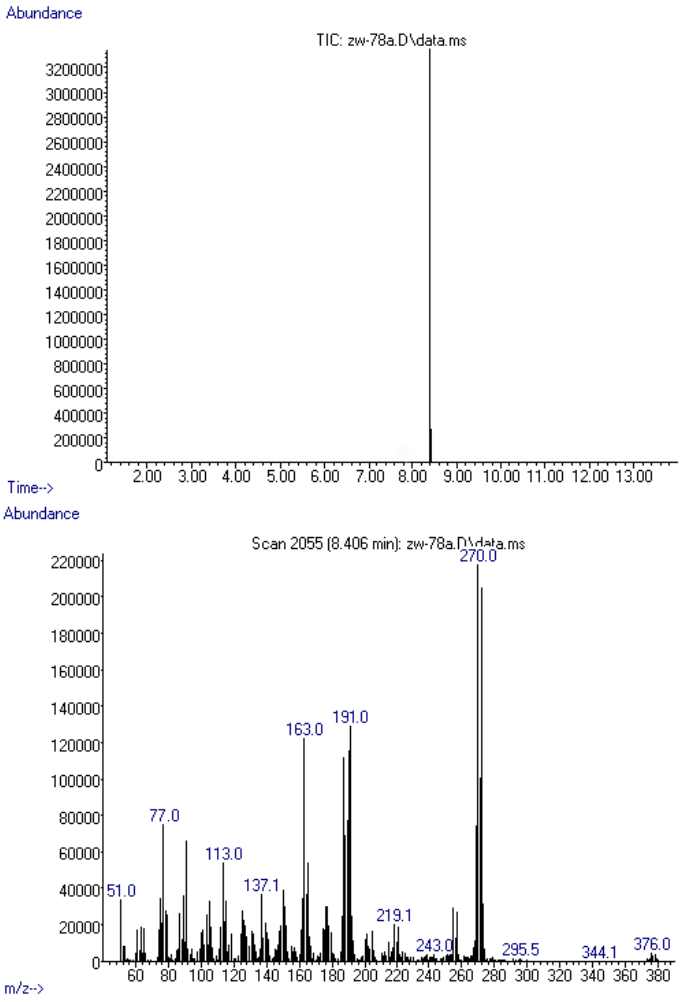

Figure 6-34. GC-MS total ion chromatogram^{TIC} and MS $(EI)_{m/z}$ of ***m*-BrTAB**.

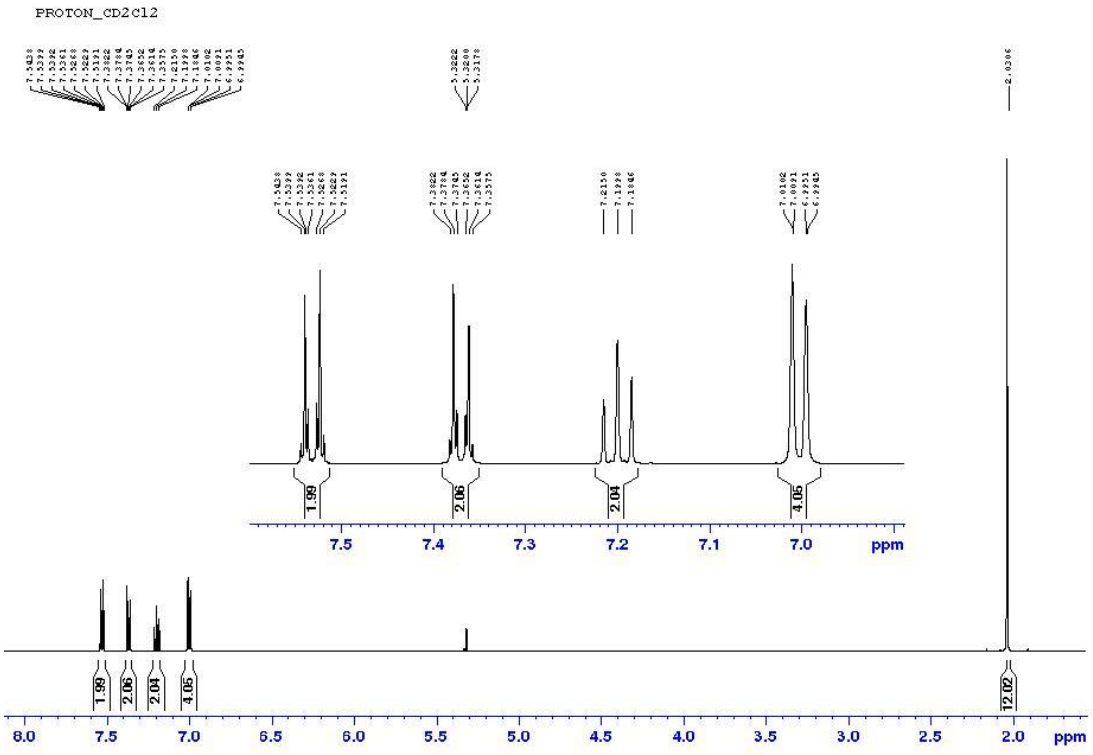

Figure 6-35. ^{1}H NMR spectrum (500 MHz, CD_2Cl_2) of ***p*-BrTAB**.

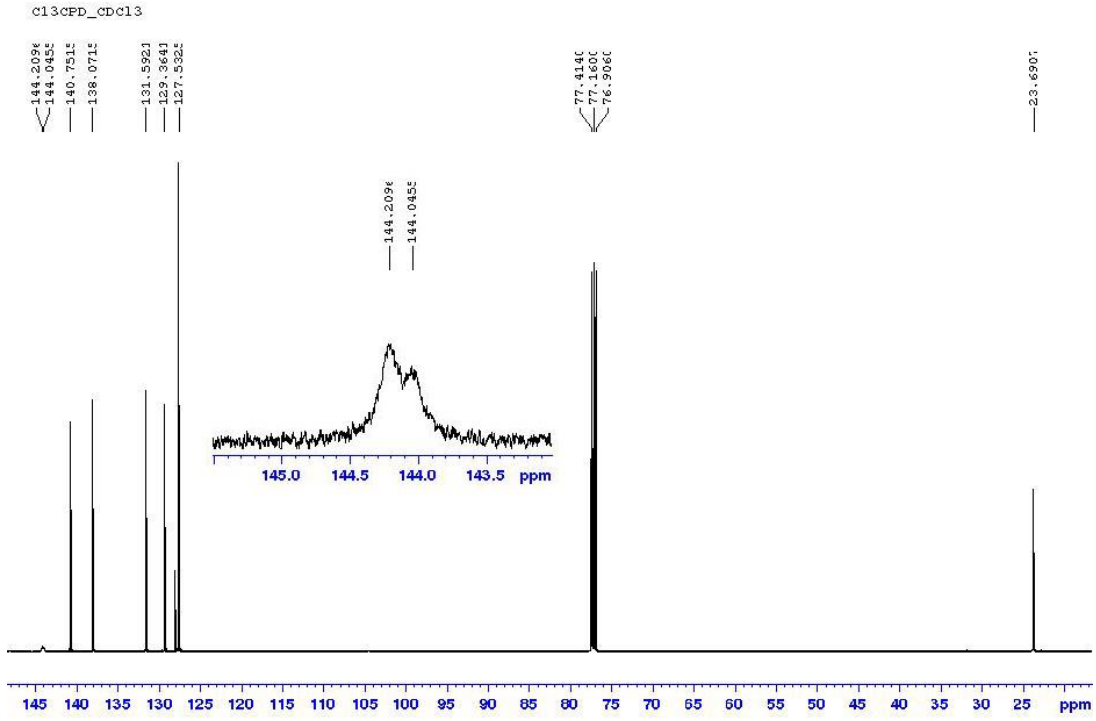

Figure 6-36. $^{13}C\{^{1}H\}$ NMR spectrum (126 MHz, $CDCl_3$) of ***p*-BrTAB**.

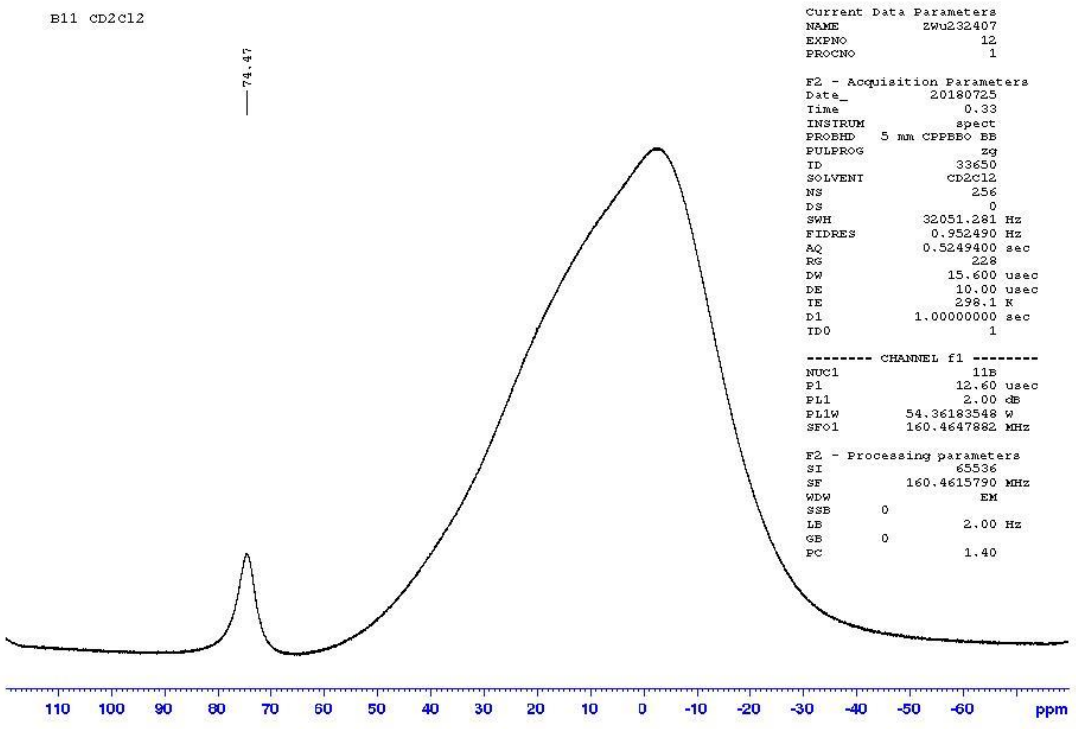

Figure 6-37. ^{11}B NMR spectrum (160 MHz, CD_2Cl_2) of ***p*-BrTAB**.

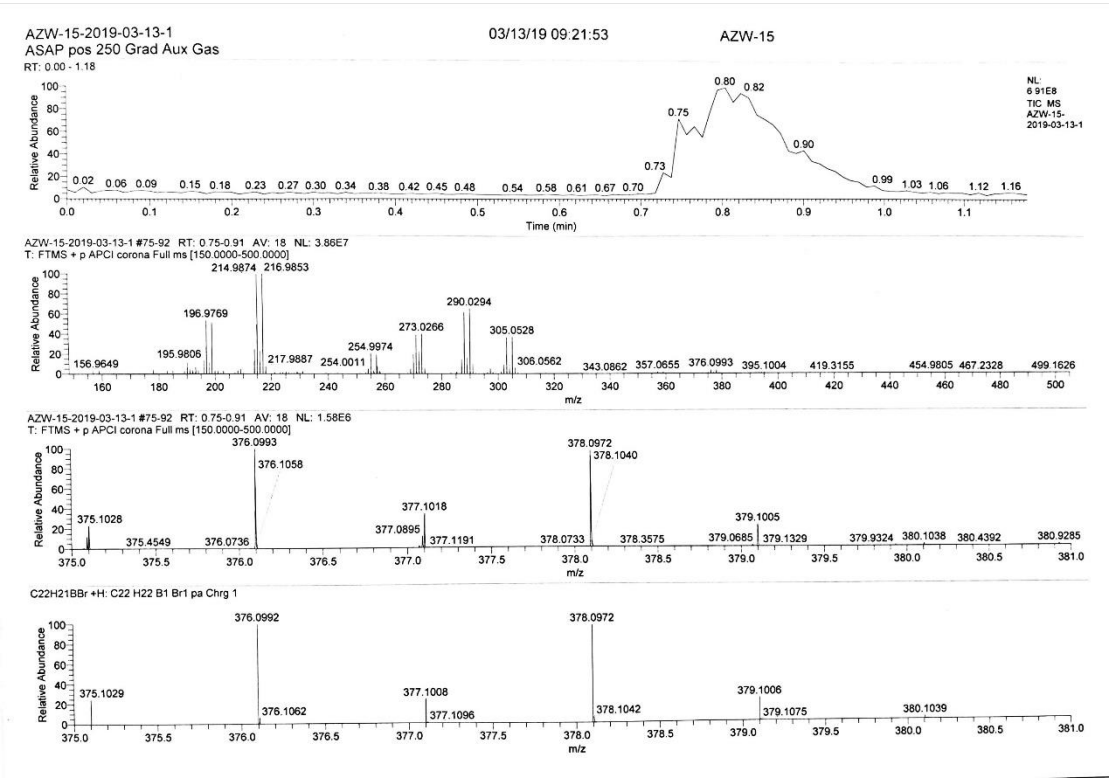

Figure 6-38. HR-ESI-MS spectrum of ***p*-BrTAB**.

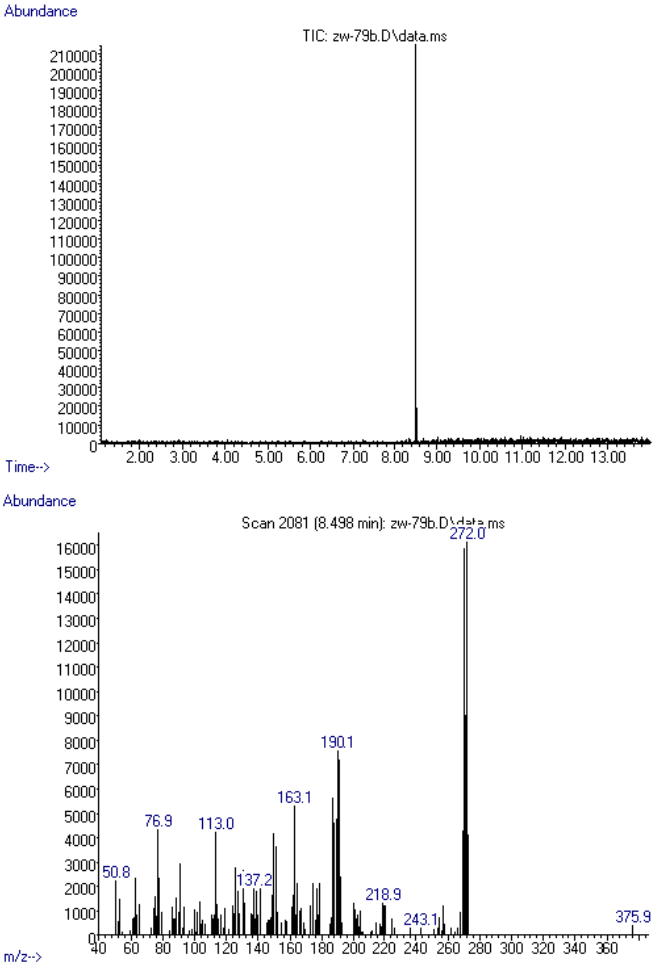

Figure 6-39. GC-MS total ion chromatogram^{TIC} and MS $(EI)_{m/z}$ of ***p*-BrTAB**.

8.1.3 Chapter 4

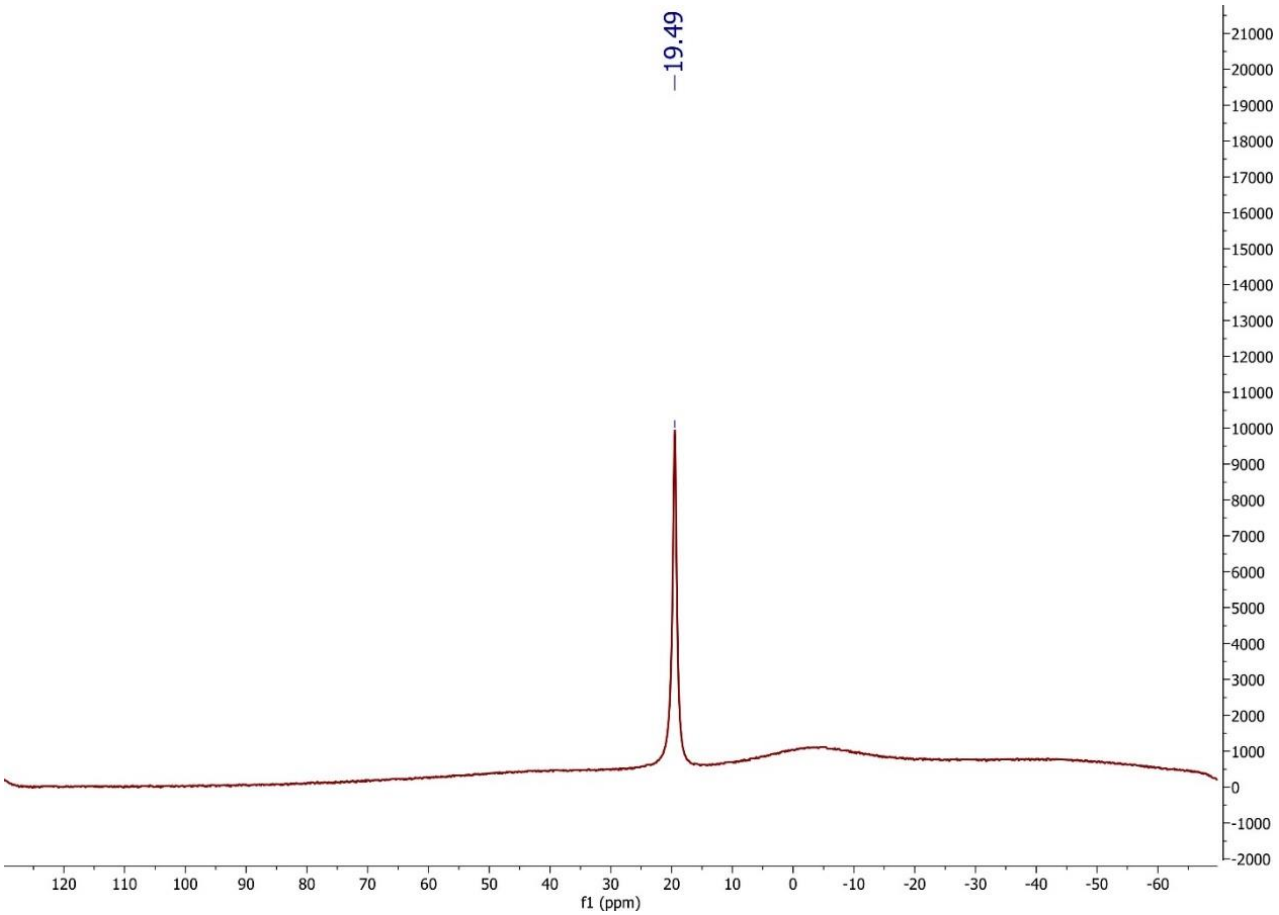

Figure 6-40. ^{11}B NMR spectrum of synthesized $B(OH)_3$ in D_2O (96 MHz).

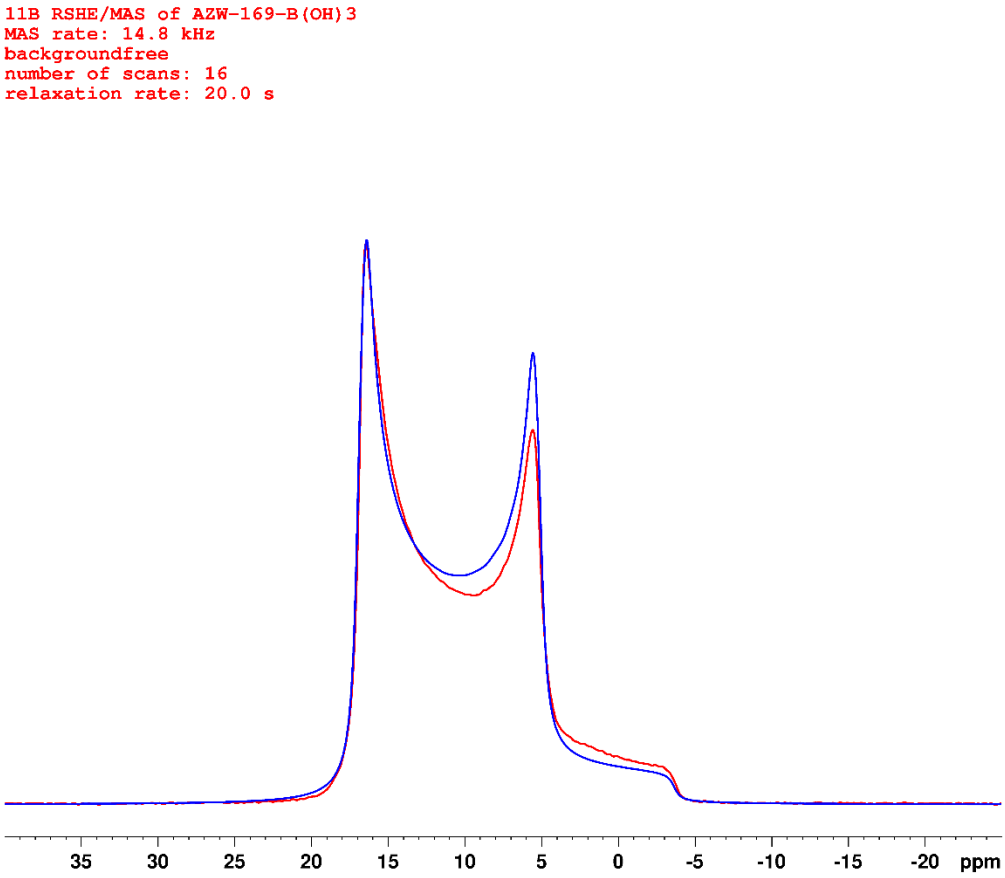

Figure 6-41. ^{11}B solid NMR spectrum (blue = fit; red = measured spectrum) of synthesized $B(OH)_3$ (MAS: 14.8 KHz).

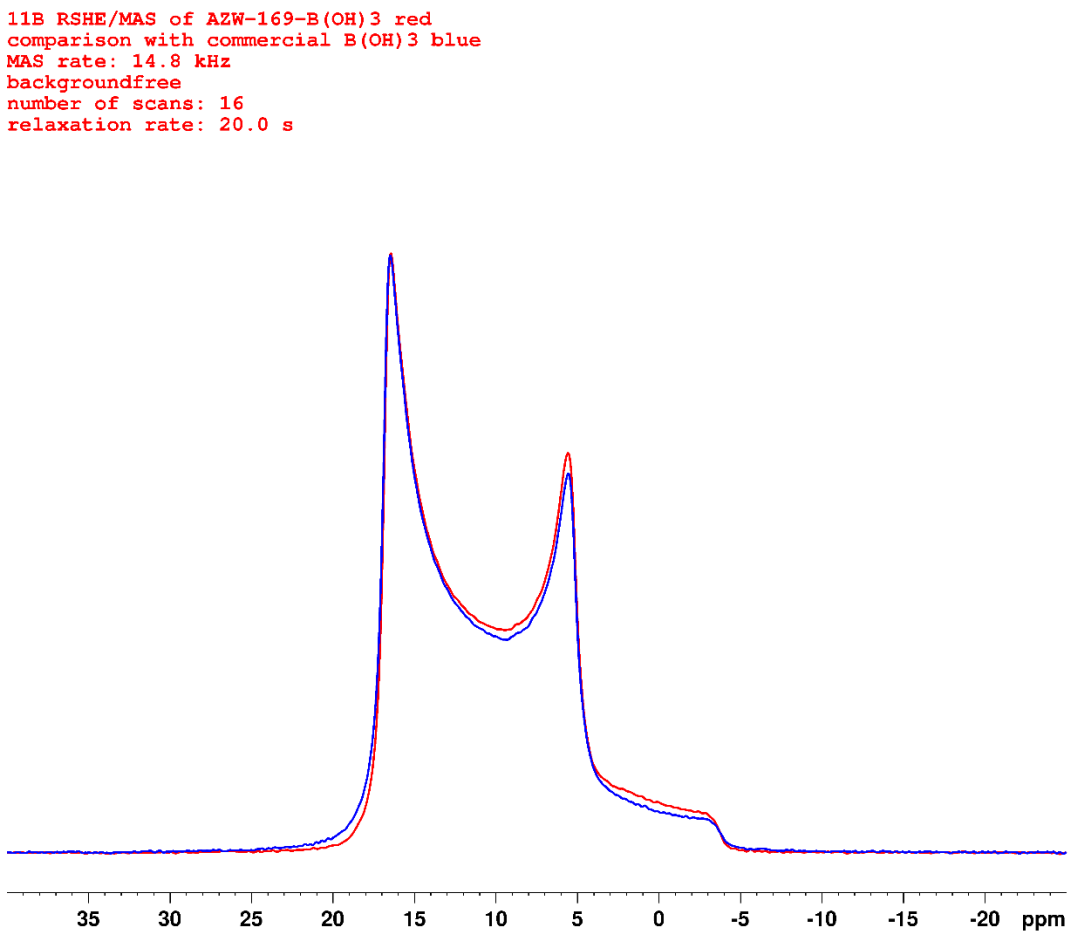

Figure 6-42. ^{11}B solid state NMR spectrum (blue = commercial $B(OH)_3$; red = synthesized $B(OH)_3$) of (MAS: 14.8 KHz).

PERMISSION OF WILEY-VCH

Persistent Room-Temperature Phosphorescence from Purely Organic Molecules and Multi-Component Systems

PERMISSION OF WILEY-VCH

Persistent Room Temperature Phosphorescence from Triarylboranes: A Combined Experimental and Theoretical Study

PERMISSION OF WILEY-VCH

Pure Boric Acid Does Not Show Room Temperature Phosphorescence (RTP)

AFFIDAVIT

I hereby confirm that my thesis entitled "*Room Temperature Phosphorescence (RTP): Experimental and Theoretical Study on Boron-Containing Materials*" is the result of my own work. I did not receive any help or support from commercial consultants. All sources and/or materials applied are listed and specified in the thesis. Furthermore, I confirm that this thesis has not yet been submitted as part of another examination process neither in identical nor similar form.

Würzburg, 15.02.2022

EIDESSTAATLICHE ERKLÄRUNG

Hiermit erkläre ich an Eides statt, die Dissertation *"Room Temperature Phosphorescence (RTP): Experimental and Theoretical Study on Boron-Containing Materials"* eigenständig, d.h. insbesondere selbstständig und ohneHilfe eines kommerziellen Promotionsberaters angefertigt und keinen anderen als die von mir angegebenen Quellen und Hilfsmittel verwendet zu haben. Ich erkläre außerdem, dass die Dissertation weder in gleicher noch ähnlicher Form bereits in einem anderen Prüfungsverfahren vorgelegt hat.

Würzburg, 15.02.2022